

INFORMATION TO USERS

This manuscript has been reproduced from the microfilm master. UMI films the text directly from the original or copy submitted. Thus, some thesis and dissertation copies are in typewriter face, while others may be from any type of computer printer.

The quality of this reproduction is dependent upon the quality of the copy submitted. Broken or indistinct print, colored or poor quality illustrations and photographs, print bleedthrough, substandard margins, and improper alignment can adversely affect reproduction.

In the unlikely event that the author did not send UMI a complete manuscript and there are missing pages, these will be noted. Also, if unauthorized copyright material had to be removed, a note will indicate the deletion.

Oversize materials (e.g., maps, drawings, charts) are reproduced by sectioning the original, beginning at the upper left-hand corner and continuing from left to right in equal sections with small overlaps. Each original is also photographed in one exposure and is included in reduced form at the back of the book.

Photographs included in the original manuscript have been reproduced xerographically in this copy. Higher quality 6" x 9" black and white photographic prints are available for any photographs or illustrations appearing in this copy for an additional charge. Contact UMI directly to order.

U·M·I

University Microfilms International
A Bell & Howell Information Company
300 North Zeeb Road, Ann Arbor, MI 48106-1346 USA
313.761-4700 800/521-0600

Order Number 9234369

**Mathematical simulation of gas transport and acid/base
regulation by blood flowing in microvessels**

Huang, Nancy Shu-Hui, Ph.D.

Rice University, 1991

U·M·I
300 N. Zeeb Rd.
Ann Arbor, MI 48106

RICE UNIVERSITY

MATHEMATICAL SIMULATION OF GAS TRANSPORT AND ACID/
BASE REGULATION BY BLOOD FLOWING IN MICROVESSELS

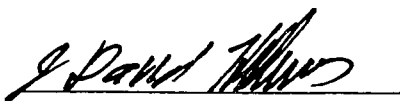
by

NANCY SHU-HUI HUANG

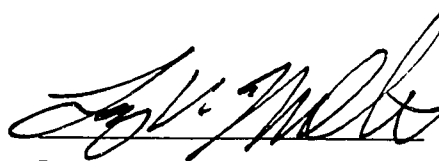
A THESIS SUBMITTED
IN PARTIAL FULFILLMENT OF THE
REQUIREMENTS FOR THE DEGREE

DOCTOR OF PHILOSOPHY

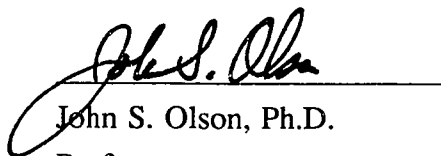
APPROVED, THESIS COMMITTEE:



J. David Hellums, Ph.D.
A. J. Hartsook Professor
Department of Chemical Engineering



Larry V. McIntire, Ph.D.
E. D. Butcher Professor
Department of Chemical Engineering
and Director
Institute of Bioscience and Bioengineering



John S. Olson, Ph.D.
Professor
Department of Biochemistry and Cell Biology

Houston, Texas
November, 1991

ABSTRACT

MATHEMATICAL SIMULATION OF GAS TRANSPORT AND ACID/ BASE REGULATION BY BLOOD FLOWING IN MICROVESSELS

by

Nancy Shu-Hui Huang

A simple model has been developed for simulation of oxygen (O_2) transport by red blood cells (RBCs) to and from blood flowing in vessels with diameters of 20 microns and larger where a substantial fraction of the microcirculatory O_2 transport occurs. This model is derived from a more complete model which has been validated experimentally. Detailed calculations of the oxygen concentration distribution reveal that the dominant resistance to O_2 transport is distributed in the plasma and that relatively little resistance is present within or in the immediate vicinity of the RBCs. Based on these findings, the complete model is simplified from four simultaneous nonlinear partial differential equations (PDEs) to one PDE by: (1) assuming chemical equilibrium within the RBCs, (2) neglecting intracellular and extracellular boundary layer resistances, and (3) incorporating transport in the RBC-free plasma region adjacent to the vessel wall into the boundary condition. The simplified model is much easier to apply mathematically to new situations. A comparison between the two models shows that they give similar predictions which agree well with experimental measurements.

In order to investigate the coupling between the oxygen and carbon dioxide (CO_2) transport, an extended model is developed to incorporate CO_2 , as well as the

various blood buffer systems that are closely connected to the transport of these gases. The blood is treated as two continuous coexisting phases: a RBC phase and a plasma phase. The microvessel is divided into two regions: the central, RBC-rich and the outer, cell-free region. The radial distribution of RBCs, and transport of various species due to bulk convection are taken into account. Chemical and transport processes which are included in the model are (1) interactions of hemoglobin with O_2 and CO_2 , (2) the Bohr and Haldane effects, (3) CO_2 hydration/dehydration reactions, (4) buffering actions of hemoglobin and plasma proteins, and (5) anion exchange across the RBC membrane. Predictions of the discrete model of simultaneous O_2/CO_2 transport by flowing blood are shown to be in excellent agreement with prior workers' experimental results from large artificial membrane tubes. A previous mathematical model which treats blood as a homogeneous continuum and uses a local chemical equilibrium approximation to describe the gas transport is shown to satisfactorily predict the amount of O_2 transport for blood oxygenation accompanied by CO_2 elimination cases, but significantly underpredict O_2 transfer for blood deoxygenation accompanied by CO_2 uptake cases. Furthermore, this previous model disagrees substantially with the CO_2 transport results under both oxygenation and deoxygenation conditions.

To my parents Yueh-Shing and Tong-Thy Huang

ACKNOWLEDGEMENTS

I would like to express my sincere appreciation to the following persons for their help and support in the completion of this research project and in the writing of this thesis:

Dr. J. David Hellums for serving as my thesis advisor, for his insight and guidance in directing this research, for his support and encouragement, and for many helpful discussions and suggestions.

Dr. Larry V. McIntire for serving as a member of my thesis committee, and for his helpful professional advices.

Dr. John S. Olson for serving as a member of my thesis committee, and for many stimulating discussions.

Dr. Colin B. McKay for his constructive discussions on the experimental aspect of this investigation.

Dr. Douglas D. Lemon for many helpful discussions, valuable suggestions, and use of his experimental data.

The faculty of the Chemical Engineering Department for contributing to my education and intellectual development.

All the special friends in the Institute of Biosciences and Bioengineering and the Department of Chemical Engineering for their friendship and moral support.

Ms. Marcella Estrella and Ms. Nancy Turner for their technical assistance.

My parents, Yueh-Shing and Tong-Thy Huang, for many years of sacrifice and encouragement.

This project was supported financially by the Texas Advanced Technology Program Grant 4073, the Robert A. Welch Foundation Grant C-612, and NIH Grants GM 35649 and HL 19824.

TABLE OF CONTENTS

Abstract.....	ii
Acknowledgements	v
Table of Contents.....	vi
List of Tables	xi
List of Figures	xv
Nomenclature	xxvii
Chapter 1 Introduction.....	1
Chapter 2 Physical Situation of Gas Transport and Blood Rheology	9
2.1 General Description of Blood-Gas Interaction	9
2.1.1 Carriage of Oxygen in Blood	12
2.1.1.a Oxygen Hemoglobin Equilibrium.....	14
2.1.1.b Equations for Standard Oxyhemoglobin	
Dissociation Curve	17
2.1.1.c Equations for Nonstandard Oxyhemoglobin	
Dissociation Curve	19
2.1.2 Carriage of Carbon Dioxide in Blood.....	25
2.1.2.a Bicarbonate System.....	27
2.1.2.b Carbamino Carriage	33
2.1.2.c Anion Transporter.....	37
2.1.2.d Buffers in Blood.....	40
2.2 Fluid Mechanics of Blood Flowing in Tubes and Enhancement of	
Gas Transport Due to Migrations of RBCs	45
2.2.1 Distribution of Cells and Velocity Profiles	
of Flowing Blood	45

2.2.1.a Hematocrit Profile.....	47
2.2.1.b Velocity Profiles	48
2.2.2 Shear-induced Augmentation of Gas Transport in Blood	49
Chapter 3 Review of Coupled Oxygen and Carbon Dioxide Transport Models	54
3.1 Exchange between Red Blood Cells and Plasma alone and Transport of Gas to and from Blood Flowing in Capillaries.....	55
3.2 Mutual Transfer of Oxygen and Carbon Dioxide to and from Blood in Artificial Membrane Tubes	62
Chapter 4 Oxygen Transport Models.....	78
4.1 Mathematical Models.....	79
4.1.1 Discrete Models.....	79
4.1.1.a Recap of Nair <i>et al.</i> 's Discrete Model.....	80
4.1.1.b Simplified Discrete Model (Simplified DM)	82
4.1.2 Continuum Models.....	85
4.1.2.a Continuum Model (Oxyhemoglobin Augmentation).....	85
4.1.2.b Continuum Model (Local Chemical Equilibrium).....	86
4.2 Numerical Analysis.....	87
4.2.1 Oxygen-Hemoglobin Equilibrium Relationship	87
4.2.2 Parameter Values and Solutions of Transport Equations	88
4.2.3 Processing of Simulation Results for Comparison of Model Predictions with Experimental Measurements	91
4.2.3.a Diller <i>et al.</i> and Schmukler and Chien	91
4.2.3.b Boland <i>et al.</i>	94
4.3 Results and Discussion.....	94
4.3.1 Simplified Discrete Model versus Nair <i>et al.</i> 's Model	94

4.3.2 Comparison with Diller <i>et al.</i> 's Membrane Oxygenator Data (300 μm , 630 μm and 1000 μm in diameters).....	95
4.3.2.a Uptake Experiments with Saturated Blood.....	100
4.3.2.b Uptake Experiments with Unsaturated Blood	103
4.3.2.c Analysis of Enhanced Transfer.....	114
4.3.3 Comparison with Schmukler and Chien's Membrane Deoxygenator Data (100 μm in diameter)	117
4.3.4 Comparison with Boland <i>et al.</i> 's Artificial Membrane Tube Data (27 μm in diameter)	124
4.4 Summary.....	137
Chapter 5 The Anion Transporter.....	139
5.1 Mathematical Analysis of The Anion Transporter.....	140
5.1.1 Established Conditions on The Anion Transporter.....	140
5.1.2 Previous Approaches	143
5.1.2.a Constant Field Electrodifussion Approach	143
5.1.2.b Michaelis-Menten Kinetic Approach.....	146
5.1.3 Simplified Ping-pong Mechanism.....	148
5.2 Experimental Validation of Flux Expression	157
5.2.1 Methods of Measurement of $\text{Cl}^-/\text{HCO}_3^-$ Exchange	157
5.2.1.a pH Changes and Jacobs-Stewart Cycle	158
5.2.1.b Uncatalyzed Hydration/Dehydration of CO_2	159
5.2.2 Description of Experimental Systems and Development of Analysis.....	162
5.2.2.a Klocke's Experimental System.....	162
5.2.2.b Weith's Experimental System.....	164
5.2.2.c Illsley and Verkman's Experimental System.....	166

5.2.2.d Lemon's Experimental System.....	168
5.2.3 Solution Methods.....	172
5.3 Results and Discussion.....	173
5.3.1 Comparison of the Simulation Results with the Experimental Data.....	173
5.3.1.a Comparison with Klocke's Data	173
5.3.1.b Comparison with Weith's Data.....	176
5.3.1.c Comparison with Illsley and Verkman's Data	180
5.3.1.d Comparison with Lemon's Data	183
5.3.2 Comparison of the Determined Kinetic Parameters to Previous Determinations.....	192
5.4 Summary.....	195
Chapter 6 A Theoretical Model for Gas Transport and Acid/Base Regulation by Blood Flowing in Microvessels	197
6.1 Development of Mathematical Model.....	199
6.1.1 Physical Situation	199
6.1.2 Transport Equations.....	203
6.1.3 Simplification of Transport Equations	209
6.1.3.a Type I Model (10 PDEs)	209
6.1.3.b Type II Model (7 PDEs)	217
6.1.4 Dimensionless Equations and Conditions	218
6.1.5 Parameter Values	224
6.1.5.a Geometrical Parameters	224
6.1.5.b Physical Parameters	227
6.1.5.c Equilibrium and Kinetic Parameters	239
6.1.5.d Hydrodynamic Parameters.....	241

6.1.5.e System Parameters.....	243
6.1.6 Numerical Method and Processing of Simulation Results for Comparison of Model Predictions with Experimental Measurements.....	247
6.2 Results and Discussion.....	250
6.2.1 Comparison with Voorhees' Membrane Oxygenator Data	250
6.2.2 Analysis of the Effects of Several Important Determinants on O ₂ /CO ₂ Exchange in Microvessels	282
6.2.2.a Effects of the Bohr and Haldane Phenomena.....	283
6.2.2.b Effects of Extracellular Carbonic Anhydrase Activity and Buffering Capacity	294
6.2.2.c Effects of Red Blood Cell HCO ₃ ⁻ /Cl ⁻ Exchange Kinetics.....	302
6.2.2.d Effects of Hematocrit on Gas Transfer.....	310
6.3 Summary.....	321
Chapter 7 Future Directions	326
References.....	330
Appendix A Validation of Space Average Oxygen Saturation Calculation Involved in Simulation of Boland <i>et al.</i> 's System.....	351
Appendix B Estimation of the Extracellular Mass Transfer Coefficient of CO ₂ in A Stopped-flow Rapid-mixing Apparatus.....	358
Appendix C Dedimensionalization of Type I Discrete Model Which Consists of Equations (6.1.1) - (6.1.10).....	363

LIST OF TABLES

Table 2.1	Models describing the oxygen-hemoglobin equilibrium curve	18
Table 2.2	Reaction rate equilibrium constants for hydration/dehydration reactions in aqueous media.....	32
Table 4.1	Parameters used in the oxygen transport calculations	89
Table 4.2	Summary of oxygen transfer models which are considered in Chapter 4	90
Table 4.3a	Experimental conditions for the saturated blood experiments (runs S1 - S4) conducted by Diller.....	101
Table 4.3b	Experimental conditions for the unsaturated blood experiments (runs U1 - U6, US1 and US2) conducted by Diller	101
Table 4.4	Values of local and overall operating slopes of ODC and average shear rate for the unsaturated blood experiments conducted by Diller	109
Table 4.5	Comparison of Diller's oxygen transfer data to the simulation results generated by simplified DM using three different values of $D_{O_2,eff}$	115
Table 4.6	Comparison of Diller's oxygen transfer data to the simulation results generated by CMequ using three different values of $D_{O_2,eff}$	116
Table 4.7	Comparison of Chien and Schmukler's oxygen transfer data to the simulation results generated by both simplified DM and CMequ using three different values of $D_{O_2,eff}$	123
Table 4.8	Comparison of Boland <i>et al.</i> 's oxygen transfer data to the simulation results generated by simplified DM using three different values of $D_{O_2,eff}$	136
Table 5.1	Permeabilities of HCO_3^- and Cl^- for anion exchanges in RBCs calculated based Goldman's solution for the electrodiffusion of ions.....	145

Table 5.2 Rates (observed v_{\max} and extrapolated v_{\max}) and concentration of Cl^- and HCO_3^- giving half maximum rates (K_M) of anion exchanges in human red blood cells or red cell ghosts at 37 °C.....	148
Table 5.3 Apparatuses, detection methods and experimental conditions in $\text{Cl}^-/\text{HCO}_3^-$ exchange experiments used by various investigators.....	161
Table 5.4 Parameter values and objective function used in analysis of Klocke's data	164
Table 5.5 Parameter values and objective function used in analysis of Weith's data.....	166
Table 5.6 Parameter values and objective function used in analysis of Illsley and Verkman's data	167
Table 5.7 Parameter values and objective function used in analysis of Lemon's data.....	170
Table 5.8 Kinetic parameters obtained for $\text{Cl}^-/\text{HCO}_3^-$ exchange across the RBC membrane from analyzing different workers' experimental data using Equation (5.11).....	193
Table 5.9 Best-fitted permeability coefficients obtained for $\text{Cl}^-/\text{HCO}_3^-$ exchange across the RBC membrane from analyzing different workers' experimental data using Equation (5.1)	194
Table 6.1 Partial differential equations describing the coupled O_2 and CO_2 transport and pH regulation by blood flowing in microvessels.....	214
Table 6.2 Values of parameters used in the numerical computations for the discrete O_2 and CO_2 transport model	224
Table 6.3 Solubility coefficients for O_2 in water (and/or saline), plasma and hemoglobin solution with equivalent heme concentration as that in RBC	228

Table 6.4 Solubility coefficients for CO ₂ in water (and/or saline), plasma and hemoglobin solution with equivalent heme concentration as that in RBC	229
Table 6.5 The diffusivity of O ₂ in water, plasma and concentrated hemoglobin solution.....	230
Table 6.6 The diffusivity of CO ₂ in water and plasma	231
Table 6.7 Comparison of $D_{O_2,pl}/D_{O_2,H_2O}$ and $D_{CO_2,pl}/D_{CO_2,H_2O}$ for different plasma protein concentrations at T=25 °C	231
Table 6.8 Estimation of $\tilde{D}_{H,pl}$, $\tilde{D}_{HCO_3,pl}$ and $\tilde{D}_{Cl,pl}$ at 25 °C	240
Table 6.9 Estimation of $\tilde{D}_{H,pl}$, $\tilde{D}_{HCO_3,pl}$ and $\tilde{D}_{Cl,pl}$ at 37 °C	240
Table 6.10 Values of parameters used in the numerical computations for the continuum O ₂ and CO ₂ transport model.....	248
Table 6.11 Description of the two types of artificial membrane tubes considered and values of the system parameters used in computations	283
Table 6.12 Influence of the Bohr effect on O ₂ transfer for both oxygenation and deoxygenation cases in artificial membrane tubes	284
Table 6.13 Influence of the Haldane effect on CO ₂ transfer for both oxygenation and deoxygenation cases in artificial membrane tubes	294
Table 6.14 Effect of extracellular catalysis of CO ₂ hydration/dehydration reactions (\hat{A}_{pl}) and extracellular buffering capacity (β_{pl}) on CO ₂ transfer for both oxygenation (accompanied by CO ₂ elimination) and deoxygenation (accompanied by CO ₂ uptake) cases in artificial membrane tubes.....	300
Table 6.15 Effect of extracellular catalysis of CO ₂ hydration/dehydration reactions (\hat{A}_{pl}) and extracellular buffering capacity (β_{pl}) on plasma pH changes for both oxygenation (accompanied by CO ₂ elimination) and deoxygenation (accompanied by CO ₂ uptake) cases in artificial membrane tubes.....	301

Table 6.16 Effect of anion exchange on CO ₂ transfer for both oxygenation (accompanied by CO ₂ elimination) and deoxygenation (accompanied by CO ₂ uptake) cases in artificial membrane tubes.....	307
Table 6.17 Effect of anion exchange on both intra- and extracellular pH changes for both oxygenation (accompanied by CO ₂ elimination) and deoxygenation (accompanied by CO ₂ uptake) cases in artificial membrane tubes.....	308
Table 6.18 Effect of discharge hematocrit (H _D) on O ₂ and CO ₂ transfer for both oxygenation (accompanied by CO ₂ elimination) and deoxygenation (accompanied by CO ₂ uptake) cases in artificial membrane tubes.....	320

LIST OF FIGURES

Figure 2.1 Exchange of oxygen and carbon dioxide in a pulmonary capillary	11
Figure 2.2 The quaternary structure of hemoglobin (copied directly from Lehninger (1975)).....	13
Figure 2.3 Carbon dioxide dissociation curve of human blood at 37 °C plotted on a linear (A) and logarithmic (B) axes.....	26
Figure 2.4 RBC and plasma velocity profiles and hematocrit profile of RBC suspensions flowing in microvessels	46
Figure 4.1 Comparison of models for O ₂ release from RBC suspensions with a H _D of 30% and P ₅₀ of 27 mmHg flowing at 12 µl/hr in a 27-µm-diameter membrane tube at 37 °C.....	96
Figure 4.2 Comparison of models for O ₂ uptake by RBC suspensions with a H _D of 30% and P ₅₀ of 27 mmHg flowing at 12 µl/hr in a 27-µm-diameter membrane tube at 37 °C.....	97
Figure 4.3 Comparison of models for O ₂ release from RBC suspensions with a H _D of 20% and P ₅₀ of 27 mmHg flowing at 12 µl/hr in a 27-µm-diameter membrane tube at 37 °C.....	98
Figure 4.4 Comparison of models for O ₂ uptake by RBC suspensions with a H _D of 20% and P ₅₀ of 20 mmHg flowing at 23 µl/hr in a 27-µm-diameter membrane tube at 37 °C.....	99
Figure 4.5 Comparison of models for oxygen uptake results for fully saturated fresh human blood flowing in silicone-rubber membrane tubes at 37 °C.....	102
Figure 4.6 Comparison of models for oxygen uptake by fresh human blood with a H _D of 44% and P ₅₀ of 28 mmHg flowing at 0.376 ml/min in a 305-µm- diameter silicone-rubber membrane tube at 37 °C	104

Figure 4.7 Comparison of models for oxygen uptake by fresh human blood with a H_D of 42% and P_{50} of 28 mmHg flowing at 0.376 ml/min in a 635- μ m-diameter silicone-rubber membrane tube at 37 °C	105
Figure 4.8 Comparison of models for oxygen uptake by fresh human blood with a H_D of 42% and P_{50} of 27 mmHg flowing at 0.329 ml/min in a 635- μ m-diameter silicone-rubber membrane tube at 37 °C	106
Figure 4.9 Comparison of models for oxygen uptake by fresh human blood with a H_D of 45% and P_{50} of 27 mmHg flowing at 0.329 ml/min in a 635- μ m-diameter silicone-rubber membrane tube at 37 °C	107
Figure 4.10 Comparison of models for oxygen uptake by fresh human blood with a H_D of 42% and P_{50} of 28 mmHg flowing at 0.329 ml/min in a 635- μ m-diameter silicone-rubber membrane tube at 37 °C	108
Figure 4.11 Comparison of oxygen uptake result by blood with a H_D of 40% and P_{50} of 28.5 mmHg flowing at 0.376 ml/min in a 305- μ m-diameter silicone-rubber membrane tube at 37 °C to the simulation result generated by CMequ using three different values of $D_{O_2,eff}$	111
Figure 4.12 Comparison of oxygen uptake result by blood with a H_D of 42% and P_{50} of 26.5 mmHg flowing at 3.29 ml/min in a 635- μ m-diameter silicone-rubber membrane tube at 37 °C to the simulation result generated by CMequ using three different values of $D_{O_2,eff}$	112
Figure 4.13 Comparison of oxygen uptake result by blood with a H_D of 40% and P_{50} of 28.5 mmHg flowing at 0.376 ml/min in a 305- μ m-diameter silicone-rubber membrane tube at 37 °C to the simulation result generated by both simplified DM and CMequ using two different values of $D_{O_2,eff}$	113

Figure 4.14 Comparison of models for oxygen release from red cell suspensions with H_D of 1.5, 5 and 10% and P_{50} of 27 mmHg flowing in microporous polypropylene fibers with diameters of 100 μm at 37 $^{\circ}\text{C}$	119
Figure 4.15 Comparison of oxygen release from red cell suspensions with a H_D of 10% and P_{50} of 27 mmHg flowing in microporous polypropylene fibers with diameters of 100 μm at 37 $^{\circ}\text{C}$ to the simulation result generated by CMequ using three different values of $D_{O_2, \text{eff}}$	120
Figure 4.16 Comparison of oxygen release from red cell suspensions with a H_D of 5% and P_{50} of 27 mmHg flowing in microporous polypropylene fibers with diameters of 100 μm at 37 $^{\circ}\text{C}$ to the simulation result generated by CMequ using different values of $D_{O_2, \text{eff}}$	121
Figure 4.17 Comparison of oxygen release from red cell suspensions with a H_D of 1.5% and P_{50} of 27 mmHg flowing in microporous polypropylene fibers with diameters of 100 μm at 37 $^{\circ}\text{C}$ to the simulation result generated by CMequ using different values of $D_{O_2, \text{eff}}$	122
Figure 4.18 Comparison of models for oxygen release from RBC suspensions with a H_D of 30% and P_{50} of 27 mmHg flowing at 12 $\mu\text{l/hr}$ in a 27 μm -diameter-membrane tube at 37 $^{\circ}\text{C}$	125
Figure 4.19 Comparison of models for oxygen uptake by RBC suspensions with a H_D of 30% and P_{50} of 27 mmHg flowing at 12 $\mu\text{l/hr}$ in a 27 μm -diameter-membrane tube at 37 $^{\circ}\text{C}$	126
Figure 4.20 Comparison of models for oxygen release from RBC suspensions with a H_D of 20% and P_{50} of 27 mmHg flowing at 12 $\mu\text{l/hr}$ in a 27 μm -diameter-membrane tube at 37 $^{\circ}\text{C}$	127

Figure 4.21 Comparison of models for oxygen uptake by RBC suspensions with a H_D of 20% and P_{50} of 20 mmHg flowing at 23 $\mu\text{l/hr}$ in a 27 μm -diameter-membrane tube at 37 $^{\circ}\text{C}$	128
Figure 4.22 Comparison of the internal profiles of oxyhemoglobin saturation as function of axial distance and dimensionless radial position for an oxygen release case which are generated by simplified DM, CMequ and CMaug.....	130
Figure 4.23 Comparison of the internal profiles of oxyhemoglobin saturation as function of axial distance and dimensionless radial position for an oxygen uptake case which are generated by simplified DM, CMequ and CMaug.....	131
Figure 4.24 Comparison of oxygen release from RBC suspensions with a H_D of 30% and P_{50} of 27 mmHg flowing at 12 $\mu\text{l/hr}$ in a 27- μm -diameter membrane tube at 37 $^{\circ}\text{C}$ to the simulation result generated by simplified DM using three different values of $D_{O_2, \text{eff}}$	132
Figure 4.25 Comparison of oxygen uptake by RBC suspensions with a H_D of 30% and P_{50} of 27 mmHg flowing at 12 $\mu\text{l/hr}$ in a 27- μm -diameter membrane tube at 37 $^{\circ}\text{C}$ to the simulation result generated by simplified DM using three different values of $D_{O_2, \text{eff}}$	133
Figure 4.26 Comparison of oxygen release from RBC suspensions with a H_D of 20% and P_{50} of 27 mmHg flowing at 12 $\mu\text{l/hr}$ in a 27- μm -diameter membrane tube at 37 $^{\circ}\text{C}$ to the simulation result generated by simplified DM using three different values of $D_{O_2, \text{eff}}$	134
Figure 4.27 Comparison of oxygen uptake by RBC suspensions with a H_D of 20% and P_{50} of 20 mmHg flowing at 23 $\mu\text{l/hr}$ in a 27- μm -diameter membrane tube at 37 $^{\circ}\text{C}$ to the simulation result generated by simplified DM using three different values of $D_{O_2, \text{eff}}$	135

Figure 5.1 Diagram of the ping-pong mechanism for anion transport (exchange of an intracellular Cl^- for an extracellular HCO_3^-).....	141
Figure 5.2 Description of the catalytic cycle of anion exchange according to the ping-pong scheme.....	149
Figure 5.3 Transport cycle of the anion transporter: $^{35}\text{Cl}^-$ and $^{37}\text{Cl}^-$ NMR data specifies that at both low and physiological temperatures the translocation step is the rate limiting step.....	153
Figure 5.4 Operation of the Jacobs-Stewart cycle and rapid acidification of the extracellular medium by $\text{Cl}^-/\text{HCO}_3^-$ exchange after addition of packed RBCs to a Cl^- -free media which contains carbonic anhydrase enzyme.....	158
Figure 5.5 Operation of the $\text{Cl}^-/\text{HCO}_3^-$ exchange after intracellular carbonic anhydrase activity is blocked so that simultaneous movement of CO_2 is eliminated.....	160
Figure 5.6 Comparison of models for simulating the change in extracellular Cl^- concentration following mixture of Cl^- -loaded RBCs with HCO_3^- -containing buffer at 37 °C	174
Figure 5.7 Comparison of models for simulating the change in extracellular HCO_3^- concentration following mixture of HCO_3^- -loaded RBCs with Cl^- -containing buffer at 37 °C	175
Figure 5.8 Comparison of change in HCO_3^- concentration inside and outside RBC ghosts as a consequence of $\text{Cl}^-/\text{HCO}_3^-$ countertransport at 0 °C to the simulation result generated by the simplified ping-pong model.....	178
Figure 5.9 Comparison of change in HCO_3^- concentration inside and outside RBC ghosts as a consequence of $\text{Cl}^-/\text{HCO}_3^-$ countertransport at 0 °C to the simulation result generated by the electrodiffusion approach	179

Figure 5.10 Comparison of models for simulating the change in intracellular Cl^- concentration following mixture of Cl^- -loaded RBCs with a Cl^- -free, HCO_3^- -containing buffer at 37 °C	181
Figure 5.11 Comparison of models for simulating the change in intracellular Cl^- concentration following mixture of Cl^- -loaded RBCs with a Cl^- -free, SO_4^{2-} -containing buffer at 37 °C	182
Figure 5.12 Comparison of models for kinetics of $\text{Cl}^-/\text{HCO}_3^-$ exchange at 25 °C (the experimental conditions are given in Table 5.7, case I.1).....	184
Figure 5.13 Comparison of models for kinetics of $\text{Cl}^-/\text{HCO}_3^-$ exchange at 25 °C (the experimental conditions are given in Table 5.7, case I.2).....	185
Figure 5.14 Comparison of models for kinetics of $\text{Cl}^-/\text{HCO}_3^-$ exchange at 25 °C (the experimental conditions are given in Table 5.7, case II.1).....	186
Figure 5.15 Comparison of models for kinetics of $\text{Cl}^-/\text{HCO}_3^-$ exchange at 25 °C (the experimental conditions are given in Table 5.7, case II.2).....	187
Figure 5.16 Comparison of models for kinetics of $\text{Cl}^-/\text{HCO}_3^-$ exchange at 25 °C (the experimental conditions are given in Table 5.7, case II.3).....	188
Figure 5.17 Comparison of models for kinetics of $\text{Cl}^-/\text{HCO}_3^-$ exchange at 25 °C (the experimental conditions are given in Table 5.7, case II.4).....	189
Figure 5.18 Comparison of models for kinetics of $\text{Cl}^-/\text{HCO}_3^-$ exchange at 25 °C (the experimental conditions are given in Table 5.7, case II.5).....	190
Figure 5.19 Comparison of models for kinetics of $\text{Cl}^-/\text{HCO}_3^-$ exchange at 25 °C (the experimental conditions are given in Table 5.7, case II.6).....	191
Figure 6.1a Comparison of models for oxygenation accompanied by CO_2 elimination of RBC suspensions flowing in a 1.47-mm-diameter membrane tube at 22 °C with $H_D=0.42$, $P_{50,\text{in}}=10.1$ mmHg, $K_{\text{eq}}=257.9$, $\beta=31.8$ mM H^+/pH , $\text{pH}_{\text{pl},\text{in}}=7.66$, $[\text{O}_2]_{\text{total},\text{in}}=7.08$ mM, $[\text{CO}_2]_{\text{total},\text{in}}=31.1$ mM.....	252

Figure 6.2a Comparison of models for oxygenation accompanied by CO ₂ elimination of RBC suspensions flowing in a 1.47-mm-diameter membrane tube at 22 °C with $H_D=0.46$, $P_{50,in}=13.6$ mmHg, $K_{eq}=105.0$, $\beta=32.6$ mM H ⁺ /pH, $pH_{pl,in}=7.28$, $[O_2]_{total,in}=7.08$ mM, $[CO_2]_{total,in}=32.5$ mM.....	253
Figure 6.3a Comparison of models for oxygenation accompanied by CO ₂ elimination of RBC suspensions flowing in a 1.47-mm-diameter membrane tube at 22 °C with $H_D=0.43$, $P_{50,in}=17.6$ mmHg, $K_{eq}=22.9$, $\beta=27.8$ mM H ⁺ /pH, $pH_{pl,in}=6.98$, $[O_2]_{total,in}=6.63$ mM, $[CO_2]_{total,in}=16.3$ mM.....	254
Figure 6.4a Comparison of models for oxygenation accompanied by CO ₂ elimination of RBC suspensions flowing in a 1.47-mm-diameter membrane tube at 27 °C with $H_D=0.42$, $P_{50,in}=19.4$ mmHg, $K_{eq}=54.2$, $\beta=32.1$ mM H ⁺ /pH, $pH_{pl,in}=7.19$, $[O_2]_{total,in}=6.04$ mM, $[CO_2]_{total,in}=24.4$ mM.....	255
Figure 6.5a Comparison of models for oxygenation accompanied by CO ₂ elimination of RBC suspensions flowing in a 1.47-mm-diameter membrane tube at 24 °C with $H_D=0.57$, $P_{50,in}=15.3$ mmHg, $K_{eq}=58.0$, $\beta=40.2$ mM H ⁺ /pH, $pH_{pl,in}=7.28$, $[O_2]_{total,in}=8.84$ mM, $[CO_2]_{total,in}=27.5$ mM.....	256
Figure 6.6a Comparison of models for oxygenation accompanied by CO ₂ elimination of RBC suspensions flowing in a 1.47-mm-diameter membrane tube at 25 °C with $H_D=0.43$, $P_{50,in}=16.8$ mmHg, $K_{eq}=46.1$, $\beta=32.4$ mM H ⁺ /pH, $pH_{pl,in}=7.23$, $[O_2]_{total,in}=6.56$ mM, $[CO_2]_{total,in}=23.1$ mM.....	257
Figure 6.7a Comparison of models for oxygenation accompanied by CO ₂ elimination of RBC suspensions flowing in a 1.57-mm-diameter membrane tube at 26 °C with $H_D=0.43$, $P_{50,in}=16.7$ mmHg, $K_{eq}=45.7$, $\beta=31.8$ mM H ⁺ /pH, $pH_{pl,in}=7.32$, $[O_2]_{total,in}=6.39$ mM, $[CO_2]_{total,in}=19.2$ mM.....	258
Figure 6.8a Comparison of models for oxygenation accompanied by CO ₂ elimination of RBC suspensions flowing in a 1.57-mm-diameter membrane tube	

at 25 °C with $H_D=0.43$, $P_{50,in}=20.6$ mmHg, $K_{eq}=24.2$, $\beta=31.3$ mM H^+/pH , $pH_{pl,in}=6.99$, $[O_2]_{total,in}=6.57$ mM, $[CO_2]_{total,in}=17.1$ mM.....	259
Figure 6.9a Comparison of models for deoxygenation accompanied by CO_2 uptake of RBC suspensions flowing in a 1.47-mm-diameter membrane tube at 25 °C with $H_D=0.43$, $P_{50,in}=17.6$ mmHg, $K_{eq}=40.3$, $\beta=31.5$ mM H^+/pH , $pH_{pl,in}=7.18$, $[O_2]_{total,in}=6.38$ mM, $[CO_2]_{total,in}=21.3$ mM.....	260
Figure 6.10 Comparison of the $\Delta[CO_2]_{total}$ results calculated by the continuum and discrete (via different values of \hat{A}_{pl}) models for RBC suspensions flowing in a 1.47-mm-diameter membrane tube with H_D of 42% at 25 °C.....	261
Figure 6.1b Mixed mean values of O_2 tension, O_2 saturation, CO_2 tension and intracellular $HbCO_2$ concentration at different axial positions along the membrane oxygenator for an oxygenation case at different flow rates.....	264
Figure 6.1c Mixed mean values of intra- and extracellular pH and intra- and extracellular HCO_3^- concentrations at different axial positions along the membrane oxygenator for an oxygenation case at different flow rates.....	265
Figure 6.2b Mixed mean values of O_2 tension, O_2 saturation, CO_2 tension and intracellular $HbCO_2$ concentration at different axial positions along the membrane oxygenator for an oxygenation case at different flow rates.....	266
Figure 6.2c Mixed mean values of intra- and extracellular pH and intra- and extracellular HCO_3^- concentrations at different axial positions along the membrane oxygenator for an oxygenation case at different flow rates.....	267
Figure 6.3b Mixed mean values of O_2 tension, O_2 saturation, CO_2 tension and intracellular $HbCO_2$ concentration at different axial positions along the membrane oxygenator for an oxygenation case at different flow rates.....	268

Figure 6.3c Mixed mean values of intra- and extracellular pH and intra- and extracellular HCO_3^- concentrations at different axial positions along the membrane oxygenator for an oxygenation case at different flow rates.....	269
Figure 6.4b Mixed mean values of O_2 tension, O_2 saturation, CO_2 tension and intracellular HbCO_2 concentration at different axial positions along the membrane oxygenator for an oxygenation case at different flow rates.....	270
Figure 6.4c Mixed mean values of intra- and extracellular pH and intra- and extracellular HCO_3^- concentrations at different axial positions along the membrane oxygenator for an oxygenation case at different flow rates.....	271
Figure 6.5b Mixed mean values of O_2 tension, O_2 saturation, CO_2 tension and intracellular HbCO_2 concentration at different axial positions along the membrane oxygenator for an oxygenation case at different flow rates.....	272
Figure 6.5c Mixed mean values of intra- and extracellular pH and intra- and extracellular HCO_3^- concentrations at different axial positions along the membrane oxygenator for an oxygenation case at different flow rates.....	273
Figure 6.6b Mixed mean values of O_2 tension, O_2 saturation, CO_2 tension and intracellular HbCO_2 concentration at different axial positions along the membrane oxygenator for an oxygenation case at different flow rates.....	274
Figure 6.6c Mixed mean values of intra- and extracellular pH and intra- and extracellular HCO_3^- concentrations at different axial positions along the membrane oxygenator for an oxygenation case at different flow rates.....	275
Figure 6.7b Mixed mean values of O_2 tension, O_2 saturation, CO_2 tension and intracellular HbCO_2 concentration at different axial positions along the membrane oxygenator for an oxygenation case at different flow rates.....	276

Figure 6.7c Mixed mean values of intra- and extracellular pH and intra- and extracellular HCO_3^- concentrations at different axial positions along the membrane oxygenator for an oxygenation case at different flow rates.....	277
Figure 6.8b Mixed mean values of O_2 tension, O_2 saturation, CO_2 tension and intracellular HbCO_2 concentration at different axial positions along the membrane oxygenator for an oxygenation case at different flow rates.....	278
Figure 6.8c Mixed mean values of intra- and extracellular pH and intra- and extracellular HCO_3^- concentrations at different axial positions along the membrane oxygenator for an oxygenation case at different flow rates.....	279
Figure 6.9b Mixed mean values of O_2 tension, O_2 saturation, CO_2 tension and intracellular HbCO_2 concentration at different axial positions along the membrane oxygenator for a deoxygenation case at different flow rates	280
Figure 6.9c Mixed mean values of intra- and extracellular pH and intra- and extracellular HCO_3^- concentrations at different axial positions along the membrane oxygenator for a deoxygenation case at different flow rates	281
Figure 6.11 Influence of the Bohr effect on rate of O_2 uptake by human whole blood flowing in a 1.47-mm-diameter artificial membrane tube	285
Figure 6.12 Influence of the Bohr effect on rate of O_2 uptake by human whole blood flowing in a 27- μm -diameter artificial membrane tube	286
Figure 6.13 Influence of the Bohr effect on rate of O_2 release from human whole blood flowing in a 1.47-mm-diameter artificial membrane tube	287
Figure 6.14 Influence of the Bohr effect on rate of O_2 release from human whole blood flowing in a 27- μm -diameter artificial membrane tube	288
Figure 6.15 Influence of the Haldane effect on rate of CO_2 elimination from human whole blood flowing in a 1.47-mm-diameter artificial membrane tube	290

Figure 6.16 Influence of the Haldane effect on rate of CO ₂ elimination from human whole blood flowing in a 27- μ m-diameter artificial membrane tube	291
Figure 6.17 Influence of the Haldane effect on rate of CO ₂ uptake by human whole blood flowing in a 1.47-mm-diameter artificial membrane tube	292
Figure 6.18 Influence of the Haldane effect on rate of CO ₂ uptake by human whole blood flowing in a 27- μ m-diameter artificial membrane tube	293
Figure 6.19 Effect of extracellular catalysis of CO ₂ hydration/dehydration reactions on rate of CO ₂ elimination from human whole blood flowing in a 1.47-mm-diameter artificial membrane tube.....	295
Figure 6.20 Effect of extracellular catalysis of CO ₂ hydration/dehydration reactions on rate of CO ₂ elimination from human whole blood flowing in a 27- μ m-diameter artificial membrane tube.....	296
Figure 6.21 Effect of extracellular catalysis of CO ₂ hydration/dehydration reactions on rate of CO ₂ removal by human whole blood flowing in a 1.47-mm-diameter artificial membrane tube	297
Figure 6.22 Effect of extracellular catalysis of CO ₂ hydration/dehydration reactions on rate of CO ₂ removal by human whole blood flowing in a 27- μ m-diameter artificial membrane tube.....	298
Figure 6.23 Effect of RBC HCO ₃ ⁻ /Cl ⁻ exchange on rate of CO ₂ elimination from human whole blood flowing in a 27- μ m-diameter artificial membrane tube.....	303
Figure 6.24 Effect of RBC anion exchange on rate of CO ₂ elimination from human whole blood flowing in a 27- μ m-diameter artificial membrane tube	304
Figure 6.25 Effect of RBC HCO ₃ ⁻ /Cl ⁻ exchange on rate of CO ₂ uptake by human whole blood flowing in a 27- μ m-diameter artificial membrane tube	305
Figure 6.26 Effect of RBC anion exchange on rate of CO ₂ uptake by human whole blood flowing in a 27- μ m-diameter artificial membrane tube	306

Figure 6.27 Effect of discharge hematocrit on rate of O ₂ uptake by human whole blood flowing in a 1.47-mm-diameter artificial membrane tube	311
Figure 6.28 Effect of discharge hematocrit on rate of CO ₂ elimination from human whole blood flowing in a 1.47-mm-diameter artificial membrane tube	312
Figure 6.29 Effect of discharge hematocrit on rate of O ₂ uptake by human whole blood flowing in a 27-μm-diameter artificial membrane tube	313
Figure 6.30 Effect of discharge hematocrit on rate of CO ₂ elimination from human whole blood flowing in a 27-μm-diameter artificial membrane tube	314
Figure 6.31 Effect of discharge hematocrit on rate of O ₂ release from human whole blood flowing in a 1.47-mm-diameter artificial membrane tube	315
Figure 6.32 Effect of discharge hematocrit on rate of CO ₂ uptake by human whole blood flowing in a 1.47-mm-diameter artificial membrane tube	316
Figure 6.33 Effect of discharge hematocrit on rate of O ₂ release from human whole blood flowing in a 27-μm-diameter artificial membrane tube	317
Figure 6.34 Effect of discharge hematocrit on rate of CO ₂ uptake by human whole blood flowing in a 27-μm-diameter artificial membrane tube	318
Figure A.1 Explanation of coordinates	354
Figure A.2 Comparison of O ₂ saturation values computed by two independent methods	357

NOMENCLATURE

Symbol	Explanation
a	particle radius of red cell
a_i	i = integer, equilibrium constant in equations for the ODC models (Table 2.1) under standard conditions ($T=37\text{ }^{\circ}\text{C}$, $pH=7.4$, $P_{CO_2}=40\text{ mmHg}$ and the molar ratio of $[DPG]/[Hb_4]=0.9$ where Hb_4 denotes hemoglobin)
A	constant in the velocity profiles which needs to be determined
\hat{A}	carbonic anhydrase activity
\hat{A}_{pl}	carbonic anhydrase activity in the plasma
\hat{A}_{rbc}	carbonic anhydrase activity in the RBC
B	blunting factor in the velocities profiles
B_i	i = integer, equilibrium constant in equations for ODC models (Equations (2.2) or (2.4)) under nonstandard conditions
B_{σ}	Bromley interaction term
C_{DH}	Debye-Hückel constant
C_{heme}	total heme concentration in the suspension (continuum approach)
$C_{heme,rbc}$	total heme concentration inside the RBC
d	half-thickness of the artificial membrane film
D	constant in the velocity profiles which needs to be determined
D_i	effective diffusion coefficient of species i in the suspension (continuum approach)
D_i°	diffusion coefficient of ionic species i in infinitely dilute solution
$D_{i,34g\%Hb}$	diffusion coefficient of species i in concentrated hemoglobin solution
D_{i,H_2O}	diffusion coefficient of species i in water
$D_{i,k}$	diffusion coefficient of species i in phase k

$D_{i,pl}$	diffusion coefficient of species i in the plasma
D_{i,T_0}	diffusion coefficient of species i at temperature T_0
$D_{O_2,eff}$	effective diffusivity of O_2 under shared condition
$D_{O_2,pl}^S$	shear-induced O_2 diffusivity in the plasma phase
$D_{O_2,rbc}^S$	shear-induced O_2 diffusivity in the red cell phase
$D_{O_2,SF}$	effective diffusivity of O_2 under unshared condition
D_{rbc}	shear-induced diffusion coefficient of RBCs
\tilde{D}_i	diffusion coefficient for ionic species i in the suspension
$\tilde{D}_{i,pl}$	diffusion coefficient of ionic species i in the plasma
E_c	equilibrium parameter in the Easton ODC model (Table 2.1)
E_i	intercept of linearized dissolved CO_2 content vs. total CO_2 content curve
E_{lp}	lumped parameter in the Easton ODC model
f_{water}	volume fraction of water inside the RBC
F	Faraday constant
F_s	slope of linearized dissolved CO_2 content vs. total CO_2 content curve
$Flux_{CO_2}$	CO_2 flux crossing the RBC wall, a function of r and z
$Flux_{HCO_3}$	net flux of extracellular HCO_3^- entering the RBCs or, equivalently, the net flux of intracellular Cl^- entering the plasma
$Flux_{O_2}$	O_2 flux crossing the RBC wall, a function of r and z
g	a measure of the departure of the hemoglobin-oxygen binding reaction from equilibrium ($0 \leq g \leq 1$); in the limit of reaction equilibrium, $g=1$
G_i	intercept of linearized dissolved CO_2 content vs. HCO_3^- content curve
GF	geometric factor; $GF=r_o/r_c$ in both Diller <i>et al.</i> 's and Schmukler and Chien's systems, and $GF=4d/\pi r_c$, in Boland <i>et al.</i> 's system
$h(r)$	hematocrit profile, the volume fraction of RBCs at any radius r
h_m	constant in the hematocrit profile which needs to be determined

H_D	discharge hematocrit
H_T	tube hematocrit
H_s	slope of linearized dissolved CO_2 content vs. HCO_3^- content curve
I	ionic strength of the medium calculated using molar concentrations
I_m	ionic strength of the medium calculated using the molality of ions
j	dissociation rate constants for O_2 binding to hemoglobin
j'	association rate constants for O_2 binding to hemoglobin
k	dissociation rate constant of Reaction (6.V)
k'	association rate constant of Reaction (6.V)
k_a	deoxyhemoglobin- CO_2 reaction forward rate constant (Reaction (6.VI))
k'_a	oxyhemoglobin- CO_2 reaction forward rate constant (Reaction (6.VII))
k_d	deoxyhemoglobin- CO_2 reaction reverse rate constant (Reaction (6.VI))
k'_d	oxyhemoglobin- CO_2 reaction reverse rate constant (Reaction (6.VII))
k_i	$i=1, 3, 4$ and 6 ; association rate constants for anion-protein complex
k_i	$i=2$ and 5 ; outward translocation rate constant of bound anion
k_{-i}	$i=1, 3, 4$ and 6 ; dissociation rate constants for anion-protein complex
k_{-i}	$i=2$ and 5 ; inward translocation rate constant of bound anion
k_{trans}	translocation rate constant of bound Cl^- and HCO_3^- in the simplified ping-pong model
k_u	CO_2 hydration rate constant
k_v	H_2CO_3 dehydration rate constant
K'	apparent first acid dissociation constant for H_2CO_3
K_1	first acid dissociation constant for H_2CO_3
K_2	second acid dissociation constant for H_2CO_3
K_a	amino group ionization constant for deoxygenated hemoglobin carbamate (Reaction (6.VI))

K_a'	amino group ionization constant for oxygenated hemoglobin carbamate (Reaction (6.VII))
K_A	equilibrium association rate constant for Cl^- -protein and HCO_3^- -protein complexes in the simplified ping-pong model
K_{buffer}	equilibrium constant of the buffer
K_{CO_2}	CO_2 permeability of the artificial membrane
K_{DPG}	pH-dependent association constant of DPG and hemoglobin
K_{eq}	pseudo equilibrium constant in approximate CO_2 dissociation curve
K_i	$i=1$ and 3 ; microscopic equilibrium association constants for Cl^- -protein complex in the inward and outward membrane compartments, respectively (Equation 5.10)
K_i	$i=4$ and 6 ; microscopic equilibrium association constants for HCO_3^- -protein complex in the outward and inward membrane compartments, respectively (Equation 5.10)
$K_{I,Cl}$	dissociation constant of the carrier- Cl^- complex
K_{I,HCO_3}	dissociation constant of the carrier- HCO_3^- complex
K_M	Michaelis constant
K_{O_2}	O_2 permeability of the artificial membrane
K_{water}	dissociation constant of water
K_z	amino group ionization constant for the reduced hemoglobin, (Reaction (6.IV))
L	axial length of the artificial membrane tube
m	O_2 carriage potential of hemoglobin calculated based on the local operating slope of the ODC (Equation (2.19b))
m'	constant in the hematocrit profile which needs to be determined
m_1	local operating slope along the unsaturated portions of the ODC

m_2	local operating slope along the almost saturated portions of the ODC
M	O ₂ carriage potential of hemoglobin calculated based on the overall operating slope of the ODC (Equation (2.20b))
n	Hill equilibrium parameter, an index for cooperativity of hemoglobin
N_i	flux of species i
pH	$-\log_{10}$ [hydrogen ion concentration]
pH_{pl}	extracellular pH
$pH_{pl,in}$	extracellular pH of inlet RBC suspension
pH_{rbc}	intracellular pH
$pH_{rbc,in}$	intracellular pH of inlet RBC suspension
pK	$-\log_{10}$ [equilibrium constant]
P_{50}	Hill equilibrium parameter, P_{O_2} at which O ₂ saturation is 50%
P_{CO_2}	partial pressure of CO ₂
$P_{CO_2,ext}$	partial pressure of CO ₂ in the gas space surrounding the artificial membrane tube
$P_{CO_2,in}$	inlet partial pressure of CO ₂
P_{Cl}	phenomenological permeability coefficient of Cl ⁻ in the constant field electrodiffusion model (Equation (5.1))
P_{HCO_3}	phenomenological permeability coefficient of HCO ₃ ⁻ in the constant field electrodiffusion model (Equation (5.1))
P_{O_2}	partial pressure of O ₂
$P_{O_2}^*$	P_{O_2} at which maximum slope for modified Easton model occurs
$\overline{P_{O_2}}$	equilibrated mixed mean oxygen tension in the collected sample
$P_{O_2,ext}$	partial pressure of O ₂ in the gas space surrounding the artificial membrane tube
$P_{O_2,in}$	inlet partial pressure of O ₂

$P_{O_2,NS}$	partial pressure of O_2 under nonstandard conditions (Equation (2.3))
$P_{O_2,S}$	partial pressure of O_2 under standard conditions (Equation (2.3))
Q	volumetric flow rate of the RBC suspension in the tube
r	radial coordinate
r'	dimensionless concentration of HCO_3^- in the RBC-rich plasma region
r''	dimensionless concentration of HCO_3^- in the RBC-free plasma region
r_c	inner radius of the artificial membrane tube
r_o	outer radius of the artificial membrane tube
r_r	radius of the cell-rich region, the difference of tube radius and the thickness of the cell-free layer
r_{rbc}	radius of the RBC
R	gas constant
\bar{R}_{GD}	Gibbs-Donnan ratio
R_{HbCO_2}	rate of formation of hemoglobin carbamate per unit RBC volume
R_{HbO_2}	rate of formation of oxyhemoglobin per unit RBC volume
$R_{HCO_3,pl}$	rate of consumption of CO_2 per unit plasma volume by the hydration reaction
$R_{HCO_3,rbc}$	rate of consumption of CO_2 per unit RBC volume by the hydration reaction catalyzed by the intracellular carbonic anhydrase
$R_{i,k}$	rate of reaction which generates i in phase k
$R_{O_2HbCO_2}$	rate of formation of oxyhemoglobin carbamate per unit RBC volume
s	red cell surface area
s'	dimensionless concentration of Cl^- in the RBC-rich plasma region
$\left(\frac{s}{v}\right)_{rbc}$	surface to volume ratio of the RBC
slp	slip constant in the RBC velocity profile
S	fractions of available hemoglobin sites saturated with O_2

\bar{S}	physically mixed mean oxyhemoglobin saturation in the equilibrated sample
S_{max}	scaling factor of the modified Easton model (Table 2.1)
S_{min}	scaling factor of the modified Easton model (Table 2.1)
S_{mm}	calculated overall mixed mean oxyhemoglobin saturation in the tube
$Sl_{P_{O_2}=P_{O_2,ext}}$	fractional saturation of the hemoglobin molecules under the O_2 partial pressure of $P_{O_2,ext}$
$Sl_{P_{O_2}=P_{O_2,in}}$	fractional saturation of the hemoglobin molecules under the O_2 partial pressure of $P_{O_2,in}$
S_{sa}	space average oxygen saturation of the hemoglobin molecules
t	dimensionless axial coordinate
t_{rbc}	maximum thickness of the RBC
T	temperature of the system
T_o	reference temperature
T_{pl}	unloaded form of the transporter in which a single anion binding/transport site is accessible to only extracellular anions
T_{rbc}	unloaded form of the transporter in which a single anion binding/transport site is accessible to only intracellular anions
T_{tot}	total number of anion transporters per RBC
TX_{pl}	complex of the transporter with extracellular anion X (Cl^-)
TX_{rbc}	complex of the transporter with intracellular anion X (Cl^-)
TY_{pl}	complex of the transporter with extracellular anion Y (HCO_3^-)
TY_{rbc}	complex of the transporter with intracellular anion Y (HCO_3^-)
u	dimensionless concentration of O_2 inside the RBC
v	dimensionless concentration of CO_2 inside the RBC
v''	dimensionless concentration of CO_2 in the RBC-free plasma region

v_{max}	the maximum reaction rate of an enzyme-catalyzed reaction described via Michaelis-Menten equation
v_o	initial rate of an enzyme-catalyzed reaction described via Michaelis-Menten equation
$V(r)$	velocity profile in the z direction
\vec{V}	velocity vector
$\langle V \rangle$	average velocity in the tube; $\langle V \rangle = Q / \pi r_c^2$
$V_{pl}(r)$	plasma velocity at radius r in the cell-rich region
$V'_{pl}(r)$	plasma velocity at radius r in the cell-free region
$\langle V \rangle_{pl}$	average plasma velocity; $\langle V \rangle_{pl} = Q (1-H_D) / \pi r_c^2 (1-H_T)$
$V_{rbc}(r)$	RBC velocity at radius r in the cell-rich region
$\langle V \rangle_{rbc}$	average red cell velocity; $\langle V \rangle_{rbc} = Q H_D / \pi r_c^2 H_T$
V_R	volume of the CSTR reactor
w	dimensionless concentration of H^+ inside the RBC
w'	dimensionless concentration of H^+ in the RBC-rich plasma region
w''	dimensionless concentration of H^+ in the RBC-free plasma region
x	dimensionless radial coordinate in the RBC-rich plasma region
x'	dimensionless radial coordinate in the RBC-free plasma region
X_{pl}	extracellular Cl^- concentration
X_{rbc}	intracellular Cl^- concentration
Y_{pl}	extracellular HCO_3^- concentration
Y_{rbc}	intracellular HCO_3^- concentration
z	axial coordinate
Z_i	electrical valence of ion i
$[buffer]_{pl}$	molar concentration of the buffer in the extracellular medium
$[C_i]$	concentration of species i in the suspension (continuum approach)

$[C_i]_k$	concentration of species i in phase k
$[C_i]_{mm}$	mixed mean concentration of species i in the suspension (continuum approach)
$[C_i]_{mm,rbc}$	mixed mean concentration of species i inside the RBC
$[C_i]_{mm,pl}$	mixed mean concentration of species i in the plasma
$[C_i]_{mm,wb}$	mixed mean concentration of species i in the whole blood
$[C_i]_o$	normalized concentration for species i
$[C_i]_{pl}$	concentration of species i in the RBC-rich plasma region
$[C_i]'_{pl}$	concentration of species i in the RBC-free plasma region
$[C_i]_{pl,calc}$	predicted concentration of species i in the extracellular phase
$[C_i]_{pl,exp}$	experimentally determined concentration of species i in the extracellular phase
$[C_i]_{pl,in}$	inlet concentration of species i in the extracellular phase
$[C_i]_{pl,out}$	outlet concentration of species i in the extracellular phase
$[C_i]_{pl,rw}$	concentration of species i at the RBC wall in the plasma
$[C_i]_{rbc}$	concentration of species i inside the RBC
$[C_i]_{rbc,calc}$	predicted concentration of species i in the intracellular phase
$[C_i]_{rbc,exp}$	experimentally determined concentration of species i in the intracellular phase
$[C_i]_{rbc,in}$	inlet concentration of species i in the intracellular phase
$[C_i]_{rbc,out}$	outlet concentration of species i in the intracellular phase
$[C_i]_{rbc,rw}$	concentration of species i at the RBC wall in the RBC
$[C_i]_{total}$	total concentration of species i
$[C_i]_{total,in}$	total inlet concentration of species i
$[C_i]_{total,out}$	total outlet concentration of species i
$[CO_2]_{reacted}$	concentration of reacted CO_2 in blood (continuum approach)

$[CO_2]_{total}$	total CO_2 content which including HCO_3^- , carbamino hemoglobin, dissolved CO_2 and H_2CO_3
$[DPG]$	intracellular concentration of 2,3-diphosphoglycerate
$\overline{[O_2]}$	physically mixed mean oxygen concentration in the equilibrated sample
$[O_2]_{total}$	total O_2 content which including both oxyhemoglobin and dissolved O_2
$[S]_o$	initial substrate concentration of an enzyme-catalyzed reaction described via Michaelis-Menten equation
α_i	effective solubility coefficient of species i in the suspension (continuum approach)
α_{i,H_2O}	solubility coefficient of species i in water
$\alpha_{i,pl}$	solubility coefficient of species i in plasma
$\alpha_{i,rbc}$	solubility coefficient of species i in RBC
$\alpha_{i,saline}$	solubility coefficient of species i in saline
β	amount of base added or acid removed per pH unit change which can be determined experimentally
β_{pl}	extracellular buffer capacity
β_{rbc}	intracellular buffer capacity
γ	local shear rate
Γ	temperature correction constant in Equation (6.50)
γ_{avg}	average shear rate
γ_i	activity coefficient of species i
δ	thickness of the RBC-free layer
$\Delta[C_i]_{total}$	total content change of species i
ζ	empirical parameter in the calculation of shear-induced diffusivity of RBCs (Equation (2.16))

η_{CO_2}	effective, lumped mass transfer coefficient for CO_2 in Lemon's stopped-flow apparatus
κ	equilibrium parameter in the equations for ODC models (Table 2.1) under standard conditions
κ_S	equilibrium parameter in the modified Easton ODC model under standard conditions (Equation (2.7))
κ_{NS}	equilibrium parameter in the modified Easton ODC model under nonstandard conditions (Equation (2.7))
λ_α (or λ')	pH-dependent association constant for CO_2 binding for the α -amino groups of the α -chain of hemoglobin
λ_β (or λ'')	pH-dependent association constant for CO_2 binding for the α -amino groups of the β -chain of hemoglobin
λ_i	equivalent conductance of ion i in solution
λ_i^o	equivalent conductance of ion i in infinitely dilute solution
μ	viscosity of the solvent
π	constant=3.14159...
σ	empirical parameter in the calculation of shear-induced diffusivity of RBCs (Equation (2.16))
σ_1	amount of H^+ released per O_2 molecule that is bound to hemoglobin (Reaction (6.IV))
σ_2	amount of H^+ released per CO_2 molecule that is bound to deoxy-hemoglobin (Reactions (6.IV) and (6.VI))
σ_3	amount of H^+ released per CO_2 molecule that is bound to oxyhemoglobin (Reactions (6.IV) and (6.VII))
ν	turnover rate of the anion transporter
ϕ	the moles of CO_2 bound per mole hemoglobin tetramer

ψ	electrical potential (Equation (5.1))
Ψ_m	membrane potential (Equation (6.51))

CHAPTER 1

INTRODUCTION

Blood can be described as a circulating organ which ensures the optimal supply of oxygen (O_2) and essential nutrients and removal of carbon dioxide (CO_2) and other metabolic by-products from all the cells of the body. Blood is an intricate physicochemical system, even when one isolates the phenomena governing its role as a carrier of O_2 and CO_2 . Basically the complexity arises from: (1) the division of the blood into effectively two phases, the erythrocytes (red blood cells, RBCs) and the plasma, between which there is transmembrane exchange of gases and anions; (2) the simultaneous interactions of RBC hemoglobin with O_2 , CO_2 , hydrogen ions (H^+ s) and the metabolic intermediate, 2,3-diphosphoglycerate (DPG); and (3) intra- and extracellular hydration/dehydration reactions of CO_2 and buffering of H^+ by hemoglobin and plasma proteins. Consequently, blood O_2 and CO_2 chemistries are no more separable than they are from acid/base chemistry, and the coupling between the blood-gas transfer and acid/base balance is significant. Additionally, analysis of gas transport and pH regulation by blood flowing in blood vessels or artificial, permeable membrane tubes requires information on the hydrodynamic characteristics of blood flowing through narrow tubes. Therefore, blood-gas transport is mediated not only by chemical reaction, but also by diffusion and convection. Thus, many of the related issues involved concern physicochemical phenomena and fluid mechanics.

One long-standing problem is to determine the relative CO_2 transport resistances within capillary blood and metabolizing tissue. This requires analysis and/or suitably scaled experimental modeling of mass transfer and chemical reactions in capillaries containing flowing RBCs. Several studies on the transport of O_2 in the microcirculation

indicated that the resistance to O_2 transport in blood is significant in comparison to the resistance in the surrounding tissue (Hellums, 1977; Artigue and Bruley, 1983; Honig *et al.*, 1984; Federspiel and Popel, 1986). Hellums (1977) was the first to give a clear mathematical estimate of this effect; his analysis showed that the fraction of total O_2 transport resistance that resides inside the capillary is influenced significantly by the discrete nature of blood. He estimated that half of the O_2 partial pressure (P_{O_2}) driving force between RBC interior and distal tissue is dissipated in the blood. From spectroscopic measurements of O_2 binding to myoglobin in cryogenically frozen tissue, Honig *et al.* (1984) deduced that muscle P_{O_2} ranges from 1 to 3 mmHg. This implies a much greater intracapillary P_{O_2} gradient and thus a more substantial fraction of resistance to O_2 transport being located in the blood phase than previously believed.

Although the true capillaries, blood vessels with diameters of 10 μm and less, are considered to be the primary exchange location; it has been observed that 25-30% of the microcirculatory gas transport occurs in the arterioles and larger vessels, 20-100 μm in diameter (Popel and Gross, 1979; Ivanov *et al.*, 1982; Roth and Wade, 1986; Pittman, 1987). In addition, membrane oxygenators used in cardiopulmonary bypass surgery and in membrane lungs involve oxygen transport from relatively large conduits (about 100 μm and larger); and in most of these devices, similar to the *in vivo* situation, the mass transfer resistance attributable to the blood phase is a significant fraction of the total resistance. To design and evaluate increasingly efficient artificial lungs, it is necessary to understand the reactive, diffusive and convective mechanisms of O_2 and CO_2 transport in flowing blood. Therefore, it is important that we develop general models for describing intracapillary oxygen transport which are valid over a wide range of vessel diameters; for vessels with diameters of 20 up to several hundred microns, as well as for capillaries. This work focuses on the transport phenomena in the large vessels (20 -

several hundred microns in diameters) where the mass transfer and hydrodynamic characteristics are known to be different from those in the small capillaries.

The mechanisms of gas transport to and from different sizes of vessels in the microcirculation are different; the steps involved are the same, but the distributions of resistance are dissimilar. In large vessels (diameters of 20 μm and greater), most of the resistance lies in the plasma phase; in the intermediate diameter range, the intracapillary resistance within the red cells becomes comparable to that in the plasma; and in the capillaries (diameters of 8 μm and less), most of the resistance lies in the red cell phase (Nair *et al.*, 1989). In true capillaries with diameters of 5 μm or less, RBCs are restricted to a single-file flow, and they tend to fold along a major axis which is parallel to the vessel axis. In larger capillaries, RBCs are observed to be travelling in either a single- or multi-file pattern depending on tube hematocrit and vessel diameter, and they often take on nonaxisymmetric shape which is resulted from a shift of internal hemoglobin solution from the trailing-edge into the leading-edge part of the cell (Cokelet, 1987). In still larger vessels, the RBCs more or less retain their disc shape, and there is a radial distribution of RBCs with higher hematocrit at the center and lower near the walls, and cell deviations from straight stream lines are somewhat suppressed (Gaehtgens *et al.*, 1980). However, in even larger vessels, the vessel walls do not impose such constraint on the cell motion, and when the blood is subject to shear flow, its formed elements undergo almost random motion. Various investigators (Colton and Drake, 1971; Dorson and Voorhees, 1974; Diller *et al.*, 1980; and Wang and Keller, 1985) had reported that these shear-induced particle migrations and the associated fluid motion can significantly augment transport of oxygen under certain circumstances. Various processes involving in the gas transport and *pH* regulation by blood and the hydrodynamic characteristics of RBCs flowing in the microvessels are discussed in Chapter 2.

Considerable attention has been focused on the theoretical description of O₂ transfer to and from blood, and several reviews have appeared on the subject: Spaeth (1973), Artigue (1980), Nair (1988), and Popel (1989). The general convective-diffusive mass balance has been employed to describe gas transfer to and from blood. A rigorous application of such theory would be exceedingly complex, and several assumptions and approximations are necessary. Some investigators (Reneau *et al.*, 1967; Buckles *et al.*, 1968; Weissman and Mockros, 1969; Bradley and Pike, 1971; Villarroel *et al.*, 1971; Benn *et al.*, 1975; Voorhees, 1976; Diller *et al.*, 1980) have simplified the problem by treating the blood as a continuous and homogeneous hemoglobin solution; while others (Hellums, 1977; Baxley and Hellums, 1983; Artigue and Bruley, 1983; Nair *et al.*, 1989) have attempted to take into account the discrete nature of the blood. For tubes of large diameter, over 300 μm , where the characteristic radial length is much larger than the red cell size, the continuum approach has proven satisfactory (Weissman and Mockros, 1969; Bradley and Pike, 1971; Villarroel *et al.*, 1971; Voorhees, 1976; and Diller *et al.*, 1980). The flow in smaller vessels (arterioles and venules) is characterized by a nonuniform hematocrit distribution, at least by a cell-depleted plasma layer near the tube wall which is about 2 - 4 μm and is, in this situation, a considerable fraction of the entire tube diameter; and the characteristic radial length approaches that of the RBC size. Therefore, the applicability of the continuum models becomes questionable in these small microvessels. A brief review on the development and validation of the continuum models is included in Chapter 3.

Various investigators have used different sets of assumptions to reduce the complex governing equations to a tractable set. It has been difficult to critically test the assumptions of the various models, because experimental measurements of sufficient detail and accuracy are not readily available. Several prior workers have reported experimental data obtained from membrane oxygenator whose diameters range from 300

μm and up (Buckles *et al.*, 1968; Weissman and Mockros, 1969; Bradley and Pike, 1971; Villarroel *et al.*, 1971; Voorhees, 1976; Diller *et al.*, 1980). However, until recently there has been insufficient experimental validation of the various assumptions used for the microvessels (vessels with diameters less than $100\ \mu\text{m}$). Boland *et al.* (1987) developed an *in vitro* microvessel microspectrophotometer system which allowed accurate determination of oxygen fluxes to and from RBC suspensions in small cylindrical conduits (diameter $\approx 30\ \mu\text{m}$) under physiologically relevant conditions. In this system flow, transport and geometrical parameters can be controlled and measured accurately. Thus, validation of the various proposed models for application to the small microvessel has become possible.

Nair *et al.*'s (1989) discrete model for calculating O_2 transport rates in blood flowing through microvessels is entirely predictive. That is to say all parameters in the model were determined from the literature or by other means independent of oxygen transfer experiments. The model was shown to be in excellent agreement with the experimental oxygen transport results from $27\text{-}\mu\text{m}$ -diameter artificial membrane tubes (Boland *et al.*'s system), as well as with deoxygenation results obtained by Schmulker and Chien (1985) in $100\text{-}\mu\text{m}$ -diameter membrane tubes. Prior mathematical models were shown to be significantly less successful. Detailed calculations of the O_2 concentration distribution from Nair *et al.*'s model revealed that the dominant resistance to O_2 transport is distributed in the plasma and relatively little resistance is present within or in the immediate vicinity of the RBCs. Using the above results as a guide, Nair *et al.*'s model can be simplified from four simultaneous nonlinear partial differential equations (PDEs) to one PDE by introduction of a set of well-founded assumptions. The development of this simplified, discrete model and comparison of the two models are presented in Chapter 4. Other objectives of Chapter 4 include mapping out the

regime of applicability for both the continuum and discrete models and consideration of shear-induced augmented transport in blood.

While O_2 and CO_2 transfer are of comparable importance and the coupling between the two processes is significant, most prior analyses have focused on O_2 transfer. In general, a lesser extent of effort and attention has been paid to the blood's companion task of stripping CO_2 from tissue, eliminating it in the lung and to its influence on the overall mass transfer rate. Indeed, in many investigators' papers, artificial lungs are usually called oxygenators, as if their only task was blood oxygenation. Previous attempts on modeling the coupled transport have been along a semi-empirical and lumped-parameter approach. The majority of these theories treated blood as a homogeneous fluid. This approach has proved to be valid for the description of O_2 transfer in macro channel devices but not necessary appropriate for small microvessels. Although it was suggested by several investigators (Weissman and Mockros, 1969; Bradley and Pike, 1971; Dorson *et al.*, 1971; Villarroel *et al.*, 1971; Benn *et al.*, 1975; Voorhees, 1976) that this continuum assumption may be valid for CO_2 transfer modeling under the conditions of low flow rates and large channel dimensions, typical of commercial oxygenators; the validity of this approximation over a range of diameters is questionable. Additionally, local chemical equilibrium was generally assumed. This assumption overlooks some of the more subtle aspects of CO_2 -blood interactions. These interactions include the synergistic actions between hemoglobin bound O_2 and CO_2 and the fact that the reaction scheme for CO_2 is much more complex than that depicted by the CO_2 dissociation curve. More importantly, the CO_2 hydration/dehydration reactions in the plasma are definitely far from being at equilibrium. Another problem in the use of this simplified equilibrium assumption arises in interpretation of the diffusive flux. Total CO_2 , as defined by the equilibrium treatment, is a combination of bicarbonate ion (HCO_3^-), carbamino- CO_2 and dissolved

CO_2 . As a result, adjustments for the effects of the individual species and the heterogeneity of blood have to be incorporated into the definition of an effective diffusivity. The interpretation of this effective property is not completely straightforward because of the highly complex nature of blood. Finally, it should be mentioned that most prior analyses have not treated the interrelationship of O_2 carriage in the blood to the amount of CO_2 in the blood (the Bohr effect) and CO_2 storage to the amount of O_2 in the blood (the Haldane effect). A literature review on the models for coupled O_2 and CO_2 transport is given in Chapter 3.

In order to investigate the coupling between the O_2 and CO_2 transport, an extended model is developed to incorporate the study of CO_2 , as well as, a study of the various blood buffer systems that are closely connected to the transport of these gases. The blood is treated as two continuous coexisting phases: a RBC phase and a plasma phase. The microvessel is divided into two regions: the central, RBC-rich and the outer, cell-free region. The radial distribution of RBCs, and transport of various species due to bulk convection are taken into account. Chemical and transport processes which are included in the model are (1) association and dissociation of O_2 with hemoglobin, (2) association and dissociation of CO_2 with hemoglobin, (3) the Bohr and Haldane effects (the interdependence of O_2 and CO_2 transport), (4) CO_2 hydration/dehydration reactions, (5) buffering actions of hemoglobin and plasma proteins, and (6) anion exchange across the RBC membrane via an anion transporter. The anion transporter is a transmembrane protein that catalyzes the one-for-one exchange of two monovalent anions in opposite directions across the red cell membrane. The monovalent anions are bicarbonate, produced by the hydration of CO_2 , and chloride. The exchange of these anions by the anion transporter has been shown to be essential to the respiration of CO_2 . It is, therefore, important that we are able to describe this exchange system. The formulation and validation of a simplified kinetic model for the anion transporter is presented in

Chapter 5. Finally, the governing equations of the complete transport model subjected to the imposed inlet and boundary conditions are derived and solved numerically in Chapter 6 to provide the concentration distributions of various species in blood that are important in the O_2 and CO_2 exchange process.

The objectives of this work include the followings:

- (1) To review and discuss phenomena, including the blood gas chemistry and rheology, that are important for blood gas transport and pH regulation by flowing blood.
- (2) To conduct a literature survey on the existing models for describing the coupled O_2 and CO_2 transport phenomena.
- (3) To formulate a simpler and workable mathematical model for predicting O_2 transport rates by blood flowing in microvessels based on the model of Nair *et al.* (1989).
- (4) To investigate the feasible diameter regime for application of several existing models (both continuum and discrete models) for prediction of O_2 transport in vessels with diameters ranging from 20 up to several hundred μm .
- (5) To assess the importance of shear-induced augmentation on O_2 transport as a function of vessel diameter, shear rate and O_2 storage potential of the blood.
- (6) To develop a simplified model for describing the anion exchange across the RBC membrane based on the available literature information on this protein; to test the validity of the flux expression with available experimental data; and to incorporate this anion exchange model into an extended model of O_2 and CO_2 transport.
- (7) To incorporate CO_2 transport and pH regulation by blood into the O_2 transport model so that we will be able to further elucidate the inter-dependence of blood gas transport and acid/base balance and to validate the model with data from the literature.

CHAPTER 2

PHYSICAL SITUATION OF GAS TRANSPORT AND BLOOD RHEOLOGY

2.1 General Description of Blood-Gas Interaction

Blood is a heterogeneous fluid composed of both a continuous plasma phase with colloidally suspended proteins and suspended cells. Plasma is a complex aqueous fluid that contains various inorganic ions, proteins and organic substances; it is composed of 90% water and about 7% protein. Among the major protein constituents of plasma are albumins and globulins which maintain osmotic balance and thereby control the movement of water between blood and various tissues. Some globulins serve as protection against disease. Fibrinogen is a protein which plays an important role in the clotting mechanism of blood. Some blood proteins act as buffers for the blood.

There are about 5×10^9 cells in a milliliter of human blood. About 0.2% of the cells are white blood cells, or leukocytes, which protect the body against invasion by foreign micro-organism (Middleman, 1972). About 5% of the cells are platelets, or thrombocytes, which perform a function related to blood clotting. The red blood cells (RBCs), or erythrocytes, by far the largest volume of the formed elements, play the important dual roles of

1. Reversibly binding O_2 in the lungs and distributing it throughout the body for cellular metabolism;
2. Removal of CO_2 formed by metabolic processes from the tissues and transporting it to the lung where it is eliminated. The RBC is composed of about 72% water and 25%

hemoglobin (by volume). The rest of the cell consists of protein, mostly associated with the structure of the cell membrane, and ions such as bicarbonate (HCO_3^-), chloride (Cl^-), sodium (Na^+) and potassium (K^+).

While O_2 is carried by the blood mainly through a reversible chemical reaction with hemoglobin, the transport of CO_2 involves a complex interaction of many phenomena. The chemical and transport events that occur in blood during gas exchange in a lung capillary (excluding the transcellular water movement) are shown schematically in Figure 2.1 (modified from Klocke (1987) and Nunn (1987)). Reactions 1, 2 and 3 represent O_2 diffusion across the alveolar capillary membrane, diffusion into the RBC and chemical reaction with intracellular hemoglobin molecule. Under normal conditions in human circulation, greater than 95% of O_2 is reversibly bound to hemoglobin; and the remaining O_2 is in a free form, dissolved in both blood plasma and in the hemoglobin solution inside the RBCs. The remaining reactions in the respiration diagram deal with CO_2 transport and $p\text{H}$ regulation. Under normal physiological conditions, roughly 0.7 H^+ (Bohr protons) are released from intracellular hemoglobin every time an O_2 molecule is bound (reaction 4). In native RBCs, these acid equivalents rapidly equilibrate with HCO_3^- in the presence of carbonic anhydrase (represented as CA in Figure 2.1) to produce H_2O and CO_2 . Free CO_2 then diffuses out of the cell rapidly since plasma membrane is highly permeable to apolar gases (reaction 6). CO_2 persists in the plasma phase and then is exchanged into the alveolus (reaction 7). Therefore, reactions 5-7 allow intracellular HCO_3^- to be expelled as CO_2 in the lung. However, the bulk of venous HCO_3^- , about 80%, is present initially in the plasma. In the absence of extracellular carbonic anhydrase, the CO_2 dehydration reaction (reaction 8) occurs much too slowly to be of importance. Therefore, in order for these extracellular HCO_3^- to be evolved as CO_2 from lung capillaries, it must be transported across the RBC membrane (reaction 9). This involves one-for-one exchange of Cl^- for HCO_3^- to maintain

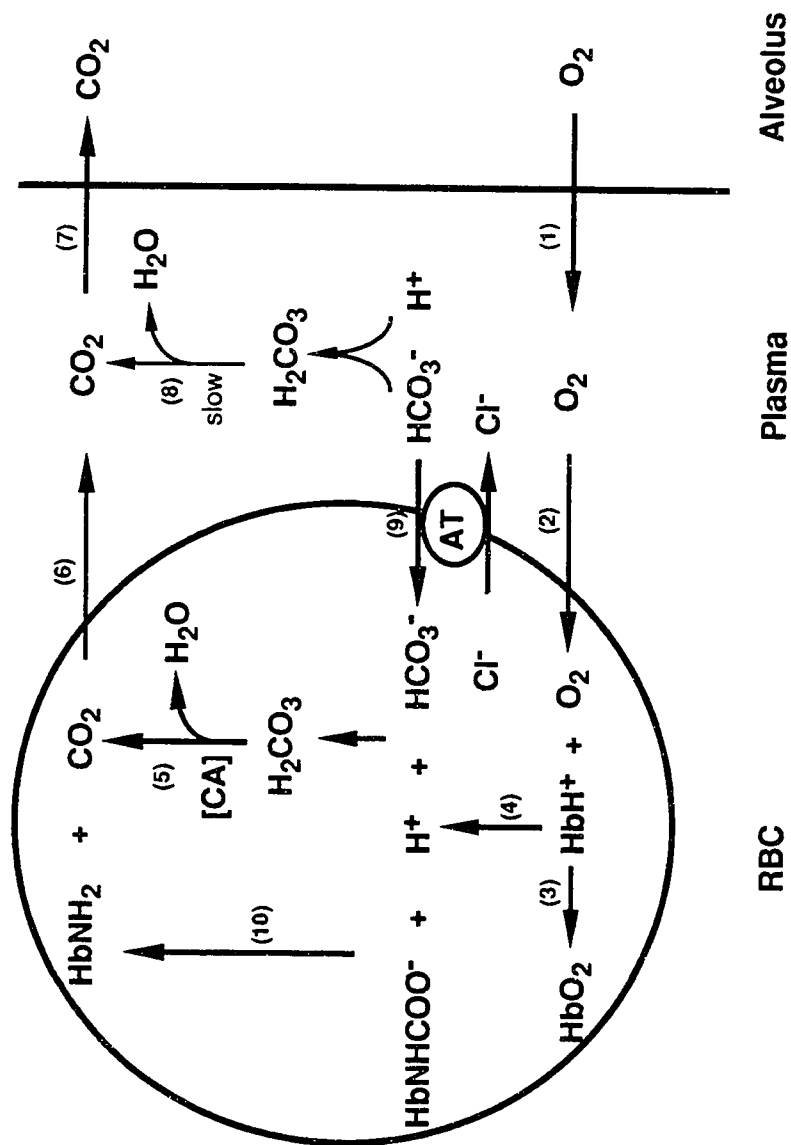


Figure 2.1: Exchange of oxygen and carbon dioxide in a pulmonary capillary.

electroneutrality, and it is mediated by the anion transporter (AT). As result, 81% of CO_2 is carried along with the plasma and RBCs from the tissue to the lung as HCO_3^- . The other mechanism which CO_2 is carried by the blood is through direct reversible chemical combination with the N-terminal valines of α and β chains of hemoglobin (reaction 10). In this form, 11% of the CO_2 is transported by the blood to the lung. Finally, dissolved CO_2 accounts for 8% of CO_2 being transported to the lung. In the case of the O_2 and CO_2 exchange between the blood and the respiring muscle tissues, the same processes occur in the reverse direction.

2.1.1 Carriage of Oxygen in Blood

O_2 dissolves physically throughout in the blood, but over 95% of the available O_2 is transported principally through reversible combination with the protein hemoglobin. A hemoglobin molecule is made up of four subunits united in a tetrameric conformation as illustrated in Figure 2.2 (taken from Lehninger, 1975). Each subunit contains a heme moiety conjugated to a polypeptide. The polypeptides are referred to collectively as the globin portion of the hemoglobin molecule. There are two pairs of polypeptides in each molecule, two of subunits containing one type (alpha chains) and two containing another (beta chains). The alpha (α) subunits and beta (β) subunits pair to form asymmetric dimers, denoted arbitrarily, $\alpha_1\beta_1$ and $\alpha_2\beta_2$. Therefore, these dimers of unlike chains are the fundamental structural units of the hemoglobin tetramer, and in the RBC, the hemoglobin molecules continually dissociate into dimers and reassociate into tetramers (Baumann *et al.*, 1987).

The hemoglobin molecule and its subunits contain mostly hydrophobic amino acids internally and hydrophilic amino acids on their surface. Therefore, the molecule is soluble in water but impermeable to water. The heme prosthetic groups are in the four largely hydrophobic pockets, one being formed in each globin peptide chain

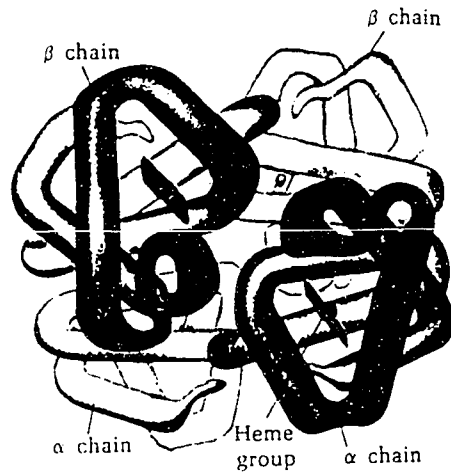


Figure 2.2: The quaternary structure of hemoglobin (copied directly from Lehninger (1975)).

(Figure 2.2). Heme is an iron-containing porphyrin derivative; it is the active center of the hemoglobin molecule, the binding site for O_2 . The non-aqueous environment around the the iron atom allows it to remain in the ferrous state even in the presence of O_2 molecules, and imparts to the iron-oxygen bond a coordination character that makes it strength intermediate between a non-covalent and a covalent bond. This property is important in allowing the reversibility of O_2 binding. The four interacting subunits of hemoglobin molecule generate a cooperative effect. The positive cooperative effect of the tetrameric hemoglobin can be described as follows: if a hemoglobin molecule takes up one O_2 , it tends to go on and acquire two or three more O_2 molecules; and vice-versa, hemoglobin's affinity for O_2 decreases with decreasing O_2 saturation. Hemoglobin is a protein molecule that changes its structure in response to chemical stimuli such as the O_2 molecule; it is known that the stable quaternary structure of the oxygenated hemoglobin is significantly different from that of the deoxygenated form (Perutz, 1978). Additionally, the striking feature of protein chemistry in relation to O_2 -

hemoglobin interaction is allosterism - the coupling of ligand (an organic molecule that donates the necessary electrons to form coordinate covalent bonds with metallic ions, as O_2 is bound to the central iron atom of hemoglobin) binding at one protein site to change in the conformation of the macromolecule due to the binding at a second site.

2.1.1.a *Oxygen Hemoglobin Equilibrium*

The O_2 -binding characteristics of hemoglobin can be described by a curve, oxyhemoglobin dissociation curve (ODC), obtained by plotting the fractions of available hemoglobin sites saturated with O_2 (S) as a function of the partial pressure of O_2 (P_{O_2}) in equilibrium with the solution. One way of characterizing the O_2 affinity of hemoglobin consists of determining P_{50} , which is the P_{O_2} leads to 50% saturation. For example, at 37 °C and pH 7.4 (physiological conditions), P_{50} for intraerythrocytic hemoglobin is about 26 mmHg. As the hemoglobin O_2 affinity is decreased (P_{50} is increased), relatively less O_2 is bound to hemoglobin; or alternatively, a greater P_{O_2} is needed to bind the same amount of O_2 . Another way to describe the behavior of hemoglobin towards O_2 is to characterize the degree of sigmoidicity of the ODC. The sigmoidal shape of this curve reflects the cooperative effect of O_2 binding to hemoglobin, which is the result of conformational changes of different subunits during the oxygenation or deoxygenation process. The sigmoid character of the ODC can be described quantitatively by Hill's coefficient, n . When the cooperativity of hemoglobin is modified, this results in a decrease of Hill's coefficient (e.g., $n=1$ for myoglobin, which binds O_2 in a non-cooperative manner, and $n=2.5-3$ for normal intraerythrocytic hemoglobin); and its value can thus be considered as a useful reflection of the efficiency of O_2 -carrying function (Lehninger, 1975). The sigmoidal nature of O_2 equilibrium curve itself contributes greatly to the efficiency of hemoglobin by causing a release of much O_2 over a narrow range of tissue P_{O_2} values (20-40 mmHg) and regaining maximal O_2 with a limited increase in P_{O_2} (100 mmHg) as it returns to the lung.

Many physicochemical conditions within the blood determine, in concert, the actual values of P_{50} and n . Several effectors or regulators of hemoglobin affect O_2 affinity and hence shift the ODC. For example, the curve is shifted right (increased P_{50} or decreased O_2 affinity) with elevated H^+ , CO_2 , 2,3-diphosphoglycerate (DPG) and temperature (Hlastala, 1984). The dependence of the ODC on CO_2 concentration is known as the Bohr effect (Hlastala and Woodson, 1983). CO_2 is bound preferentially to deoxygenated hemoglobin, and therefore the O_2 affinity of hemoglobin decreases. However, only part of Bohr effect is due to molecular CO_2 , the remainder being due to the presence of H^+ , formed by the hydration of CO_2 and subsequent dissociation of carbonic acid. The latter effect is called the fixed acid Bohr effect which is determined when the pH is changed by addition of fixed acid or base alone. Therefore, CO_2 lowers hemoglobin's O_2 affinity, not only by carbamino formation at the amino-terminal residues of alpha and beta chains, but also by its action in the form of HCO_3^- , as an anionic effector of hemoglobin function. Briefly, Bohr effect enhances O_2 transport in blood in the following manner. As blood pass through the lung, CO_2 diffuses from the blood into alveoli. This reduces the partial pressure of CO_2 (P_{CO_2}) and the concentration of H^+ in blood. Both effects shift the ODC to the left and upward; so that the quantity of O_2 that binds with hemoglobin at any given P_{O_2} becomes considerably increased, thus allowing greater O_2 transport to the tissues. Then when blood reaches the respiring tissue capillaries, exactly the opposite effects occur. The pH of blood passing through the capillaries drops continuously due to uptake of CO_2 and other acids; this displace O_2 from the hemoglobin and delivers O_2 to the tissue at a higher P_{O_2} than would otherwise occur. Thus Bohr effect is particularly important under the conditions of heavy muscular exercise.

Because the preferential binding of DPG, which is an erythrocyte metabolic intermediate, with the deoxygenated form of hemoglobin, the presence of DPG has

several forms of action. It has a direct effect on hemoglobin; binding of DPG to hemoglobin reduces the affinity to O_2 because it stabilizes the deoxygenated form of hemoglobin by cross-linking the beta chains and contributing additional salt bridges that must be broken for the deoxygenated form to click into the oxygenated form of hemoglobin (Martin, 1981). In addition, because the binding of DPG to the N-terminal (amino-terminal) valine of beta chains, the presence of DPG decreases the effect of CO_2 . Several other organic and inorganic phosphates had also been found to have similar effects *in vitro* (Chanutin and Curnish, 1967). However, in human RBCs, only DPG and adenosine triphosphate (ATP) are present in sufficient quantity to influence the O_2 affinity of blood. However, the concomitant presence in human RBCs of a divalent cation such as Mg^{2+} , which binds to ATP to form an unreactive Mg-ATP complex, minimizes the allosteric effect of ATP on human hemoglobin. Moreover, 70 to 80% of intraerythrocytic ATP is bound to Mg^{2+} ; therefore, it appears plausible to exclude ATP concentrations from the computations (Bunn *et al.*, 1971). Finally, increased temperature has a direct effect on hemoglobin, reducing its affinity for O_2 . It also decreases the fixed-acid Bohr effect and increases the effect of molecular CO_2 . Increased temperature also decreases the binding of DPG to hemoglobin (Hlastala, 1984).

Such intricacy has precluded even a phenomenological model of blood O_2 -hemoglobin equilibria at varying CO_2 , acidity, DPG and temperature levels. However, several research teams have developed convenient representations of experimental data obtained over wide ranges of conditions, and these equations of state are discussed in more details in the following two sections. On the other hand, O_2 binding to hemoglobin also affects transport of other substances. Particularly, the dependence of CO_2 transport on O_2 concentration is called the Haldane effect which is the O_2 -linked lowering of blood's CO_2 affinity and is discussed in more details in a later section.

Together the Bohr and Haldane effects linked the problem of CO₂ transport intimately to the problem of O₂ transport, and the interactions result in facilitation of gas exchange at the lung and in the systemic tissue.

2.1.1.b *Equations for Standard Oxyhemoglobin Dissociation Curve*

An excellent review on modeling blood ODC was published by O’Riordan and Colleagues (1985) in which they compare nine different models fitted to normal human data. Some of these models are summarized in Table 2.1. It is not the intent here to review all models for the ODC, but rather to compare them. Among many models for ODC, the empirical Hill (1910) and the more theoretical Adair (1925) equations are best known. The Hill model gives a good characterization over the saturation range 20-98% which is the range of major physiological interest. The significance of the Hill parameters, P_{50} and n , is well known; P_{50} reflects the affinity of hemoglobin molecule toward O₂, and n is an empirical index of cooperativity of O₂ binding to hemoglobin. Under standard conditions ($T=37$ °C, $pH=7.4$, $P_{CO_2}=40$ mmHg and the molar ratio of $[DPG]/[Hb_4]=0.9$ where Hb_4 denotes hemoglobin), it has been reported that the mean P_{50} is 26.7 ± 1.7 mmHg and n is about 2.6-2.8 (O’Riordan *et al.*, 1983; Winslow *et al.*, 1983).

Adair’s stepwise hypothesis paved the way for modern conception of the hemoglobin molecule. He proposed that four O₂ molecules bind to a single hemoglobin molecule sequentially, giving four equilibrium constants, one for each sequential reaction. This type of equation is difficult to fit because the parameters are rather closely correlated (i.e., the parameters are redundant) (Winslow *et al.*, 1977; Fell, 1979). Margaria (1963) simplified the Adair model by equating the first three equilibrium constants because they were of similar magnitude while the forth was much higher. k and η of the of the Margaria approximation are constants; the value of η is generally given as 125 while k is a function of P_{50} ($k=0.0124$ when $P_{50}=27$ mmHg). The

Margaria model with its two parameters would certainly be easier to fit than the four-parameter Adair model from whence it was derived.

Table 2.1: Models describing the oxygen-hemoglobin equilibrium curve.

ODC Model	Equation
Hill (1910)	$S = \frac{(P_{O2}/P_{50})^n}{1 + (P_{O2}/P_{50})^n}$
Adair (1925)	$S = \frac{a_1 P_{O2} + 2a_2 P_{O2}^2 + 3a_3 P_{O2}^3 + 4a_4 P_{O2}^4}{4(1 + a_1 P_{O2} + a_2 P_{O2}^2 + a_3 P_{O2}^3 + a_4 P_{O2}^4)}$
Margaria (1963)	$S = \frac{(\kappa P_{O2})^3 + \eta - 1}{(\kappa P_{O2})^4 + \eta - 1} \quad \text{where } \kappa P_{O2} = \frac{1 + k P_{O2}}{k P_{O2}}$
Kelman (1966)	$S = \frac{a_1 P_{O2} + a_2 P_{O2}^2 + a_3 P_{O2}^3 + P_{O2}^4}{a_4 + a_5 P_{O2} + a_6 P_{O2}^2 + a_7 P_{O2}^3 + P_{O2}^4}$
Easton (1979)	$S = (S_{max} - S_{min}) \exp\{-\exp[\kappa(P_{O2}^* - P_{O2})]\} + S_{min}$ where $P_{O2}^* = \frac{\ln(E_d/\kappa)}{\kappa}$

Kelman (1966) used one of the more complicated equation for the ODC, a ratio of two polynomials, requiring seven parameters (a_1 - a_7) for standard conditions. Kelman completely generalized Adair equation parameters to allow greater flexibility; thus the model may be able to provide a better fit even through that it has no theoretical basis. Unfortunately, this also caused the parameter redundancy to reach unacceptable levels. Easton's (1979) model for the ODC is based on a theoretical relationship between the partial pressure and equilibrium kinetics. The model requires two parameters: a rate coefficient E_c and a rate parameter κ , and two scaling factors, S_{max}

and S_{min} . S_{max} represents the maximum (upper) saturation scale, and S_{min} represents the minimum (lower) saturation scale. The Easton lumped parameter E_{lp} which is a ratio of (E_c/κ) can be shown to be a grouping of the two scaling parameters such that: $E_{lp} = \ln[(S_{min} - S_{max})/S_{min}]$. The E_{lp} factor describes the leftward or rightward shift of the ODC, much like the Hill parameter P_{50} ; additionally, his parameter κ is supposed to determine the slope of the ODC, like the Hill parameter n .

As a result of O’Riordan *et al.*’s (1985) investigations, they reported that for most applications, the Hill equation still appears to give an adequate characterization over the physiologically important part of the ODC. As expected, when compared with the Hill model, an increase in accuracy was obtained with the models such as Adair, Kelman and Easton. Although these models are also applicable over the complete range of saturation, this extra information is in their opinion of little physiological interest. In addition, they also suggested that when the most accurate description of the ODC is required, as when looking for small changes in ODC; the Easton model would appear to be the best choice. The three parameters are relatively easy to determine although the slightly higher parameter redundancy necessitates good initial parameter estimates. Independently, Buerk (1985) evaluated the Easton model and found it to be superior to the Hill equation and comparable to the Adair equation in the saturation range from 0 to 95%. Reich and Zinke (1984) also examined the parameter redundancy for different models. They found that the Kelman model fit their data best. However, the uncertainty in the seven parameters was large. They found some parameter redundancy with all models and suggested that the simpler ODC may ultimately be the most useful.

2.1.1.c *Equations for Nonstandard Oxyhemoglobin Dissociation Curve*

Understanding the gas exchange processes can not be accomplished without detailed empirical knowledge of hemoglobin, oxygen and effectors in interactions in the blood. Therefore, it is necessary that we are able to describe O₂-hemoglobin

equilibrium relationship and the important aspects of how ODC varies with P_{CO_2} , pH , DPG and temperature. It is essential that we are able to compute the full range of the curve; such that if P_{O_2} , pH and P_{CO_2} are given, S can be calculated; this is to account for the Bohr effect which is attributed to pH changes, due to CO_2 , and consequent allosteric effects. It is also important that we understand the allosteric effect of DPG on hemoglobin. It is well known that in some pathological and adaptive conditions DPG concentration within the RBC can vary widely. Some of these conditions are anaemia, hexokinase and pyruvate kinase deficiencies, acidosis, shock, massive blood transfusion, congenital and acquired heart disease, chronic lung disease, and high altitude adaptation (Samaja and Winslow, 1979).

Arturson *et al.* (1974) tabulated the “effector ligand coefficients”,

$$\left(\frac{\partial \log P_{O_2}}{\partial \log X_i} \right)_{S, X_{j \neq i}} \quad \text{where } X_i = [H^+], P_{CO_2} \text{ or } [DPG].$$

The use of such coefficient is motivated by the analysis of “allosteric linkage” by Wyman (1964). Wyman derived “reciprocal relationships” - comparable to Maxwell’s relations in thermodynamics - such as the following:

$$\left(\frac{\partial [H^+]}{\partial [HbO_2]} \right)_{pH} = - \left(\frac{\partial \log P_{O_2}}{\partial pH} \right)_S \quad (2.1)$$

The derivative on the right is called the “Bohr coefficient” which is a measure of change in O_2 affinity with pH . On the left of Equation (2.1) is the “Haldane coefficient” which is a measure of release or gain of protons accompanying oxygenation or deoxygenation. Tyuma and Ueda (1975) also experimentally substantiated this theoretically derived equivalence of the Bohr and Haldane coefficients in a wide range of O_2 saturation.

Samaja *et al.* (1981) developed an empirical method for the ODC variation with pH , P_{CO_2} and $[DPG]/[Hb_4]$ molar ratio based on Hill's equation. They examined how the Hill parameters varied by fitting human blood data obtained under a variety of conditions, and the effects of temperature were not determined. Because $\log P_{50}$ was observed to be a linear function of pH in the range of 6.9 to 7.6, its value at any pH in this range can be interpolated by use of the following formulas (Samaja *et al.*, 1981):

$$\log P_{50}(pH) = \frac{\{(pH - 7.0) [\log P_{50}(pH=7.6) - \log P_{50}(pH=7.0)]\}}{0.6} + \log P_{50}(pH=7.0) \quad (2.2a)$$

$$\log P_{50}(pH=7.0) = (B_1 P_{CO_2} + B_2) \left(\frac{[DPG]}{[Hb_4]} \right) + B_3 P_{CO_2} + B_4 \quad (2.2b)$$

$$\log P_{50}(pH=7.6) = (B_5 P_{CO_2} + B_6) \left(\frac{[DPG]}{[Hb_4]} \right) + B_7 P_{CO_2} + B_8 \quad (2.2c)$$

where $B_1 = -6.912 \times 10^{-4}$, $B_2 = 0.3365$, $B_3 = 3.598 \times 10^{-4}$, $B_4 = 1.599$, $B_5 = -1.380 \times 10^{-3}$, $B_6 = 0.3607$, $B_7 = 9.089 \times 10^{-4}$, $B_8 = 1.360$; P_{CO_2} is in mmHg, and $[DPG]/[Hb_4]$ is a molar ratio. It should be mentioned that Samaja *et al.*'s empirical relationship allows the estimate of normal human whole blood P_{50} at any given pH (range 6.9 to 7.6), P_{CO_2} (range 20 to 90 mmHg), and $[DPG]/[Hb_4]$ ratio (range 0.3 to 2.5), with 0.73 mmHg SD. Together with the above, it was also assumed that Hill's factor, n , would be approximately constant under various conditions of pH and $[DPG]/[Hb_4]$. Therefore, the Bohr effect and organic phosphate (DPG) effect on the ODC can be accounted for through the fact that P_{50} is now a function of P_{CO_2} , pH and DPG.

However, characterization of the ODC by Hill's approximation does not account for changes in shape under various conditions of pH and $[DPG]/[Hb_4]$; consequently, Winslow *et al.* (1983) set out to correlate not only the position but also the shape of the curve to the values of the various effectors. They developed an algorithm for the

oxygen saturation with pH , P_{CO_2} and DPG based on Adair's equation because the four Adair parameters appeared to be sensitive to these effects. In order to generate the nonstandard ODC, they examined how the Adair model parameters (a_i ; $i=1, 2, 3, 4$) varied by fitting human blood data under a variety of conditions. The resulting set of Adair parameters were then empirically fit to quadratic equations, requiring a total of 72 coefficients. The temperature effects were not determined, but would require that an additional 24 coefficients be estimated in order to extend this algorithm. Their data base were more extensive than had previously been available: P_{O_2} up to 150 mmHg, pH between 7.2 and 7.8, P_{CO_2} between 7 and 70 mmHg, and $[DPG]$ between 1 and 14 mM. Kelman (1966) determined the effect of temperature variation and used the following empirical relationship, requiring three coefficients, given by

$$P_{O_2,S} = P_{O_2,NS} 10^{[0.024 (37 - T) + 0.4 (pH - 7.4) + 0.06 \log (40/P_{CO_2})]} \quad (2.3)$$

where subscripts "S" and "NS" denote standard and nonstandard conditions, respectively; and T is in °C and P_{CO_2} is in mmHg. The effects of DPG were not included, since its effects were not known at the time. Saturation can then be computed after correcting the nonstandard P_{O_2} to standard conditions and substitute into a standard ODC.

The Easton model was shown to be comparable to the Adair equation; however, the Easton model involves only two parameters and a scaling factor while Adair model requires four parameters. In addition, Easton's model offers a computational advantage, since explicit mathematical equations can be written for either oxyhemoglobin saturation as a function of O_2 partial pressure, or vice versa; and numerical methods are required to invert Adair's equation. Furthermore, Easton (1979) had shown that only one of the model parameters will vary with nonstandard conditions, which would simplify

calculations for nonstandard ODC. Recognizing these advantages, Buerk and Bridges (1986) modified Easton's model and developed an algorithm for which nonstandard ODCs can be computed. They rewrote Easton's model by defining a new parameter, $P_{O_2}^*$, which is the O_2 partial pressure where the slope of ODC (dS/dP_{O_2}) is at maximum. They showed that the maximum slope for the Easton's model occurs at

$$P_{O_2}^* = \frac{\ln\left(\frac{E_c}{\kappa}\right)}{\kappa} \quad (2.4)$$

Using their redefined parameter, the saturation is given by the double exponential (Buerk and Bridges, 1986):

$$S = (S_{max} - S_{min}) \exp\left\{-\exp\left[\kappa(P_{O_2}^* - P_{O_2})\right]\right\} + S_{min} \quad (2.5)$$

As they had defined the model, the dimensionless product $\kappa P_{O_2}^*$ would not vary under nonstandard conditions. P_{O_2} can be computed explicitly from

$$P_{O_2} = \frac{\left\{\kappa P_{O_2}^* - \ln\left[\ln\left(\frac{S_{max} - S_{min}}{S - S_{min}}\right)\right]\right\}}{\kappa} \quad (2.6)$$

They estimated the Easton parameters for the standard human ODC (@ $T=37^\circ\text{C}$, $pH=7.4$, $P_{CO_2}=40$ mmHg and $[DPG]/[Hb_4]=0.9$) from ten previously reported human blood data in the literature. Overall, the mean values (\pm SE) were $\kappa=0.0725\pm0.0059$ (mmHg) $^{-1}$ and $P_{O_2}^*=20.70\pm0.30$ mmHg. By restricting the fit to data in the saturation range from 0 to 95%, they found an upper scaling factor $S_{max}=96.01\pm0.22\%$ and lower scaling factor $S_{min}=1.23\pm0.23\%$. It should be mentioned that the corresponding P_{50} is 26.8 mmHg for those ten data sets. They then determined how $P_{O_2}^*$ and κ vary under

nonstandard conditions by comparing the modified model with two previous nonstandard ODC algorithms (Kelman, 1966 and Winslow *et al.*, 1983) in the literature. They found that the conditions can be characterized by additional four parameters. The rate constant κ for the modified Easton model varies with all four factors as

$$\kappa_{NS} = \kappa_S \exp \left\{ B_1(pH - 7.4) + B_2(P_{CO_2} - 40) + B_3(T - 37) + B_4 \left(\sqrt{\frac{[DPG]}{[Hb_4]}} - 0.9 \right) \right\} \quad (2.7)$$

where subscripts “S” and “NS” denote standard and nonstandard conditions; $B_1=0.765$ (pH)⁻¹, $B_2=-1.47 \times 10^{-3}$ (mmHg)⁻¹, $B_3=-0.0611$ (°C)⁻¹ and $B_4=-0.291$. The applicable range for the description of ODC is for P_{O_2} 0-150 mmHg, T 20-40 °C, pH 6.8-8.0, P_{CO_2} 7-70 mmHg, and $[DPG]/[Hb_4]$ 0.6-2.0.

Because this model also describes hemoglobin solutions as well as whole blood (Easton, 1979), it would also be useful for characterizing O₂ transport and delivery with hemoglobin-based artificial blood substitutes. New estimates for the model parameters (κ , $P_{O_2}^*$, S_{max}) and nonstandard coefficients (B_1 - B_4) would be required for the specific blood substitute. This modified Easton algorithm would be superior than Samaja’s modified Hill model for the obvious reason that it is of adequate accuracy over a variety of conditions; while the modified Hill model accounts for changes in shifting but not in shape of the dissociation curve under various conditions. It also offers computational advantages over the previous algorithms by Kelman (1966) and Winslow *et al.* (1983). First, explicit forms of $S=S(P_{O_2})$ and $P_{O_2}=P_{O_2}(S)$ are readily obtainable (Equations (2.5) and (2.6)), avoiding the iterative numerical procedures that are required to invert either Adair or Kelman’s equations. Second, less computer time is required to compute new parameters for nonstandard conditions, since only one parameter is involved.

2.1.2 Carriage of Carbon Dioxide in Blood

The uptake and release of CO_2 take place during the passage of the blood through tissue and lung capillaries, respectively. The processes occurring in the lung capillaries are depicted schematically in Figure 2.1. Under normal circumstances, only about 5% of the total CO_2 content of blood is carried as free CO_2 . Predominantly, CO_2 is found in blood chemically combined into two species: as bicarbonate, the primary CO_2 carriers in both plasma and RBCs, and as carbamino - CO_2 in combination with amino groups on proteins, particularly as hemoglobin carbamate. The portions of different form of CO_2 depends largely upon the acid/base status of the blood. While the vast bulk (typically about 97%) of O_2 is carried by hemoglobin inside the RBCs, CO_2 is somewhat more evenly distributed between the blood phases. Plasma HCO_3^- is normally the major CO_2 -bearing species because of the greater plasma volume, CO_2 solubility and pH . Because the volume fraction occupied by water is 0.94 in plasma and 0.72 in the cells; solubility coefficient of CO_2 is 0.031 mM/mmHg in the plasma, while it is 0.023 mM/mmHg in the RBC. With a normal hematocrit of 0.40-0.45, plasma transports about two-thirds of all CO_2 carried in blood.

The simple shape of the CO_2 dissociation curve (Figure 2.3) is deceptive, since the reaction scheme for CO_2 is far more complex than that for O_2 , as illustrated in Figure 2.1. For the case which CO_2 is removed in the lung or with an artificial membrane oxygenator, bicarbonate and hydrogen ions form carbonic acid which is then decomposed to liberate CO_2 . However, the dehydration reaction of carbonic acid to form CO_2 in the plasma is very slow, thus HCO_3^- is the predominant species. HCO_3^- can translocate into RBC, although slowly, in exchange of other anions, in particular Cl^- , where the same chain reactions then occur. In the RBC, however, dehydration of carbonic acid is catalyzed by the enzyme carbonic anhydrase. The predominant mode for liberation of CO_2 from blood is therefore translocation of bicarbonate into the RBC

where it reacts with hydrogen ion to form carbonic acid. Dehydration of carbonic acid liberates CO_2 which, in turn, diffuses out of the RBC into the plasma, diffuses and convects within the bulk of the plasma, and then diffuses across the blood-membrane interface. Decomposition of carbamino hemoglobin is an additional source of CO_2 . Carbamate compounds that arise from combination of CO_2 with plasma proteins have a much smaller effect because of the relatively unfavorable equilibria for their formation. Finally, various ionic species, such as organic and inorganic phosphates, amino acids, and proteins, behave as weak acids at physiological pH range. The buffering power of hemoglobin is particularly strong and has a marked effect in influencing the shape of the CO_2 dissociation curve.

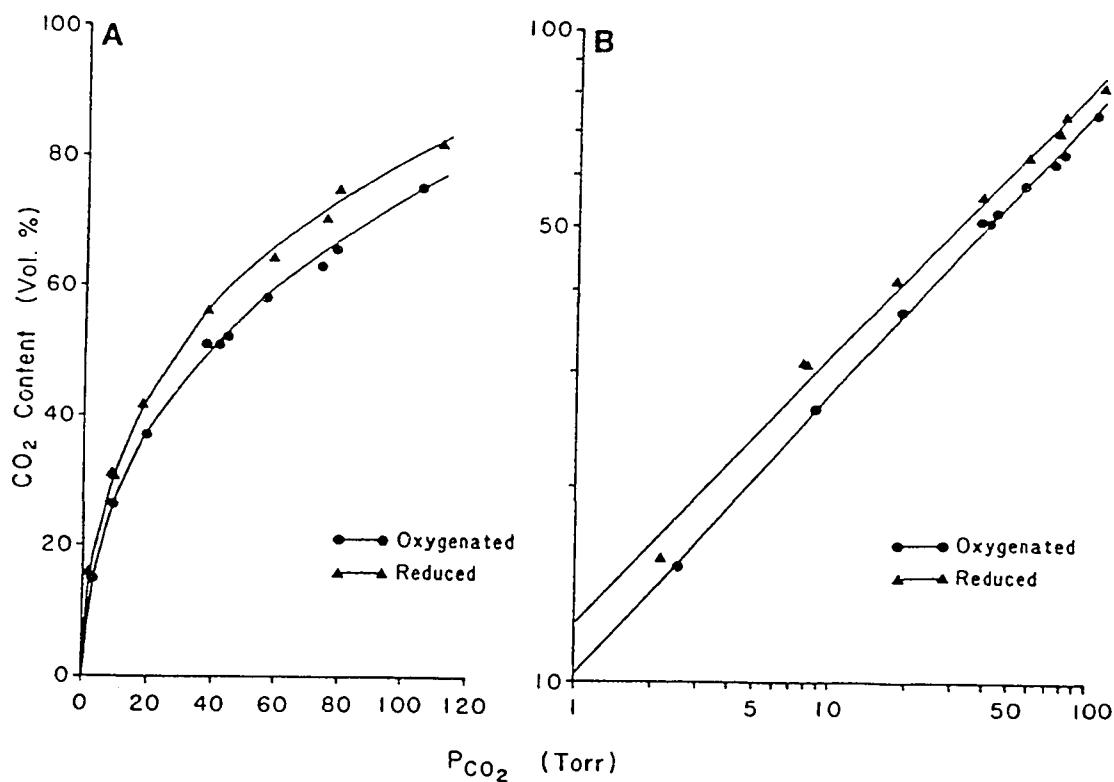
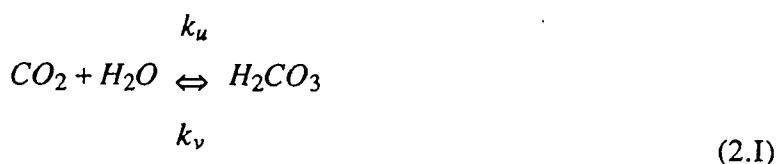


Figure 2.3: Carbon dioxide dissociation curve of human blood at 37 °C plotted on a linear (A) and logarithmic (B) axes. [Copied directly from Klocke (1987)].

A carrier mechanism has been established in which O_2 and hemoglobin combine rapidly to form oxyhemoglobin which then diffuses in parallel with the diffusing O_2 . The transfer of the O_2 is thus augmented or facilitated by the cooperative movement of oxyhemoglobin. For mathematical analysis of O_2 transport by flowing blood in microvessels, assumption of the reactants to be at chemical equilibrium, was shown to be a good approximation (Nair *et al.*, 1990). This is due to the fact that in the microvessels (vessels with diameter of 30 μm and larger) the fraction of resistance to O_2 transport which is attributed to the RBC interior is very small, and to the fact that almost all O_2 is carried inside the RBC; thus the chemical equilibrium assumption is appropriate for the O_2 transfer problem. On the other hand, the transport of CO_2 through the bicarbonate solutions is enhanced by the hydration of CO_2 . The hydrated CO_2 in the form of bicarbonate ion; diffuses along with dissolved CO_2 . Intracellular hydration reaction is catalyzed by the carbonic anhydrase enzyme; thus the chemical equilibrium assumption would again be applicable. However, the extracellular hydration reaction is very slow, and the involving species are, in general, far from chemical equilibrium. Moreover, about two-thirds of CO_2 transport is carried out in the plasma region. Therefore, the simplifying approach of utilizing the CO_2 dissociation curve to describe the transfer of CO_2 might not be valid. This implies that perhaps one would not be able to consider the CO_2 transfer problem by considering the CO_2 dissociation curve alone; one would need to consider the intracellular and extracellular CO_2 transport events separately and then tie these processes together with interphase exchange of various species.

2.1.2.a Bicarbonate System

Carbonic acid and CO_2 are linked through the hydration/dehydration



where k_u and k_v are the forward and backward reaction rate constants, respectively, for the hydration/dehydration reactions. Under normal circumstances, this reaction is extremely slow; however, in the RBC, the enzyme carbonic anhydrase greatly speeds up the rates of both forward and reverse reactions. Carbonic anhydrase is a zinc-containing enzyme of low molecular weight. It is inhibited by a large number of unsubstituted sulphonamides (general formula $R-SO_2NH_2$). Acetazolamide is the most important of all these active inhibitors; this drug produces complete inhibition at 5-20 mg/kg in all organism and has no other pharmacological effects of importance. Acetazolamide has been much used in the study of carbonic anhydrase and has revealed the surprising fact that it is not essential to life. With total inhibition, P_{CO_2} gradients between tissues and alveolar gas are increased. Pulmonary ventilation is increased and alveolar P_{CO_2} is decreased (Kernohan, 1965; Dodgson and Forster, 1983; Bidani and Crandall, 1985). Otto and Quinn (1971) had shown that at enzyme concentrations approaching those found in the RBC the reaction rate is no longer linearly dependent on enzyme concentration but passes through a maximum followed by a region where the activity is independent of the carbonic anhydrase enzyme. Measurements of the catalytic activity of RBC hemolysates and suspensions have given a value of 6,500-15,000 for the catalytic factor inside the intact RBC (Itada and Forster, 1973; Dodgson and Forster, 1983).

At the pH of physiological significance, carbonic acid instantly dissociates into H^+ and HCO_3^- .



where K_1 is the first acidic dissociation constant of carbonic acid. According to the law of mass action: $[H^+][HCO_3^-]/[H_2CO_3]=K_1$. The pK_1 is about 6.1; therefore, carbonic acid is about 96% dissociated under physiological conditions (Otto and Quinn, 1971). Bicarbonate can further dissociate into carbonate ion with liberation of a proton.



where K_2 is the second dissociation constant of carbonic acid. However, the second dissociation occurs only at high pH (above 9), because $pK_2 > 10$; and it is, therefore, not a factor in the carriage of CO_2 by the blood.

Interconversion of HCO_3^- and CO_2 can also be achieved through the following pathway which involves the combination of hydroxyl ion with CO_2 :



This reaction only becomes significant with increasing pH because of the greater OH^- concentration. Klocke (1987) calculated that at pH 7.4 and 37 °C, only 9% of reaction product is formed via the hydroxyl pathway; and at pH 7.2 and 7.6, this fraction becomes 6% and 14% respectively. Therefore, at pH values less than 7.6; the contribution from Reaction (2.IV) is reasonably small and will be neglected in the analysis.

Consequently, the physiologically relevant pathways for hydration/dehydration reactions are Reactions (2.I) and (2.II). The rate of hydration of CO_2 per unit volume of aqueous media can be expressed as (Garg and Maren, 1972; Bidani *et al.*, 1978)

$$-\frac{d[CO_2]}{dt} = \hat{A} \left(k_u [CO_2] - \frac{k_v}{K_1} [H^+] [HCO_3^-] \right) \quad (2.8)$$

where

$[CO_2]$ is the dissolved CO_2 concentration expressed in unit volume of aqueous media.

$[H^+]$ and $[HCO_3^-]$ are the concentrations of hydrogen and bicarbonate ions, respectively; and they are expressed in unit volume of aqueous media.

\hat{A} is a parameter that varies with the presence of carbonic anhydrase activity. If the reaction is uncatalyzed, i.e., no carbonic anhydrase is present, then $\hat{A}=1.0$. The rate expression can be used for both the intra- and extracellular compartments. Extracellular carbonic anhydrase activity is thought to be normally absent ($\hat{A}=1.0$), but may be present if hemolysis did occur ($\hat{A}>1.0$).

There, however, had been some experimental evidences which indicated that a relatively small concentration of carbonic anhydrase is localized to the capillary endothelium in some tissues and can catalyze the plasma CO_2 hydration to some extent (Forster, 1982; Bidani and Crandall, 1985). In the present analysis, it will be assumed that carbonic anhydrase exists only in the RBCs and that plasma hydration is uncatalyzed. However, the analysis can readily be modified to include catalyzed plasma bicarbonate formation. Due to high intracellular concentration of carbonic anhydrase, the CO_2 hydration/ dehydration is enzymatically catalyzed to proceed to about 10^4 times faster than the uncatalyzed process in plasma. Therefore, intracellular hydration/ dehydration reactions can be assumed to be at equilibrium relative to exchanges of CO_2 ; and the interacting influences of bicarbonate, hydrogen ions and dissolved CO_2 can then be described quantitatively by Equation (2.9a) (Klocke, 1987):

$$[H^+]_{rbc} = K' f_{water} \left(\frac{[CO_2]_{rbc}}{[HCO_3^-]_{rbc}} \right) \quad (2.9a)$$

where

$[CO_2]_{rbc}$ is the dissolved CO_2 concentration inside the RBC expressed in per unit volume of RBCs.

$[H^+]_{rbc}$ and $[HCO_3^-]_{rbc}$ are the concentrations of intracellular hydrogen and bicarbonate ions, respectively; and they are expressed in per unit volume of RBCs.

K' is the apparent first dissociation constant of carbonic acid, and it includes a factor which allows for the substitution of total dissolved CO_2 concentration for carbonic acid.

f_{water} is the fraction of water inside the RBC, and it is approximately 0.72 under normal conditions (Meldon, 1984). f_{water} is introduced here to account for the fact that the concentrations of the involving species are expressed in unit volume of RBC phase instead of unit volume of cell water.

Transforming Equation (2.9a) to the logarithmic form results in the familiar Henderson-Hasselbalch equation

$$pH_{rbc} = pK' + \log \left(\frac{[HCO_3^-]_{rbc}}{[CO_2]_{rbc}} \right) - \log(f_{water}) \quad (2.9b)$$

where $pH = -\log([H^+]_{rbc})$ and $pK' = -\log(K')$. The kinetic and equilibrium constants for hydration and dehydration reactions which were taken from the literature (Gibbson and Edsall, 1963; Garg and Maren, 1972; Nunn, 1987) are summarized in Table 2.2.

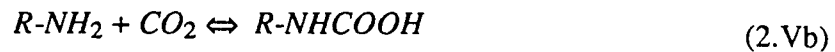
Table 2.2

Reaction rate equilibrium constants for hydration/dehydration reactions in aqueous media.

Reactions	Constants	Water		Buffered Saline		Plasma	
		25 °C	37 °C	25 °C	37 °C	25 °C	37 °C
$\text{CO}_2 + \text{H}_2\text{O} \rightleftharpoons \text{H}_2\text{CO}_3$	Forward Rate Constant k_u (sec ⁻¹)	0.03	0.223	0.0318	0.134	0.0318	0.134
	Reverse Rate Constant k_v (sec ⁻¹)	20.0	70.4	18.5	59.4	18.5	57.5
$\text{H}_2\text{CO}_3 \rightleftharpoons \text{H}^+ + \text{HCO}_3^-$	First acid dissociation constant of H_2CO_3	1.74x10 ⁻⁴	1.58x10 ⁻⁴	4.06x10 ⁻⁴	3.40x10 ⁻⁴	4.19x10 ⁻⁴	3.50x10 ⁻⁴
	K_1 (M)						
$\text{CO}_2 + \text{H}_2\text{O} \rightleftharpoons \text{H}^+ + \text{HCO}_3^-$	Apparent first dissociation constant of H_2CO_3	2.63x10 ⁻⁷	5.01x10 ⁻⁷	6.92x10 ⁻⁷	7.59x10 ⁻⁷	7.24x10 ⁻⁷	8.12x10 ⁻⁷
	K' (M)						

2.1.2.b Carbamino Carriage

Amino groups of hemoglobin and plasma proteins have the ability to combine directly with CO₂ (Klocke,1987):



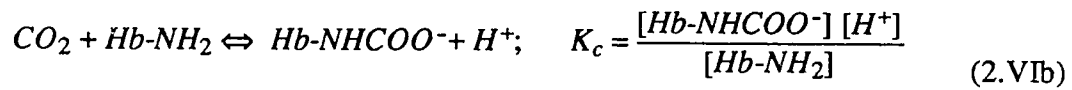
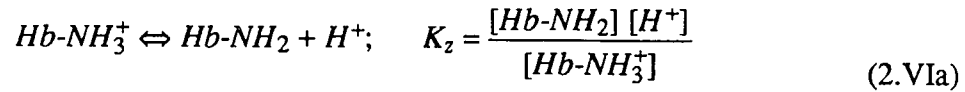
where R is the protein moiety. In a protein, the amino groups involved in the peptide linkages between amino acid residues cannot combine with CO₂. Carbamino carriage is therefore restricted to the one terminal group (α -amino) in each protein and to the side chain amino groups (ϵ -amino). However, the ϵ -amino groups of hemoglobin have a high pK_z (where K_z is the acidic dissociation constant of the amino group, see Reaction (2.Va)), $pK_z \approx 10$; this precludes any significant contribution to CO₂ binding under physiological circumstances (Klocke (1987)). It was calculated that the arterial-venous difference of carbamate accounted for 10.5% (normal DPG concentration) and 27% (in the absence of DPG) of the CO₂ excreted by the lung despite a relatively low absolute concentration. This accounts for the major part of Haldane effect, which is the difference in the quantity of CO₂ carried, at constant P_{CO_2} , in oxygenated and reduced blood. The remainder of the effect is due to the increased buffering capacity of deoxygenated (reduced) hemoglobin (Nunn, 1987). In other words, the Haldane effect is due to the fact that combination of O₂ with hemoglobin causes hemoglobin to become a stronger acid, and this in turn displaces CO₂ from the blood in two ways. Firstly, the more acidic hemoglobin has less tendency to combine with CO₂, thereby releasing additional CO₂ from carbamino hemoglobin. Secondly, the increased acidity of hemoglobin causes it to release excess of H⁺, and this favors the conversion of more HCO₃⁻ into carbonic acid which then dissociates and releases CO₂.

The amount of CO_2 combined with $-\text{NH}_2$ groups of plasma protein to form carbamino compound is so small as to be physiologically negligible. Almost all is carried by hemoglobin, and deoxygenated hemoglobin is about 3.5 times as effective as oxyhemoglobin. The actual P_{CO_2} has very little effect upon the quantity of CO_2 carried in this manner, throughout the physiological range of P_{CO_2} (Nunn, 1987). Formation of carbamino compounds does not require the dissolved CO_2 to be hydrated and so is independent of carbonic anhydrase. The reaction would be of particular importance in a patient who had received a carbonic anhydrase inhibitor. The arterial/venous difference in carbamino carriage had been reported to be lost in certain regions of the body when a patient inhales 100% O_2 at a pressure of about 3 atmospheres absolute, since the O_2 dissolved in the arterial blood is then sufficient for metabolic requirements and very little reduced hemoglobin appears in the venous blood (Nunn, 1987). It was suggested that the loss of the arterial/venous difference in carbamino carriage of CO_2 under these conditions resulted in tissue retention of CO_2 , and was a major factor in the cerebral toxic effect produced by high O_2 tension (Klocke, 1987).

The competition effect between CO_2 and DPG binding to hemoglobin is known to be resulting from the fact that CO_2 combines with the α -amino groups of the α - and β -chains of hemoglobin and DPG interacts with the α -amino group of the β chain. The mechanism of the antagonism between CO_2 and DPG binding to hemoglobin was established by Bunn and Briehl (1970). Such an effect was first demonstrated by showing that substantial decrease in alkaline (pH) Bohr effect (measured as $\Delta \log P_{50} / \Delta pH$) caused by CO_2 was abolished by stoichiometric amounts of DPG. However, O_2 affinity of hemoglobin in the presence of DPG was still considerably decreased by CO_2 , showing that deoxyhemoglobin still combined with more CO_2 than oxyhemoglobin. The explanation for these results was that DPG was displacing the CO_2 from the α -amino group of the β -chain and that the increase in the pH Bohr effect

caused by DPG described earlier exactly balances the decrease caused by the combination of the α -amino group of the α -chain.

It has been shown that in the absence of organic phosphates (DPG and ATP) the binding curve of CO_2 to human deoxyhemoglobin cannot be fitted to single values of K_c (K_c is the pH-independent association constant for carbamino CO_2 binding to hemoglobin) and K_z (K_z is the ionization constant for Hb-NH_3^+ , the protonated form of the amino groups of hemoglobin that are able to form carbamino CO_2) (Kilmartin and Rossi-Bernardi, 1973).



This suggested that α - and β -chains have a different reactivity toward CO_2 . A good fit to the CO_2 -binding data was obtained if two pH-dependent association constants for CO_2 binding are assumed, a high affinity ($\lambda' = 650 \text{ M}^{-1}$) and a low affinity constant ($\lambda'' = 240 \text{ M}^{-1}$). On addition of DPG or ATP, the carbamino CO_2 binding to human deoxyhemoglobin at 37°C is decreased by about 30% at P_{CO_2} of 40 mmHg. As mentioned previously, although ATP exerts effects on hemoglobin similar to those of DPG, it appears to be largely chelated with Mg^{2+} and Ca^{2+} inside the RBC, so that the “free” ATP concentration is low and that DPG is the more important allosteric factor of these two organic phosphates. Experimentally, it was observed that the carbamino CO_2 binding curve with DPG or ATP coincided exactly with the binding curve for the higher affinity binding site (λ') (Kilmartin and Rossi-Bernardi, 1973). Their interpretation for this finding was that DPG or ATP completely displaced CO_2 from the low-affinity site (λ''); thus this site must be the β -chain α -amino group because it was clearly involved in

DPG binding to deoxyhemoglobin. The higher affinity CO_2 binding site (λ') is therefore the α -chain α -amino group. The preceding simplified structural interpretation allowed Kilmartin and Rossi-Bernardi (1973) to derive the equations for competitive interaction between DPG and CO_2 . The total carbamino CO_2 bound by the α - and β -chains of hemoglobin in the presence of DPG is

$$\phi = \frac{2 \lambda_{\alpha} [\text{CO}_2]}{1 + \lambda_{\alpha} [\text{CO}_2]} + \frac{2 \lambda_{\beta} [\text{CO}_2]}{1 + \lambda_{\beta} [\text{CO}_2] + K_{DPG} [\text{DPG}]} \quad (2.10)$$

where

ϕ is the moles of CO_2 bound per mole hemoglobin tetramer.

λ_{α} (or λ') and λ_{β} (or λ'') are the pH-dependent association constants for CO_2 binding for the α -amino groups of the α -chain and β -chain, respectively.

K_{DPG} is the pH-dependent association constant of DPG and hemoglobin.

It is worth noting that λ_{β} and K_{DPG} are the pH-dependent association constants; their pH dependence in the physiological range operates in the opposite directions. K_{DPG} increases with decreasing pH , leading to a higher affinity for DPG, whereas λ_{β} decreases since the fraction of charged β -chain α -amino groups able to combine with CO_2 decreases.

It should be emphasized that these equations provide only a simplified treatment of interaction between CO_2 , DPG and hemoglobin. In particular the problem of a hemoglobin tetramer with one CO_2 molecule bound has not been considered because it was not clear whether this would totally exclude DPG binding or merely reduce it. The assumption made by Kilmartin and Rossi-Bernardi, that two CO_2 molecules bound per tetramer would completely exclude DPG binding, seems reasonable on stereochemical grounds. In the physiological pH range, ϕ will vary between 0 and 4. Equation (2.10)

was used to fit CO₂-binding to human deoxyhemoglobin with values of $\lambda_{\alpha}=650 \text{ M}^{-1}$ and $\lambda_{\beta}=240 \text{ M}^{-1}$ at pH 7.4 and 37 °C (Kilmartin and Rossi-Bernardi, 1973). While Garby and de Verdier (1971) and Kilmartin and Rossi-Bernardi (1973) calculated the association rate constant for DPG binding to deoxyhemoglobin to be in the range of $5 \times 10^2 \text{ M}^{-1}$ and $1.5 \times 10^3 \text{ M}^{-1}$.

Ferguson (1936) examined the effect of oxygen saturation at various level on the carbamino carriage of CO₂, and found that the difference in bound carbamino CO₂ between oxy- and deoxyhemoglobin is linear with oxygen saturation (data is given in *Applied Respiratory Physiology* by Nunn, 1987).

2.1.2.c Anion Transporter

In the tissue P_{CO_2} is 46 mmHg, while the P_{CO_2} of the arterial blood entering the tissue capillary is 40 mmHg. Although the pressure difference is small, CO₂ easily diffuses from the tissue to the blood. The diffusion process is governed both by a high lipid solubility of CO₂ and by a short diffusion distance. As CO₂ enters the blood, it dissolves physically in the extracellular water phases, forms carbamino compounds predominantly by binding to intracellular hemoglobin; and most of CO₂ is hydrated to carbonic acid, which subsequently dissociates into bicarbonate and hydrogen ions. The extracellular spontaneous hydration of CO₂ is too slow a process to provide any significant contribution. Therefore, the bicarbonate production takes place almost entirely within the RBC. The intracellular bicarbonate formation is accompanied by a production of hydrogen ions, which are buffered to a greater extent, mainly by hemoglobin. The removal of H⁺ is very efficient because the buffer properties of hemoglobin are amplified by the O₂-linked pK shifts that accompany the transition from oxyhemoglobin to deoxyhemoglobin, the Haldane effect. Unless bicarbonate ions are also removed from the intracellular phase, the formation of bicarbonate ions will stop when the bicarbonate concentration is in equilibration with P_{CO_2} and pH according to the

Henderson-Hasselbalch equation. In fact, intracellular bicarbonate is removed by the so-called chloride-bicarbonate exchange (also known as the “Hamburger shift” or the “chloride shift”) across the RBC membrane, whereby 75% of the formed bicarbonate is stored in the plasma until the blood reaches the lung capillary, where the reactions would run backward in this so-called “Jacobs-Stewart cycle” (Weith *et al.*, 1982; Frohlich and Gunn, 1986). Most of the CO_2 liberated in the lung capillaries is generated from the plasma HCO_3^- . As intracellular HCO_3^- decreases, plasma HCO_3^- enters the RBC in exchange for Cl^- and the production of free CO_2 through the action of carbonic anhydrase. Although the contribution of plasma to the total CO_2 carriage is greater than that of the RBC, almost all CO_2 excreted from the plasma must first enter the RBCs so that it can be processed to a form (molecular CO_2) that is readily excreted.

$\text{HCO}_3^-/\text{Cl}^-$ exchange across the RBC membrane plays a major determinant role in the CO_2 exchange and transport for the reason mentioned above that under normal physiological conditions 80% of CO_2 transfer/exchange is derived from the hydration of plasma and RBC bicarbonate. In addition, this pathway provides a crucial link between two compartments with different H^+ buffering characteristics. It has been shown that a specialized transport system, involving a major RBC membrane protein (band 3), is involved in the electroneutral translocation of anions into and out of RBCs. It is designated as the band 3 protein because it can be easily localized on sodium dodecyl sulfate (SDS) polyacrylamide gel electrophorograms, where it is found in the third major band from the top. The exchange of these anions by band 3 is essential to the respiration of CO_2 ; as a result, there exists an extensive amount of literature on the band 3 anion transport system. There are various reviews on band 3 biochemistry, exchange kinetics and anion transport inhibitors (Cabantchik *et al.*, 1978; Lowe and Lambert, 1983; Jennings, 1985; Frohlich and Gunn, 1986; Brahm, 1986; Passow, 1986; Jennings, 1989). Some investigators have reported that the largest of the resistances

involved in CO₂ transport is associated with anion exchange (Weith and Brahm, 1980; Crandall and Bidani, 1981). For instance, Crandall *et al.*'s (1981) study in isolated rat lungs suggested that CO₂ transfer in capillary beds is adversely affected *in vivo* when the rate of RBC HCO₃⁻/Cl⁻ exchange is abnormally low. While others have reported that this exchange is not rate limiting in CO₂ transport under resting conditions; however, this exchange becomes a bottleneck for CO₂ transport under exercising conditions due to the significantly reduced transit time through the capillary (Weith *et al.*, 1982). Therefore, it is important that we are able to describe this transmembrane exchange process.

Hyperventilation under resting conditions appears when the elimination of CO₂ from the tissue is impeded. Possible conditions causing a reduced CO₂ elimination are restricted diffusion of CO₂ in pulmonary diseases accompanied by hypercapnia, inhibition of intracellular carbonic anhydrase, and an impaired anion transport due to a reduced number of transport sites per RBC and/or inhibition of Jacobs-Stewart cycle (Weith *et al.*, 1982). Since carbonic anhydrase activity greatly exceeds the needs of the organism, a pronounced reduction of the enzyme activity may have no pathophysiological consequences. In contrast, a slight reduction of anion exchange capacity causes an immediate compensatory hyperventilation which seems to indicate that anion transport system has practically no reserve capacity at all. Crandall *et al.* (1981) conducted experiments to confirm the hypothesis that inhibition of RBC anion exchange can significantly affect both CO₂ excretion and postcapillary pH equilibration. Furthermore, because a number of commonly used drugs, such as salicylate, furosemide and anesthetics are known to inhibit the rate of RBC anion exchange, these results thus imply a potential clinically significant effect on CO₂ transfer *in vivo* by inhibition of the anion exchange kinetics, especially in patients with limited cardiopulmonary reserve (Crandall *et al.*, 1982; Weith and Brahm, 1985). In order to

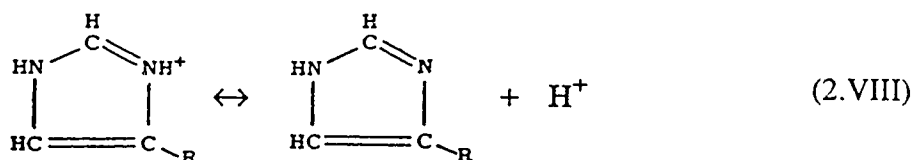
study the respiratory function of blood, it is important to develop a mathematical expression for describing this anion exchange across the RBC membrane. The development of the flux equation as a function of two kinetic parameters and the intra- and extracellular anion compositions is discussed in Chapter 5.

2.1.2.d *Buffers in Blood*

CO₂ produced by aerobic metabolism is transported in such a way that excess H⁺s are produced, both through dissociation of carbonic acid and the formation of carbamino compounds. Anaerobic metabolism produces lactic acid, a further source of H⁺s. The total amount of H⁺ produced daily in man in the form of nonvolatile acids is 50-70 mEq. Accordingly, blood must possess potent buffering system to prevent large changes in acidity associated with CO₂ transport. In the blood, proteins - for example, the plasma proteins - can serve as buffers because both their free carboxyl and their free amino groups dissociate.



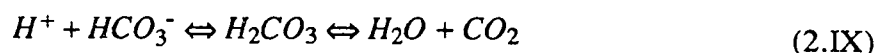
A more important buffer system is produced by the dissociation of the imidazole groups of the histidine residues in hemoglobin.



In the *pH* 7.0 - 7.7 range, the free carboxyl and amino groups of hemoglobin contribute relatively little to its buffering capacity. However, the hemoglobin molecule contains 38 histidine residues and it is present in large amounts. Thus, the hemoglobin in blood has

six times the buffering capacity of the plasma proteins. In addition, the action of hemoglobin is unique because the imidazole groups of deoxygenated hemoglobin dissociate less than those of oxyhemoglobin, making deoxygenated hemoglobin a weaker acid and therefore a better buffer than oxygenated hemoglobin.

Another major buffer system in the blood is the carbonic acid-bicarbonate system because the H_2CO_3 level is in equilibrium with dissolved CO_2 , and the amount of dissolved CO_2 is controlled by respiration.



Although blood contains other buffers, such as phosphate, they are not particularly important for short term *pH* regulation. The system $H_2PO_4^- \rightleftharpoons H^+ + HPO_4^{2-}$ has a *pK* of 6.8. In human plasma, the phosphate concentration is too low (e.g., $[HPO_4^{2-}]_{pl}$ and $[H_2PO_4^-]_{pl}$ are about 2 mM as compare to $[HCO_3^-]_{pl}$ of about 30 mM) for this system to be a quantitatively important buffer.

As illustrated in Figure 2.1, generation of free CO_2 via the carbamate and dehydration reactions consume H^+ . Conversion of HCO_3^- to CO_2 requires an equal number of protons. Release of CO_2 from carbamate utilizes even more H^+ . The formation of carbamic acid from the carbamate ion consumes a single proton. As CO_2 is released from the carbamic acid, the concentration of uncharged amino groups increases. A portion of these groups ionizes, consuming more H^+ . Generation of CO_2 by carbamate pathway requires more than a single proton, the exact number depending on the values of K_z and K_c and their change with oxygenation. The number has been estimated to vary between 1.2 and 1.8 protons from *pH* 6.9 to 7.9 in human blood. Also it appears to be a function of O_2 saturation (Klocke, 1973). Hemoglobin, which is the principal source of protons for both reactions, provides H^+ by two mechanisms.

First, the intracellular contents are potent buffers, releasing about 3 moles of proton per mole of hemoglobin monomer with a unit pH change (Siggaard-Anderson, 1971). Second, the pK values of certain acidic groups on the hemoglobin molecule change with oxygenation, releasing Bohr protons (Perutz, 1978). The number of H^+ s released with binding of a molecule of O_2 can be computed from the relationship between two linked functions (Equation 2.1), as described by Wyman (1964). As an approximation, about 0.5-0.7 H^+ is released with binding of one O_2 molecule under normal circumstances, but this ratio varies significantly, depending on pH , P_{CO_2} , 2,3-DPG concentration, and even the O_2 saturation of blood (Hlastala and Woodson, 1975).

Consequently, for the opposite event of CO_2 uptake and O_2 release in the tissue capillaries, the hydration reaction, the carbamino reactions, the dissociation of the positively charged amino groups, and the deoxygenation of hemoglobin all produce H^+ s. However, as a result of the various buffer systems mentioned above, the actual increase in H^+ concentration is considerably less than that indicated by these reactions. The buffering action can be expressed through the following equation

$$\frac{d[H^+]}{dt} = \frac{d[H^+]}{d(pH)} \frac{d(pH)}{d[H^+]_{app}} \frac{d[H^+]_{app}}{dt} = \frac{2.303 [H^+]}{\beta} \frac{d[H^+]_{app}}{dt} \quad (2.11)$$

where

$d[H^+]/dt$ is the actual rate of increase in H^+ concentration.

$d[H^+]_{app}/dt$ is the apparent rate of increase in H^+ concentration.

$-d[H^+]_{app}/d(pH)$ is the buffering capacity of the medium, β . β is the amount of base added or acid removed per pH unit change and it can be determined experimentally.

In addition, because $pH = -\log[H^+]$ and $d[H^+]/d(pH) = -2.303[H^+]$, $d[H^+]/dt$ can then be rewritten as $(2.303[H^+] d[H^+]_{app}/dt)/\beta$.

Buffering capacity can be determined in two ways. First, all the detailed reaction schemes can be combined with a statement of electroneutrality to include the ionic equilibria reactions to form a complete, but cumbersome, set of equations which describe the exact interactions (Butler, 1964). This approach is, however, primarily useful in model systems that contain one or at most two, buffers for which the equilibrium constants and exact concentrations are known. In blood, this type of a development is generally not applicable due to the complex mixture of buffers. The second approach which describes buffer action has found more widespread application to describe mixtures of buffers. It relies on the definition of buffers as “substances which by their presence in solution increase the amount of acid or alkali that must be added to cause a unit change in pH ”. A good buffer has a large value of β . This value is always positive, so that the addition of base increases the pH while the addition of acid decreases the pH . β is normally determined experimentally, and is, in general, a function of pH .

For very simple systems, β can be determined from chemical equilibrium, the first method described above. In mixtures of buffers, β can be determined experimentally by titration of solution of interest. The usefulness of this approach when applied to plasma and hemoglobin solutions at physiological pH is twofold. First their titration curves, $d[H^+]_{app}$ vs. $d(pH)$, are effectively linear. Second, when dissolved CO_2 levels are varied, the differential change in bicarbonate ion is equal to the non-bicarbonate buffer value as (Klocke, 1987):

$$-\frac{d[HCO_3^-]_{pl}}{d(pH)_{pl}} = \beta_{pl} \quad (2.12a)$$

$$-\frac{d[HCO_3^-]_{rbc}}{d(pH)_{rbc}} = \beta_{rbc} \quad (2.12b)$$

where β_{rbc} and β_{pl} are the intracellular and extracellular buffering factors, respectively. Therefore, the non- HCO_3^- buffering power of physiological solutions is expressed in $\{d[\text{HCO}_3^-]/d(pH)\}$ with HCO_3^- concentration expressed as millimoles per liter. Addition of buffers to a solution improves buffering capacity and thus the increment in HCO_3^- concentration with any given change in pH . The buffer value for plasma varies with the total proteins and phosphates present. For hemoglobin, production of H^+ s via carbamate and oxyhemoglobin formation can be regarded as a change in the buffer value from some standard condition.

Plasma separated from RBCs and then equilibrated with CO_2 has the ability to absorb CO_2 because the buffering provided by plasma proteins. The capacity of “separated” plasma is proportional to protein concentration. However, this is substantially less than the apparent buffering power of “true” plasma - plasma that has been separated from RBCs after equilibration with CO_2 . Plasma CO_2 content then reflects not only plasma buffering but also buffering provided by intracellular hemoglobin. HCO_3^- formed due to buffering of CO_2 inside the cell exchanges for plasma Cl^- , thereby increasing plasma HCO_3^- more than could be achieved by plasma buffering alone. Erythrocyte buffering power, corrected for the intracellular water content, is greater than that of plasma. Whole blood, a mixture of plasma and RBCs, has an intermediate value. The buffering powers of “true” plasma, erythrocytes, and whole blood are predominantly a function of hemoglobin concentration; and these buffering powers all pertain to solutions equilibrated *in vitro*.

2.2 Fluid Mechanics of Blood Flowing in Tubes and Enhancement of Gas Transport Due to Migrations of RBCs

The development of a mathematical model of mass transport in microvessel requires knowledge not only of the basic mechanism of transport and the complex chemical and physical interactions but also the hydrodynamics of the system. In this section, the rheology of red cell suspensions is described. Emphasis is given to the rheology of blood in tube flow and its possible relationship to gas transport which is the main goal of this work. The rheological properties of blood have been studied in detail using coaxial cylinder and capillary viscometers. Since these viscometers are large-scale devices, the measurements can be applied to a homogeneous fluid theory. The viscosity of blood has been found to be non-Newtonian at very low shear rates, presumably due to breakup of RBC clusters. In a strongly sheared system (shear rate $> 100 \text{ sec}^{-1}$) the viscosity of blood approaches a constant, “Newtonian” value. Plasma always exhibits Newtonian behavior. The specification of the velocity field is simplified considerably if the non-Newtonian behavior of blood is neglected. The approximation is reasonably acceptable for a system operating in a high shear rate region.

2.2.1 Distribution of Cells and Velocity Profiles of Flowing Blood

In large microvessels, many red cells are intersected by a cross section of the vessel; the flow is then complicated by the interactions between cells. Observations *in vivo* as well as *in vitro* show that there is a thin layer near the wall which has fewer red blood cells in it than average. This is due partly to wall exclusion and also lateral migration of cells which leads to a radial distribution of hematocrit with a higher hematocrit at the center and lower near the wall. Another feature is that velocity is blunted in the central portion of the tube compared to Poiseuille flow (Figure 2.4).

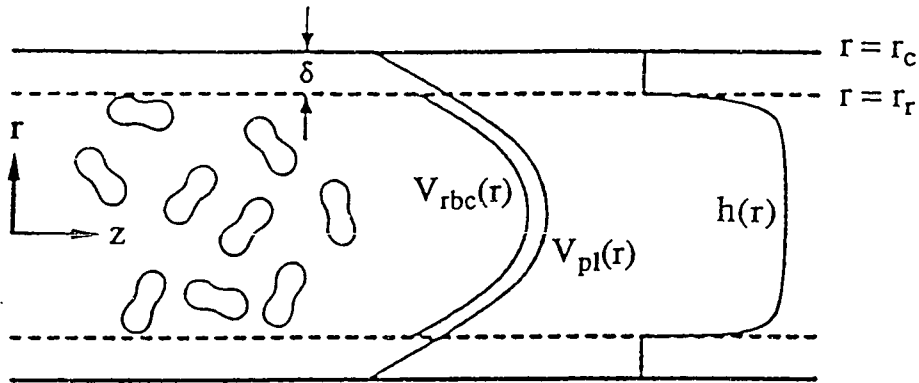


Figure 2.4: RBC and plasma velocity profiles and hematocrit profile of RBC suspensions flowing in microvessels.

Blunting of the flow profile is a function of hematocrit, flow rate and microvessel diameter; profiles were found to be blunt at high hematocrits and low flowrates, and/or in small microvessels. With increasing diameter, the profile approaches a parabolic form, such that in vessels above $75\ \mu\text{m}$ in diameter the deviation from a parabolic profile is below 5% under *in vitro* conditions (Bugliarello and Sevilla, 1970; Lee *et al.*, 1983). However, it should be mentioned that more blunted profiles were reported from *in vivo* measurements in arterioles and venules (Pittman and Ellsworth, 1986). The central region travels at higher velocity than the average for the suspension as a whole. This together with the existence of the cell-depleted layer near the vessel wall cause the average hematocrit in the tube, H_T , to be generally less than that in the reservoir to which the blood is discharged to, H_D , under steady-state conditions. This phenomenon of H_T/H_D being less than one in vessels with diameter smaller than about $500\ \mu\text{m}$ is generally referred to as the Fahraeus effect (Cokelet, 1987).

Several flow models which take into account some or all of above mentioned flow characteristics have been proposed by different investigators with varying degrees of success. Most of the models assume a two layered flow consisting of a cell-depleted

wall layer surrounding a core of suspension. The hematocrit and flow relationships used in this work are the same as those which were used by *Nair et al.* (1989). The description of RBC distribution in the vessel used by *Nair et al.* (1989) is of the form suggested by Lih (1969), with a modification to exclude the cell-free region. The velocity profile of RBC suspension in microvessel was treated as parabolic with a slight blunting in the center to account for the deviation from the Poiseuillean profile.

2.2.1.a Hematocrit Profile

From observations of hematocrit profiles (*Caro et al.*, 1978; Goldsmith and Turitto, 1986), it has been found that the radial hematocrit distribution can be expressed as:

$$h(r) = h_m \left[1 - \left(\frac{r}{r_r} \right)^{m'} \right] \quad (2.13a)$$

$$h(r) = 0 \quad (2.13b)$$

$$(h_m \geq 0, m' \geq 0)$$

where

r is the radial coordinate.

$h(r)$ is the hematocrit profile, the volume fraction of RBCs at any radius r .

r_r is the radius of the cell-rich region, the difference of tube radius and the thickness of the cell-free layer.

r_c is the radius of the microvessel.

h_m and m' are constants which need to be determined.

The cell-free layer adjacent to the capillary wall, δ , was taken as that due to geometric consideration alone (see Figure 2.4):

$$\delta = r_c + t_{rbc} - \sqrt{r_c^2 - r_{rbc}^2} \quad (2.14)$$

where

r_{rbc} is the radius of the RBC disc.

t_{rbc} is the maximum half thickness of the RBC disc.

2.2.1.b Velocity Profiles

Different velocity profiles are used for the plasma and the RBCs (Figure 2.4). The profiles are parabolic with a slight blunting, and differ by a constant - the slip.

$$V'_{pl}(r) = A \left[1 - \left(\frac{r}{r_c} \right)^2 \right] \quad r_r \leq r \leq r_c \quad (2.15a)$$

$$V_{pl}(r) = D \left[1 - B \left(\frac{r}{r_c} \right)^2 \right] \quad 0 \leq r \leq r_r \quad (2.15b)$$

$$V_{rbc}(r) = D (1 - slp) \left[1 - B \left(\frac{r}{r_c} \right)^2 \right] \quad 0 \leq r \leq r_c \quad (2.15c)$$

$$(0 \leq B \leq 1) \text{ and } (0 \leq slp \leq 1)$$

where

B is the blunting factor based on Pittman and Ellsworth's work (1986).

$V_{pl}(r)$ and $V'_{pl}(r)$ are the plasma velocities at radius r in the cell-free and cell-rich region, respectively.

slp is a "slip" constant based on Sinha's work (1936). It is the difference in the velocity of the suspending fluid and the particle at a particular point due to the finite size of the particle, used as 0.1 in all cases.

$V_{rbc}(r)$ is the RBC velocity at radius r in the cell-rich region.

A and D are constants corresponding to centerline velocities which need to be determined for each case.

Because RBCs are semi-solid entities suspending in the plasma, the properties such as velocities and hematocrit actually vary with position in a discontinuous fashion.

However, as a simplification, these properties are treated here as varying continuously. So, for example, the RBC velocity at a given radial position is an average velocity averaging over time, even though at any given instant of time that particular position may or may not be occupied by a RBC. The parameters A , D , h_m , and m can be obtained by simultaneous solution of equations which describe: the continuity of the plasma velocity profile, the overall RBC mass balance, the overall plasma mass balance and the definition of tube hematocrit (see Section 6.1.5.d).

2.2.2 Shear-induced Augmentation of Gas Transport in Blood

The presence of particles is expected to increase the rate of transverse mass transport in flowing suspensions over the rate in the suspending medium alone. It is postulated that the augmentation in transport rates is due to lateral fluid movements caused by particle rotations and collisions. Prediction of mass transfer rates is generally more complicated for flowing suspensions than for simple Newtonian fluids. However, mass transfer equations and correlations for Newtonian fluids might work well for suspensions provided the proper “effective” diffusivity is used. In reality, the transverse mass flux vector is consisted of two parts, effective diffusion under stationary flow condition and convection due to the lateral fluid movements; consequently, the “effective” diffusivity lumps these two terms together.

Leal (1973) and Nir and Acrivos (1976) considered the cases of dilute suspensions of deformable droplets in the limit of low and high Peclet numbers, respectively; both suggested a linear dependence of enhanced diffusivity on particle concentration, H_D . Increases in H_D should causes increases in transport rates; until particle crowding begins to restrict the lateral excursions of the particles. At very high particle concentrations ($H_D=0.99$), dispersive particle migration of particle is reduced, suggesting that augmentation is zero. Using these type of augments, Zydeny and Colton

(1988) have suggested the following empirical correlation for this enhanced solute (O_2) transport:

$$D_{rbc} = a^2 \gamma \zeta H_D (1 - H_D)^\sigma \quad (2.16)$$

where

D_{rbc} is the shear-induced diffusion coefficient of red blood cells.

a is the particle radius of red cell.

γ is the local shear rate.

ζ and σ are empirically fitted parameters.

H_D is the volume fraction of the suspended red blood cells or hematocrit.

For deformable particles (liquid drops and red cells) of characteristics radius a in a local shear rate γ , the numerous data on particle and saturated red cell diffusion were empirically fitted to give values for parameters ζ and σ , and the best fit values are $\zeta=0.15$ and $\sigma=0.8$. The excellent agreement between the above correlation and the experimental data suggested that their concept of augmented solute transport arising primarily from shear-induced particle and fluid migration and not from particle rotation is reasonable, at least for particle volume fractions which are either very low nor extremely high. This empirical model can be used to quantify the augmentation of oxygen transport observed under condition in which hemoglobin is not actively involved in the transfer process.

Since oxygen is largely transported by attachment to the hemoglobin of red cells, diffusion of red cells can produce an additional increased rate of mass transfer. Lateral migrations of red cells move oxygen-saturated red cells to unsaturated region where oxyhemoglobin could serve as a strong source for release of oxygen; conversely, unsaturated hemoglobin could serve as a strong sink for oxygen uptake on subsequent radial migration into an oxygen-saturated region. In an attempt to incorporate the

amplifying effect due to the oxygen storage potential of the hemoglobin into the picture, the red cells are treated as flat disks with their faces parallel to the wall and occasionally undergo flip-flop end over end. Consequently, one-dimensional oxygen transfer from plane sheets of hemoglobin is assumed. The total oxygen flux through the suspension can be expressed as follows (Zydney and Colton, 1988):

$$\begin{aligned} \text{Total } O_2 \text{ flux} = & -D_{O_2, SF} \frac{\partial}{\partial r} [h(r) [O_2]_{rbc} + (1 - h(r)) [O_2]_{pl}] \\ & - D_{O_2, rbc}^S \frac{\partial}{\partial r} [h(r) ([O_2]_{rbc} + [HbO_2])] - D_{O_2, pl}^S \frac{\partial}{\partial r} [(1 - h(r)) [O_2]_{pl}] \end{aligned} \quad (2.17)$$

where

r is the direction which is parallel to the velocity gradient.

$D_{O_2, SF}$ is the effective diffusivity of oxygen under unshared condition.

$D_{O_2, rbc}^S$ and $D_{O_2, pl}^S$ are the shear-induced oxygen diffusivities in the red cell and plasma phases, respectively.

$[O_2]_{rbc}$ and $[O_2]_{pl}$ are the dissolved oxygen concentrations inside the RBC and in the plasma, respectively.

$[HbO_2]$ is the concentration of oxygen that is bound as oxyhemoglobin.

If particle rotations make a negligible contribution to the overall oxygen flux, then $D_{O_2, rbc}^S = D_{O_2, pl}^S = D_{rbc}$; and D_{rbc} is given by Equation (2.16). If the gradient in RBC volume fraction is negligible, then $h(r)$ is a constant which is independent of position and is equal to H_D . In addition, if chemical reaction of oxygen and hemoglobin takes place rapidly by comparison to diffusion, it may be assumed that the free and bound oxygen are in instantaneous equilibrium and that the two concentrations are related through the ODC. Furthermore, if the solubility coefficients of oxygen in the red cell and the plasma are assumed approximately equal, then the total oxygen flux may be written as

$$Total\ O_2\ flux = -D_{O_2,SF} \frac{\partial[O_2]}{\partial r} - D_{rbc} \frac{\partial[O_2]}{\partial r} - H_D D_{rbc} C_{heme,rbc} \left(\frac{dS}{d[O_2]} \right) \frac{\partial[O_2]}{\partial r} \quad (2.18)$$

With the driving force taken to be the concentration of the total dissolved oxygen in the suspension, $[O_2]$, the effective diffusion coefficient becomes

$$D_{O_2,eff} = D_{O_2,SF} + D_{rbc} (1 + m) \quad (2.19a)$$

$$\text{and } m = \frac{H_D C_{heme,rbc}}{\alpha_{O_2}} \frac{dS}{dP_{O_2}} \quad (2.19b)$$

where

$D_{O_2,eff}$ is the effective diffusivity of oxygen under shared condition.

$C_{heme,rbc}$ is the heme concentration inside the RBC.

α_{O_2} is the Bunsen solubility coefficient of O_2 in the blood.

$\frac{dS}{dP_{O_2}}$ is the slope of the ODC, and it is a nonlinear function of P_{O_2} .

m is the oxygen carriage potential of hemoglobin calculated based on the local operating slope of the ODC (Equation (2.19b)).

The expression for $D_{O_2,eff}$ derived here is the same as that obtained by Zydney and Colton (1988), except that they had a different interpretation of m . They defined m as the ratio of bound to free oxygen concentrations and assumed it to be approximately constant.

Zydney and Colton (1988) were not the first to derive an O_2 augmentation model. In fact, Diller and Mikic (1983) had previously developed a similar model for augmented oxygen transport in blood which was based on the concept that shear-induced motion of red cell can be modeled in an analogous manner to the Brownian motion of molecules. Their results for $D_{O_2,eff}$ can be expressed as

$$D_{O2,eff} = D_{O2,SF} + D_{rbc} g (H_D + M) \quad (2.20a)$$

$$\text{and } M = \frac{H_D C_{heme,rbc}}{\alpha_{O2}} \left(\frac{S|_{P_{O2}=P_{O2,ext}} - S|_{P_{O2}=P_{O2,in}}}{P_{O2,ext} - P_{O2,in}} \right) \quad (2.20b)$$

where

$P_{O2,ext}$ is the oxygen tension in the environmental chamber surrounding the membrane film.

$P_{O2,in}$ is the oxygen tension of the inlet red cell suspension.

$S|_{P_{O2}=P_{O2,ext}}$ and $S|_{P_{O2}=P_{O2,in}}$ are the fractional saturations of the hemoglobin molecules under the oxygen partial pressures of $P_{O2,ext}$ and $P_{O2,in}$, respectively.

g is a measure of the departure of the hemoglobin-oxygen binding reaction from equilibrium ($0 \leq g \leq 1$); in the limit of reaction equilibrium, $g=1$.

M is the oxygen carriage potential of hemoglobin calculated based on the overall operating slope of the ODC (Equation (2.20b)).

Equation (2.20a) contains one slight error; namely, the factor g multiplied by both H_D and M terms. This is inappropriate, since nonequilibrium only effects the bound oxygen concentration and not the dissolved oxygen. In the limit of reaction equilibrium, $g=1$, Equations (2.20a) and (2.20b) yield an effective diffusivity that is different from that given by Equations (2.19a) and (2.19b). The major difference is that Diller and Mikic replaces m , the local operating slope, with M , the overall operating slope. Another difference is that Equation (2.20a) does not include the term $(1-H_D)D_{rbc}$; this is due to the fact that Diller and Mikic neglected the effect of dispersive fluid migrations in their analysis. For unsaturated blood where $M \gg 1$, $D_{O2,eff}$ is dominated by dispersive cell motion; and as a result, the contribution due to $(1-H_D)D_{rbc}$ is negligible. However, the dispersive fluid motion could become more important under conditions of high shear rates and low values of overall operating slopes.

CHAPTER 3

REVIEW OF COUPLED OXYGEN AND CARBON DIOXIDE TRANSPORT MODELS

A great number of mathematical analyses of various aspects of respiratory gas exchange has appeared in the literature. These can be divided into the following categories:

1. Models of exchange between RBC and plasma alone (e.g. Sirs, 1970; Klocke, 1973; Forster and Crandall, 1975; Coin and Olson, 1978; Salathe, 1981; Vandegriff and Olson, 1984b and 1984c; for recent reviews on O₂ and CO₂ transport see Baumann *et al.*, 1987 and Klocke, 1987). These studies aimed specifically at a determination of the rate-limiting steps in O₂/CO₂ exchange between two phases of the blood, and have contributed to our knowledge of RBC membrane permeability to gases and exchange of anions, as well as the kinetics of diffusion and chemical reaction within the red cell.
2. Models of exchange of O₂ and CO₂ between blood and the alveoli (Forster, 1957; Wagner and West, 1972; Hill *et al.*, 1973; Hlastala, 1973; Bidani *et al.*, 1978; Singh *et al.*, 1980; Sharan *et al.*, 1987; for a recent review on CO₂ exchange in the lung, see Bidani and Crandall, 1988). These analyses considered the Bohr and Haldane effects, and the implications of a finite diffusional resistance in the lung membrane.
3. Analysis of O₂ transport to tissue (Reneau *et al.*, 1967; McCracken *et al.*, 1972; Meldon and Garby, 1975; Artigue, 1980; Baxley and Hellums, 1983; Federspiel and Popel, 1986; Nair, 1988; Ellsworth *et al.*, 1988; Weerappuli and Popel, 1989; for a recent review on the subject, see Popel, 1989). Consideration was given to the diffusion of O₂ in up to three dimensions, as well as in tissue surrounding the capillary networks. Metabolic O₂ consumption has been modeled by either a zero order, first order, or

Michaelis-Menten kinetic expression. Through the application of complex mathematical analysis, a firmer theoretical base has been given to speculations regarding the distribution of O_2 in tissue, and also in regard to vessel orientation and flow directions within the capillary clusters. Most of the models, however, involved a simplified representation of blood chemistry.

4. Calculations of the rate of gas exchange between flowing blood and gas phase in membrane oxygenators (diameters of several hundred μm) or artificial membrane microvessels (diameters less than 100 μm). While these have been directed mostly towards the design of artificial lungs, and not *in vivo* transport, much of the physics and chemistry is the same as have been applied to the analyses of physiological processes. Therefore, these models have utility in providing guidance in designing oxygenators and aiding in the interpretation of membrane lung function, but also in providing guidance in the understanding of gas transport in arterioles and venules of the microcirculation.

A more detailed review on the subject matter of category 4 will be present here because the subject is closely related to the objective of this thesis which is to model the gas transport by flowing blood in microvessels.

3.1 Exchange between Red Blood Cells and Plasma alone and Transport of Gas to and from Blood Flowing in Capillaries

Under equilibrium conditions, the total amount of CO_2 held by the blood may be calculated from the CO_2 dissociation curve of total CO_2 content versus dissolved CO_2 (measured as P_{CO_2}) which depends on pH and O_2 saturation; as in the case of O_2 , the dissociation curve may be measured experimentally. However, during CO_2 exchange the reaction rates and transport effects may be important. Although the rate of each individual processes (as illustrated in Figure 2.1) had been measured separately *in vitro*,

these processes occur simultaneously during blood O_2/CO_2 exchange. To obtain an estimate of the rate of overall gas exchange, or the importance of each step in limiting its rate, these measurements must be considered in a model system, including all different chemical reactions and diffusion elements. A number of investigations have been undertaken to determine the specific influence of the interrelated reaction rates and transport mechanisms on gas transport in the lungs and tissues both experimentally and mathematically. Only a sampling of the literature is quoted here in this chapter; excellent summaries of the results from previous research are included in *Biophysics and Physiology of Carbon Dioxide* (Bauer *et al.*, 1980), *Blood Oxygen Transport* (Baumann *et al.*, 1987) and *Carbon Dioxide Transport* (Klocke, 1987) in *Handbook of Physiology*, and in Popel's review paper on Theory of Oxygen Transport to Tissue (Popel, 1989) in *Critical Reviews in Biomedical Engineering*.

Roughton (1935) in his classical review of CO_2 transport should be given credit for pointing out the slow *pH* reaction and suggesting that uncatalyzed hydration of CO_2 in the plasma ultimately would limit the exchange of CO_2 . This idea was extended by Sirs (1970) whose approximate calculation indicated that while carbonic anhydrase accelerates the equilibration between $[CO_2]_{rbc}$, $[H^+]_{rbc}$ and $[HCO_3^-]_{rbc}$ inside the RBC, it has no effect on the speed of these processes in the plasma, so that the necessary alkalization of this phase takes place by the uncatalyzed dehydration of HCO_3^- . The exchanges of Cl^- and HCO_3^- across the RBC membrane have a negligible effect on plasma *pH*. This uncatalyzed reaction requires several tens of seconds to complete and does not have time to occur in the lung capillaries, but must continue in the blood as it travels through the pulmonary veins and into the arterial tree.

The rates at which blood O_2 and CO_2 equilibrate with alveolar gas depend on the rates of the various chemical reaction events as well as the pulmonary diffusing capacity and affinity of the blood for O_2 and CO_2 . Roughton and Forster (1957) measured the

overall reaction rate of O_2 with hemoglobin and indicated its importance to the rate of gas exchange in the lungs. Earlier mathematical simulations of pulmonary gas exchange had generally not consider chemical reactions. For example, Defares and Visser (1962) and Milhorn and Pulley (1968) calculated changes in P_{O_2} and P_{CO_2} along the pulmonary capillaries on the basis of mixed venous values, diffusing capacities, and simplifying assumptions about the dissociation curve shapes. Neither of these studies attempted to consider chemical reaction rates. Wagner and West (1972) presented calculations which included CO_2 reaction rates as well as O_2 reaction rates and O_2/CO_2 interactions. They allowed for the finite rate of chemical reactions of CO_2 by choosing representative values for the overall rate of CO_2 reaction with blood to predict changes in P_{O_2} and P_{CO_2} as function of time during the capillary transit. They also considered the effects of diffusion limitation and ventilation-to-perfusion inequality on pulmonary gas exchange. This was essentially a compartmental model in which a mean value of P_{O_2} was used in the formulation.

Hill *et al.* (1973a) presented a computer simulation study of a model for the exchange of CO_2 and O_2 between fetal and maternal blood in the placenta, which they subsequently modified to describe pulmonary CO_2 and O_2 exchange (Hill *et al.*, 1973b). It was a one-dimensional model of gas exchange that takes place in the lungs, and the role played by convection and diffusion in the transport of the gases was not taken into account. Rather than using an overall rate constant for CO_2 , as did Wagner and West, they included the commonly recognized reactions and processes, including the chloride shift and O_2/CO_2 interactions. The reaction of CO_2 with hemoglobin was included in their studies, and the description of the anion exchange was based on an empirical relationship for the Gibbs-Donnan ratio. Incorporating exchange between cells and plasma, they predicted a slow readjustment of plasma pH and related effects after capillary transit. Calculations performed that assumed the rate of hydration of CO_2 in the

plasma to be equal to that in RBC did not change appreciably the total transfer rate of CO_2 , although the reaction path was different. Sirs (1970) and Hill *et al.*'s findings were consistent with the experimental work of Forster and Crandall (1975).

In vitro confirmation of Roughton's postulate was provided by Forster and Crandall (1975) when they showed that the rate of *pH* equilibration in RBC suspensions was two orders of magnitude slower than the rate of uptake of CO_2 (half time of 2 and 0.045 sec, respectively). It was further shown that the slow readjustment of plasma *pH* can be eliminated by adding carbonic anhydrase to the plasma. They also considered a simplified model for describing the time course of exchange between RBCs and the extracellular fluid during O_2 uptake. This model included some of the chemical processes important in CO_2 uptake by blood but not the reaction of CO_2 with hemoglobin. In addition, the description of the exchange of anions between the plasma and RBCs in their model was based on the theory of electrodiffusion of ions (Goldman's solution to the Nernst-Planck equation which is given in *Biophysical Chemistry of Membrane Functions* by Kotyk *et al.*, 1988). A slightly more elaborate model for pulmonary exchange was later on given by Bidani *et al.* (1978). Agreement of both catalyzed and uncatalyzed experiments with a simplified compartment model led them to conclude that *pH* does not reach its eventual equilibrium value in the lung. Result of experiments by Klocke (1973) also suggested that even dissolved CO_2 may not attain equilibrium during capillary transit.

Several investigators then designed experimental protocols to verify the presence of such slow *pH* changes in the arterial circulation in anesthetized animals. If plasma *pH* does not achieve chemical equilibration with P_{CO_2} and the bicarbonate system during transit through the lung, one would expect effluent blood *pH* to change with time. Using a stopped-flow *pH* apparatus, Hill *et al.* (1977) and Bidani *et al.* (1978) measured the *pH* of blood as a function of time after it had passed through the lungs and observed

a smaller than predicted pH change in blood leaving the lungs. Whereas in the laboratories of Crandall and O'Brasky (1978), Effros *et al.* (1978) and Klocke (1980), the question was approached from a different angle. Isolated lungs were perfused with fluid containing no hemoglobin or carbonic anhydrase and the effects on capillary exchanges observed. They observed no effluent perfusate pH disequilibrium which indicated that the perfusate CO_2 reactions was completed during the pulmonary capillary transits. Moreover, addition of carbonic anhydrase inhibitor (such as acetazolamide) to the perfusate yielded an increase in effluent pH with time. Consequently, they reached the conclusion that carbonic anhydrase was available to the perfusate in the lung capillaries and it was bound to the luminal surface of the endothelial cells. Carbonic anhydrase had been reported in cultured pulmonary endothelium (Ryan and Ryan, 1984) which provided the morphological support for such an enzyme location and distribution.

Salathe *et al.* (1981) presented a time-dependent study of acid/base balance in the microcirculation which involved the study of CO_2 transport and its relationship to O_2 transport, as well as a study of the buffer systems that are intimately connected to the transport of these gases. Their study did not take into account the transport of species due to diffusion, convection; and the exchange of HCO_3^- and Cl^- was regarded as passive electrodiffusion.

Singh *et al.* (1980) considered a model of a capillary slit exchanging O_2 and CO_2 through the plane walls. They formulated five balance equations for O_2 , CO_2 , Hb, HbO_2 and $HbCO_2$, and presented an order-of-magnitude analysis of the problem. These equations described convection of substances along the capillary, and facilitated transport of O_2 and CO_2 were included in the model. These researchers used the governing equations subsequently in a series of publications that presented numerical solution to the problem, took into account axial diffusion in the capillary and pulmonary membrane resistance, and considered unsteady processes (as summarized in Sharan *et al.*, 1987).

However, their governing O_2 - CO_2 -hemoglobin reaction appeared to be based on the assumption that O_2 and CO_2 compete for the same sites on the hemoglobin molecules which is significantly different from the known mechanism of gas transfer by blood.

Based on Krogh tissue cylinder geometry, Reneau *et al.*'s (1967, 1969) models for O_2 transport in a systematic capillary included a constant metabolic rate, radial O_2 gradients in the capillary, and the nonlinear aspects of O_2 storage within the RBCs. Under steady-state conditions, the effect of the blood velocity profile was studied while ignoring the existence of axial diffusion in both the capillary and tissue. In addition, the effects of variations in arterial P_{CO_2} were also studied. The unsteady or transient situation of O_2 transport were created by allowing arterial P_{O_2} to increase suddenly by keeping other factors constant. It was seen that the reaction in the capillary predominates over convection and molecular diffusion during initial times.

McCracken *et al.* (1972) studied the interacting effects of O_2 , CO_2 and glucose in the capillaries and tissue of the human brain. They did not consider the facilitated diffusion of the species and the kinetics of hemoglobin with O_2 and CO_2 in their model. They solved the system of interactive equations for describing the simultaneous transport of O_2 , CO_2 and glucose and concluded that the interaction of components such as O_2 and CO_2 in the capillary blood is very important in the transport of O_2 to tissue. Artigue (1980) used McCracken *et al.*'s work as a basis for further investigation. He considered both the steady-state and dynamic models of transport of O_2 , CO_2 , glucose and lactic acid. The facilitated diffusion and the interactions of O_2 and CO_2 (the Bohr and Haldane effects) were taken into account with empirical equations which were developed based on experimental data. However, the convective diffusive equations were simplified by assuming local chemical equilibrium. The effects of blood pH on the dissociation curves for O_2 and CO_2 were not included. He attempted to take into account the two-phase nature of blood by considering the RBCs to be a separate phase which is uniformly

distributed in the blood according to the prescribed hematocrit. Diffusional resistance between the cells and the plasma was taken into account by a means of a mass transfer coefficient.

Baxley and Hellums (1983) developed a model for intracapillary transport in which they considered RBCs to be cylindrical slugs and included radial diffusion and reaction within the RBC and also included diffusion in the plasma gap between the RBCs and the capillary wall. They also took into account the effective flux from the RBCs due to the presence of alternate plasma gaps between them. Federspiel and Popel (1986) developed a somewhat different model for small capillaries in which they treated RBCs as spheres and took RBC spacing, RBC velocity and RBC clearance as parameters. They solved the problem of intracapillary O_2 transport numerically and presented the result in terms of a mass transfer coefficient. Both groups found an increased resistance due to the discrete nature of blood over hemoglobin solutions. There are other theoretical studies on intracapillary gas transport; however, none of these models have yet been validated by experiments.

These studies offered insight into the integrated changes which occur during physiological transfer. However, for a number of reasons, the results and conclusions may not apply directly when considering gas transport in microvessels and artificial membrane oxygenators. Although the steps involved for gas transport are the same, but the mass transfer and flow characteristics are significantly different. On one hand, the diffusional process is very efficient at nearly capillary dimensions; on the other hand, diffusion in blood becomes an inefficient means of transport and is known to limit gas transfer in large microvessels and macroscopic flow channels whose diameters are orders of magnitude greater than that of lung or tissue capillaries. Additionally, cellular level effects are somewhat masked in the large microvessels due to the fact that most of the transport resistance lies in the plasma phase. Therefore, a rigorous and detailed

description of intraerythrocytic activities is probably not necessary for the formulation of large microvessel models.

3.2 Mutual Transfer of Oxygen and Carbon Dioxide to and from Blood in Artificial Membrane Tubes

Mathematical models for describing the mass transfer of O_2 and CO_2 by blood flowing in blood vessels or artificial membrane tubes can be obtained from the species continuity equation which includes convection, diffusion and chemical reaction of various species in the blood. A general approach to the transfer of O_2 and CO_2 would require a three phase model of the blood with interphase exchange of various species. Therefore, equations for various species can be written for the RBC, RBC membrane and extracellular plasma phases. A material balance for species i in phase k can be written as:

$$\frac{\partial [C_i]_k}{\partial t} + \text{div} (\vec{V} [C_i]_k) = \nabla \cdot D_{i,k} \nabla [C_i]_k + R_{i,k} \quad (3.1)$$

where

\vec{V} is the velocity vector.

$[C_i]_k$ is the concentration of species i in phase k .

$D_{i,k}$ is the diffusion coefficient of species i in phase k .

$R_{i,k}$ is the rate of reaction which generates i in phase k .

The material balance of species i inside the RBC phase would be coupled through continuity of flux and concentration of i to the continuity equation of species i for the RBC membrane phase at the inside surface of the membrane. Similarly, continuity of

equation of specie i for the plasma phase would be coupled to the equation for the RBC membrane at the outside surface of the membrane.

The simplified approach which had been used by most of the investigators who modeled O_2 and CO_2 transfer was to consider overall mass balances for O_2 and CO_2 that are applied to a combined RBC-RBC membrane-plasma continuum. In addition, the majority of analysis also considered steady state transfer and local chemical equilibrium. Thus Equation (3.2), written for one phase, is applicable, but the diffusion coefficients must be interpreted as effective values for the continuum to account for the heterogeneity of the blood.

$$\sum_i \text{div}(\vec{V}[C_i]) = \sum_i \nabla \cdot D_i \nabla [C_i] \quad (3.2)$$

Equation (3.2) represents summation over the sets of equations obtained for various forms of O_2 and CO_2 in the blood individually; and it sums both total reaction for O_2 and CO_2 separately to be zero. Therefore, Equation (3.2) is applicable to both species, O_2 and CO_2 . Furthermore, assuming a tubular channel with axial symmetry and invoking assumptions (1) - (3), listed below, leads to Equations (3.3) and (3.4).

- (1) There is negligible axial and angular diffusion.
- (2) Transport by convection occurs only in the axial direction.
- (3) Species i has constant diffusivity.

$$V(r) \frac{\partial [O_2]_{total}}{\partial [O_2]} \frac{\partial [O_2]}{\partial z} = \frac{D_{O_2}}{r} \frac{\partial}{\partial r} \left[\left(1 + \frac{D_{HbO_2}}{D_{O_2}} \frac{\partial [HbO_2]}{\partial [O_2]} \right) \left(r \frac{\partial [O_2]}{\partial r} \right) \right] \quad (3.3)$$

$$V(r) \frac{\partial [CO_2]_{total}}{\partial [CO_2]} \frac{\partial [CO_2]}{\partial z} = \frac{D_{CO_2}}{r} \frac{\partial}{\partial r} \left[\left(1 + \frac{D_{HCO_3}}{D_{CO_2}} \frac{\partial [HCO_3^-]}{\partial [CO_2]} + \frac{D_{HbCO_2}}{D_{CO_2}} \frac{\partial [HbCO_2]}{\partial [CO_2]} \right) \left(r \frac{\partial [CO_2]}{\partial r} \right) \right] \quad (3.4)$$

where

r and z are the radial and axial coordinates, respectively, of the tubular channel.

$V(r)$ is the velocity profile in the z direction.

D_{O_2} and D_{CO_2} are the effective diffusivities of dissolved O_2 and CO_2 in the suspension, respectively.

D_{HbO_2} and D_{HbCO_2} are the effective diffusivities of oxyhemoglobin and carbamino hemoglobin in the suspension, respectively.

$D_{HCO_3^-}$ is the effective diffusivity of bicarbonate ion in the suspension.

$[O_2]$ and $[CO_2]$ are the physically dissolved concentration of O_2 and CO_2 in the suspension, respectively.

$[HbO_2]$ and $[HbCO_2]$ are the concentrations of oxyhemoglobin and carbamino hemoglobin in the suspension, respectively.

$[HCO_3^-]$ is the concentration of bicarbonate ion in the suspension.

$[O_2]_{total}$ is the total O_2 content which includes both oxyhemoglobin and dissolved O_2 .

$[CO_2]_{total}$ is the total CO_2 content which includes bicarbonate ion, carbamino hemoglobin, dissolved CO_2 and carbonic acid.

Here, the differential balances have been written in terms of the dissolved O_2 and CO_2 , $[O_2]$ and $[CO_2]$. The convective terms in Equations (3.3) and (3.4) account for axial transport of all O_2 and CO_2 species (denoted by $[O_2]_{total}$ and $[CO_2]_{total}$, respectively). The diffusive terms account for only the major diffusing species - specifically, for O_2 there are dissolved O_2 and oxyhemoglobin; and for CO_2 there are dissolved CO_2 , bicarbonate ion and carbamino hemoglobin. Again, the diffusion coefficients are effective values in the above development. The following review is presented in chronological order.

Buckles (1966) and Buckles *et al.* (1968)

Buckles and coworkers studied the steady-state transfer of O_2 to flowing blood, using a straight silicone rubber membrane tube system. Their analysis was based on a microscopic local equilibrium model, but involved the convective terms and even incorporated a correction for non-Newtonian flow effects. The continuity equation for O_2 is given in Equation (3.5), except for the fact that Buckles *et al.* used the Casson model for the velocity profile. Buckles also did a full analysis of the gas transport through the wall and considered the wall flux as one of the boundary conditions. Experimental measurements of O_2 uptake by deoxygenated (or reduced) blood at 38 °C and constant P_{CO_2} agreed moderately well with the transfer rates predicted by the numerical solution of Equation (3.5), using an effective value of $D_{O_2}=1.4 \times 10^{-5} \text{ cm}^2/\text{sec}$, although the data did not follow the shape of the theoretical curve closely.

Weissman and Mockros (1967 and 1969)

The O_2 transport model developed by Weissman and Mockros is very similar in nature to the model developed by Buckles (1966). Weissman and Mockros' O_2 transport differential equation, transformed to the symbols used elsewhere in this paper, is given below. Equation (3.5) was obtained from Equation (3.3) by further introducing the approximation that the diffusion of oxyhemoglobin is sufficiently small relative to the diffusion of O_2 to be neglected.

$$V(r) \left(1 + \frac{d[HbO_2]}{d[O_2]} \right) \frac{\partial [O_2]}{\partial z} = \frac{D_{O_2}}{r} \frac{\partial}{\partial r} \left(r \frac{\partial [O_2]}{\partial r} \right) \quad (3.5)$$

where

$V(r)$ is a parabolic velocity profile in tubes. Because the non-Newtonian nature of the blood, the velocity profile should be more appropriately described by an integrated form of Casson equation. However, the Casson model approximates a parabolic profile

in the flow range of conditions investigated by these investigators; therefore, a simple parabolic Newtonian type model is reasonable here.

$d[HbO_2]/d[O_2]$ is a function proportional to the slope of oxyhemoglobin dissociation curve (ODC); and it is related to the ODC through the following relationship:

$$\frac{d[HbO_2]}{d[O_2]} = \frac{C_{heme,total}}{\alpha_{O_2}} \frac{dS}{dP_{O_2}} \quad (3.6)$$

where S is the fraction of the total hemoglobin O_2 binding sites that are occupied by O_2 ; $C_{heme,total}$ is the total heme concentration in the medium; α_{O_2} is the Bunsen solubility coefficient O_2 in blood; and P_{O_2} is the partial pressure of O_2 . dS/dP_{O_2} is the slope of the ODC. Weissman and Mockros obtained the description of the relationship between S and P_{O_2} by fitting an exponential function to the ODC.

They also ignored the effect of the wall on the overall gas transport rate; i.e., they neglected the mass transfer resistance of the wall. The boundary conditions which were imposed for this problem are

$$[O_2] = [O_2]_o \quad \text{at } z = 0 \quad \text{for } 0 \leq r \leq r_c \quad (3.7a)$$

$$\frac{\partial [O_2]}{\partial r} = 0 \quad \text{at } r = 0 \quad \text{for } z > 0 \quad (3.7b)$$

$$[O_2] = [O_2]_\infty \quad \text{at } r = r_c \quad \text{for } z > 0 \quad (3.7c)$$

The term, $d[HbO_2]/d[O_2]$, makes this equation nonlinear. Any attempt at linearization, such as replacing the slope of ODC by a constant, for instance, eliminates a major aspect of the problem; thus the above system of equations, Equations (3.5) - (3.7), was solved numerically. Weissman and Mockros did not predict a priori an O_2 diffusivity for blood.

Instead, for each experiment they calculated the appropriate diffusivity which would bring the solution of their equations close to agreement with the experimental findings. In addition, the experimental device which they used was an oxygenator alone which did not simulate the lung's function; a constant CO_2 partial pressure was maintained to prevent simultaneous diffusion of CO_2 .

As an extension, Weissman and Mockros used a simplified form of Equation (3.4) to theoretically predict CO_2 removal in a permeable membrane tube. They neglected the diffusion of bicarbonate ion and carbamino hemoglobin; and assumed that in the physiological pressure range $[\text{CO}_2]_{\text{total}}$ and $[\text{CO}_2]$ for arterial blood are related through the following linear relationship

$$[\text{CO}_2]_{\text{total}} \left(\frac{\text{moles}}{\text{liter}} \right) = 1.14 \times 10^{-2} + 10.0 [\text{CO}_2] \quad (3.8)$$

The slope of total CO_2 versus dissolved species relationship was given as $d[\text{CO}_2]_{\text{total}}/d[\text{CO}_2] = 10$. In addition, only diffusion of dissolved CO_2 was considered; thus Equation (3.4) was simplified to the following

$$10 V(r) \frac{\partial [\text{CO}_2]}{\partial z} = \frac{D_{\text{CO}_2}}{r} \frac{\partial}{\partial r} \left(r \frac{\partial [\text{CO}_2]}{\partial r} \right) \quad (3.9)$$

Equation (3.9) is a linear partial differential equation and the boundary conditions selected were similar to those that are imposed on the O_2 transfer problem, Equations (3.7a) - (3.7c). The solution to this boundary problem, a nonreactive problem for the tubular geometry, was given by Graetz's solution. However, no experimental corroboration were offered to verify the CO_2 transport model. Therefore, Weissman and Mockros' model did not allow the influence of CO_2 and H^+ content of the blood on the O_2 transport (the Bohr effect) and vice versa the impact of oxygen saturation on the CO_2

transport (the Haldane effect). They neglected the interdependence of O₂ and CO₂ transport and decoupled the problem into two independent transfer processes.

Bradley (1969); Bradley and Pike (1971)

Bradley and Pike also considered CO₂ transport in the presence of simultaneous O₂ transport in a tubular geometry. Two models were developed, and the first one considered the steady state oxygenation as independent of CO₂ removal. The second model considered CO₂ transfer on the simultaneous O₂ transfer. The resulting convective-diffusive equations for O₂ and CO₂ were similar to that obtained by Weissman and Mockros; except for the fact that the influence of a changing O₂ saturation on the CO₂ transfer was included. Bradley and Pike modeled the ODC by an exponential fit. In addition, they also assumed a linear relationship between total CO₂ content and P_{CO_2} and included a linear correction for oxygen saturation to account for the Haldane effect.

$$[CO_2]_{total} \left(\frac{\text{moles}}{\text{liter}} \right) = 1.67 \times 10^{-2} - 3.34 \times 10^{-3} S + 2.04 \times 10^{-4} P_{CO_2} \quad (3.10)$$

This correlation was reported for T at 38 °C and hematocrit of 45%, and P_{CO_2} is the partial pressure of CO₂ in mmHg.

The equation for CO₂ transport which is given by Equation (3.11) was solved numerically and simultaneously with an O₂ transport equation.

$$V(r) \left[\frac{2.04 \times 10^{-4}}{\alpha_{CO_2}} \frac{\partial [CO_2]}{\partial z} - 3.34 \times 10^{-3} \frac{\partial S}{\partial z} \right] = \frac{D_{CO_2}}{r} \frac{\partial}{\partial r} \left(r \frac{\partial [CO_2]}{\partial r} \right) \quad (3.11)$$

where α_{CO_2} is the effective solubility coefficient for CO₂ in the suspension. Boundary conditions, Equations (3.7a) and (3.7b) were used. Furthermore, they relaxed the

assumption of negligible wall resistance made by Weissman and Mockros which would not be valid for membrane tubes that are not as permeable and/or have a fairly high wall thickness to inner diameter ratio. They introduced the flux matching boundary condition

$$D_{CO_2} \frac{\partial [CO_2]}{\partial r} = D_{CO_2,m} \frac{\partial [CO_2]_m}{\partial r} \quad \text{at } r = r_c \quad \text{for } z > 0 \quad (3.12)$$

where

$D_{CO_2,m}$ is the diffusion coefficient of CO_2 in the membrane.

$[CO_2]_m$ is the concentration of CO_2 in the membrane.

Although data was taken using only partial pressure measurements, there was large scatter in the results. In addition, Bradley and Pike's model predicted the amount of CO_2 transferred to be less than that found experimentally. The fact that the model underpredicted the measured transfer rates might be due to the neglect of simultaneous diffusion of CO_2 in the form of bicarbonate ion.

Villarroel (1970) and Villarroel *et al.* (1971)

In continued studies of the gas exchange processes with flowing blood in membrane system, Villarroel *et al.* explored the effect of steady versus pulsatile flow conditions, using a macroscopic model similar to that used by Weissman and Mockros but incorporating non-Newtonian flow effects and accounting for the tube wall resistance. They found that use of the Casson equation was not necessary for the steady-state flow range studied. Therefore, a parabolic Newtonian velocity profile was incorporated for the steady-state flow conditions, and a flux matching boundary condition was employed. The ODC was curve fitted with a function which consists of two dependent variables, P_{CO_2} and pH . The total CO_2 content approximation used was that of Weissman and Mockros (Equation (3.8)). Therefore, only the fixed acid Bohr

effect was accounted for here and the CO_2 Bohr effect and the Haldane effect were neglected. As with previous investigators, bicarbonate ion diffusion was neglected. In addition, they provided for shear augmented diffusion but found this unnecessary for the flow range studied.

A numerical solution to this model was developed which allowed both O_2 and unfacilitated CO_2 profiles to be computed simultaneously. This, in turn, permitted the evaluation of the pH profile in the tube using the standard Henderson-Hasselbalch equation; however, the gross assumption that HCO_3^- was constant in the vessel was utilized for the above calculation. The ODC could then be corrected to these local conditions during the numerical integration. The application of this more detailed, coupled macroscopic model to experimental data obtained by previous workers, Buckles (1966) and Weissman and Mockros (1967), and their own data was found to result in improved fits. However, it should be mentioned that all those experiments considered only O_2 transfer in isolation because a constant CO_2 partial pressure was maintained to prevent simultaneous diffusion of CO_2 .

Fair and Weissman (1971)

Fair and Weissman modified the earlier Weissman and Mockros' straight tube theory to include the interrelationship of O_2 storage in the blood and the amount of CO_2 in the blood (the Bohr effect) and of CO_2 storage to the amount of O_2 in the blood (the Haldane effect). Empirically fit ODC including the Bohr effect and CO_2 buffer equation including the Haldane effect were used. However, a constant wall concentration was employed again. In order to avoid numerical difficulties in the solution, the wall concentration was chosen as a nominal small value (corresponding to $P_{\text{CO}_2}=1$ mmHg). By comparison with prior work of Weissman and Mockros (i.e., no coupling), it was shown that the inclusion of the Bohr and Haldane effects (i.e., coupling) did result in

changes in uptake rates; however, these are only on the order of $\pm 20\%$ and thus considered to be of secondary importance.

Dorson *et al.* (1971)

Dorson *et al.* treated blood as an overall continuum which has only dissolved and reacted CO_2 species in local equilibrium, and for tube flow at steady state the convective removal is balanced against the effective radial diffusion as represented by Equation (3.4). They neglected the carbamino hemoglobin's contribution to diffusion on the basis of its large molecular weight. Additionally, they assumed that the relationships of total CO_2 content and bicarbonate ion with dissolved CO_2 can be approximated in a linear form:

$$[\text{CO}_2]_{\text{total}} = E_i + F_s [\text{CO}_2] \quad (3.13a)$$

$$[\text{HCO}_3] = G_i + H_s [\text{CO}_2] \quad (3.13b)$$

where

E_i and F_s are the intercept and slope, respectively, of linearized dissolved CO_2 content versus total CO_2 content curve.

G_i and H_s are the intercept and slope, respectively, of linearized dissolved CO_2 content versus HCO_3^- content curve.

Upon introducing these additional assumptions, Equation (3.4) becomes

$$V(r) \frac{\partial [\text{CO}_2]}{\partial z} = \frac{D_{\text{CO}_2} \left(1 + \frac{D_{\text{HCO}_3}}{D_{\text{CO}_2}} H_s \right)}{F_s} \frac{1}{r} \frac{\partial}{\partial r} \left(r \frac{\partial [\text{CO}_2]}{\partial r} \right) \quad (3.14)$$

Along with the standard conditions which include Equations (3.7a) and (3.7b), the wall flux matching condition was used to determine the variable wall concentration:

$$D_{CO_2} \left(1 + \frac{D_{HCO_3}}{D_{CO_2}} H_s \right) \frac{\partial [CO_2]}{\partial r} = D_{CO_2, m} \frac{\partial [CO_2]_m}{\partial r} \quad (3.15)$$

Therefore, the entire complexity of multiple reacting and diffusing species is lumped into the ratio, $D_{CO_2} (1 + D_{HCO_3} H_s / D_{CO_2}) / F_s$, and the flux matching boundary condition, Equation (3.15).

Comparison of the model calculations with their experimental data were not completely satisfactory. A basic problem was that this approach relied on appropriate slope determinations for estimating the values of F_s and H_s . When blood acid/base was altered significantly from standard condition, the generalized charts that they used were of little value. In addition, for small wall resistances, steep internal CO_2 profiles further complicated selection of F_s and H_s . Furthermore, for large CO_2 transfer rates, a linear approximation of the total CO_2 content and HCO_3^- content versus $[CO_2]$ became a poor assumptions. However, they did report that the comparison was improved when measured slopes were used.

Chen (1972)

Chen theoretically studied CO_2 transfer in a single permeable tube. Total content curves were generated by using a published nomogram in conjunction with the plasma pH and plasma bicarbonate relationship. Numerical results were computed with and without bicarbonate ion diffusion. The relationship between the dissolved species and the convected and diffused reacted species were expressed mathematically as implicit derivatives which multiplied the convective and diffusive terms. He concluded that if bicarbonate ion diffusion occurred, it would significantly enhance CO_2 transfer. However, no data were reported to support this contention.

Sosa and Merchuck (1972)

This group of researchers studied the gas transfer in a film of blood flowing through a rectangular membrane artificial lung. Their mathematical analysis treated blood as a homogeneous, non-Newtonian fluid, in which the system P_{O_2} , P_{CO_2} and pH

were in equilibrium due to the reaction rate in the RBCs. They used more complicated empirical expressions to account for the interdependence of O₂ and CO₂ transport. For instance, the extent of hemoglobin saturation was fitted to be a function of the partial pressures of O₂ and CO₂, temperature and *pH* in the following form:

$$S = \frac{(a_1 w + a_2 w^2 + a_3 w^3 + w^4)}{(a_4 + a_5 w + a_6 w^2 + a_7 w^3 + w^4)} \quad (3.16)$$

where

a_1, \dots, a_7 are constants given by Kelman (1966).

w is a corrected P_{O_2} given by the following equation:

$$w = P_{O_2} 10^{[0.024(37 - T) + 0.04(pH - 7.4) + 0.06(\log 40 - \log P_{CO_2})]}.$$

The *pH* of blood was given as the following

$$pH = 8.059 + 0.012(1 - S) + 0.011(1 - S)C_{heme, total} - [HCO_3^-] \left\{ \frac{0.02}{C_{heme, total}} [0.273 - 0.01(1 - S)] \right\} \quad (3.17)$$

where $[HCO_3^-]$ is the concentration of bicarbonate ion in the blood and is derived from the Henderson-Hasselbalch equation: $[HCO_3^-] = \alpha_{CO_2} P_{CO_2} 10^{(pH - pK')}$; and K' is the apparent first dissociation constant of carbonic acid and includes a factor which allows for the substitution of total dissolved CO₂ concentration for carbonic acid.

They used these analytical approximations for O₂ and CO₂ dissociation curves and solved the following two coupled partial differential equations:

$$V_z \left[1 + C_{heme, total} \frac{\partial S}{\partial (\alpha_{O_2} P_{O_2})} \right] \frac{\partial (\alpha_{O_2} P_{O_2})}{\partial z} = D_{O_2} \frac{\partial^2 (\alpha_{O_2} P_{O_2})}{\partial x^2} \quad (3.18)$$

$$V_z \left[1 + 10^{(pH - pK')} \right] \frac{\partial (\alpha_{CO_2} P_{CO_2})}{\partial z} = D_{CO_2} \frac{\partial^2 (\alpha_{CO_2} P_{CO_2})}{\partial x^2} \quad (3.19)$$

where x and z are the spatial coordinates of their experimental system. A flux boundary condition resulting from the mass balance of either O_2 or CO_2 at the blood membrane interface was used; the suffix i indicates either O_2 or CO_2 .

$$D_i \alpha_i \frac{\partial P_i}{\partial x} = \frac{D_{i,m} \alpha_{i,m} (P_{i,ext} - P_i)}{d} \quad (3.20)$$

where

P_i and $P_{i,ext}$ are the gas pressures in the blood side and outside of the membrane, respectively.

α_i and $\alpha_{i,m}$ are the solubility coefficients of the gas in the blood and in the membrane material, respectively.

d is the thickness of the membrane film.

The authors reported that calculated values of oxygen saturation agree with the experimental data to within an error of 5-10%; however, it should be mentioned that there was some scatter in the results. In addition, no CO_2 transport related quantities, such as P_{CO_2} and pH were reported for the validation of the entire model. Furthermore, there is question to the applicable operating regime of the correlations they used.

Villarroel and Lanham (1973)

Villarroel and Lanham proposed a design method for tubular membrane oxygenators which included a modified version of their earlier models. Although bicarbonate diffusion was neglected, they employed a normal CO_2 dissociation curve by using experimental data which accounted for the Haldane effect. The flux matching boundary condition was used, and data in the form of bulk exit P_{CO_2} values were

reported. There was good agreement between the data and theory on a P_{O_2} basis, but the agreement was due in part to the wall limited nature of their experimental devices. Total CO_2 transfer rates were reported.

Benn (1974) and Benn *et al.* (1975)

Benn and colleagues conducted a study of CO_2 transfer from weak acids and blood flowing in permeable tubes. They included the facilitation of CO_2 transport by bicarbonate ion, the kinetics of carbonic anhydrase (assumed to be uniformly distributed throughout the blood), and the effects of the predominant weak acids present in blood. Their experimental results suggested that dehydration of carbonic acid could be treated as being at equilibrium. However, the sensitivity of the measurements to a departure from equilibrium of the carbonic anhydrase reaction was diminished by a significant membrane mass transfer resistance for CO_2 .

CO_2 transfer theory in flowing blood was modeled by these researchers as an extension of the theory that they developed for their weak acid study. Blood was considered to be a homogeneous fluid composed of three CO_2 species; dissolved CO_2 , bicarbonate ions, and carbamino-bound CO_2 . Again, Equation (3.1) applies for each species, but was written only for dissolved CO_2 and bicarbonate ion.

$$\vec{V} \cdot \nabla [C_i] = D_i \nabla^2 [C_i] + R_i \quad (3.21)$$

Carbamino CO_2 was incorporated into the dissolved CO_2 equation by assuming it to be in equilibrium with the dissolved CO_2 everywhere in the blood channel. A lumped buffering behavior of all weak acids was assumed, and a simplified reaction between bicarbonate and dissolved CO_2 similar to Reactions (2.I) and (2.II) was used. O_2 linked effects were included via simultaneous solution of an O_2 convection equation. Major conclusions from their work were

1. Diffusion of weak acids was negligible since hemoglobin, the major weak acid in blood, does not diffuse.
2. Data verified CO₂ transfer theory when the O₂ linked effects are minimal.
3. Under normal artificial lung operating conditions, their model predicted a 15% increase in CO₂ transport due to O₂ related effects. However, the difficulty of measuring simultaneous O₂ and CO₂ transfer to within an error less than 15% prevented experimental validation of O₂ enhanced CO₂ transfer.

Voorhees (1976)

Voorhees attempted to improve upon Dorson *et al.*'s (1971) model by treating the CO₂ equilibrium with blood differently. Basically, Equation (3.22) was used to relate the dissolved and reacted forms of CO₂:

$$[CO_2] = \frac{[CO_2]_{reacted}}{K_{eq}} 10^{([CO_2]_{reacted}/\beta)} \quad (3.22)$$

where

$[CO_2]_{reacted}$ is the concentration of reacted CO₂ in blood.

K_{eq} is a pseudo equilibrium constant in approximate CO₂ dissociation curve which was determined from experimental measurements.

β is the apparent buffering capacity of the blood which was determined semi-empirically.

Knowing K_{eq} and β , all values of $[CO_2]$ and $[CO_2]_{reacted}$ can then be related through Equation (3.22). With the assumption concerning the relationship between the dissolved and reacted CO₂ and assumptions (1) - (3), listed previously for the derivation of Equation (3.4), Equation (3.2) can then be expressed as

$$V(r) \frac{\partial}{\partial z} ([CO_2] + [CO_2]_{reacted}) = \frac{D_{CO_2}}{r} \frac{\partial}{\partial r} \left[r \frac{\partial}{\partial r} \left([CO_2] + \frac{D_{CO_2,reacted}}{D_{CO_2}} [CO_2]_{reacted} \right) \right] \quad (3.23)$$

where $D_{CO_2,reacted}$ is the effective, lumped diffusivity of reacted CO_2 . In addition, the advancing front concept (Dorson and Voorhees, 1974) which decoupled the convective and diffusive contribution was applied to the O_2 transfer problem. Finally, his treatment of O_2 , CO_2 equilibrium with blood was consistent with the assumption of blood being a homogeneous fluid. However, those correlations overlooked some of the subtle aspects of O_2 - CO_2 -blood interactions which included the Bohr and Haldane effects.

Agreement between data and theory for CO_2 transfer from blood was good for experiments to which carbonic anhydrase was added to the plasma portion of the sample. This further confirmed the validity of the homogeneous, local chemical equilibrium model developed by Voorhees. However, for most cases, CO_2 transfer data was over predicted by theory. This overprediction could be attributed to the fact that the model was underestimating the transport resistance by assuming the CO_2 hydration/dehydration to be in equilibrium in the plasma. For the cases of CO_2 transfer with either simultaneous oxygenation or deoxygenation and addition of extracellular carbonic anhydrase, the theory under calculated the amount of transport. This underprediction could be linked to the factor that the Haldane effect was not taken into account.

CHAPTER 4

OXYGEN TRANSPORT MODELS

There has been considerable activity in past years on the mathematical simulation of oxygen transport in the microcirculation. Various investigators have used different sets of assumptions to reduce the complex governing equations to a tractable set. Although there were experimental data available for the larger diameter microvessels (several hundred microns in diameter) from artificial membrane oxygenators, previously there has been insufficient experimental validation of the various assumptions for applying to the smaller diameter microvessels (less than 100 μm in diameter). Recently, Boland *et al.* (1987) have developed an *in vitro* microvessel microspectrophotometer system which allows accurate determination of oxygen fluxes to and from RBC suspensions in small cylindrical conduits ($\approx 30 \mu\text{m}$ in diameter) under physiologically relevant conditions. In this system flow, transport and geometrical parameters can be controlled and measured accurately. Thus, validation of the various proposed models over a wider range of diameters has become possible.

Nair *et al.* (1989) have developed a small microvessel model which is entirely predictive. That is to say all parameters in the model are determined from the literature or by other means independent of capillary oxygen transport experiments. In addition, the model is discrete in the sense that the particulate (two-phase) nature of blood is considered. The model was shown to be in excellent agreement with the experimental oxygen transport results from 27 μm diameter artificial membrane tubes (Nair *et al.*, 1989), as well as with deoxygenation results obtained by Schmukler and Chien (1985) in 100 μm vessels. The first part of this chapter can be regarded as an extension of Nair

et al.'s model in which the results of their study is used as a guide to formulate a much simpler discrete model.

Another objective of this chapter is both to further investigate the feasible diameter regime for application of the continuum (assuming that blood is a continuous and homogeneous hemoglobin solution) and discrete models and to assess the importance of the shear-induced augmentation on oxygen transport as a function of tube diameter, shear rate and oxygen storage potential of the blood. For this previously developed mathematical models of oxygen transport by flowing blood were adapted to model the *in vitro* experimental systems of Diller *et al.* (1980), Schmukler and Chien (1985) and Boland *et al.* (1987).

4.1 Mathematical Models

4.1.1 Discrete Models

In the case of uptake, oxygen must diffuse through the artificial membrane medium (*in vitro* situation) or the tissue region (*in vivo* situation), then convect and diffuse through the blood plasma. Subsequently, it diffuse through the red cell membrane; once it is inside the red blood cell, oxygen simultaneously diffuses and reacts in the hemoglobin solution ("facilitated diffusion"). In the case of release, the same processes occur in the reverse order. The approach is to estimate each of the resistances to oxygen transport and use these estimates with the appropriate differential equations of change in a model which yields the O_2 concentration distribution. First, for continuity the main features of Nair *et al.*'s model (1989) is briefly recapitulated. Then it will be shown that by introduction of certain well-founded assumptions, Nair *et al.*'s model which consists a system of four simultaneous, nonlinear partial differential equations can be reduced to one partial differential equation (PDE). The comparison

given in section 4.3.1 will show the two methods give essentially equivalent results and are in good agreement with experiments.

4.1.1.a *Recap of Nair et al.'s Discrete Model*

A brief outline of the Nair *et al.*'s model is given below. More detail is given by Nair (1988) and Nair *et al.* (1989). The red cell suspension is treated as two continuous, coexisting phases: a RBC phase and a plasma phase. Intracellular diffusion and reaction resistances are estimated by solution of the transport equations for a typical RBC under a prescribed O_2 flux at the RBC wall. The extracellular diffusion boundary layer resistance is obtained from the low Reynolds' number solution for mass transfer from a disc to fluid flowing past it. The model takes into account convection of both the plasma and RBCs, and radial diffusion in the plasma. The equations for O_2 transport by the RBCs are:

$$V_{rbc}(r) \frac{\partial [O_2]_{rbc}}{\partial z} = - \left(\frac{S}{v} \right)_{rbc} Flux_{O_2} + C_{heme,rbc} F([O_2]_{rbc}, S) \quad (4.1)$$

$$V_{rbc}(r) \frac{\partial (C_{heme,rbc} S)}{\partial z} = - C_{heme,rbc} F([O_2]_{rbc}, S) \quad (4.2)$$

where

$C_{heme,rbc} F([O_2]_{rbc}, S)$ is the reaction rate expressed as a rate of O_2 appearance per unit volume of RBC. It can be treated by any of the variable-rate-coefficient methods (Moll, 1969; Clark *et al.*, 1985; Vandegriff and Olson, 1984b).

$C_{heme,rbc}$ is the total heme concentration in RBC, a constant.

$[O_2]_{rbc}$ is the mean dissolved O_2 concentration in the RBC. $[O_2]_{rbc}$ is a value averaged within each individual RBC but varying with position of the RBC in the vessel.

S is the mean fraction O_2 saturation of the hemoglobin molecules.

$(s/v)_{rbc}$ is the surface to volume ratio of the RBC.

$Flux_{O_2}$ is the O_2 flux crossing the RBC wall, a function of r and z .

In the plasma only one species - dissolved oxygen is considered.

$$(1 - h(r)) V_{pl}(r) \frac{\partial [O_2]_{pl}}{\partial z} = \frac{D_{O_2,pl}}{r} \frac{\partial}{\partial r} \left(r \frac{\partial [O_2]_{pl}}{\partial r} \right) + h(r) \left(\frac{s}{v} \right)_{rbc} Flux_{O_2} \quad 0 \leq r \leq r_r \quad (4.3)$$

$$V'_{pl}(r) \frac{\partial [O_2]'_{pl}}{\partial z} = \frac{D_{O_2,pl}}{r} \frac{\partial}{\partial r} \left(r \frac{\partial [O_2]'_{pl}}{\partial r} \right) \quad r_r \leq r \leq r_c \quad (4.4)$$

where

$D_{O_2,pl}$ is the diffusivity of O_2 in the plasma.

$[O_2]_{pl}$ and $[O_2]'_{pl}$ are the dissolved O_2 concentrations in the RBC-rich and RBC-free plasma region, respectively.

The velocity variables used here may be thought of as profile variables. Different velocity variables are sometimes used in flow of heterogeneous fluids. Specifically, $h(r)V_{rbc}(r)$ gives the local volumetric flux of RBCs (volume of RBCs per unit time per unit area). Similarly $(1-h(r))V_{pl}(r)$ is the local volumetric flux of plasma. Velocity profiles for the RBCs and the plasma, $V_{rbc}(r)$, $V_{pl}(r)$ and $V'_{pl}(r)$; radial hematocrit, $h(r)$; and the method for estimation of the cell-free layer thickness are summarized in section 2.2.1.

At the RBC-rich and RBC-free region interface, continuity of oxygen tensions and fluxes is imposed; and the symmetry condition is used at the center of vessel. In the *in vitro* experimental systems of Diller *et al.* (1980) and Schmukler and Chien (1985), the cylindrical vessel is embedded in the center of a film with circular cross section; in Boland *et al.*'s (1987), the microvessel is embedded in a thin film of rectangular section.

For simulating the experimental results, transport in the outer membrane film is incorporated as a boundary condition at the vessel wall. Therefore, the steady-state asymptotic solution of the Laplace equation in the film yields the vessel wall O₂ flux (Balcerzak and Raynor, 1961):

$$-D_{O_2,pl} \frac{\partial [O_2]_{pl}}{\partial r} \Big|_{r=r_c} = \frac{K_{O_2}}{\alpha_{O_2,pl} \ln(GF)} \left([O_2]_{pl} \Big|_{r=r_c} - \alpha_{O_2,pl} P_{O_2,ext} \right) \quad (4.5)$$

where

K_{O_2} is the oxygen permeability of the silicone rubber film.

$\alpha_{O_2,rbc}$ and $\alpha_{O_2,pl}$ are the solubility coefficients for O₂ in the RBC and the plasma, respectively.

GF is the geometric factor. $GF=r_o/r_c$, where r_o is the outer radius of the membrane oxygenator, in both Diller *et al.*'s and Schmukler and Chien's systems; and $GF=4d/\pi r_c$, where d is the half-sheet thickness of the silicone rubber film in Boland *et al.*'s system.

Finally, to complete the description, inlet conditions are imposed at $z=0$ where $[O_2]_{rbc}$, S , $[O_2]_{pl}$, and $[O_2]_{pl}'$ are assumed to be in equilibrium and uniform with respect to radius. Therefore, Nair *et al.*'s model consists of a system of four simultaneous nonlinear PDEs which determine the O₂ transport variables $[O_2]_{rbc}$, $[O_2]_{pl}$, $[O_2]_{pl}'$ and S as functions of r and z for given values of the various parameters.

4.1.1.b Simplified Discrete Model (Simplified DM)

Nair *et al.*'s discrete model revealed that within the 27 μm diameter microvessel, only about 2% of the resistance lies inside the RBCs, and only another 2% is associated with the plasma boundary layer close to the RBC wall. Thus, some 96% of the intracapillary resistance is distributed in the plasma - not inside or directly adjacent to the

cells. Furthermore, for larger microvessels the resistance associated with the red cells is even less important. Since the resistances attributed to the RBC interior and the diffusion boundary layers close to the RBC wall are small, the assumptions of chemical equilibrium within the red cell and negligible intracellular and cell boundary layer resistances can be introduced to simplify Nair *et al.*'s model.

By combining Equations (4.1) and (4.2) and invoking the chemical equilibrium assumption, one obtains

$$V_{rbc}(r) \left(1 + \frac{C_{heme,rbc}}{\alpha_{O_2,rbc}} \frac{dS}{dP_{O_2}} \right) \frac{\partial [O_2]_{rbc}}{\partial z} = - Flux_{O_2} \quad (4.6)$$

Since chemical equilibrium within the RBC is assumed, the fractional saturation of hemoglobin, S , can be expressed as a function of the O_2 concentration, $[O_2]_{rbc}$. The term dS/dP_{O_2} is the slope of the oxyhemoglobin dissociation curve and is a nonlinear function of P_{O_2} . It is also assumed that there is no transport resistance in the RBC membrane; thus the oxygen tension is continuous at the RBC wall (i.e., $[O_2]_{rbc,rw}/\alpha_{O_2,rbc} = [O_2]_{pl,rw}/\alpha_{O_2,pl}$; where $[O_2]_{rbc,rw}$ and $[O_2]_{pl,rw}$ are the O_2 concentrations at the RBC wall in the RBC and in the plasma, respectively). In addition, if the intra- and extra-cellular boundary layer resistances are neglected (i.e., $[O_2]_{rbc} = [O_2]_{rbc,rw}$ and $[O_2]_{pl} = [O_2]_{pl,rw}$), then it follows that

$$[O_2]_{pl} = \left(\frac{\alpha_{O_2,pl}}{\alpha_{O_2,rbc}} \right) [O_2]_{rbc} \quad (4.7)$$

Multiplication of Equation (4.6) by $h(r)$, addition of the resultant expression to Equation (4.3) and substitution of $(\alpha_{O_2,pl}/\alpha_{O_2,rbc})[O_2]_{rbc}$ for $[O_2]_{pl}$ yields the following mass balance for dissolved O_2 in the RBC:

$$\left[(1 - h(r)) V_{pl}(r) + \left(\frac{\alpha_{O_2, rbc}}{\alpha_{O_2, pl}} \right) h(r) V_{rbc}(r) \left(1 + \frac{C_{heme, rbc}}{\alpha_{O_2, rbc}} \frac{dS}{dP_{O_2}} \right) \right] \frac{\partial [O_2]_{rbc}}{\partial z} = \frac{D_{O_2, pl}}{r} \frac{\partial}{\partial r} \left(r \frac{\partial [O_2]_{rbc}}{\partial r} \right) \quad 0 \leq r \leq r_r \quad (4.8)$$

The plasma O₂ concentration in the cell-rich region is obtained through Equation (4.7).

To further simplify Nair *et al.*'s model, the mass balance for dissolved O₂ in the cell-free region can be solved analytically and incorporated as a boundary condition to Equation (4.8). This solution uses the finding that convective transport of O₂ in the cell-free plasma region is small relative to transport by molecular diffusion. Hence, the term $V'_{pl}(r) \partial [O_2]_{pl} / \partial z$ can be dropped from Equation (4.4). The simplified equation can be integrated and expressed in terms of the wall flux or in terms of the flux from the cell-rich region (Equation (4.9)):

$$- D_{O_2, pl} \frac{\partial [O_2]_{pl}}{\partial r} \Big|_{r=r_r} = \frac{- D_{O_2, pl} ([O_2]_{pl}|_{r=r_c} - [O_2]_{pl}|_{r=r_r})}{r_r \ln \left(\frac{r_c}{r_r} \right)} \quad (4.9)$$

The vessel wall oxygen flux is the product of the left hand side of Equation (4.9) and the ratio, r_r/r_c . Equation (4.9) can easily be incorporated into the boundary conditions of the O₂ transport problem. For example, in the simplest case of specified vessel wall O₂ concentration, Equation (4.9) as it stands is the boundary condition on Equation (4.8). In applying these conditions, expression in terms of $[O_2]_{rbc}$ instead of $[O_2]_{pl}$ is derived from use of Equation (4.7) and from conditions of continuity ($[O_2]_{pl} = [O_2]_{pl}$ and $\partial [O_2]_{pl} / \partial r = \partial [O_2]_{pl} / \partial r$ at $r=r_r$).

In the particular case of the boundary condition for the artificial membrane tube system, Equation (4.5), the usual summation of resistance approach gives:

$$-D_{O2,pl} \frac{\partial [O_2]_{rbc}}{\partial r} \Big|_{r=rr} = \frac{-D_{O2,pl} (\alpha_{O2,rbc} P_{O2,ext} - [O_2]_{rbc} \Big|_{r=rr})}{r_r \left[\frac{D_{O2,pl} \alpha_{O2,pl} \ln(GF)}{K_{O2}} + \ln\left(\frac{r_c}{r_r}\right) \right]} \quad (4.10)$$

4.1.2 Continuum Models

Many assumptions are implicit in the derivation of the continuum models investigated in this paper, but one is of particular importance. That is on a microscopic scale, blood can be treated as a homogeneous continuum. In other words, blood is statistically homogeneous over a sufficiently large sample volume, even though it is microscopically heterogeneous. Within such a volume one expects that a linear relation, analogous to Fick's first law, will exist between the average diffusive flux and the average concentration gradient, where the average concentration is the volume fraction-weighted sum of the concentrations in RBCs and plasma, and the coefficient of proportionality is the effective diffusion coefficient.

4.1.2.a Continuum Model (Oxyhemoglobin Augmentation)

This model (CMAug) treats blood as homogeneous hemoglobin (Hb) solution, taking into account the transport mechanism of molecular diffusion, convection and the facilitated diffusion of O_2 due to the presence of Hb (Lemon *et al.*, 1987):

$$\frac{2Q}{\pi r_c^2} \left[1 - \left(\frac{r}{r_c} \right)^2 \right] \frac{\partial [O_2]}{\partial z} = \frac{D_{O2}}{r} \frac{\partial}{\partial r} \left(r \frac{\partial [O_2]}{\partial r} \right) + C_{heme} [j S - j' [O_2] (1-S)] \quad (4.11)$$

$$\frac{2Q}{\pi r_c^2} \left[1 - \left(\frac{r}{r_c} \right)^2 \right] \frac{\partial S}{\partial z} = \frac{D_{HbO2}}{r} \frac{\partial}{\partial r} \left(r \frac{\partial S}{\partial r} \right) - [j S - j' [O_2] (1-S)] \quad (4.12)$$

where

Q is the volumetric flowrate in the tube.

C_{heme} is the total heme concentration in the suspension.

j and j' are the dissociation and association rate constants for O_2 binding to hemoglobin, respectively; j is a constant, and j' is a nonlinear function of $[O_2]$.

The appropriate boundary conditions are

$$@ z = 0, \quad [O_2] = [O_2]_{in}; \quad S = F_{eq}\{[O_2]_{in}\} \quad (4.13a)$$

$$@ r = 0, \quad \frac{\partial [O_2]}{\partial r} = 0; \quad \frac{\partial S}{\partial r} = 0 \quad (4.13b)$$

$$@ r = r_r, \quad -D_{O_2} \frac{\partial [O_2]}{\partial r} = \frac{K_{O_2}}{\alpha_{O_2} r_c \ln(GF)} ([O_2] - \alpha_{O_2} P_{O_2,ext}); \quad \frac{\partial S}{\partial r} = 0 \quad (4.13c)$$

corresponding to uniform inlet concentrations, symmetry about centerline, and wall flux matching, respectively; and α_{O_2} is the effective solubility coefficient for O_2 in blood.

4.1.2.b Continuum Model (Local Chemical Equilibrium)

This continuum model (CMequ) is slightly different from the previous one due to the fact that the augmentation of oxygen transport by diffusion of oxyhemoglobin is neglected (Reneau *et al.*, 1967; Buckles *et al.*, 1968; Weissman and Mockros, 1969; Bradley and Pike, 1971; Villarroel *et al.*, 1971; Benn *et al.*, 1975; Voorhees, 1976; Diller *et al.*, 1980). It assumes that the rate of reaction between O_2 and hemoglobin is sufficiently fast, when compared to the rate of diffusion of O_2 within the red cell, and that the reaction can be considered at local equilibrium. Therefore, the concentration of hemoglobin-bound O_2 is directly related to the concentration of dissolved O_2 via the oxyhemoglobin dissociation curve.

$$\frac{2Q}{\pi r_c^2} \left[1 - \left(\frac{r}{r_c} \right)^2 \right] \left(1 + \frac{C_{heme}}{\alpha_{O_2}} \frac{dS}{dP_{O_2}} \right) \frac{\partial [O_2]}{\partial z} = \frac{D_{O_2}}{r} \frac{\partial}{\partial r} \left(r \frac{\partial [O_2]}{\partial r} \right) \quad (4.14)$$

Equation (4.14) is solved subject to the appropriate inlet and boundary conditions similar to those that are imposed on Equation (4.11).

4.2 Numerical Analysis

4.2.1 Oxygen-Hemoglobin Equilibrium Relationship

Different investigators have used different approaches to handle the ODC. For instance, Diller *et al.* (1980) used a saturation curve which was based on the four-step Adair reaction scheme and developed by Margaria. If the Margaria approximation, Equation (4.15a), is chosen to describe the ODC; dS/dP_{O_2} is then given by Equation (4.15b).

$$S = \frac{(\kappa P_{O_2})^3 + \eta - 1}{(\kappa P_{O_2})^4 + \eta - 1} \quad (4.15a)$$

$$\frac{dS}{dP_{O_2}} = \frac{(\kappa P_{O_2})^6 + (\eta - 1)[4(\kappa P_{O_2})^3 - 3(\kappa P_{O_2})^2]}{k P_{O_2}^2 [(\kappa P_{O_2})^4 + \eta - 1]^2} \quad (4.15b)$$

where $\kappa P_{O_2} = \frac{1 + k P_{O_2}}{k P_{O_2}}$; k and η are constants.

Nair *et al.* (1990), however, chose the Hill equation to approximate the ODC (Equation (4.16a)), and the derivative is given by Equation (4.16b).

$$S = \frac{\left(\frac{P_{O_2}}{P_{50}}\right)^n}{1 + \left(\frac{P_{O_2}}{P_{50}}\right)^n} \quad (4.16a)$$

$$\frac{dS}{dP_{O_2}} = \frac{n \left(\frac{P_{O_2}}{P_{50}}\right)^n}{P_{O_2} \left[1 + \left(\frac{P_{O_2}}{P_{50}}\right)^n\right]^2} \quad (4.16b)$$

where P_{50} and n are the equilibrium parameters from experimental data.

There are other and slightly better approximations to the oxygen-hemoglobin equilibrium relationship, but those in general are more complicated (see Section 2.1.1.a). The selections here represent the simpler and reasonable choices; incorporation of both equilibrium approximations into the transport models results in similar predictions (differences of less than 1-2% in fractional saturation). Although equilibrium parameters from both kinetic models, k , η , P_{50} and n , can be considered as useful indexes of the oxygen-carrying function of hemoglobin, P_{50} and n seem to reflect this property in a more direct fashion (they are directly obtainable from the ODC). Consequently, the Hill approximation was chosen for simulation of oxygen transport.

4.2.2 Parameter Values and Solutions of Transport Equations

The values for the parameters used in this study are listed in Table 4.1. For the continuum models, the effective physical properties (Brownian diffusion and solubility coefficients) are estimated by regarding the suspension as a hemolysate of the blood in the tube where the hemoglobin concentration is determined by the discharge hematocrit (solubility data from Christoforides and Hedley-Whyte (1969); diffusivity data from Kreuzer (1970), Keller *et al.* (1971) and Spaan *et al.* (1980)). However, the chemical environment is not altered as a result of this hypothetical hemolysis; thus equilibrium parameters of the blood; namely, P_{50} and n , remain unchanged and are estimated using the oxygen saturation and partial pressure data obtained from the blood gas analyzer for the red cell suspensions. For the discrete model, parameters for the interior of the red cell are the same as those used and discussed in detail by Nair *et al.* (1988). In addition, parameters for the plasma region are needed: the diffusion coefficients comes from Kreuzer (1970) and the solubility coefficient from Christoforides and Hedley-Whyte (1969).

Table 4.1

Parameters used in the oxygen transport calculations.

Discrete model parameters	Diller <i>et al.</i>	Schmukler and Chien	Boland <i>et al.</i>
$C_{heme,rbc}$ (mM)	20.8	20.8	20.8
$\left(\frac{d}{v}\right)_{rbc}$ (μm^{-1})	1.87	1.87	1.87
$\alpha_{O_2,rbc}$ (M/mm Hg)	1.43×10^{-6}	1.43×10^{-6}	1.43×10^{-6}
$\alpha_{O_2,pl}$ (M/mm Hg)	1.27×10^{-6}	1.33×10^{-6}	1.33×10^{-6}
$D_{O_2,pl}$ (cm^2/sec)	2.25×10^{-5}	2.70×10^{-5}	2.70×10^{-5}
δ (μm)	≈ 1.4	≈ 1.5	≈ 2.0
B (blunting factor)	≈ 1.0	≈ 0.95	≈ 0.9
H_T/H_D	0.95 ($r_c=150 \mu\text{m}$) 1.00 ($r_c \geq 300 \mu\text{m}$)	0.94	0.83 (flowrate=12 $\mu\text{l/hr}$) 0.80 (flowrate=23 $\mu\text{l/hr}$)
Continuum model parameters	Diller <i>et al.</i>	Schmukler and Chien	Boland <i>et al.</i>
C_{heme} (mM)	(calculated from H_D)		
α_{O_2} (M/mm Hg)	1.31×10^{-6} ($H_D=0.45$) 1.30×10^{-6} ($H_D=0.24$)	1.34×10^{-6}	1.36×10^{-6} ($H_D=0.3$) 1.35×10^{-6} ($H_D=0.2$)
D_{O_2} (cm^2/sec)	1.65×10^{-5} ($H_D=0.45$) 2.23×10^{-5} ($H_D=0.24$)	2.55×10^{-5} ($H_D=0.1$) 2.63×10^{-5} ($H_D=0.05$) 2.68×10^{-5} ($H_D=0.015$)	2.30×10^{-5} ($H_D=0.3$) 2.44×10^{-5} ($H_D=0.21$)
D_{HbO_2} (cm^2/sec)	3.80×10^{-7} ($H_D=0.45$) 4.60×10^{-7} ($H_D=0.24$)	$\approx 11.9 \times 10^{-7}$	7.60×10^{-7} ($H_D=0.3$) 9.00×10^{-7} ($H_D=0.2$)

Table 4.2

Summary of oxygen transfer models which are considered in Chapter 4.

Model	Transport equation(s)	Dependent variable(s) calculated in the numerical solution	Equation(s) used to determine other dependent variable(s)
Nair <i>et al.</i> 's discrete model	Equation (4.1) -	$[O_2]_{rbc}(r,z)$ and $S(r,z)$ $0 \leq r \leq r_r$	
	Equation (4.4)	$[O_2]_{pl}(r,z)$ $0 \leq r \leq r_r$	
		$[O_2]'_{pl}(r,z)$ $r_r \leq r \leq r_c$	
Simplified DM	Equation (4.8)	$[O_2]_{rbc}(r,z)$ $0 \leq r \leq r_r$	$S(r,z) = F_{eq} \{ [O_2]_{rbc}(r,z) \}$ $0 \leq r \leq r_r$ Equation (4.16a) $[O_2]_{pl}(r,z) = G \{ [O_2]_{rbc}(r,z) \}$ $0 \leq r \leq r_c$ Equation (4.17)
CMaug	Equations (4.11) and (4.12)	$[O_2](r,z)$ and $S(r,z)$ $0 \leq r \leq r_c$	
CMequ	Equation (4.14)	$[O_2](r,z)$ $0 \leq r \leq r_c$	$S(r,z) = F_{eq} \{ [O_2](r,z) \}$ $0 \leq r \leq r_c$ Equation (4.16a)

Solutions to these transport models are complicated by nonlinear kinetic terms, and in one case there is also coupling among the equations. Therefore, these equations are solved numerically using a finite element B-spline collocation method (described and evaluated elsewhere; Baxley and Hellums, 1983). The numerical solutions provide the spatial profiles of free and bound oxygen concentrations as functions of r and z for given values of various parameters (see Tables 4.1 and 4.2). In addition, for the discrete model, the dissolved O_2 concentration in the plasma phase can be obtained through Equation (4.17).

$$[O_2]_{pl}(r) = \left(\frac{\alpha_{O_2,pl}}{\alpha_{O_2,rbc}} \right) [O_2]_{rbc}(r) \quad (4.17a)$$

$$[O_2]'_{pl}(r) = \left[\frac{\alpha_{O_2,pl} P_{O_2,ext} - \left(\frac{\alpha_{O_2,pl}}{\alpha_{O_2,rbc}} \right) [O_2]_{rbc}|_{r=r_r}}{\frac{D_{O_2,pl} \alpha_{O_2,pl} \ln(GF)}{K_{O_2}} + \ln\left(\frac{r_c}{r_r}\right)} \right] \ln\left(\frac{r}{r_r}\right) + \left(\frac{\alpha_{O_2,pl}}{\alpha_{O_2,rbc}} \right) [O_2]_{rbc}|_{r=r_r} \quad (4.17b)$$

where $[O_2]'_{pl}$ is the dissolved O_2 concentration in the RBC-free plasma region ($r_r < r < r_c$).

4.2.3 Processing of Simulation Results for Comparison of Model Predictions with Experimental Measurements

4.2.3.a Diller *et al.* (1980) and Schmukler and Chien (1985)

To compare theoretical predictions with experimental measurements obtained by Diller *et al.* (1980) and Schmukler and Chien (1985), the physically mixed mean concentrations of the blood at the tube outlet are required. It is first necessary to calculate the velocity-weighted bulk average values of dissolved oxygen concentration and oxyhemoglobin saturation. Then, the composition that would be measured if the

blood issuing from the tube were physically mixed and allowed to equilibrate can be calculated from the following relationship which pertains to the hemoglobin solutions:

$$[O_2]_{mm} + C_{heme} S_{mm} = \overline{[O_2]} + C_{heme} \bar{S} \quad (4.18)$$

where

$[O_2]_{mm}$ and S_{mm} are the calculated overall mixed mean oxygen concentration and oxyhemoglobin saturation in the tube, respectively.

$\overline{[O_2]}$ and \bar{S} are the physically mixed mean oxygen concentration and oxyhemoglobin saturation in the equilibrated sample, respectively.

Because enough time elapsed between collection of a sample and measurements on the sample via a blood gas analyzer to allow bulk equilibration of the entire RBC suspension; \bar{S} is related to $\overline{[O_2]}$ via the equilibrium relationship; i.e., $\bar{S} = F_{eq}(\overline{[O_2]})$.

For the continuum models, if the Hill approximation is used, Equation (4.18) can be rewritten as the followings:

$$[O_2]_{mm} + C_{heme} S_{mm} = \alpha_{O_2} \overline{P_{O_2}} + C_{heme} \left[\frac{\left(\frac{\overline{P_{O_2}}}{P_{50}} \right)^n}{1 + \left(\frac{\overline{P_{O_2}}}{P_{50}} \right)^n} \right] \quad (4.19)$$

where $\overline{P_{O_2}}$ is the equilibrated mixed mean oxygen tension in the collected sample. The mixed mean averages in Equation (4.19), $[O_2]_{mm}$ and S_{mm} , are calculated as

$$[O_2]_{mm}(z) = \frac{1}{\pi r_c^2} \int_0^{r_c} 4 \pi r \left[1 - \left(\frac{r}{r_c} \right)^2 \right] [O_2](r, z) dr \quad (4.20a)$$

$$S_{mm}(z) = \frac{1}{\pi r_c^2} \int_0^{r_c} 4 \pi r \left[1 - \left(\frac{r}{r_c} \right)^2 \right] y(r, z) dr \quad (4.20b)$$

For the discrete model, Equation (4.18) can be rewritten as the following:

$$[O_2]_{mm} + H_D C_{heme, rbc} S_{mm} = H_D \alpha_{O_2, rbc} \overline{P_{O_2}} + (1 - H_D) \alpha_{O_2, pl} \overline{P_{O_2}} + H_D C_{heme, rbc} \left[\frac{\left(\frac{\overline{P_{O_2}}}{P_{50}} \right)^n}{1 + \left(\frac{\overline{P_{O_2}}}{P_{50}} \right)^n} \right] \quad (4.21)$$

where

$$H_D \text{ is the discharge hematocrit, and } H_D = \frac{1}{\pi r_c^2 \langle V \rangle} \int_0^{r_r} 2 \pi r h(r) V_{rbc}(r) dr.$$

$\langle V \rangle$ is the average velocity in the tube, and $\langle V \rangle = Q / \pi r_c^2$.

In this case, the mixed mean averages in Equation (4.21), $[O_2]_{mm}$ and S_{mm} , are calculated as

$$\begin{aligned} [O_2]_{mm}(z) = & \frac{1}{\pi r_c^2 \langle V \rangle} \int_0^{r_r} 2 \pi r h(r) V_{rbc}(r) [O_2]_{rbc}(r, z) dr \\ & + \frac{1}{\pi r_c^2 \langle V \rangle} \int_0^{r_r} 2 \pi r (1 - h(r)) V_{pl}(r) [O_2]_{pl}(r, z) dr \\ & + \frac{1}{\pi r_c^2 \langle V \rangle} \int_{r_r}^{r_c} 2 \pi r V'_{pl}(r) [O_2]'_{pl}(r, z) dr \end{aligned} \quad (4.22a)$$

$$S_{mm}(z) = \frac{1}{\pi r_c^2 H_D \langle V \rangle_{rbc}} \int_0^{r_c} 2 \pi r h(r) V_{rbc}(r) S(r, z) dr \quad (4.22b)$$

where $\langle V \rangle_{rbc}$ is the average red cell velocity, and $\langle V \rangle_{rbc} = Q H_D / \pi r_c^2 H_T$.

4.2.3.b Boland *et al.* (1987)

Boland *et al.*'s (1987) dual-wavelength microspectrophotometric system measures the space average oxygen saturation of the hemoglobin molecules, S_{sa} , at various axial positions along the microvessel. To compare the simulation results with experimental data, the following operations are carried out:

For the continuum models,

$$S_{sa}(z) = \frac{1}{\pi r_c^2} \int_0^{r_c} 2 \pi r S(r,z) dr \quad (4.23)$$

For the discrete model,

$$S_{sa}(z) = \frac{1}{\pi r_c^2 H_T} \int_0^{r_c} 2 \pi r h(r) S(r,z) dr \quad (4.24)$$

The validity of Equation (4.24) is critically examined in Appendix A.

4.3 Results and Discussion

4.3.1 Simplified Discrete Model versus Nair *et al.*'s Model

A comparison is given of results from Nair *et al.*'s model and the simpler model (simplified DM) with experimental determinations from the artificial membrane tube system of Boland *et al.* (1987) which is described in Section 4.3.4. Equation (4.8) subject to the imposed inlet and boundary (Equation (4.10)) conditions was solved numerically by a finite element basis spline collocation method (described and evaluated

elsewhere; Baxley and Hellums, 1983). Figures 4.1 - 4.4 give the fractional saturation curves of hemoglobin, both S_{sa} and S_{mm} , for release and uptake of O_2 comparing calculated results by Nair *et al.*'s model to those by the simplified model. The calculations were made for values of the parameters corresponding to specific experiments in the artificial membrane tube system, and the experimentally determined O_2 saturation values are given in the figures for comparison with the calculated values.

From these figures, it is clear that both models generate equally accurate predictions. The maximum deviation between the experimental data and the theoretical curve generated by either model is 0.1 fractional saturation units; the mean absolute deviation (calculated as $\left(\sum_{i=1}^{i=N} |deviation_i| \right) / N$ where N is the number of experimental data points) and absolute algebraic deviation (calculated as $\left| \left(\sum_{i=1}^{i=N} (deviation)_i \right) / N \right|$) for any one curve does not exceed 0.05 and 0.04 fractional saturation units, respectively. A difference of no more than 0.03 in S_{sa} and 0.02 in S_{mm} are observed between the models for both the uptake and release cases. To put this small discrepancy into perspective, it is important to note that the difference between these models cannot be distinguished within the experimental error involved. Another observation is that the rate of change in O_2 saturation predicted by Nair *et al.*'s model is slightly lower than that predicted by the simplified model. This finding is consistent with the additional assumptions of the simplified model - some small transport resistances were neglected.

4.3.2 Comparison with Diller *et al.*'s Membrane Oxygenator Data (300 μm , 630 μm and 1000 μm in diameters)

Diller (1977) measured oxygenation of fresh human whole blood flowing through silicone-rubber membrane tubes with diameters ranging from 300 to 1000 μm . In this oxygen transfer apparatus, the membrane tube was divided into two by a

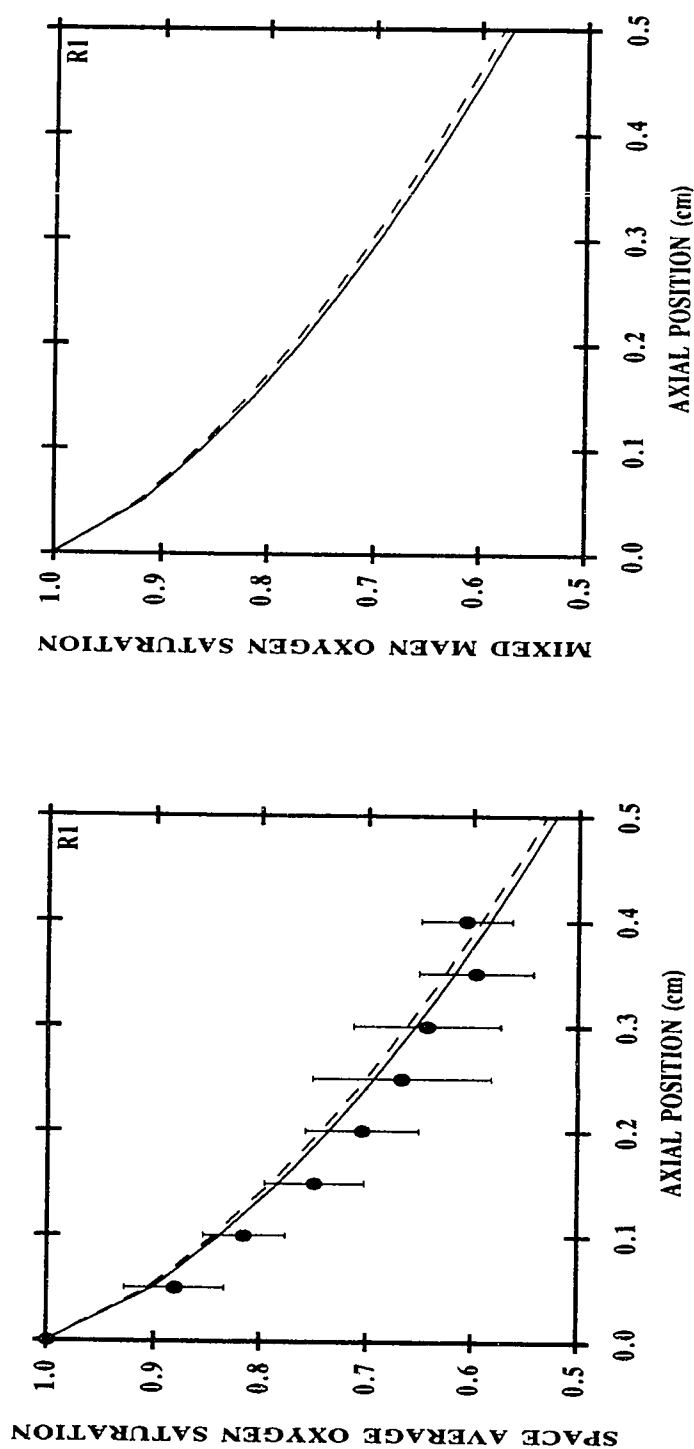


Figure 4.1: Comparison of models for O_2 release from RBC suspensions with a H_D of 30% and P_{50} of 27 mmHg flowing at 12 $\mu\text{l/hr}$ in a 27- μm -diameter membrane tube at 37 $^{\circ}\text{C}$. The left panel gives the space average O_2 saturation (S_{sa}) at different axial positions along the artificial membrane tube; and the right panel, the mixed mean O_2 saturation (S_{mm}). Circles: experimental results, mean \pm S.D. for 8 replicate experiments. Curves: theoretical simulation curves for the same conditions, (—) simplified discrete model and (---) Nair *et al.*'s model.

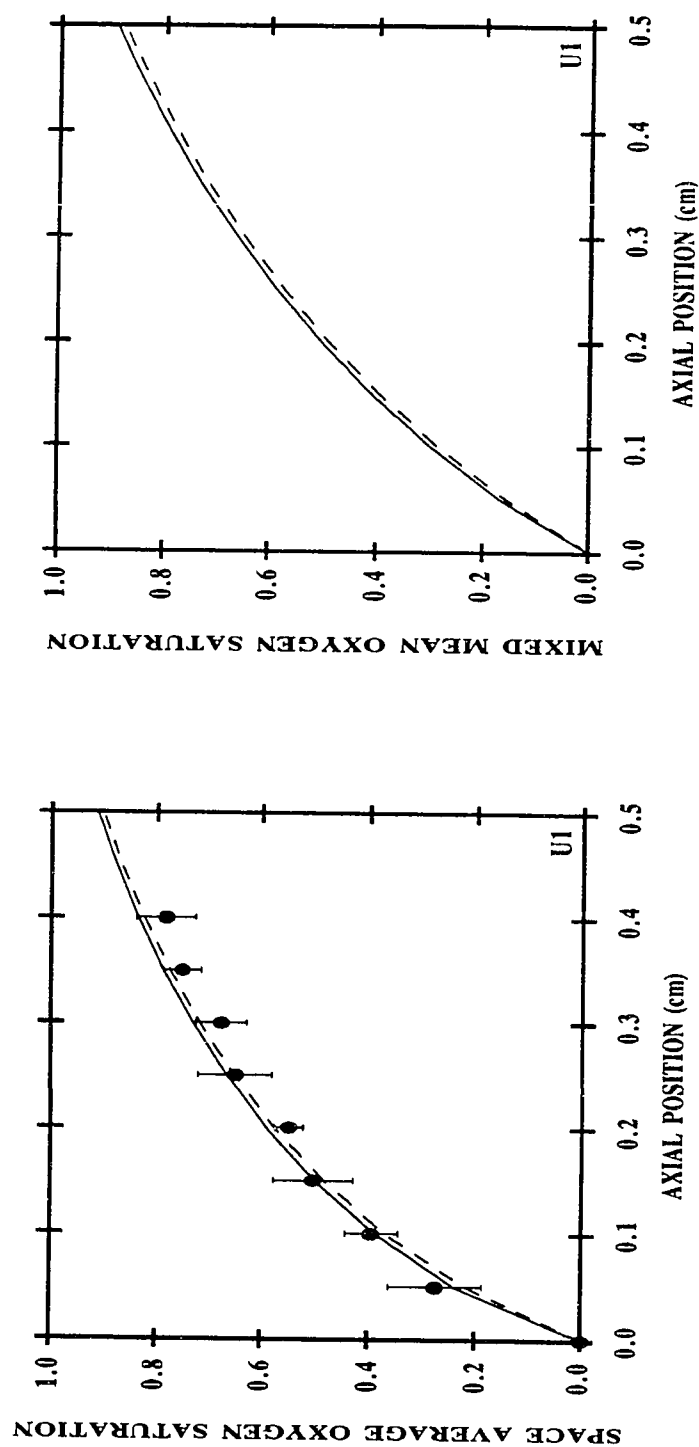


Figure 4.2: Comparison of models for O_2 uptake by RBC suspensions with a H_D of 30% and P_{50} of 27 mmHg flowing at 12 $\mu\text{l/hr}$ in a 27- μm -diameter membrane tube at 37 $^{\circ}\text{C}$. The left panel gives the space average O_2 saturation (S_{sa}) at different axial positions along the artificial membrane tube; and the right panel, the mixed mean O_2 saturation (S_{mm}). Circles: experimental results, mean \pm S.D. for 8 replicate experiments. Curves: theoretical simulation curves for the same conditions, (—) simplified discrete model and (---) Nair *et al.*'s model.

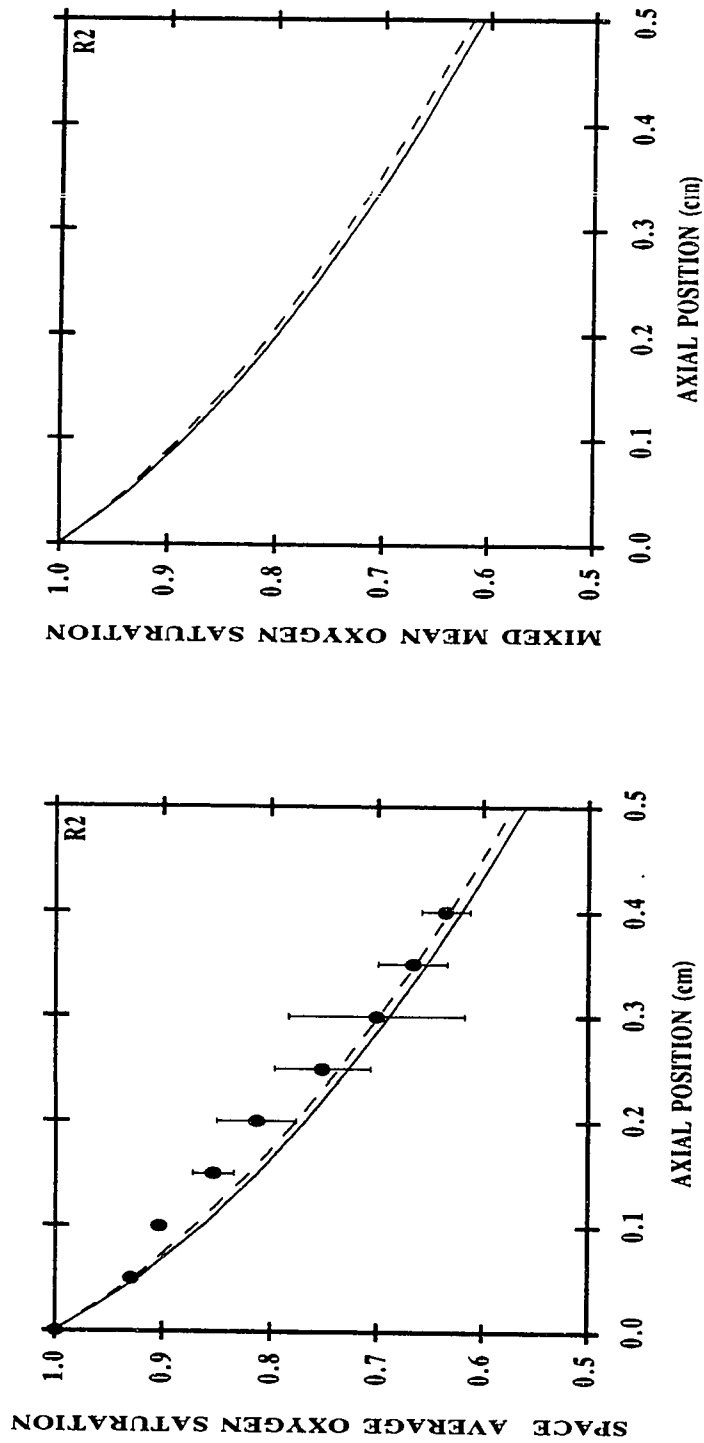


Figure 4.3: Comparison of models for O_2 release from RBC suspensions with a H_D of 20% and P_{50} of 27 mmHg flowing at 12 $\mu\text{l/hr}$ in a 27- μm -diameter membrane tube at 37 $^\circ\text{C}$. The left panel gives the space average O_2 saturation (S_{sa}) at different axial positions along the artificial membrane tube; and the right panel, the mixed mean O_2 saturation (S_{mm}). Circles: experimental results, mean \pm S.D. for 8 replicate experiments. Curves: theoretical simulation curves for the same conditions, (—) simplified discrete model and (---) Nair *et al.*'s model.

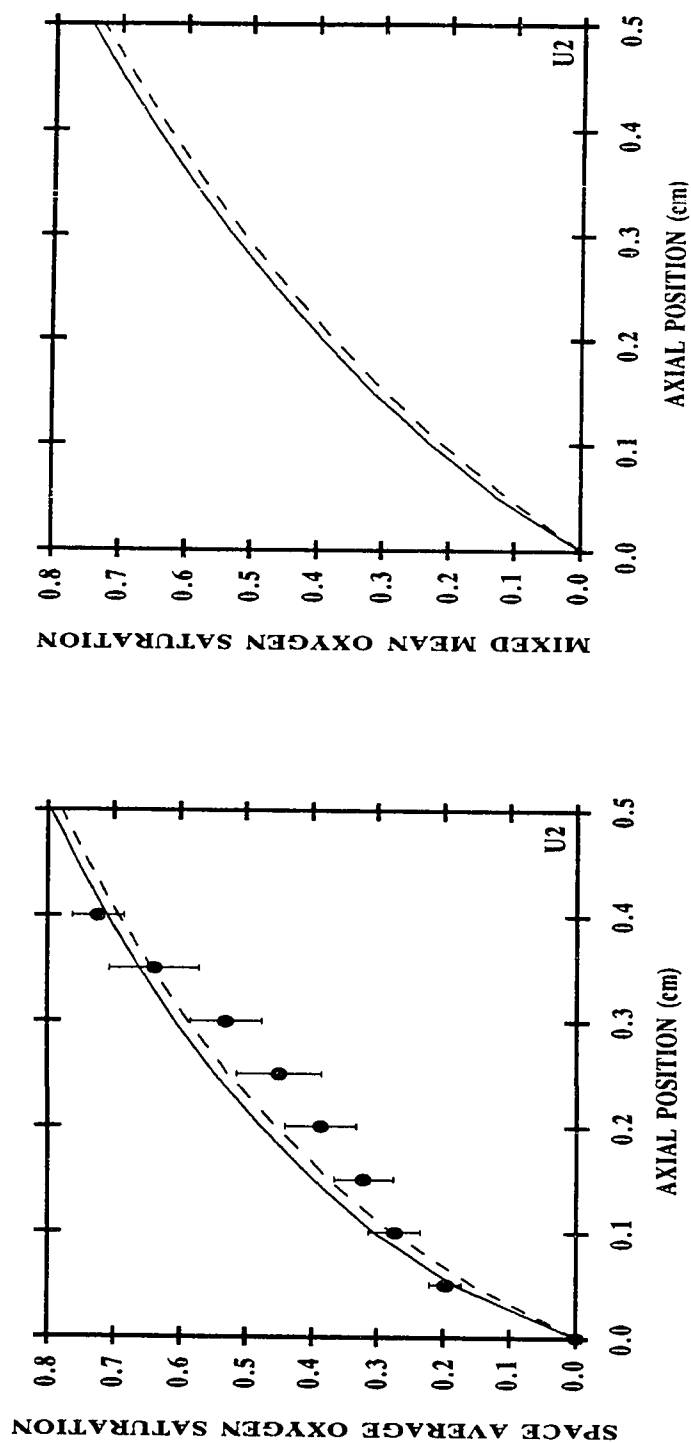


Figure 4.4: Comparison of models for O_2 uptake by RBC suspensions with a H_D of 20% and P_{50} of 20 mmHg flowing at 23 $\mu\text{l/hr}$ in a 27- μm -diameter membrane tube at 37 $^{\circ}\text{C}$. The left panel gives the space average O_2 saturation (S_{sa}) at different axial positions along the artificial membrane tube; and the right panel, the mixed mean O_2 saturation (S_{mm}). Circles: experimental results, mean \pm S.D. for 8 replicate experiments. Curves: theoretical simulation curves for the same conditions, (—) simplified discrete model and (---) Nair *et al.*'s model.

moveable plug. One part of the membrane tube served as the feed reservoir, and its environmental chamber was thus circulated with the same gas stream which was used to set the initial gas concentration of the fluid, $P_{O_2, in}$. The measured transfer, driven by the oxygen tension, $P_{O_2, ext}$, occurred in the other chamber. By moving the moveable plug, any of the ten different effective transfer lengths (10-100 cm) could be achieved for each sample. The permeability to oxygen of the medical grade silicone rubber is 3.1×10^{-10} M cm²/sec/mmHg (Diller, 1977).

4.3.2.a Uptake Experiments with Saturated Blood

Figure 4.5 shows the results of the calculations obtained from both CMequ and simplified DM methods for simulating Diller's uptake experiments with saturated blood (runs S1 - S4). These experiments ($P_{O_2, in} > 100$ mmHg and $P_{O_2, ext} > 700$ mmHg) were designed to minimize the effect on transfer of the oxygen-hemoglobin reaction. Consequently, the hemoglobin saturation was maintained near 100%, and the value of $dS/dP_{O_2} \approx 0$. Details on the experimental conditions of runs S1 - S4 are given in Table 4.3a. For oxygen saturated blood the continuum models, CMaug and CMequ, give the same predictions; so only one is shown. It can be seen that simplified DM generally predicts more transport than CMequ (for runs S1-S3, at $z=100$ cm, DM predicts \bar{P}_{O_2} that is ≈ 30 mmHg that is higher than that predicted by CMequ); this is due to the fact that the value of $D_{O_2, pl}$ used ($D_{O_2, pl} = 2.25 \times 10^{-5}$ cm²/sec; discrete model) is slightly higher than the value of D_{O_2} ($D_{O_2} = 1.65 \times 10^{-5}$ cm²/sec; homogeneous solution model). If $V(r) = V_{rbc}(r) = V_{pl}(r)$, $h(r) = H_D$ and $\alpha_{O_2} = \alpha_{O_2, rbc} = \alpha_{O_2, pl}$; then simplified DM can be reduced to CMequ. Therefore, for large vessels where $r_c \gg a$, $H_T/H_D \approx 1$, the cell-depleted layer thickness is only a negligible fraction of the tube diameter, and the velocity profile is nearly parabolic, the difference between the simulation results obtained by simplified DM and CMequ can be accounted for by the differences between the values used for $D_{O_2, pl}$ and D_{O_2} ; and between α_{O_2} , $\alpha_{O_2, rbc}$ and $\alpha_{O_2, pl}$. In run S4, a

Table 4.3a

Experimental conditions for the saturated blood experiments (runs S1 - S4) conducted by Diller (1977).

Run #	I.D. (μm)	O.D. (μm)	Q (ml/min)	H_D	$P_{O_2, in}$ (mmHg)	$P_{O_2, ext}$ (mmHg)	γ_{avg} (sec ⁻¹)
S1	635	1219	3.76	0.44	105	711	1250
S2	1016	2158	1.90	0.40	120	710	150
S3	635	1219	3.29	0.41	130	715	1100
S4	1016	2158	3.29	0.24	148	708	270

Table 4.3b

Experimental conditions for the unsaturated blood experiments (runs U1 - U6, US1 and US2) conducted by Diller (1977).

Run #	I.D. (μm)	O.D. (μm)	Q (ml/min)	pH	P_{50}	H_D	$P_{O_2, in}$ (mmHg)	$P_{O_2, ext}$ (mmHg)
U3	305	635	0.376	7.30	28.0	0.44	47.4	120
U4	635	1219	0.376	7.35	28.0	0.42	23.3	119
U5	635	1219	0.329	7.35	27.0	0.42	30.3	118
U6	635	1219	0.329	7.30	27.0	0.45	42.0	119
US2	635	1219	0.329	7.40	28.0	0.42	24.7	712
U1	305	635	0.376	7.30	28.5	0.40	18.5	116
US1	635	1219	3.290	7.30	26.5	0.42	18.2	716

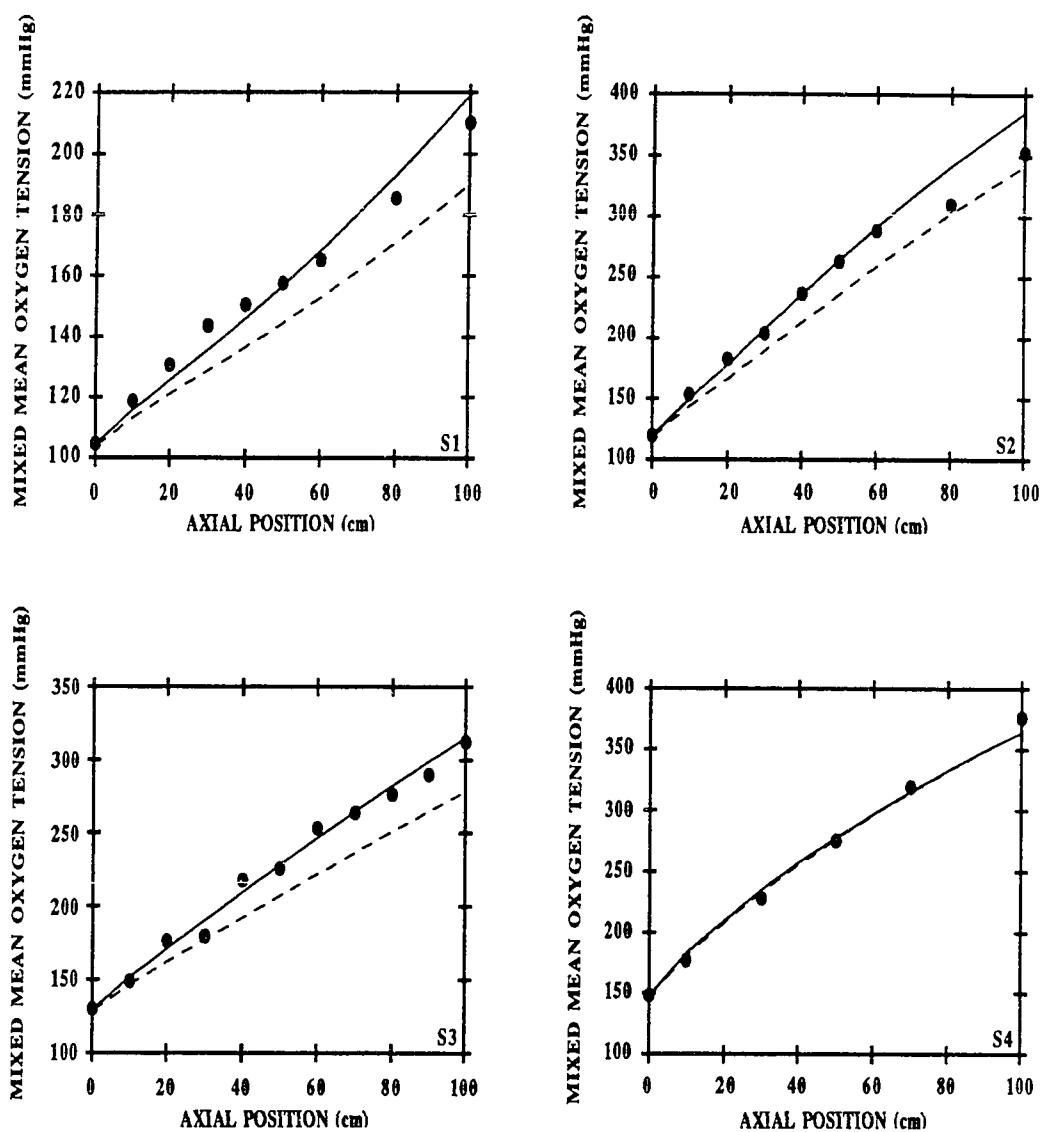


Figure 4.5: Comparison of models for oxygen uptake results for fully saturated fresh human blood flowing in silicone-rubber membrane tubes at 37 °C (details on the experimental conditions for runs S1 - S4 are given in Table 4.3a). Circles: experimental data from Diller (1977). Curves: theoretical simulation curves for the same conditions; (—) simplified DM and (----) CMequ.

lower hematocrit ($H_D \approx 24\%$) sample was used; consequently, a higher value was estimated for D_{O_2} ; and coincidentally, $D_{O_2} \approx D_{O_2,pl}$ ($D_{O_2} = 2.23 \times 10^{-5} \text{ cm}^2/\text{sec}$). The maximum deviation between the theoretical curve generated by simplified DM and the experimental data is 33.5 mmHg units; the mean absolute deviation and absolute algebraic deviation for any one curve does not exceed 9.1 and 7.2 mmHg units, respectively. On the other hand, the maximum deviation between the theoretical curve generated by CMequ and the experimental data is 33.5 mmHg units; the mean absolute deviation and absolute algebraic deviation for any one curve does not exceed 18.6 and 18.6 mmHg units, respectively. Thus, it is seen that the simplified discrete model generates more accurate predictions than the continuum model; except for run S4 where both models give almost equivalent predictions.

4.3.2.b *Uptake Experiments with Unsaturated Blood*

Figures 4.6 - 4.12 show the experimental data on both the equilibrated mixed mean oxyhemoglobin saturation (\bar{S}) and oxygen tension ($\overline{P_{O_2}}$) in comparison to the predictions generated by both the continuum and discrete models. The oxygen transfer measurements are made with the blood initially at partial saturation ($P_{O_2,in} \approx 20\text{-}50 \text{ mmHg}$). Some of these experiments (runs U1 - U6) were designed to operate almost on the steep portion of the saturation curve ($P_{O_2,ex} < 120 \text{ mmHg}$); while other experiments (runs US1 and US2) were to operate over the full range of the curve ($P_{O_2,ex} > 700 \text{ mmHg}$). Details on the experimental conditions of these runs are given in Tables 4.3b and 4.4.

U3 - U6 and US2: runs where shear-induced augmentation of oxygen is negligible

Molecular diffusivity was used in these simulations; with fresh human blood at 37°C and $H_D \approx 40\%$, for the continuum models: $D_{O_2} = 1.65 \times 10^{-5} \text{ cm}^2/\text{sec}$ and $D_{HbO_2} = 3.8 \times 10^{-7} \text{ cm}^2/\text{sec}$, for the discrete model: $D_{O_2,pl} = 2.25 \times 10^{-5} \text{ cm}^2/\text{sec}$ (see Table 4.1). From Figures 4.6 - 4.10, it is seen that CMaug consistently predicts more

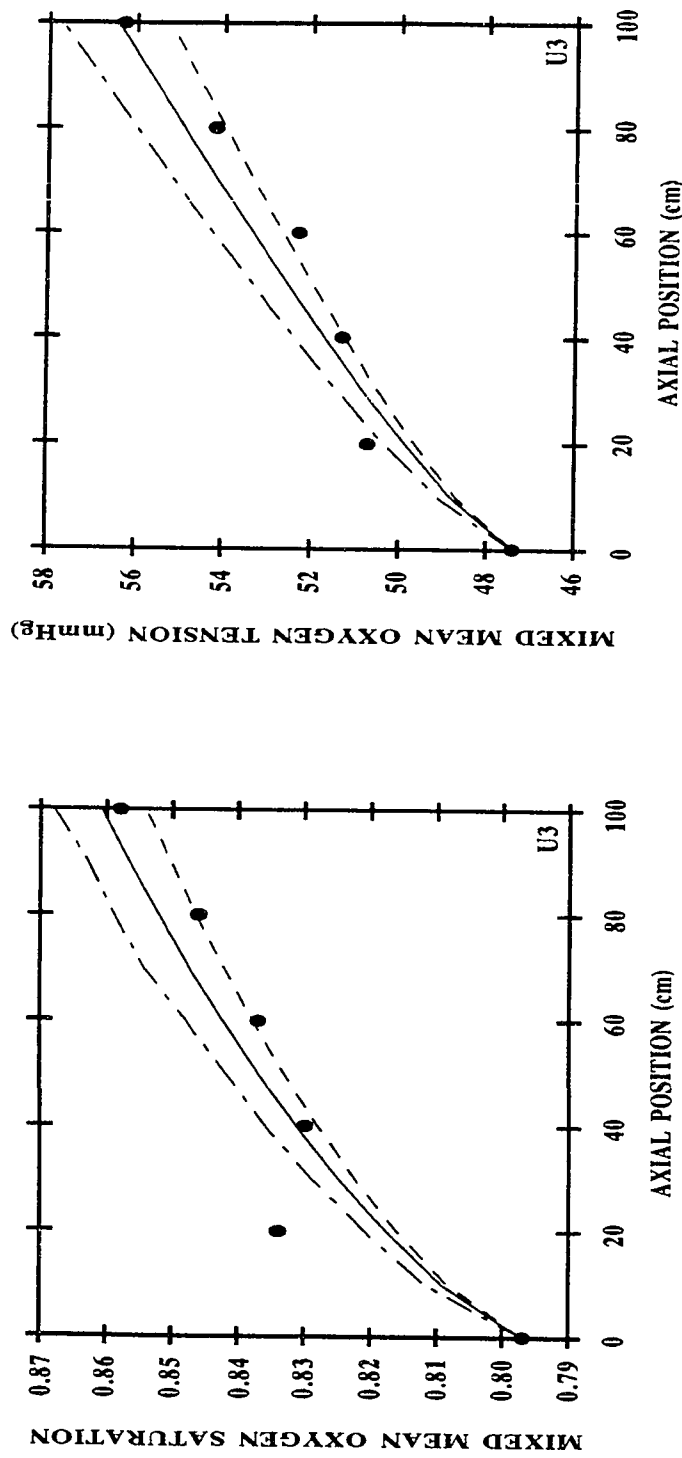


Figure 4.6: Comparison of models for oxygen uptake by fresh human blood with a H_D of 44% and P_{50} of 28 mmHg flowing at 0.376 ml/min in a 305- μ m-diameter silicone-rubber membrane tube at 37 °C (more detail on the experimental conditions for run U3 is given in Table 4.3b). The left panel gives the equilibrated mixed mean oxyhemoglobin saturation (\bar{S}) at different axial positions along the membrane oxygenator; and the right panel, the equilibrated mixed mean O_2 partial pressure (\bar{P}_{O_2}). Circles: experimental data from Diller (1977). Curves: theoretical simulation curves for the same conditions; (—) simplified DM, (---) CMequ and (- - -) CMAug.

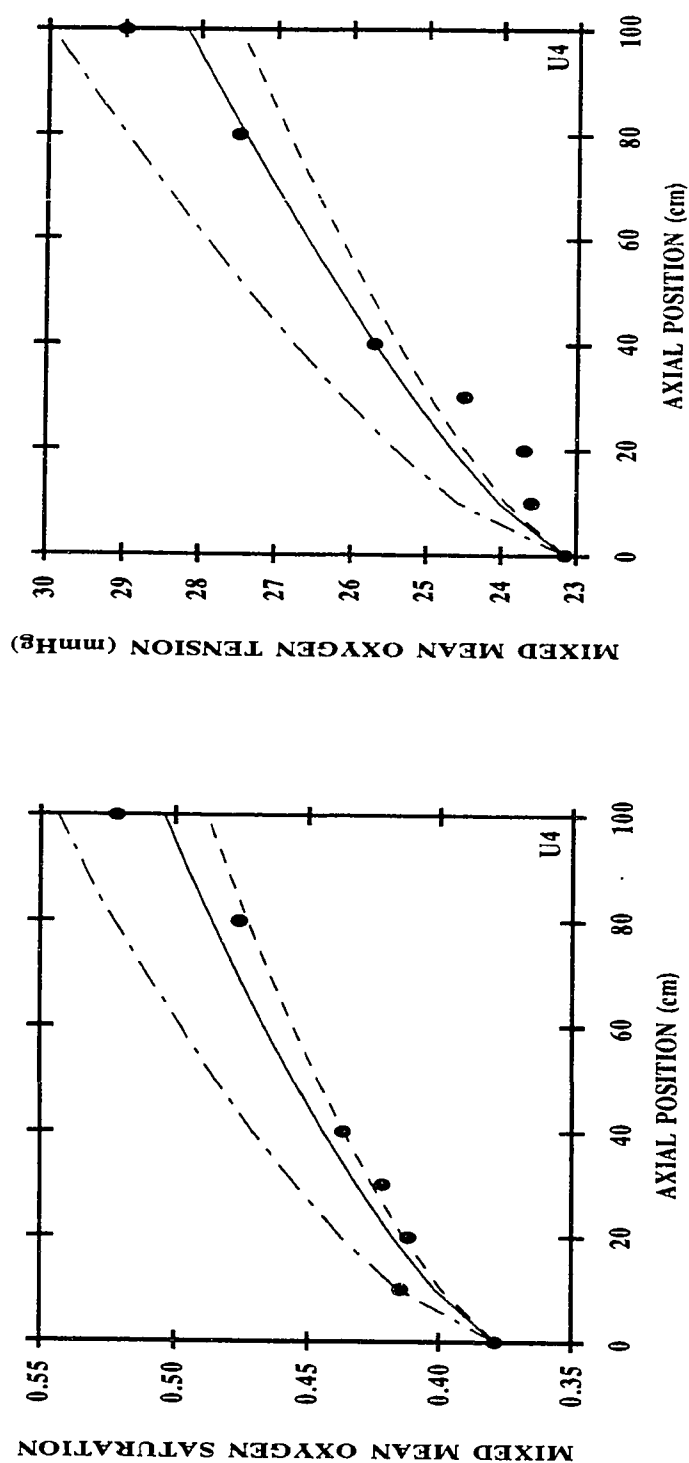


Figure 4.7: Comparison of models for oxygen uptake by fresh human blood with a H_D of 42% and P_{50} of 28 mmHg flowing at 0.376 ml/min in a 635- μ m-diameter silicone-rubber membrane tube at 37 °C (more detail on the experimental conditions for run U4 is given in Table 4.3b). The left panel gives the equilibrated mixed mean oxyhemoglobin saturation (\bar{S}) at different axial positions along the membrane oxygenator; and the right panel, the equilibrated mixed mean O_2 partial pressure (\bar{P}_{O_2}). Circles: experimental data from Diller (1977). Curves: theoretical simulation curves for the same conditions; (—) simplified DM, (---) CMequ and (---) CMaug.

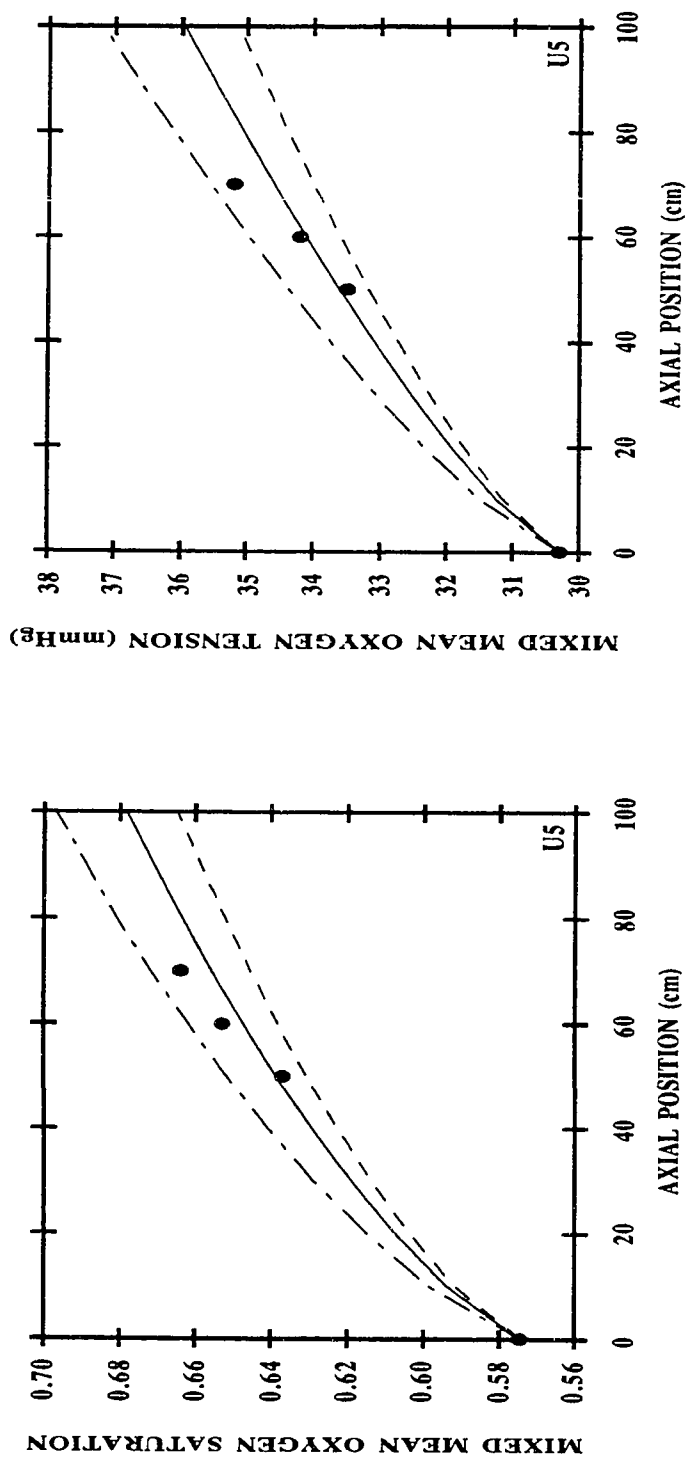


Figure 4.8: Comparison of models for oxygen uptake by fresh human blood with a H_D of 42% and P_{50} of 27 mmHg flowing at 0.329 ml/min in a 635- μ m-diameter silicone-rubber membrane tube at 37 °C (more detail on the experimental conditions for run U5 is given in Table 4.3b). The left panel gives the equilibrated mixed mean oxyhemoglobin saturation (\bar{S}) at different axial positions along the membrane oxygenator; and the right panel, the equilibrated mixed mean O_2 partial pressure (\bar{P}_{O_2}). Circles: experimental data from Diller (1977). Curves: theoretical simulation curves for: the same conditions; (—) simplified DM, (---) CMequ and (- - -) CMaug.

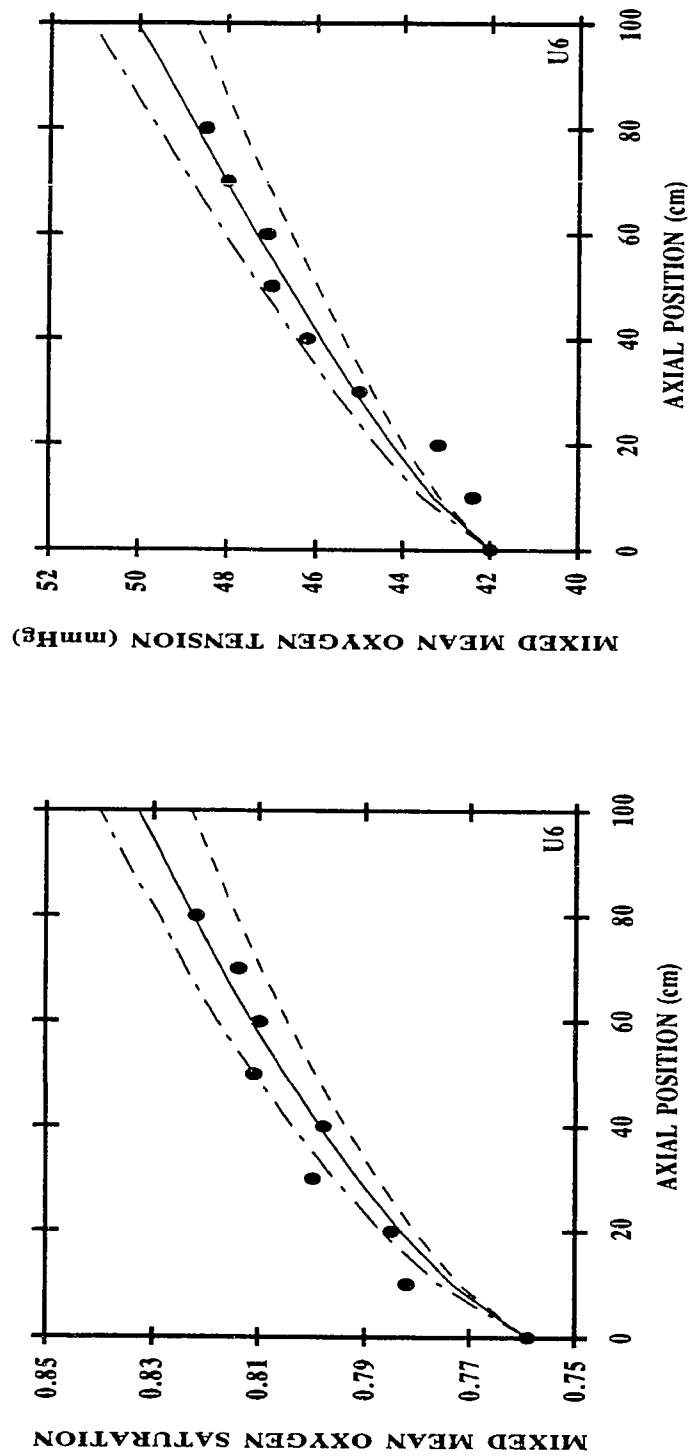


Figure 4.9: Comparison of models for oxygen uptake by fresh human blood with a H_D of 45% and P_{50} of 27 mmHg flowing at 0.329 ml/min in a 635- μ m-diameter silicone-rubber membrane tube at 37 °C (more detail on the experimental conditions for run U6 is given in Table 4.3b). The left panel gives the equilibrated mixed mean oxyhemoglobin saturation (\bar{S}) at different axial positions along the membrane oxygenator; and the right panel, the equilibrated mixed mean O_2 partial pressure (\bar{P}_{O_2}). Circles: experimental data from Diller (1977). Curves: theoretical simulation curves for the same conditions; (—) simplified DM, (---) CMequ and (- - -) CMaug.

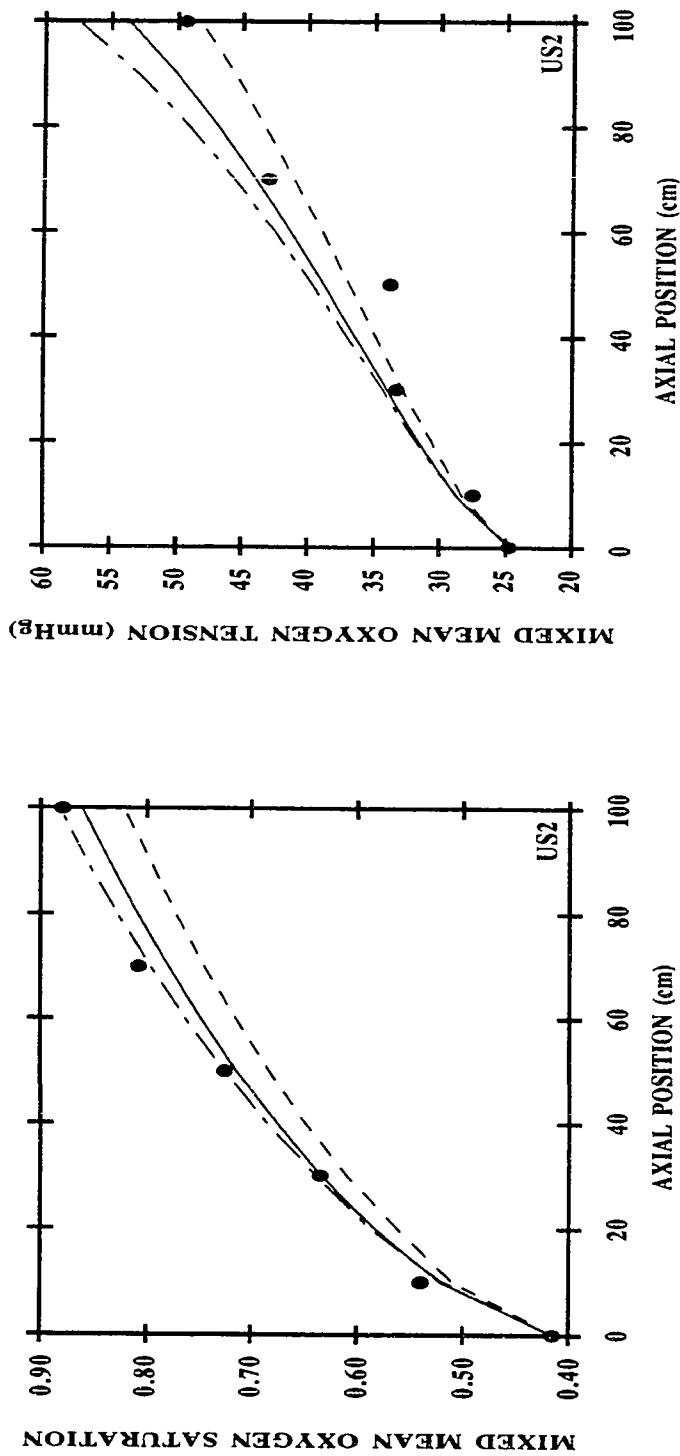


Figure 4.10: Comparison of models for oxygen uptake by fresh human blood with a H_D of 42% and P_{50} of 28 mmHg flowing at 0.329 ml/min in a 635- μ m-diameter silicone-rubber membrane tube at 37 °C (more detail on the experimental conditions for run US2 is given in Table 4.3b). The left panel gives the equilibrated mixed mean oxyhemoglobin saturation (\bar{S}) at different axial positions along the membrane oxygenator; and the right panel, the equilibrated mixed mean O_2 partial pressure (\bar{P}_{O_2}). Circles: experimental data from Diller (1977). Curves: theoretical simulation curves for the same conditions; (—) simplified DM, (---) CMequ and (---) CMaug.

transport than the other two models. However, upon setting the value of D_{HbO_2} zero, the calculations generated by CMAug and CMequ become identical. In addition, both simplified DM and CMequ generate accurate predictions which agree with the measured values (equilibrated mixed mean oxygen saturation and tension) for runs U3 - U6 and US2 to well within the experimental error. Here simplified DM approach predicts slightly more transport than CMequ; this is, again, due to the values used for $D_{O_2,pl}$ and D_{O_2} . For runs U3 - U6 and US2 differences of no more than 0.35 mM in $[O_2]_{total}$, total O_2 content, were observed between simulation results generated by DM and CMAug; and differences of no more than 0.35 mM in $[O_2]_{total}$ were observed between the DM and CMequ. The maximum deviations between the theoretical curves generated by simplified DM, CMAug and CMequ from the experimental data are 0.24 mM, 0.41 mM, and 0.54 mM in $[O_2]_{total}$, respectively. The algebraic deviations for any one curve generated by simplified DM, CMAug and CMequ from the experimental data do not exceed 0.10 mM, 0.21 mM and 0.32 mM in $[O_2]_{total}$, respectively.

Table 4.4: Values of local and overall operating slopes of ODC and average shear rate for the unsaturated blood experiments conducted by Diller (1977).

Run #	$m = \frac{H_D C_{heme}}{\alpha_{O_2}} \frac{dS}{dP_{O_2}}$	$M = \frac{H_D C_{heme,rbc}}{\alpha_{O_2}} \left(\frac{S _{P_{O_2}=P_{O_2,ex}} - S _{P_{O_2}=P_{O_2,in}}}{P_{O_2,ex} - P_{O_2,in}} \right)$	$\gamma_{avg} \text{ (sec}^{-1}\text{)}$
U3	42	18.9	985
U4	138	41.5	110
U5	124	30.8	110
U6	44	20.5	110
US2	$m_1^\dagger = 158$ $m_2^\dagger = 70$	5.4	110
U1	154	46.3	1125
US1	150	6.8	1095

[†] m_1 and m_2 for run US2 in Table 4.4 represent the local operating slopes along the unsaturated and almost saturated portions of the ODC, respectively.

U1 and US1: runs where shear-induced augmentation of oxygen is important

Figures 4.11 and 4.12 give the comparison of the results computed by CMequ using different values of effective diffusivity for O_2 , $D_{O_2,eff}$, with the experimental data from runs U1 and US1. The bottom curve in both plots is generated using ordinary diffusivities ($D_{O_2}=1.65 \times 10^{-5} \text{ cm}^2/\text{sec}$ and $D_{O_2,pl}=2.25 \times 10^{-5} \text{ cm}^2/\text{sec}$). It is clear that without the usage of the effective diffusivity which includes the contribution from shear-induced augmentation, CMequ under estimates the amount of transport. The uppermost curve is generated using effective diffusivity estimated from Equations (2.19a) and (2.19b); the intermediate set is generated using Equations (2.19a) and (2.19b) with m , the local operating slope, being replaced with M , the overall operating slope. The effective RBC diffusion coefficient, D_{rbc} , is evaluated from Zydney and Colton's correlation (1988). Using the equivalent spherical radius of red cell, $a=2.75 \text{ }\mu\text{m}$, and whole blood hematocrit, $H_D=0.4$, D_{rbc} is calculated to be $(3 \times 10^{-9} \text{ cm}^2) (\gamma_{avg} \text{ sec}^{-1})$ from Equation (2.16). The effective oxygen diffusivity in the suspension is then the sum of the ordinary diffusivity and the shear-induced diffusivity. If one were to use m to estimate the effective diffusivity; the models end up over predicting the transport observed in both runs U1 and US1. Better agreements between the model simulations and experimental measurements were achieved by using M in place of m (see Figures 4.11 and 4.12). Figure 4.13 provides a comparison between simplified DM and CMequ under the experimental condition of U1 and using both $D_{O_2,eff}=D_{O_2,SF}$ and $D_{O_2,eff}=D_{O_2,SF}+D_{rbc}(1+M)$. It is clear from this plot that the differences in the results generated by the two models are small for both sets of diffusivity values. In addition, for both models the usage of a modified diffusivity, $D_{O_2,eff}=D_{O_2,SF}+D_{rbc}(1+M)$, to also include the shear-induced augmentation of O_2 provides a better agreement between the simulation and experimental results.

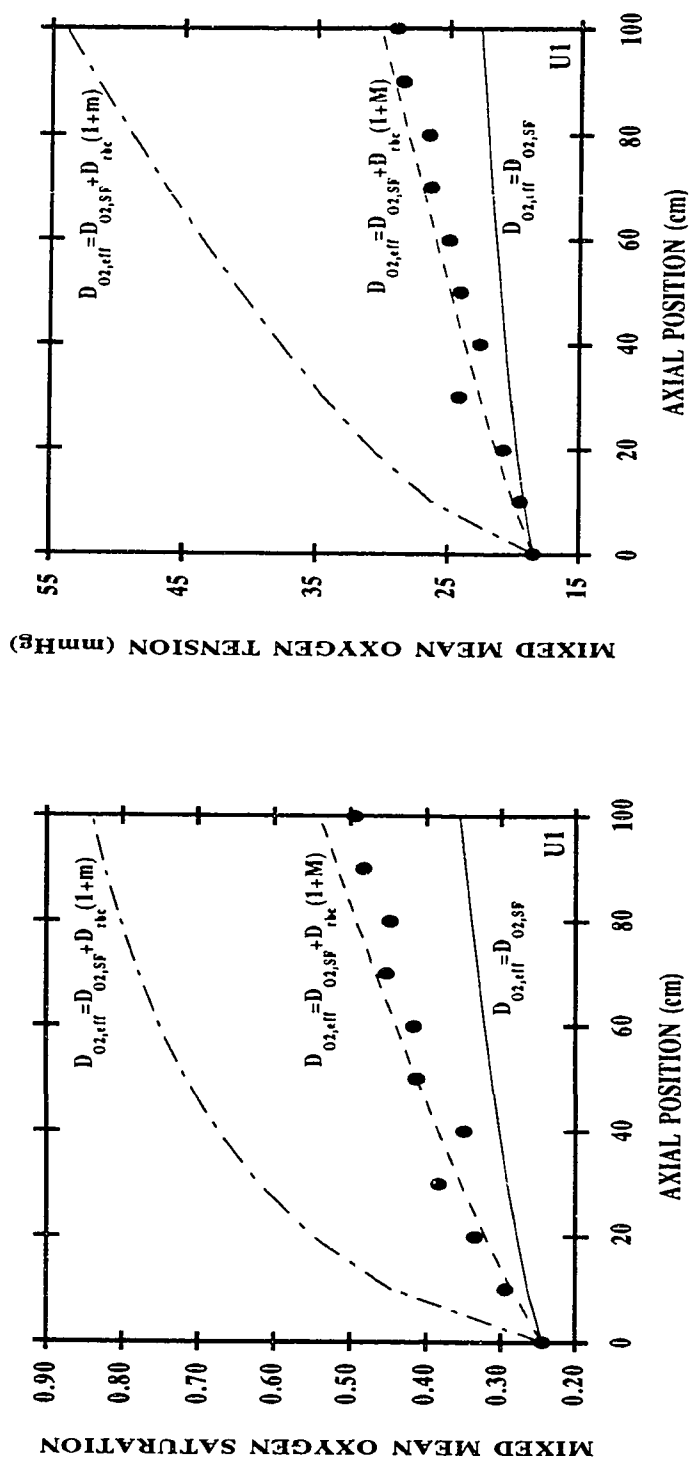


Figure 4.11: Oxygen uptake result by fresh human blood with a H_D of 40% and P_{50} of 28.5 mmHg flowing at 0.376 ml/min in a 305- μ m-diameter silicone-rubber membrane tube at 37 °C (more detail on the experimental conditions of run U1 is given in Tables 4.3b and 4.4). The left panel gives the equilibrated mixed mean oxyhemoglobin saturation (\bar{S}) at different axial positions along the membrane oxygenator; and the right panel, the equilibrated mixed mean O_2 partial pressure (\bar{P}_{O2}). Circles: experimental data from Diller (1977). Curves: theoretical simulation of experiments generated by CMequ: the bottom curve (—) is generated using $D_{O2,eff} = 1.65 \times 10^{-5} \text{ cm}^2/\text{sec}$; the intermediate curve (- - -) is generated using $D_{O2,eff} = 17.6 \times 10^{-5} \text{ cm}^2/\text{sec}$; the uppermost curve (— · —) is generated using $D_{O2,eff} = 54.0 \times 10^{-5} \text{ cm}^2/\text{sec}$.

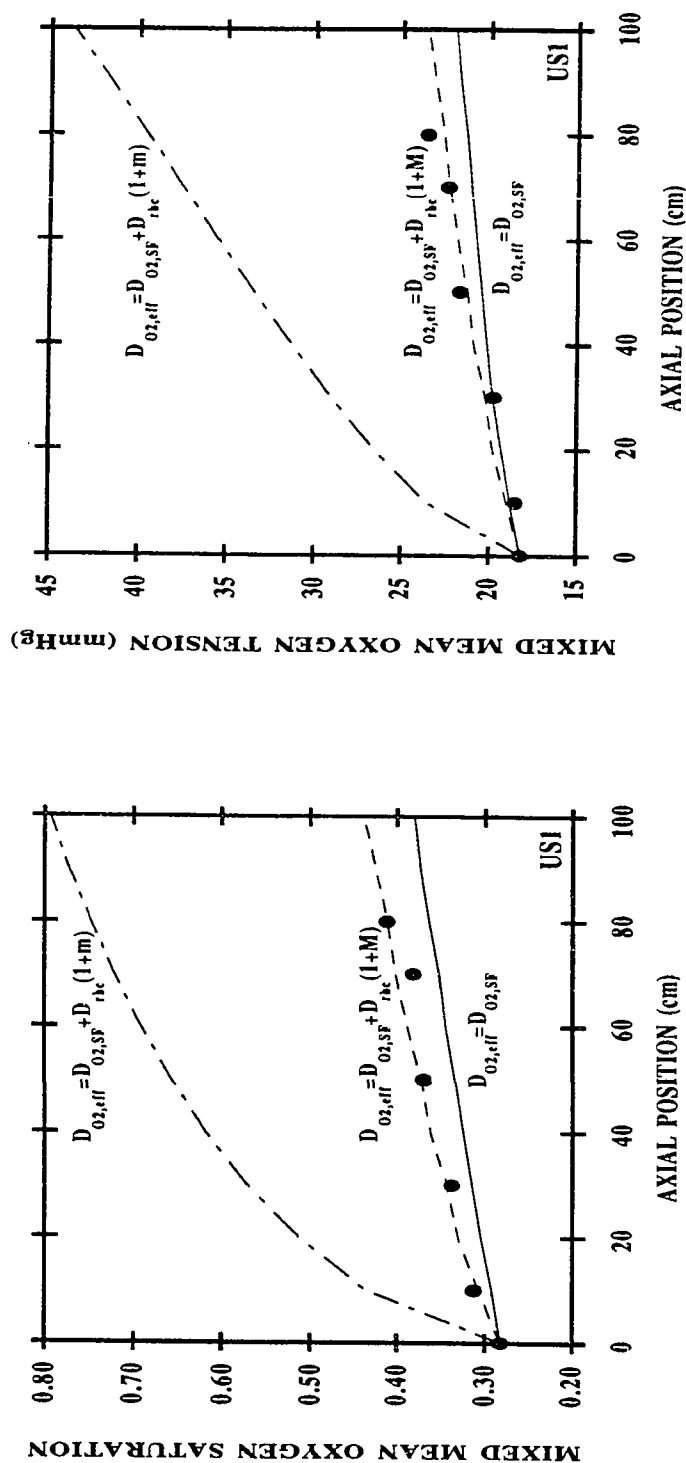


Figure 4.12: Oxygen uptake result by fresh human blood with a H_D of 42% and P_{50} of 26.5 mmHg flowing at 3.29 ml/min in a 635- μ m-diameter silicone-rubber membrane tube at 37 °C (more detail on the experimental conditions of run US1 is given in Tables 4.3b and 4.4). The left panel gives the equilibrated mixed mean oxyhemoglobin saturation (\bar{S}) at different axial positions along the membrane oxygenator; and the right panel, the equilibrated mixed mean O_2 partial pressure (\bar{P}_{O_2}). Circles: experimental data from Diller (1977). Curves: theoretical simulation of experiments generated by CMequ: the bottom curve (—) is generated using $D_{O_2,eff} = 1.65 \times 10^{-5}$ cm²/sec; the intermediate curve (- - -) is generated using $D_{O_2,eff} = 4.21 \times 10^{-5}$ cm²/sec; the uppermost curve (---) is generated using $D_{O_2,eff} = 51.2 \times 10^{-5}$ cm²/sec.

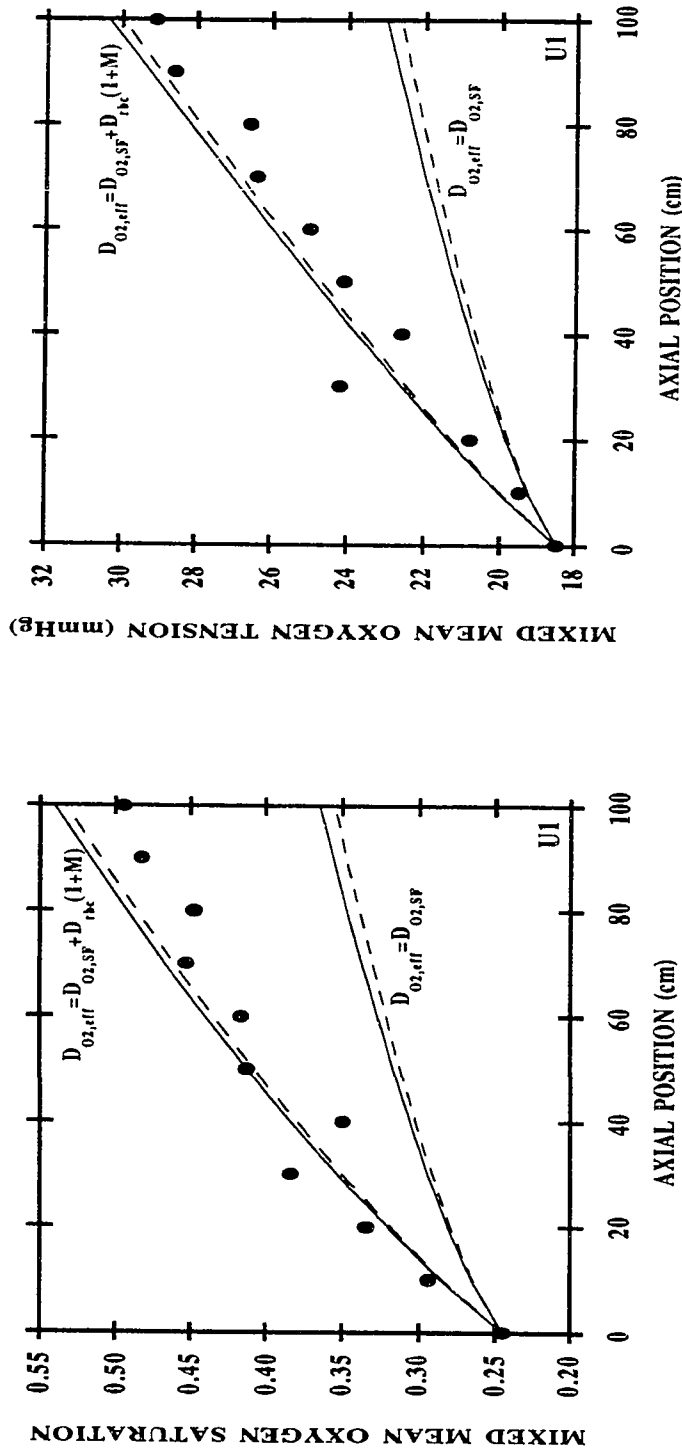


Figure 4.13: Comparison of oxygen uptake result by fresh human blood with a H_D of 40% and P_{50} of 28.5 mmHg flowing at 0.376 ml/min in a 305- μ m-diameter silicone-rubber membrane tube at 37 °C (more detail on the experimental condition of run U1 is given in Tables 4.3b and 4.4). The left panel gives the equilibrated mixed mean oxyhemoglobin saturation (\bar{S}) at different axial positions along the membrane oxygenator; and the right panel, the equilibrated mixed mean O_2 partial pressure (\bar{P}_{O_2}). Circles: experimental data from Diller (1977). Curves: theoretical simulation of experiments; (—) simplified DM and (---) CMequ. The bottom set of curves is generated using $D_{O_2,eff} = 2.25 \times 10^{-5}$ cm²/sec for simplified DM and $D_{O_2,eff} = 1.65 \times 10^{-5}$ cm²/sec for CMequ; the upper set of curves is generated using $D_{O_2,eff} = 18.2 \times 10^{-5}$ cm²/sec for simplified DM and $D_{O_2,eff} = 17.6 \times 10^{-5}$ cm²/sec for CMequ.

4.3.2.c Analysis of Enhanced Transfer

The values for m , M and γ_{avg} for various runs are listed in Table 4.4. The local operating slopes for these runs are approximately constant, except for run US2 in which the blood experiences both the unsaturated and almost saturated regions of the ODC (m_1 and m_2 for run US2 in Table 4.4 represent the local operating slopes in the unsaturated and almost saturated portions of the dissociation curve, respectively). From Table 4.4, it is seen that runs U1 and US1 were operated both along the steep portion of the ODC ($m > 150$) and under high shear rate environment ($\gamma_{avg} > 1000 \text{ sec}^{-1}$); while other runs were operated similarly with high oxygen sink strength but at low shear rate (runs U4, U5 and US2), or low oxygen carriage potential but at high shear rate (run U3), or low m and low shear rate (run U6). The result indicates that shear-dependent augmentation is not significant in saturated whole blood flowing through an oxygenated environment. The presence of an oxygen sink inside the red cells would provide an additional mechanism of augmented transport only if high shear rate is also available in the flow field. From the simple analysis outlined earlier in Section 2.2.2, it is seen that the magnitude of the augmentation due to the lateral migration of unsaturated RBCs in the radial direction, which could be potentially large, is theoretically related to the product of $D_{rbc}m$. However, from analyzing Diller's experimental results on runs U1 and US1, the outcome seems to demonstrate that the values of m along with γ can be used as indicators for monitoring whether the effect of shear-induced augmentation is substantial or not; but the magnitude of the augmentation is related to $D_{rbc}M$. Tables 4.5 and 4.6 summarize the difference between Diller *et al.*'s experimental results and the calculations generated by simplified DM and CMequ using three different values of $D_{O2,eff}$.

These results illustrate that for vessels with diameters of 300 μm and larger augmented O_2 transport is significant only under the conditions of both high m and γ . In addition, the magnitude of this effect was shown theoretically to be related to the

Table 4.5

Comparison of Diller's oxygen transfer data to the simulation results generated by simplified DM using three different values of $D_{O_2,eff}$. Both the maximum deviation and algebraic deviation[†] of the numerical calculations from the experimental data are given here for $[O_2]_{total}$, the total O_2 content.

$D_{O_2,eff}$	$D_{O_2,pl}=D_{O_2,SF}$		$D_{O_2,pl}=D_{O_2,SF}+D_{rbc}(1+M)$		$D_{O_2,pl}=D_{O_2,SF}+D_{rbc}(1+m)$	
Error	lmax. deviation	algebraic deviation	lmax. deviation	algebraic deviation	lmax. deviation	algebraic deviation
Run U3	0.057 mM	0.001 mM ↓*	0.512 mM	0.275 mM ↑*	0.887 mM	0.585 mM ↑
Run U4	0.154 mM	0.005 mM ↑	0.352 mM	0.144 mM ↑	0.799 mM	0.491 mM ↑
Run U5	0.071 mM	0.025 mM ↓	0.083 mM	0.078 mM ↑	0.423 mM	0.312 mM ↑
Run U6	0.032 mM	0.001 mM ↓	0.101 mM	0.050 mM ↑	0.266 mM	0.137 mM ↑
Run US2	0.242 mM	0.108 mM ↓	0.189 mM	0.119 mM ↑	1.54 mM	1.00 mM ↑
Run U1	1.09 mM	0.644 mM ↓	0.326 mM	0.077 mM ↑	3.06 mM	2.10 mM ↑
Run US1	0.351 mM	0.191 mM ↓	0.212 mM	0.062 mM ↑	2.44 mM	1.45 mM ↑

[†] The algebraic deviation is calculated as $\sum_{i=1}^{i=N} (deviation)_i / N$ where N is the number of data points.

* ↓ indicates that a model on the average under predicts the amount of transport, and ↑ indicates that a model on the average over predicts the amount of transport.

Table 4.6

Comparison of Diller's oxygen transfer data to the simulation results generated by CMequ using three different values of $D_{O_2,eff}$. Both the maximum deviation and algebraic deviation[†] of the numerical calculations from the experimental data are given here for $[O_2]_{total}$, the total O_2 content.

$D_{O_2,eff}$	$D_{O_2}=D_{O_2,SF}$		$D_{O_2}=D_{O_2,SF}+D_{rbc}(1+M)$		$D_{O_2}=D_{O_2,SF}+D_{rbc}(1+m)$	
Error	lmax. deviation	algebraic deviation	lmax. deviation	algebraic deviation	lmax. deviation	algebraic deviation
Run U3	0.037 mM	0.035 mM ↓*	0.520 mM	0.282 mM ↑*	0.938 mM	0.636 mM ↑
Run U4	0.296 mM	0.018 mM ↑	0.288 mM	0.084 mM ↑	0.985 mM	0.373 mM ↑
Run U5	0.162 mM	0.086 mM ↓	0.094 mM	0.040 mM ↑	0.439 mM	0.323 mM ↑
Run U6	0.116 mM	0.061 mM ↓	0.067 mM	0.004 mM ↑	0.250 mM	0.131 mM ↑
Run US2	0.544 mM	0.318 mM ↓	0.383 mM	0.206 mM ↓	1.40 mM	0.925 mM ↑
Run U1	1.17 mM	0.704 mM ↓	0.386 mM	0.112 mM ↑	3.33 mM	2.37 mM ↑
Run US1	0.403 mM	0.216 mM ↓	0.045 mM	0.032 mM ↑	2.58 mM	1.60 mM ↑

[†] The algebraic deviation is calculated as $\sum_{i=1}^{i=N} (deviation)_i / N$ where N is the number of data points.

* ↓ indicates that a model on the average under predicts the amount of transport, and ↑ indicates that a model on the average over predicts the amount of transport.

magnitude of $D_{rbc}m$; however, Diller *et al.*'s experimental results seem to point toward $D_{rbc}M$. As a result, more experimental data is needed for further investigation and quantification of this phenomena as a function of vessel diameter, oxygen storage potential (m or M) and shear rate. Furthermore, it should be mentioned that for runs U1 and US1 implementation of Equation (2.20), which was developed by Diller and Mikic (1983) for estimating $D_{O2,eff}$ in the O_2 transport models generated results which were similar to that predicted by using Equation (2.19) with m being replaced with M . Equation (2.19) is on a theoretically more sound basis in the sense that Equation (2.20) does not include the effect of dispersive fluid migration which is proportional to $(1-H_D)D_{rbc}$. The effect of dispersive fluid migration is minor when $M \gg 1$, but it could become important under the conditions of small M and high γ .

4.3.3 Comparison with Schmukler and Chien's Membrane Deoxygenator Data (100 μm in diameter)

Schmukler and Chien (1985) measured deoxygenation of red cells flowing through 100- μm -diameter microporous polypropylene hollow fibers. The deoxygenators were composed of fiber beds consisting of 96 or 144 parallel fibers and with 5 or 10 cm active length. The incoming sample to the deoxygenator was preoxygenated to give a $P_{O2,in} \approx 91$ mmHg. A stream of humidified 95% nitrogen - 5% carbon dioxide ($P_{O2,ext} = 0$ mmHg) flowed counter-currently in the environmental chamber. The outgoing sample from the deoxygenator was directly connected to a blood gas analyzer, and time was allowed for equilibration before readings were obtained. The permeability of the polypropylene hollow fibers used in the deoxygenator was obtained by analyzing the authors' results on hemoglobin solution, and it was determined to be 1×10^{-11} $\text{Mcm}^2/\text{sec}/\text{mmHg}$ (Boland *et al.*, 1987). The P_{50} of the blood was taken to be 27 mmHg as typical of red cell suspensions at the experimental pH of

7.4. All other parameters required for the theoretical simulation were specified by Schmukler and Chien.

Figure 4.14 shows the results of the calculations generated by the models corresponding to both the outgoing equilibrated mixed mean oxygen tension and saturation as functions of the residence time of the red cell suspension. The residence time in the deoxygenator is defined as the ratio of the active fiber length to the average fluid velocity in the tube. From both plots, it is clear that the differences in simulation results for these models are small. Differences of no more than 2.2 mmHg in oxygen tension and 0.03 in fractional saturation of hemoglobin were observed between the results from the simplified DM and CMAug; and differences of no more than 0.5 mmHg in oxygen tension and 0.01 in saturation of hemoglobin between the simplified DM and CMequ. Furthermore, the agreement between the theoretical curves and the experimental data is excellent. In the worst case, the hematocrit of 1.5%, the maximum deviations and the algebraic average deviations between the theoretical results generated by simplified DM, CMAug, CMequ and the experimental data are 7.7, 7.2, 6.7 and 3.4, 3.0, 2.3 mmHg units, respectively.

It has been reported that in dilute suspensions particle rotation augments the mass transport (Keller, 1971; Wang and Keller, 1985). However, this effect was found to be insignificant in analyzing Schmukler and Chien's data. As illustrated in Figures 4.15 - 4.16, usage of the ordinary molecular diffusivity is sufficient for predicting the observed transport phenomena. Introduction of shear-induced diffusivity into the models leads to over prediction of the transport for the $H_D=10\%$ and 5% cases. Table 4.7 summarizes the maximum deviation and algebraic average deviation of the numerical results generated by simplified DM and CMequ using three different values of effective diffusivity for O_2 from the experimental data.

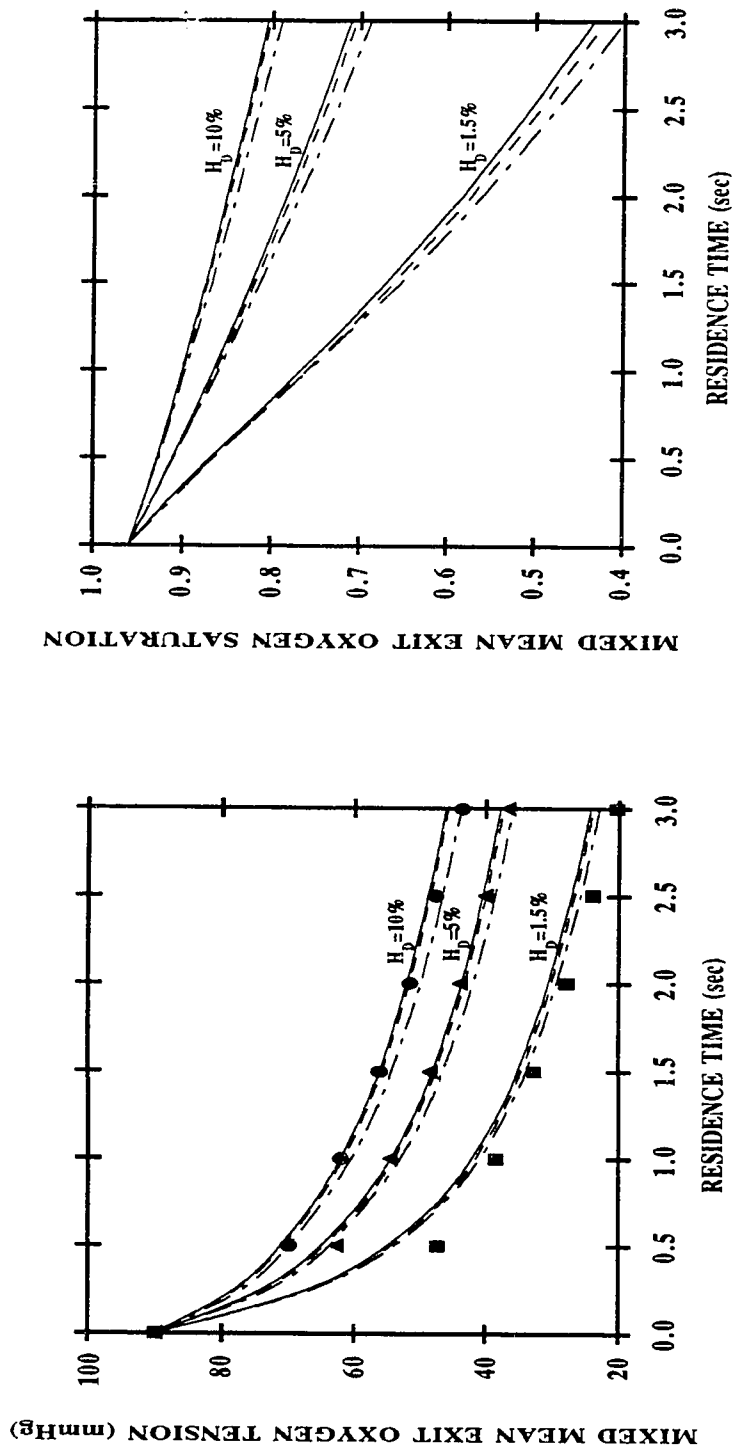


Figure 4.14: Comparison of models for oxygen release from red cell suspensions with P_{50} of 27 mmHg flowing in microporous polypropylene hollow fibers with 100 μm in I.D. and 130 μm in O.D. at 37 $^{\circ}\text{C}$. The left panel gives the equilibrated mixed mean O_2 partial pressure ($\overline{P_{\text{O}_2}}$) as a function of residence time; and the right panel, the equilibrated mixed mean oxyhemoglobin saturation (\overline{S}). Data points: means of experiments from Schmukler and Chien (1985). Curves: theoretical simulation curves for the same conditions; (—) simplified DM, (-.-.-) CMequ and (---) CMAug.

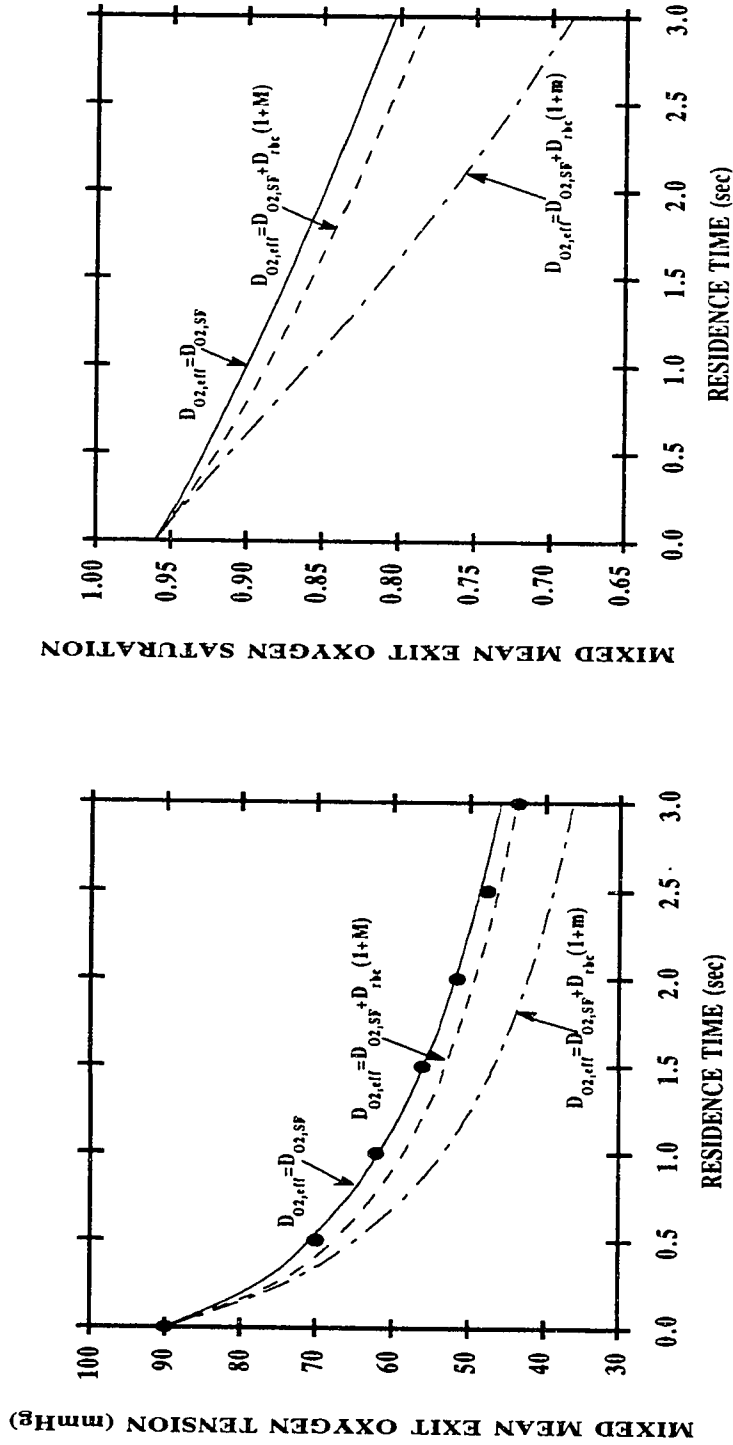


Figure 4.15: Oxygen release from red cell suspensions with a H_D of 10% and P_{50} of 27 mmHg flowing in microporous polypropylene hollow fibers with 100 μm in I.D. and 130 μm in O.D. at 37 $^{\circ}\text{C}$. The left panel gives the equilibrated mixed mean O_2 partial pressure (\bar{P}_{O_2}) as a function of residence time; and the right panel, the equilibrated mixed mean oxyhemoglobin saturation (\bar{S}). Data points: means of experiments from Schmukler and Chien (1985). Curves: theoretical simulation of experiments generated by CMequ: the upper curve (—) is generated using $D_{O_2,eff} = D_{O_2,SF} + D_{r,bc}(1+M)$ where $M = 16.5$; the intermediate curve (- - -) is generated using $D_{O_2,eff} = D_{O_2,SF} + D_{r,bc}(1+m)$ where m is given by Equation (2.19b); the bottom curve (- · - ·) is generated using $D_{O_2,eff} = D_{O_2,SF}$.

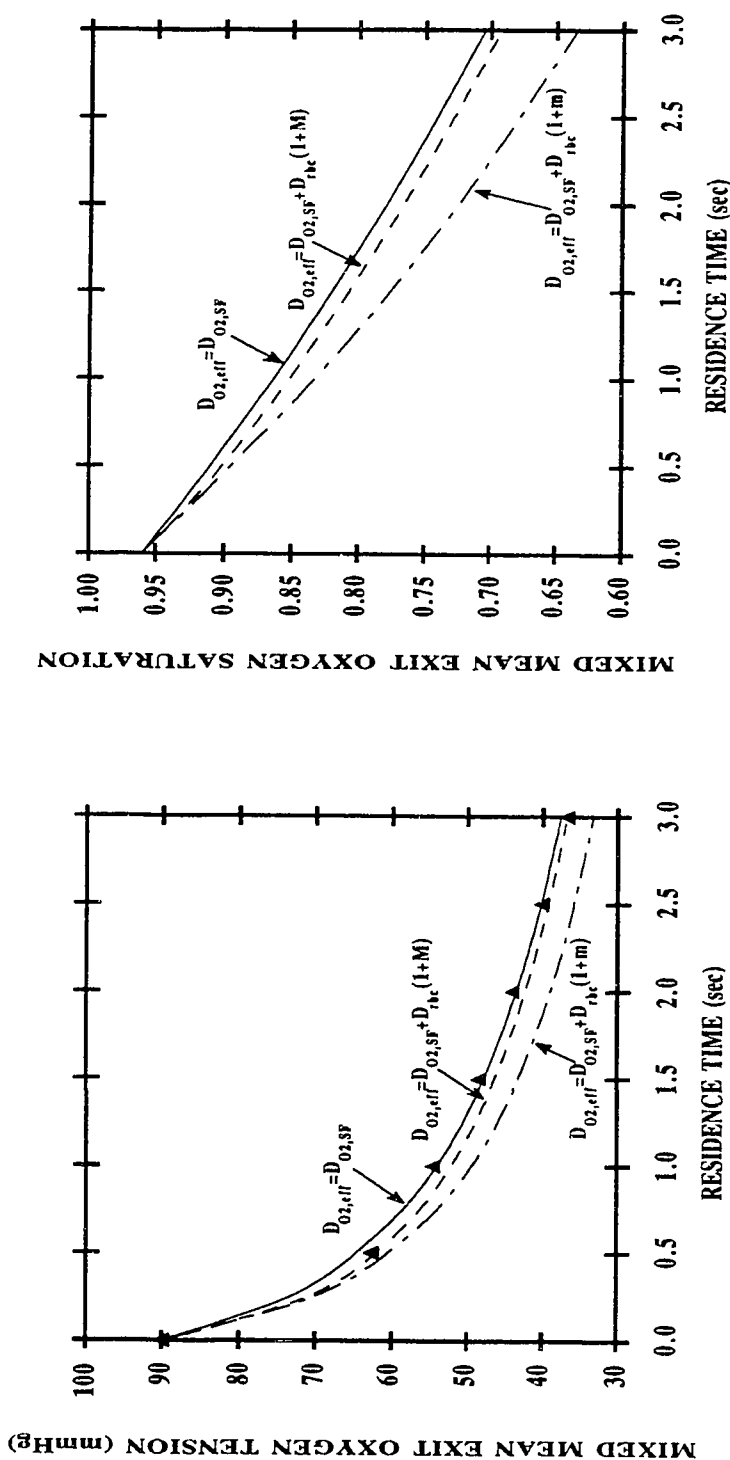


Figure 4.16: Oxygen release from red cell suspensions with a H_D of 5% and P_{50} of 27 mmHg flowing in microporous polypropylene hollow fibers with 100 μm in I.D. and 130 μm in O.D. at 37 $^{\circ}\text{C}$. The left panel gives the equilibrated mixed mean O_2 partial pressure (\bar{P}_{O_2}) as a function of residence time; and the right panel, the equilibrated mixed mean oxyhemoglobin saturation (\bar{S}). Data points: means of experiments from Schmukler and Chien (1985). Curves: theoretical simulation of the experiments generated by CMequ: the upper curve (—) is generated using $D_{O_2,eff} = 1.65 \times 10^{-5} \text{ cm}^2/\text{sec}$; the intermediate curve (- - -) is generated using $D_{O_2,eff} = D_{O_2,SF} + D_{rbc}(1+M)$ where $M=8.3$; the bottom curve (- · -) is generated using $D_{O_2,eff} = D_{O_2,SF} + D_{rbc}(1+m)$ where m is given by Equation (2.19b).

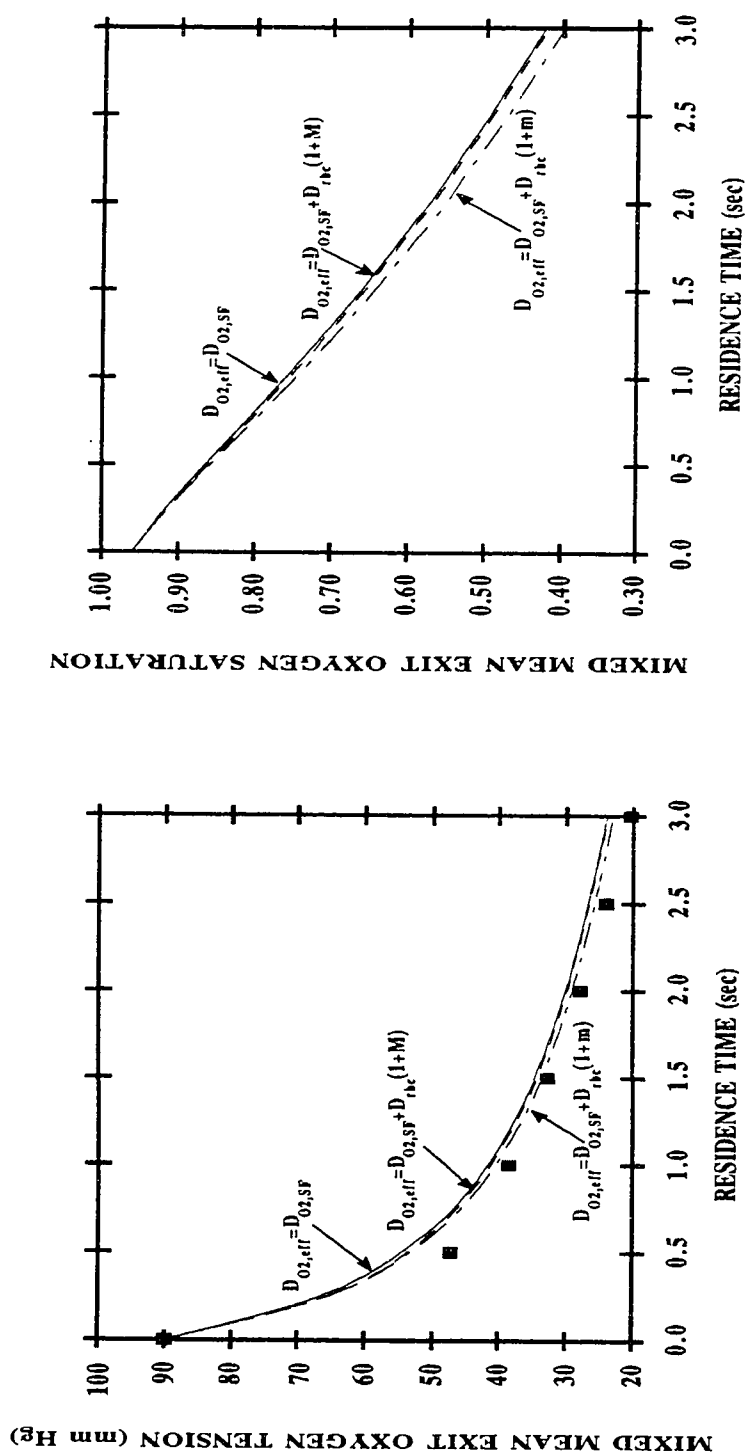


Figure 4.17: Oxygen release from red cell suspensions with a H_D of 1.5% and P_{50} of 27 mmHg flowing in microporous polypropylene hollow fibers with 100 μm in I.D. and 130 μm in O.D. at 37 $^{\circ}\text{C}$. The left panel gives the equilibrated mixed mean O_2 partial pressure (\bar{P}_{O_2}) as a function of residence time; and the right panel, the equilibrated mixed mean oxyhemoglobin saturation (\bar{S}). Data points: means of experiments from Schumaker and Chien (1985). Curves: theoretical simulation of experiments generated by CMequ: the upper curve (—) is generated using $D_{\text{O}_2,eff} = D_{\text{O}_2,SF} + D_{\text{O}_2,rc}(1+M)$; the intermediate curve (- - -) is generated using $D_{\text{O}_2,eff} = D_{\text{O}_2,SF} + D_{\text{O}_2,rc}$ where $M=2.5$; the bottom curve (- . -) is generated using $D_{\text{O}_2,eff} = D_{\text{O}_2,SF}$ where m is given by Equation (2.19b).

Table 4.7

Comparison of Chien and Schukler's oxygen transfer data to the simulation results generated by simplified DM and CMequ using three different values of $D_{O_2,eff}$. Both the maximum deviation and algebraic deviation of the numerical calculations from the experimental data are given here for $\overline{P_{O_2}}$, the equilibrated mixed mean outgoing P_{O_2} .

Discrete model: simplified DM					
$D_{O_2,eff}$	$D_{O_2,pl} = D_{O_2,SF}$		$D_{O_2,pl} = D_{O_2,SF} + D_{rbc}(1+M)$		$D_{O_2,pl} = D_{O_2,SF} + D_{rbc}(1+m)$
Error	lmax. deviation	algebraic deviation	lmax. deviation	algebraic deviation	lmax. deviation algebraic deviation
$H_D = 10\%$	2.5 mmHg	0.79 mmHg ↓*	2.9 mmHg	1.2 mmHg ↑*	4.9 mmHg 4.1 mmHg ↑
$H_D = 5\%$	1.2 mmHg	0.48 mmHg ↓	1.5 mmHg	0.57 mmHg ↑	3.3 mmHg 2.0 mmHg ↑
$H_D = 1.5\%$	7.7 mmHg	3.4 mmHg ↓	7.1 mmHg	3.2 mmHg ↓	6.9 mmHg 2.8 mmHg ↓
Continuum model: CMequ					
$D_{O_2,eff}$	$D_{O_2} = D_{O_2,SF}$		$D_{O_2} = D_{O_2,SF} + D_{rbc}(1+M)$		$D_{O_2} = D_{O_2,SF} + D_{rbc}(1+m)$
Error	lmax. deviation	algebraic deviation	lmax. deviation	algebraic deviation	lmax. deviation algebraic deviation
$H_D = 10\%$	2.2 mmHg	0.48 mmHg ↓	3.1 mmHg	1.8 mmHg ↑	9.4 mmHg 7.0 mmHg ↑
$H_D = 5\%$	1.9 mmHg	0.50 mmHg ↓	2.5 mmHg	1.2 mmHg ↑	5.4 mmHg 3.7 mmHg ↑
$H_D = 1.5\%$	7.2 mmHg	3.0 mmHg ↓	6.4 mmHg	2.7 mmHg ↓	6.0 mmHg 2.1 mmHg ↓

* ↓ indicates that a model on the average under predicts the amount of transport, and ↑ indicates that a model on the average over predicts the amount of transport.

4.3.4 Comparison with Boland *et al.*'s Artificial Membrane Tube Data (27 μm in diameter)

Another comparison was performed by utilizing data obtained by Boland *et al.* for red cell suspensions flowing in a 27- μm -diameter and 5-mm-active length silicone rubber capillary which is embedded in a 170- μm -thickness slab. The permeability of the silicone copolymer is $4.17 \times 10^{-10} \text{ M cm}^2/\text{sec}/\text{mmHg}$ (Boland *et al.*, 1987; Nair *et al.*, 1989). Oxygen uptake experiments were conducted by suffusing the gas space surrounding the capillary with oxygen-nitrogen mixture ($P_{O_2, \text{ext}} = 159.6 \text{ mmHg}$) and perfusing the capillary with deoxygenated samples ($P_{O_2, \text{in}} = 0 \text{ mmHg}$). Oxygen release experiments were carried out by suffusing the gas space with pure nitrogen ($P_{O_2, \text{ext}} = 0 \text{ mmHg}$) and perfusing the capillary with deoxygenated samples ($P_{O_2, \text{in}} = 159.6 \text{ mmHg}$). Experimental determinations were obtained over a rectangular field of view of approximately $28 \times 40 \mu\text{m}$ with a dual-wavelength microspectrophotometer to yield space-averaged fractional saturations of hemoglobin at different axial positions along the microvessel.

Figures 4.18 - 4.21 show both the space and mixed mean averages of oxygen saturation as functions of axial position; results are shown for both release and uptake for several values of the parameters P_{50} , H_D and Q . The left-hand-side panels of these plots which present the comparison of the experimentally obtained space-averaged oxygen saturation of hemoglobin to the predictions generated by various models indicate that simplified DM gives better agreement than the continuum models. Both continuum models, CMAug and CMequ, underestimate the resistance to oxygen transport and thus over predict the amount of transport that occurs in the small microvessels. It is also observed that the continuum model, CMequ, which assumes local chemical equilibrium and thus neglects the facilitated diffusion due to oxyhemoglobin predicts a higher resistance and results in a closer fit to the experimental data. A more appropriate means

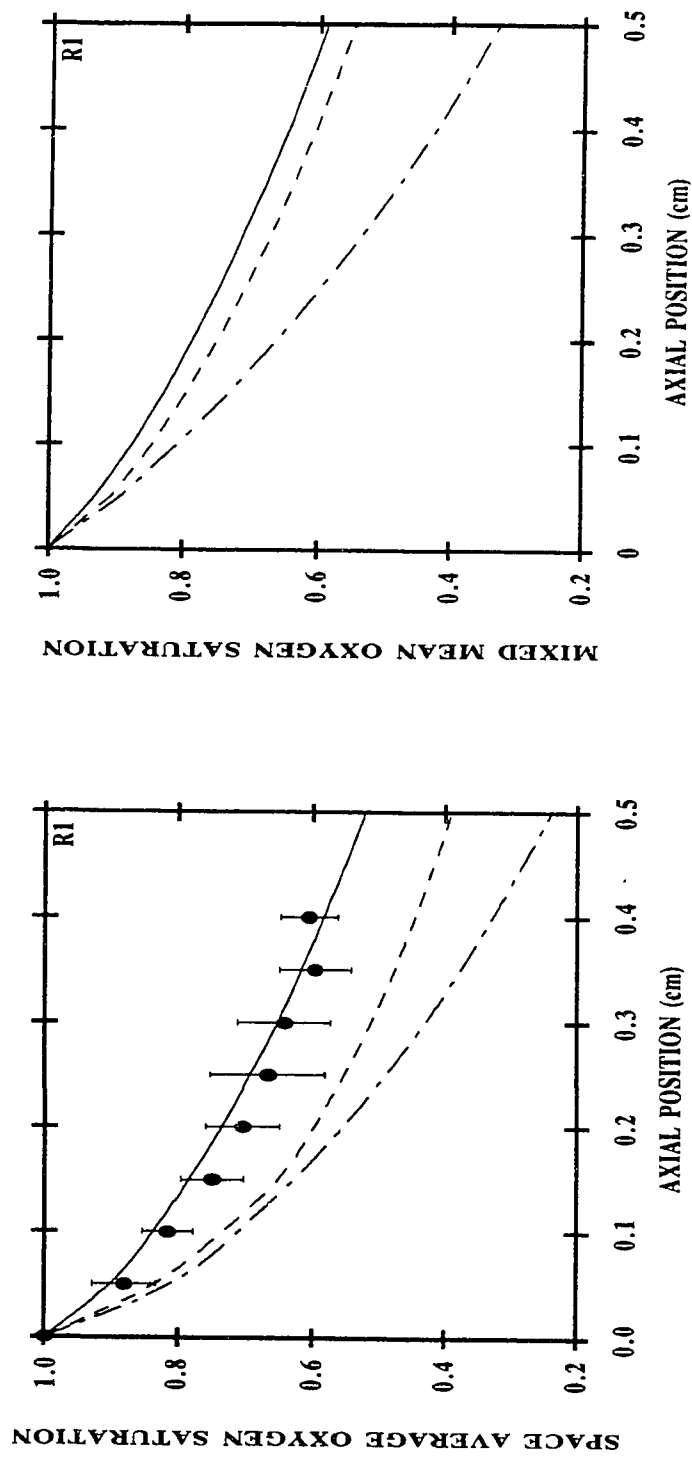


Figure 4.18: Comparison of models for oxygen release from RBC suspensions with a H_D of 30% and P_{50} of 27 mmHg flowing at 12 $\mu\text{l/hr}$ in a 27 μm -diameter-membrane tube at 37 $^{\circ}\text{C}$. The left panel gives the space average O_2 saturation (S_{sa}) at different axial positions along the artificial membrane tube; and the right panel, the mixed mean O_2 saturation (S_{mm}). Circles: experimental results, mean \pm S.D. for 8 replicate experiments. Curves: theoretical simulation curves for the same conditions; (—) simplified DM, (---) CMequ and (- - -) CMAug.

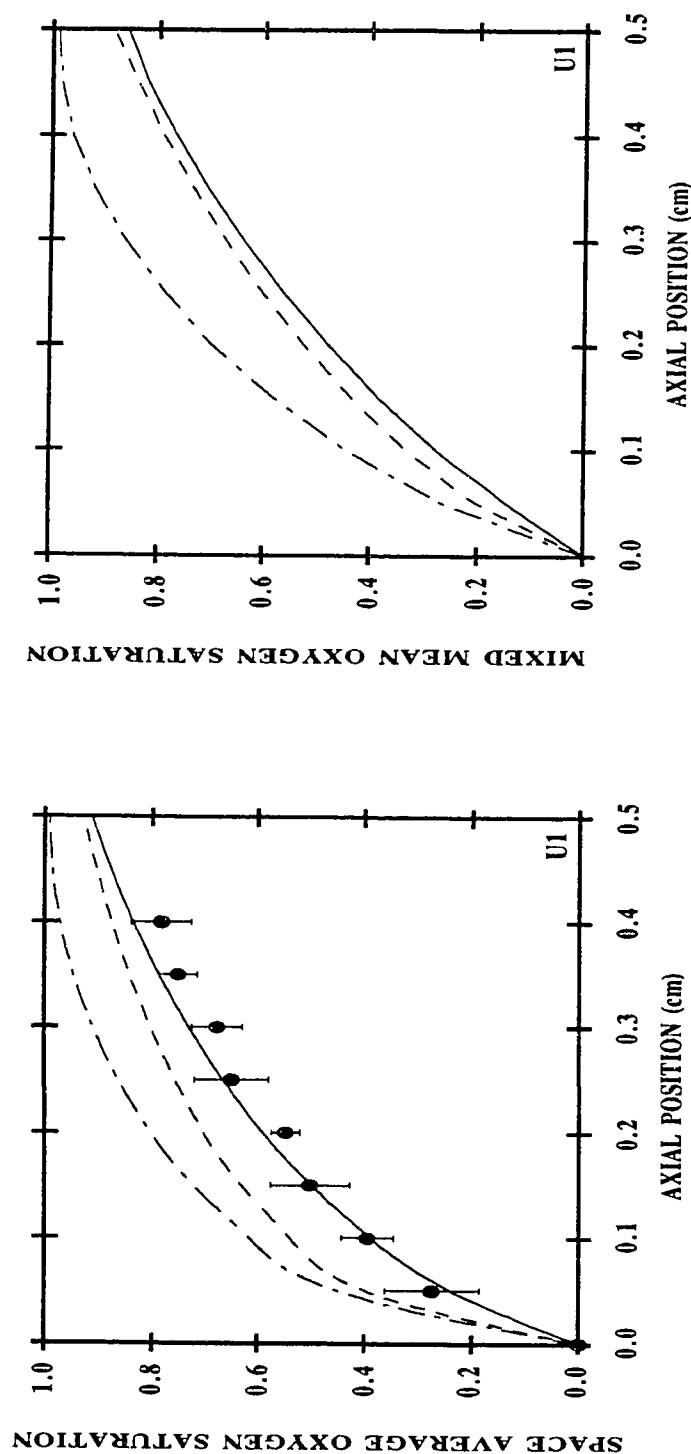


Figure 4.19: Comparison of models for oxygen uptake by RBC suspensions with a H_D of 30% and P_{50} of 27 mmHg flowing at 12 $\mu\text{l/hr}$ in a 27- μm -diameter membrane tube at 37 $^{\circ}\text{C}$. The left panel gives the space average O_2 saturation (S_{sa}) at different axial positions along the artificial membrane tube; and the right panel, the mixed mean O_2 saturation (S_{mm}). Circles: experimental results, mean \pm S.D. for 8 replicate experiments. Curves: theoretical simulation curves for the same conditions; (—) simplified DM, (---) CMequ and (-.-.-) CMaug.

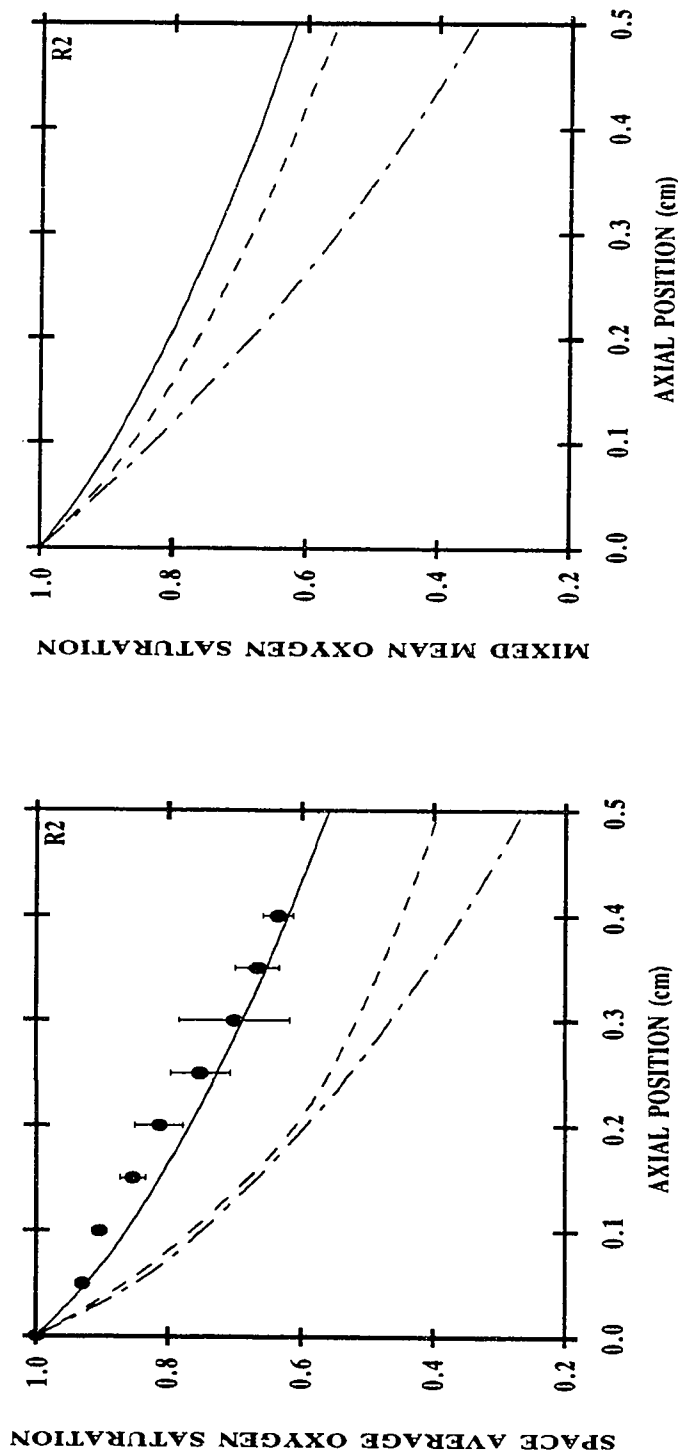


Figure 4.20: Comparison of models for oxygen release from RBC suspensions with a H_D of 20% and P_{50} of 27 mmHg flowing at 12 $\mu\text{l/hr}$ in a 27- μm -diameter membrane tube at 37 °C. The left panel gives the space average O_2 saturation (S_{sa}) at different axial positions along the artificial membrane tube; and the right panel, the mixed mean O_2 saturation (S_{mm}). Circles: experimental results, mean \pm S.D. for 8 replicate experiments. Curves: theoretical simulation curves for the same conditions; (—) simplified DM, (---) CMequ and (- - -) CMaug.

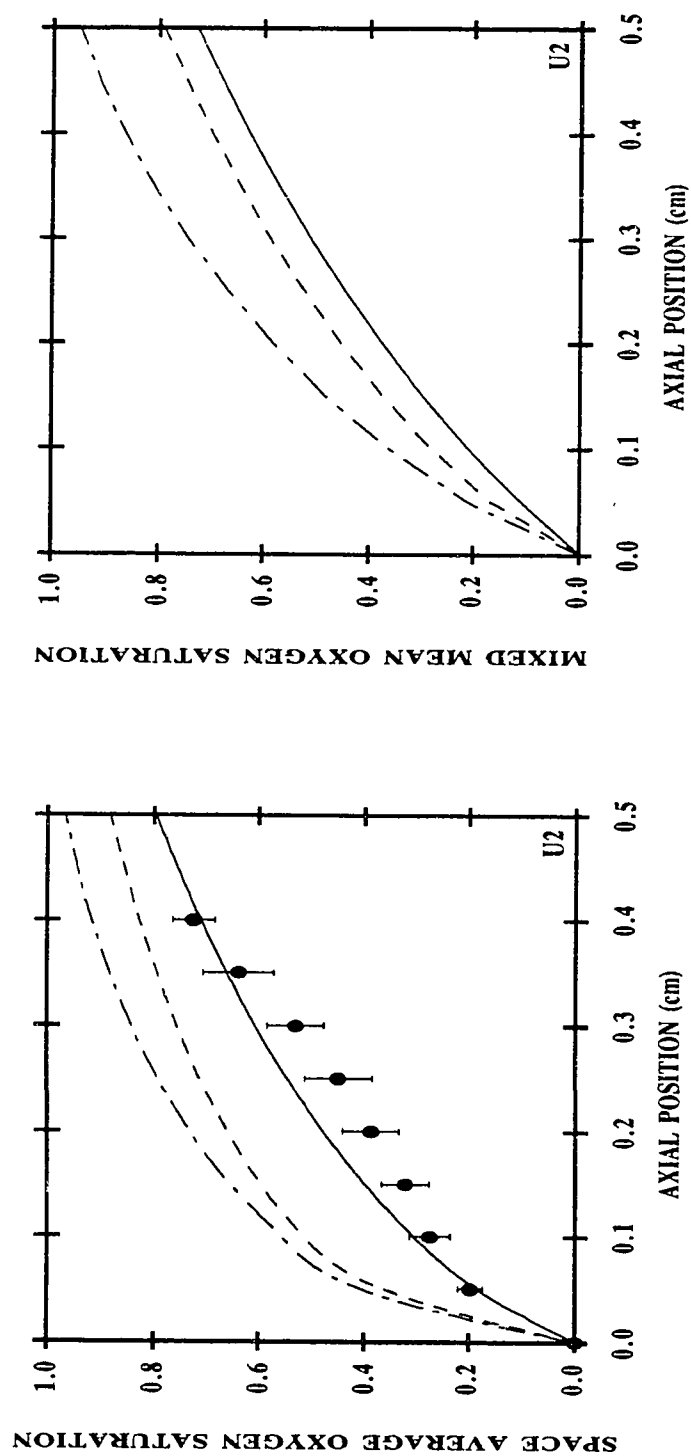


Figure 4.21: Comparison of models for oxygen uptake by RBC suspensions with a H_D of 20% and P_{50} of 20 mmHg flowing at 23 $\mu\text{l/hr}$ in a 27- μm -diameter membrane tube at 37 $^{\circ}\text{C}$. The left panel gives the space average O_2 saturation (S_{sa}) at different axial positions along the artificial membrane tube; and the right panel, the mixed mean O_2 saturation (S_{mm}). Circles: experimental results, mean \pm S.D. for 8 replicate experiments. Curves: theoretical simulation curves for the same conditions; (—) simplified DM, (---) CMegu and (— · —) CMaug.

of comparing these models is to compare the calculated mixed mean concentrations (the right-hand-side panels of Figures 4.18 - 4.21). It is observed that the difference between DM and CMequ on this basis is smaller. There is a difference of no more than 0.1 in S_{mm} which would be within the experimental error involved. This seems to indicate that CMequ is satisfactory for predicting oxygen transport in a 27- μm -diameter microvessel, although it slightly over predicts the amount of transport.

Figures 4.22 and 4.23 give plots of the internal (calculated) radial profiles of hemoglobin oxygen saturation at several axial positions for both release and uptake cases. Comparing the detailed oxygen saturation profiles for these models, it can be seen that the profiles generated by simplified DM and CMequ are in reasonable agreement except at the cell-depleted region. CMAug predicts notably more transport than DM across almost the entire tube, except for the region near the tube wall. The space average receives a larger contribution from the blood travelling near the wall; while on the contrary, the mixed mean weights blood in the center of the tube more heavily. Consequently, when the models are judged based on the mixing-cup averages, CMequ gives similar predictions as DM, but CMAug performs poorly; while if the determining criteria is space-averaged saturations, both CMequ and CMAug predict significantly more transport than DM does.

Although the hemoglobin in these runs operated mostly over the steep portion of the ODC ($m_1 \approx 120$ and $m_2 \approx 30$; $M \approx 20$) and at average shear rates of about 800 to 1500 sec^{-1} , shear-induced enhancement of oxygen transfer to and from the blood was not observed. As illustrated in Figures 4.24 - 4.27, with the usage of molecular diffusivity the simplified DM accurately predicts the transfer rate. On the other hand, upon incorporation of an effective diffusivity to account for the the possible shear-induced augmentation of O_2 transport, the model generates results which are substantially in error (see Table 4.8). This is not surprising because it is known that red cell rotation

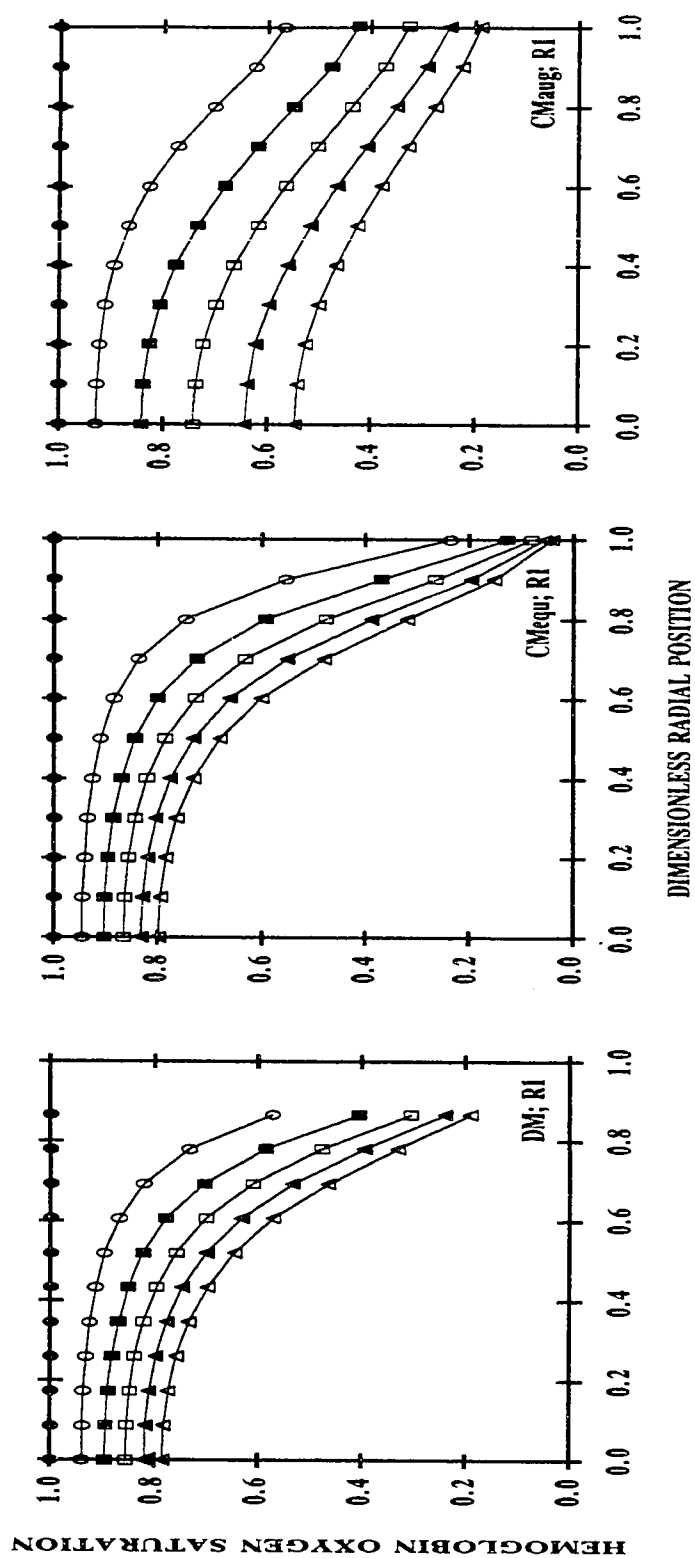


Figure 4.22: Comparison of the internal (nonmeasurable) profiles of oxyhemoglobin saturation as function of axial distance and dimensionless radial position which are generated by simplified DM, CMegu and CMAug for the experimental conditions of R1. (—●—) $z = 0$ mm; (—■—) $z = 1$ mm; (---□---) $z = 2$ mm; (---▲---) $z = 3$ mm; (---△---) $z = 4$ mm; (---○---) $z = 5$ mm.

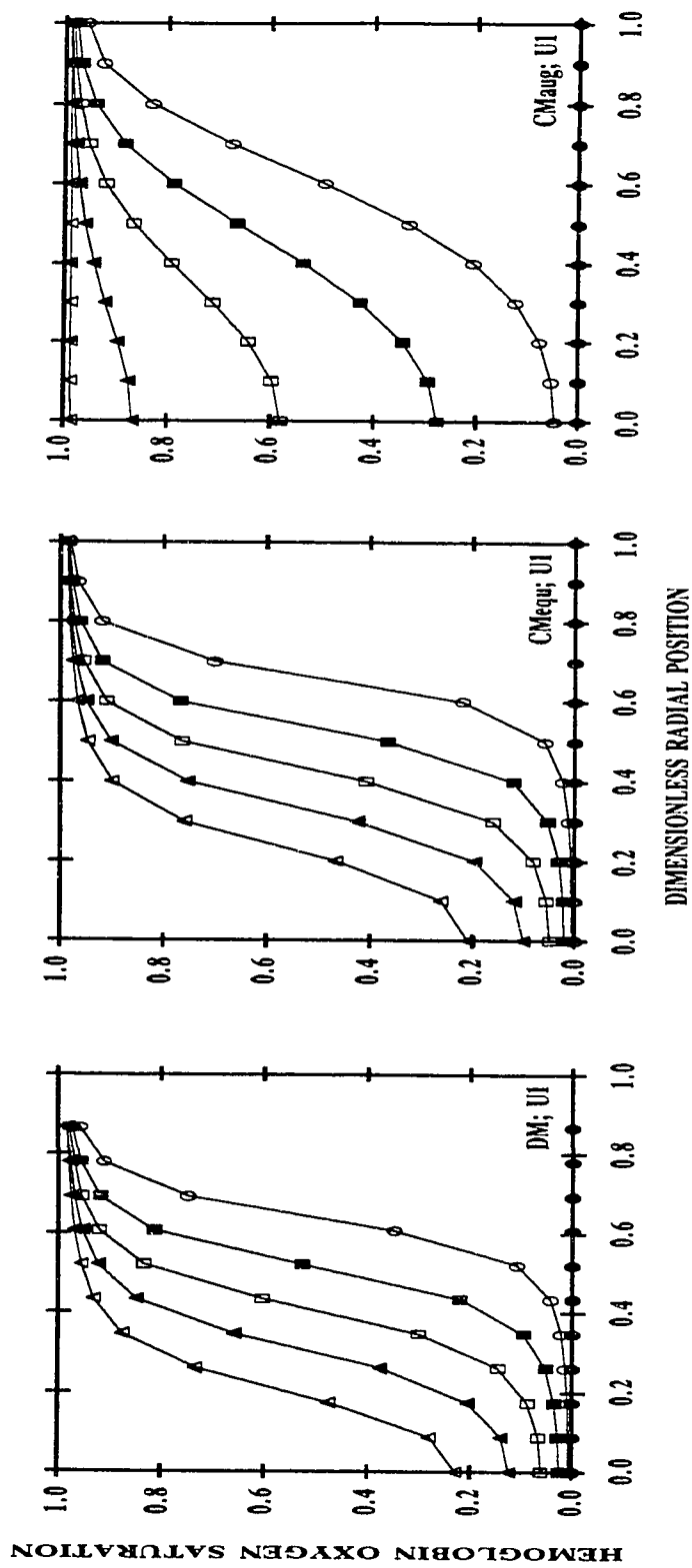


Figure 4.23: Comparison of the internal (nonmeasurable) profiles of oxyhemoglobin saturation as function of axial distance and dimensionless radial position which are generated by simplified DM, CMequ and CMaug for the experimental conditions of U1. (—●—) $z = 0$ mm; (---□---) $z = 1$ mm; (---■---) $z = 2$ mm; (---◇---) $z = 3$ mm; (---▲---) $z = 4$ mm; (---△---) $z = 5$ mm.

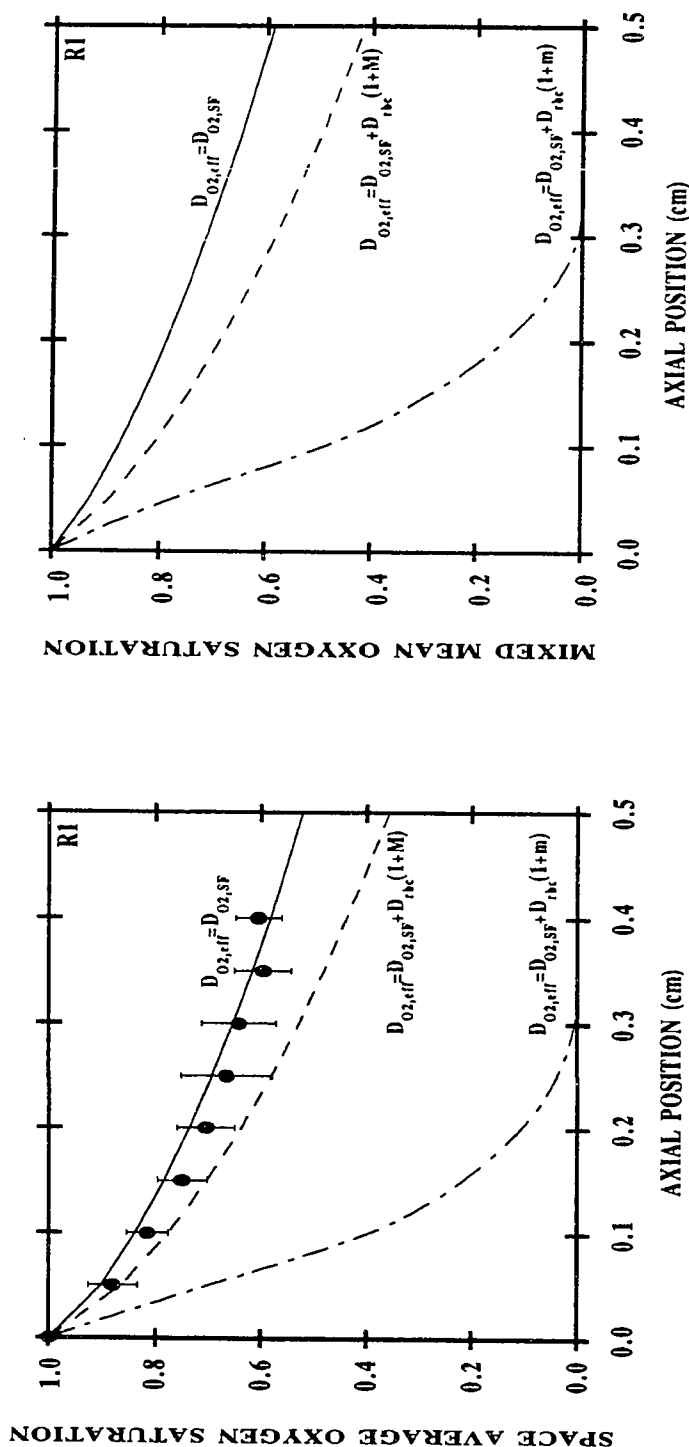


Figure 4.24: Oxygen release from RBC suspensions with a H_D of 30% and P_{50} of 27 mmHg flowing at 12 $\mu\text{L/hr}$ in a 27- μm -diameter membrane tube at 37 $^{\circ}\text{C}$. The left panel gives the space average O_2 saturation (S_{sa}) at different axial positions along the artificial membrane tube; and the right panel, the mixed mean O_2 saturation (S_{mm}). Circles: experimental results, mean \pm S.D. for 8 replicate experiments. Curves: theoretical simulation of experiments generated by simplified DM: the upper curve (—) is generated using $D_{O2,eff} = 2.25 \times 10^{-5} \text{ cm}^2/\text{sec}$; the intermediate curve (- - -) is generated using $D_{O2,eff} = D_{O2,SF} + D_{rc}(1+m)$ where $M=26$ and $\gamma_{avg} = 773 \text{ sec}^{-1}$; the bottom curve (- · - ·) is generated using $D_{O2,eff} = D_{O2,SF} + D_{rc}(1+m)$ where m is given by Equation (2.19b) and $\gamma_{avg} = 773 \text{ sec}^{-1}$.

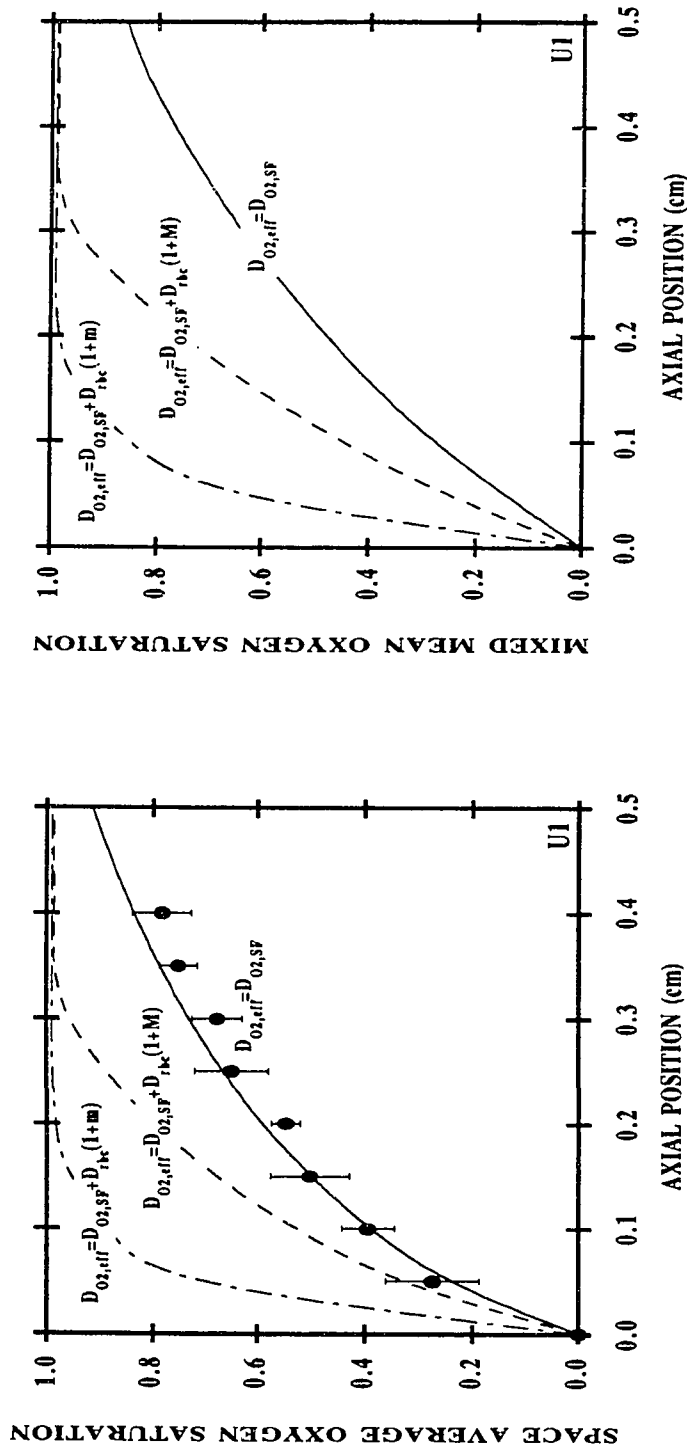


Figure 4.25: Oxygen uptake by RBC suspensions with a H_D of 30% and P_{50} of 27 mmHg flowing at 12 $\mu\text{l/hr}$ in a 27- μm -diameter membrane tube at 37 $^{\circ}\text{C}$. The left panel gives the space average O_2 saturation (S_{sa}) at different axial positions along the artificial membrane tube; and the right panel, the mixed mean O_2 saturation (S_{mm}). Circles: experimental results, mean \pm S.D. for 8 replicate experiments. Curves: theoretical simulation of experiments generated by simplified DM: the bottom curve (-----) is generated using $D_{\text{O}_2, \text{eff}} = 2.25 \times 10^{-5} \text{ cm}^2/\text{sec}$; the intermediate curve (- - - -) is generated using $D_{\text{O}_2, \text{eff}} = D_{\text{O}_2, \text{SF}} + D_{rbc}(1+M)$ where $M=26$ and $\gamma_{\text{avg}} = 773 \text{ sec}^{-1}$; the upper curve (---) is generated using $D_{\text{O}_2, \text{eff}} = D_{\text{O}_2, \text{SF}} + D_{rbc}(1+m)$ where m is given by Equation (2.19b) and $\gamma_{\text{avg}} = 773 \text{ sec}^{-1}$.

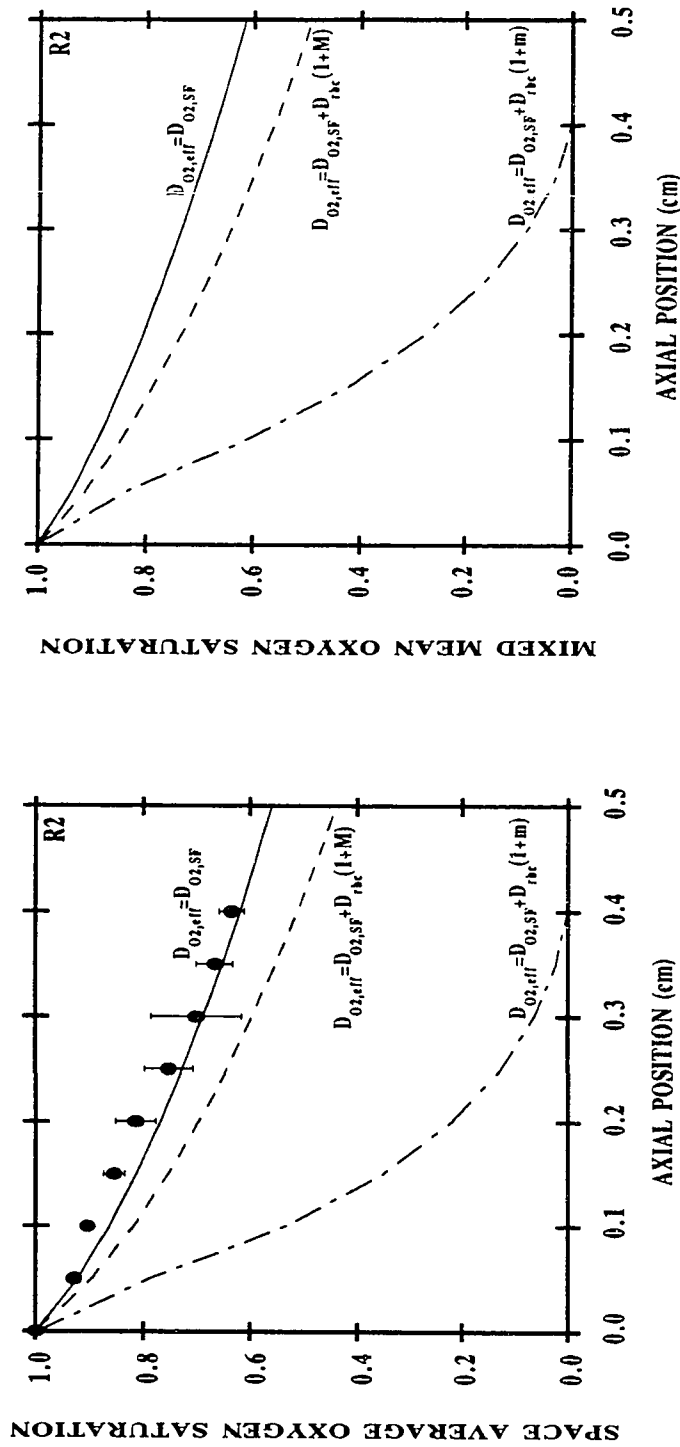


Figure 4.26: Oxygen release from RBC suspensions with a H_D of 20% and P_{50} of 27 mmHg flowing at 12 $\mu\text{l/hr}$ in a 27- μm -diameter membrane tube at 37 $^\circ\text{C}$. The left panel gives the space average O_2 saturation (S_{sa}) at different axial positions along the artificial membrane tube; and the right panel, the mixed mean O_2 saturation (S_{mm}). Circles: experimental results, mean \pm S.D. for 8 replicate experiments. Curves: theoretical simulation of experiments generated by simplified DM: the upper curve (—) is generated using $D_{O_2,eff} = 2.25 \times 10^{-5} \text{ cm}^2/\text{sec}$; the intermediate curve (- - -) is generated using $D_{O_2,eff} = D_{O_2,SF} + D_{rbc}(1+M)$ where $M=18$ and $\gamma_{avg}=773 \text{ sec}^{-1}$; the bottom curve (- · - ·) is generated using $D_{O_2,eff} = D_{O_2,SF} + D_{rbc}(1+m)$ where m is given by Equation (2.19b) and $\gamma_{avg}=773 \text{ sec}^{-1}$.

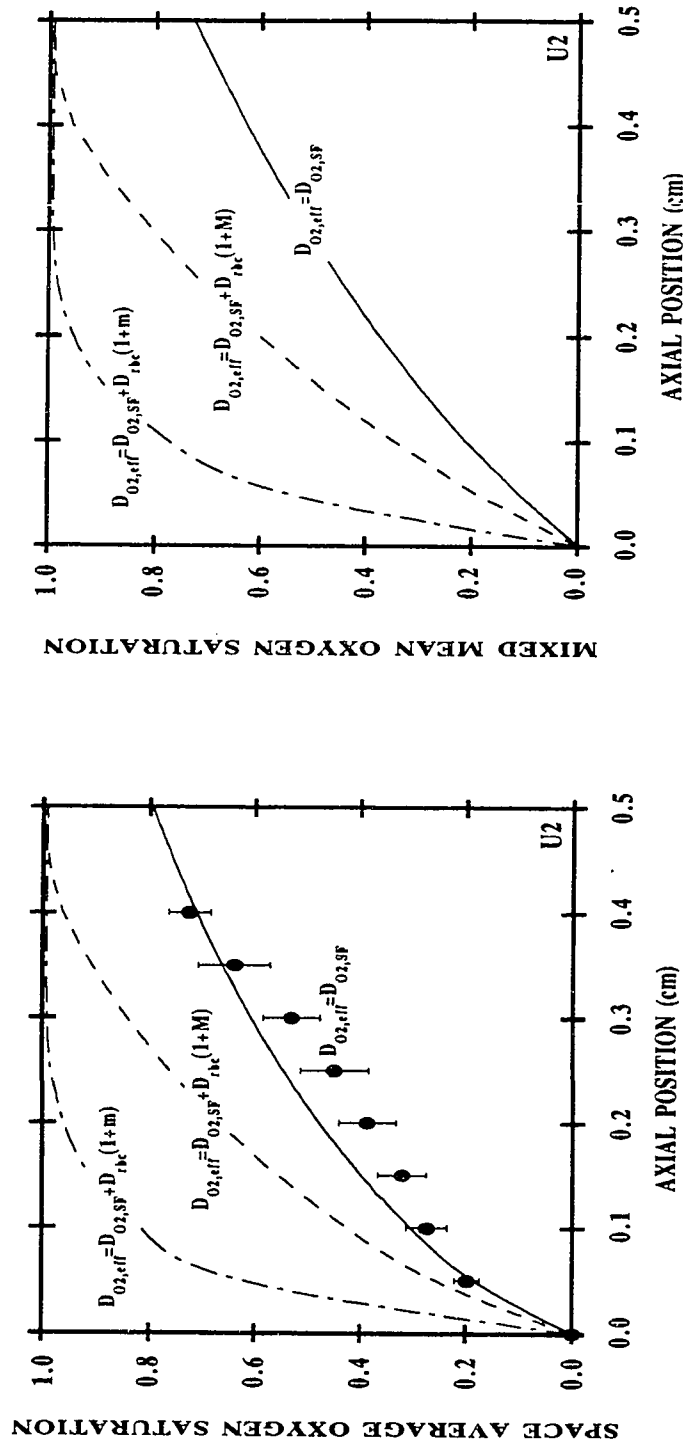


Figure 4.27: Oxygen uptake by RBC suspensions with a H_D of 20% and P_{50} of 20 mmHg flowing at 23 $\mu\text{l/hr}$ in a 27- μm -diameter membrane tube at 37 °C. The left panel gives the space average O_2 saturation (S_{sa}) at different axial positions along the artificial membrane tube; and the right panel, the mixed mean O_2 saturation (S_{mm}). Circles: experimental results, mean \pm S.D. for 8 replicate experiments. Curves: theoretical simulation of the experiments generated by simplified DM: the bottom curve (-----) is generated using $D_{O_2,eff} = 2.25 \times 10^{-5} \text{ cm}^2/\text{sec}$; the intermediate curve (- - - -) is generated using $D_{O_2,eff} = D_{O_2,SF} + D_{rbc}(1+M)$ where $M = 18$ and $\gamma_{avg} = 1482 \text{ sec}^{-1}$; the upper curve (---) is generated using $D_{O_2,eff} = D_{O_2,SF} + D_{rbc}(1+m)$ where m is given by Equation (2.19b) and $\gamma_{avg} = 1482 \text{ sec}^{-1}$.

Table 4.8

Comparison of Boland *et al.*'s oxygen transfer data to the simulation results generated by simplified DM using three different values of $D_{O_2,eff}$. Both the maximum deviation and algebraic deviation[†] of the numerical calculations from the experimental data are given here for S_{sa} , space average O_2 saturation .

$D_{O_2,eff}$	$D_{O_2,pl}=D_{O_2,SF}$		$D_{O_2,pl}=D_{O_2,SF}+D_{rbc}(1+M)$		$D_{O_2,pl}=D_{O_2,SF}+D_{rbc}(1+m)$	
Error	lmax. deviation	algebraic deviation	lmax. deviation	algebraic deviation	lmax. deviation	algebraic deviation
Run R1	0.03	0.02 ↓*	0.16	0.07 ↑*	0.61	0.46 ↑
Run U1	0.05	0.02 ↑	0.28	0.17 ↑	0.52	0.33 ↑
Run R2	0.05	0.02 ↑	0.12	0.09 ↑	0.74	0.54 ↑
Run U2	0.10	0.04 ↑	0.31	0.21 ↑	0.64	0.43 ↑

[†] The algebraic derviation is calculated as $\sum_{i=1}^{i=N} (deviation)_i / N$ where N is the number of data points.

* ↓ indicates that a model on the average under predicts the amount of transport, and ↑ indicates that a model on the average over predicts the amount of transport.

and excursions from straight streamlines are highly suppressed in small vessels (Gaehtgens *et al.*, 1980). Therefore, the augmentation of oxygen transport from these mechanisms would tend to be less than that observed in the large vessels.

4.4 Summary

As mentioned previously, all the parameters in Nair *et al.*'s model are either physical properties or are determined by ways independent of the oxygen transport experiments. Hence, it is a predictive model that has been validated by well-defined experiments in microvessels of 27 μm and 100 μm diameters (Nair *et al.*, 1989). Because the simplified DM presented here is in excellent agreement with Nair *et al.*'s model, it is concluded that the simple 1 PDE model presented here accurately predicts oxygen transport rates by flowing blood in microvessels. The simple model has the advantage of being more tractable mathematically and easier to apply in practice. These models have been verified for application to microvessels of 25-100 μm , and they may be assumed to apply to larger diameters for laminar flow. However, the models should be used with caution if applied to smaller microvessels where the flow and mass transfer characteristics are different than those in the larger vessels.

The predictions of all three models, CMaug, CMequ and simplified DM, prove to be in good agreement with the data obtained by Diller *et al.* (1980) and Schmukler and Chien (1985) for vessels with diameters of 100 μm and larger. Shear-induced augmentation is established to be important in vessels of 300 μm diameter and larger and under the conditions of operating both along the steepest portion of the ODC ($m > 150$) and high shear rate ($\gamma_{avg} \geq 1000 \text{ sec}^{-1}$). This transport enhancement is found to be insignificant in small microvessels (diameters of 30 μm and less). This result, however, raises the question: in what tube diameter range does the shear-induced augmentation

mechanism cease to be important? Schmukler and Chien's result was obtained for low hematocrit suspensions ($H_D=1.5\%$ to 10%) where shear-induced dispersive migration of red cells due to cell collisions is not expected to play an important role (Zydeny and Colton, 1988). Therefore, this work does not exclude the possibility that shear-induced augmentation of oxygen transport is of significance for $100\text{-}\mu\text{m}$ -diameter vessels with higher hematocrits.

Another finding is that both continuum models underestimate the resistance to oxygen transport by flowing blood in small microvessels (diameter of $30\text{ }\mu\text{m}$ and less) and thus over predict the amount of transfer; while the discrete model, as previously stated, gives good agreement with the experimental measurements (space-averaged oxygen saturations). In these small vessels, the characteristic vessel dimension and the red cell size are of comparable size, and the cell-depleted layer constitutes a measurable fraction of the circular lumen. Thus, assumptions that hemoglobin is uniformly distributed over the tube and that the RBC velocity is described by a Poiseuille distribution are not valid. The discrete nature of blood begins to play more important role in determining the transport resistance for oxygen uptake and release by blood in this diameter regime. It is worth noting that, however, when the models are considered based on the mixed-mean or flow-average fractional saturation of hemoglobin (see the left panels of Figures 4.18 - 4.21), CMequ gives predictions that are reasonably close to those generated by simplified DM; while CMAug still seriously over predicts the amount of transport.

CHAPTER 5

THE ANION TRANSPORTER

Because the rate of chloride shift may indeed be rate-limiting under certain conditions *in vivo*, a basic understanding of the exchange mechanism is needed to learn about the effect of alterations in anion exchange kinetics on overall CO₂ transport by blood. Hence, the purpose of this chapter is to formulate a well-founded mathematical relationship to represent RBC anion exchange. In Section 5.1, the established characteristics on anion transporter are briefly described; and three approaches for quantitative characterization of Cl⁻/HCO₃⁻ exchange are considered: (1) a phenomenological permeability coefficient approach with appropriate chemical potential gradients, (2) a Michaelis-Menten type of approach and (3) a carrier-mediated type of model derived based on a “ping-pong” mechanism. Methods for measurements of anion exchange are briefly discussed in Section 5.2 to secure background information on the experimental techniques. In addition, a discussion on the experimental measurements carried out in both continuous flow (Klocke, 1976) and stopped-flow rapid-reaction devices (Weith, 1979; Illsley and Verkman, 1987; Lemon, 1989), and on development of mathematical models to describe these systems is included. Application of the anion flux expressions developed in Section 5.1 to analyze data is discussed in Section 5.3 with regard to the determination of kinetic parameters. The assessments of the anion exchange models are carried out by direct comparison of results from mathematical simulations with experimental data from the literature.

5.1 Mathematical Analysis of The Anion Transporter

5.1.1 Established Conditions on The Anion Transporter

There are reported to be $0.8\text{--}1.2 \times 10^6$ band 3 monomers per RBC - based on the number of stilbene binding sites per RBC depending on the individual donor. Stilbene competitively inhibits anion exchange when bound to the transporters (Gunn *et al.*, 1973). Most of the experimental evidence on the exchange kinetics point toward the single-site “ping-pong” mechanism with obligatory exchange (Cabantchik *et al.*, 1978; Lowe and Lambert, 1983; Falke and Chan, 1985; Jennings, 1985; Frohlich and Gunn, 1986; Passow, 1986; Jennings, 1989). The general features of the ping-pong mechanism are illustrated in Figure 5.1. In the ping-pong mechanism, the anions take turns crossing the membrane rather than switching place simultaneously; and the protein has two structurally distinct states, an inward-facing state and an outward-facing state. Thus it is an alternating site transporter possessing a single transport site which is alternatively exposed to the opposite sides of the membrane. This site can only cross the membrane when it is occupied by a substrate anion; it then undergoes a conformational change to face the opposite side of the membrane and releases the transported ion. The transported site can now bind another (or the same) anion and return to the original membrane face, release the anion to complete a cycle of anion exchange.

Although there are arguments for a sequential mechanism (two coupled transport sites, one on each side of the membrane that must be occupied for the simultaneous and reciprocal transfer of both anions) (Salhany and Rauenbuehler, 1983), the characteristics of the ping-pong mechanism has been experimentally demonstrated by various investigators. For instance, Jennings (1982) showed that a gradient of chloride concentration (with Cl^- higher inside than outside of the cells) appeared to recruit anion carriers to an outward-facing conformation; and this behavior is that expected for a ping-

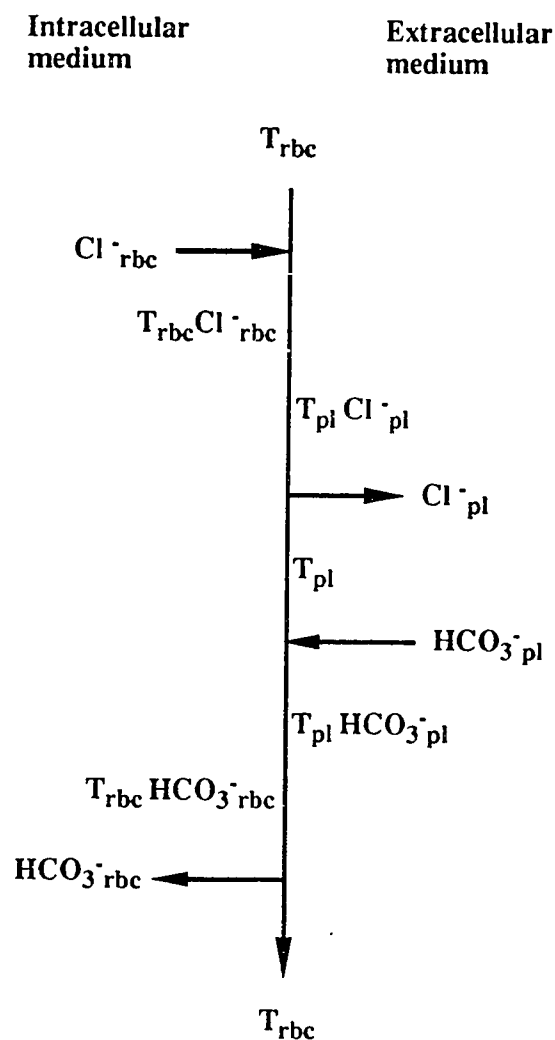


Figure 5.1: Diagram of a ping-pong mechanism for anion transport. Shown here is the exchange of an intracellular Cl^- for an extracellular HCO_3^- .

pong mechanism. If there are no transportable anions on one side of the membrane, all the transport sites will be recruited to this side by transporting an anion across to this side but are locked in this position and not able to transport one back because of the lack of substrate ion with which the transporter can form a complex. On the other hand, the sequential mechanism would require that half of the transport sites be on each side of the

membrane, and the fraction of the loaded sites would depend on the substrate concentrations on the two sides.

Other evidence came from the experimental demonstration of the half-turnover of the transporters, i.e. the transport of 10^6 Cl^- ions per RBC from inside to the outside when 10^6 transport sites are recruited from the inside to the outside and blocked by an external irreversible inhibitor. Jennings (1982) demonstrated this by adding RBC ghosts (resealed erythrocytes) containing a low concentration of $^{36}\text{Cl}^-$ to a chloride and bicarbonate-free medium containing sulfate. There was a rapid loss of about 10^6 Cl^- per cell equivalent to one half-turnover of each transport site. Because SO_4^{2-} was transported very slowly (Schnell *et al.*, 1977), the ping-pong mechanism predicts an initial “burst” of Cl^- due to one-half of a cycle followed by a much slower exchange of extracellular SO_4^{2-} for intracellular Cl^- . Exchange of Cl^- for SO_4^{2-} was found to be accompanied by movement of protons with a stoichiometry of one proton plus one sulfate, HSO_4^- , to one chloride. This experimental evidence supports the notion that translocation of an anion from one side of the membrane to the other does not require simultaneous translocation of an anion in the opposite direction, i.e. the efflux half-cycle and influx half-cycle are separated, as specified in the ping-pong model. Moreover, because the number of anion transporters per RBC is 10^6 , this observation also suggested that the stoichiometry of anion transport is one ion per translocation per band 3 monomer.

Chloride binding to band 3 had also been studied using $^{35}\text{Cl}^-$ nuclear magnetic resonance (NMR) (Falke and Chan, 1985). Their results showed that there is a class of high-affinity Cl^- binding sites that behave as the transport site might behave with respect to displacement by other anions, inhibitors and recruitment. However, the previously postulated modifier site, which was proposed by Dalmark (1976) to explain the inhibition of anion exchange at large anion concentration, was NMR-invisible and had

no effects on Cl^- binding to the transport site. Their results are quantitatively consistent with the ping-pong model, which states that the transport site is the only site involved in the transport cycle. Therefore, mechanisms with a ternary complex between band 3 and two chloride ions seem to be excluded by these observations.

5.1.2 Previous Approaches

5.1.2.a Constant Field Electrodifffusion Approach

Previously, the exchange of HCO_3^- and Cl^- had generally been regarded as passive electrodiffusion. Various investigators (Crandall *et al.*, 1971; Chow *et al.*, 1976; Klocke, 1976; Salathe *et al.*, 1981) recognized that RBC anion exchange process involves some form of membrane-anion interaction, and that passive diffusion down electrochemical gradient implies a specification of a mechanism. As a result, they used a phenomenological approach in which appropriate phenomenological permeability coefficients (P_{HCO_3} and P_{Cl}) were introduced to quantitatively characterize $\text{HCO}_3^-/\text{Cl}^-$ exchange under physiological conditions. Using Goldman's assumption of a linear decrease in electrical potential across the cell membrane, flux of a univalent ion across the RBC membrane is equal to (Goldman's equation which is given in *Biophysical Chemistry of Membrane Functions* by Kotyk *et al.*, 1988)

$$\text{Flux}_{\text{HCO}_3} = \frac{P_{\text{HCO}_3} F \Psi_m}{R T} \left[\frac{[\text{HCO}_3^-]_{\text{pl}} - [\text{HCO}_3^-]_{\text{rbc}} \exp(-\Psi_m F/RT)}{1 - \exp(-\Psi_m F/RT)} \right] \quad (5.1)$$

where the intracellular and extracellular concentrations are expressed in (mole/liter RBC) and (mole/liter plasma), respectively; Ψ_m is the membrane potential; and P_{HCO_3} is the permeability of HCO_3^- which was obtained based on experimental kinetic data. With appropriate concentrations and permeability, Equation (5.1) can also be written for Cl^-

flux. Upon imposing the electroneutrality condition, i.e. requiring the fluxes of HCO_3^- and Cl^- to sum to zero, the membrane potential can then be expressed as

$$\Psi_m = -\frac{RT}{F} \ln \left(\frac{P_{\text{Cl}} [\text{Cl}^-]_{\text{pl}} + P_{\text{HCO}_3} [\text{HCO}_3^-]_{\text{pl}}}{P_{\text{Cl}} [\text{Cl}^-]_{\text{rbc}} + P_{\text{HCO}_3} [\text{HCO}_3^-]_{\text{rbc}}} \right) \quad (5.2)$$

Other implicit assumptions involved in deriving Equation (5.2) are that activity coefficients are identical both inside and outside the RBCs, and that permeabilities are independent of the direction of ionic movement.

Computation of the permeabilities using the constant field assumption can be simplified by conducting the initial rate approach (Chow *et al.*, 1976). Assuming that P_{HCO_3} and P_{Cl} remain constant at any given pH in spite of different experimental conditions, the initial membrane potential depends upon the intra- and extracellular concentrations present immediately after mixing of reactants. For example, at the start of experiments with Cl^- -loaded cells, since $[\text{Cl}^-]_{\text{pl}}$ and $[\text{HCO}_3^-]_{\text{rbc}}$ are small, if both permeabilities are not widely different Equation (5.2) simplifies to

$$\Psi_m = -\frac{RT}{F} \ln \left(\frac{P_{\text{HCO}_3} [\text{HCO}_3^-]_{\text{pl}}}{P_{\text{Cl}} [\text{Cl}^-]_{\text{rbc}}} \right) \quad (5.3)$$

and the membrane potential is dependent on $[\text{Cl}^-]_{\text{rbc}}$ and $[\text{HCO}_3^-]_{\text{pl}}$ and the respective permeabilities. In addition, the total flux of HCO_3^- from plasma to RBC was calculated from the initial kinetic measurements. Hence, by varying the initial reactant compositions, at least two sets of independent data were required here, the three unknowns (P_{HCO_3} , P_{Cl} and Ψ_m) can then be calculated. Klocke (1976), on the other hand, used the integral method to analyze his kinetic data. Using Equations (5.1) and (5.2) and assumed permeabilities forward integration was conducted from the initial

conditions to give a relation between composition of the reaction mixture and time. A trial-and-error procedure was continued until the best fit of the theoretical curves to the observed data was achieved by the method of least square. Table 5.1 summarizes the permeability coefficients calculated by Chow *et al.* (1976) and Klocke (1976):

Table 5.1: Permeabilities of HCO_3^- and Cl^- for anion exchanges in RBCs calculated based Goldman's solution for the electrodiffusion of ions.

Experimenters	P_{HCO_3} (cm/sec)			P_{Cl} (cm/sec)	
	0 °C	25 °C	37 °C	25 °C	37 °C
Chow <i>et al.</i>	3.8×10^{-6}	1.2×10^{-4}	2.2×10^{-4}	1.0×10^{-4}	---
Klocke	---	---	$1.1 \times (10^{-5} - 10^{-3})$	---	1.1×10^{-4}

It is interesting to note that P_{Cl} obtained by Klocke (1976) averaged 1.1×10^{-4} cm/sec and were not significantly correlated with experimental conditions; in contrast, to the relatively constant value of P_{Cl} , the P_{HCO_3} varied widely. In addition the relatively low temperature dependence of P_{Cl} is difficult to reconcile with the values of the activation energy that were reported in the literature.

However, discrepancies of several orders of magnitude between the Cl^- permeability as measured by isotope exchange and by net (or conductive) flow with direct electrical measurements practically ruled out the possibility that anions as such diffuse across the membrane (Cabantchik *et al.*, 1978). Those data alone with other experimental evidence suggest that the exchange mechanism is carrier-mediated; the carrier is capable of one-for one exchange of anions, but does not permit the net flow of anions across the membrane. As a result, these permeability values are only "effective" and must be interpreted accordingly. Therefore, modifications needed to be introduced

to include the possibility of passive mediated-transport system. Such transport system includes a specific protein which contains binding site(s) complementary to the substrate(s) transported and serves as a carrier of the substrate(s) (Lehninger, 1975). In addition, the process is completely reversible, and the movement of the substrate(s) may be in either direction, depending on the relative concentration(s) of the substrate(s) in the two compartments.

5.1.2.b Michaelis-Menten Kinetic Approach

Because saturation effects were observed in the $\text{HCO}_3^-/\text{Cl}^-$ exchange system, some investigators (Lambert and Lowe, 1978 and 1980; London *et al.*, 1987) used Michaelis-Menten equation to characterize their data. Basically the Michaelis-Menten equation expresses the mathematical relationship between the initial rate (v_o) of an enzyme-catalyzed reaction, the concentration of the substrate ($[S]_o$), and certain characteristics of the enzyme. This equation is derived by making the steady-state approximation for the intermediate enzyme-substrate complex and utilizing the conservation equation for total enzyme concentration.

$$v_o = \frac{v_{max} [S]_o}{K_M + [S]_o} \quad (5.4)$$

where v_{max} is the maximum reaction rate and K_M is known as the Michaelis constant. An important numerical relationship emerges from the above equation in the special case when $v_o = 0.5v_{max}$; consequently, K_M is equal to the concentration of $[S]_o$ which gives the half maximum reaction rate. v_{max} and K_M can be determined by a reciprocal plot which is based on the rearrangement of Equation (5.4) into the following form.

$$\frac{1}{v_o} = \frac{1}{v_{max}} + \frac{K_M}{v_{max} [S]_o} \quad (5.5)$$

If the data fit the model, a plot of $1/v_o$ versus $1/[S]_o$ should be linear with a slope of K_M/v_{max} and intercept of $1/v_{max}$. Although Michaelis-Menten expression is applicable to a wide variety of enzyme catalyzed reactions; it is not appropriate for reversible reactions and multiple-substrate reactions. As a result, the values for K_M and v_{max} reported in the literature can only be considered as effective and apparent because they were obtained by assuming that this saturable carrier system is analogous to an enzyme which obeys Michaelis-Menten kinetic.

Lowe and Lambert (1983) analyzed various studies (Brahm, 1977; Lambert and Lowe, 1980; Weith and Brahm, 1980) and reported the apparent values for K_M and v_{max} which were extracted from those experimental studies (see Table 5.2). Lowe and Lambert (1983) had also attempted to make some sort of correction on the fact that they were using a single-substrate kinetic expression to describe an bisubstrate reaction. For instance, in a case where the driving force was set up for the net exchange of intracellular Cl^- with extracellular HCO_3^- , they regarded competition between Cl^- and HCO_3^- at extracellular sites as lowering the effective concentration of HCO_3^- by a factor of $1/(1+[Cl^-]_{pl}/K_{I,Cl})$ where $K_{I,Cl}$ is the dissociation constant of the carrier- Cl^- complex. In an analogous fashion, intracellular HCO_3^- compete with Cl^- for transport sites; and this is treated as having effect of reducing the rates of exchange by a factor of $1/(1+[HCO_3^-]_{rbc}/K_{I,HCO_3})$ where K_{I,HCO_3} is the dissociation constant of the carrier- HCO_3^- complex. Another correction applied in this case for obtaining the extrapolated v_{max} was to assume Michaelis-Menten kinetics with the apparent K_M and extrapolate v_{max} to infinite intracellular Cl^- concentration. The apparent discrepancies in the results of different workers probably arise, in part at least, from the different conditions of pH and competitive effects between anions prevailing under the different experimental conditions. More importantly, the issue is that Michaelis-Menten equation is not

applicable for characterizing the anion transporter because of the fundamental assumptions and specific mechanism that are associated with this kinetic model.

Table 5.2: Rates (observed v_{max} and extrapolated v_{max}) and concentration of Cl^- and HCO_3^- giving half maximum rates (K_M) of anion exchanges in human red blood cells or red cell ghosts at 37 °C.

	Apparent K_M^* (mM)	Observed v_{max}^\parallel (nmole $\text{cm}^{-2} \text{sec}^{-1}$)	Extrapolated $v_{max}^\#$ (nmole $\text{cm}^{-2} \text{sec}^{-1}$)
Cl^-/Cl^- exchange [†]			
Brahm	65.0	56.6	81.2
Weith and Brahm	---	49.0	68.3
$\text{HCO}_3^-/\text{HCO}_3^-$ [†]			
Weith and Brahm	43.0	24.0	30.3
$\text{Cl}^-/\text{HCO}_3^-$ [†]			
Weith and Brahm	---	26.0	32.8
Lambert and Lowe	11.1	10.2	61.6
$\text{HCO}_3^-/\text{Cl}^-$ [†]			
Weith and Brahm	---	48.0	66.9

[†] For hetro-exchange the first named anion is intracellular.

^{*} Uncorrected for the inhibitory effects of anions. K_M is for HCO_3^- in the case of heteroexchange.

[¶] With anions usually present at 150-165 mM inside and outside the cell.

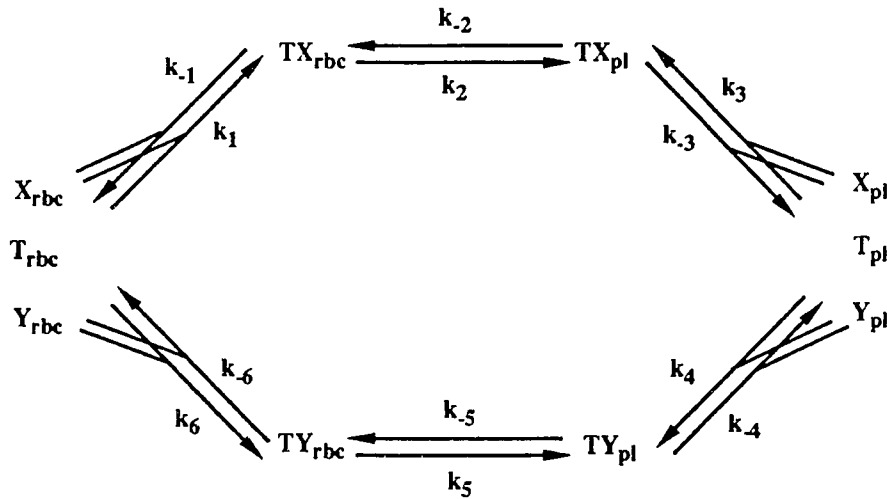
[#] Extrapolated assuming Michaelis-Menten kinetics and the apparent K_M stated.

5.1.3 Simplified Ping-pong Mechanism

The scheme illustrated in Figure 5.2 was proposed by Frohlich and Gunn (1986). They attempted to use the minimal number of reaction steps and different kinetic states of the anion transporter that are necessary to describe the one-for-one

exchange of the anions. They decomposed the exchange process into three steps: (1) binding of the anion to the transport molecule at one surface of the membrane, (2) translocation of the anion across the membrane, and (3) dissociation of the anion from the transport molecule at the opposite surface. Reaction rate expression for enzymatic reactions are usually derived by making the steady-state approximation for the intermediate enzyme-substrate complexes. This is an appropriate assumption when the substrate concentration greatly exceeds that of the enzyme (the usual laboratory situation) or when there is both a continuous supply of reactant and a continuous removal of products (the usual cellular concentration).

Figure 5.2: Description of the catalytic cycle of anion exchange according to the ping-pong scheme.



where

T_{rbc} and T_{pl} are the unloaded forms of the transporter in which a single anion binding/transport site is accessible to only intra- or extracellular anions, respectively,

TX_{rbc} , TX_{pl} , TY_{rbc} and TY_{pl} denote the complexes of the transporter with the anions X (Cl^-) and Y (HCO_3^-).

k_1, k_3, k_4 and k_6 are the association rate constants.

k_{-1}, k_{-3}, k_{-4} and k_{-6} are the dissociation rate constants.

k_2 and k_5 are the outward translocation rate constants.

k_{-2} and k_{-5} are the inward translocation rate constants.

Based on the above kinetic scheme, Frohlich and Gunn (1986) derived the differential equations which describe how the concentrations of the different transporter conformations change with the substrate and product concentrations. Then they applied the generalized steady-state analysis (i.e., the concentrations of different states of the transporter are constant) to solve for the steady-state concentrations of different states of the anions. The resulting concentrations are given in Frohlich and Gunn (1986). T_{rbc}/T_{tot} , T_{pl}/T_{tot} , TX_{rbc}/T_{tot} , TX_{pl}/T_{tot} , TY_{rbc}/T_{tot} and TY_{pl}/T_{tot} are functions of $\{k_i$, where $i=\pm 1, \dots, \pm 6$; and $X_{rbc}, X_{pl}, Y_{rbc}, Y_{pl}\}$ and T_{tot} is the total number of band 3 transporter molecules; these expressions give the fraction of the transporter molecules that are in the given state (or the probability of a given transporter molecule being in a particular state). The flux equation which describes the anion concentrations on the two sides of the membrane can be constructed from the steady concentrations by expressing the net reaction rate between any two adjacent points in the reaction scheme (Figure 5.2).

$$v = \frac{Flux_{HCO_3}}{T_{tot}} = k_1 \frac{T_{rbc} X_{rbc}}{T_{tot}} - k_{-1} \frac{TX_{rbc}}{T_{tot}} = k_2 \frac{TX_{rbc}}{T_{tot}} - k_{-2} \frac{TX_{pl}}{T_{tot}} = etc. \quad (5.6)$$

where

v is the turnover rate.

$Flux_{HCO_3}$ is the net flux of extracellular HCO_3^- entering the RBCs or equivalently, the net flux of intracellular Cl^- entering the plasma.

T_{tot} is the total number of band 3 transporter molecules per RBC ($0.8-1.2 \times 10^6$).

$$\begin{aligned}
v = & (X_{rbc} Y_{pl}) \left[c X_{rbc} + \left(\frac{bc}{a} \right) X_{pl} + \left(\frac{bc}{d} \right) Y_{rbc} + b Y_{pl} + c K_3 \left(1 + \frac{1}{K_2} \right) X_{rbc} X_{pl} \right. \\
& + b K_6 \left(1 + \frac{1}{K_5} \right) Y_{rbc} Y_{pl} + (g+f) X_{rbc} Y_{pl} + \left(\frac{K_3 K_5 K_6}{K_1 K_2 K_4} \right) (h+e) X_{pl} Y_{rbc} \left. \right]^{-1} \\
& - (X_{pl} Y_{rbc}) \left[d X_{pl} + \left(\frac{ad}{b} \right) X_{rbc} + \left(\frac{ad}{c} \right) Y_{pl} + a Y_{rbc} + d K_1 (1 + K_2) X_{rbc} X_{pl} \right. \\
& + a K_4 (1 + K_5) Y_{rbc} Y_{pl} + (h+e) X_{pl} Y_{rbc} + \left(\frac{K_1 K_2 K_4}{K_3 K_5 K_6} \right) (g+f) X_{rbc} Y_{pl} \left. \right]^{-1}
\end{aligned} \tag{5.7}$$

where

$$X_{rbc} = [Cl^-]_{rbc}, Y_{rbc} = [HCO_3^-]_{rbc}, X_{pl} = [Cl^-]_{pl} \text{ and } Y_{pl} = [HCO_3^-]_{pl}.$$

$$a = \frac{k_{-1} k_{-2} + k_{-1} k_{-3} + k_2 k_{-3}}{k_{-1} k_{-2} k_3} \quad e = \frac{k_{-1} + k_2 + k_{-2}}{k_{-1} k_{-2}} \tag{5.8a}$$

$$b = \frac{k_{-1} k_{-2} + k_{-1} k_{-3} + k_2 k_{-3}}{k_1 k_2 k_{-3}} \quad f = \frac{k_2 + k_{-2} + k_{-3}}{k_2 k_{-3}} \tag{5.8b}$$

$$c = \frac{k_{-4} k_5 + k_{-4} k_{-6} + k_{-5} k_{-6}}{k_4 k_{-5} k_{-6}} \quad g = \frac{k_5 + k_{-5} + k_{-6}}{k_{-5} k_{-6}} \tag{5.8c}$$

$$d = \frac{k_{-4} k_5 + k_{-4} k_{-6} + k_{-5} k_{-6}}{k_{-4} k_5 k_6} \quad h = \frac{k_{-4} + k_5 + k_{-5}}{k_{-4} k_5} \tag{5.8d}$$

$$K_j = \frac{k_j}{k_{-j}} \quad (j = 1, 2, \dots, 6)$$

Equation (5.7) is recited here for the purpose of a discussion on how additional assumptions are introduced to simplify the flux expression. Detailed description of the exchange kinetic at this level would be too cumbersome; as seen from Equation (5.7), it is rather unyielding. The nature of the transmembrane processes could depend largely on the identity of the reaction or reactions that are rate-limiting in the transport cycle. Falke and coworkers (1985a, 1985b) utilized $^{35}Cl^-$ nuclear magnetic resonance (NMR) and $^{37}Cl^-$ NMR to set lower limits on the rates of chloride binding and dissociation at

the saturated inward- and outward-facing band 3 transport sites. The physical basis of the NMR technique is the large difference in the spectral widths of the bound and free Cl^- , the spectral width of Cl^- bound to a macromolecule is typically $\geq 10^4$ times than the spectral width of solution Cl^- . As a result when solution Cl^- visits a macromolecular binding site sufficiently rapidly, the solution Cl^- NMR resonance can be measurably broadened. When line broadening is observed, it contains information on the rate of Cl^- migration between the binding site and the bulk solution. The exchange of Cl^- between a binding site and solution can be slow, intermediate, or rapid on the Cl^- NMR time scale. For slow exchange the $^{35}\text{Cl}^-$ or $^{37}\text{Cl}^-$ line broadening exactly specifies the exchange rate. At both 0-3 and 37 °C, their NMR data specified that Cl^- binding and dissociation at the saturated sites are not rate-limiting, indicating that translocation of bound Cl^- across the membrane is the slowest step in the overall transport cycle. The Cl^- binding and dissociation rates determined by Falke *et al.* (1985) allow important features of the kinetic equation for a ping-pong transport cycle to be described (see Figure 5.3). However, it should be mentioned that at the inward-facing transport site the turnover rate at 37 °C has become comparable to the rate of Cl^- binding and dissociation, so these rates need to be examined more closely.

If the translocation step is also relatively slower than the HCO_3^- dissociation step, one can then simplify the kinetic analysis by letting the translocation step be rate limiting or alternatively by letting the association and dissociation reactions be at equilibrium and by eliminating terms in the kinetic equation which are now known to be negligibly small. The simplified version of lumped kinetic parameters, $a - h$, is as followings:

$$a = \frac{1}{k_{-2} k_3} \quad e = \frac{1}{k_{-2}} \quad (5.9a)$$

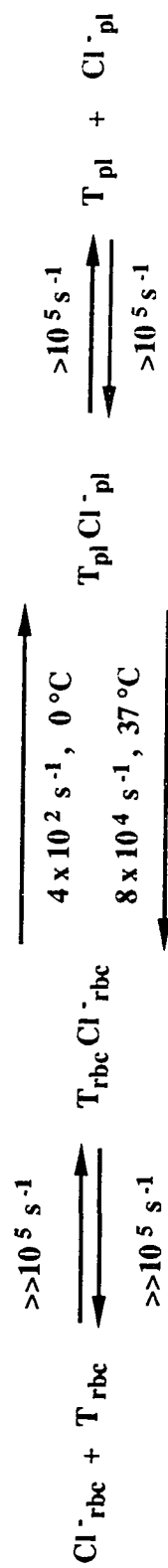


Figure 5.3: Transport cycle of the anion transporter. Falke *et al.*'s $^{35}\text{Cl}^-$ and $^{37}\text{Cl}^-$ NMR data specifies that at both low and physiological temperatures, the binding and dissociation events at both orientations of the transport site are measurably faster than the translocation step.

$$b = \frac{1}{k_2 k_1} \quad f = \frac{1}{k_2} \quad (5.9b)$$

$$c = \frac{1}{k_{-5} k_4} \quad g = \frac{1}{k_{-5}} \quad (5.9c)$$

$$d = \frac{1}{k_5 k_6} \quad h = \frac{1}{k_5} \quad (5.9d)$$

In addition, the principle of microscopic reversibility for a passive system requires that for the hexagonal scheme of Figure 5.2: $k_1 k_2 k_{-3} k_4 k_{-5} k_{-6} = k_{-1} k_{-2} k_3 k_{-4} k_5 k_6$ which in turn becomes: $K_1 K_2 K_4 / K_3 K_5 K_6 = 1$. Upon introducing above assumptions, the flux equation (Equation (5.7)) is simplified to the following:

$$\begin{aligned} v = (X_{rbc} Y_{pl}) & \left[\frac{X_{rbc}}{k_{-5} K_4} + \frac{K_3 X_{pl}}{k_{-5} K_1 K_2 K_4} + \frac{K_5 K_6 Y_{rbc}}{k_2 K_1 K_4} + \frac{Y_{pl}}{k_2 K_1} + \frac{K_3}{k_{-5} K_4} \left(1 + \frac{1}{K_2} \right) X_{rbc} X_{pl} \right. \\ & + \frac{k_6}{k_2 K_1} \left(1 + \frac{1}{K_5} \right) Y_{rbc} Y_{pl} + \left(\frac{1}{k_{-5}} + \frac{1}{k_2} \right) X_{rbc} Y_{pl} + \left(\frac{1}{k_5} + \frac{1}{k_{-2}} \right) X_{pl} Y_{rbc} \left. \right]^{-1} \\ & - (X_{pl} Y_{rbc}) \left[\frac{X_{pl}}{k_5 K_6} + \frac{K_4 Y_{pl}}{k_{-2} K_3 K_5 K_6} + \frac{K_1 K_2 X_{rbc}}{k_5 K_3 K_6} + \frac{Y_{pl}}{k_{-2} K_3} + \frac{K_1 (1 + K_2)}{k_5 K_6} X_{rbc} X_{pl} \right. \\ & + \frac{k_4 (1 + K_5)}{k_{-2} K_3} Y_{rbc} Y_{pl} + \left(\frac{1}{k_{-5}} + \frac{1}{k_2} \right) X_{rbc} Y_{pl} + \left(\frac{1}{k_5} + \frac{1}{k_{-2}} \right) X_{pl} Y_{rbc} \left. \right]^{-1} \end{aligned} \quad (5.10)$$

where

X_{rbc} denotes $[Cl^-]_{rbc}$, Y_{rbc} denotes $[HCO_3^-]_{rbc}$, X_{pl} denotes $[Cl^-]_{pl}$ and Y_{pl} denotes $[HCO_3^-]_{pl}$.

$K_j = k_j / k_{-j}$ for $j=1, 3, 4$ and 6 . K_1 and K_3 are the microscopic equilibrium association constants for Cl^- -protein complex in the inward and outward membrane compartments, respectively. K_4 and K_6 are the microscopic equilibrium association constants for HCO_3^- -protein complex in the outward and inward membrane compartments, respectively.

k_2, k_{-2} (k_5, k_{-5}), the rates of translocation of bound Cl^- (HCO_3^-), are defined in the ping-pong model as the microscopic rate constant for conversion of an intracellular carrier-anion binary complex to an extracellular carrier complex and vice-versa.

It should be mentioned that inhibitory effects on anion exchange are not taken into account. Inhibitory effects can be divided into the following three types: (a) self inhibition by the high concentrations of the transported anions (Dalmark, 1976; Lambert and Lowe, 1980; Weith *et al.*, 1980; Weith and Bjerrum, 1982), (b) competitive inhibition by other anions where the inhibitor compete for the same unloaded anion transporter (Dalmark, 1976; Lambert and Lowe, 1978), and (c) other inhibitors which inactive the anion carrier through predominantly non-competitive mechanism where the inhibitors bind to both the loaded and unloaded transporters (Lambert and Lowe, 1978 and 1980; Weith *et al.*, 1980). The phenomena of self-inhibition has been observed at relatively high extracellular concentrations of Cl^- and HCO_3^- compared to the physiological concentrations. Therefore, it is reasonable for a first approximation to neglect it. The mechanism behind these different types of inhibition are still not known well. There are some apparent discrepancies in the results of different workers on the studies of competitive inhibition. This probably arises, in part at least, from the different conditions of *pH*, temperature and competitive effects between anions prevailing under different experimental conditions.

For a first order approximation of the anion exchange, additional assumptions are introduced to further simplify the expression for the flux (Equation (5.10)):

- (1) The translocation step is assumed to be the rate limiting step.
- (2) k_{trans} , the translocation rate constant, is assumed to be independent of the type of bound anions as well as independent of the direction of the translocation. Therefore, $k_{trans}=k_2=k_{-2}=k_5=k_{-5}$.

(3) Equilibrium association constants (K_A s) for Cl^- and HCO_3^- are assumed to be the same in both membrane compartments (i.e., facing-inward and facing-outward). Therefore, $K_A = K_1 = K_3 = K_4 = K_6$ (Lemon, 1989).

(4) In the literature, it has been reported that $\text{HCO}_3^-/\text{Cl}^-$ exchange is essentially independent of internal pH in the range of intracellular pH from 7.0 to 8.0. In addition, it is approximately independent of extracellular pH in the range from 7.0 to 9.0 (Obaid and Crandall, 1979; Weith *et al.*, 1980; Weith and Bjerrum, 1982; Weith *et al.*, 1982). Thus, k_{trans} and K_A are assumed to be independent of pH .

Upon introducing assumptions (1) - (4), Equation (5.10) is simplified to the following equation which is mathematically more tractable and contains only two kinetic parameters, k_{trans} and K_A .

$$\begin{aligned} Flux_{HCO_3} = T_{tot} k_{trans} K_A \left([Cl^-]_{rbc} [HCO_3^-]_{pl} - [Cl^-]_{pl} [HCO_3^-]_{rbc} \right) / \\ \left\{ [Cl^-]_{rbc} + [Cl^-]_{pl} + [HCO_3^-]_{rbc} + [HCO_3^-]_{pl} + 2 K_A \left([Cl^-]_{rbc} [Cl^-]_{pl} + \right. \right. \\ \left. \left. [HCO_3^-]_{rbc} [HCO_3^-]_{pl} + [Cl^-]_{rbc} [HCO_3^-]_{pl} + [Cl^-]_{pl} [HCO_3^-]_{rbc} \right) \right\} \quad (5.11) \end{aligned}$$

Equation (5.11) predicts that there is a net influx of HCO_3^- into RBCs or a net efflux of Cl^- entering the extracellular medium as long as

$$\frac{[HCO_3^-]_{pl}}{[HCO_3^-]_{rbc}} > \frac{[Cl^-]_{pl}}{[Cl^-]_{rbc}} \quad (5.12a)$$

For a long time it has been known that the ratios of the inside and outside concentrations of the various permeable anions (and of the cation, H^+ , because $[H^+]_{rbc}[OH^-]_{rbc} = [H^+]_{pl}[OH^-]_{pl}$) were approximately given by the Gibbs-Donnan relationship (Van Slyke *et al.*, 1923).

$$R_{GD} = \frac{[Cl^-]_{rbc}}{[Cl^-]_{pl}} = \frac{[HCO_3^-]_{rbc}}{[HCO_3^-]_{pl}} = \frac{[SO_4^{2-}]_{rbc}}{[SO_4^{2-}]_{pl}} = \frac{[OH^-]_{rbc}}{[OH^-]_{pl}} = \frac{[H^+]_{pl}}{[H^+]_{rbc}} \quad (5.12b)$$

where R_{GD} is the so called “Donnan ratio”. That is the ions behave as if they are all in equilibrium with the same membrane potential. This is exactly what would be predicted if the ions were to diffuse across the membrane in response to their electrochemical potential difference. Cabantchik *et al.* (1978) pointed out that for thermodynamic reasons even in the carrier model in which no electrical driving force is considered and in which ions are assumed to carry no current across the membrane, one would predict the same relationship between the equilibrium distribution ratio of the various ions. Therefore Equation (5.12a) derived from Equation (5.11) is consistent with the Donnan-type distribution of ions (Equation (5.12b)) which is approached at equilibrium when the net flux must be zero.

5.2 Experimental Validation of Flux Expression

5.2.1 Methods of Measurement of Cl^-/HCO_3^- Exchange

The transmembrane movements of the Cl^- can be monitored without serious complications, but movements of HCO_3^- involve an additional feature which must be taken into account in any technique adopted. This complication is the involvement in the following equilibria: $CO_2 + H_2O \rightleftharpoons H_2CO_3 \rightleftharpoons H^+ + HCO_3^-$. Basically, two methods of overcoming this difficulty during measurements of HCO_3^- movements had been used. Details of these techniques are discussed below, because in assessing the significance of results obtained using one of these methods in relation to those obtained using the other it is necessary to consider carefully the experimental procedures used.

5.2.1.a *pH Changes and Jacobs-Stewart Cycle*

When an intracellular Cl^- exchanges for an extracellular HCO_3^- , subsequent operation of Jacobs-Stewart Cycle (Figure 5.4) leads to production of one extracellular H^+ and the absorption of one intracellular H^+ . In principle, it is therefore possible to measure $\text{Cl}^-/\text{HCO}_3^-$ exchange by following changes in extracellular *pH*, provided that the anion exchange is the rate-limiting step in the cycle and that *pH* measuring technique has a sufficiently fast response. In human red blood cells under normal circumstances steps 2 and 3, as illustrated in Figure 5.4, are very much faster than anion exchange

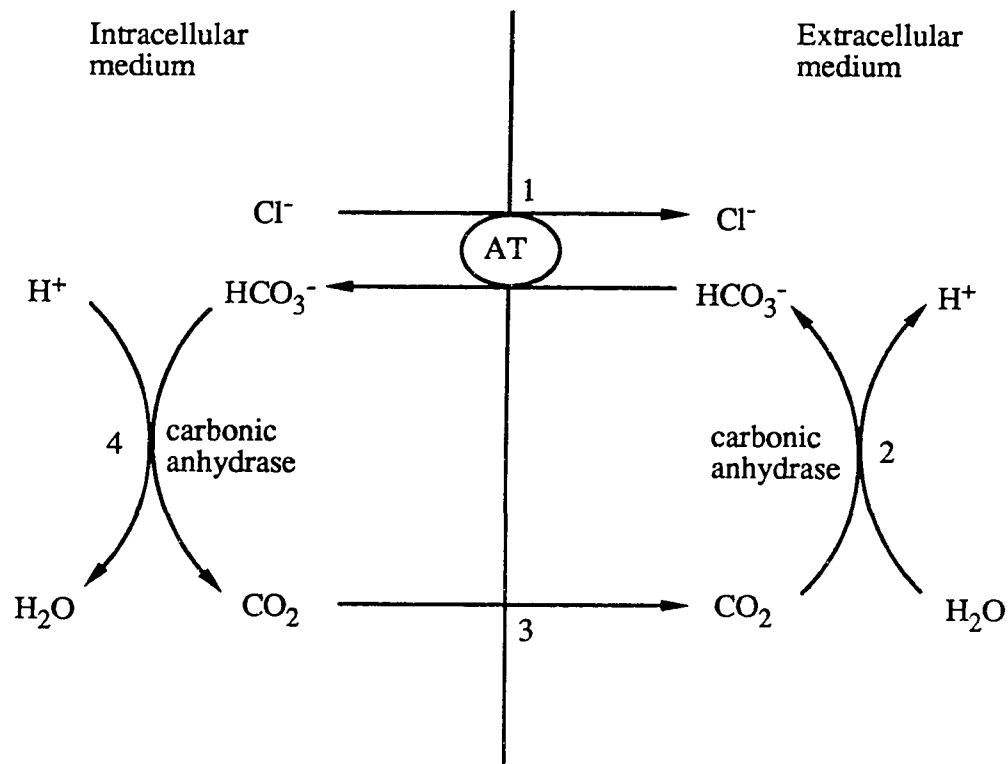


Figure 5.4: Operation of the Jacobs-Stewart cycle and rapid acidification of the extracellular medium by $\text{Cl}^-/\text{HCO}_3^-$ exchange after addition of packed RBCs to a Cl^- -free media which contains carbonic anhydrase enzyme.

(step 1) because intracellular hydration of CO_2 is catalyzed by carbonic anhydrase which is present at high activity levels in RBCs and the physical diffusion of CO_2 cross the membrane is very rapid. However, the rate of hydration of extracellular H_2CO_3 is much slower in comparison to the anion exchange process. This difficulty can be overcome by adding carbonic anhydrase to the extracellular medium in a concentration sufficient to leave $\text{Cl}^-/\text{HCO}_3^-$ exchange as the rate-limiting step in the cycle. The rate of change in pH which reflects the operation of Jacobs-Stewart cycle, can then be taken as a measure of the rate of $\text{Cl}^-/\text{HCO}_3^-$ exchange. The types of apparatuses and detection methods that were used by Chow *et al.* (1976), Obaid and Crandall (1979) and Lemon (1989) who measured the anion exchange with the method described above are summarized in Table 5.3.

5.2.1.b *Uncatalyzed Hydration/Dehydration of CO_2*

An alternative approach to measurement of the anion exchange is one in which the Jacobs-Stewart cycle is prevented by inhibiting the catalyzed hydration of CO_2 by carbonic anhydrase (Figure 5.5). When this is done, rates of CO_2 transport become very slow compared with rates of anion exchange and isotopically labeled HCO_3^- can be used to monitor HCO_3^- movement. The carbonic anhydrase activity was effectively eliminated by, firstly, using resealed red cell ghost from which most of the enzyme had been lost during lysis and, secondly, incorporating into the ghost an inhibitor of carbonic anhydrase (e.g., acetazolamide or 2,6-pyridine dicarboxylic acid which chelates the zinc ions). If the formation of intracellular $^{14}\text{CO}_2$ is not eliminated, the tracer will permeate the membrane in the form $^{14}\text{CO}_2$. Due to the high membrane permeability to CO_2 , intra- and extracellular CO_2 will equilibrate rapidly, and this will lead to rapid loss of the tracer. Therefore, under the conditions described previously, after mixing of Cl^- -containing cells to a Cl^- -free medium that contains $\text{H}^{14}\text{CO}_3^-$ ion, the influx of $^{14}\text{CO}_2$ would be very much slower than the influx of $[^{14}\text{C}]\text{bicarbonate}$ and so

the rate of entry of radioactivity would be a good measure of HCO_3^- transport (Weith, 1979). Along this same line of conducting experiments in the presence of carbonic anhydrase inhibitor, Cl^- -sensitive fluorescent probe have also been used to follow the exchange (Ilsley and Verkman, 1987). The types of apparatus and detection methods that were used by Klocke (1976), Weith (1979), Ilsley and Verkman (1987) who measured the anion exchange with the method described above are synopsized in Table 5.3.

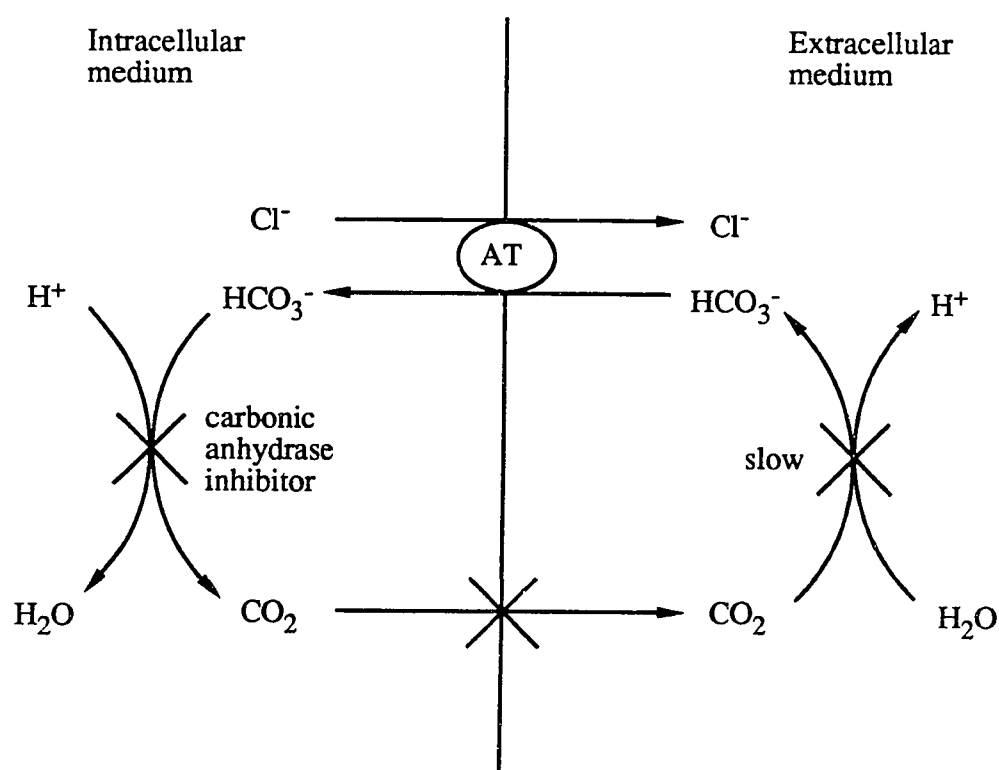


Figure 5.5: Operation of the $\text{Cl}^-/\text{HCO}_3^-$ exchange after intracellular carbonic anhydrase activity is blocked so that simultaneous movement of CO_2 is eliminated.

Table 5.3: Apparatuses, detection methods and experimental conditions in $\text{Cl}^-/\text{HCO}_3^-$ exchange experiments used by various investigators.

Experiments where Jacobs-Stewart cycle is in operation in the presence of added extracellular carbonic anhydrase.			
Workers	Apparatuses	Detection methods	RBCs/ghosts
Chow <i>et al.</i> (1976) Obaid and Crandall (1979)	stopped-flow rapid-reaction device ($T=5-40\text{ }^\circ\text{C}$)	pH electrode	intact RBCs ($Ht=16\%$)
Lemon (1989)	stopped-flow rapid-reaction device ($T=25\text{ }^\circ\text{C}$)	pyranine [†] or SPQ* (pH-sensitive or Cl^- -sensitive fluorescent dye)	intact RBCs ($Ht=6.7\%$)
Experiments where intracellular carbonic anhydrase activity is eliminated.			
Workers	Apparatuses	Detection methods	RBCs/ghosts
Klocke (1976)	continuous-flow rapid-reaction device ($T=37\text{ }^\circ\text{C}$)	chloridometer gas chromatography	intact RBCs ($Ht=19\%$)
Weith (1979)	stopped-flow rapid-reaction device ($T=25\text{ }^\circ\text{C}$)	tracer method $[^{14}\text{C}]\text{HCO}_3^-$	resealed ghosts ($Ht=1\%$)
Illsley and Verkman (1987)	stopped-flow rapid-reaction device ($T=37\text{ }^\circ\text{C}$)	SPQ (Cl^- -sensitive fluorescent probe)	resealed ghosts ($Ht=0.03\%$)

[†] Pyranine is 8-hydroxy-1,3,6-pyrene trisulfonic acid.

* SPQ denotes 6-methoxy-N-(3-sulfopropyl) quinolinium.

5.2.2 Description of Experimental Systems and Development of Analysis

5.2.2.a Klocke's Experimental System (1976)

Klocke studied $\text{Cl}^-/\text{HCO}_3^-$ exchange in a continuous-flow rapid-reaction apparatus at 37 °C. The Reynolds number was greater than 5000 so that turbulent flow was ensured to promote mixing. The residence time can be estimated from the flow rate and the distance travelled in the tube. Thus, one can model Klocke's system as an ideal, isothermal continuous flow stirred tank reactor. It is a two-compartment system between which there exists a transmembrane gradient for both anions, and this gradient is produced by having RBCs which were loaded with one ion reacted with an isoosmotic solution which contained the other ion. Carbonic anhydrase activity was inhibited, so that simultaneous movement of CO_2 can be avoided and free CO_2 concentration, $[\text{CO}_2]_{pl,free}$ remained essentially constant during the experimental period. During sample collection, RBCs were trapped in the mesh of the filter, so that extracellular Cl^- and HCO_3^- concentrations can be determined. Extracellular Cl^- concentration was determined coulometrically. Total extracellular CO_2 content, $[\text{CO}_2]_{pl,total}$ was measured with gas chromatography; then extracellular HCO_3^- concentration was calculated through the following relationship: $[\text{HCO}_3^-]_{pl} = [\text{CO}_2]_{pl,total} - [\text{CO}_2]_{pl,free}$.

The mathematical description of Klocke's system follows:

Intracellular phase

$$([\text{HCO}_3^-]_{rbc,out} - [\text{HCO}_3^-]_{rbc,in}) = \left(\frac{S}{V}\right)_{rbc} \text{Flux}_{\text{HCO}_3} \left(\frac{V_R}{Q}\right) \quad (5.13)$$

$$([Cl^-]_{rbc,out} - [Cl^-]_{rbc,in}) = - \left(\frac{S}{V} \right)_{rbc} Flux_{HCO_3} \left(\frac{V_R}{Q} \right) \quad (5.14)$$

Extracellular phase

$$(1 - Ht) ([HCO_3^-]_{pl,out} - [HCO_3^-]_{pl,in}) = - Ht \left(\frac{S}{V} \right)_{rbc} Flux_{HCO_3} \left(\frac{V_R}{Q} \right) \quad (5.15)$$

$$(1 - Ht) ([Cl^-]_{pl,out} - [Cl^-]_{pl,in}) = Ht \left(\frac{S}{V} \right)_{rbc} Flux_{HCO_3} \left(\frac{V_R}{Q} \right) \quad (5.16)$$

where

$[HCO_3^-]_{rbc,out}$ ($[HCO_3^-]_{rbc,in}$) and $[Cl^-]_{rbc,out}$ ($[Cl^-]_{rbc,in}$) are the intracellular concentrations of HCO_3^- and Cl^- , respectively; subscripts “out” and “in” denote outlet and inlet compositions, respectively.

$[HCO_3^-]_{pl,out}$ ($[HCO_3^-]_{pl,in}$) and $[Cl^-]_{pl,out}$ ($[Cl^-]_{pl,in}$) are the extracellular concentrations of HCO_3^- and Cl^- , respectively; subscripts “out” and “in” denote outlet and inlet compositions, respectively.

Ht is the hematocrit or the volume fraction of RBCs in the suspension.

$Flux_{HCO_3} = Function \{k_{trans}, K_A; [HCO_3^-]_{rbc}, [Cl^-]_{rbc}, [HCO_3^-]_{pl}, [Cl^-]_{pl}\}$ or
 $Flux_{HCO_3} = Function' \{P_{HCO_3}, P_{Cl}; [HCO_3^-]_{rbc}, [Cl^-]_{rbc}, [HCO_3^-]_{pl}, [Cl^-]_{pl}\}$ which is given by either Equation (5.11) or (5.1), respectively.

V_R/Q is the residence time of the reactor where V_R is the volume of the CSTR and Q is the volumetric flowrate of the RBC suspension.

Table 5.4: Parameter values and objective function used in analysis of Klocke's data.

System parameters	$T = 37\text{ }^{\circ}\text{C}$, $Ht = 19\%$ RBC
RBC parameters	$(s/v)_{rbc} = 1.87\text{ }\mu\text{m}^{-1}$ $T_{tot} = 1 \times 10^6$ transporters/RBC
Case 1: Chloride-loaded RBCs with bicarbonate-containing buffer @ pH 7.7	
Inlet concentrations (mM)	$[\text{HCO}_3^-]_{rbc} = 25.0$, $[\text{Cl}^-]_{rbc} = 125.0$ $[\text{HCO}_3^-]_{pl} = 130.4$, $[\text{Cl}^-]_{pl} = 19.6$
Minimization objective function	$F(k_{trans}, K_A) = \frac{\sum ([\text{Cl}^-]_{pl,exp} - [\text{Cl}^-]_{pl,calc})^2}{\sum ([\text{Cl}^-]_{pl,exp})^2}$
Case 2: Bicarbonate-loaded RBCs with chloride-containing buffer @ pH 7.7	
Inlet concentrations (mM)	$[\text{HCO}_3^-]_{rbc} = 146.0$, $[\text{Cl}^-]_{rbc} = 4.0$ $[\text{HCO}_3^-]_{pl} = 20.5$, $[\text{Cl}^-]_{pl} = 129.5$
Minimization objective function	$F(k_{trans}, K_A) = \frac{\sum ([\text{HCO}_3^-]_{pl,exp} - [\text{HCO}_3^-]_{pl,calc})^2}{\sum ([\text{HCO}_3^-]_{pl,exp})^2}$

5.2.2.b Weith's Experimental System (1979)

Counter-transport of [^{14}C]bicarbonate into human erythrocyte ghosts driven by a Cl^- gradient was followed at a low cytocrit (volume fraction of ghosts in the suspension) of 1%, under the conditions where the amount of permeating anions in the ghosts is significant compared to the amount of permeating anions in the extracellular phase. Weith (1979) conducted the experiments in a stopped-flow rapid-reaction device at $0\text{ }^{\circ}\text{C}$ by having ghosts containing 165 mM KCl and 1 mM acetazolamide reacted with a Cl^- -free medium containing $4.2\text{ }\mu\text{M}$ $\text{H}^{14}\text{CO}_3^-$. As mentioned previously, his experiments utilized the fact that uncatalyzed rates of hydration/dehydration of carbonic acid proceed very slowly relative to the rate of anion exchange and isotopically labeled $\text{H}^{14}\text{CO}_3^-$ can be used to monitor HCO_3^- movement. The decrease of extracellular $\text{H}^{14}\text{CO}_3^-$

concentration was followed by determinations of the extracellular radioactivity. The intracellular radioactivity was calculated from the disappearance of $H^{14}CO_3^-$ from the medium. It had been reported in the literature that the maximum transport capacity of anion transporter decreased by 10-15% when ghosts were stored at 0 °C for 24 hours (Funder and Weith, 1976). However, Weith's investigations were reported to be carried out with ghosts that were prepared on the day of the experiment; therefore 1×10^6 band 3 monomers per ghost is used in the simulation.

Because the transmembrane anion transport is, by comparison, a much slower process than the diffusion of anions in both the cell and extracellular medium, as a result, resistances to the diffusion of HCO_3^- and Cl^- in the intra- and extracellular boundary layers are neglected in this analysis. Weith's system is modeled as an ideal, isothermal batch reactor with two compartments; consequently, a simple model which consists a system of four simultaneous, nonlinear ordinary differential equations (ODEs) is obtained.

Intracellular phase

$$\frac{d[HCO_3^-]_{rbc}}{dt} = \left(\frac{s}{v}\right)_{rbc} Flux_{HCO_3} \quad (5.17)$$

$$\frac{d[Cl^-]_{rbc}}{dt} = -\left(\frac{s}{v}\right)_{rbc} Flux_{HCO_3} \quad (5.18)$$

Extracellular phase

$$(1 - Ht) \frac{d[HCO_3^-]_{pl}}{dt} = -Ht \left(\frac{s}{v}\right)_{rbc} Flux_{HCO_3} \quad (5.19)$$

$$(1 - Ht) \frac{d[Cl^-]_{pl}}{dt} = Ht \left(\frac{s}{v}\right)_{rbc} Flux_{HCO_3} \quad (5.20)$$

where

$[HCO_3^-]_{rbc}$ and $[Cl^-]_{rbc}$ are the intracellular concentrations of HCO_3^- and Cl^- , respectively.

$[HCO_3^-]_{pl}$ and $[Cl^-]_{pl}$ are the extracellular concentrations of HCO_3^- and Cl^- , respectively.

Table 5.5: Parameter values and objective function used in analysis of Weith's data.

System parameters	$T = 0\text{ }^\circ\text{C}, pH = 8.7, Ht = 1\%$ ghost
RBC parameters	$(s/v)_{rbc} = 1.58\text{ }\mu\text{m}^{-1\dagger}$ $T_{tot} = 1 \times 10^6$ transporters/ghost*
Initial concentrations	$[HCO_3^-]_{rbc} = 0\text{ M}, [Cl^-]_{rbc} = 165\text{ mM}$ $[HCO_3^-]_{pl} = 4.2\text{ }\mu\text{M}, [Cl^-]_{pl} = 0\text{ M}$
Minimization objective function	$F(k_{trans}, K_A) = \frac{\sum ([HCO_3^-]_{pl,exp} - [HCO_3^-]_{pl,calc})^2}{\sum ([HCO_3^-]_{pl,exp})^2} + \frac{\sum ([HCO_3^-]_{rbc,exp} - [HCO_3^-]_{rbc,calc})^2}{\sum ([HCO_3^-]_{rbc,exp})^2}$

[†] It was reported that ghost resealed with KCl had a membrane area of $1.42 \times 10^{-6}\text{ cm}^2$ per cell, and a cell volume of $90\text{ }\mu\text{m}^3$ (Funder and Weith, 1976).

* Weith *et al.*'s (1980) studies had demonstrated that the anion transport capacity of resealed ghosts is not hampered by the technique for preparing ghosts.

5.2.2.c Illsley and Verkman's Experimental System (1987)

Illsley and Verkman measured anion exchange using a Cl^- sensitive fluorescent probe which is 6-methoxy-N-(3-sulfopropyl) quinolinium (SPQ). It was reported that SPQ fluorescence was not altered by other physiological anions or pH . The experiments were conducted by having sealed RBC ghosts which were loaded with 100 mM Cl^- and 1 mM SPQ reacted with isoosmotic Cl^- -free solutions containing either

HCO_3^- or SO_4^{2-} in a stopped-flow rapid-reaction apparatus at 37 °C. Addition of ghosts to the Cl^- -free medium caused a rapid increase in fluorescence as intracellular Cl^- was exchanged for external HCO_3^- and SPQ fluorescence was unquenched. Knowing the quenching constant of SPQ, initial and final Cl^- concentrations and the corresponding fluorescences, one can then use the Stern-Volmer relationship to translate the fluorescence intensity to intracellular Cl^- concentration. Equations (5.17) - (5.20) can be used to describe this system.

Table 5.6: Parameter values and objective function used in analysis of Illsley and Verkman's data.

System parameters	$T = 37\text{ }^\circ\text{C}, Ht = 0.03\% \text{ ghost}$
RBC parameters	$(s/v)_{rbc} = 1.58\text{ }\mu\text{m}^{-1}$ $T_{tot} = 1 \times 10^6 \text{ transporters/ghost}$
Case 1: Chloride-loaded ghosts with bicarbonate-containing isoosmotic buffer	
Initial concentrations (mM)	$[\text{HCO}_3^-]_{rbc} = 0, [\text{Cl}^-]_{rbc} = 100$ $[\text{HCO}_3^-]_{pl} = 20, [\text{Cl}^-]_{pl} = 0$
Minimization objective function	$F(k_{trans}, K_A) = \frac{\sum ([\text{Cl}^-]_{rbc,exp} - [\text{Cl}^-]_{rbc,calc})^2}{\sum ([\text{Cl}^-]_{rbc,exp})^2}$
Case 2: Chloride-loaded ghosts with sulfate-containing isoosmotic buffer	
Initial concentrations (mM)	$[\text{SO}_4^{2-}]_{rbc} = 0, [\text{Cl}^-]_{rbc} = 100$ $[\text{SO}_4^{2-}]_{pl} = 66, [\text{Cl}^-]_{pl} = 0$
Minimization objective function	$F(k_{trans}, K_A) = \frac{\sum ([\text{Cl}^-]_{rbc,exp} - [\text{Cl}^-]_{rbc,calc})^2}{\sum ([\text{Cl}^-]_{rbc,exp})^2}$

5.2.2.d *Lemon's Experimental System* (1989)

Lemon measured the pH changes of the Jacobs-Stewart cycle using a fluorescent indicator, pyranine (8-hydroxy-1,3,6-pyrene trisulfonic acid), in the extracellular medium in a stopped-flow mixing device at 25 °C. Special ion jump experiments, designed to minimize competition between Cl^- and HCO_3^- , were performed by mixing 1 volume of essentially HCO_3^- -free, Cl^- -loaded packed cells with 14 volumes of various Cl^- -free, HCO_3^- -containing pyranine solutions. The following approach was implemented to formulate a model for describing Lemon's system:

- (1) After mixing, the RBCs were assumed to be uniformly distributed in the mixing cuvette of the stopped-flow device.
- (2) Extracellular resistance to CO_2 transport was taken into account with an estimated mass transfer coefficient. This transport resistance was included because CO_2 diffusion across the RBC membrane is a very rapid process in comparison to CO_2 diffusion through the unstirred layer which is a much slower process, perhaps one to two order magnitude slower depending on the P_{CO_2} of the system. The magnitude of this external diffusion effect is estimated from a simple boundary layer analysis as given in Appendix B (Coin and Olson, 1979; Kagawa and Mochizuki, 1982; Vandegriff and Olson, 1984a and 1984b).
- (3) Since additional carbonic anhydrase enzyme was added to the extracellular medium, CO_2 hydration/dehydration reactions are assumed to be at chemical equilibrium both intra- and extracellularly.
- (4) Intra- and extracellular buffering capacities are taken into account. The dependence of extracellular buffering capacity on pH and $[HCO_3^-]_{pl}$ is taken into consideration as shown in Equation (5.21) (Butler, 1964).

$$\beta_{pl} = 2.303 \left[\frac{K_{buffer} [buffer]_{pl} [H^+]_{pl}}{(K_{buffer} + [H^+]_{pl})^2} + \frac{K_{water}}{[H^+]_{pl}} + [H^+]_{pl} \right] \quad (5.21)$$

where

β_{pl} is the buffering capacity of the extracellular medium.

K_{buffer} is the equilibrium constant of the buffer.

$[buffer]_{pl}$ is the molar concentration of the buffer in the extracellular medium.

K_{water} is the dissociation constant of water.

The last two terms of Equation (5.21) are due to buffering effect of water; the first term is due to the conjugate acid base pair. In most cases of interest, the last two terms can be neglected. It should be mentioned that the contributions are additive; thus when there is a mixture of noninteractive buffers present in solution, their buffering effects are additive.

Intracellular phase

$$\left(1 - \frac{\beta_{rbc}}{2.303[H^+]_{rbc}} \frac{d[H^+]_{rbc}}{d[HCO_3^-]_{rbc}}\right) \frac{d[HCO_3^-]_{rbc}}{dt} = \left(\frac{s}{v}\right)_{rbc} Flux_{HCO_3} \quad (5.22)$$

$$\frac{d[Cl^-]_{rbc}}{dt} = -\left(\frac{s}{v}\right)_{rbc} Flux_{HCO_3} \quad (5.23)$$

$$\left(1 + \frac{\beta_{rbc}}{2.303[H^+]_{rbc}} \frac{d[H^+]_{rbc}}{d[CO_2]_{rbc}}\right) \frac{d[CO_2]_{rbc}}{dt} = \left(\frac{s}{v}\right)_{rbc} \eta_{CO_2} \left(\frac{[CO_2]_{pl}}{\alpha_{CO_2,pl}} - \frac{[CO_2]_{rbc}}{\alpha_{CO_2,rbc}}\right) \quad (5.24)$$

Extracellular phase

$$(1 - Ht) \left(1 - \frac{\beta_{pl}}{2.303[H^+]_{pl}} \frac{d[H^+]_{pl}}{d[HCO_3^-]_{pl}}\right) \frac{d[HCO_3^-]_{pl}}{dt} = -Ht \left(\frac{s}{v}\right)_{rbc} Flux_{HCO_3} \quad (5.25)$$

$$(1 - Ht) \frac{d[Cl^-]_{pl}}{dt} = Ht \left(\frac{s}{v}\right)_{rbc} Flux_{HCO_3} \quad (5.26)$$

$$(1 - Ht) \left(1 + \frac{\beta_{pl}}{2.303[H^+]_{pl}} \frac{d[H^+]_{pl}}{d[CO_2]_{pl}} \right) \frac{d[CO_2]_{pl}}{dt} = - Ht \left(\frac{s}{v} \right)_{rbc} \eta_{CO_2} \left(\frac{[CO_2]_{pl}}{\alpha_{CO_2,pl}} - \frac{[CO_2]_{rbc}}{\alpha_{CO_2,rbc}} \right) \quad (5.27)$$

where

$$\frac{d[H^+]_{rbc}}{d[HCO_3^-]_{rbc}} = - \frac{K' f_{water} [CO_2]_{rbc}}{([HCO_3^-]_{rbc})^2} \text{ and } \frac{d[H^+]_{pl}}{d[HCO_3^-]_{pl}} = - \frac{K' f_{water} [CO_2]_{pl}}{([HCO_3^-]_{pl})^2}$$

$$\frac{d[H^+]_{rbc}}{d[CO_2]_{rbc}} = \frac{K' f_{water}}{[HCO_3^-]_{rbc}} \text{ and } \frac{d[H^+]_{pl}}{d[CO_2]_{pl}} = \frac{K' f_{water}}{[HCO_3^-]_{pl}}$$

f_{water} is the fraction of water inside the RBC, and it is introduced here to account for the fact that concentrations inside the RBCs are expressed per unit cell volume instead per unit cell water volume.

$\alpha_{CO_2,rbc}$ and $\alpha_{CO_2,pl}$ are the solubility coefficients for CO_2 in the RBC and the plasma, respectively.

η_{CO_2} is the effective, lumped mass transfer coefficient for CO_2 ; and its value is estimated in Appendix B.

Table 5.7: Parameter values and objective function used in analysis of Lemon's data.

System parameters	$T = 25^\circ\text{C}$, $Ht = 6.7\%$ RBC
RBC parameters	$(s/v)_{rbc} = 1.87 \mu\text{m}^{-1}$ $T_{tot} = 1 \times 10^6$ transporters/RBC $f_{water} = 0.72$, $\beta_{rbc} = 0.057$ M/pH
Extracellular parameters	β_{pl} (calculated from Equation (5.21))
Physical properties of CO_2	$\alpha_{CO_2,rbc} = 3.60 \times 10^{-5}$ M/mmHg $\alpha_{CO_2,pl} = 4.05 \times 10^{-5}$ M/mmHg
Mass transfer coefficient	$\eta_{CO_2} = 6.0 \times 10^{-5}$ cm/sec/mmHg
Equilibrium parameter	$pK' = 6.16$

Table 5.7: continued

Case I: Chloride-loaded RBCs with buffer containing bicarbonate and pyranine	
Initial concentrations (mM)	
(1) $[CO_2]_{rbc} = 0.116$, $[HCO_3^-]_{rbc} = 1.25$, $[Cl^-]_{rbc} = 21.6$ $[CO_2]_{pl} = 0.161$, $[HCO_3^-]_{pl} = 3.52$, $[Cl^-]_{pl} = 5.22 \times 10^{-4}$	
(2) $[CO_2]_{rbc} = 0.227$, $[HCO_3^-]_{rbc} = 3.23$, $[Cl^-]_{rbc} = 21.6$ $[CO_2]_{pl} = 0.316$, $[HCO_3^-]_{pl} = 7.07$, $[Cl^-]_{pl} = 5.22 \times 10^{-4}$	
Minimization objective function	$F(k_{trans}, K_A) = \frac{\sum ([H^+]_{pl,exp} - [H^+]_{pl,calc})^2}{\sum ([H^+]_{pl,exp})^2}$
Case II: Chloride-loaded RBCs with buffer containing bicarbonate and SPQ	
Initial concentrations (mM)	
(1) $[CO_2]_{rbc} = 0.0137$, $[HCO_3^-]_{rbc} = 0.236$, $[Cl^-]_{rbc} = 50.4$ $[CO_2]_{pl} = 0.0190$, $[HCO_3^-]_{pl} = 0.330$, $[Cl^-]_{pl} = 0.442$	
(2) $[CO_2]_{rbc} = 0.0342$, $[HCO_3^-]_{rbc} = 0.583$, $[Cl^-]_{rbc} = 50.4$ $[CO_2]_{pl} = 0.0475$, $[HCO_3^-]_{pl} = 0.827$, $[Cl^-]_{pl} = 0.442$	
(3) $[CO_2]_{rbc} = 0.0683$, $[HCO_3^-]_{rbc} = 1.14$, $[Cl^-]_{rbc} = 50.4$ $[CO_2]_{pl} = 0.0949$, $[HCO_3^-]_{pl} = 1.60$, $[Cl^-]_{pl} = 0.442$	
(4) $[CO_2]_{rbc} = 0.340$, $[HCO_3^-]_{rbc} = 5.03$, $[Cl^-]_{rbc} = 50.4$ $[CO_2]_{pl} = 0.473$, $[HCO_3^-]_{pl} = 8.33$, $[Cl^-]_{pl} = 0.442$	
(5) $[CO_2]_{rbc} = 0.678$, $[HCO_3^-]_{rbc} = 8.85$, $[Cl^-]_{rbc} = 50.4$ $[CO_2]_{pl} = 0.941$, $[HCO_3^-]_{pl} = 16.7$, $[Cl^-]_{pl} = 0.442$	
(6) $[CO_2]_{rbc} = 1.35$, $[HCO_3^-]_{rbc} = 14.6$, $[Cl^-]_{rbc} = 50.4$ $[CO_2]_{pl} = 1.87$, $[HCO_3^-]_{pl} = 24.4$, $[Cl^-]_{pl} = 0.442$	
Minimization objective function	$F(k_{trans}, K_A) = \frac{\sum ([Cl^-]_{pl,exp} - [Cl^-]_{pl,calc})^2}{\sum ([Cl^-]_{pl,exp})^2}$

5.2.3 Solution Methods

All the numerical computations are carried out on a Vax 2000 station. With all the parameters and inlet conditions being specified (Table 5.4), Equations (5.13) - (5.16) which is a set of nonlinear algebraic equations can be solved using a modification of the Powell hybrid method from MINPACK-1 (Moré *et al.*, 1980) to give concentrations for various species as functions of reactor residence time. MINPACK-1 is a collection of efficient and robust optimization software. Entirely satisfactory global convergence results are available from the algorithms; and, in addition, the package's properties allow scale invariant implementations. Along the same line, with all the parameters and initial conditions specified (Tables 5.5 and 5.6 and Table 5.7), Equations (5.17) - (5.20) and Equations (5.22) - (5.26), which are systems of simultaneous nonlinear ODEs, can be numerically integrated with EPISODE (Byrne *et al.*, 1977) to give concentrations for various species as a function of reactor holding time. EPISODE is ideally suited for "stiff" differential equation systems (i.e., systems with widely varying time constants).

However, the goal here is to solve the inverse problem of characterizing k_{trans} and K_A (or P_{HCO_3} and P_{Cl}) by utilizing available experimental data in the literature. Therefore, the numerical procedure is initiated by input of the experimental measurements, immediately followed by the usage of a natural cubic spline to smooth the raw data and generate $\{[C_i]_{exp}\}$, where C_i denotes all the species that are involved in a particular system}. The next step is to supply the inlet or initial conditions and guesses for k_{trans} and K_A (or P_{HCO_3} and P_{Cl}). The material balance equations are then solved with the appropriate numerical method; and k_{trans} and K_A (or P_{HCO_3} and P_{Cl}) are then searched for by a nonlinear least squares fitting method. The nonlinear least squares fitting method searches for the values of both parameters that best fit the experimental data $\{[C_i]_{exp}\}$. In other words one seeks the values of k_{trans} and K_A (or

P_{HCO_3} and P_{Cl}) which minimize the objective function $F(k_{trans}, K_A)$ (or $F(P_{HCO_3}, P_{Cl})$). The nonlinear function, $F(k_{trans}, K_A)$ (or $F(P_{HCO_3}, P_{Cl})$), is minimized using a non-gradient based minimization method based on the simplex method of Nelder and Meads (1965). This minimization algorithm has the advantages of simple calculations, uncomplicated logic and few adjustable parameters which need to be supplied. A major disadvantage of this algorithm is that the optimum values for the parameters may not represent a global minimum. To determine whether a set of parameters corresponds to a global minimum, different sets of initial guess can be used to initiate the search. The iterative procedure is continued until the error between the calculated and the experimental concentrations is sufficiently small. Numerical values for RBC/ghost parameters, inlet or initial conditions, and the minimization objective functions for various experimental systems used in the analysis are listed in Tables 5.4 - 5.7.

5.3 Results and Discussion

5.3.1 Comparison of the Simulation Results with the Experimental Data

5.3.1.a Comparison with Klocke's Data (1976)

Two sets of computations are performed for the experimental conditions given in Table 5.4. The first simulates the increase in extracellular Cl^- concentration following mixture of Cl^- -loaded RBCs with bicarbonate buffer which is shown in Figure 5.6. The second computation simulates the change in extracellular HCO_3^- content following mixture of HCO_3^- -loaded cells with chloride buffer which is given in Figure 5.7. In Figures 5.6 and 5.7, the solid lines represent the computed $[Cl^-]_{pl}$ and $[HCO_3^-]_{pl}$, respectively, versus residence time calculated using the flux expression based on the ping-pong model (Equation (5.11)) with $k_{trans}=4 \times 10^4 \text{ sec}^{-1}$, $K_A=200 \text{ M}^{-1}$ and $k_{trans}=6 \times 10^4 \text{ sec}^{-1}$, $K_A=200 \text{ M}^{-1}$, respectively. The dashed lines in the right-hand-side

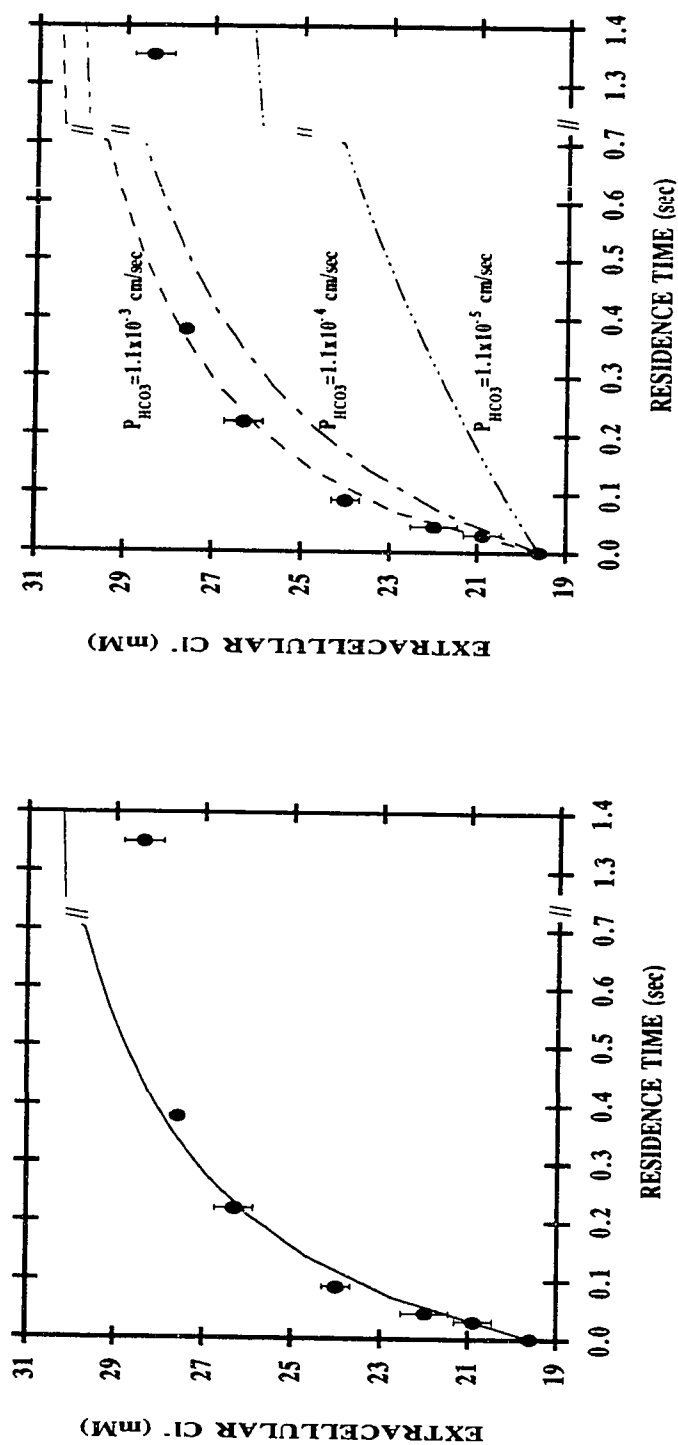


Figure 5.6: Change in extracellular Cl^- concentration following mixture of Cl^- -loaded RBCs with HCO_3^- -containing buffer at 37°C (more detail on the experimental conditions is given in Table 5.4). Klocke's experimental results (Klocke, 1976) are represented as mean \pm S.E. of the multiple analyses of each filtered sample. The left panel gives the comparison of simulation result generated using simplified ping-pong model with the experimental data. The theoretical line (—) is calculated with $k_{\text{trans}}=4 \times 10^4 \text{ sec}^{-1}$ and $K_A=200 \text{ M}^{-1}$. The right panel gives the comparison of simulation result generated using the constant field electrodiffusion with phenomenological permeability coefficients with the experimental data. The theoretical curve (---) is calculated assuming $P_{\text{HCO}_3^-}=1.10 \times 10^{-3}$ and $P_{\text{Cl}^-}=1.10 \times 10^{-4} \text{ cm/sec}$; (— · — · —), $P_{\text{HCO}_3^-}=1.10 \times 10^{-4}$ and $P_{\text{Cl}^-}=1.10 \times 10^{-4} \text{ cm/sec}$; (— · · — · ·), $P_{\text{HCO}_3^-}=1.10 \times 10^{-5}$ and $P_{\text{Cl}^-}=1.10 \times 10^{-4} \text{ cm/sec}$.

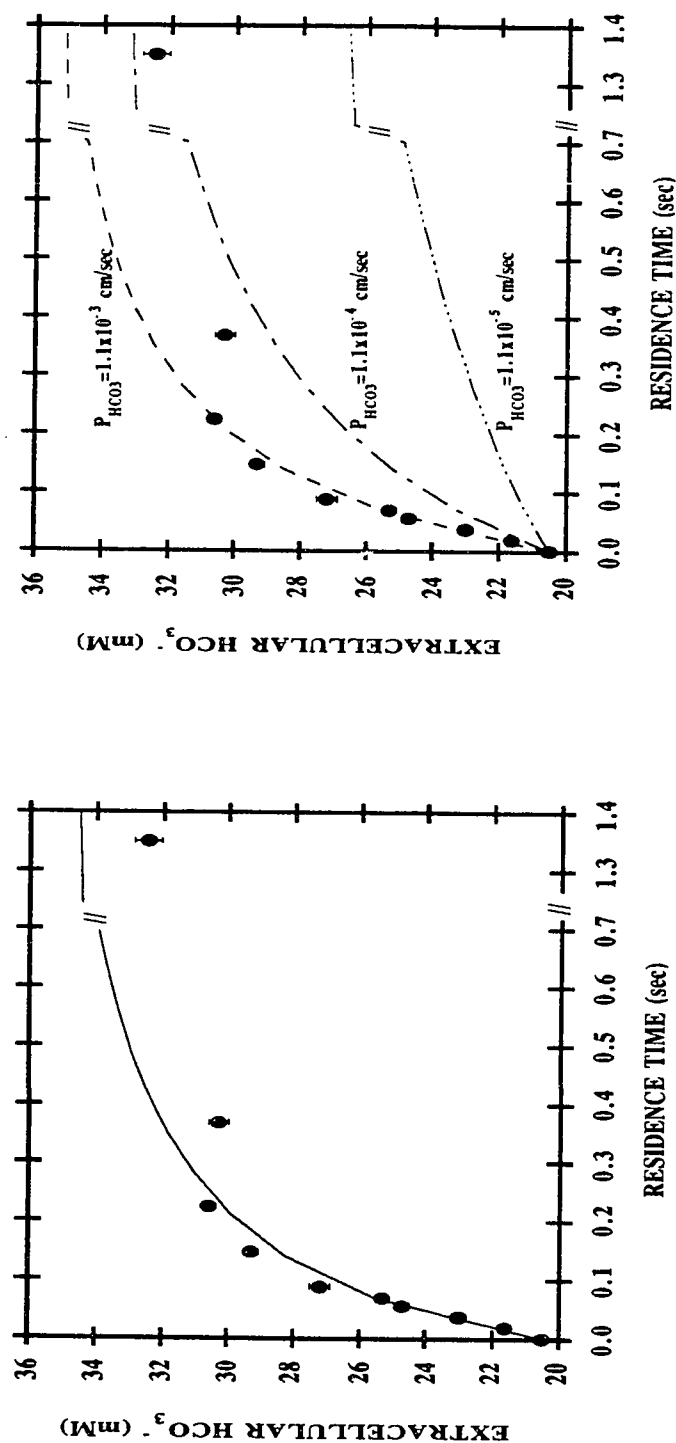


Figure 5.7: Change in extracellular HCO_3^- concentration following mixture of HCO_3^- -loaded RBCs with Cl^- -containing buffer at 37°C (more detail on the experimental conditions is given in Table 5.4). Klocke's experimental results (Klocke, 1976) are represented as mean \pm S.E. of the multiple analyses of each filtered sample. The left panel gives the comparison of simulation result generated using simplified ping-pong model with the experimental data. The theoretical line (—) is calculated with $k_{\text{trans}} = 6 \times 10^4 \text{ sec}^{-1}$ and $K_A = 200 \text{ M}^{-1}$. The right panel gives the comparison of simulation result generated using the constant field electrodiffusion with phenomenological permeability coefficients with the experimental data. The theoretical curve (---) is calculated assuming $P_{\text{HCO}_3} = 1.10 \times 10^{-3}$ and $P_{\text{Cl}} = 1.10 \times 10^{-4} \text{ cm/sec}$; (— · — · —) $P_{\text{HCO}_3} = 1.10 \times 10^{-4}$ and $P_{\text{Cl}} = 1.10 \times 10^{-4} \text{ cm/sec}$; (— · · — · ·) $P_{\text{HCO}_3} = 1.10 \times 10^{-5}$ and $P_{\text{Cl}} = 1.10 \times 10^{-4} \text{ cm/sec}$; (— · · · — · · ·) $P_{\text{HCO}_3} = 1.10 \times 10^{-6}$ and $P_{\text{Cl}} = 1.10 \times 10^{-4} \text{ cm/sec}$.

panels are the computational results generated using flux expression derived based on constant field electrodiffusion (Equation (5.1)) using the range of permeability coefficients reported in the literature. These curves are calculated assuming $P_{Cl}=1.1 \times 10^{-4}$ cm/sec and $P_{HCO_3}=1.1 \times 10^{-3}$ cm/sec for the topmost of this group of curves, $P_{HCO_3}=1.1 \times 10^{-4}$ cm/sec for the middle curves, $P_{HCO_3}=1.1 \times 10^{-5}$ cm/sec for the bottom curves.

The experimental data points seem to indicate that 97% of reaction is complete in 0.4 sec, while simplified ping-pong model predicts 93% and constant field electrodiffusion model predicts 91% of reaction is complete in 0.4 sec. As can be seen the agreement between the experimental data and the computational results generated by simplified ping-pong model and constant field passive diffusion theory (assuming $P_{HCO_3}=1.1 \times 10^{-3}$ and $P_{Cl}=1.1 \times 10^{-4}$ cm/sec) in the first 0.4 sec is good; both models, however, over predict the final concentrations. The simplified ping-pong model over predicts final $[Cl^-]_{pl}$ and $[HCO_3^-]_{pl}$ by 1.82 and 2.03 mM, respectively; and the constant field electrodiffusion model over predicts by 2.09 and 2.71 mM, respectively. The reason for this discrepancy is unclear; with the limited data it is difficult to sort out whether it is due to some experimental errors and/or artifacts or due to the fact that inhibitory effects on the anion transporter became significant at the later stage of the measurements which is not accounted for in the model. The algebraic deviations from the experimental data for the curves generated by the simplified ping-pong equation are 0.10 mM in $[Cl^-]_{pl}$ and 0.17 mM in $[HCO_3^-]_{pl}$. On the other hand, the algebraic deviations for the curves computed by passive electrodiffusion equation are 0.16 mM in $[Cl^-]_{pl}$ and 0.29 mM in $[HCO_3^-]_{pl}$.

5.3.1.b Comparison with Weith's Data (1979)

Figures 5.8 and 5.9 give the comparison of the simulation result generated using both models with Weith's experimental data. The numerical values used for the

pertinent parameters and initial chemical compositions are given in Table 5.5. In Figure 5.8, the solid line represents the computed $[HCO_3^-]_{rbc}$ and $[HCO_3^-]_{pl}$ versus time by the simplified ping-pong model with $k_{trans}=504 \text{ sec}^{-1}$, $K_A=390 \text{ M}^{-1}$. In Figure 5.9, the results are shown for different values of permeability coefficients, using the set $P_{HCO_3}=3.8 \times 10^{-6}$ and $P_{Cl}=1.7 \times 10^{-6} \text{ cm/sec}$ which represents typical values reported in the literature for anion transport at 2°C , and the set $P_{HCO_3}=3.02 \times 10^{-5}$ and $P_{Cl}=1.35 \times 10^{-5} \text{ cm/sec}$ which represents the best-fitted values obtained in this study. From these figures, it is clear that excellent agreement is obtained between both model calculations and the experimental result. Although usage of the literature values for the permeability coefficients in the constant field electrodiffusion theory under estimates the transport by a substantial amount, a 10-fold increase of the permeabilities then give calculation that agrees closely with the experimental data.

It is noteworthy that after addition of Cl^- -loaded ghosts to a Cl^- -free, HCO_3^- -containing medium, efflux of Cl^- was accompanied by an accumulation of HCO_3^- inside and depletion of medium HCO_3^- to give a final ratio of $[HCO_3^-]_{rbc}/[HCO_3^-]_{pl}=662$, this being very similar to the ratio of $[Cl^-]_{rbc}/[Cl^-]_{pl}=660$ at the end of experiment. Both flux expressions predict the final intracellular concentration is 647 times the extracellular concentration owing to the new Gibbs-Donnan equilibrium which is in agreement with the experimental observation. The maximum deviations between the results generated by the simplified ping-pong model and the experimental data are $14.4 \mu\text{M}$ in $[HCO_3^-]_{rbc}$ and $0.035 \mu\text{M}$ in $[HCO_3^-]_{pl}$; the algebraic deviations for both curves are $6.58 \mu\text{M}$ in $[HCO_3^-]_{rbc}$ and $0.015 \mu\text{M}$ in $[HCO_3^-]_{pl}$, respectively. On the other hand, the maximum deviations between the results simulated by the passive electrodiffusion model ($P_{HCO_3}=3.02 \times 10^{-5}$ and $P_{Cl}=1.35 \times 10^{-5} \text{ cm/sec}$) and the experimental data are $15.2 \mu\text{M}$ in $[HCO_3^-]_{rbc}$ and $0.066 \mu\text{M}$ in $[HCO_3^-]_{pl}$; the algebraic deviations for both curves are $7.38 \mu\text{M}$ in $[HCO_3^-]_{rbc}$ and $0.016 \mu\text{M}$ in $[HCO_3^-]_{pl}$, respectively.

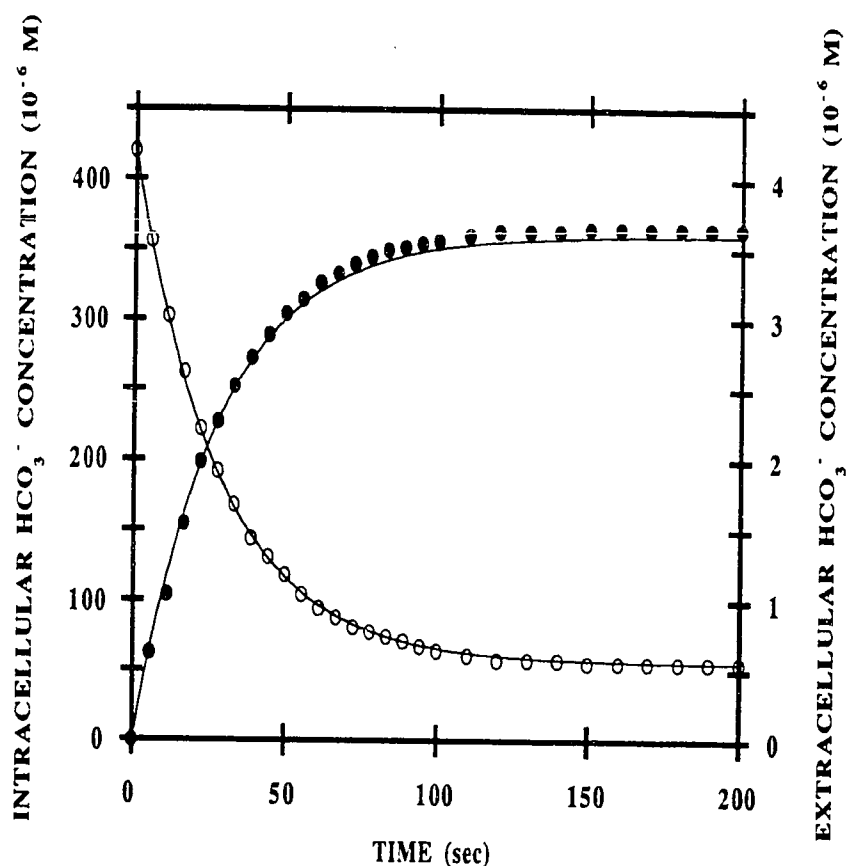


Figure 5.8: Change in HCO_3^- concentration inside and outside human RBC ghosts as a consequence of $\text{Cl}^-/\text{HCO}_3^-$ countertransport at 0 °C (more detail on the experimental conditions is given in Table 5.5). Intracellular HCO_3^- concentrations are indicated on the left-hand ordinate, and extracellular concentrations on the right-hand ordinate; note difference of ordinate scales. Data points: experimental data from Weith (1978); filled circles for intracellular HCO_3^- concentrations and open circles for extracellular HCO_3^- concentrations. Curve: theoretical simulation of the experiment using the simplified ping-pong model; $k_{\text{trans}}=504 \text{ sec}^{-1}$ and $K_A=390 \text{ M}^{-1}$.

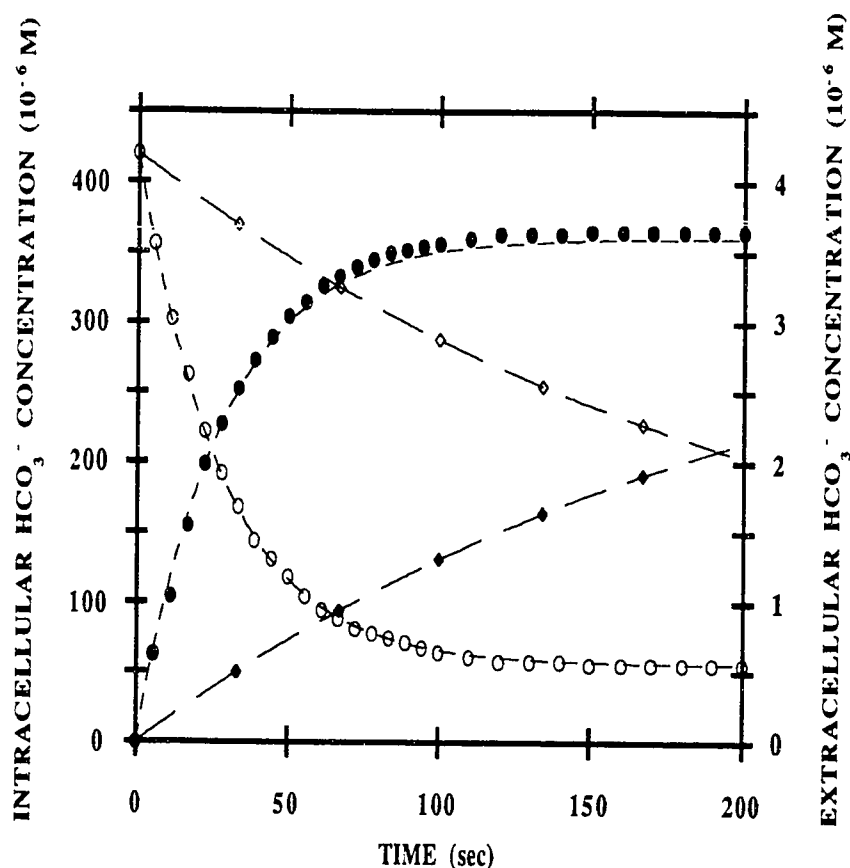


Figure 5.9: Change in HCO_3^- concentration inside and outside human RBC ghosts as a consequence of $\text{Cl}^-/\text{HCO}_3^-$ countertransport at 0°C (more detail on the experimental conditions is given in Table 5.5). Intracellular HCO_3^- concentrations are indicated on the left-hand ordinate, and extracellular concentrations on the right-hand ordinate; note difference of ordinate scales. Data points: experimental data from Weith (1978); filled circles for intracellular HCO_3^- concentrations and open circles for extracellular HCO_3^- concentrations. Curve: theoretical simulation of the experiment using the constant field electrodiffusion with phenomenological permeability coefficients; (---) $P_{\text{HCO}_3}=3.02\times 10^{-5}$ and $P_{\text{Cl}}=1.35\times 10^{-5}$ cm/sec, and (—◆— for intracellular HCO_3^- , —◇— extracellular for HCO_3^-) $P_{\text{HCO}_3}=3.80\times 10^{-6}$ and $P_{\text{Cl}}=1.70\times 10^{-6}$ cm/sec.

5.3.1.c Comparison with Illsley and Verkman's Data (1987)

Figures 5.10 and 5.11 show the comparison of the calculations obtained by both models and Illsley and Verkman's (1987) red cell ghost chloride/anion exchange results; experimental conditions and relevant parameters for these cases are given in Table 5.6. Figure 5.10 illustrates the decrease in intracellular Cl^- concentration following mixture of Cl^- -containing ghosts with bicarbonate buffer. Figure 5.11 demonstrates the change in intracellular Cl^- content following mixture of Cl^- -loaded ghosts with K_2SO_4 buffer. In both figures, the solid lines represent the computed $[\text{Cl}^-]_{rbc}$ versus time calculated using the simplified ping-pong model with $k_{trans}=4.5 \times 10^4 \text{ sec}^{-1}$, $K_A=200 \text{ M}^{-1}$ for the $\text{Cl}^-/\text{HCO}_3^-$ exchange; and $k_{trans}=400 \text{ sec}^{-1}$, $K_A=180 \text{ M}^{-1}$ for the $\text{Cl}^-/\text{SO}_4^{2-}$ exchange. It is reported in the literature that anion transporter site has much lower affinity for SO_4^{2-} than for Cl^- ; i.e., K_{SO_4} is much smaller than K_{Cl} (Schnell *et al.*, 1977). Therefore, the transporter model developed in this work is not exactly appropriate for describing $\text{Cl}^-/\text{SO}_4^{2-}$ exchange due to the assumption that the association equilibrium constants are the same for both anions. A more appropriate model for considering $\text{Cl}^-/\text{SO}_4^{2-}$ exchange would be to relax this assumption and use $k_{trans} \approx 4.5 \times 10^4 \text{ sec}^{-1}$, $K_{\text{Cl}} \approx 200 \text{ M}^{-1}$ and $K_{\text{SO}_4} \approx 2 \text{ M}^{-1}$ in the rederived flux expression.

The dashed lines in the right-hand-side panels are the computational results generated using the phenomenological permeability coefficients. In Figure 5.10, the results are shown for different values of permeability coefficients, using the set $P_{\text{HCO}_3}=1.1 \times 10^{-3}$ and $P_{\text{Cl}}=1.1 \times 10^{-4} \text{ cm/sec}$ which represents typical values reported in the literature for anion transport at 37°C , and the set $P_{\text{HCO}_3}=1.58 \times 10^{-3}$ and $P_{\text{Cl}}=4.6 \times 10^{-4} \text{ cm/sec}$ which represents the best-fitted values obtained in this study. In Figure 5.11, the dashed line is obtained by using $P_{\text{HCO}_3}=2.4 \times 10^{-6}$ and $P_{\text{SO}_4}=2.95 \times 10^{-6} \text{ cm/sec}$ which represents the set of permeabilities that gives the best-fitted result.

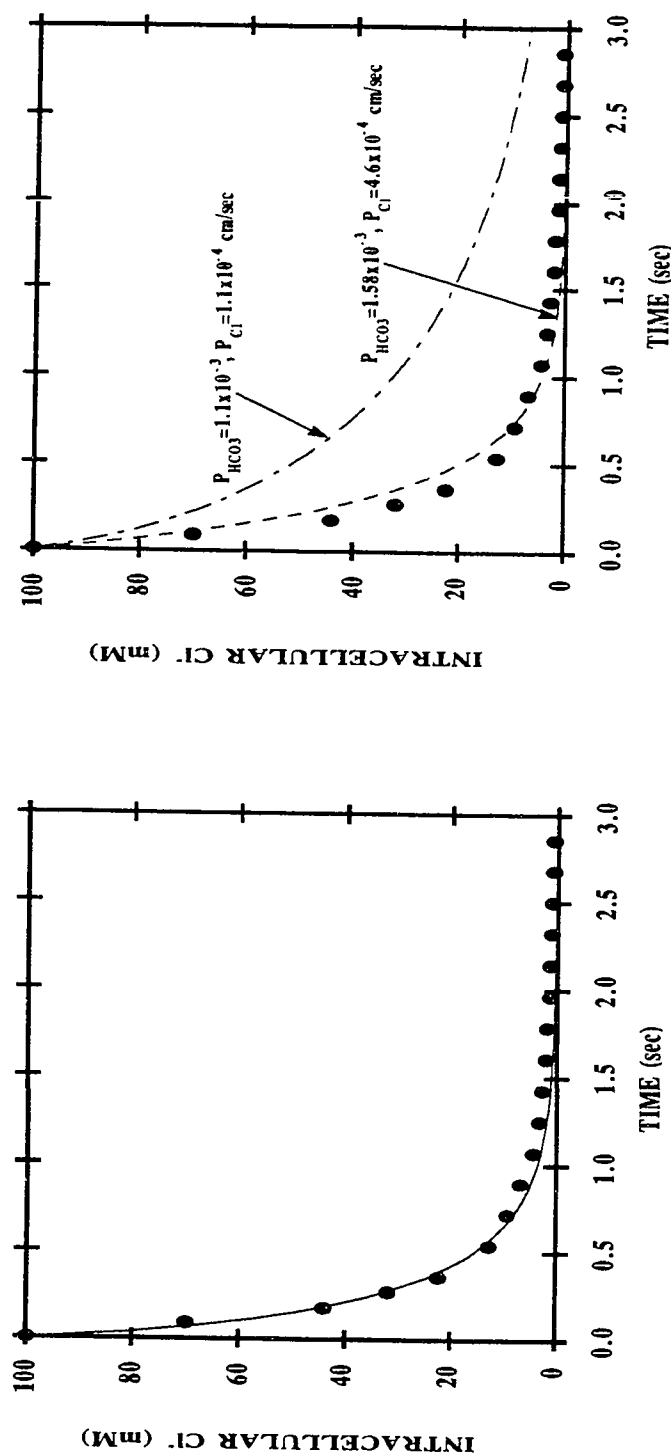


Figure 5.10: Change in intracellular Cl^- concentration following mixture of Cl^- -loaded RBCs with a Cl^- -free, HCO_3^- -containing buffer at 37°C (more detail on the experimental conditions is given in Table 5.6). Illsley and Verkman's experimental results (Illsley and Verkman, 1987) are represented as filled circles. The left panel gives the comparison of simulation result generated using simplified ping-pong model with the experimental data. The theoretical line (—) is calculated with $k_{\text{trans}}=4.5 \times 10^4 \text{ sec}^{-1}$ and $K_A=200 \text{ M}^{-1}$. The right panel gives the comparison of simulation result generated using the constant field electrodiffusion with phenomenological permeability coefficients with the experimental data. The theoretical curve (---) is calculated assuming $P_{\text{HCO}_3}=1.58 \times 10^{-3}$ and $P_{\text{Cl}}=4.60 \times 10^{-4} \text{ cm/sec}$; (— · —), $P_{\text{HCO}_3}=1.10 \times 10^{-3}$ and $P_{\text{Cl}}=1.10 \times 10^{-4} \text{ cm/sec}$.

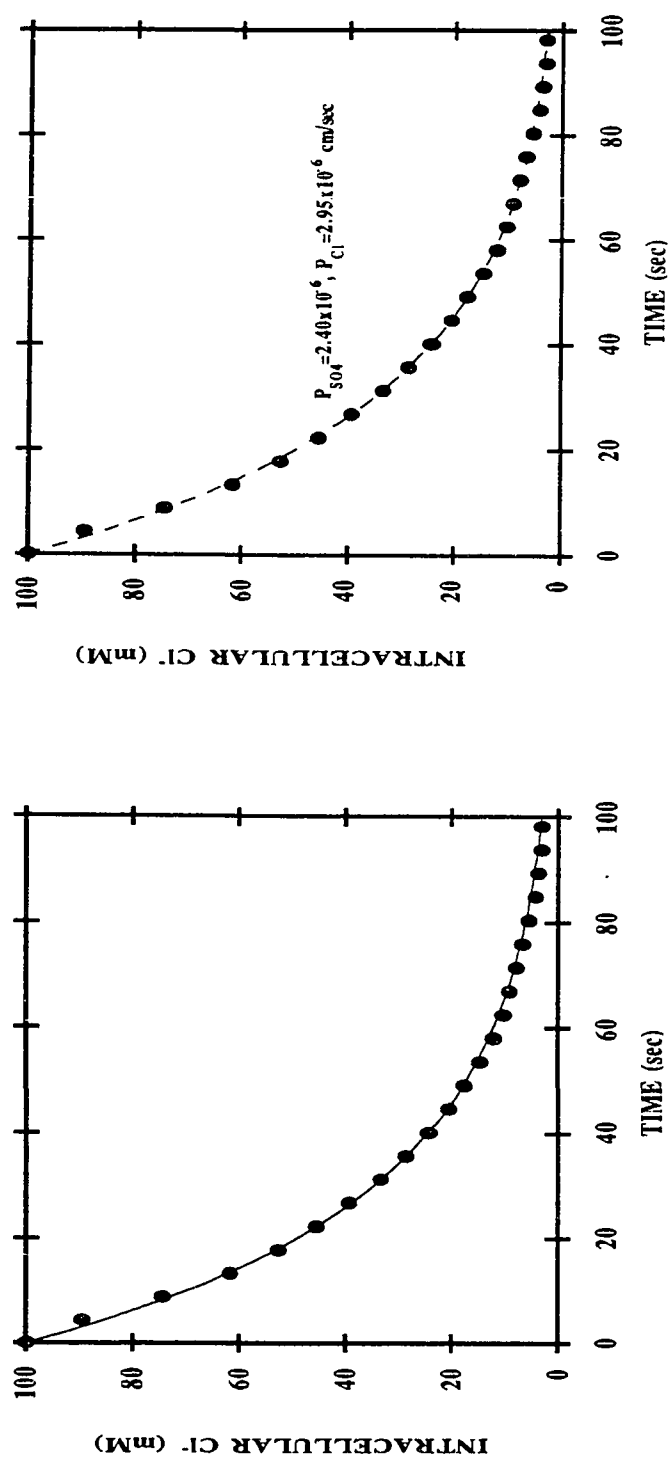


Figure 5.11: Change in intracellular Cl^- concentration following mixture of Cl^- -loaded RBCs with a Cl^- -free, SO_4^{2-} -containing buffer at $37^\circ C$ (more detail on the experimental conditions is given in Table 5.6). Illsley and Verkman's experimental results (Illsley and Verkman, 1987) are represented as filled circles. The left panel gives the comparison of simulation result generated using simplified ping-pong model with the experimental data; the theoretical line (-----) is calculated with $k_{trans} = 400 \text{ sec}^{-1}$ and $K_A = 180 \text{ M}^{-1}$. The right panel gives the comparison of simulation result generated using the constant field electrodiffusion with phenomenological permeability coefficients with the experimental data; the theoretical curve (-----) is calculated assuming $P_{SO_4} = 2.40 \times 10^{-6}$ and $P_{Cl^-} = 2.95 \times 10^{-6} \text{ cm/sec}$.

The maximum deviations between the calculations generated by the simplified ping-pong model and the experimental data are 4.87 mM and 3.67 mM in $[Cl^-]_{rbc}$ for cases 1 and 2, respectively; the algebraic deviations for these curves are 0.505 mM and 1.23 mM in $[Cl^-]_{rbc}$ for cases 1 and 2, respectively. On the other hand, the maximum deviations between the result calculated by the passive electrodiffusion model and the experimental data are 13.0 mM and 4.2 mM in $[Cl^-]_{rbc}$ for case 1 and 2, respectively; the algebraic deviations for these curves are 2.04 mM and 0.61 mM in $[Cl^-]_{rbc}$ for cases 1 and 2, respectively. As can be seen the agreement between the experimental data and the computational results generated by simplified ping-pong model is slightly better than that calculated by constant field electrodiffusion model.

5.3.1.d Comparison with Lemon's Data (1989)

Figures 5.12 and 5.13 show the extracellular pH , and Figures 5.14 - 5.19 show the extracellular Cl^- concentration computed by the simplified ping-pong (solid line) and passive electrodiffusion models (dashed line) for the experimental conditions listed in Table 5.7, with the experimentally determined time courses of extracellular pH or Cl^- concentration from the stopped-flow experiments of Lemon (1989) which are redrawn here for comparison. The ping-pong simulations agree well with the experimental data with the values of $k_{trans}=1.1 \times 10^4 \text{ sec}^{-1}$, $K_A=200 \text{ M}^{-1}$. On the other hand, the calculations obtained by using constant values of P_{HCO_3} and P_{Cl} (both have values of $3.16 \times 10^{-4} \text{ cm/sec}$ which represent the best-fitted permeability coefficients) over estimate the observed transport rates by a noticeable amount. The maximum deviations between the results generated by the simplified ping-pong model and the experimental data are 0.494 nM in $[H^+]_{pl}$ and 0.129 mM in $[Cl^-]_{pl}$; the algebraic deviations for both curves are 0.276 nM in $[H^+]_{pl}$ and 0.11 mM in $[Cl^-]_{pl}$, respectively. On the other hand, the maximum deviations between the results simulated by the passive electrodiffusion model and the experimental data are 1.00 nM in $[H^+]_{pl}$ and 0.903 mM in $[Cl^-]_{pl}$; the algebraic

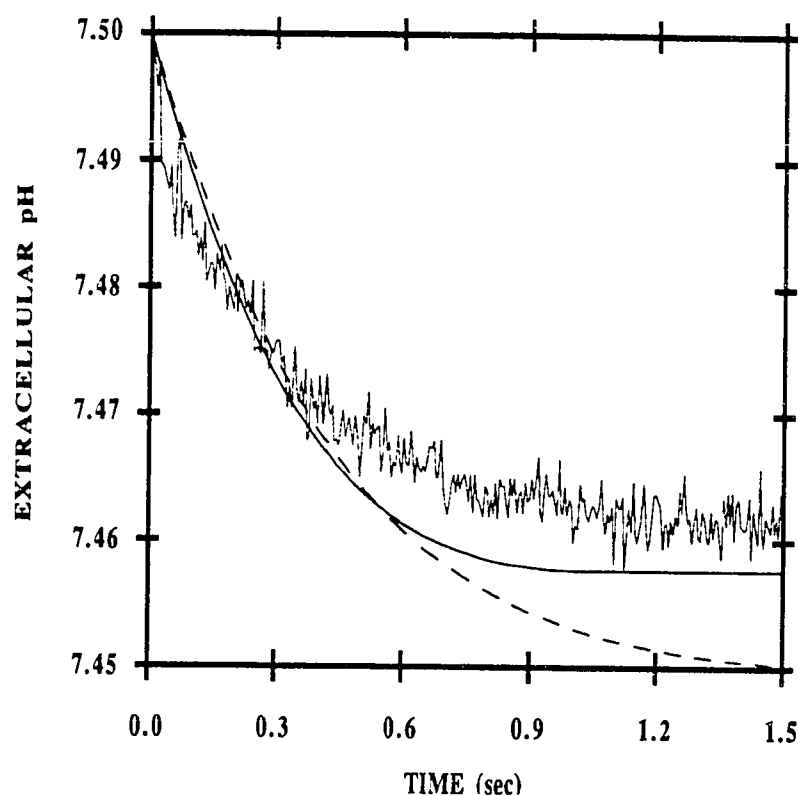


Figure 5.12: Comparison of models for kinetics of $\text{Cl}^-/\text{HCO}_3^-$ exchange at 25 °C (more detail on the experimental conditions is given in Table 5.7, case I.1). The chloride jump pH time course was collected by mixing Cl^- -loaded RBCs with a Cl^- -free 200 μM pyranine solution. Data: experimental trace of the extracellular pH from Lemon (1989). Curves: theoretical simulations of the experiment; (—) the simplified ping-pong model with $k_{trans}=1.1 \times 10^4 \text{ sec}^{-1}$ and $K_A=200 \text{ M}^{-1}$, and (- - -) the constant field electrodiffusion with phenomenological permeability coefficients $P_{\text{HCO}_3}=3.16 \times 10^{-4}$ and $P_{\text{Cl}}=3.16 \times 10^{-4} \text{ cm/sec}$.

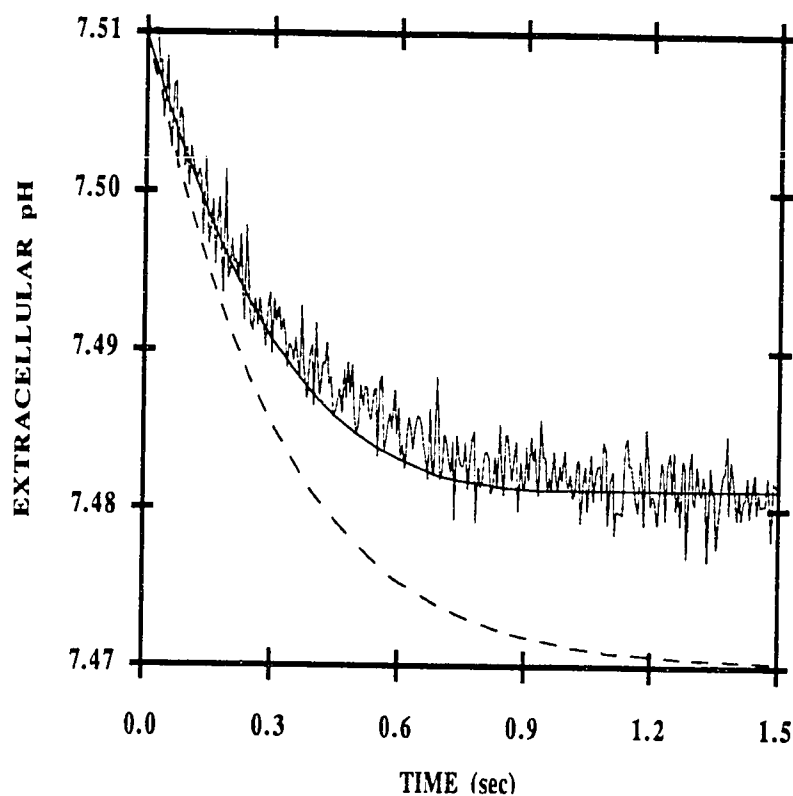


Figure 5.13: Comparison of models for kinetics of $\text{Cl}^-/\text{HCO}_3^-$ exchange at 25 °C (more detail on the experimental conditions is given in Table 5.7, case I.2). The chloride jump pH time course was collected by mixing Cl^- -loaded RBCs with a Cl^- -free 200 μM pyranine solution. Data: experimental trace of the extracellular pH from Lemon (1989). Curves: theoretical simulations of the experiment; (—) the simplified ping-pong model with $k_{trans}=1.1 \times 10^4 \text{ sec}^{-1}$ and $K_A=200 \text{ M}^{-1}$, and (- - - -) the constant field electrodiffusion with phenomenological permeability coefficients $P_{\text{HCO}_3}=3.16 \times 10^{-4}$ and $P_{\text{Cl}}=3.16 \times 10^{-4} \text{ cm/sec}$.

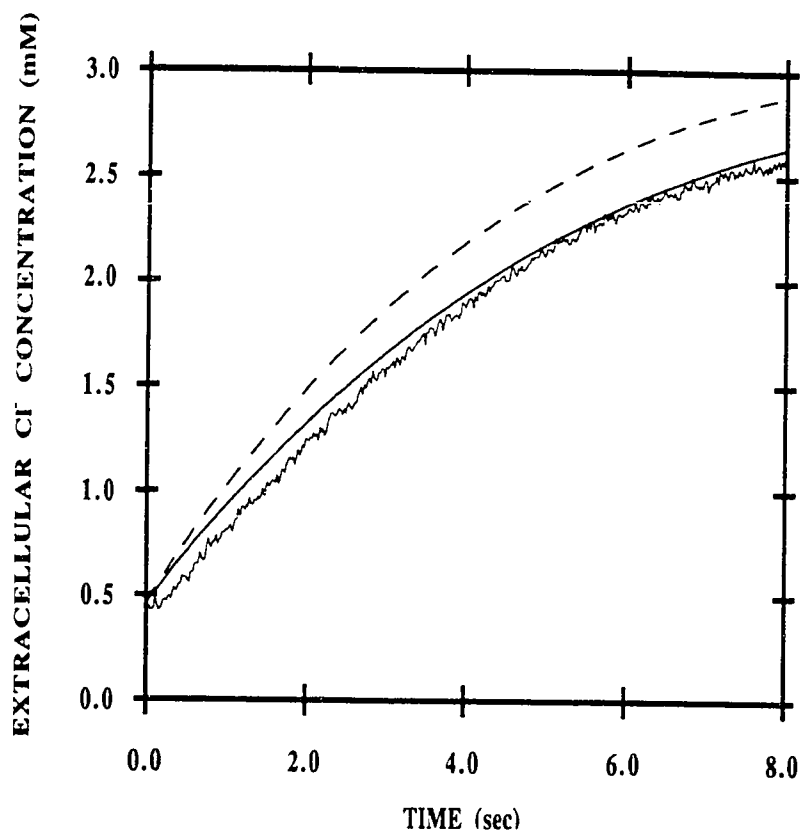


Figure 5.14: Comparison of models for kinetics of $\text{Cl}^-/\text{HCO}_3^-$ exchange at 25 °C (more detail on the experimental conditions is given in Table 5.7, case II.1). The chloride jump Cl^- time course was collected by mixing Cl^- -loaded RBCs with a HCO_3^- -containing 220 μM SPQ solution. Data: experimental trace of the extracellular Cl^- concentration from Lemon (1989). Curves: theoretical simulations of the experiment; (—) the simplified ping-pong model with $k_{\text{trans}}=1.1 \times 10^4 \text{ sec}^{-1}$ and $K_A=200 \text{ M}^{-1}$, and (- - - -) the constant field electrodiffusion with phenomenological permeability coefficients $P_{\text{HCO}_3}=3.16 \times 10^{-4}$ and $P_{\text{Cl}}=3.16 \times 10^{-4} \text{ cm/sec}$.

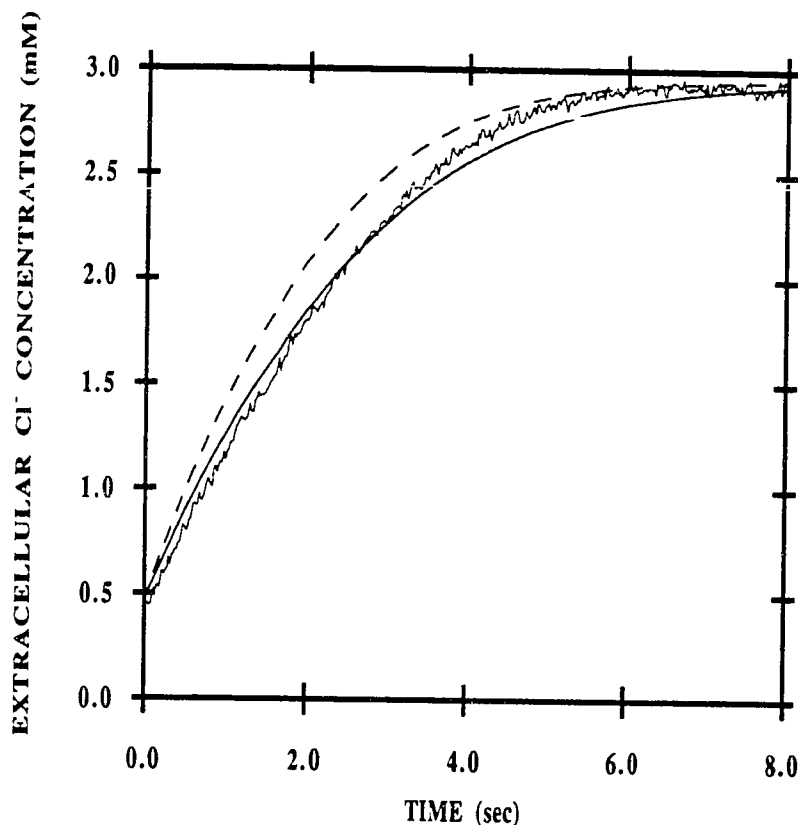


Figure 5.15: Comparison of models for kinetics of $\text{Cl}^-/\text{HCO}_3^-$ exchange at 25 °C (more detail on the experimental conditions is given in Table 5.7, case II.2). The chloride jump Cl^- time course was collected by mixing Cl^- -loaded RBCs with a HCO_3^- -containing 220 μM SPQ solution. Data: experimental trace of the extracellular Cl^- concentration from Lemon (1989). Curves: theoretical simulations of the experiment; (—) the simplified ping-pong model with $k_{\text{trans}}=1.1 \times 10^4 \text{ sec}^{-1}$ and $K_A=200 \text{ M}^{-1}$, and (---) the constant field electrodiffusion with phenomenological permeability coefficients $P_{\text{HCO}_3}=3.16 \times 10^{-4}$ and $P_{\text{Cl}}=3.16 \times 10^{-4} \text{ cm/sec}$.

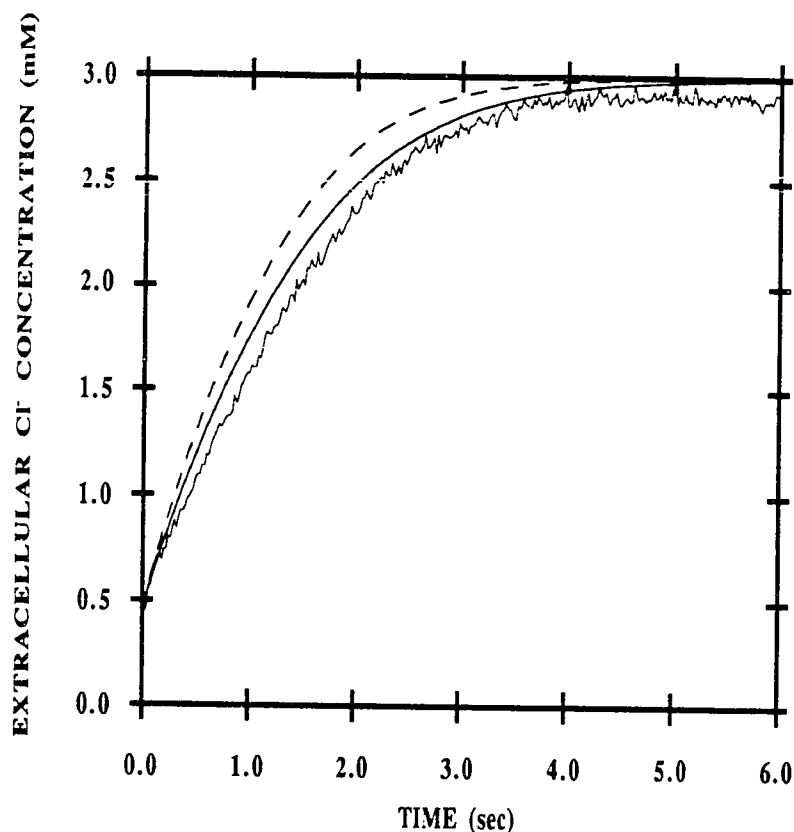


Figure 5.16: Comparison of models for kinetics of $\text{Cl}^-/\text{HCO}_3^-$ exchange at 25 °C (more detail on the experimental conditions is given in Table 5.7, case II.3). The chloride jump Cl^- time course was collected by mixing Cl^- -loaded RBCs with a HCO_3^- -containing 220 μM SPQ solution. Data: experimental trace of the extracellular Cl^- concentration from Lemon (1989). Curves: theoretical simulations of the experiment; (—) the simplified ping-pong model with $k_{\text{trans}}=1.1 \times 10^4 \text{ sec}^{-1}$ and $K_A=200 \text{ M}^{-1}$, and (- - -) the constant field electrodiffusion with phenomenological permeability coefficients $P_{\text{HCO}_3}=3.16 \times 10^{-4}$ and $P_{\text{Cl}}=3.16 \times 10^{-4} \text{ cm/sec}$.

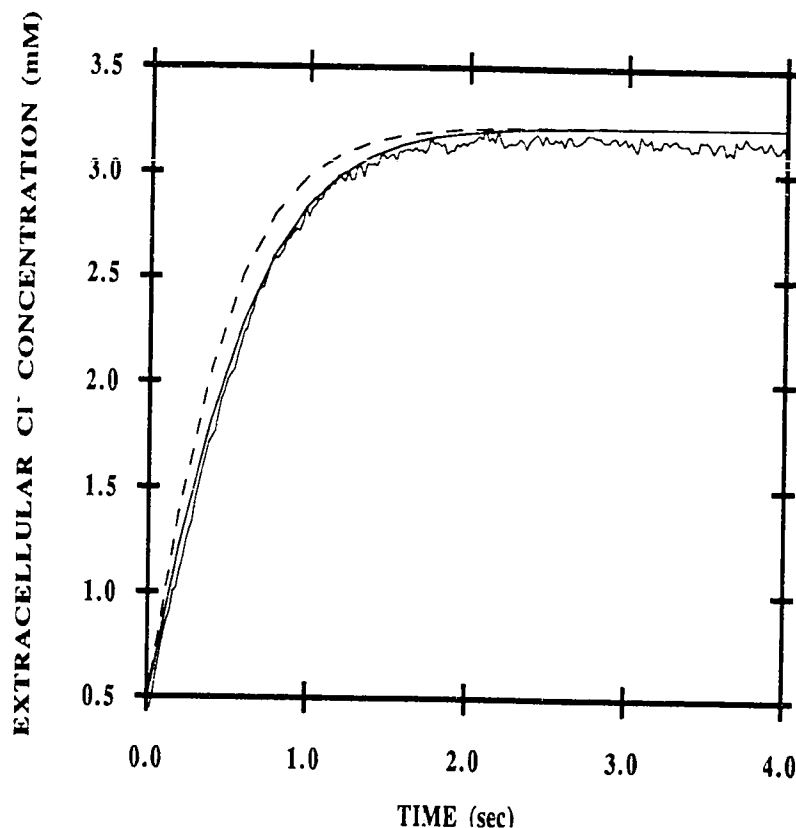


Figure 5.17: Comparison of models for kinetics of $\text{Cl}^-/\text{HCO}_3^-$ exchange at 25 °C (more detail on the experimental conditions is given in Table 5.7, case II.4). The chloride jump Cl^- time course was collected by mixing Cl^- -loaded RBCs with a HCO_3^- -containing 220 μM SPQ solution. Data: experimental trace of the extracellular Cl^- concentration from Lemon (1989). Curves: theoretical simulations of the experiment; (—) the simplified ping-pong model with $k_{\text{trans}}=1.1 \times 10^4 \text{ sec}^{-1}$ and $K_A=200 \text{ M}^{-1}$, and (---) the constant field electrodiffusion with phenomenological permeability coefficients $P_{\text{HCO}_3}=3.16 \times 10^{-4}$ and $P_{\text{Cl}}=3.16 \times 10^{-4} \text{ cm/sec}$.

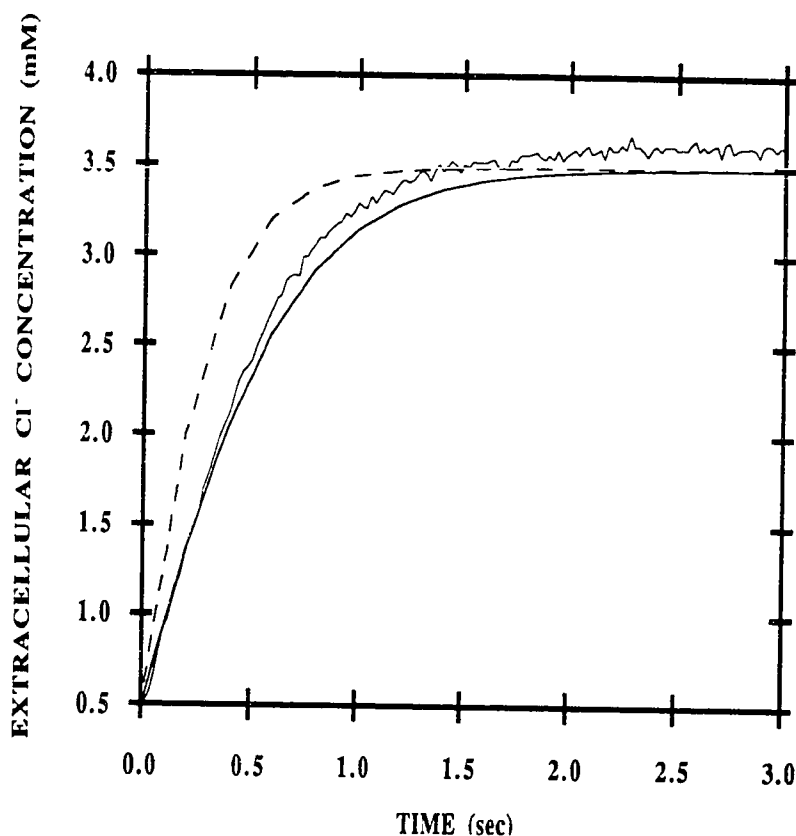


Figure 5.18: Comparison of models for kinetics of $\text{Cl}^-/\text{HCO}_3^-$ exchange at 25 °C (more detail on the experimental conditions is given in Table 5.7, case II.5). The chloride jump Cl^- time course was collected by mixing Cl^- -loaded RBCs with a HCO_3^- -containing 220 μM SPQ solution. Data: experimental trace of the extracellular Cl^- concentration from Lemon (1989). Curves: theoretical simulations of the experiment; (—) the simplified ping-pong model with $k_{\text{trans}}=1.1 \times 10^4 \text{ sec}^{-1}$ and $K_A=200 \text{ M}^{-1}$, and (- - -) the constant field electrodifffusion with phenomenological permeability coefficients $P_{\text{HCO}_3}=3.16 \times 10^{-4}$ and $P_{\text{Cl}}=3.16 \times 10^{-4} \text{ cm/sec}$.

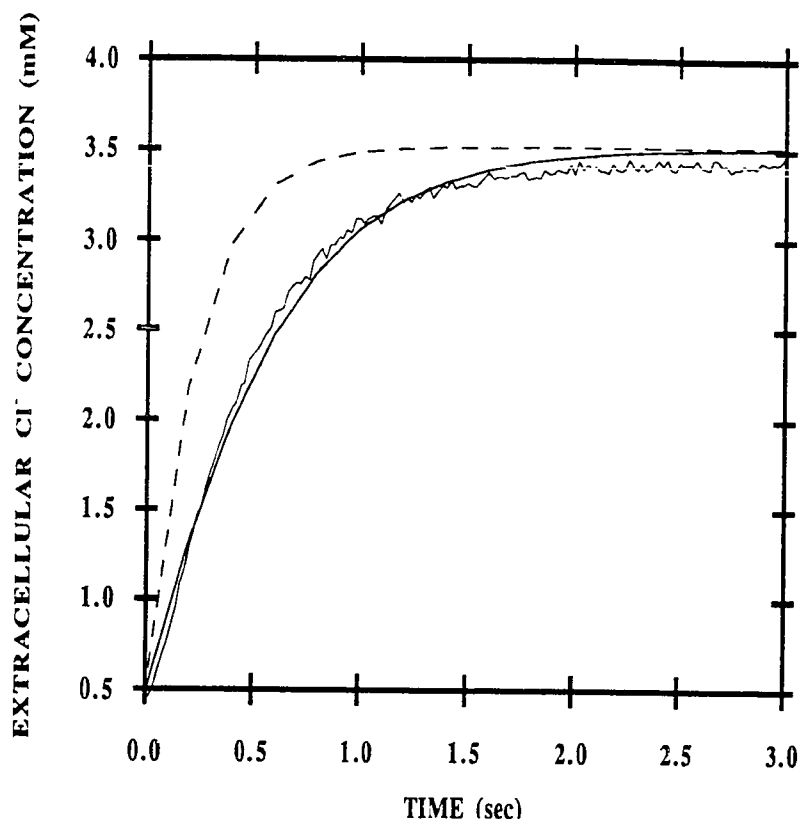


Figure 5.19: Comparison of models for kinetics of $\text{Cl}^-/\text{HCO}_3^-$ exchange at 25 °C (more detail on the experimental conditions is given in Table 5.7, case II.6). The chloride jump Cl^- time course was collected by mixing Cl^- -loaded RBCs with a HCO_3^- -containing 220 μM SPQ solution. Data: experimental trace of the extracellular Cl^- concentration from Lemon (1989). Curves: theoretical simulations of the experiment; (—) the simplified ping-pong model with $k_{\text{trans}}=1.1 \times 10^4 \text{ sec}^{-1}$ and $K_A=200 \text{ M}^{-1}$, and (- - -) the constant field electrodiffusion with phenomenological permeability coefficients $P_{\text{HCO}_3}=3.16 \times 10^{-4}$ and $P_{\text{Cl}}=3.16 \times 10^{-4} \text{ cm/sec}$.

deviations for both curves are 0.571 nM in $[H^+]_{pl}$ and 0.290 mM in $[Cl^-]_{pl}$, respectively. As can be seen the agreement between the experimental data and the computational results generated by simplified ping-pong model is better than that calculated by constant field electrodiffusion model.

5.3.2 Comparison of the Determined Kinetic Parameters to Previous Determinations

Kinetic parameters used for the best-fitted simplified ping-pong simulations for various experimental systems are listed in Table 5.8. Literature values for K_A are difficult to come by because most of the binding constants reported in the literature are “apparent” values which depend strongly on the experimental conditions. As Lemon (1989) pointed out, a better estimate of the intrinsic binding rate constant comes from studies of competition between anions. Lemon’s argument was that by definition a competitive inhibitor binds to the transport site, and the point at which the transport rate for a given substrate is halved by a competitive anion should define the affinity of the site for the competing anion. The competitive inhibition binding constant for HCO_3^- competing against extracellular Cl^- in Cl^-/HCO_3^- exchange at 0 °C was reported to be in the range of 167 - 333 M^{-1} (Gunn *et al.*, 1973). The competitive inhibition binding constant for Cl^- competing with the binding of the specific anion transport inhibitor was reported to be 190 M^{-1} at 20 °C (Frohlich and Gunn, 1986). In addition, a value of 200 M^{-1} was reported for the competitive inhibition binding constant for HCO_3^- at 37 °C (Lambert and Lowe, 1980). Finally, it should be mentioned that Lemon’s analysis on his own data which involved a different mathematical formulation of ping-pong model also indicated that usage of $k_{trans}=1.1 \times 10^4 \text{ sec}^{-1}$, $K_{HCO_3}=K_{Cl}=200 \text{ M}^{-1}$ did result in a more satisfactory fit between experimental data and model calculations. Therefore, it is

seen that the agreement between the K_A values estimated in this work and the literature values for different temperatures is excellent.

Estimates for k_{trans} in the literature come from Brahm's (1977) calculations of the anion transporter turnover number and Falke *et al.*'s (1985) NMR studies on the transport cycle. Using his data for Cl^-/Cl^- exchange, Brahm (1977) calculated a turnover number of $1.3 \times 10^4 \text{ sec}^{-1}$ at 25°C and $5 \times 10^4 \text{ sec}^{-1}$ at 37°C . Because the translocation step is the rate-limiting step, the translocation rate must approximately equal the turnover rate of the transport cycle. Falke *et al.*'s NMR data specified that the translocation rate constant is $\approx 400 \text{ sec}^{-1}$ at 0°C and $\approx 8 \times 10^4 \text{ sec}^{-1}$ at 37°C (see Figure 5.3). Again, the k_{trans} values determined in this analysis and reported literature values are in good agreement for different temperatures.

Table 5.8: Kinetic parameters obtained for $\text{Cl}^-/\text{HCO}_3^-$ exchange across the RBC membrane from analyzing different workers' experimental data using Equation (5.11).

	$k_{trans} (\text{sec}^{-1})$	$K_A (\text{M}^{-1})$
Exchange at 0°C Weith; $\text{Cl}^-/\text{HCO}_3^-$	504	390
Exchange at 25°C Lemon; $\text{Cl}^-/\text{HCO}_3^-$	1.1×10^4	200
Exchange at 37°C Klocke; $\text{Cl}^-/\text{HCO}_3^-$	$4-6 \times 10^4$	200
Illsley and Verkman; $\text{Cl}^-/\text{HCO}_3^-$	4.5×10^4	200

Permeability coefficients used for the best-fitted constant field electrodiffusion computations for various experimental systems are listed in Table 5.9. With the usage of permeabilities which are reported in the literature (Table 5.1), the phenomenological electrodiffusion theory generates the predictions that are sometimes in poor agreement with the observed rate of transport. For instance, the best-fitted result for Weith's system is achieved using permeabilities which are an order of magnitude higher than the reported literature values. Although the flux predicted by the constant field equation fits the data adequately, there are some discrepancies between the best-fitted values for P_{HCO_3} and P_{Cl} obtained in this study and the literature values. It is observed that there is a wide variation of permeability coefficients reported both in the literature and in this study. This is because the concentrations of Cl^- and HCO_3^- were varied experimentally over a wide range. In some cases, the carrier is saturated. In others, the processes are like permeation and effectively bimolecular or diffusion driven.

Table 5.9: Best-fitted permeability coefficients obtained for Cl^-/HCO_3^- exchange across the RBC membrane from analyzing different workers' experimental data using Equation (5.1).

	P_{HCO_3} (cm/sec)	P_{Cl} (cm/sec)
Exchange at 0 °C		
Weith; Cl^-/HCO_3^-	3.02×10^{-5}	1.35×10^{-5}
Exchange at 25 °C		
Lemon; Cl^-/HCO_3^-	3.16×10^{-4}	3.16×10^{-4}
Exchange at 37 °C		
Klocke; Cl^-/HCO_3^-	1.10×10^{-3}	1.10×10^{-4}
Illsley and Verkman; Cl^-/HCO_3^-	1.58×10^{-3}	4.60×10^{-4}

5.4 Summary

Most of data on univalent anion movement across the RBC membrane have been interpreted by the use of a constant field diffusion of ion down an electrochemical gradient, slightly modified in the sense that phenomenological permeability coefficients were introduced to replace the ion mobilities in Goldman's solution. Although with appropriate values of P_{HCO_3} and P_{Cl} , the passive electrodiffusion model generates simulation results which are reasonably compatible with some of the experimental data in the literature, this interpretation of anion exchange has been questioned because of the numerous evidences which indicate that anion exchange is mediated by a carrier mechanism. Furthermore, the derivation of Goldman's equation for ion fluxes and the membrane potential is not free of contradictions. On the one hand, one must assume that the membrane is so thin that the electrical potential profile may be considered as linear; on the other hand, integration of the differential equation across the thickness of the membrane should be physically meaningful. This inconsistency itself already circumscribes the validity of Equation (5.1). Therefore, the computed permeability values are only "effective" and must be interpreted accordingly.

Because the mechanism is dependent on carrier mediation which proceeds with obligatory exchange of an electrically neutral complex, the simplified ping-pong model is theoretically a more appropriate framework for analysis of anion transport data. Despite the assumptions which were introduced to simplify the model, the simplified ping-pong scheme appears to be of sufficient accuracy for describing the anion exchange. It is important to realize that while the curve-fitting technique used to obtain the kinetic parameters is accurate, its usefulness is limited by both the experimental error and the validity of the model. If the model comes close in representing the actual physical situation, then proper estimation of the kinetic parameters becomes possible

when accurate experimental data is available. In addition, these parameters are not phenomenological but true intrinsic properties.

As mentioned previously, it is difficult to reconcile the fundamental observations and concepts on anion exchange kinetics with the notion of electrodiffusion of aqueous soluble anions. The simplified ping-pong model is both on a more satisfactory theoretical basis, and consistently provides better agreement with the available experimental data. Therefore, the conclusion of present work is that simplified ping-pong model has substantial advantages over the constant-field electrodiffusion model in the mathematical simulation of anion exchange.

CHAPTER 6

A THEORETICAL MODEL FOR GAS TRANSPORT AND ACID/BASE REGULATION BY BLOOD FLOWING IN MICROVESSELS

As has already been mentioned, the binding of O_2 at one hemoglobin site is coupled with binding of other substances at other sites due to conformational change of the hemoglobin molecule. In particular, O_2 binding to hemoglobin is affected by P_{CO_2} , pH , $[DPG]$ and other factors; and, in turn, O_2 binding affects transport of other substances, such as CO_2 and H^+ . Thus a more complete description of gas transport can be achieved by considering simultaneous interactions between hemoglobin, O_2 , CO_2 , H^+ , and other intermediate compounds. CO_2 exchange involves multiple interrelated physical and chemical events as depicted in Figure 2.1. Although there is a great deal of data dealing with the kinetics of individual events in CO_2 exchange, due to the fact that these processes are entwined in a complex manner, there have been limited attempts in studying the integrated system as a whole by incorporating the complete set of chemical and physical events into a computational model. Most of the work thus far in computational models which aimed at providing insights into the coupled O_2 and CO_2 transfer have been achieved by a semi-empirical, lumped-parameter approach.

Due to the complex nature of an exact transport model, various simplifications were introduced by previous investigators in order to develop tractable theoretical analyses. An adequate theory for the O_2 and CO_2 transfer problem has not been developed and verified for a wide range of tube diameters. Existing theories which treated blood as a homogeneous fluid and assumed local chemical equilibrium have been validated to some extent for macrochannel devices with diameters of several

hundred μm , but not for small microvessels. In addition, the interdependence of all species had been represented by O_2 and CO_2 dissociation curves. Theoretical developments along this line neglected not only the synergism among various species in the blood but also posed some problems in the interpretation of the effective, lumped properties. From the O_2 transport studies, it is observed that continuum models become less satisfactory for describing the transport in small microvessels where the discrete nature of blood begins to play a more important role. Therefore, there is a question on the validity of the continuum assumption for CO_2 transport when the flow channel dimension and RBC diameter are of comparable size. A local chemical equilibrium assumption is expected to be a good approximation for describing the chemical behavior of intracellular CO_2 due to the presence of carbonic anhydrase. However, this assumption is likely not appropriate for describing extracellular CO_2 hydration/dehydration reactions.

This work aims at utilizing available literature data which deals with the rate of individual events in O_2 and CO_2 exchange for the development of a mathematical model which is discrete in nature and takes into account the important physiological and biochemical processes underlying gas transport and $p\text{H}$ regulation by flowing blood. Experimental validation of the model is necessary; however, only few works in the literature have been accompanied with data that included measured total CO_2 transfer rates. Additionally, these experimental data were obtained for vessels whose diameters are several hundred μm and larger. No data is yet available for small vessels whose diameters are less than 100 μm . As a result, critical validation of this mathematical model over a wide range of diameters is still not possible. In this study, Voorhees' quantitative data on simultaneous O_2 and CO_2 transfer to and from blood flowing in tubular membrane oxygenators with diameters of ≈ 1.5 mm (Voorhees,

1976) is used to check on the performance of this mathematical model in this very large diameter regime.

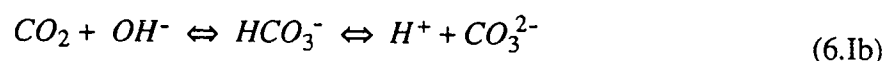
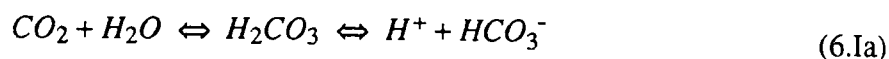
In addition to the development and limiting-case validation of the computational model, this analysis is used to address several specific questions. The first pertains to the incorporation of the coupled CO_2 transport by blood in relationship to O_2 transport in small microvessels with diameters of about $27\text{ }\mu\text{m}$. Many previous analyses of gas transport by blood flowing in microvessels have been concerned with the O_2 transport problem alone. As a result, the effects of change in O_2 affinity as a result of $p\text{H}$ and P_{CO_2} variations and the acid/base balance in blood were not evaluated by those models. Therefore, an O_2 transport model is evaluated in comparison to the more complete O_2/CO_2 exchange model to assess the error incurred by neglect of CO_2 transport effects. Often in prior model studies if CO_2 transport was considered, the description was simplified by treating blood as a continuum with the transferring species in local chemical equilibrium. Thus, the second question relates to the significance of those simplifications. The third question pertains to the effects of RBC $\text{HCO}_3^-/\text{Cl}^-$ exchange kinetics on CO_2 transfer. It has been suggested that under certain circumstances the transfer of CO_2 is limited by the rate of anion exchange across the RBC membrane (Weith and Brahm, 1980; Crandall and Bidani, 1981; Crandall *et al.*, 1981). Finally, a study is made to determine the regime of applicability of the continuum and discrete models.

6.1 Development of Mathematical Model

6.1.1 Physical Situation

Before preceding to derive the necessary equations for the gas transport model, the chemistry and kinetics of the reactions will be considered. The reactions and

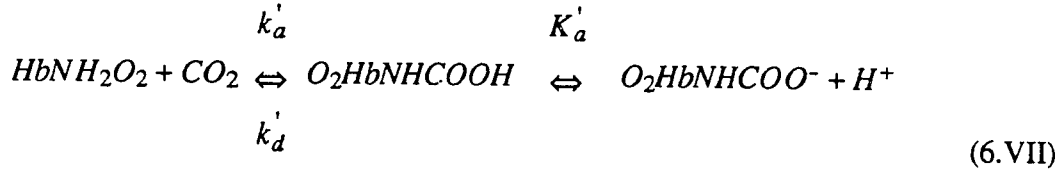
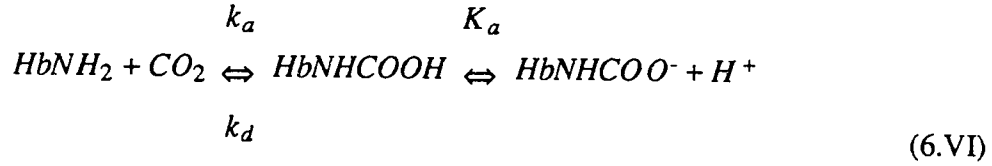
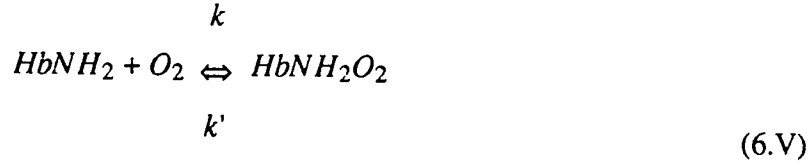
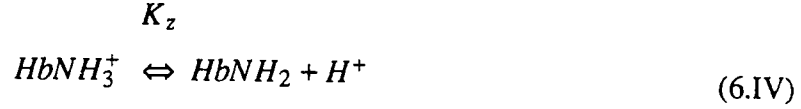
transport of O_2 and CO_2 in blood are complex phenomena. The scheme illustrated in Figure 2.1 is a simplified representation of the actual system. However, Figure 2.1 is a justifiable depiction of the system for the reasons discussed below. The following reactions are known to be taking place in both the RBC and plasma phases.



Reactions (6.Ia) - (6.Ic) and (6.IIIa) are typical of reactions of CO_2 in aqueous media. However, at physiological *pH* the contribution to the formation of HCO_3^- via Reaction (6.Ib) is small, and negligible amount of carbonate ion (CO_3^{2-}) is formed relative to the amounts of dissolved CO_2 and HCO_3^- present; as a result, Reaction (6.Ib) is neglected. Although blood contains other buffer systems, such as phosphates (Reactions (6.IIa) - (6.IIc)), their effects are minimal due to their small concentrations. Ionic species, such as Na^+ and K^+ , are not involved in any important reactions but in

maintaining electroneutrality; nevertheless, it is necessary to account for their compositions in the medium when estimating the diffusivities of H^+ , HCO_3^- and Cl^- .

Inside the RBC, Reactions (6.I) - (6.III) and Reactions (6.IV) - (6.VII) are known to take place.



where

K_z is the amino group ionization constant for the reduced hemoglobin, (Reaction (6.IV)).

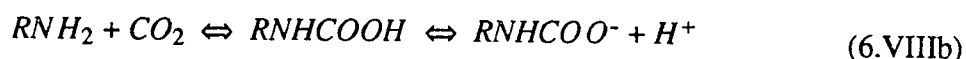
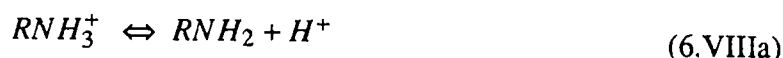
k and k' are the dissociation and association rate constants of Reaction (6.V), respectively; and $k' = \frac{k}{[O_2]_{rbc}} \left(\frac{P_{O_2}}{P_{50}} \right)^n$ according to the one-step variable rate coefficient method (Moll, 1969; Clark *et al.*, 1985; Vandegriff and Olson, 1984b).

K_a and K'_a are the amino group ionization constants for deoxygenated and oxygenated hemoglobin carbamate, respectively (Reactions (6.VI) and (6.VII)).

k_a and k'_a are the hemoglobin- CO_2 reaction forward rate constants for Reactions (6.VI) and (6.VII), respectively.

k_d and k'_d are the hemoglobin- CO_2 reaction reverse rate constants for Reactions (6.VI) and (6.VII), respectively.

In the plasma, Reactions (6.I) - (6.III) and Reaction (6.VIII) are known to be taking place.



Reaction (6.VIII) represents the reaction of CO_2 with proteins, amino acids and aliphatic aminos contained in the plasma. However, the carbamate or carbamino compounds that arise from combination of CO_2 with plasma proteins have a much smaller effect as compared to carbamino hemoglobin because of the relatively unfavorable equilibria for their formation. Consequently, the formation of plasma carbamate is neglected, but the buffering action of the plasma proteins is taken into account.

It should also be mentioned that RBC membrane is relatively impermeable to cations and that there are three anionic species that move across the RBC membrane which are potentially important in gas exchange - HCO_3^- , Cl^- and OH^- . Because the concentration of OH^- is extremely low relative to HCO_3^- and Cl^- , the corresponding flux of OH^- across the RBC membrane is small and negligible (Crandall *et al.*, 1971). Furthermore, since water vapor pressure varies with osmolality, transfer of water is inevitable. As RBCs pass through the lung, HCO_3^- undergoes CO_2 hydration reaction, and Cl^- moves out the RBCs; this leads to a decrease in osmolality which causes water

to move out. At the venous, the opposite situation occurs, and RBCs take up water. However, this effect is not significant because there is only 2-3% difference in the hematocrit of arterial and venous blood. As a result, transfer of OH^- and water across the RBC membrane is neglected in this analysis.

6.1.2 Transport Equations

This model is an extension of the previous O_2 transport model which considered only reactions (2) and (3) in Figure 2.1. In the present model additional complexities, namely CO_2 transport and $p\text{H}$ regulation by blood, are incorporated. As in the previous model, the RBC suspension is treated as two continuous, coexisting phases consisting of RBCs and plasma. The microvessel is divided into two regions: the central RBC-rich plasma region and the outer, RBC-free region. Radial distribution of RBCs and flow velocity profiles of RBCs and plasma are included. A description of the events shown in Figure 2.1 plus Reaction (6.VII) can be obtained by making mass balances for each of the chemical species involved. These include oxygen, oxyhemoglobin, carbon dioxide, hemoglobin carbamate and hydrogen, bicarbonate and chloride ions. Since some of these species exist at different concentrations in the intra- and extracellular compartments, the behavior of 18 chemical species are described as a function of r and z . The mass balances describing the change of each of the 18 species involve (a) transport of the species due to bulk convection of both the RBCs and plasma and radial diffusion in the plasma, (b) rate of consumption or production of that species by chemical reaction within its compartments, and/or (c) net transport of some of the species into or out of its compartment. The equations defining the analysis are developed below.

RBC Phase ($0 \leq r \leq r_r$)

The equations of continuity for the various species involved inside the RBCs are:

$$V_{rbc}(r) \frac{\partial [O_2]_{rbc}}{\partial z} = - \left(\frac{s}{v} \right)_{rbc} Flux_{O_2} - R_{HbO_2} \quad (6.1)$$

$$V_{rbc}(r) \frac{\partial [HbO_2]_{rbc}}{\partial z} = R_{HbO_2} - R_{O_2HbCO_2} \quad (6.2)$$

$$V_{rbc}(r) \frac{\partial [CO_2]_{rbc}}{\partial z} = \left(\frac{s}{v} \right)_{rbc} Flux_{CO_2} - R_{HCO_3, rbc} - R_{HbCO_2} - R_{O_2HbCO_2} \quad (6.3)$$

$$V_{rbc}(r) \frac{\partial [HbCO_2]_{rbc}}{\partial z} = R_{HbCO_2} \quad (6.4)$$

$$V_{rbc}(r) \frac{\partial [O_2HbCO_2]_{rbc}}{\partial z} = R_{O_2HbCO_2} \quad (6.5)$$

$$V_{rbc}(r) \frac{\partial [H^+]_{rbc}}{\partial z} = (R_{HCO_3, rbc} + \sigma_1 R_{HbO_2} + \sigma_2 R_{HbCO_2} + \sigma_3 R_{O_2HbCO_2}) \left(\frac{2.303 [H^+]_{rbc}}{\beta_{rbc}} \right) \quad (6.6)$$

$$V_{rbc}(r) \frac{\partial [HCO_3^-]_{rbc}}{\partial z} = \left(\frac{s}{v} \right)_{rbc} Flux_{HCO_3} + R_{HCO_3, rbc} \quad (6.7)$$

$$V_{rbc}(r) \frac{\partial [Cl^-]_{rbc}}{\partial z} = - \left(\frac{s}{v} \right)_{rbc} Flux_{HCO_3} \quad (6.8)$$

where

$[O_2]_{rbc}$ and $[CO_2]_{rbc}$ are the mean dissolved O_2 and CO_2 concentrations in the RBC, respectively.

$[HbO_2]_{rbc}$ and $[HbCO_2]_{rbc}$ are the concentrations of reduced heme which are in combination with O_2 and CO_2 , respectively.

$[O_2HbCO_2]_{rbc}$ is the concentration of oxygenated heme which is in combination with CO_2 .

$[H^+]_{rbc}$, $[HCO_3^-]_{rbc}$ and $[Cl^-]_{rbc}$ are the concentrations of H^+ , HCO_3^- and Cl^- in the RBC, respectively.

R_{HbO_2} is the rate of formation of oxyhemoglobin per unit RBC volume, and
 $R_{HbO_2} = k' [O_2]_{rbc} [Hb]_{rbc} - k [HbO_2]_{rbc}$.

R_{HbCO_2} is the rate of formation of hemoglobin carbamate per unit RBC volume, and $R_{HbCO_2} = k_a [CO_2]_{rbc} [Hb]_{rbc} - \frac{k_d}{K_a} [HbCO_2]_{rbc} [H^+]_{rbc}$ (Forster, 1969).

$R_{O_2HbCO_2}$ is the rate of formation of oxyhemoglobin carbamate per unit RBC volume, and $R_{O_2HbCO_2} = k'_a [CO_2]_{rbc} [HbO_2]_{rbc} - \frac{k'_d}{K'_a} [O_2HbCO_2]_{rbc} [H^+]_{rbc}$ (Forster, 1969).

$R_{HCO_3, rbc}$ is the rate of consumption of CO_2 per unit RBC volume by the hydration reaction catalyzed by the intracellular carbonic anhydrase, and
 $R_{HCO_3, rbc} = \hat{A}_{rbc} \left(k_d [CO_2]_{rbc} - \frac{k_v}{K_1 f_{water}} [H^+]_{rbc} [HCO_3^-]_{rbc} \right)$ where \hat{A}_{rbc} is the intracellular carbonic anhydrase activity factor (Garg and Maren, 1972; Bidani *et al.*, 1978).

σ_1 is the amount of H^+ released per O_2 molecule that is bound to hemoglobin (Reaction (6.IV)); literature value of σ is about 0.5-0.7 (Hlastala and Woodson, 1975).

σ_2 is the amount of H^+ released per CO_2 molecule that is bound to hemoglobin; literature value of γ is about 1.5-1.8 (Gros *et al.*, 1976). γ is greater than 1 and almost 2 because CO_2 does not react with positively charged amino group, Reaction (6.IV).

In addition, in the physiological range, carbamino hemoglobin exists almost completely in the ionized state, thus Reaction (6.VI).

σ_3 is the amount of H^+ released per CO_2 molecule that is bound to oxyhemoglobin (Reactions (6.IV) and (6.VII)).

$Flux_{CO_2}$ is the flux of CO_2 crossing the RBC wall; it is a function of r and z and has the unit of moles per unit area per unit time.

$Flux_{HCO_3}$ is the net flux of extracellular HCO_3^- entering the RBCs; or, equivalently, the net flux of intracellular Cl^- entering the plasma. It is a function of the intra- and extracellular HCO_3^- and Cl^- compositions and is given by Equation (5.11), moles per unit area per unit time.

β_{rbc} is the intracellular hemoglobin buffering factor, equivalents of base per pH unit.

It should be mentioned that the concentrations for the various species inside the RBC are values averaged within each individual RBC but varying with the position of the RBC in the tube. In addition, these intracellular concentrations are expressed in the basis of per unit RBC volume. Because no hemoglobin escapes from the RBCs, $[Hb]_{total} = [Hb]_{rbc} + [HbO_2]_{rbc} + [HbCO_2]_{rbc} + [O_2HbCO_2]_{rbc}$ remains constant.

Therefore, only three independent mass balances are written for the four different species of hemoglobin that are considered in this study.

RBC-Rich Plasma Region ($0 \leq r \leq r_r$)

In the RBC-rich plasma region, the following species are considered.

$$(1 - h(r)) V_{pl}(r) \frac{\partial [O_2]_{pl}}{\partial z} = \frac{D_{O_2,pl}}{r} \frac{\partial}{\partial r} \left(r \frac{\partial [O_2]_{pl}}{\partial r} \right) + h(r) \left(\frac{S}{V} \right)_{rbc} Flux_{O_2} \quad (6.9)$$

$$(1 - h(r)) V_{pl}(r) \frac{\partial [CO_2]_{pl}}{\partial z} = \frac{D_{CO_2,pl}}{r} \frac{\partial}{\partial r} \left(r \frac{\partial [CO_2]_{pl}}{\partial r} \right) - h(r) \left(\frac{S}{V} \right)_{rbc} Flux_{CO_2} - (1 - h(r)) R_{HCO_3,pl} \quad (6.10)$$

$$(1 - h(r)) V_{pl}(r) \frac{\partial [H^+]_{pl}}{\partial z} = \frac{\tilde{D}_{H,pl}}{r} \frac{\partial}{\partial r} \left(r \frac{\partial [H^+]_{pl}}{\partial r} \right) + (1 - h(r)) R_{HCO_3,pl} \left(\frac{2.303 [H^+]_{pl}}{\beta_{pl}} \right) \quad (6.11)$$

$$(1 - h(r)) V_{pl}(r) \frac{\partial [HCO_3^-]_{pl}}{\partial z} = \frac{\tilde{D}_{HCO_3,pl}}{r} \frac{\partial}{\partial r} \left(r \frac{\partial [HCO_3^-]_{pl}}{\partial r} \right) - h(r) \left(\frac{S}{V} \right)_{rbc} Flux_{HCO_3} + (1 - h(r)) R_{HCO_3,pl} \quad (6.12)$$

$$(1 - h(r)) V_{pl}(r) \frac{\partial [Cl^-]_{pl}}{\partial z} = \frac{\tilde{D}_{Cl,pl}}{r} \frac{\partial}{\partial r} \left(r \frac{\partial [Cl^-]_{pl}}{\partial r} \right) + h(r) \left(\frac{S}{V} \right)_{rbc} Flux_{HCO_3} \quad (6.13)$$

where

$[O_2]_{pl}$ and $[CO_2]_{pl}$ are the dissolved O_2 and CO_2 concentrations, respectively, in the RBC-rich plasma.

$[H^+]_{pl}$, $[HCO_3^-]_{pl}$ and $[Cl^-]_{pl}$ are the concentrations of H^+ , HCO_3^- and Cl^- in the RBC-rich plasma, respectively.

$R_{HCO_3,pl}$ is the rate of consumption of CO_2 per unit plasma volume by the hydration reaction, and $R_{HCO_3,pl} = \hat{A}_{pl} \left(k_u [CO_2]_{pl} - \frac{k_v}{K_1} [H^+]_{pl} [HCO_3^-]_{pl} \right)$ where \hat{A}_{pl} is the extracellular carbonic anhydrase activity factor.

$D_{O_2,pl}$ and $D_{CO_2,pl}$ are the molecular diffusivities of O_2 and CO_2 in the plasma, respectively.

$\tilde{D}_{H,pl}$, $\tilde{D}_{HCO_3,pl}$ and $\tilde{D}_{Cl,pl}$ are the effective ionic diffusivities of H^+ , HCO_3^- and Cl^- in the plasma, respectively.

β_{pl} is the extracellular plasma buffering capacity, equivalents of base per pH unit.

In the RBC-free plasma region, the continuity equations for various species can be obtained from the mass balances for various species in the RBC-rich plasma region by requiring $h(r)$ to be zero.

$$V'_{pl}(r) \frac{\partial [O_2]_{pl}}{\partial z} = \frac{D_{O_2,pl}}{r} \frac{\partial}{\partial r} \left(r \frac{\partial [O_2]_{pl}}{\partial r} \right) \quad (6.14)$$

$$V'_{pl}(r) \frac{\partial [CO_2]_{pl}}{\partial z} = \frac{D_{CO_2,pl}}{r} \frac{\partial}{\partial r} \left(r \frac{\partial [CO_2]_{pl}}{\partial r} \right) - R'_{HCO_3,pl} \quad (6.15)$$

$$V'_{pl}(r) \frac{\partial [H^+]_{pl}}{\partial z} = \frac{\tilde{D}_{H,pl}}{r} \frac{\partial}{\partial r} \left(r \frac{\partial [H^+]_{pl}}{\partial r} \right) + R'_{HCO_3,pl} \left(\frac{2.303 [H^+]_{pl}}{\beta_{pl}} \right) \quad (6.16)$$

$$V'_{pl}(r) \frac{\partial [HCO_3^-]_{pl}}{\partial z} = \frac{\tilde{D}_{HCO_3,pl}}{r} \frac{\partial}{\partial r} \left(r \frac{\partial [HCO_3^-]_{pl}}{\partial r} \right) + R'_{HCO_3,pl} \quad (6.17)$$

$$V'_{pl}(r) \frac{\partial [Cl^-]_{pl}}{\partial z} = \frac{\tilde{D}_{Cl,pl}}{r} \frac{\partial}{\partial r} \left(r \frac{\partial [Cl^-]_{pl}}{\partial r} \right) \quad (6.18)$$

where

$[O_2]_{pl}$ and $[CO_2]_{pl}$ are the dissolved O_2 and CO_2 concentrations in the RBC-free plasma, respectively.

$[H^+]_{pl}$, $[HCO_3^-]_{pl}$ and $[Cl^-]_{pl}$ are the concentrations of H^+ , HCO_3^- and Cl^- in the RBC-free plasma, respectively.

$R'_{HCO_3,pl}$ is the rate of consumption of CO_2 per unit plasma volume by the hydration reaction, and $R'_{HCO_3,pl} = \hat{A}_{pl} \left(k_u [CO_2]_{pl} - \frac{k_v}{K_1} [H^+]_{pl} [HCO_3^-]_{pl} \right)$.

6.1.3 Simplification of Transport Equations

6.1.3.a Type I Model (10 PDEs)

To understand the basic aspects of gas transport and pH regulation by flowing blood, simplifications are made to render the problem tractable from a mathematical point of view, while still retaining the terms in the continuity equations which are believed to be primarily important. Basically the following assumptions are introduced to simplify the above model which consists a system of 18 simultaneous nonlinear PDEs.

From the detailed O_2 transport studies, it was reported that only a small fraction of the resistance to transport lies inside the RBCs. The carbonic anhydrase enzyme which is present in high concentration in RBCs speeds up the CO_2 hydration/dehydration reactions by approximately 6,500 fold. In addition, because CO_2 has higher solubilities in the blood than O_2 (see Tables 6.3 and 6.4) and that the diffusion of CO_2 across the RBC membrane has been shown to be very rapid (Gros and Moll, 1971), it is assumed that the diffusion occurs rapidly enough that any P_{CO_2} gradient across the RBC membrane is negligible. Therefore, assumptions of chemical equilibrium within the RBC and negligible intra- and extracellular boundary resistances are appropriate for describing the transport of both O_2 and CO_2 .

By combining Equations (6.1), (6.2) and (6.5) and invoking the chemical equilibrium, one obtains

$$V_{rbc}(r) \left(1 + \frac{\partial[HbO_2]_{rbc}}{\partial[O_2]_{rbc}} + \frac{\partial[O_2HbCO_2]_{rbc}}{\partial[O_2]_{rbc}} \right) \frac{\partial[O_2]_{rbc}}{\partial z} = - \left(\frac{s}{v} \right)_{rbc} Flux_{O_2} \quad (6.19)$$

Because chemical equilibrium inside the RBC is imposed, oxyhemoglobin and oxyhemoglobin carbamate can be incorporated into the dissolved O_2 equation. If the Hill model, Equation (4.16a), is chosen to describe the ODC, then the slope of the

ODC is specified by Equation (4.16b) where P_{50} is a function of P_{CO_2} , pH , $[DPG]$ and is given by Equation (2.2). On the other hand, if the modified Easton model, Equation (2.5), is selected to describe the dissociation curve, then $\partial[HbO_2]_{rbc}/\partial[O_2]_{rbc}$ is given by

$$\frac{\partial[HbO_2]_{rbc}}{\partial[O_2]_{rbc}} = \frac{C_{heme,rbc}}{\alpha_{O_2,rbc}} \kappa (S_{max} - S_{min}) \exp[\kappa(P_{O_2}^* - P_{O_2})] \exp\{-\exp[\kappa(P_{O_2}^* - P_{O_2})]\} \quad (6.20)$$

where κ is a function of P_{CO_2} , pH , $[DPG]$ and is characterized by Equation (2.5). For an approximation, it is also assumed that $\partial[O_2HbCO_2]_{rbc}/\partial[O_2]_{rbc} \ll (1 + \partial[HbO_2]_{rbc}/\partial[O_2]_{rbc})$. The reason is that at every pH value reduced hemoglobin has a much greater ability to bind CO_2 than does oxyhemoglobin, and this difference increases with pH ; thus Reaction (6.VII) is of secondary importance in comparison to Reaction (6.VI). Moreover, available literature data is insufficient for the estimation of this derivative.

In a similar fashion, Equations (6.3), (6.4), (6.5) and (6.7) are combined to give Equation (6.21). Again, because the chemical equilibrium assumption is enforced intracellularly, both carbamino hemoglobin species and HCO_3^- can be incorporated into the dissolved CO_2 equation.

$$V_{rbc}(r) \left(1 + \frac{\partial[HbCO_2]_{total}}{\partial[CO_2]_{rbc}} + \frac{\partial[HCO_3^-]_{rbc}}{\partial[CO_2]_{rbc}} \right) \frac{\partial[CO_2]_{rbc}}{\partial z} = \left(\frac{\mathcal{L}}{V} \right)_{rbc} Flux_{CO_2} + \left(\frac{\mathcal{L}}{V} \right)_{rbc} Flux_{HCO_3} \quad (6.21)$$

where $[HbCO_2]_{total} = [HbCO_2]_{rbc} + [O_2HbCO_2]_{rbc}$ If Equation (2.10) is chosen to describe the total carbamino CO_2 bound by the hemoglobin, this derivative, $\partial[HbCO_2]_{total}/\partial[CO_2]_{rbc}$, is given by

$$\frac{\partial[HbCO_2]_{total}}{\partial[CO_2]_{rbc}} = \frac{C_{heme,rbc}}{4} \left[\frac{2\lambda_\alpha + 4\lambda_\alpha^2[CO_2]_{rbc}}{(1 + \lambda_\alpha[CO_2]_{rbc})^2} + \frac{2\lambda_\beta(1 + K_{DPG}[DPG]) + 4\lambda_\beta^2[CO_2]_{rbc}}{(1 + \lambda_\beta[CO_2]_{rbc} + K_{DPG}[DPG])^2} \right] \quad (6.22)$$

If the Henderson-Hasselbalch equation (Equation (2.9a)) is used to quantify the equilibrium relationship between the interacting species that are involved in the CO_2 hydration/dehydration reactions, then $\partial[HCO_3^-]_{rbc}/\partial[CO_2]_{rbc} = K' f_{water}/[H^+]_{rbc}$.

Another assumption introduced here is that the reaction term $R_{O_2HbCO_2}$ is neglected in the derivation of Equation (6.23) for the reason mentioned previously that Reaction (6.VII) is of less importance than Reaction (6.VI) under physiologically relevant conditions. Multiplication of Equation (6.2) by $-\sigma_1$, Equation (6.4) by $-\sigma_2$; Equation (6.7) by -1 , Equation (6.6) by $\beta_{rbc}/(2.303[H^+]_{rbc})$, and addition of the above resultant equations yield the following equation:

$$V_{rbc}(r) \left(\frac{\beta_{rbc}}{2.303 [H^+]_{rbc}} - \sigma_1 \frac{\partial[HbO_2]_{rbc}}{\partial[H^+]_{rbc}} - \sigma_2 \frac{\partial[HbCO_2]_{rbc}}{\partial[H^+]_{rbc}} - \frac{\partial[HCO_3^-]_{rbc}}{\partial[H^+]_{rbc}} \right) \frac{\partial[H^+]_{rbc}}{\partial z} = - \left(\frac{S}{V} \right)_{rbc} Flux_{HCO_3} \quad (6.23)$$

where

$\partial[HbO_2]_{rbc} / \partial[H^+]_{rbc}$ is related to the inverse of the number of release or gain of protons by hemoglobin protein accompanying oxygenation or deoxygenation; i.e., $\partial[HbO_2]_{rbc} / \partial[H^+]_{rbc} = \sigma_1^{-1}$.

$\partial[HbCO_2]_{rbc} / \partial[H^+]_{rbc}$ is related to the inverse of the number of gain or lose of protons by hemoglobin protein accompanying release or uptake of CO_2 ; i.e., $\partial[HbCO_2]_{rbc} / \partial[H^+]_{rbc} = \sigma_2^{-1}$.

$\partial[HCO_3^-]_{rbc} / \partial[H^+]_{rbc} = -(K' f_{water} [CO_2]_{rbc}) / [H^+]_{rbc}^2$ which is obtained through Equation (2.9a).

It is also assumed that there is no transport resistance in the RBC membrane for O_2 and CO_2 ; thus P_{O_2} and P_{CO_2} are continuous at the RBC wall. In addition, if $\alpha_{O_2,rbc} = \alpha_{O_2,pl}$ and $\alpha_{CO_2,rbc} = \alpha_{CO_2,pl}$, then $[O_2]_{rw,rbc} = [O_2]_{rw,pl}$ and $[CO_2]_{rw,rbc} = [CO_2]_{rw,pl}$ where $[O_2]_{rw,rbc}$ and $[CO_2]_{rw,rbc}$ are the concentrations of O_2 and CO_2 , respectively, at the RBC wall in the RBC; and $[O_2]_{rw,pl}$ and $[CO_2]_{rw,pl}$ are the concentrations of O_2 and CO_2 , respectively, at the RBC wall in the plasma. Furthermore, if the intra- and extracellular boundary resistances are neglected (i.e., $[O_2]_{rbc} = [O_2]_{rw,rbc}$, $[O_2]_{pl} = [O_2]_{rw,pl}$ and $[CO_2]_{rbc} = [CO_2]_{rw,rbc}$, $[CO_2]_{pl} = [CO_2]_{rw,pl}$) then it follows that

$$[O_2]_{pl} = \left(\frac{\alpha_{O_2,pl}}{\alpha_{O_2,rbc}} \right) [O_2]_{rbc} \quad (6.24)$$

$$[CO_2]_{pl} = \left(\frac{\alpha_{CO_2,pl}}{\alpha_{CO_2,rbc}} \right) [CO_2]_{rbc} \quad (6.25)$$

Multiplication of Equation (6.19) by $h(r)$, addition of the resultant expression to Equation (6.9) and substitution of $(\alpha_{O_2,pl}/\alpha_{O_2,rbc})[O_2]_{rbc}$ for $[O_2]_{pl}$ yields the following mass balance for dissolved O_2 in the RBC:

$$\left[\left(\frac{\alpha_{O_2,rbc}}{\alpha_{O_2,pl}} \right) h(r) V_{rbc}(r) \left(1 + \frac{\partial [HbO_2]_{rbc}}{\partial [O_2]_{rbc}} \right) + (1 - h(r)) V_{pl}(r) \right] \frac{\partial [O_2]_{rbc}}{\partial z} = \frac{D_{O_2,pl}}{r} \frac{\partial}{\partial r} \left(r \frac{\partial [O_2]_{rbc}}{\partial r} \right) \quad (6.26)$$

In an analogous fashion, Equations (6.21) and (6.10) can be combined to give the following mass balance for dissolved CO_2 :

$$\begin{aligned}
& \left[h(r) V_{rbc}(r) \left(1 + \frac{\partial[HCO_3^-]_{rbc}}{\partial[CO_2]_{rbc}} + \frac{\partial[HbCO_2]_{total}}{\partial[CO_2]_{rbc}} \right) + \left(\frac{\alpha_{CO_2,pl}}{\alpha_{CO_2,rbc}} \right) (1 - h(r)) V_{pl}(r) \right] \frac{\partial[CO_2]_{rbc}}{\partial z} \\
& = \left(\frac{\alpha_{CO_2,pl}}{\alpha_{CO_2,rbc}} \right) \frac{D_{CO_2,pl}}{r} \frac{\partial}{\partial r} \left(r \frac{\partial[CO_2]_{rbc}}{\partial r} \right) + h(r) \left(\frac{\mathcal{L}}{V} \right)_{rbc} Flux_{HCO_3} - (1 - h(r)) R_{HCO_3,pl}
\end{aligned} \tag{6.27}$$

To further simplify the model, the mass balances for dissolved O_2 and Cl^- in the cell-free plasma region, Equations (6.14) and (6.18), can be solved analytically and incorporated as boundary conditions to Equations (6.26) and (6.13), respectively. This approach uses the finding that convective transport of these species in the cell-free plasma region is small relative to transport by diffusion. Hence, the term $V'_{pl} \partial[C_i]/\partial z$, where $i=O_2$ or Cl^- , can be dropped from Equations (6.14) and (6.18). The simplified equations were then solved subject to conditions of a specified concentration at $r=r_r$, the RBC-rich and RBC-free region interface; and continuity of flux at $r=r_c$, the vessel wall. The solutions to these simplified equations can then be incorporated as boundary conditions to Equations (6.26) and (6.13), respectively, at $r=r_r$.

After introducing the above assumptions, the original model is simplified down to a model with 10 PDEs which is summarized in Table 6.1:

Table 6.1: Type I Model. Partial differential equations describing the coupled O₂ and CO₂ transport and *pH* regulation by blood flowing in microvessels.

$$\left[\left(\frac{\alpha_{O_2, rbc}}{\alpha_{O_2, pl}} \right) h(r) V_{rbc}(r) \left(1 + \frac{\partial [HbO_2]_{rbc}}{\partial [O_2]_{rbc}} \right) + (1 - h(r)) V_{pl}(r) \right] \frac{\partial [O_2]_{rbc}}{\partial z} = \frac{D_{O_2, pl}}{r} \frac{\partial}{\partial r} \left(r \frac{\partial [O_2]_{rbc}}{\partial r} \right) \quad (6.1.1)$$

$$\begin{aligned} \left[h(r) V_{rbc}(r) \left(1 + \frac{\partial [HCO_3^-]_{rbc}}{\partial [CO_2]_{rbc}} + \frac{\partial [HbCO_2]_{total}}{\partial [CO_2]_{rbc}} \right) + \left(\frac{\alpha_{CO_2, pl}}{\alpha_{CO_2, rbc}} \right) (1 - h(r)) V_{pl}(r) \right] \frac{\partial [CO_2]_{rbc}}{\partial z} = \\ \left(\frac{\alpha_{CO_2, pl}}{\alpha_{CO_2, rbc}} \right) \frac{D_{CO_2, pl}}{r} \frac{\partial}{\partial r} \left(r \frac{\partial [CO_2]_{rbc}}{\partial r} \right) + h(r) \left(\frac{s}{v} \right)_{rbc} Flux_{HCO_3} - (1 - h(r)) R_{HCO_3, pl} \end{aligned} \quad (6.1.2)$$

$$V_{rbc}(r) \left(\frac{\beta_{rbc}}{2.303 [H^+]_{rbc}} - \sigma_1 \frac{\partial [HbO_2]_{rbc}}{\partial [H^+]_{rbc}} - \sigma_2 \frac{\partial [HbCO_2]_{rbc}}{\partial [H^+]_{rbc}} - \frac{\partial [HCO_3^-]_{rbc}}{\partial [H^+]_{rbc}} \right) \frac{\partial [H^+]_{rbc}}{\partial z} = - \left(\frac{s}{v} \right)_{rbc} Flux_{HCO_3} \quad (6.1.3)$$

$$V_{rbc}(r) \frac{\partial [Cl^-]_{rbc}}{\partial z} = - \left(\frac{s}{v} \right)_{rbc} Flux_{HCO_3} \quad (6.1.4)$$

$$(1 - h(r)) V_{pl}(r) \frac{\partial [H^+]_{pl}}{\partial z} = \frac{\tilde{D}_{H, pl}}{r} \frac{\partial}{\partial r} \left(r \frac{\partial [H^+]_{pl}}{\partial r} \right) + (1 - h(r)) R_{HCO_3, pl} \left(\frac{2.303 [H^+]_{pl}}{\beta_{pl}} \right) \quad (6.1.5)$$

$$(1 - h(r)) V_{pl}(r) \frac{\partial [HCO_3^-]_{pl}}{\partial z} = \frac{\tilde{D}_{HCO_3, pl}}{r} \frac{\partial}{\partial r} \left(r \frac{\partial [HCO_3^-]_{pl}}{\partial r} \right) - h(r) \left(\frac{s}{v} \right)_{rbc} Flux_{HCO_3} + (1 - h(r)) R_{HCO_3, pl} \quad (6.1.6)$$

$$(1 - h(r)) V_{pl}(r) \frac{\partial [Cl^-]_{pl}}{\partial z} = \frac{\tilde{D}_{Cl, pl}}{r} \frac{\partial}{\partial r} \left(r \frac{\partial [Cl^-]_{pl}}{\partial r} \right) + h(r) \left(\frac{s}{v} \right)_{rbc} Flux_{HCO_3} \quad (6.1.7)$$

$$V'_{pl}(r) \frac{\partial [CO_2]_{pl}}{\partial z} = \frac{D_{CO_2, pl}}{r} \frac{\partial}{\partial r} \left(r \frac{\partial [CO_2]_{pl}}{\partial r} \right) - R'_{HCO_3, pl} \quad (6.1.8)$$

$$V'_{pl}(r) \frac{\partial [H^+]_{pl}}{\partial z} = \frac{\tilde{D}_{H, pl}}{r} \frac{\partial}{\partial r} \left(r \frac{\partial [H^+]_{pl}}{\partial r} \right) + R'_{HCO_3, pl} \left(\frac{2.303 [H^+]_{pl}}{\beta_{pl}} \right) \quad (6.1.9)$$

$$V'_{pl}(r) \frac{\partial [HCO_3^-]_{pl}}{\partial z} = \frac{\tilde{D}_{HCO_3, pl}}{r} \frac{\partial}{\partial r} \left(r \frac{\partial [HCO_3^-]_{pl}}{\partial r} \right) + R'_{HCO_3, pl} \quad (6.1.10)$$

Finally, to complete the mathematical description, inlet and boundary conditions are imposed. At lines of symmetry, the following boundary conditions hold:

$$\frac{\partial [O_2]_{rbc}}{\partial r} = 0 \quad (6.28a)$$

$$\frac{\partial [CO_2]_{rbc}}{\partial r} = 0 \quad (6.28b)$$

$$\frac{\partial [H^+]_{pl}}{\partial r} = 0 \quad (6.28c)$$

$$\frac{\partial [HCO_3^-]_{pl}}{\partial r} = 0 \quad (6.28d)$$

$$\frac{\partial [Cl^-]_{pl}}{\partial r} = 0 \quad (6.28e)$$

At the RBC-rich and RBC-free region interface, the modified flux boundary conditions for O_2 and Cl^- and continuity of concentration and flux for the other species are imposed:

$$-D_{O_2,pl} \frac{\partial [O_2]_{rbc}}{\partial r} = \frac{-D_{O_2,pl} (\alpha_{O_2,rbc} P_{O_2,ext} - [O_2]_{rbc})}{r_r \left[\frac{D_{O_2,pl} \alpha_{O_2,pl} \ln(GF)}{K_{O_2}} + \ln\left(\frac{r_c}{r_r}\right) \right]} \quad (6.29a)$$

$$\left(\frac{\alpha_{CO_2,pl}}{\alpha_{CO_2,rbc}} \right) [CO_2]_{rbc} = [CO_2]_{pl}' \quad (6.29b)$$

$$-D_{CO_2,pl} \left(\frac{\alpha_{CO_2,pl}}{\alpha_{CO_2,rbc}} \right) \frac{\partial [CO_2]_{rbc}}{\partial r} = -D_{CO_2,pl} \frac{\partial [CO_2]_{pl}'}{\partial r} \quad (6.29c)$$

$$[H^+]_{pl} = [H^+]_{pl}' \quad (6.29d)$$

$$- \tilde{D}_{H,pl} \frac{\partial [H^+]_{pl}}{\partial r} = - \tilde{D}_{H,pl} \frac{\partial [H^+]_{pl}'}{\partial r} \quad (6.29e)$$

$$[HCO_3^-]_{pl} = [HCO_3^-]_{pl}' \quad (6.29f)$$

$$- \tilde{D}_{HCO_3,pl} \frac{\partial [HCO_3^-]_{pl}}{\partial r} = - \tilde{D}_{HCO_3,pl} \frac{\partial [HCO_3^-]_{pl}'}{\partial r} \quad (6.29g)$$

$$- \tilde{D}_{Cl,pl} \frac{\partial [Cl^-]_{pl}}{\partial r} = 0 \quad (6.29h)$$

At the vessel wall, the following flux conditions are prescribed:

$$- D_{CO_2,pl} \frac{\partial [CO_2]_{pl}'}{\partial r} = \frac{K_{CO_2}}{\alpha_{CO_2,pl} r_c \ln(GF)} ([CO_2]_{pl}' - \alpha_{CO_2,pl} P_{CO_2,ext}) \quad (6.30a)$$

$$- \tilde{D}_{H,pl} \frac{\partial [H^+]_{pl}'}{\partial r} = 0 \quad (6.30b)$$

$$- \tilde{D}_{HCO_3,pl} \frac{\partial [HCO_3^-]_{pl}'}{\partial r} = 0 \quad (6.30c)$$

where

K_{O_2} and K_{CO_2} are the gas permeability constants of the artificial membrane film for O_2 and CO_2 , respectively.

$P_{O_2,ext}$ and $P_{CO_2,ext}$ are the partial pressures of O_2 and CO_2 , respectively, in the gas space surrounding the artificial membrane tubes.

At the entrance, the compositions are assumed to be uniform and in equilibrium.

$$[O_2]_{rbc} = [O_2]_{in} \quad (6.31a)$$

$$[CO_2]_{rbc} = [CO_2]_{in} \quad (6.31b)$$

$$[H^+]_{rbc} = [H^+]_{rbc,in} \quad (6.31c)$$

$$[Cl^-]_{rbc} = R_{GD} [Cl^-]_{pl,in} \quad (6.31d)$$

$$[H^+]_{pl} = [H^+]_{pl,in} \quad (6.31e)$$

$$[HCO_3^-]_{pl} = \frac{K' \left(\frac{\alpha_{CO_2,pl}}{\alpha_{CO_2,rbc}} \right) [CO_2]_{rbc,in}}{[H^+]_{pl,in}} \quad (6.31f)$$

$$[Cl^-]_{pl} = [Cl^-]_{pl,in} \quad (6.31g)$$

$$[CO_2]_{pl}' = \left(\frac{\alpha_{CO_2,pl}}{\alpha_{CO_2,rbc}} \right) [CO_2]_{in} \quad (6.31h)$$

$$[H^+]_{pl}' = [H^+]_{pl,in} \quad (6.31i)$$

$$[HCO_3^-]_{pl}' = \frac{K' \left(\frac{\alpha_{CO_2,pl}}{\alpha_{CO_2,rbc}} \right) [CO_2]_{rbc,in}}{[H^+]_{pl,in}} \quad (6.31j)$$

$$\text{where } R_{GD} = \left(\frac{[HCO_3^-]_{rbc,in}}{[HCO_3^-]_{pl,in}} \right) = \frac{K' f_{water} [CO_2]_{rbc,in}}{[H^+]_{rbc,in} [HCO_3^-]_{pl,in}}.$$

6.1.3.b Type II Model (7 PDEs)

This transport model can be further reduced to a system of 7 simultaneous, nonlinear PDEs consisting of Equations (6.1.1) - (6.1.7) by incorporating the continuity equations for CO_2 , H^+ and HCO_3^- in the RBC-free plasma region, Equations (6.1.8) - (6.1.10), as boundary conditions to Equations (6.1.2), (6.1.5) and (6.1.6), respectively. Again, these solutions use the finding that convective transport of various species is small relative to transport by diffusion. Hence the convective transport terms can be dropped from Equations (6.1.8) - (6.1.10). Additionally, the reaction term, $R'_{HCO_3,pl}$ in these equations is deleted for the reason that the CO_2

hydration/dehydration reaction is very slow in the absence of the carbonic anhydrase enzyme. Even if there were some carbonic anhydrase enzyme added to the extracellular medium to speed up the reaction, it will still be reasonable to neglect $R'_{HCO_3,pl}$ because the RBC-free region represents only a small fraction of the vessel. Therefore, the simplified RBC-free plasma phase mass balances for CO_2 , H^+ and HCO_3^- are solved analytically and incorporated as boundary conditions at $r=r_r$:

$$-D_{CO_2,pl} \frac{\partial [CO_2]_{rbc}}{\partial r} = \frac{-D_{CO_2,pl} (\alpha_{CO_2,rbc} P_{CO_2,ext} - [CO_2]_{rbc})}{r_r \left[\frac{D_{CO_2,pl} \alpha_{CO_2,pl} \ln(GF)}{K_{CO_2}} + \ln\left(\frac{r_c}{r_r}\right) \right]} \quad (6.32a)$$

$$-D_{H,pl} \frac{\partial [H^+]_{pl}}{\partial r} = 0 \quad (6.32b)$$

$$-D_{HCO_3,pl} \frac{\partial [HCO_3^-]_{pl}}{\partial r} = 0 \quad (6.32c)$$

6.1.4 Dimensionless Equations and Conditions

Before solving these equations, it will be convenient to rewrite them in terms of the following dimensionless variables:

$$\begin{aligned} t &= \frac{z}{L}, \quad x = \frac{r}{r_r}, \quad x' = \frac{r_c - r}{r_c - r_r}, \\ u &= \frac{[O_2]_{rbc}}{[O_2]_o}, \quad v = \frac{[CO_2]_{rbc}}{[CO_2]_o}, \quad w = \frac{[H^+]_{rbc}}{[H^+]_o}, \quad s = \frac{[Cl^-]_{rbc}}{[Cl^-]_o}, \\ w' &= \frac{[H^+]_{pl}}{[H^+]_o}, \quad r' = \frac{[HCO_3^-]_{pl}}{[HCO_3^-]_o}, \quad s' = \frac{[Cl^-]_{pl}}{[Cl^-]_o}, \\ v'' &= \frac{[CO_2]_{pl}}{[CO_2]_o}, \quad w'' = \frac{[H^+]_{pl}}{[H^+]_o}, \quad r'' = \frac{[HCO_3^-]_{pl}}{[HCO_3^-]_o} \end{aligned} \quad (6.33)$$

where

L is the length of the artificial membrane tube.

$[O_2]_o$, $[CO_2]_o$, $[H^+]_o$, $[HCO_3^-]_o$ and $[Cl^-]_o$ are the normalized concentrations for various species.

t is the dimensionless axial coordinate.

x and x' are the dimensionless radial coordinates in the RBC-rich and RBC-free plasma regions, respectively.

u , v , w and s are the dimensionless concentrations of O_2 , CO_2 , H^+ and Cl^- inside the RBCs.

w' , r' and s' are the dimensionless concentrations of H^+ , HCO_3^- and Cl^- in the RBC-rich plasma region.

v'' , w'' and r'' are the dimensionless concentrations of CO_2 , H^+ , and HCO_3^- in the RBC-free plasma region.

Details on the dedimensionalization of Type I model are outlined in Appendix C. In terms of the dimensionless variables, the partial differential equations and boundary and inlet conditions may be written

$$\frac{\partial u}{\partial t} = \frac{a_{2u} \frac{1}{x} \frac{\partial}{\partial x} \left(x \frac{\partial u}{\partial x} \right)}{\left[\left(\frac{1}{a_{1u}} \right) h(x) (1-slp) (1-Bb^2x^2) \left(1 + a_{6u} \frac{\partial S}{\partial u} \right) + (1-h(x)) (1-Bb^2x^2) \right]} \quad (6.34)$$

$$\frac{\partial v}{\partial t} = \frac{a_{1v} a_{2v} \frac{1}{x} \frac{\partial}{\partial x} \left(x \frac{\partial v}{\partial x} \right) + a_7 a_{4kr} \left(\frac{1}{d_4} \right) Flux_{HCO_3}^* - (1-h(x)) R_{HCO_3,pl}^*}{\left[h(x) (1-slp) (1-Bb^2x^2) \left(1 + a_{6v} \frac{\partial \phi}{\partial v} + a_{6w} \frac{1}{w} \right) + a_{1v} (1-h(x)) (1-Bb^2x^2) \right]} \quad (6.35)$$

$$\frac{\partial w}{\partial t} = \frac{-\alpha_7 \alpha_{4k} \left(\frac{d_3}{d_4} \right) Flux_{HCO3}^*}{(1-s/p)(1-Bb^2x^2) \left[\left(\frac{1}{\alpha_{5c}} \right) \frac{1}{w} + \alpha_{12w} d_3 \frac{v}{w^2} - 2 \right]} \quad (6.36)$$

$$\frac{\partial s}{\partial t} = \frac{-\alpha_7 \alpha_{4k} Flux_{HCO3}^*}{(1-s/p)(1-Bb^2x^2)} \quad (6.37)$$

$$\frac{\partial w'}{\partial t} = \frac{\alpha_{2w} \frac{1}{x} \frac{\partial}{\partial x} \left(x \frac{\partial w'}{\partial x} \right) + \alpha_{5p} d_3 (1-h(x)) w' R_{HCO3,pl}^*}{(1-h(x))(1-Bb^2x^2)} \quad (6.38)$$

$$\frac{\partial r'}{\partial t} = \frac{\alpha_{2r} \frac{1}{x} \frac{\partial}{\partial x} \left(x \frac{\partial r'}{\partial x} \right) - \alpha_7 \alpha_{4k} h(x) Flux_{HCO3}^* + d_4 (1-h(x)) R_{HCO3,pl}^*}{(1-h(x))(1-Bb^2x^2)} \quad (6.39)$$

$$\frac{\partial s'}{\partial t} = \frac{\alpha_{2s} \frac{1}{x} \frac{\partial}{\partial x} \left(x \frac{\partial s'}{\partial x} \right) + \alpha_7 \alpha_{4k} d_5 h(x) Flux_{HCO3}^*}{(1-h(x))(1-Bb^2x^2)} \quad (6.40)$$

$$\frac{\partial v''}{\partial t} = \frac{\alpha_{8v1} \frac{\partial^2 v''}{\partial x'^2} - \alpha_{8v2} \left[\frac{1}{(1-(1-b)x')} \right] \frac{\partial v''}{\partial x'} - \left(\frac{1}{1-b} \right) R_{HCO3,pl}^{*'}}{[2-(1-b)x']x'} \quad (6.41)$$

$$\frac{\partial w''}{\partial t} = \frac{\alpha_{8w1} \frac{\partial^2 w''}{\partial x'^2} - \alpha_{8w2} \left[\frac{1}{(1-(1-b)x')} \right] \frac{\partial w''}{\partial x'} + \alpha_{5p} d_3 \left(\frac{1}{1-b} \right) w'' R_{HCO3,pl}^{*'}}{[2-(1-b)x']x'} \quad (6.42)$$

$$\frac{\partial r''}{\partial t} = \frac{\alpha_{8r1} \frac{\partial^2 r''}{\partial x'^2} - \alpha_{8r2} \left[\frac{1}{(1-(1-b)x')} \right] \frac{\partial r''}{\partial x'} + d_4 \left(\frac{1}{1-b} \right) R_{HCO3,pl}^{*'}}{[2-(1-b)x']x'} \quad (6.43)$$

where

$$Flux_{HCO3}^* = \frac{a_7 a_{4k} (s r' - s' r)}{(s + s') + d_5 (r + r') + 2 [d_6 s s' + d_7 r' r + d_8 (s r' + s' r)]}.$$

$$R_{HCO3,pl}^* = \hat{A}_{pl} (a_{4ku} a_{1v} v - a_{4kv} d_1 w' r').$$

$$R_{HCO3,pl}^{*'} = \hat{A}_{pl} (a_{9ku} v'' - a_{9kv} d_1 w'' r'').$$

The boundary conditions that go with the simplified equations for type I model are listed below. At lines of symmetry,

$$\frac{\partial u}{\partial x} = 0 \quad (6.44a)$$

$$\frac{\partial v}{\partial x} = 0 \quad (6.44b)$$

$$\frac{\partial w'}{\partial x} = 0 \quad (6.44c)$$

$$\frac{\partial r'}{\partial x} = 0 \quad (6.44d)$$

$$\frac{\partial s'}{\partial x} = 0 \quad (6.44e)$$

At the RBC-rich and RBC-free region interface,

$$\frac{\partial u}{\partial x} + a_{3u}(u - u_{ext}) = 0 \quad (6.45a)$$

$$a_{1v} v - v'' = 0 \quad (6.45b)$$

$$a_{1v} \frac{\partial v}{\partial x} + \left(\frac{b}{1-b} \right) \frac{\partial v''}{\partial x'} = 0 \quad (6.45c)$$

$$w' - w'' = 0 \quad (6.45d)$$

$$\frac{\partial w'}{\partial x} + \left(\frac{b}{1-b} \right) \frac{\partial w''}{\partial x'} = 0 \quad (6.45e)$$

$$r' - r'' = 0 \quad (6.45f)$$

$$\frac{\partial r'}{\partial x} + \left(\frac{b}{1-b} \right) \frac{\partial r''}{\partial x'} = 0 \quad (6.45g)$$

$$\frac{\partial s'}{\partial x} = 0 \quad (6.45h)$$

At the vessel wall,

$$\frac{\partial v''}{\partial x'} - a_{3v} (v'' - a_{1v} v_{ex}) = 0 \quad (6.46a)$$

$$\frac{\partial w''}{\partial x'} = 0 \quad (6.46b)$$

$$\frac{\partial r''}{\partial x'} = 0 \quad (6.46c)$$

At the entrance,

$$u = u_{in} \quad (6.47a)$$

$$v = v_{in} \quad (6.47b)$$

$$w = w_{rbc,in} \quad (6.47c)$$

$$s = R_{GD} s_{pl,in} \quad (6.47d)$$

$$w' = w_{pl,in} \quad (6.47e)$$

$$r' = \left(\frac{a_{1v} d_9}{d_1} \right) \frac{v_{in}}{w_{pl,in}} \quad (6.47f)$$

$$s' = s_{pl,in} \quad (6.47g)$$

$$v'' = v_{in} \quad (6.47h)$$

$$w'' = w_{pl,in} \quad (6.47i)$$

$$r'' = \left(\frac{a_{1v} d_9}{d_1} \right) \frac{v_{in}}{w_{pl,in}}$$

(6.47j)

where

$$a_{1u} = \frac{\alpha_{O2,pl}}{\alpha_{O2,rbc}}, \quad a_{1v} = \frac{\alpha_{CO2,pl}}{\alpha_{CO2,rbc}},$$

$$a_{2u} = \frac{D_{O2,pl} L}{D r_f^2}, \quad a_{2v} = \frac{D_{CO2,pl} L}{D r_f^2}, \quad a_{2w} = \frac{\tilde{D}_{H,pl} L}{D r_f^2}, \quad a_{2r} = \frac{\tilde{D}_{HCO3,pl} L}{D r_f^2}, \quad a_{2s} = \frac{\tilde{D}_{Cl,pl} L}{D r_f^2},$$

$$a_{3u} = \frac{K_{O2}}{D_{O2,pl} \alpha_{O2,pl} \ln(GF) + K_{O2} \ln\left(\frac{r_c}{r_f}\right)}, \quad a_{3v} = \frac{K_{CO2} \left(1 - \frac{r_f}{r_c}\right)}{D_{CO2,pl} \alpha_{CO2,pl} \ln(GF)},$$

$$a_{4ku} = \frac{k_u L}{D}, \quad a_{4kv} = \frac{k_v L}{D}, \quad a_{4kz} = \frac{k_{trans} L}{D},$$

$$a_{5c} = \frac{2.303 [H^+]_o}{\beta_{rbc}}, \quad a_{5p} = \frac{2.303 [H^+]_o}{\beta_{pl}},$$

$$a_{6u} = \frac{C_{heme,rbc}}{[O_2]_o}, \quad a_{6v} = \frac{C_{heme,rbc}}{4 [CO_2]_o}, \quad a_{6w} = \frac{K' f_{water}}{[H^+]_o}, \quad a_7 = \left(\frac{s}{v}\right)_{rbc} T_{tot} K_A,$$

$$a_{8v1} = \frac{D_{CO2,pl} L}{A r_c^2 (1-b)^3}, \quad a_{8v2} = \frac{D_{CO2,pl} L}{A r_c^2 (1-b)^2},$$

$$a_{8w1} = \frac{\tilde{D}_{H,pl} L}{A r_c^2 (1-b)^3}, \quad a_{8w2} = \frac{\tilde{D}_{H,pl} L}{A r_c^2 (1-b)^2},$$

$$a_{8r1} = \frac{\tilde{D}_{HCO3,pl} L}{A r_c^2 (1-b)^3}, \quad a_{8r2} = \frac{\tilde{D}_{HCO3,pl} L}{A r_c^2 (1-b)^2},$$

$$a_{9ku} = \frac{k_u L}{A}, \quad a_{9kv} = \frac{k_v L}{A},$$

$$d_1 = \frac{[H^+]_o [HCO_3^-]_o}{K_1 [CO_2]_o}, \quad d_2 = \frac{[O_2]_o}{[H^+]_o}, \quad d_3 = \frac{[CO_2]_o}{[H^+]_o}, \quad d_4 = \frac{[CO_2]_o}{[HCO_3^-]_o},$$

$$d_5 = \frac{[HCO_3^-]_o}{[Cl^-]_o}, \quad d_6 = K_A [Cl^-]_o, \quad d_7 = \frac{K_A [HCO_3^-]_o^2}{[Cl^-]_o}, \quad d_8 = K_A [HCO_3^-]_o, \quad d_9 = \frac{K'}{K_1},$$

$$u_{ext} = \frac{\alpha_{O2,rbc} P_{O2,ext}}{[O_2]_o}, \quad v_{ext} = \frac{\alpha_{CO2,rbc} P_{CO2,ext}}{[CO_2]_o}.$$

6.1.5 Parameter Values

In order to simulate O_2/CO_2 transport and pH regulation by blood, various parameters which are summarized in Table 6.2 must be known or evaluated. Whenever possible, the parameters are based on experimental observations. Where no data is available, estimates are made from existing correlations and theory. When necessary, the values of the parameters found in the literature were corrected for temperature, protein concentration or ionic strength of the medium. A detailed discussion on the evaluation and selection parameters is given in this section.

6.1.5.a Geometrical Parameters

Consider first the geometrical parameters which are listed in Table 6.2. The specification of RBC characteristic dimensions is well established; for the most part, values that are typical of recent work are selected (Nair *et al.*, 1989). The dimensions of the artificial membrane oxygenator come from experimental determinations.

Table 6.2: Values of parameters used in the numerical computations for the discrete model.

(a) Geometrical parameters		
Red blood cell		
s	Red cell surface area	$163 \times 10^{-8} \text{ cm}^2$
$\left(\frac{s}{v}\right)_{rbc}$	Surface to volume ratio of the RBC	$1.87 \mu\text{m}^{-1}$
t_{rbc}	Maximum thickness of the RBC	$1.3 \mu\text{m}$
r_{rbc}	Radius of the RBC	$4.0 \mu\text{m}$
Artificial membrane oxygenator		
r_c	Inner radius of the artificial membrane tube	
r_o	Outer radius of the artificial membrane tube	
d	Half thickness of the artificial membrane film	
L	Axial length of the artificial membrane tube	

Table 6.2: continued

(b) Physical parameters		
Red blood cell		
$C_{heme,rbc}$	Total heme concentration in the RBC	20.8 mM
$[DPG]$	Intracellular concentration of DPG	6.1 mM
f_{water}	Water fraction of RBC volume	0.72
T_{tot}	Total number of anion transporters per RBC	1×10^6
β_{rbc}	Intracellular buffer capacity	54.5 mM H ⁺ /pH
$\alpha_{O_2,rbc}$	Bunsen solubility coefficient for O ₂ in RBC	Table 6.3
$\alpha_{CO_2,rbc}$	Bunsen solubility coefficient for CO ₂ in RBC	Table 6.4
Plasma		
β_{pl}	Extracellular buffer capacity	5.5 mM H ⁺ /pH
$\alpha_{O_2,pl}$	Bunsen solubility coefficient for O ₂ in plasma	Table 6.3
$\alpha_{CO_2,pl}$	Bunsen solubility coefficient for CO ₂ in plasma	Table 6.4
$D_{O_2,pl}$	Diffusion coefficient for O ₂ in the plasma	Table 6.5
$D_{CO_2,pl}$	Diffusion coefficient for CO ₂ in the plasma	Table 6.6
$\tilde{D}_{H,pl}$	Diffusion coefficient for H ⁺ in the plasma	Tables 6.8, 6.9
$\tilde{D}_{HCO_3,pl}$	Diffusion coefficient for HCO ₃ ⁻ in the plasma	Tables 6.8, 6.9
$\tilde{D}_{Cl,pl}$	Diffusion coefficient for Cl ⁻ in the plasma	Tables 6.8, 6.9
Artificial membrane oxygenator		
K_{O_2}	O ₂ permeability of the artificial membrane	
K_{CO_2}	CO ₂ permeability of the artificial membrane	

Table 6.2: continued

(c) Equilibrium and kinetic parameters		
Oxygen-hemoglobin equilibrium relationship		
P_{50}	Hill equilibrium parameter	Equation (2.2)
n	Hill equation parameter	2.6
S_{min}, S_{max}	Scaling factors of the modified Easton model	0.12, 0.96
$P_{O_2}^*$	P_{O_2} at which maximum slope for modified Easton model occurs	20.7 mmHg
κ	Rate constant of the modified Easton model	Equation (2.7)
Carbamino-hemoglobin equilibrium relationship		
λ_{α}	Association constant for CO_2 -binding to the α -chain of hemoglobin	650 M^{-1} (@ 37 °C)
λ_{β}	Association constant for CO_2 -binding to the β -chain of hemoglobin	240 M^{-1} (@ 37 °C)
K_{DPG}	Association constant for DPG and hemoglobin	$1.5 \times 10^3 \text{ M}^{-1}$ - 5×10^2 (@ 37 °C)
Carbon dioxide hydration-dehydration reactions		
K'	Acid dissociation constant for H_2CO_3	Table 2.2
K_1	Acid dissociation constant for H_2CO_3	Table 2.2
k_u	CO_2 hydration rate constant	Table 2.2
k_v	H_2CO_3 dehydration rate constant	Table 2.2
\hat{A}_{pl}	Carbonic anhydrase activity in the plasma	1.0
Anion exchange kinetics		
k_{trans}	Translocation rate constant	Table 5.8
K_A	Equilibrium association rate constant	Table 5.8

Table 6.2: continued

(d) Hydrodynamic parameters		
H_D	Discharge hematocrit	Equations (6.65a), (6.65b) Equation (2.14) 0.1 Equations (6.65c), (6.65d)
H_T	Tube hematocrit	
m', h_m	Constants in the hematocrit profile which need to be determined	
δ	Thickness of the RBC-free layer	
Q	Volumetric flow rate of the RBC suspension	
B	Blunting factor	
slp	Slip constant	
D, A	Constants in the velocity profiles which need to be determined	
(e) System parameters		
T	Temperature of the system	
$P_{O_2,ext}$	Partial pressure of O_2 in the gas space surrounding the artificial membrane tube	
$P_{CO_2,ext}$	Partial pressure of CO_2 in the gas space surrounding the artificial membrane tube	
$P_{O_2,in}$	Inlet partial pressure of O_2	
$P_{CO_2,in}$	Inlet partial pressure of CO_2	
$[C_i]_{rbc,in}$	Inlet compositions for intracellular species i for $i = H^+$ and Cl^-	
$[C_i]_{pl,in}$	Inlet compositions for extracellular species i for $i = H^+, HCO_3^-$ and Cl^-	

6.1.5.b Physical Parameters

$C_{heme,rbc}$, $[DPG]$, f_{water} , T_{tot} , β_{rbc} and β_{pl}

Let's start with the total heme concentration in the RBC which may be calculated from the hemoglobin density within the red cell; in this study, value of 20.8 mM is used. Normal cellular DPG concentration and fraction of water content in RBC are 6.1 mM and 0.72, respectively (Meldon, 1984). The total number of anion

transporters is reported to be $\approx 1 \times 10^6$ per RBC (Gunn *et al.*, 1973). The intracellular buffering capacity is calculated using data of Rossi-Bernardi and Roughton (1967). They reported that for an 8.8 mM hemoglobin solution, β is approximately 23 (mM base)/(pH unit) for either oxygenated or deoxygenated hemoglobin; thus, β_{rbc} is calculated to be ≈ 54.5 (mM base)/(pH unit). The buffer power of plasma proteins is one-tenth the value of the intracellular buffering capacity (Davenport, 1969); therefore, β_{pl} is ≈ 5.5 (mM base)/(pH unit).

$\alpha_{O_2,rbc}$, $\alpha_{O_2,pl}$, $\alpha_{CO_2,rbc}$ and $\alpha_{CO_2,pl}$

The solubilities for most of gases of physiological interest are available in the literature. The solubilities of O_2 and CO_2 in water, plasma and concentrated hemoglobin solution, which is approximately equivalent to the RBC interior, are listed in Tables 6.3 and 6.4.

Table 6.3: Solubility coefficients for oxygen in water (and/or saline), plasma and hemoglobin solution with equivalent heme concentration as that in RBC.

Authors	α_{O_2,H_2O} [$\alpha_{O_2,saline}$] [†] (10^{-6} M/mmHg)		$\alpha_{O_2,pl}$ (10^{-6} M/mmHg)		$\alpha_{O_2,rbc}$ (10^{-6} M/mmHg)	
	25 °C	37 °C	25 °C	37 °C	25 °C	37 °C
Christoforides and Hedley-Whyte	1.67	1.41	1.51	1.27	1.70	1.42
Altman and Dittmer	1.66 [1.60]	1.41 [1.34]	1.51	1.26	1.94	1.53
Sendroy <i>et al.</i>	---	---	---	1.23	---	1.52
Albritton	---	---	1.46	---	1.80	---

[†] Value of $\alpha_{O_2,saline}$ is obtained or estimated for the condition of isotonic saline with a concentration of 0.15 N.

Table 6.4: Solubility coefficients for carbon dioxide in water (and/or saline), plasma and hemoglobin solution with equivalent heme concentration as that in RBC.

Authors	α_{CO_2,H_2O} [$\alpha_{CO_2,saline}$] [†] (10 ⁻⁵ M/mmHg)		$\alpha_{CO_2,pl}$ (10 ⁻⁵ M/mmHg)		$\alpha_{CO_2,rbc}$ (10 ⁻⁵ M/mmHg)	
	25 °C	37 °C	25 °C	37 °C	25 °C	37 °C
Altman and Dittmer	4.31 [4.36]	3.26 [3.23]	4.00	2.98	3.84	2.58
Albritton	---	---	4.10	3.12	3.37	2.55
Mochizuki and Kagawa	---	---	---	3.08	---	2.62

[†] Value of $\alpha_{CO_2,saline}$ is obtained or estimated for the condition of isotonic saline with a concentration of 0.15 N.

$D_{O_2,pl}$ and $D_{CO_2,pl}$

In this study, the flux (N_i) of any molecular species (O_2 or CO_2) is defined via binary diffusivity (D_i), that is neglecting any diffusive coupling effect,

$$N_i = - D_i \nabla [C_i] \quad (6.48)$$

where $[C_i]$ is the dissolved concentration of either O_2 or CO_2 . Spaeth and Friedlander (1967) and Kreuzer (1970) gave a comprehensive list of experimentally determined values of O_2 diffusion coefficients in distilled water, serum protein solutions and hemoglobin solutions at 25 °C and 37 °C. The mean values of these measured quantities are summarized in Table 6.5.

Table 6.5: The diffusivity of O_2 in water, plasma and concentrated hemoglobin solution.

D_{O_2,H_2O} (cm ² /sec)		$D_{O_2,pl}$ (cm ² /sec)		$D_{O_2,35\%Hb}$ (cm ² /sec)	
25 °C	37 °C	25 °C	37 °C	25 °C	37 °C
2.15×10^{-5}	2.75×10^{-5}	1.73×10^{-5}	2.24×10^{-5}	0.74×10^{-5}	0.95×10^{-5}

The value for $D_{O_2,pl}$ in Table 6.5 is given for normal human plasma. Plasma contains 8% or 9% protein by weight. Due to a wide variety of substances present in plasma and the normal variations from person to person, it is difficult to establish representative properties for plasma. Various investigators (summarized by Kreuzer (1970); Goldstick and Fatt (1970)) added bovine serum albumin to isotonic solution at the same total protein concentration as that of human plasma. When the resulting diffusion coefficient is plotted versus total protein concentration, an almost linear relationship is found. The value for $D_{O_2,35\%Hb}$ is given for the concentrated hemoglobin solution which is assumed to be equivalent to that of RBC interior. A plot of D_{O_2} in protein solutions against protein concentration and a similar plot of D_{O_2} against hemoglobin concentration at 25 °C are given in Kreuzer (1970). The effect of electrolytes on the diffusivity of O_2 in water was studied by Goldstick and Fatt (1970). Their conclusion was that saline does have a different diffusivity than distilled water. However, at isotonic concentrations, it was only about 3% lower than that for water. The difference increases drastically, though, as a molarity of 1.0 is approached.

Diffusion coefficients for CO_2 in water and plasma as reported by Altman and Dittmer (1971) Gros and Moll (1974) are summarized in Table 6.6.

Table 6.6: The diffusivity of CO₂ in water and plasma.

Authors	D_{CO_2,H_2O} (cm ² /sec)		$D_{CO_2,pl}$ (cm ² /sec)	
	25 °C	37 °C	25 °C	37 °C
Altman and Dittmer	1.85×10^{-5}	2.55×10^{-5}	$8.33 \times 10^{-6}^\dagger$	$1.17 \times 10^{-5}^\dagger$
Gros and Moll	1.74×10^{-5}	---	$1.36 \times 10^{-5}^*$	---

[†] Plasma protein concentration of 33g% methemoglobin.

* Plasma protein concentration of 11g% albumin.

The dependence of the diffusivity of O₂ and CO₂ on the protein concentration has been shown to be simply explainable on the basis of the geometry and water space in the protein solution (Gros and Moll, 1971). The diffusion coefficients for O₂ and CO₂ in plasma protein solutions are reduced as compared to their values in water; values of $D_{O_2,pl}/D_{O_2,H_2O}$ and $D_{CO_2,pl}/D_{CO_2,H_2O}$ for different plasma protein concentration is summarized in Table 6.7. These values are taken from different sources, and the result suggests that the dependence of D_{O_2} and D_{CO_2} on the protein concentration is similar; i.e., $D_{O_2,pl}/D_{O_2,H_2O} \approx D_{CO_2,pl}/D_{CO_2,H_2O}$ in the range of plasma

Table 6.7: Comparison of $D_{O_2,pl}/D_{O_2,H_2O}$ and $D_{CO_2,pl}/D_{CO_2,H_2O}$ for different plasma protein concentrations at $T=25$ °C.

plasma protein (wt)	$\frac{D_{O_2,pl}}{D_{O_2,H_2O}}$		$\frac{D_{CO_2,pl}}{D_{CO_2,H_2O}}$	
8.5 g%	0.85^\dagger	0.84^*	---	---
11.0 g%	0.79^\dagger	---	---	0.78^\P
30.0 g%	0.45^\dagger	0.36^*	---	0.44^\P
34.0 g%	0.42^\dagger	---	0.45^*	---

[†] denotes value obtained from Kreuzer (1970).

* denotes value obtained from Altman and Dittmer (1971).

[¶] denotes value obtained from Gros and Moll (1974).

concentrations considered. Altman and Dittmer reported a value of 0.46 for $D_{CO_2,pl} (@34g\%Hb)/D_{CO_2,H_2O}$ at 37 °C which is in close agreement as that reported for 25 °C. Since extensive studies of the dependence of diffusivities on protein concentration at 37 °C is not available in the literature, it is assumed that the same reduction as at 25 °C holds.

Since diffusivity measurements were sometimes taken at temperatures other than the physiological temperature, adjustments sometimes are necessary before the values for diffusivities of various species can be used in a transport model. It is a substantial alteration of experimental results and therefore needs to be considered in detail. One way to express the diffusion coefficient as a function of temperature is the Stokes-Einstein correction (Bird *et al.*, 1960):

$$\frac{T}{D_i \mu} = constant \quad (6.49)$$

where D_i is the diffusivity of species i at temperature T and μ is the viscosity of the solvent. Unfortunately the viscosity is also a function of temperature. Although the viscosity of water at different temperatures is available, that for other fluids is not. However because plasma is an aqueous based solution, its temperature corrections would be expected to be approximately the same as that for water. Spaeth and Friedlander (1967) tested the applicability of this relationship for temperature corrections of experimental data in the range of 25 °C to 37 °C. Their results indicated reasonable agreement with the theory. Their result showed that D_{O_2,H_2O} increases by a factor of ≈ 1.3 and $D_{O_2,pl}$ increases by a factor of ≈ 1.34 as T increases from 25 to 37 °C. A second means of correcting the diffusivity coefficient was discussed by Roughton (1959). Over a small temperature range, the diffusivity can be

approximated by a linear correction, usually given as a percent change of diffusivity for each degree change in temperature (T):

$$\frac{D_i}{D_{i,T_0}} = (1 + \Gamma)^{(T - T_0)} \quad (6.50)$$

where D_{i,T_0} is the diffusivity of specie i at reference temperature T_0 and Γ is given as $2.5\% (\text{°C})^{-1}$ for gases in aqueous protein solutions. For temperatures in the range of 20 to 40 °C, it gives close agreement with the Stokes-Einstein correlation. For the change between 25 and 37 °C, Equation (6.50) gives a correction factor of 1.34.

$\tilde{D}_{H,pl}$, $\tilde{D}_{HCO_3,pl}$ and $\tilde{D}_{Cl,pl}$

The situation is remarkably more complex when, as invariably turns out to be the case, the diffusivities of ionic species need to be estimated. The reason for the additional complexities in estimation of the diffusivities for ionic species is that the diffusion of different ions is coupled in the sense that the diffusive flux of any one ion depends on the concentration gradients of all ions in solution. In principle, one would have to set up the diffusion reaction equations taking this into account; the equations would then be coupled not only through the reaction terms but also the diffusion term (i.e., one would have both chemical and ionic coupling). For these reasons, only limited data exist in the literature for the diffusivities of the ionic species. Hashitani and Kigoshi (1965) measured the diffusivity of HCO_3^- in aqueous solutions as $1.09 \times 10^{-5} \text{ cm}^2/\text{sec}$ at 25 °C. Benn *et al.* (1975) used the Nernst-Hartley equation (Horvath, 1985), which is applicable to diffusion of a single anion-cation pair at infinite dilution, to calculate diffusivity of HCO_3^- in weak acid solutions as $1.18 \times 10^{-5} \text{ cm}^2/\text{sec}$ at 25 °C.

In the diffusion of any particular ion i in a mixture of ions the operative factors are: its concentration gradient (here expressed as $\nabla[C_i]$), its electrical valency (Z_i), its

fractional resistance to movement (expressed as the reciprocal of its equivalent conductivity λ_i) and the electrical gradient ($\nabla\psi$) produced by and a function of all ions present. These fundamental principles are quantitatively expressed as follows (Bird *et al.*, 1960)

$$N_i = -D_i \left(\nabla [C_i] + Z_i [C_i] \nabla \psi \right) \quad (6.51)$$

where values of D_i are available in the literature for common ions and can be evaluated from measurements of electrical conductance. Astarita *et al.* (1983) considered the problem and developed the following approximation scheme. The electrical capacity of liquids is so low that even a minor imbalance in the local charge concentration would result in very large peaks of electrical potential. Hence, to all practical purpose, the solution is electrically neutral everywhere.

$$\sum_i Z_i [C_i] = 0 \quad (6.52)$$

The flux of ion i carries a current proportional to $Z_i N_i$. Although in an electrochemical cell the total net current is non-zero; in an aqueous solutions, as in blood, there is no net electrical current and, therefore,

$$\sum_i Z_i N_i = 0 \quad (6.53)$$

Substitution of Equation (6.51) into (6.53) and algebraic rearrangement yields the electrical potential gradient

$$\nabla \psi = - \frac{\sum Z_i D_i \nabla [C_i]}{\sum Z_i^2 D_i [C_i]} \quad (6.54)$$

Notice that if all D_i s are equal, the gradient of electrical potential is zero, and Equation (6.51) reduces to the ordinary diffusion equation for non-ionic species. However, if the ionic diffusivities are sufficiently different from each other to generate a non-negligible electrical potential gradient, then the $Z_i[C_i]\nabla\psi$ term may provide strong ionic coupling of diffusion. The approximate procedure that Astarita *et al.* (1983) tried to develop was to estimate an “apparent” diffusivity of ionic species \tilde{D}_i defined by

$$N_i = - \tilde{D}_i \nabla [C_i] \quad (6.55)$$

Consider the case of plasma. The ionic species to be considered are Na^+ , Cl^- and HCO_3^- ; K^+ , H^+ , OH^- , H_2PO_4^- and HPO_4^{2-} are not considered because their concentrations are known to be negligible as compared to that of Na^+ , Cl^- and HCO_3^- . The electroneutrality condition requires

$$[\text{Na}^+]_{pl} = [\text{Cl}^-]_{pl} + [\text{HCO}_3^-]_{pl} \quad (6.56)$$

so that the electrical potential gradient is calculated from Equation (6.54) as

$$\nabla \psi = - \frac{(D_{\text{HCO}_3,pl} - D_{\text{Cl},pl}) \nabla [\text{HCO}_3^-]_{pl} - (D_{\text{Na},pl} - D_{\text{Cl},pl}) \nabla [\text{Na}^+]_{pl}}{(D_{\text{HCO}_3,pl} - D_{\text{Cl},pl}) [\text{HCO}_3^-]_{pl} + (D_{\text{Na},pl} + D_{\text{Cl},pl}) [\text{Na}^+]_{pl}} \quad (6.57)$$

However, an additional condition is imposed by the physical fact that the flux of Na^+ needs necessarily to be zero. Therefore, from the appropriate form of Equation (6.51),

$$\nabla \psi = - \frac{\nabla [Na^+]_{pl}}{[Na^+]_{pl}} \quad (6.58)$$

Substitution of Equations (6.57) and (6.58) into appropriate form of Equation (6.51) and rearrangement yields the apparent diffusivities

$$\tilde{D}_{Cl,pl} = D_{Cl,pl} \frac{2 (D_{Na,pl} + D_{HCO_3,pl} - D_{Cl,pl}) [Na^+]_{pl}}{(D_{HCO_3,pl} - D_{Cl,pl}) [HCO_3^-]_{pl} + (2 D_{Na,pl} + D_{HCO_3,pl} - D_{Cl,pl}) [Na^+]_{pl}} \quad (6.59)$$

$$\tilde{D}_{HCO_3,pl} = D_{HCO_3,pl} \frac{2 D_{Na,pl} [Na^+]_{pl}}{(D_{HCO_3,pl} - D_{Cl,pl}) [HCO_3^-]_{pl} + 2 D_{Na,pl} [Na^+]_{pl}} \quad (6.60)$$

with the equivalent diffusivity $\tilde{D}_{Na,pl}$ being zero, since flux of Na^+ is zero although $\nabla [Na^+]_{pl}$ is not.

For an ideal electrolyte solution, D_i s can be calculated directly from their equivalent conductivities using an equation derived by Nernst (Horvath, 1985):

$$D_i^o = \lambda_i^o \left(\frac{RT}{|Z_i| F^2} \right) \quad (6.61)$$

where

D_i^o is the diffusion coefficient of ion i in infinitely dilute solution, cm^2/sec .

λ_i^o is the equivalent conductance of ion i in infinitely dilute solution, $cm^2 \Omega^{-1} mole^{-1}$.

R is the universal gas constant ($=8.316 \text{ Jouels mole}^{-1} K^{-1}$).

T is the absolute temperature, K.

Z_i is the electrical valence of ion i.

F is the Faraday number ($=96,500 \text{ coulombs mole}^{-1}$)

Because D_i^o is the value of the diffusion coefficient of ion i when completely released from other ions and not under the influence of a potential gradient. As a result, corrections have to be made for the effects of protein concentration and ionic strength. As discussed above, the diffusion coefficients of O_2 and CO_2 in a 8.5 g/100 ml plasma protein solution are roughly 85% of their respective values in water (Table 6.7). As a rough estimate, it seems reasonable to assume that the protein affects the diffusion of other small molecules in a similar way. Since no experimental data is available, it is assumed that the same reduction holds for the diffusivities of the ionic species. However, the corrections dealing with the effects of non-ideal electrolyte solutions on the diffusivities of the ionic species are more complicated. A brief discussion on the relationship between the non-ideality of electrolyte solutions and the charge and concentrations is given below.

The concentration dependence of diffusion coefficient in dilute aqueous electrolyte solutions is given by the the following expression:

$$D_i = D_i^o \left(1 + \frac{d \ln \gamma_i}{d \ln [C_i]} \right) \quad (6.62)$$

where γ_i is the activity coefficient of species i . The variation of D_i with concentration is due to the thermodynamic term ($d \ln \gamma_i / d \ln [C_i]$). Generally, the methods for calculating activity coefficients in multicomponent systems are built upon the calculation of activity coefficients of single electrolyte solutions (e.g., Debye-Hückel's law; a complete review of the various approaches for dealing with single electrolyte solutions is given in Horvath, 1985) together with the application of mixing rules. Plasma is a combination of both strong (e.g., $NaCl \rightleftharpoons Na^+ + Cl^-$) and weak electrolytes (e.g., $NaHCO_3 \rightleftharpoons Na^+ + HCO_3^-$). Therefore, plasma is by definition to contain both strong electrolytes (compounds which nearly dissociates to its maximally

charged constituent ions when placed in aqueous solution) and complexing electrolytes (compounds which form a non-trivial quantities of non-maximally charged complexes). There is a vast literature dealing with the theory of multicomponent electrolyte solutions which is compiled in *Handbook of Aqueous Electrolyte Thermodynamics* by Zemaitis *et al.* (1986). For instance, Bromley's method (Zemaitis *et al.*, 1986) would be applicable for use with this system; the ionic activity coefficient of ion i is:

$$\ln \gamma_i = -\frac{C_{DH} Z_i^2 \sqrt{I}}{1 + \sqrt{I}} + \sum_j \dot{B}_{ij} Z_{ij}^2 [C_j] \quad (6.63)$$

where

C_{DH} is the Debye-Hückel constant.

I is the ionic strength, and $I = 0.5 \sum_i [C_i] Z_i^2$.

$$Z_{ij} = \frac{Z_i + Z_j}{2}.$$

$$\dot{B}_{ij} = \frac{(0.06 + 0.6 B_\sigma) |Z_i Z_j|}{\left(1 + \frac{1.5}{|Z_i Z_j|} I\right)^2} + B_\sigma.$$

and B_σ is the Bromley interaction term. Bromley's expression is applicable here due to the summation term; the species may be any of the complexes in the solution. Using this approach to estimate the non-ideality of the electrolyte solution would be reasonable from a fundamental standpoint. However, because of the lack of complete and accurate values for the interaction terms, the practicality of using this correction is diminished.

For a first order approximation, Equation (6.61) and plasma protein correction factor, listed in Table 6.7, are used to calculate $D_{Cl,pl}$, $D_{HCO_3,pl}$ and $D_{Na,pl}$; in other

words, the non-ideality of the solution is ignored and the thermodynamic term ($d \ln \gamma_i / d \ln C_i$) put equal to zero. Values of the limiting equivalent conductivities in water (λ_i^0), ionic diffusivities at infinite dilute solution (D_i^0) calculated from Equation (6.61), and apparent diffusivities ($\tilde{D}_{i, pl}$) calculated via Equations (6.59) and (6.60) are listed in Tables 6.8 and 6.9 at $T=25$ °C and $T=37$ °C, respectively.

In an attempt to correct for the effects of ionic strength, Landolt and Bronstein's experimental data (summarized by Gros and Moll, 1974) on the relation between ionic strength and conductivity of NaHCO_3 were used to estimate the reduction of HCO_3^- conductivity/diffusivity by the ionic strength. Accordingly, the diffusion coefficient is reduced to 77% of $D_{\text{HCO}_3}^0$ for $I_m=0.13$ (albumin solution with $\text{pH}=7.2$), to 73% of $D_{\text{HCO}_3}^0$ for $I_m=0.78$ (albumin solution with $\text{pH}=7.8$) where I_m is the ionic strength calculated using the molality of ions. Hence the apparent diffusivities for different ions in the plasma are calculated as follows: $D_{i, pl}^0 = 0.75 \cdot 0.85 \cdot D_i^0$. Because experimental data is not available, it is then assumed here that the effect of ionic strength and equivalent conductivity of univalent salts such as NaCl and NaHCO_3 are similar. As a result, correction by above equation is also applied to Na^+ and Cl^- . The apparent diffusivities are calculated to be the followings: $\tilde{D}_{\text{Cl}, pl} = 1.03 \times 10^{-5}$ and $\tilde{D}_{\text{HCO}_3, pl} = 0.952 \times 10^{-5}$ cm^2/sec at 25 °C; and $\tilde{D}_{\text{Cl}, pl} = 1.29 \times 10^{-5}$ and $\tilde{D}_{\text{HCO}_3, pl} = 1.25 \times 10^{-5}$ cm^2/sec at 37 °C.

6.1.5.c Equilibrium and Kinetic Parameters

Empirical relationships which allow the estimate of ODC parameters of normal human whole blood at both standard and nonstandard conditions were obtained by Samaja *et al.* (1981) and Buerk and Bridges (1986) who used direct nonlinear regression applied to available literature data; Equation (2.2) for estimating Hill parameter, P_{50} , (Samaja *et al.*, 1981) or Equation (2.7) for estimating Easton parameter, κ , (Buerk and Bridges, 1986). Parameter values for the carbamino-

Table 6.8: Estimation of $\tilde{D}_{H,pl}$, $\tilde{D}_{HCO_3,pl}$ and $\tilde{D}_{Cl,pl}$ at 25 °C.

Ionic species i	$\lambda_i^{\circ \dagger}$ (cm ² /Ω-mole)	$D_i^{\circ *}$ (cm ² /sec)	$D_{i,pl}^{\circ \P}$ (cm ² /sec)	$\tilde{D}_{i,pl}^{\S}$ (cm ² /sec)
H ⁺	350.10	9.28x10 ⁻⁵	7.89x10 ⁻⁵	7.89x10 ⁻⁵
Na ⁺	50.11	1.33x10 ⁻⁵	1.13x10 ⁻⁵	0
Cl ⁻	76.34	2.03x10 ⁻⁵	1.72x10 ⁻⁵	1.32x10 ⁻⁵
HCO ₃ ⁻	54.50	1.45x10 ⁻⁵	1.23x10 ⁻⁵	1.28x10 ⁻⁵

[†] The values of λ_i° are obtained from Table 2.10.1 in *Handbook of Aqueous Electrolyte Solutions* (Horvath, 1985).

^{*} The diffusivities of various ions are calculated from Equation (6.61).

^{\P} The calculated diffusivities are further corrected for the plasma protein concentration (8.5 g%); i.e., $D_{i,pl}^{\circ} = 0.85 D_i^{\circ}$.

^{\S} The apparent or effective ionic diffusivities are calculated via Equations (6.59) and (6.60) where $[Na^+]_{pl} = 134$ mM and $[HCO_3^-]_{pl} = 27$ mM.

Table 6.9: Estimation of $\tilde{D}_{H,pl}$, $\tilde{D}_{HCO_3,pl}$ and $\tilde{D}_{Cl,pl}$ at 37 °C.

Ionic species i	$\lambda_i^{\circ \dagger}$ (cm ² /Ω-mole)	$D_i^{\circ *}$ (cm ² /sec)	$D_{i,pl}^{\circ \P}$ (cm ² /sec)	$\tilde{D}_{i,pl}^{\S}$ (cm ² /sec)
H ⁺	404.76	1.12x10 ⁻⁴	9.52x10 ⁻⁵	9.52x10 ⁻⁵
Na ⁺	64.26	1.77x10 ⁻⁵	1.50x10 ⁻⁵	0
Cl ⁻	95.88	2.65x10 ⁻⁵	2.25x10 ⁻⁵	1.73x10 ⁻⁵
HCO ₃ ⁻	68.07	1.88x10 ⁻⁵	1.60x10 ⁻⁵	1.66x10 ⁻⁵

[†] The values of λ_i° are obtained from Tables 2.10.2 and 2.11.2 in *Handbook of Aqueous Electrolyte Solutions* (Horvath, 1985).

^{*} The diffusivities of various ions are calculated from Equation (6.61).

^{\P} The calculated diffusivities are further corrected for the plasma protein concentration (8.5 g%); i.e., $D_{i,pl}^{\circ} = 0.85 D_i^{\circ}$.

^{\S} The apparent or effective ionic diffusivities are calculated via Equations (6.59) and (6.60) where $[Na^+]_{pl} = 134$ mM and $[HCO_3^-]_{pl} = 27$ mM.

hemoglobin equilibrium listed in Table 6.2 are reported for human deoxyhemoglobin in the absence of DPG at pH 7.4 and 37 °C. In order to incorporate the oxygen saturation dependence (the Haldane effect) into account, the following information was implemented into Equation (2.10). By drawing data from various publications, Nunn (1987) reported that in the absence of DPG, the carbamino CO_2 bound to oxyhemoglobin is about 30% of that bound to deoxyhemoglobin for various P_{CO_2} . In addition, there is a linear relationship between the difference in carbamino carriage and S . Therefore, it is proposed here to extrapolate $\phi(S,[DPG])$ from $\phi(S=0,[DPG])$ via the following relationship:

$$\phi(S,[DPG]) = \phi(S=0,[DPG]) (1 - 0.7S) \quad (6.64)$$

where $\phi(S=0,[DPG])$ is calculated using Equation (2.10) with the equilibrium parameters which were determined for stripped deoxyhemoglobin. Values for various rate and equilibrium constants for the CO_2 hydration/dehydration gathered from the literature are synopsized in Table 2.2. Kinetic parameters for anion transporter operating via ping-pong mechanism are summarized in Table 5.8.

6.1.5.d Hydrodynamic Parameters

Due to the Fahraeus effect the tube hematocrit, H_T , is lower than the discharge hematocrit, H_D . The tube hematocrit used in this work is based on the measurements of Gaehtgens *et al.* (1978), who determined tube hematocrit as a function of discharge hematocrit, tube radius and flow rate. The cell-free layer thickness, δ , is calculated from Equation (2.14). The blunting factor, B , represents the deviation of velocity profile from the Poiseuille flow parabolic profile; B is known to depend on vessel diameter, hematocrit and shear rate. Because Nair *et al.*'s (1989) studies showed that their oxygen transport results are not highly sensitive to the value of B , a constant

value of B is used in this work. For instance, $B \approx 0.9$ for vessels with diameters of $\approx 30 \mu\text{m}$ and $B \approx 1$ for vessels with diameters of several hundred μm . The slip constant, slp , is the difference in the velocity of the suspending fluid and the particle at a particular point due to the finite size of the particle, and it is a function of particle position and hematocrit. For the sake of simplicity, a constant slip of 0.1 is assumed in this work.

The parameters h_m , m' , A and D can be obtained by simultaneous solution of equations which describe: the continuity of plasma velocity profile, the overall RBC mass balance, the overall plasma mass balance and the definition of tube hematocrit. The compatibility conditions of the model are integral expressions (Equations (6.65a) - (6.65d)) which when applied to the hematocrit and velocity profiles can be reduced to the closed form expressions given in Equations (6.66a) - (6.66d) (Nair *et al.*, 1989).

Continuity of plasma velocity profile:

$$V_{pl}'(r_r) = V_{pl}(r_r) \quad (6.65a)$$

Overall RBC mass balance which defines H_D , the discharge hematocrit:

$$Q H_D = \int_0^{r_c} 2 \pi r V_{rbc}(r) h(r) dr \quad (6.65b)$$

Overall plasma mass balance:

$$Q(1 - H_D) = \int_0^{r_r} 2 \pi r V_{pl}(r) (1 - h(r)) dr + \int_{r_r}^{r_c} 2 \pi r V_{pl}'(r) dr \quad (6.65c)$$

Definition of tube hematocrit, H_T , the space average hematocrit at any cross section in the tube:

$$H_T = \frac{1}{\pi r_c^2} \int_0^{r_c} 2 \pi r h(r) dr \quad (6.65d)$$

Simultaneous solution of above equations yields the followings:

$$m' = \frac{2(2\varphi - 1)}{1 - \varphi} \quad (6.66a)$$

$$h_m = \frac{H_T(m' + 2)}{m' b^2} \quad (6.66b)$$

$$D = \frac{2 Q H_D \left[1 + \frac{(1 - H_D)}{H_D} (1 - slp) \right]}{\pi r_c^2 (1 - slp) [1 + b^2 (1 - B)]} \quad (6.66c)$$

$$A = \frac{D(1 - Bb^2)}{1 - b^2} \quad (6.66d)$$

where

$$b = \frac{r_r}{r_c}$$

$$\varphi = \frac{2}{B b^2} \left\{ 1 - \frac{[1 + b^2 (1 - B)]}{2 H_T \left[1 + \left(\frac{1 - H_D}{H_D} \right) (1 - slp) \right]} \right\} \quad (\text{for } 0.5 < \varphi < 1).$$

6.1.5.e System Parameters

All the quantities which are listed under the category of system parameters should be accessible to experimental measurements. Sometimes, only some of the quantities are determined by the investigators. For illustrations, let's consider Voorhees' (1976) system where the following quantities are available from experimental determinations: T , $P_{O2,ex}$, $P_{CO2,ex}$, $P_{O2,in}$, $P_{CO2,in}$, $pH_{pl,in}$ and total inlet CO_2 content. As a result, one has to reconstruct the inlet composition for other species.

The inlet composition is assumed to be in equilibrium and uniform. In addition, if $(pH_{rbc,in} - pH_{pl,in})$ is assumed to be a function $[DPG]$ and $P_{CO_2,in}$ and independent of temperature between 25 °C and 37 °C, then the result obtained by Meldon (1984) can be used to estimate $pH_{rbc,in}$ from the experimentally determined $pH_{pl,in}$ using Equation (6.67).

$$pH_{rbc,in} = pH_{pl,in} - \Delta pH \quad (6.67)$$

where ΔpH is the difference between the pH in the RBCs from that in the plasma which was calculated by Meldon (1984). Meldon (1984) calculated pH_{pl} and pH_{rbc} and other dependent variables from P_{CO_2} and $[DPG]$ in oxygenated whole blood, *in vitro* at 37 °C by applying published data on RBC and plasma buffer capacity, RBC/plasma Donnan distribution, plus CO_2 solubility and reaction equilibrium constants and enforcing fundamental thermodynamic and conservation constraints. Because we are interested in the difference between but not the actual values of the pH in RBC and plasma, it is then reasonable to neglect the fact that the inlet O_2 saturation of blood samples in Voorhees' experiments were $\geq 70\%$ instead of 100%, and the operating temperature was 25 °C instead of 37 °C.

The inlet intracellular and extracellular concentrations of other species can then be calculated as follows.

(a) The dissolved CO_2 is in equilibrium with HCO_3^- and H^+ in both intra- and extracellular phases. Therefore,

$$\frac{[H^+]_{rbc,in} [HCO_3^-]_{rbc,in}}{[CO_2]_{rbc,in}} = K' f_{water} \quad (6.68a)$$

$$\frac{[H^+]_{pl,in} [HCO_3^-]_{pl,in}}{[CO_2]_{pl,in}} = K' \quad (6.68b)$$

Normally RBCs contain some 72% water and plasma 94% by volume. Meldon's analysis (1984) which used fundamental physiochemical constraints and equilibrium data established the fact that CO_2 -induced osmotic effects, or shift of water between cells and plasma, are small (< 3-5%). Therefore, f_{water} is taken to be a constant. In addition, from Table 2.2 it is observed that reaction and equilibrium constants for CO_2 hydration/dehydration reactions in both buffered saline and plasma are about the same; consequently, no volume correction term is incorporated into Equation (6.68b). Furthermore, because $[CO_2]_{rbc} = \alpha_{CO_2,rbc} P_{CO_2}$ and $[CO_2]_{pl} = \alpha_{CO_2,pl} P_{CO_2}$ the intra- and extracellular HCO_3^- concentrations can then be calculated via Equations (6.68a) and (6.68b), respectively.

(b) Intra- and extracellular concentrations of Cl^- were not determined in Voorhees' work. In making the calculations, extracellular Cl^- concentration under standard condition ($T=37^\circ C$, $P_{O_2}=100$ mmHg and $P_{CO_2}=40$ mmHg) is used, and intracellular Cl^- concentration is then calculated from the Donnan ratio:

$$\frac{[HCO_3^-]_{rbc,in}}{[HCO_3^-]_{pl,in}} = \frac{[Cl^-]_{rbc,in}}{[Cl^-]_{pl,in}} = R_{GD} \quad (6.69)$$

Although the actual Cl^- concentrations are not used, it is assumed that Gibbs Donnan ratio used here will set up the appropriate driving force for the transmembrane transport. The usage of the actual Cl^- concentrations here might not be essential because Cl^- is not involved in any other chemical reaction but the one-for-one exchange of Cl^- for HCO_3^- ; and the Cl^- flux is equal and opposite to that of HCO_3^- across the RBC membrane. Therefore, it is presumed that within the physiological

concentration range, if the driving force is represented appropriately, then the actual values of Cl^- should not alter the results on other components appreciably.

(c) Finally, total inlet CO_2 content, $[CO_2]_{total,in}$, can then be used as a consistency check for the above calculations.

$$\begin{aligned}
 [CO_2]_{total,in} = & [HCO_3^-]_{pl,in} (1 - H_D) + [HCO_3^-]_{rbc,in} H_D \\
 & + [\alpha_{CO_2,rbc} H_D + \alpha_{CO_2,pl} (1 - H_D)] P_{CO_2,in} \\
 & + [HbCO_2]_{in} H_D + [H_2CO_3]_{pl,in} (1 - H_D) + [H_2CO_3]_{rbc,in} H_D \quad (6.70)
 \end{aligned}$$

Carbonic acid presence is negligible because both intra- and extracellular pH in the system are much higher than the pK of the acid; therefore, it can be neglected from the calculation of $[CO_2]_{total,in}$.

In the case where the inlet pH of the blood sample was not available, then the following approach is used to estimate pH_{pl} and pH_{rbc} .

(a) Given the quantity $P_{CO_2,in}$, $[HbCO_2]_{in}$ can be calculated from Equation (6.71),

$$[HbCO_2]_{in} = \left(\frac{C_{heme,rbc}}{4} \right) \left(\frac{2 \lambda_\alpha \alpha_{CO_2} P_{CO_2,in}}{1 + \lambda_\alpha \alpha_{CO_2} P_{CO_2,in}} + \frac{2 \lambda_\beta \alpha_{CO_2} P_{CO_2,in}}{1 + \lambda_\beta \alpha_{CO_2} P_{CO_2,in} + K_{DPG} [DPG]} \right) \quad (6.71)$$

(b) From Equations (6.68a) and (6.68b), $[HCO_3^-]_{rbc,in}$ and $[HCO_3^-]_{pl,in}$ can be expressed terms of inlet CO_2 and hydrogen ion compositions:

$$[HCO_3^-]_{rbc,in} = \frac{K' f_{water} [CO_2]_{rbc,in}}{[H^+]_{rbc,in}} \quad (6.72a)$$

$$[HCO_3^-]_{pl,in} = \frac{K' [CO_2]_{pl,in}}{[H^+]_{pl,in}} \quad (6.72b)$$

In addition, from Equation (6.67), $[H^+]_{rbc} = 10^{\Delta pH} [H^+]_{pl}$ is obtained.

(c) Substituting Equations (6.71) and (6.72) into (6.70) and utilizing the relationship that $[H^+]_{rbc} = 10^{\Delta pH} [H^+]_{pl}$, an equation with $[H^+]_{pl,in}$ as the unknown is obtained. Rearrange the equation and solve for $[H^+]_{pl,in}$:

$$[H^+]_{pl,in} = \frac{K' P_{CO_2,in} [H_D f_{water} \alpha_{CO_2,rbc} + (1-H_D) \alpha_{CO_2,pl} 10^{\Delta pH}]}{10^{\Delta pH} \{ [CO_2]_{total,in} - [H_D \alpha_{CO_2,rbc} + (1-H_D) \alpha_{CO_2,pl}] P_{CO_2,in} - H_D [HbCO_2]_{in} \}} \quad (6.73)$$

6.1.6 Numerical Method and Processing of Simulation Results for Comparison of Model Predictions with Experimental Measurements

Solution of the transport equations is complicated by nonlinear reaction equilibrium and kinetic terms and coupling among the equations. Thus all the partial differential equations are solved numerically by the finite element collocation method of Madsen and Sincovec (1975) which uses basic spline polynomials for the spatial discretization. This method was described and evaluated for problems of O_2 transport in capillaries by Baxley and Hellums (1983) and it was shown to be much more efficient than finite difference methods. The numerical solution to the transport equations, subject to the imposed boundary and inlet conditions, provides the concentration profiles for various species as functions of r and z . The selection of the appropriate physical and chemical parameters is summarized in Table 6.2 for the discrete model which is consisted of Equations (6.1.1) - (6.1.7); and Table 6.10 for the continuum model which is consisted of Equations (3.23) and (4.14).

Table 6.10: Values of parameters used in the numerical computations for the continuum model.

Physical properties	
α_{O_2} , effective O ₂ solubility coefficient	$\alpha_{O_2} = H_D \alpha_{O_2, rbc} + (1 - H_D) \alpha_{O_2, pl}$
α_{CO_2} , effective CO ₂ solubility coefficient	$\alpha_{CO_2} = H_D \alpha_{CO_2, rbc} + (1 - H_D) \alpha_{CO_2, pl}$
D_{O_2} , effective O ₂ diffusion coefficient	$D_{O_2} = H_D D_{O_2, rbc} + (1 - H_D) D_{O_2, pl}$
D_{CO_2} , effective CO ₂ diffusion coefficient	$D_{CO_2} = H_D D_{CO_2, rbc} + (1 - H_D) D_{CO_2, pl}$
Equilibrium parameters for approximating CO ₂ dissociation curve	
K_{eq}^{\dagger} , pseudo equilibrium constant	$K_{eq} = 54.2 @ 25 ^\circ C^*$; $78.6 @ 37 ^\circ C^{\dagger}$
β^{\dagger} , apparent buffering capacity of the blood	$\beta = 31.7 @ 25 ^\circ C^*$; $32.5 @ 37 ^\circ C^{\dagger}$

[†] The values of K_{eq} and β used to simulate Voorhees' experiments are given in the legend for each run; K_{eq} =[dimensionless] and β =[mM H⁺/pH].

* Basis: $T=25 ^\circ C$, $H_D=45\%$, $P_{CO_2}=56$ mmHg, $[CO_2]_{total}=24.4$ mM, $pH_{pl}=7.201$ (Voorhees, 1976).

[†] Basis: $T=37 ^\circ C$, $H_D=45\%$, $P_{CO_2}=46$ mmHg, $[CO_2]_{total}=23.2$ mM, $pH_{pl}=7.37$ (Voorhees, 1976).

Gas transport predictions are obtained for the experimental runs conducted by Voorhees (1976) as the numerical solutions for either Equations (6.1.1) - (6.1.7) listed in Table 6.1 for the discrete model and Equations (3.23) and (4.14) for the continuum model. For the discrete model, mixed mean concentrations of species i inside the RBC ($[C_i]_{mm, rbc}$), in the plasma ($[C_i]_{mm, pl}$) and in the whole blood ($[C_i]_{mm, wb}$) are calculated by Equations (6.74a), (6.74b) and (6.74c), respectively.

$$[C_i]_{mm, rbc}(z) = \frac{1}{\pi r_c^2 H_T \langle V \rangle_{rbc}} \int_0^{r_c} 2 \pi r h(r) V_{rbc}(r) [C_i]_{rbc}(r, z) dr \quad (6.74a)$$

$$[C_i]_{mm, pl}(z) = \frac{1}{\pi r_c^2 (1 - H_T) \langle V \rangle_{pl}} \int_0^{r_r} 2 \pi r (1 - h(r)) V_{pl}(r) [C_i]_{pl}(r, z) dr$$

$$+ \frac{1}{\pi r_c^2 (1 - H_T) \langle V \rangle_{pl}} \int_{r_r}^{r_c} 2 \pi r V_{pl}'(r) [C_i]_{pl}'(r, z) dr \quad (6.74b)$$

$$\begin{aligned} [C_i]_{mm,wb}(z) = & \frac{1}{\pi r_c^2 \langle V \rangle} \int_0^{r_c} 2 \pi r h(r) V_{rbc}(r) [C_i]_{rbc}(r, z) dr \\ & + \frac{1}{\pi r_c^2 \langle V \rangle} \int_0^{r_r} 2 \pi r (1 - h(r)) V_{pl}(r) [C_i]_{pl}(r, z) dr \\ & + \frac{1}{\pi r_c^2 \langle V \rangle} \int_{r_r}^{r_c} 2 \pi r V_{pl}'(r) [C_i]_{pl}'(r, z) dr \end{aligned} \quad (6.74c)$$

For the continuum model, the mixed mean concentration of species i in the tube ($[C_i]_{mm}$) is evaluated as

$$[C_i]_{mm}(z) = \frac{1}{\pi r_c^2} \int_0^{r_c} 4 \pi r \left[1 - \left(\frac{r}{r_c} \right)^2 \right] [C_i](r, z) dr \quad (6.75)$$

The comparison with Voorhees' data are presented as changes in both total O_2 content, $[O_2]_{total}$, and total CO_2 content, $[CO_2]_{total}$, versus transit time. Here the transit time is defined as the ratio of active exchange length to the average fluid velocity in the tube; i.e., transit time = $\pi r_c^2 L / Q$. The total content change of O_2 or CO_2 is calculated from

$$\Delta[C_i]_{total} = [C_i]_{total,out} - [C_i]_{total,in} \quad (6.76)$$

where

$\Delta[C_i]_{total}$ is the total content change of species i .

$[C_i]_{total,out}$ and $[C_i]_{total,in}$ are the total concentrations of species i at $z=L$ and $z=0$, respectively.

For the discrete model, $[O_2]_{total}$ and $[CO_2]_{total}$ are computed as the follows:

$$[O_2]_{total} = H_D C_{heme,rbc} S_{mm,rbc} + [O_2]_{mm,wb} \quad (6.77a)$$

$$[CO_2]_{total} = [HCO_3^-]_{mm,wb} + [CO_2]_{mm,wb} + H_D [HbCO_2]_{mm,rbc} \quad (6.77b)$$

For the continuum model, these quantities are calculated as

$$[O_2]_{total} = C_{heme} S_{mm} + [O_2]_{mm} \quad (6.78a)$$

$$[CO_2]_{total} = [CO_2]_{reacted,mm} + [CO_2]_{mm} \quad (6.78b)$$

6.2 Results and Discussion

6.2.1 Comparison with Voorhees' Membrane Oxygenator Data

Experimental results by Voorhees (1976) were used for comparison with the calculations from the models. In this work, freshly drawn human blood was equilibrated to the desired inlet conditions at $\approx 25^\circ\text{C}$ and then perfused through an artificial membrane oxygenator. Simultaneous O_2 and CO_2 transfer were measured in a single straight permeable tube constructed of dimethyl silicone. Two basic transfer units were used by Voorhees (1976); and the geometrical parameters for those units were I.D.=1.47 mm, O.D.=1.96 mm, $L=179$ cm and I.D.=1.57 mm, O.D.=3.17 mm, $L=179$ cm. The O_2 and CO_2 permeabilities in dimethyl-silicone are 2.5×10^{-9} and 1.5×10^{-8} M cm²/sec/mmHg, respectively (Dorson *et al.*, 1971). Minimum and maximum experimental values were: inlet O_2 saturation from 69 to 81%, inlet CO_2 tension from 27.9 to 59.7 mmHg, inlet plasma pH from 7.0 to 7.7, and hematocrit between 42 and 57%. Oxygenation experiments, in which RBC suspensions were

taking up O_2 and eliminating CO_2 to the environment, were carried out by suffusing the environmental gas space with almost pure oxygen ($P_{O_2,ext} \approx 698-718$ mmHg and $P_{CO_2,ext} \approx 0$ mmHg). Deoxygenation experiments, in which RBC suspensions were delivering O_2 to the environment and taking up CO_2 , were conducted by suffusing the external gas chamber with a N_2 - CO_2 gas mixture ($P_{O_2,ext} \approx 0$ mmHg and $P_{CO_2,ext} \approx 115$ mmHg).

Data reported by Voorhees were taken with care in measuring not only most of the relevant blood gas parameters (e.g., T , H_D , S , P_{O_2} , P_{CO_2} , and $[CO_2]_{total}$) for the inlet and outlet blood samples, but also the biochemical status of each sample (such as K_{eq} and β which are parameters for characterizing the CO_2 dissociation curve, O_2 consumption, and/or ΔpH and ΔP_{CO_2}). However, it should be mentioned that hemoglobin O_2 affinity and cooperativity which are required for describing the O_2 dissociation curve were not reported. As a result, in order to compare the theoretical predictions with Voorhees' experimental data, these equilibrium parameters are calculated based on Equation (2.2) and the temperature coefficient ($\partial \log P_{O_2} / \partial T$) of whole blood which was tabulated by Zwart *et al.* (1984).

Figures 6.1a - 6.9a show both the total O_2 content change and CO_2 content change in comparison to the predictions generated by both the discrete and continuum models. It can be seen from the left-hand plots of these figures that both models are equally successful in predicting the O_2 transport over the conditions studied, except for the deoxygenation case (Figure 6.9a) where the continuum model under predicts the amount of transport by a substantial fraction. The discrete model consistently predicts more transport than the continuum model. As mentioned previously in Section 4.3.2, for large vessels, the discrete model reduces to the continuum model for describing O_2 transport. Therefore, the difference between the O_2 transfer rates predicted by these models can be partially explained by the fact that $D_{O_2,pl}$ used ($D_{O_2,pl} = 1.60 \times 10^{-5}$

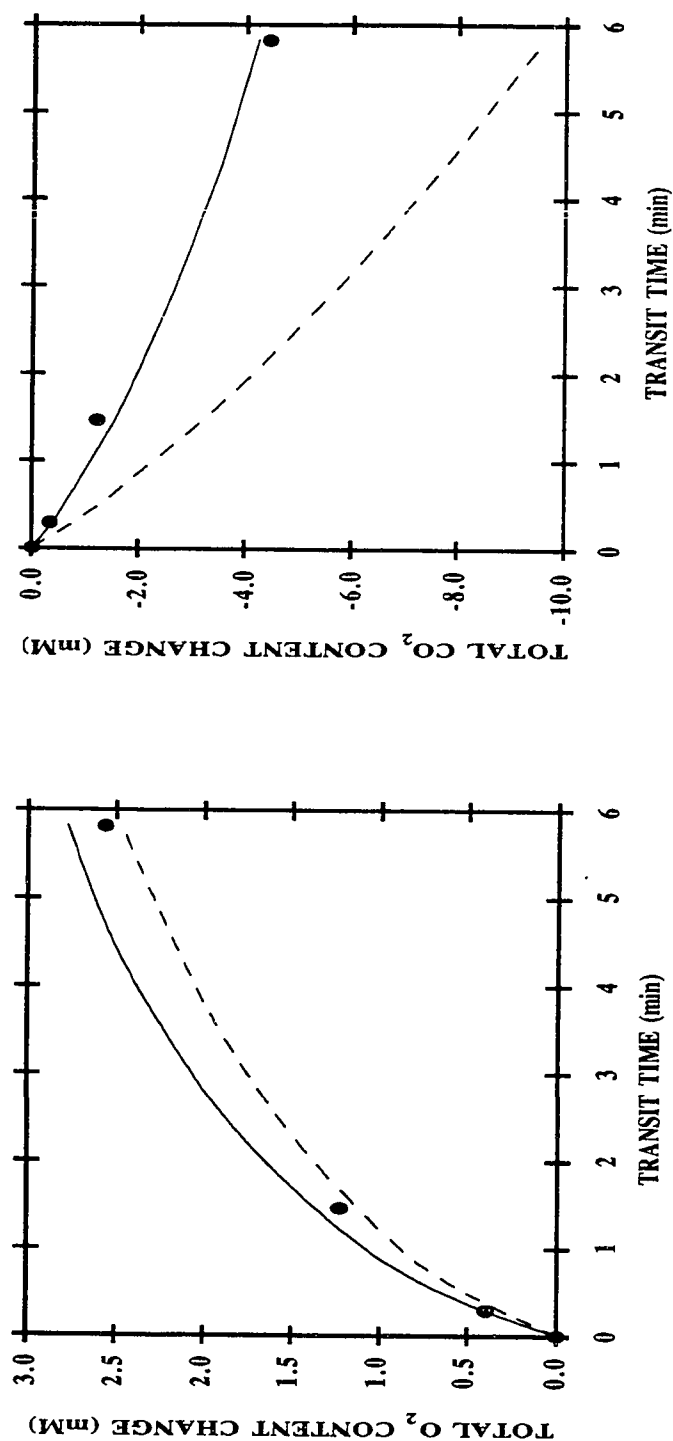


Figure 6.1a: Comparison of models for oxygenation accompanied by CO₂ elimination of RBC suspensions flowing in a 1.47-mm-diameter membrane tube at 22 °C with $H_D=0.42$, $P_{50,in}=10.1$ mmHg, $K_{eq}=257.9$, $\beta=31.8$ mM H⁺/pH, $pH_{pl,in}=7.66$, $P_{O2,in}=17.5$ mmHg (corresponding to 7.08 mM in $[O_2]_{total}$), $P_{CO2,in}=27.9$ mmHg (corresponding to 31.1 mM in $[CO_2]_{total}$), $P_{O2,ext}=718$ mmHg and $P_{CO2,ext}=0$ mmHg. The left panel gives the total O₂ content change as a function of transit time; and the right panel, the total CO₂ content change. Data points: means of experiments from Voorhees (1976). Curves: theoretical simulation curves for the same conditions; (—) the discrete model and (---) the continuum model.

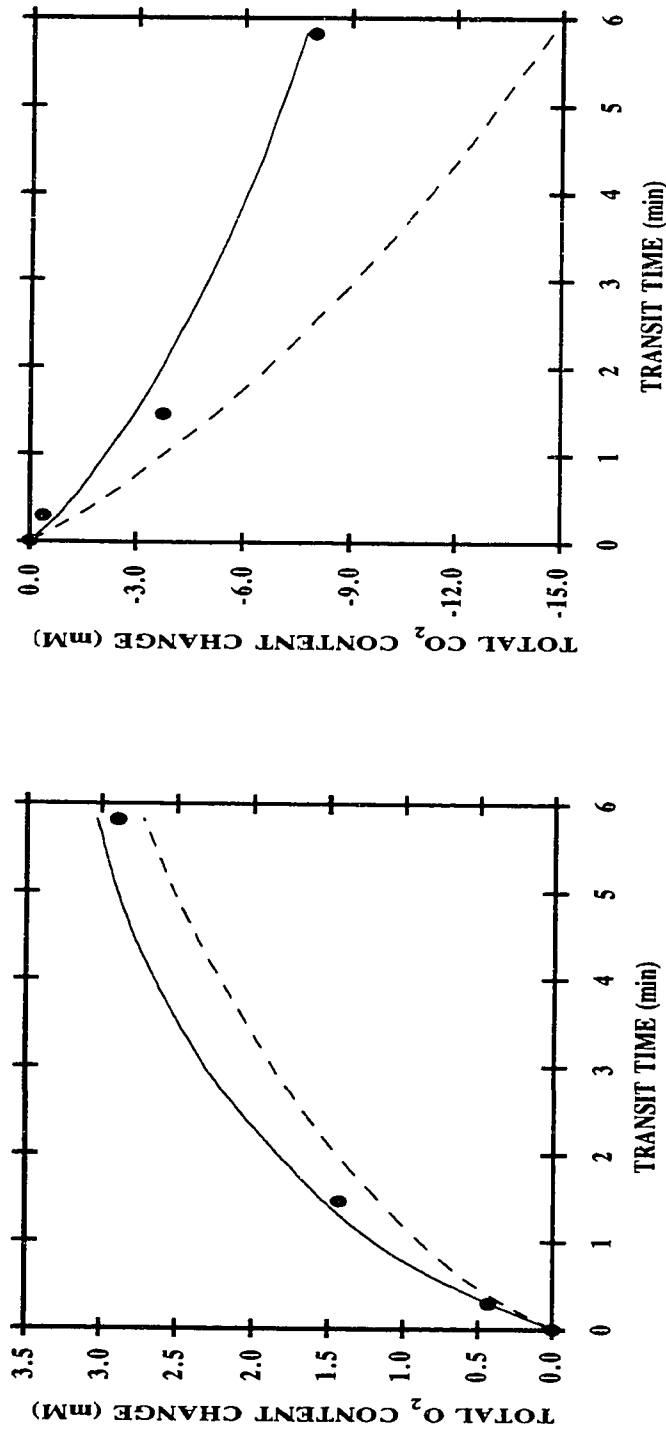


Figure 6.2a: Comparison of models for oxygenation accompanied by CO₂ elimination of RBC suspensions flowing in a 1.47-mm-diameter membrane tube at 22 °C with $H_D=0.46$, $P_{50,in}=13.6$ mmHg, $K_{eq}=105.0$, $\beta=32.6$ mM H⁺/pH, $pH_{pl,in}=7.28$, $P_{O2,in}=18.5$ mmHg (corresponding to 7.08 mM in $[O_2]_{total}$), $P_{CO2,in}=63.3$ mmHg (corresponding to 32.5 mM in $[CO_2]_{total}$), $P_{O2,ext}=718$ mmHg and $P_{CO2,ext}=0$ mmHg. The left panel gives the total O₂ content change as a function of transit time; and the right panel, the total CO₂ content change. Data points: means of experiments from Voorhees (1976). Curves: theoretical simulation curves for the same conditions; (—) the discrete model and (---) the continuum model.

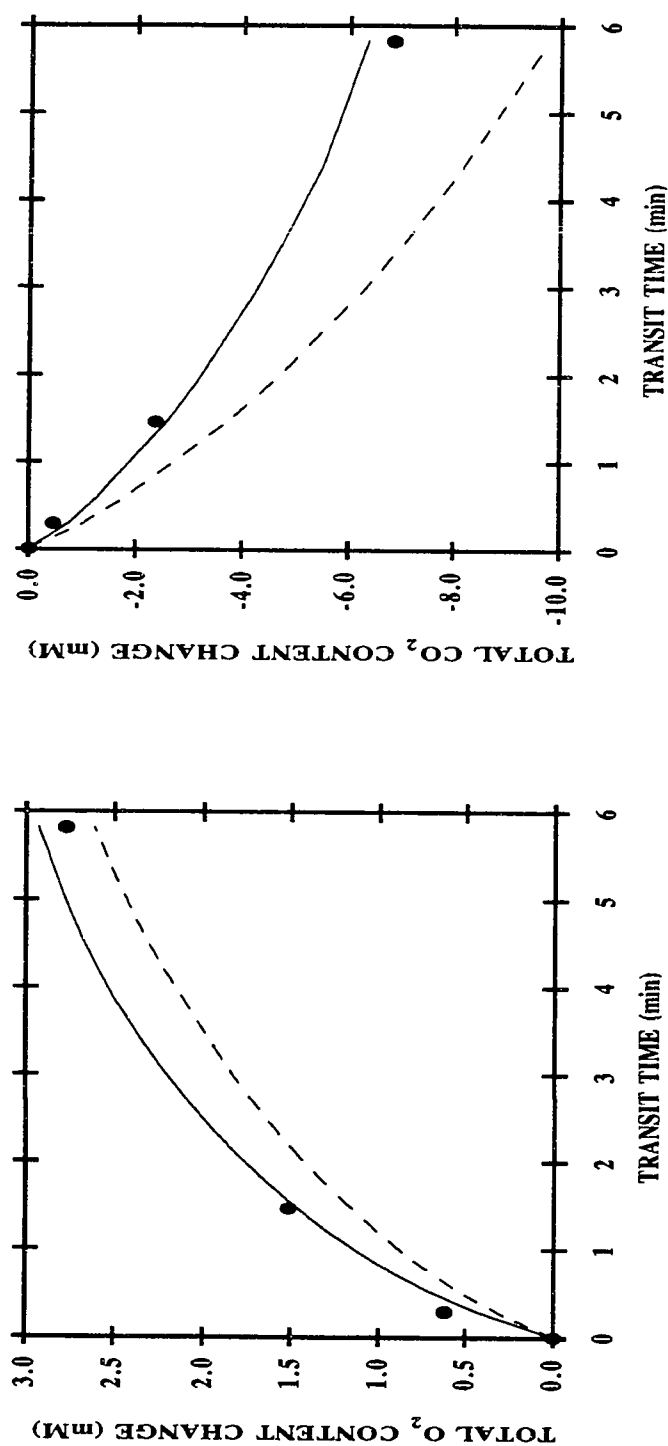


Figure 6.3a: Comparison of models for oxygenation accompanied by CO₂ elimination of RBC suspensions flowing in a 1.47-mm-diameter membrane tube at 22 °C with $H_D=0.43$, $P_{50,in}=17.6$ mmHg, $K_{eq}=22.9$, $\beta=27.8$ mM H⁺/pH, $pH_{p,i,in}=6.98$, $P_{O_2,in}=23.0$ mmHg (corresponding to 6.63 mM in $[O_2]_{total}$), $P_{CO_2,in}=57.7$ mmHg (corresponding to 16.3 mM in $[CO_2]_{total}$), $P_{O_2,ex}=720$ mmHg and $P_{CO_2,ex}=0$ mmHg. The left panel gives the total O₂ content change as a function of transit time; and the right panel, the total CO₂ content change. Data points: means of experiments from Voorhees (1976). Curves: theoretical simulation curves for the same conditions; (—) the discrete model and (---) the continuum model.

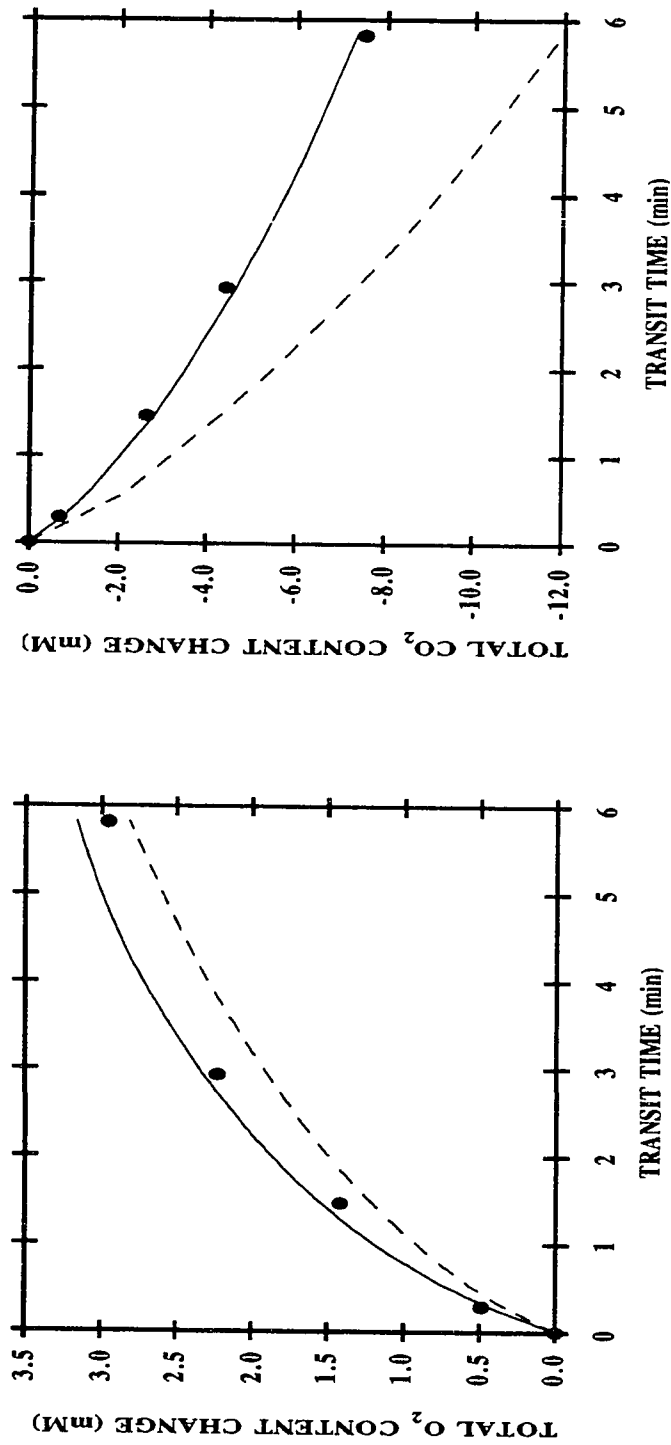


Figure 6.4a: Comparison of models for oxygenation accompanied by CO₂ elimination of RBC suspensions flowing in a 1.47-mm-diameter membrane tube at 27 °C with $H_D=0.42$, $P_{50,in}=19.4$ mmHg, $K_{eq}=54.2$, $\beta=32.1$ mM H⁺/pH, $pH_{pl,in}=7.19$, $P_{O2,in}=25.0$ mmHg (corresponding to 6.04 mM in $[O_2]_{total}$), $P_{CO2,in}=59.6$ mmHg (corresponding to 24.4 mM in $[CO_2]_{total}$), $P_{O2,ex}=698$ mmHg and $P_{CO2,ex}=0$ mmHg. The left panel gives the total O₂ content change as a function of transit time; and the right panel, the total CO₂ content change. Data points: means of experiments from Voorhees (1976). Curves: theoretical simulation curves for the same conditions; (—) the discrete model and (---) the continuum model.

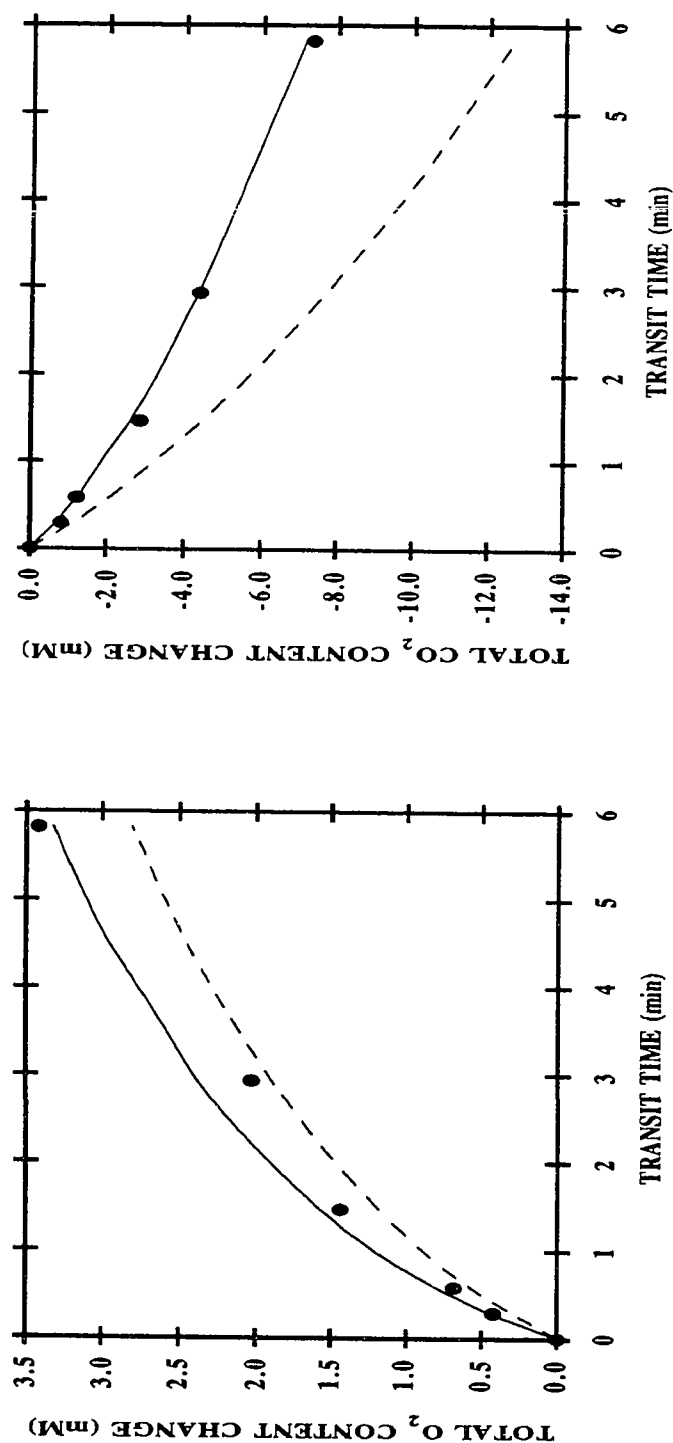


Figure 6.5a: Comparison of models for oxygenation accompanied by CO₂ elimination of RBC suspensions flowing in a 1.47-mm-diameter membrane tube at 24 °C with $H_D=0.57$, $P_{50,i}=15.3$ mmHg, $K_{eq}=58.0$, $\beta=40.2$ mM H⁺/pH, $pH_{p,i}=7.28$, $P_{O2,i}=25.0$ mmHg (corresponding to 8.84 mM in $[O_2]_{total}$), $P_{CO2,i}=51.8$ mmHg (corresponding to 27.5 mM in $[CO_2]_{total}$), $P_{O2,ex}=704$ mmHg and $P_{CO2,ex}=0$ mmHg. The left panel gives the total O₂ content change as a function of transit time; and the right panel, the total CO₂ content change. Data points: means of experiments from Voorhees (1976). Curves: theoretical simulation curves for the same conditions; (—) the discrete model and (- - -) the continuum model.

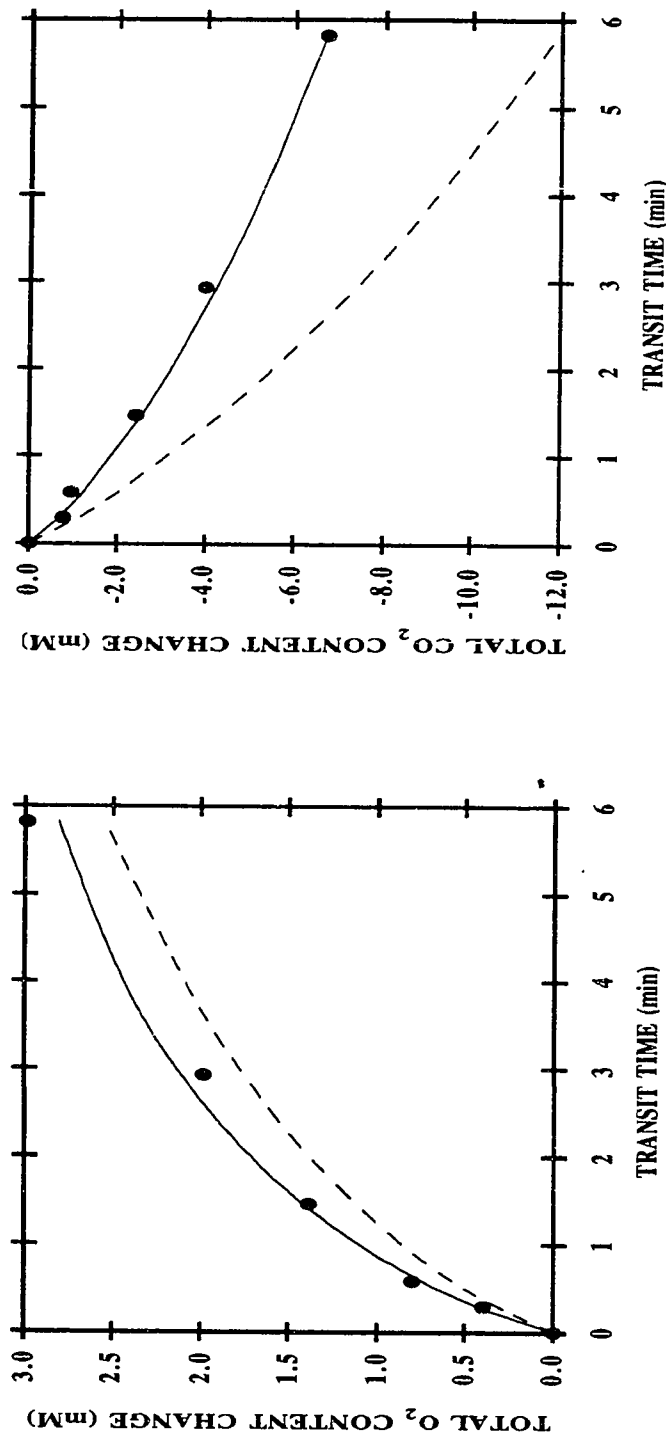


Figure 6.6a: Comparison of models for oxygenation accompanied by CO₂ elimination of RBC suspensions flowing in a 1.47-mm-diameter membrane tube at 25 °C with $H_D=0.43$, $P_{50,in}=16.8$ mmHg, $K_{eq}=46.1$, $\beta=32.4$ mM H⁺/pH, $pH_{p,i,in}=7.23$, $P_{O2,in}=22.7$ mmHg (corresponding to 6.56 mM in $[O_2]_{total}$), $P_{CO2,in}=54.4$ mmHg (corresponding to 23.1 mM in $[CO_2]_{total}$), $P_{O2,ex}=708$ mmHg and $P_{CO2,ex}=0$ mmHg. The left panel gives the total O₂ content change as a function of transit time; and the right panel, the total CO₂ content change. Data points: means of experiments from Voorhees (1976). Curves: theoretical simulation curves for the same conditions; (—) the discrete model and (---) the continuum model.

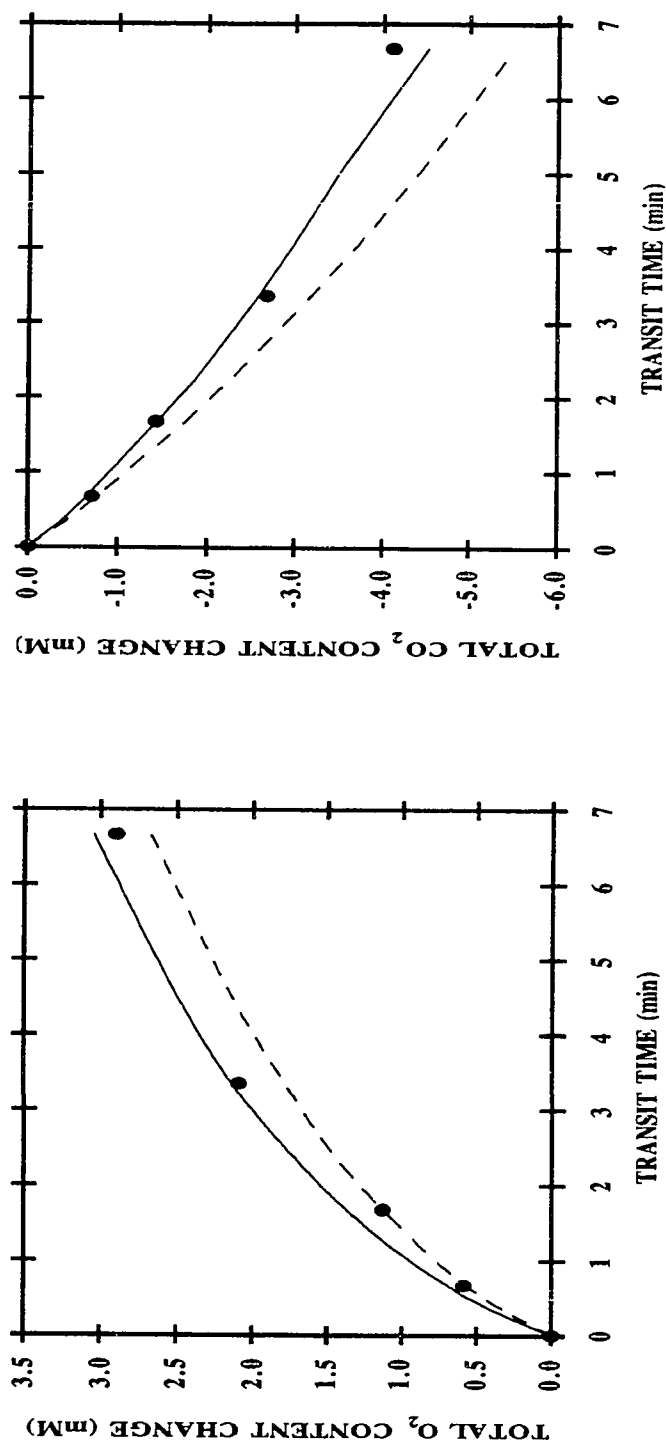


Figure 6.7a: Comparison of models for oxygenation accompanied by CO₂ elimination of RBC suspensions flowing in a 1.57-mm-diameter membrane tube at 26 °C with $H_D=0.43$, $P_{50,in}=16.7$ mmHg, $K_{eq}=45.7$, $\beta=31.8$ mM H⁺/pH, $pH_{pl,in}=7.32$, $P_{O_2,in}=22.4$ mmHg (corresponding to 6.39 mM in $[O_2]_{total}$), $P_{CO_2,in}=40.9$ mmHg (corresponding to 19.2 mM in $[CO_2]_{total}$), $P_{O_2,ex}=707$ mmHg and $P_{CO_2,ex}=0$ mmHg. The left panel gives the total O₂ content change as a function of transit time; and the right panel, the total CO₂ content change. Data points: means of experiments from Voorhees (1976). Curves: theoretical simulation curves for the same conditions; (—) the discrete model and (---) the continuum model.

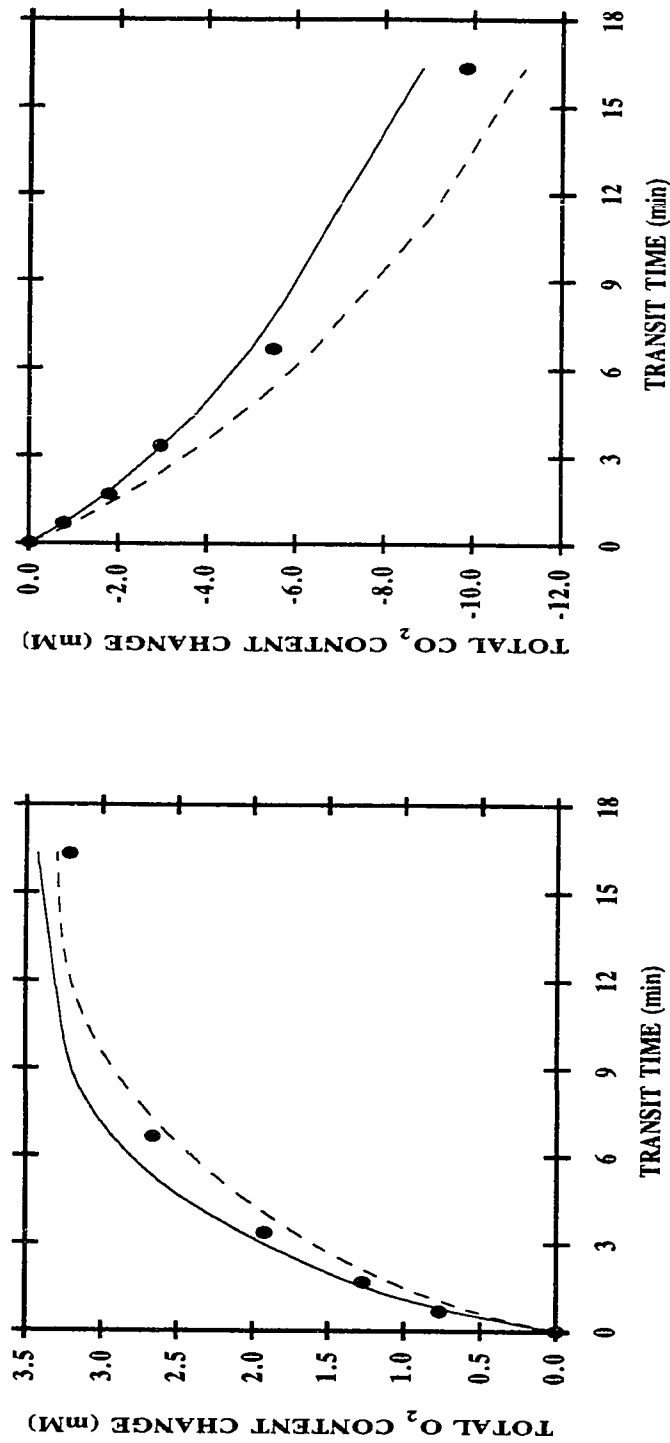


Figure 6.8a: Comparison of models for oxygenation accompanied by CO₂ elimination of RBC suspensions flowing in a 1.57-mm-diameter membrane tube at 25 °C with $H_D=0.43$, $P_{50,in}=20.6$ mmHg, $K_{eq}=24.2$, $\beta=31.3$ mM H⁺/pH, $pH_{pl,in}=6.99$, $P_{O_2,in}=32.0$ mmHg (corresponding to 6.57 mM in $[O_2]_{total}$), $P_{CO_2,in}=52.0$ mmHg (corresponding to 17.1 mM in $[CO_2]_{total}$), $P_{O_2,ex}=709$ mmHg and $P_{CO_2,ex}=0$ mmHg. The left panel gives the total O₂ content change as a function of transit time; and the right panel, the total CO₂ content change. Data points: means of experiments from Voorhees (1976). Curves: theoretical simulation curves for the same conditions; (—) the discrete model and (---) the continuum model.

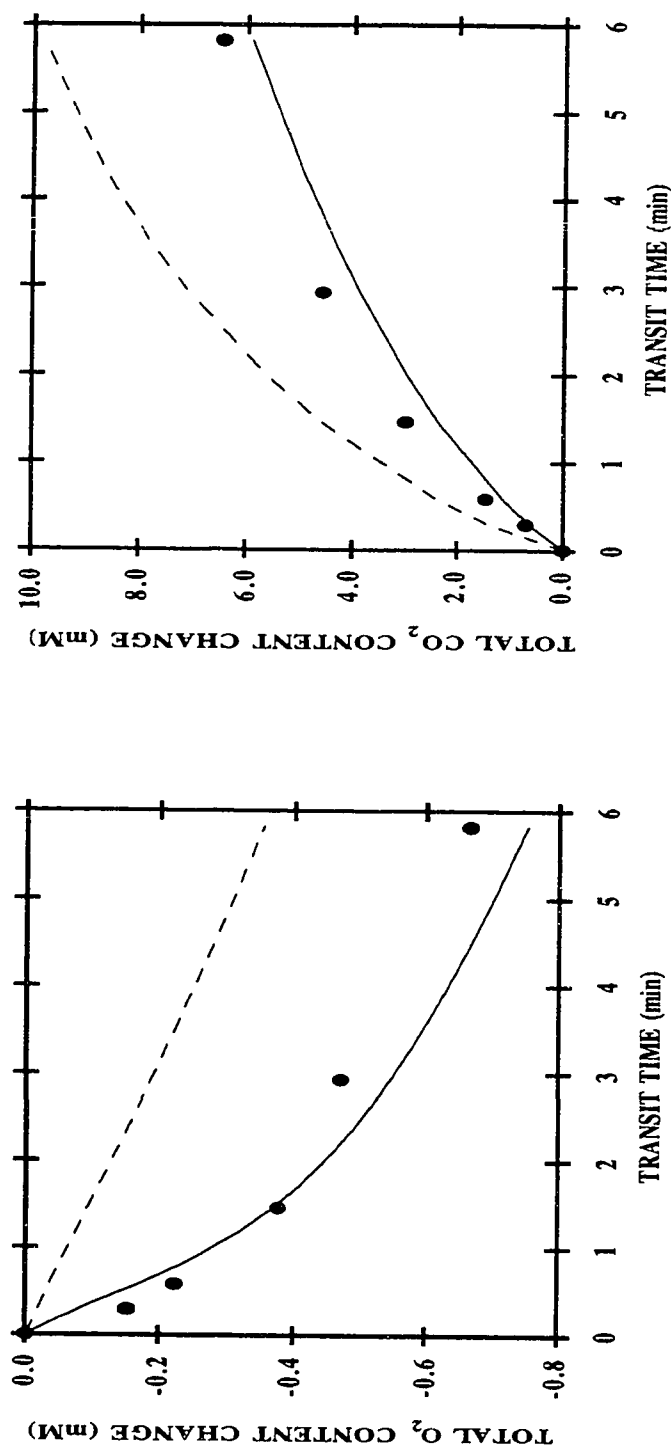


Figure 6.9a: Comparison of models for deoxygenation accompanied by CO₂ uptake of RBC suspensions flowing in a 1.47-mm-diameter membrane tube at 25 °C with $H_D=0.43$, $P_{50,i}=17.6$ mmHg, $K_{eq}=40.3$, $\beta=31.5$ mM H⁺/pH, $pH_{pl,i}=7.18$, $P_{O2,i}=22.5$ mmHg (corresponding to 6.38 mM in $[O_2]_{total}$), $P_{CO2,i}=53.9$ mmHg (corresponding to 21.3 mM in $[CO_2]_{total}$), $P_{O2,ex}=0$ mmHg and $P_{CO2,ex}=115$ mmHg. The left panel gives the total O₂ content change as a function of transit time; and the right panel, the total CO₂ content change. Data points: means of experiments from Voorhees (1976). Curves: theoretical simulation curves for the same conditions; (—) the discrete model and (---) the continuum model.

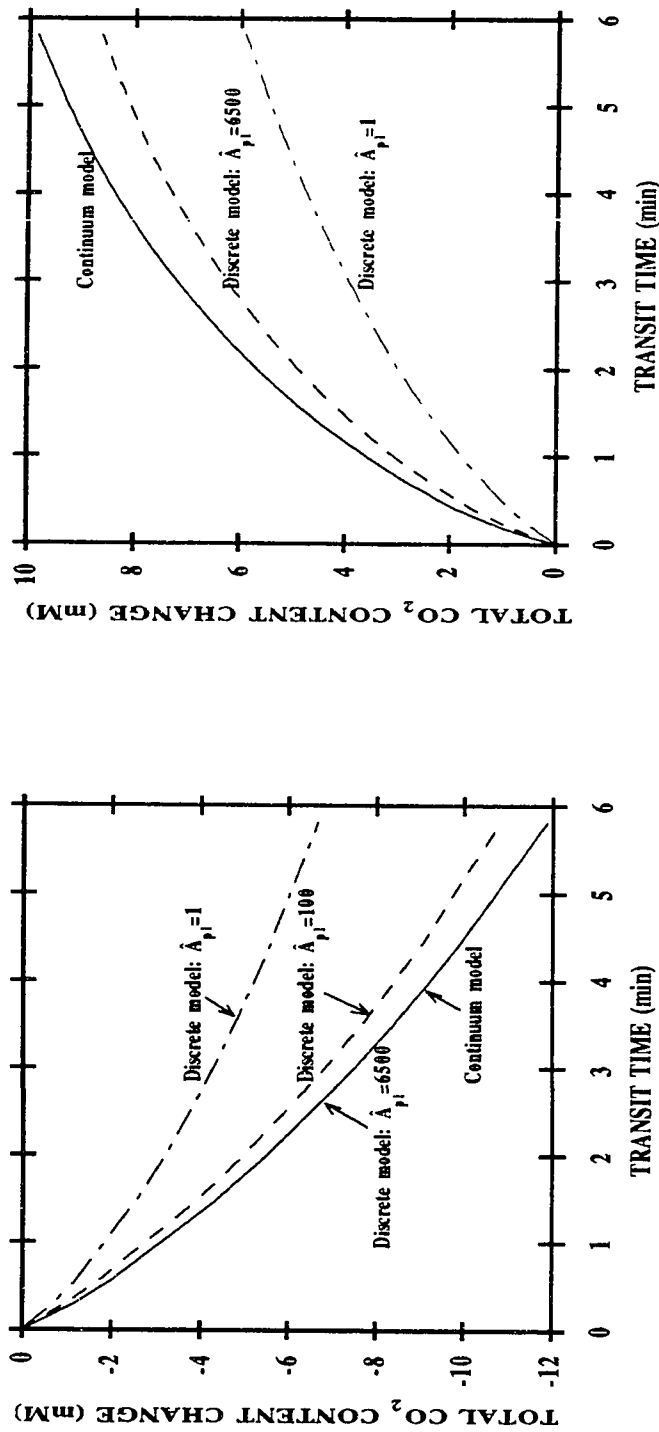


Figure 6.10: Comparison of the $\Delta[CO_2]_{total}$ results calculated by the continuum (CM) and discrete (DM) models for RBC suspensions flowing in a 1.47-mm-diameter membrane tube with discharge hematocrit of 42% at 25 °C. The left panel gives the comparison for an oxygenation (and CO_2 elimination) case: $P_{50,in}=16.8$ mmHg, $K_{eq}=46.1$, $\beta=32.4$ mM H^+/pH , $pH_{pl,in}=7.23$, $P_{O2,in}=22.7$ mmHg, $P_{CO2,in}=54.4$ mmHg, $P_{O2,ext}=708$ mmHg and $P_{CO2,ext}=0$ mmHg. Curves: theoretical simulation of the situations; (—) both CM and DM via $\hat{A}_{pl}=6500$, (---) DM via $\hat{A}_{pl}=100$, (---) DM via $\hat{A}_{pl}=1$. The right panel gives the comparison for a deoxygenation (and CO_2 uptake) case: $P_{50,in}=17.6$ mmHg, $K_{eq}=40.3$, $\beta=31.5$ mM H^+/pH , $pH_{pl,in}=7.18$, $P_{O2,in}=22.5$ mmHg, $P_{CO2,in}=53.9$ mmHg, $P_{O2,ext}=0$ mmHg and $P_{CO2,ext}=115$ mmHg. Curves: theoretical simulation of the situations; (—) CM, (---) DM via $\hat{A}_{pl}=6500$, (---) DM via $\hat{A}_{pl}=1$.

cm²/sec @ $T=25$ °C and $H_D=42\%$; discrete model) is higher than the value of D_{O_2} ($D_{O_2,pl}=1.25 \times 10^{-5}$ cm²/sec @ $T=25$ °C and $H_D=42\%$; continuum model). Another cause contributing to this difference is due to the fact that the Bohr effect is taken into consideration in the discrete model but not in the continuum model. For the oxygenation runs (Figures 6.1a - 6.8a), differences of no more than 0.51 mM in $\Delta[O_2]_{total}$ were observed between simulation results generated by the two models; this difference amounts to $\approx 15\%$ of the change in $[O_2]_{total}$. However, for the deoxygenation case (Figure 6.9a), the continuum model predicts far less transport than the discrete model; and the maximum difference between the models is 0.41 mM which amounts to $\approx 53\%$ of the change in $[O_2]_{total}$. The explanation of this observation is that the Bohr effect plays a more important role during deoxygenation run (more details in Section 6.2.2a). The maximum deviations between the experimental data and the theoretical curves generated by the discrete and continuum models are 0.35 mM and 0.71 mM in $\Delta[O_2]_{total}$, respectively. The algebraic average deviations for any one curve generated by the discrete and continuum models do not exceed 0.15 mM and 0.25 mM in $\Delta[O_2]_{total}$, respectively.

More importantly, from the right-hand plots of Figures 6.1a - 6.9a, it is clear that the discrete model represents an improvement in accuracy for predicting CO₂ transport over the continuum model. In all the cases, the continuum model predicts more transport than experimentally observed. The maximum deviations between the experimental data and the theoretical curves generated by the discrete and continuum models are 0.8 mM and 6.7 mM in $\Delta[CO_2]_{total}$, respectively. The algebraic average deviation from the experimental data for any one curve generated by the discrete and continuum models do not exceed 0.37 mM and 2.4 mM in $\Delta[CO_2]_{total}$, respectively.

A major factor in the success of the discrete model for predicting CO₂ transfer is due to the incorporation of the slow CO₂ hydration/ dehydration reactions in the

plasma. This conclusion is substantiated and demonstrated by Figure 6.10 where upon setting $\hat{A}_{pl}=6500$ the amount of CO_2 transfer predicted by the discrete model approaches that predicted by the continuum model for both oxygenation and deoxygenation cases. $\hat{A}_{pl}=6500$ represents the situation where carbonic anhydrase activity equivalent to that of the RBC interior is available to the plasma. For these runs, differences ranging from 1.0 to 7.0 mM in $\Delta[CO_2]_{total}$ were observed between simulation results generated by the two models at transit time of ≈ 5.8 min.

Figures 6.1b - 6.9b present the mixed mean values of P_{O_2} , S , P_{CO_2} and intracellular $[HbCO_2]$ for three different flow rates under the experimental conditions of runs 1 to 9; and Figures 6.1c - 6.9c show that for intra- and extracellular pH , $[HCO_3^-]_{rbc}$ and $[HCO_3^-]_{pl}$. As was expected the larger the flow rate, the smaller the change in these quantities. These figures may be useful for calculations of membrane oxygenator performance so as to ensure proper blood oxygenation and CO_2 stripping. Sizing of the oxygenator is important with respect to minimization of priming volume as well as with respect to ensurance of proper O_2 and CO_2 transfer. Over-design of the oxygenator brings blood oxygenation to the 95-100% O_2 saturation range. However, along with the above effect, over design also leads to the possibilities of blood P_{O_2} becoming intolerably great and excessive CO_2 removal. Intolerably high P_{O_2} raises the concern with oxygen toxicity; and improper removal of CO_2 is undesirable because of the associated disturbance of acid/base balance. For illustrations, Figures 6.5b and 6.5c show that at flow rate of 0.52 ml/min 95% O_2 saturation, which is normal arterial level, is reached at about $z=110$ cm. The corresponding P_{O_2} of 160 mmHg is high, and this is due to the high $P_{O_2,ext}$ used in the study. On the other hand, the normal arterial level of CO_2 tension is about 40 mmHg and plasma pH is about 7.4. These values are reached at $z=80$ cm. For an existing equipment, these results would mean

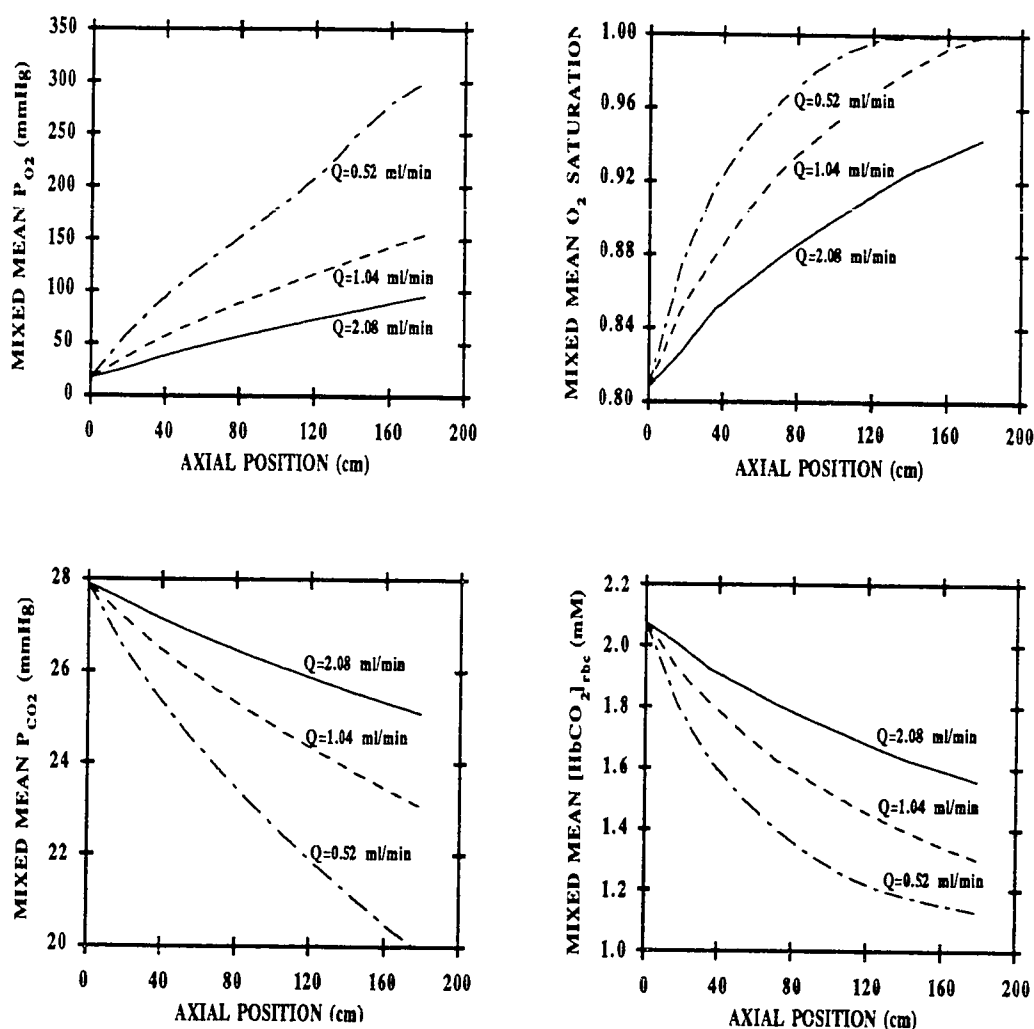


Figure 6.1b: Mixed mean values of O_2 tension, O_2 saturation, CO_2 tension and intracellular $HbCO_2$ concentration at different axial positions along the membrane oxygenator. Experimental conditions: I.D.=1.47 mm, O.D.=1.95 mm, $T=22$ °C, $H_D=0.42$, $P_{50,in}=10.1$ mmHg, $K_{eq}=257.9$, $\beta=31.8$ mM H^+/pH , $pH_{pl,in}=7.66$, $P_{O_2,in}=17.5$ mmHg, $P_{CO_2,in}=27.9$ mmHg, $P_{O_2,ext}=718$ mmHg and $P_{CO_2,ext}=0$ mmHg. Simulation curves: generated via the discrete model; (—) $Q=2.08$ ml/min, (---) $Q=1.04$ ml/min, (— · —) $Q=0.52$ ml/min.

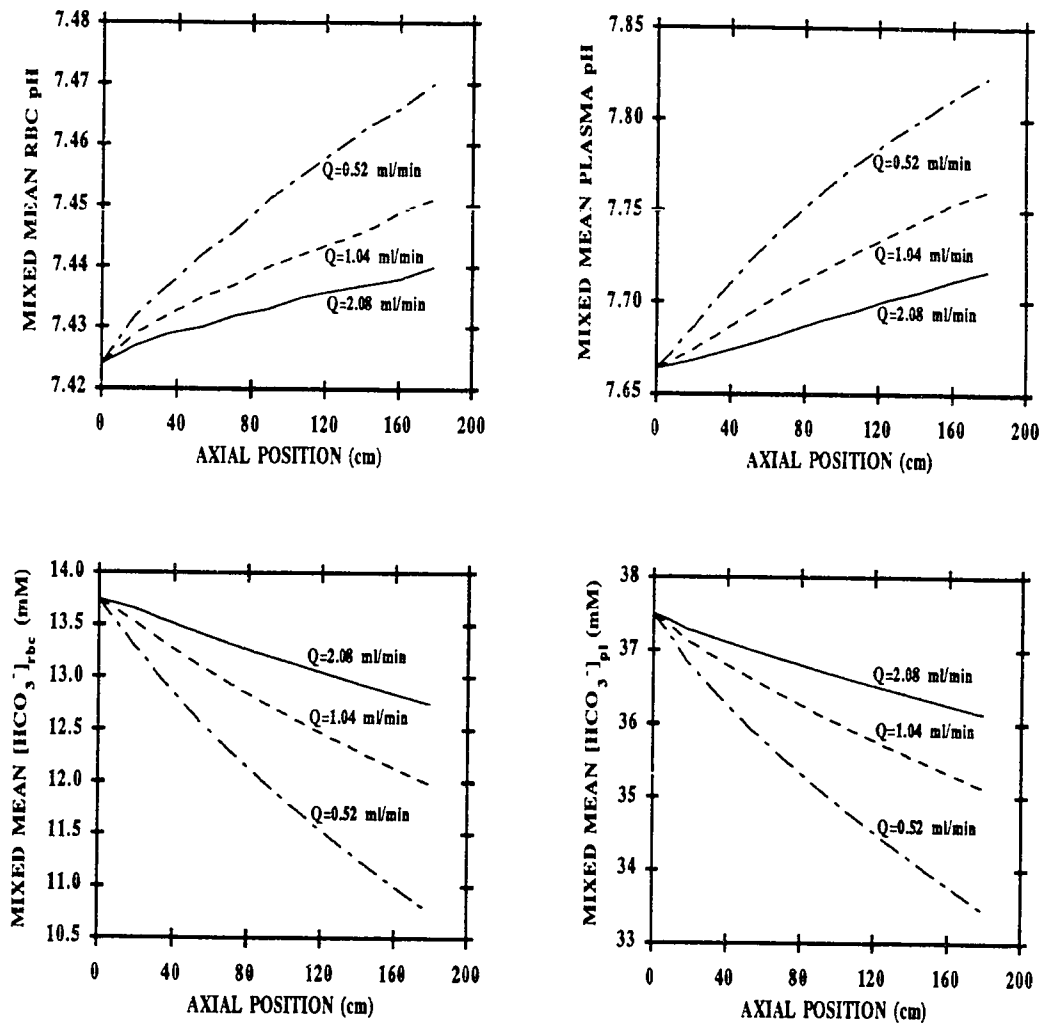


Figure 6.1c: Mixed mean values of intra- and extracellular pH and intra- and extracellular HCO_3^- concentrations at different axial positions along the membrane oxygenator. Experimental conditions: I.D.=1.47 mm, O.D.=1.95 mm, $T=22$ °C, $H_D=0.42$, $P_{50,in}=10.1$ mmHg, $K_{eq}=257.9$, $\beta=31.8$ mM H^+/pH , $pH_{pl,in}=7.66$, $P_{O2,in}=17.5$ mmHg, $P_{CO2,in}=27.9$ mmHg, $P_{O2,ex}=718$ mmHg and $P_{CO2,ex}=0$ mmHg. Simulation curves: generated via the discrete model; (—) $Q=2.08$ ml/min, (- - - -) $Q=1.04$ ml/min, (- - -) $Q=0.52$ ml/min.

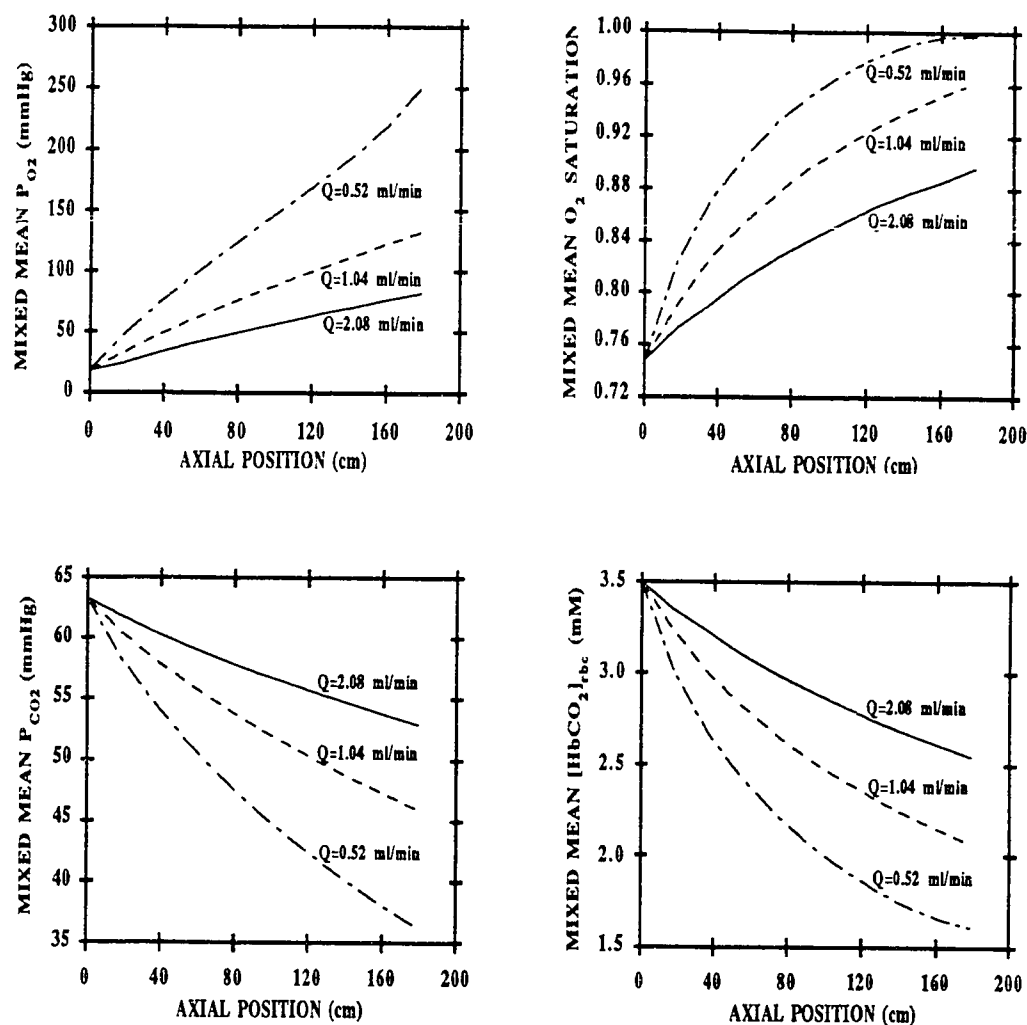


Figure 6.2b: Mixed mean values of O_2 tension, O_2 saturation, CO_2 tension and intracellular $HbCO_2$ concentration at different axial positions along the membrane oxygenator. Experimental conditions: I.D.=1.47 mm, O.D.=1.95 mm, $T=22$ °C, $H_D=0.46$, $P_{50,in}=13.6$ mmHg, $K_{eq}=105.0$, $\beta=32.6$ mM H^+/pH , $pH_{pl,in}=7.28$, $P_{O_2,in}=18.5$ mmHg, $P_{CO_2,in}=63.3$ mmHg, $P_{O_2,ext}=718$ mmHg and $P_{CO_2,ext}=0$ mmHg. Simulation curves: generated via the discrete model; (—) $Q=2.08$ ml/min, (---) $Q=1.04$ ml/min, (— —) $Q=0.52$ ml/min.

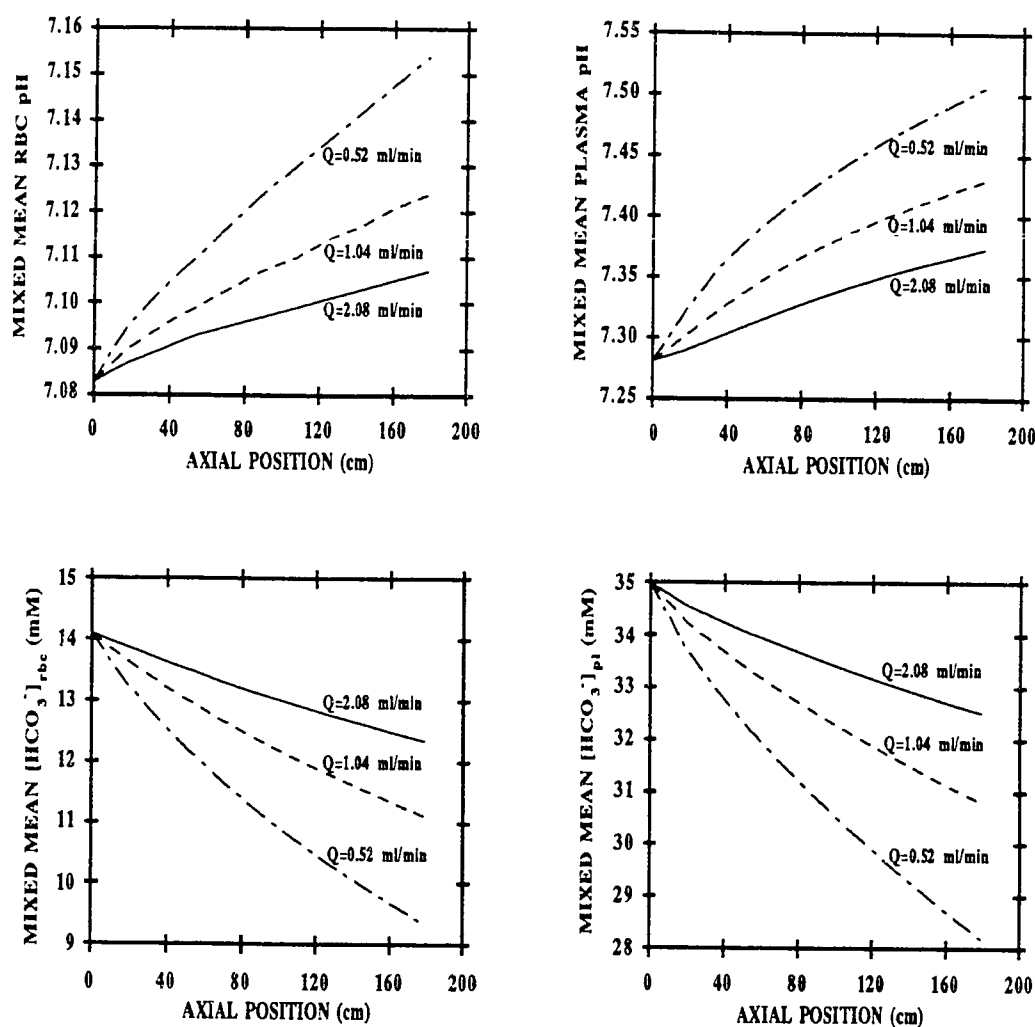


Figure 6.2c: Mixed mean values of intra- and extracellular pH and intra- and extracellular HCO_3^- concentrations at different axial positions along the membrane oxygenator. Experimental conditions: I.D.=1.47 mm, O.D.=1.95 mm, $T=22$ °C, $H_D=0.46$, $P_{50,in}=13.6$ mmHg, $K_{eq}=105.0$, $\beta=32.6$ mM H^+/pH , $pH_{pl,in}=7.28$, $P_{O2,in}=18.5$ mmHg, $P_{CO2,in}=63.3$ mmHg, $P_{O2,ext}=718$ mmHg and $P_{CO2,ext}=0$ mmHg. Simulation curves: generated via the discrete model; (—) $Q=2.08$ ml/min, (- - -) $Q=1.04$ ml/min, (- . -) $Q=0.52$ ml/min.

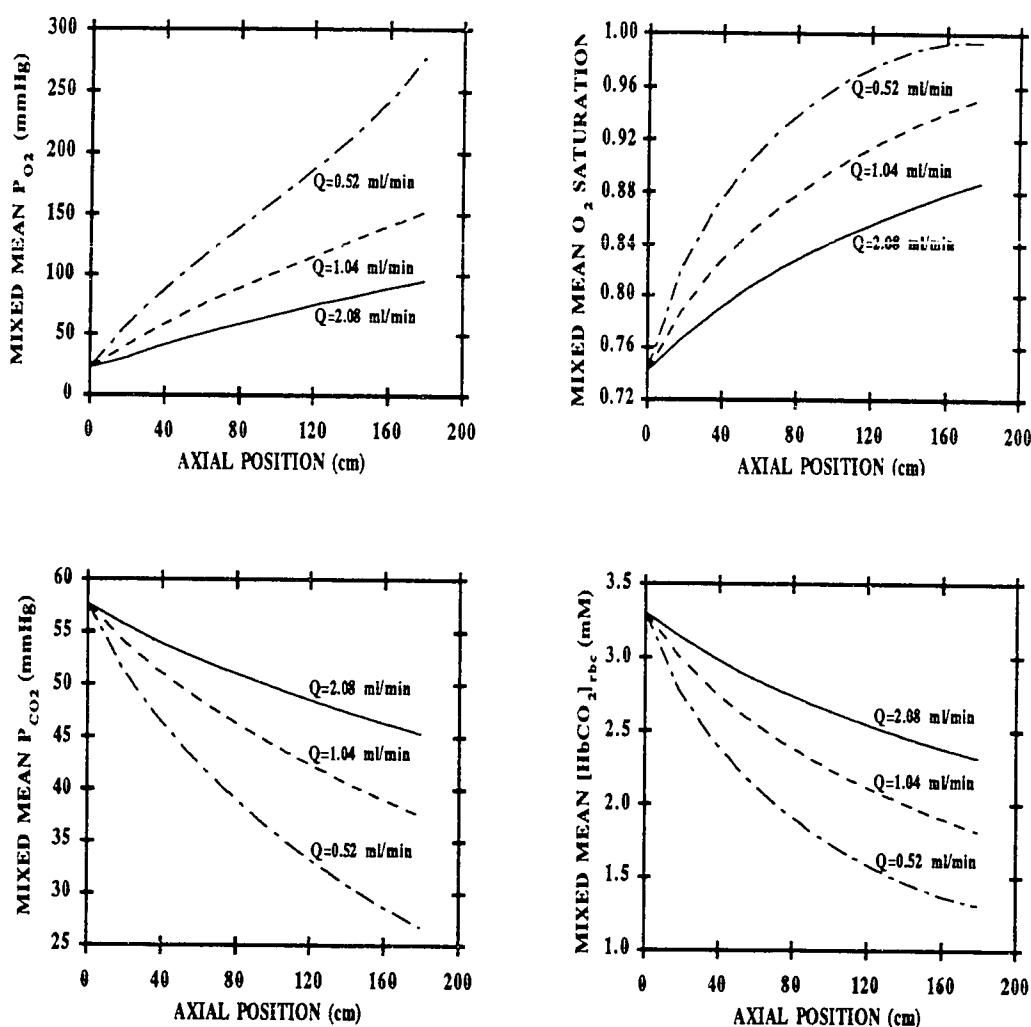


Figure 6.3b: Mixed mean values of O_2 tension, O_2 saturation, CO_2 tension and intracellular $HbCO_2$ concentration at different axial positions along the membrane oxygenator. Experimental conditions: I.D.=1.47 mm, O.D.=1.95 mm, $T=22$ °C, $H_D=0.43$, $P_{50,in}=17.6$ mmHg, $K_{eq}=22.9$, $\beta=27.8$ mM H^+/pH , $pH_{pl,in}=6.98$, $P_{O2,in}=23.0$ mmHg, $P_{CO2,in}=57.7$ mmHg, $P_{O2,ext}=720$ mmHg and $P_{CO2,ext}=0$ mmHg. Simulation curves: generated via the discrete model; (—) $Q=2.08$ ml/min, (- - - -) $Q=1.04$ ml/min, (- - -) $Q=0.52$ ml/min.

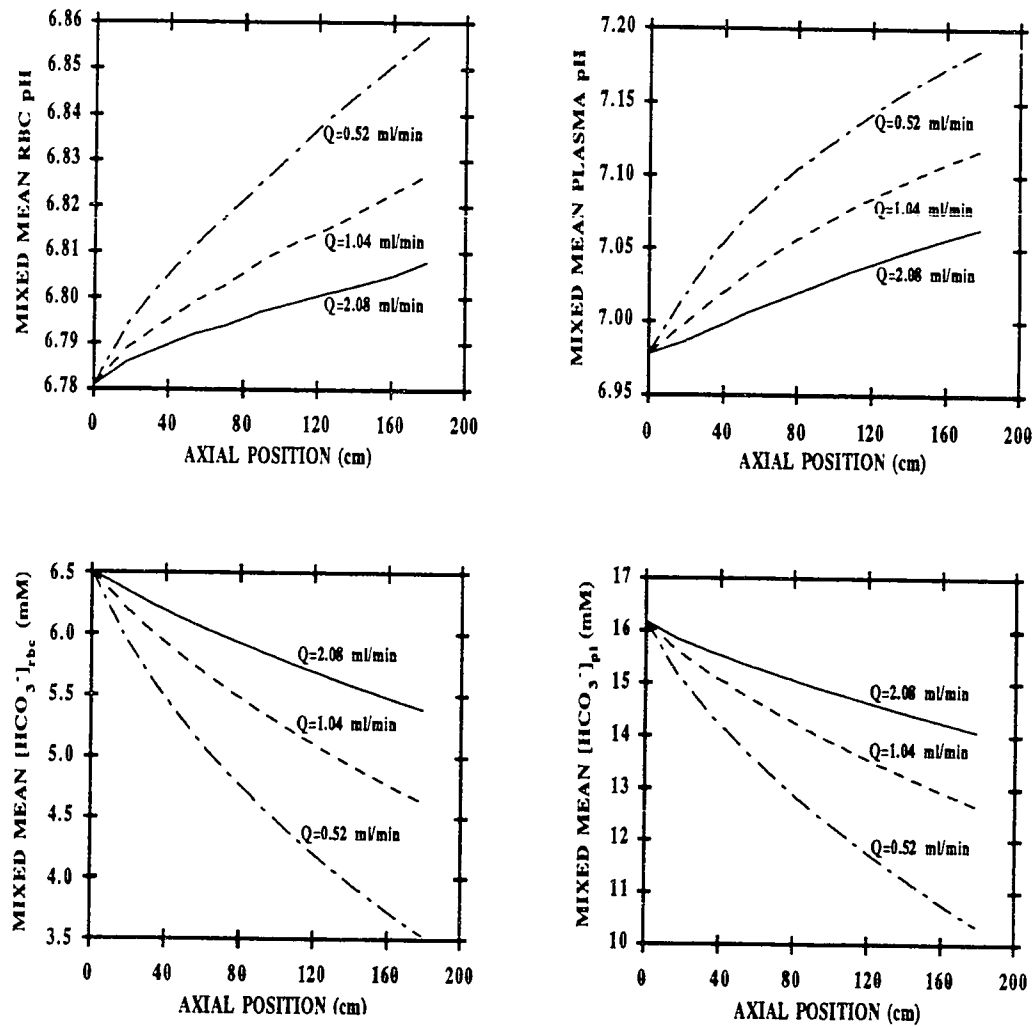


Figure 6.3c: Mixed mean values of intra- and extracellular pH and intra- and extracellular HCO_3^- concentrations at different axial positions along the membrane oxygenator. Experimental conditions: I.D.=1.47 mm, O.D.=1.95 mm, $T=22$ °C, $H_D=0.43$, $P_{50,in}=17.6$ mmHg, $K_{eq}=22.9$, $\beta=27.8$ mM H^+/pH , $pH_{pl,in}=6.98$, $P_{O2,in}=23.0$ mmHg, $P_{CO2,in}=57.7$ mmHg, $P_{O2,ext}=720$ mmHg and $P_{CO2,ext}=0$ mmHg. Simulation curves: generated via the discrete model; (—) $Q=2.08$ ml/min, (---) $Q=1.04$ ml/min, (— - —) $Q=0.52$ ml/min.

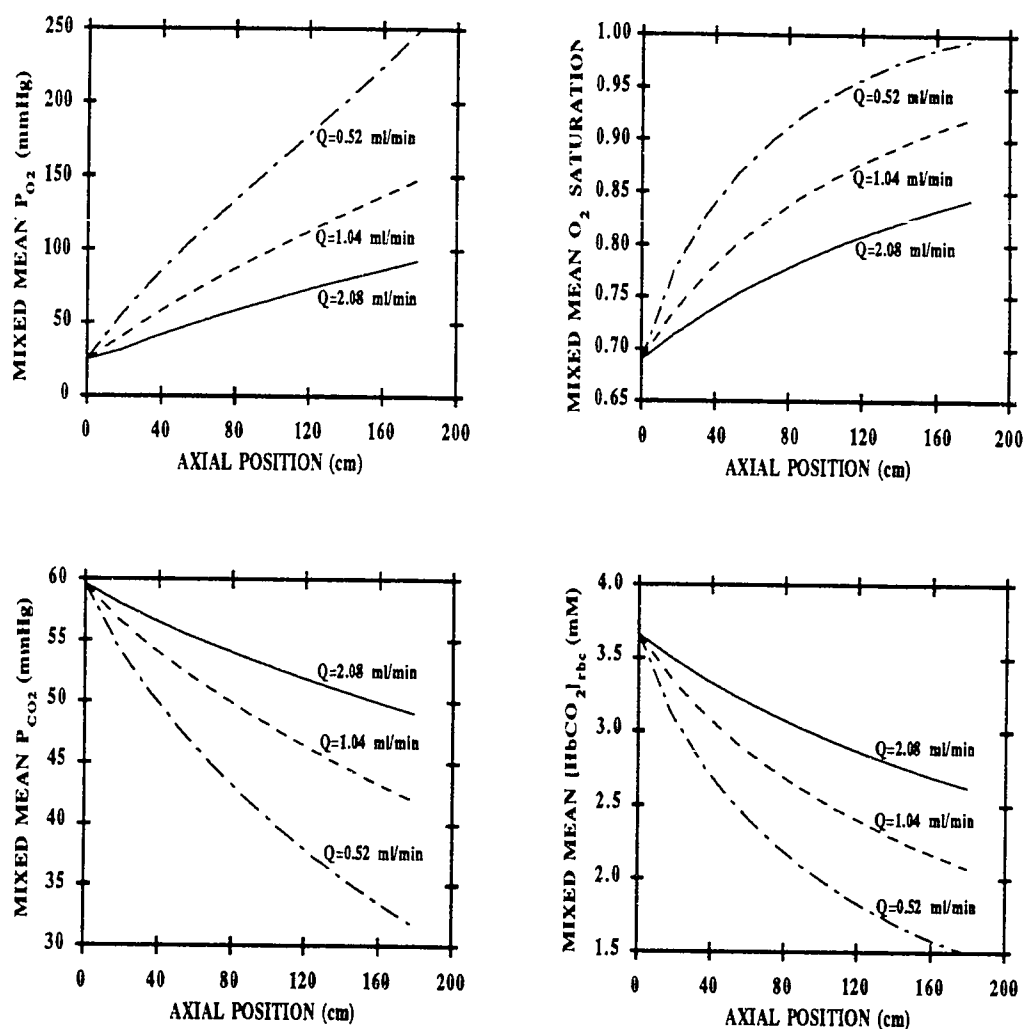


Figure 6.4b: Mixed mean values of O_2 tension, O_2 saturation, CO_2 tension and intracellular $HbCO_2$ concentration at different axial positions along the membrane oxygenator. Experimental conditions: I.D.=1.47 mm, O.D.=1.95 mm, $T=27^\circ C$, $H_D=0.42$, $P_{50,in}=19.4$ mmHg, $K_{eq}=54.2$, $\beta=32.1$ mM H^+/pH , $pH_{pl,in}=7.19$, $P_{O_2,in}=25.0$ mmHg, $P_{CO_2,in}=59.6$ mmHg, $P_{O_2,ext}=698$ mmHg and $P_{CO_2,ext}=0$ mmHg. Simulation curves: generated via the discrete model; (—) $Q=2.08$ ml/min, (---) $Q=1.04$ ml/min, (— · —) $Q=0.52$ ml/min.

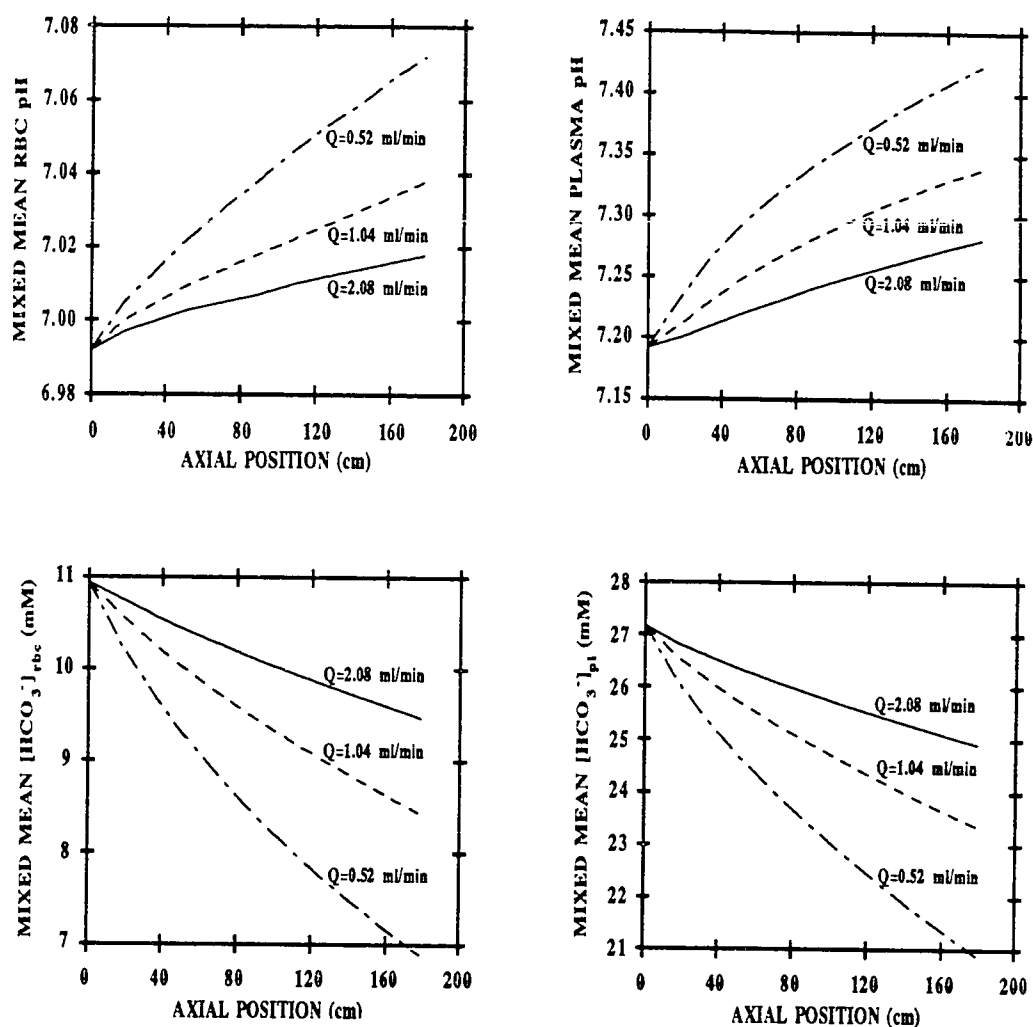


Figure 6.4c: Mixed mean values of intra- and extracellular pH and intra- and extracellular HCO_3^- concentrations at different axial positions along the membrane oxygenator. Experimental conditions: I.D.=1.47 mm, O.D.=1.95 mm, $T=27^\circ\text{C}$, $H_D=0.42$, $P_{50,in}=19.4$ mmHg, $K_{eq}=54.2$, $\beta=32.1$ mM H^+/pH , $pH_{pl,in}=7.19$, $P_{O2,in}=25.0$ mmHg, $P_{CO2,in}=59.6$ mmHg, $P_{O2,ext}=698$ mmHg and $P_{CO2,ext}=0$ mmHg. Simulation curves: generated via the discrete model; (—) $Q=2.08$ ml/min, (----) $Q=1.04$ ml/min, (— · —) $Q=0.52$ ml/min.

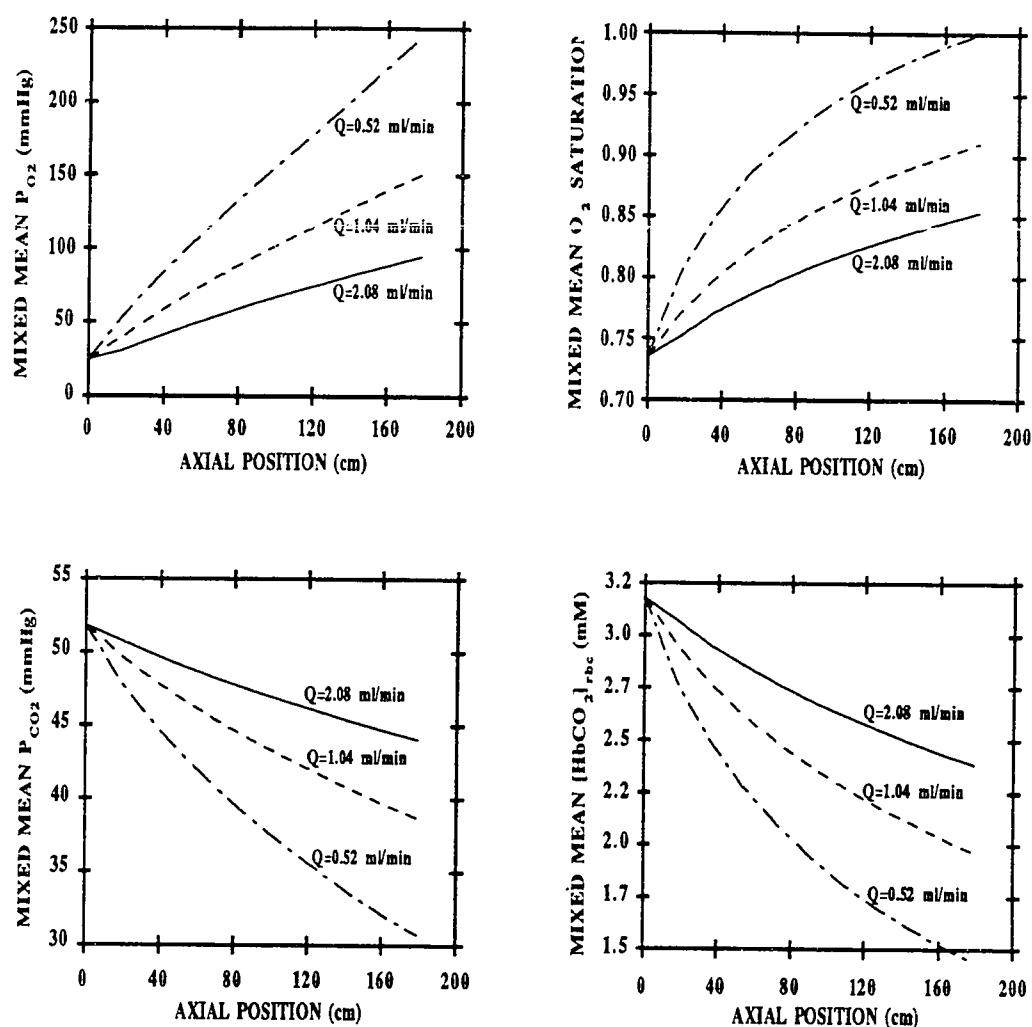


Figure 6.5b: Mixed mean values of O_2 tension, O_2 saturation, CO_2 tension and intracellular $HbCO_2$ concentration at different axial positions along the membrane oxygenator. Experimental conditions: I.D.=1.47 mm, O.D.=1.95 mm, $T=24$ °C, $H_D=0.57$, $P_{50,in}=15.3$ mmHg, $K_{eq}=58.0$, $\beta=40.2$ mM H^+/pH , $pH_{pl,in}=7.28$, $P_{O2,in}=25.0$ mmHg, $P_{CO2,in}=51.8$ mmHg, $P_{O2,ext}=704$ mmHg and $P_{CO2,ext}=0$ mmHg. Simulation curves: generated via the discrete model; (—) $Q=2.08$ ml/min, (- - -) $Q=1.04$ ml/min, (- - -) $Q=0.52$ ml/min.

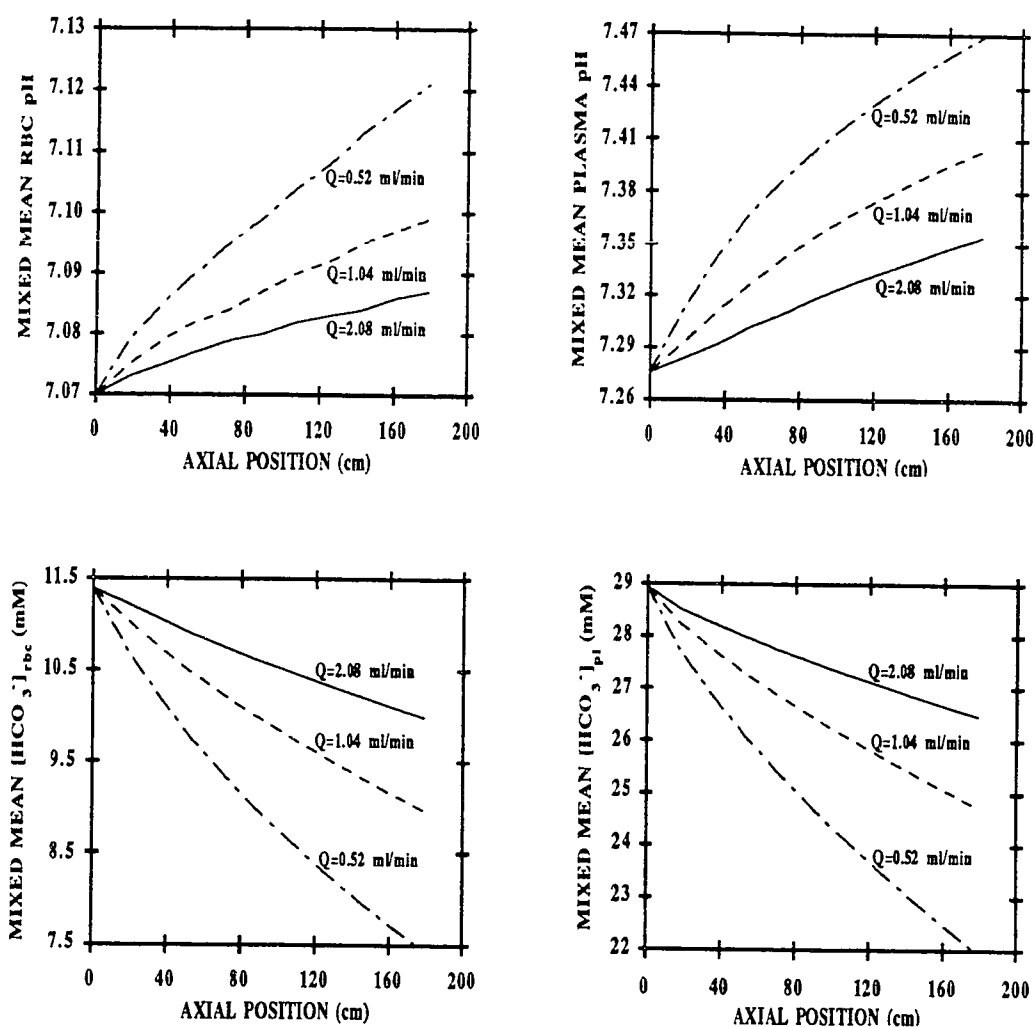


Figure 6.5c: Mixed mean values of intra- and extracellular pH and intra- and extracellular HCO_3^- concentrations at different axial positions along the membrane oxygenator. Experimental conditions: I.D.=1.47 mm, O.D.=1.95 mm, $T=24$ °C, $H_D=0.57$, $P_{50,in}=15.3$ mmHg, $K_{eq}=58.0$, $\beta=40.2$ mM H^+/pH , $pH_{pl,in}=7.28$, $P_{O2,in}=25.0$ mmHg, $P_{CO2,in}=51.8$ mmHg, $P_{O2,ext}=704$ mmHg and $P_{CO2,ext}=0$ mmHg. Simulation curves: generated via the discrete model; (—) $Q=2.08$ ml/min, (- - - -) $Q=1.04$ ml/min, (— - —) $Q=0.52$ ml/min.

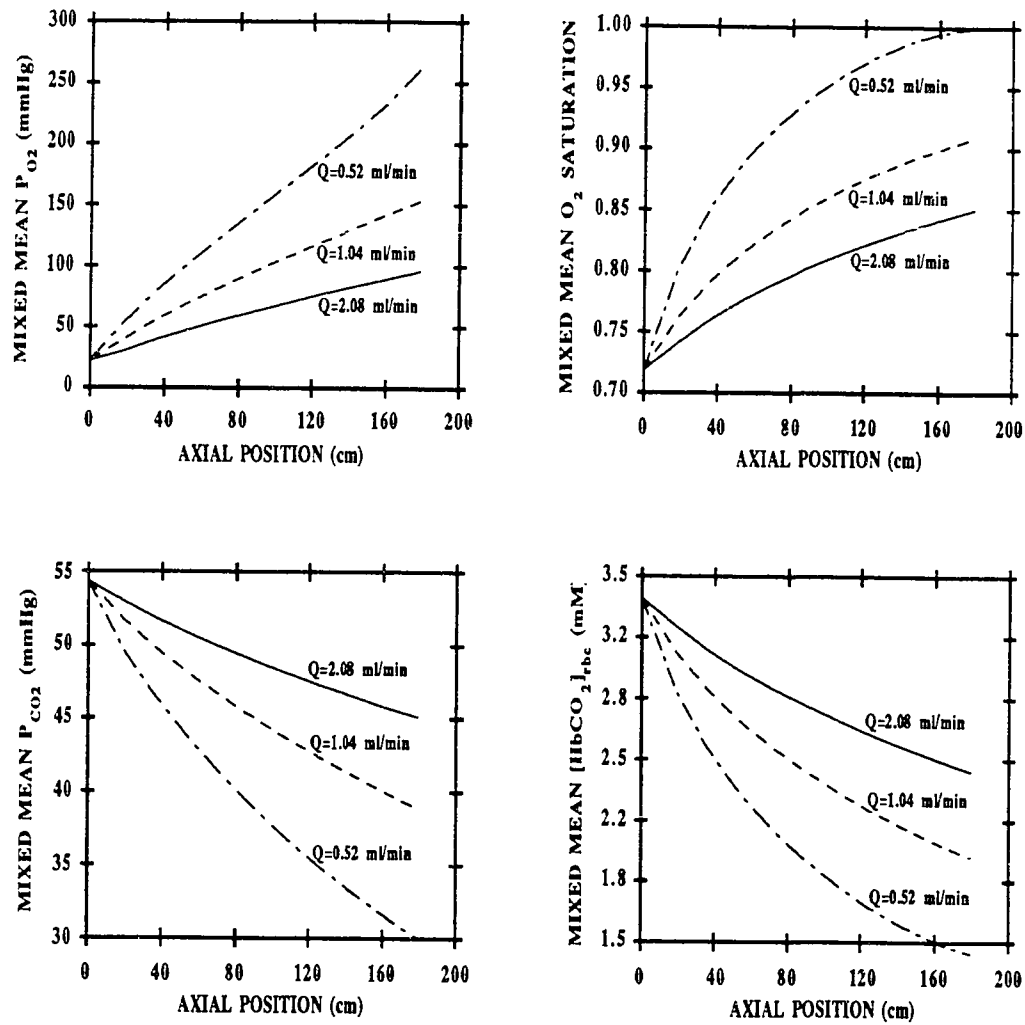


Figure 6.6b: Mixed mean values of O_2 tension, O_2 saturation, CO_2 tension and intracellular $HbCO_2$ concentration at different axial positions along the membrane oxygenator. Experimental conditions: I.D.=1.47 mm, O.D.=1.95 mm, $T=25$ °C, $H_D=0.43$, $P_{50,in}=16.8$ mmHg, $K_{eq}=46.1$, $\beta=32.4$ mM H^+ /pH, $pH_{pl,in}=7.23$, $P_{O_2,in}=22.7$ mmHg, $P_{CO_2,in}=54.4$ mmHg, $P_{O_2,ext}=708$ mmHg and $P_{CO_2,ext}=0$ mmHg. Simulation curves: generated via the discrete model; (—) $Q=2.08$ ml/min, (- - -) $Q=1.04$ ml/min, (— - —) $Q=0.52$ ml/min.

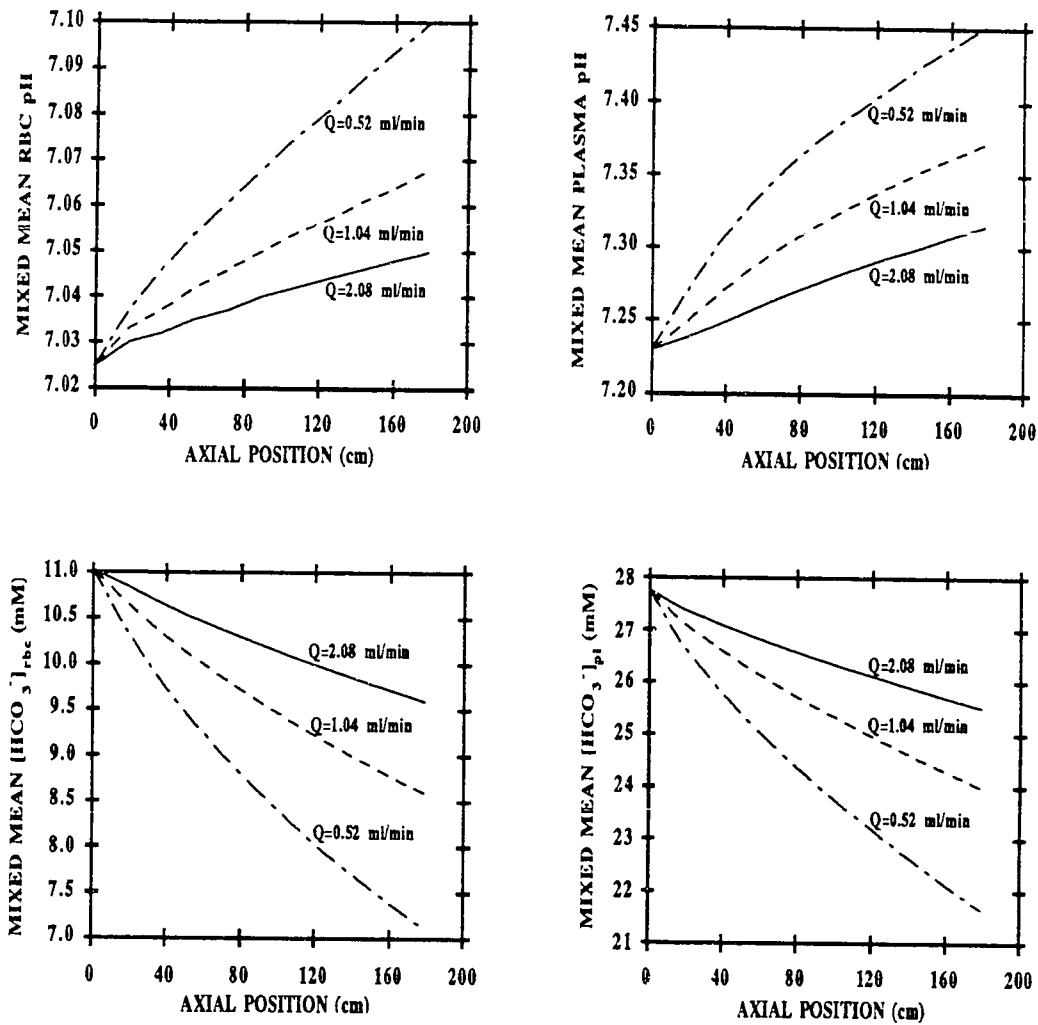


Figure 6.6c: Mixed mean values of intra- and extracellular pH and intra- and extracellular HCO_3^- concentrations at different axial positions along the membrane oxygenator. Experimental conditions: I.D.=1.47 mm, O.D.=1.95 mm, $T=25$ °C, $H_D=0.43$, $P_{50,in}=16.8$ mmHg, $K_{eq}=46.1$, $\beta=32.4$ mM H^+/pH , $pH_{pl,in}=7.23$, $P_{O2,in}=22.7$ mmHg, $P_{CO2,in}=54.4$ mmHg, $P_{O2,ext}=708$ mmHg and $P_{CO2,ext}=0$ mmHg. Simulation curves: generated via the discrete model; (—) $Q=2.08$ ml/min, (- - -) $Q=1.04$ ml/min, (- . -) $Q=0.52$ ml/min.

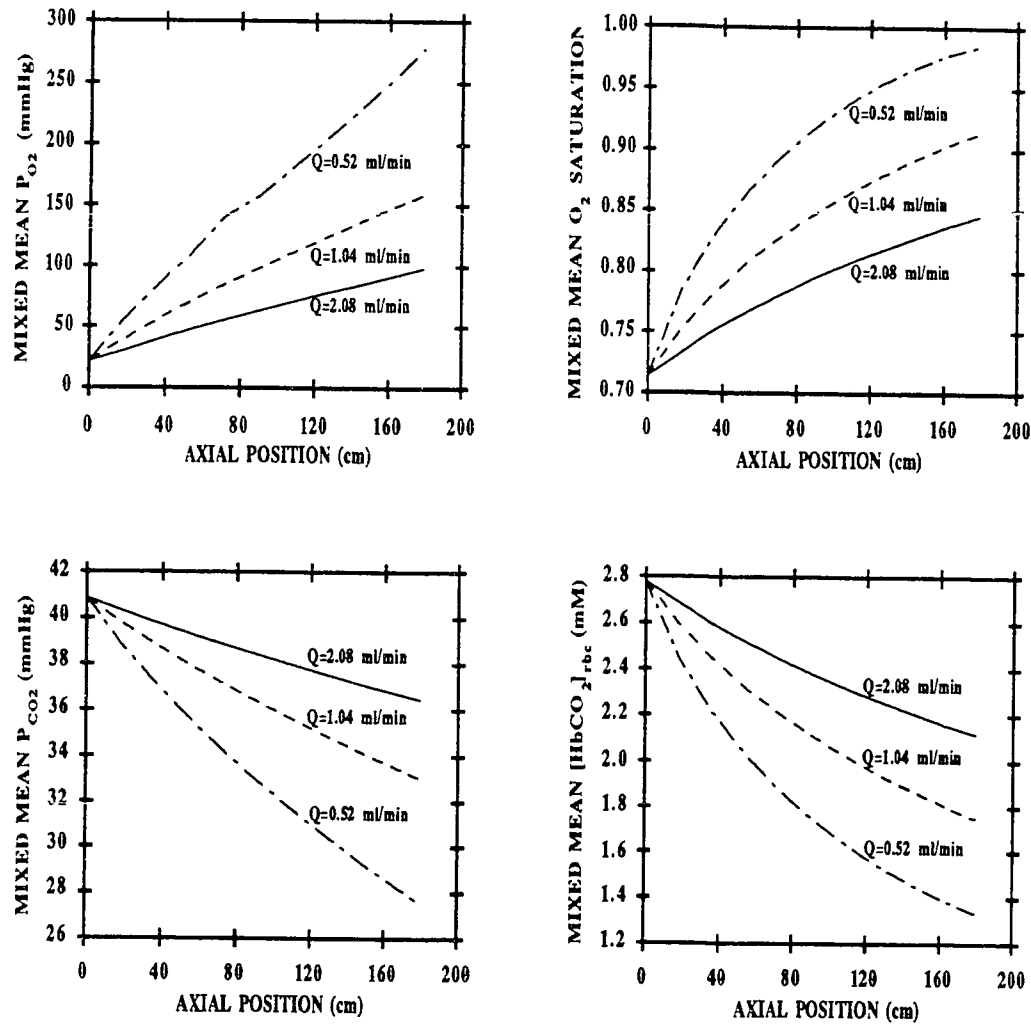


Figure 6.7b: Mixed mean values of O_2 tension, O_2 saturation, CO_2 tension and intracellular $HbCO_2$ concentration at different axial positions along the membrane oxygenator. Experimental conditions: I.D.=1.57 mm, O.D.=3.18 mm, $T=26$ °C, $H_D=0.43$, $P_{50,in}=16.7$ mmHg, $K_{eq}=45.7$, $\beta=31.8$ mM H^+ /pH, $pH_{pl,in}=7.32$, $P_{O_2,in}=22.4$ mmHg, $P_{CO_2,in}=40.9$ mmHg, $P_{O_2,ext}=707$ mmHg and $P_{CO_2,ext}=0$ mmHg. Simulation curves: generated via the discrete model; (—) $Q=2.08$ ml/min, (---) $Q=1.04$ ml/min, (— · —) $Q=0.52$ ml/min.

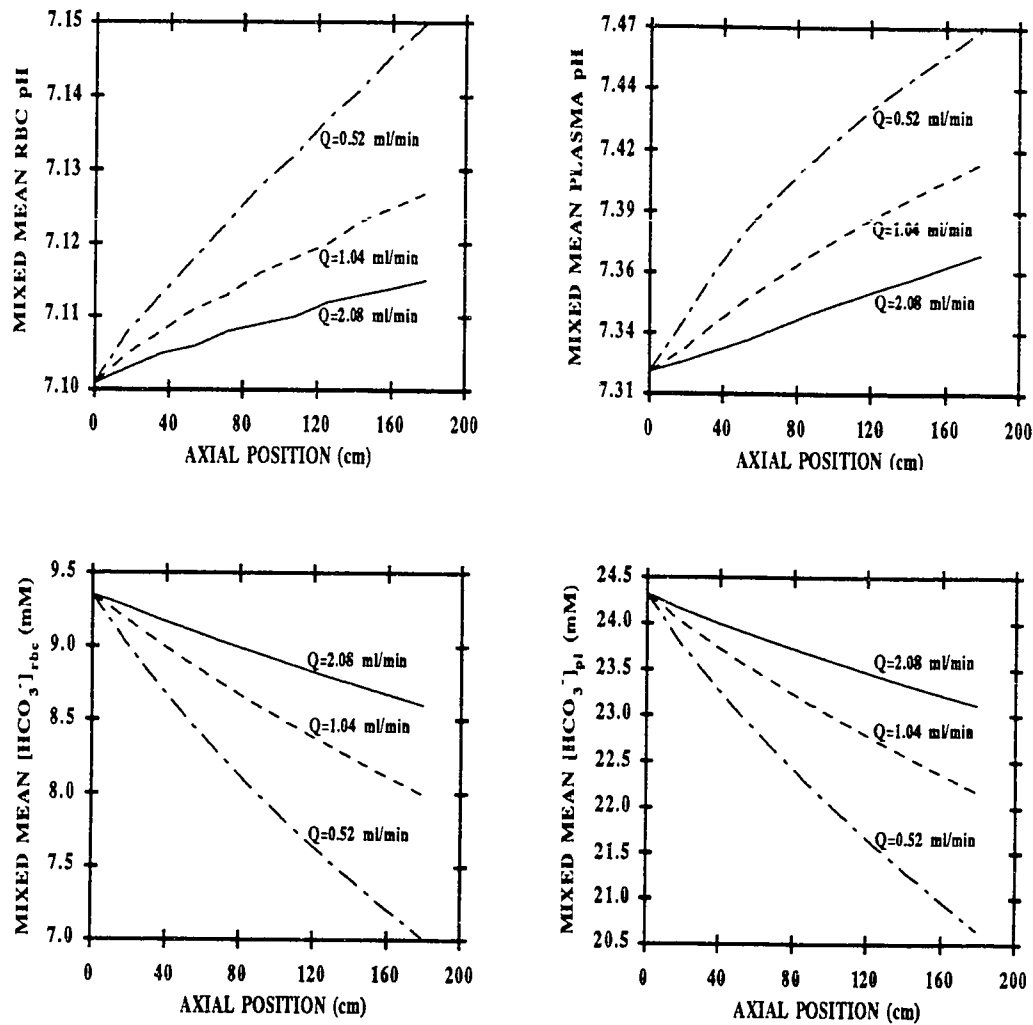


Figure 6.7c: Mixed mean values of intra- and extracellular pH and intra- and extracellular HCO_3^- concentrations at different axial positions along the membrane oxygenator. Experimental conditions: I.D.=1.57 mm, O.D.=3.18 mm, $T=26^\circ\text{C}$, $H_D=0.43$, $P_{50,\text{in}}=16.7$ mmHg, $K_{eq}=45.7$, $\beta=31.8$ mM H^+/pH , $pH_{\text{pl},\text{in}}=7.32$, $P_{\text{O}_2,\text{in}}=22.4$ mmHg, $P_{\text{CO}_2,\text{in}}=40.9$ mmHg, $P_{\text{O}_2,\text{ext}}=707$ mmHg and $P_{\text{CO}_2,\text{ext}}=0$ mmHg. Simulation curves: generated via the discrete model; (—) $Q=2.08$ ml/min, (---) $Q=1.04$ ml/min, (— - —) $Q=0.52$ ml/min.

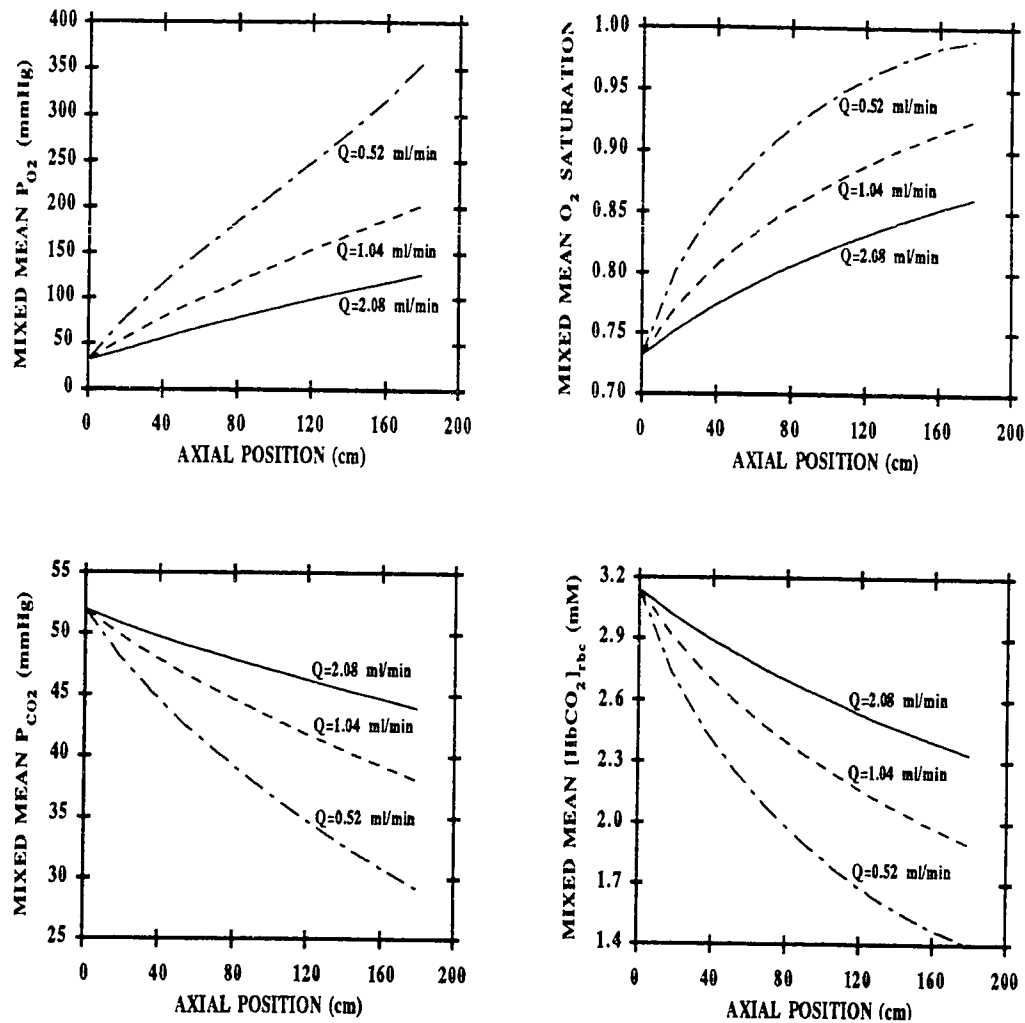


Figure 6.8b: Mixed mean values of O_2 tension, O_2 saturation, CO_2 tension and intracellular $HbCO_2$ concentration at different axial positions along the membrane oxygenator. Experimental conditions: I.D.=1.57 mm, O.D.=3.18 mm, $T=25^\circ C$, $H_D=0.43$, $P_{50,in}=20.6$ mmHg, $K_{eq}=24.2$, $\beta=31.3$ mM H^+/pH , $pH_{pl,in}=6.99$, $P_{O_2,in}=32.0$ mmHg, $P_{CO_2,in}=52.0$ mmHg, $P_{O_2,ext}=709$ mmHg and $P_{CO_2,ext}=0$ mmHg. Simulation curves: generated via the discrete model; (—) $Q=2.08$ ml/min, (----) $Q=1.04$ ml/min, (— - —) $Q=0.52$ ml/min.

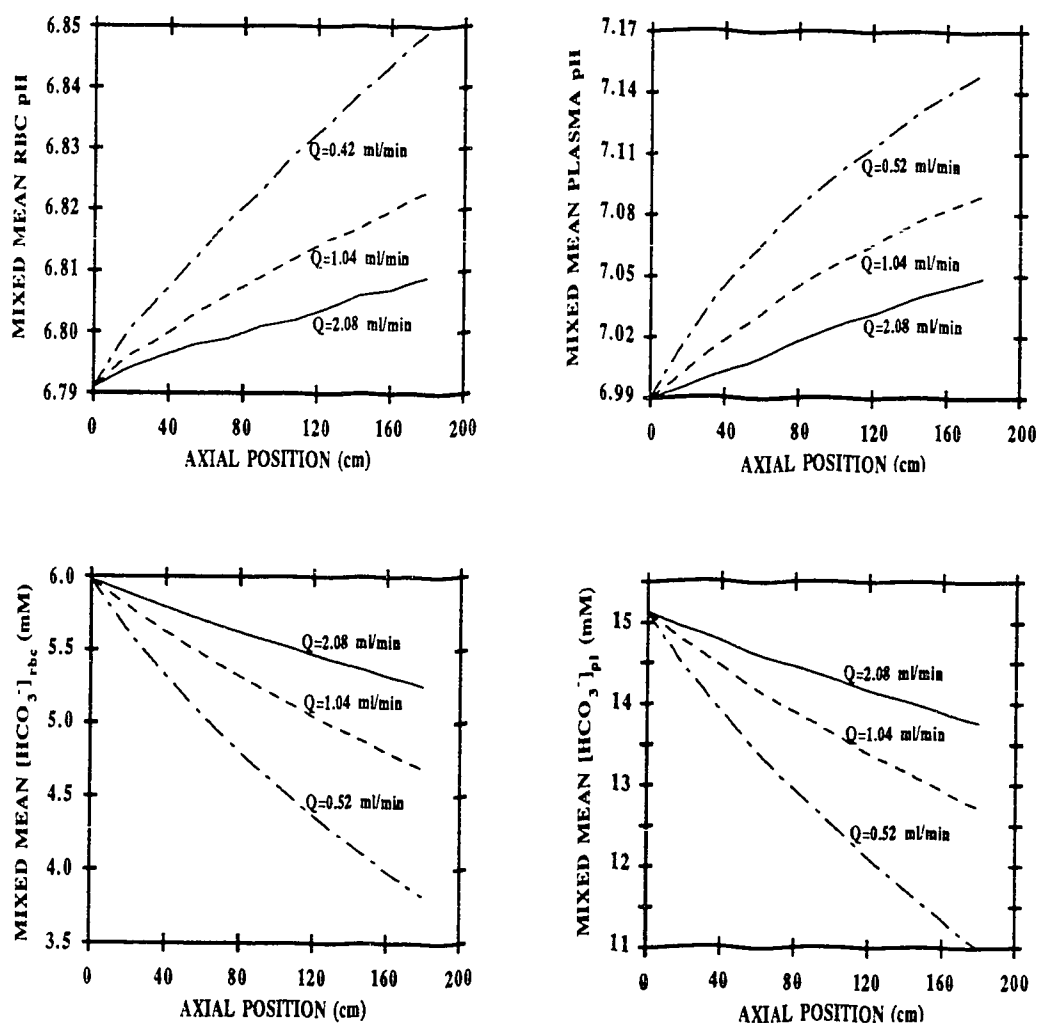


Figure 6.8c: Mixed mean values of intra- and extracellular pH and intra- and extracellular HCO_3^- concentrations at different axial positions along the membrane oxygenator. Experimental conditions: I.D.=1.57 mm, O.D.=3.18 mm, $T=25$ °C, $H_D=0.43$, $P_{50,in}=20.6$ mmHg, $K_{eq}=24.2$, $\beta=31.3$ mM H^+/pH , $pH_{pl,in}=6.99$, $P_{O2,in}=32.0$ mmHg, $P_{CO2,in}=52.0$ mmHg, $P_{O2,ext}=709$ mmHg and $P_{CO2,ext}=0$ mmHg. Simulation curves: generated via the discrete model; (—) $Q=2.08$ ml/min, (---) $Q=1.04$ ml/min, (— - —) $Q=0.52$ ml/min.

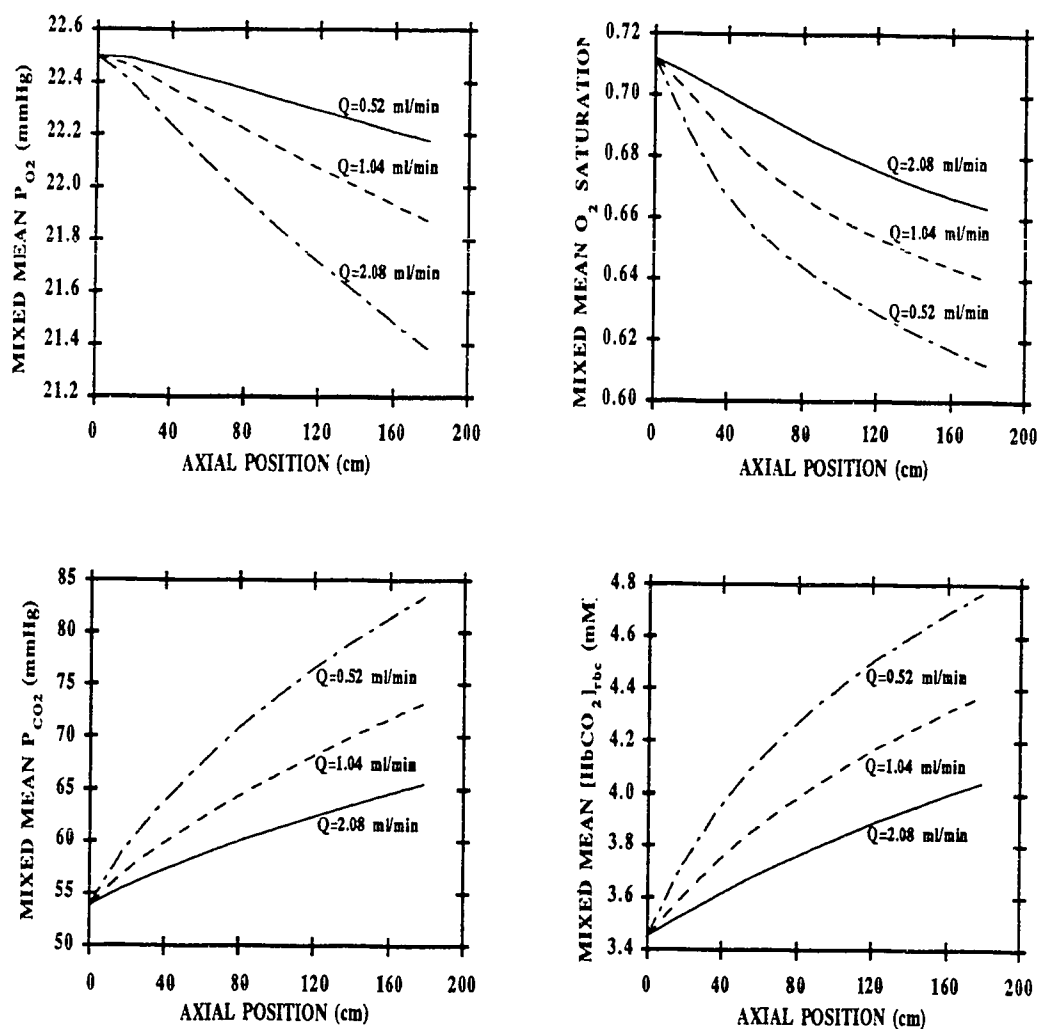


Figure 6.9b: Mixed mean values of O_2 tension, O_2 saturation, CO_2 tension and intracellular $HbCO_2$ concentration at different axial positions along the membrane oxygenator. Experimental conditions: I.D.=1.47 mm, O.D.=1.95 mm, $T=25$ °C, $H_D=0.43$, $P_{50,in}=17.6$ mmHg, $K_{eq}=40.3$, $\beta=31.5$ mM H^+ /pH, $pH_{pl,in}=7.18$, $P_{O_2,in}=22.5$ mmHg, $P_{CO_2,in}=53.9$ mmHg, $P_{O_2,ext}=0$ mmHg and $P_{CO_2,ext}=115$ mmHg. Simulation curves: generated via the discrete model; (—) $Q=2.08$ ml/min, (---) $Q=1.04$ ml/min, (- - -) $Q=0.52$ ml/min.

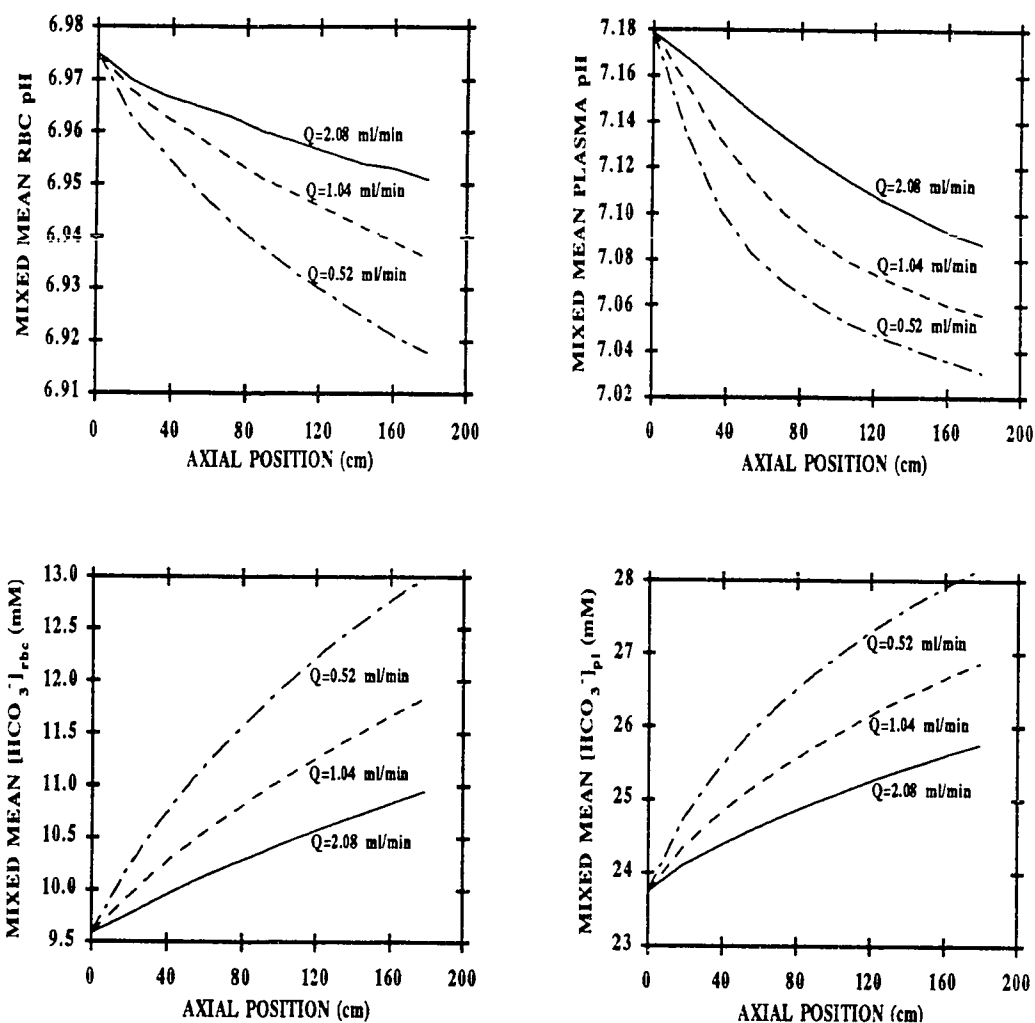


Figure 6.9c: Mixed mean values of intra- and extracellular pH and intra- and extracellular HCO_3^- concentrations at different axial positions along the membrane oxygenator. Experimental conditions: I.D.=1.47 mm, O.D.=1.95 mm, $T=25$ °C, $H_D=0.43$, $P_{50,in}=17.6$ mmHg, $K_{eq}=40.3$, $\beta=31.5$ mM H^+/pH , $pH_{pl,in}=7.18$, $P_{O2,in}=22.5$ mmHg, $P_{CO2,in}=53.9$ mmHg, $P_{O2,ext}=0$ mmHg and $P_{CO2,ext}=115$ mmHg. Simulation curves: generated via the discrete model; (—) $Q=2.08$ ml/min, (---) $Q=1.04$ ml/min, (— · —) $Q=0.52$ ml/min.

that in order to achieve normal arterial blood composition certain operating parameters need to be altered. For instance, one can either increase $P_{CO_2,in}$ or $P_{CO_2,ext}$ to prevent disproportionate stripping of CO_2 . For design purpose, the results indicate that in these operating conditions the limiting design phenomenon is the O_2 transport and not the CO_2 removal.

6.2.2 Analysis of the Effects of Several Important Determinants on O_2/CO_2 Exchange in Microvessels

Coupled O_2 and CO_2 transport are determined by the complex interaction of multiple factors. In this section, several of the major determinants which are of particular significance in determining the gas transport are considered. These factors include the influences of the Bohr and Haldane effects, the rate of CO_2 hydration/dehydration reactions within the plasma, the kinetics of RBC anion exchange, and the effects of discharge hematocrit. In order to quantify the specific effects of alterations in the various factors mentioned, the discrete model developed in Section 6.1 is used. The computations were performed for the artificial membrane tube systems of Voorhees (1976) and Boland *et al.* (1987) and for both oxygenation and deoxygenation cases. Table 6.11 summarizes the values chosen for the system parameters. For each case considered, except for the parameters specifically noted, all other physical and chemical parameters are chosen to represent the normal and typical values (see Table 6.2). Although the absolute values of various quantities of the numerical solutions depend on the choice of these values, in most cases the observations on the various trends are found not to be critical.

Table 6.11: Description of the two types of artificial membrane tubes considered and values of the system parameters used in computations.

Two types of artificial membrane tubes.		
Type 1. Voorhees' membrane oxygenator system: a 1.47-mm-diameter and 179-cm-active length tube which is embedded in a concentric film with an outer diameter of 1.95 mm.		
Type 2. Boland's membrane oxygenator system: a 27- μ m-diameter and 5-mm-active length tube which is embedded in a 170- μ m-thickness slab.		
Values of the system parameters.		
Situation	Oxygenation	Deoxygenation
Temperature	37 °C	37 °C
Discharge hematocrit	42%	42%
Inlet composition of RBC suspension	$P_{O_2,in}=14.0$ mmHg $P_{CO_2,in}=52.5$ mmHg $pH_{pl,in}=7.28$ $P_{50,in}=29.9$ mmHg	$P_{O_2,in}=68.1$ mmHg $P_{CO_2,in}=28.8$ mmHg $pH_{pl,in}=7.66$ $P_{50,in}=23.8$ mmHg
Composition of the external gas space	$P_{O_2,ext}=708$ mmHg (Type 1) $P_{O_2,ext}=160$ mmHg (Type 2) $P_{CO_2,ext}=0$ mmHg	$P_{O_2,ext}=0$ mmHg $P_{CO_2,ext}=115$ mmHg

6.2.2.a Effects of the Bohr and Haldane Phenomena

Interactions of O_2 and CO_2 exchange are included in the discrete model. To study the importance of these interactions, the exchange of O_2 and CO_2 are calculated in the presence and absence of simultaneous transfer of the other gas. The influence of the Bohr effect on oxygenation is shown for the Type 1 and 2 membrane tubes in

Figures 6.11 and 6.12, respectively; on deoxygenation, Figures 6.13 and 6.14. The left-hand plots of Figures 6.11 - 6.14 present the results of total O_2 content change versus transit time; and the right-hand plots give the change in mixed mean P_{O_2} and O_2 saturation. These figures illustrate the fact that when no CO_2 transfer is allowed, the calculated total O_2 content changes are less than in the case of simultaneous O_2/CO_2 exchange. The calculated total O_2 content changes for these cases are summarized in Table 6.12. These calculations indicated that the Bohr effect accounts for about 20% of the total O_2 exchange for the deoxygenation case; and less than 10% for the oxygenation case. The Bohr effect is more significant for the deoxygenation case as compared to the oxygenation case; and it becomes increasingly more important for smaller vessels as compared to the larger vessels.

Table 6.12: Influence of the Bohr effect on O_2 transfer for both oxygenation and deoxygenation cases in artificial membrane tubes.

Cases	$\Delta[O_2]_{total} = [O_2]_{total}(z=L) - [O_2]_{total}(z=0)$	
	O_2 transport alone	O_2/CO_2 transport
Oxygenation (I.D.=1.47 mm) [†]	8.09 mM	8.23 mM (2% ↑) [¶]
Oxygenation (I.D.=27 μ m) [*]	5.90 mM	6.45 mM (9% ↑)
Deoxygenation (I.D.=1.47 mm) [†]	- 1.28 mM	- 1.62 mM (20% ↑)
Deoxygenation (I.D.=27 μ m) [*]	- 2.10 mM	- 2.73 mM (23% ↑)

[†] Type 1 membrane tube: $Q=12.5$ ml/hr.

^{*} Type 2 membrane tube: $Q=9$ μ l/hr.

[¶] Values in parentheses denote the % increase in the amount of total O_2 transfer which is calculated as:

$$\% \uparrow = \frac{\Delta[O_2]_{total}(O_2/CO_2 \text{ transfer}) - \Delta[O_2]_{total}(O_2 \text{ transfer alone})}{\Delta[O_2]_{total}(O_2/CO_2 \text{ transfer})} .$$

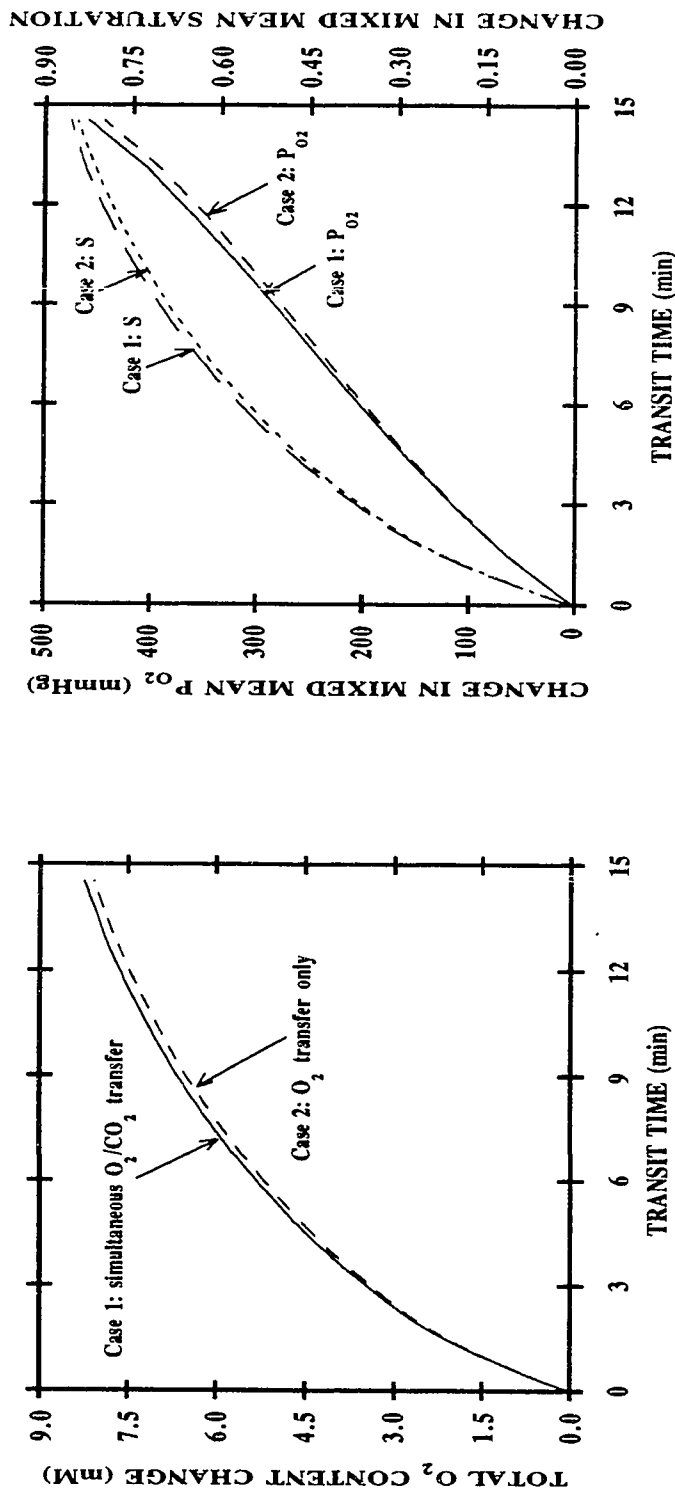


Figure 6.11: Influence of the Bohr effect on rate of O₂ uptake by human whole blood flowing in a Type 1 artificial membrane tube (see Table 6.11). The left panel gives the total O₂ content change as a function of transit time ($[O_2]_{total, in} = 1.09$ mM). Curves: theoretical simulation of the situations; (—) O₂ transfer in the presence of CO₂ exchange, (---) O₂ transfer in the absence of CO₂ exchange. The right panel gives both changes in mixed mean P_{O₂} and O₂ saturation as functions of transit time ($P_{O_2, in} = 14.0$ mmHg, $S_{in} = 0.12$). Curves: theoretical simulation of the situations; (—, left-hand scale) and (—, right-hand scale) O₂ transfer in the presence of CO₂ exchange; (---, left-hand scale) and (---, right-hand scale) O₂ transfer in the absence of CO₂ exchange.

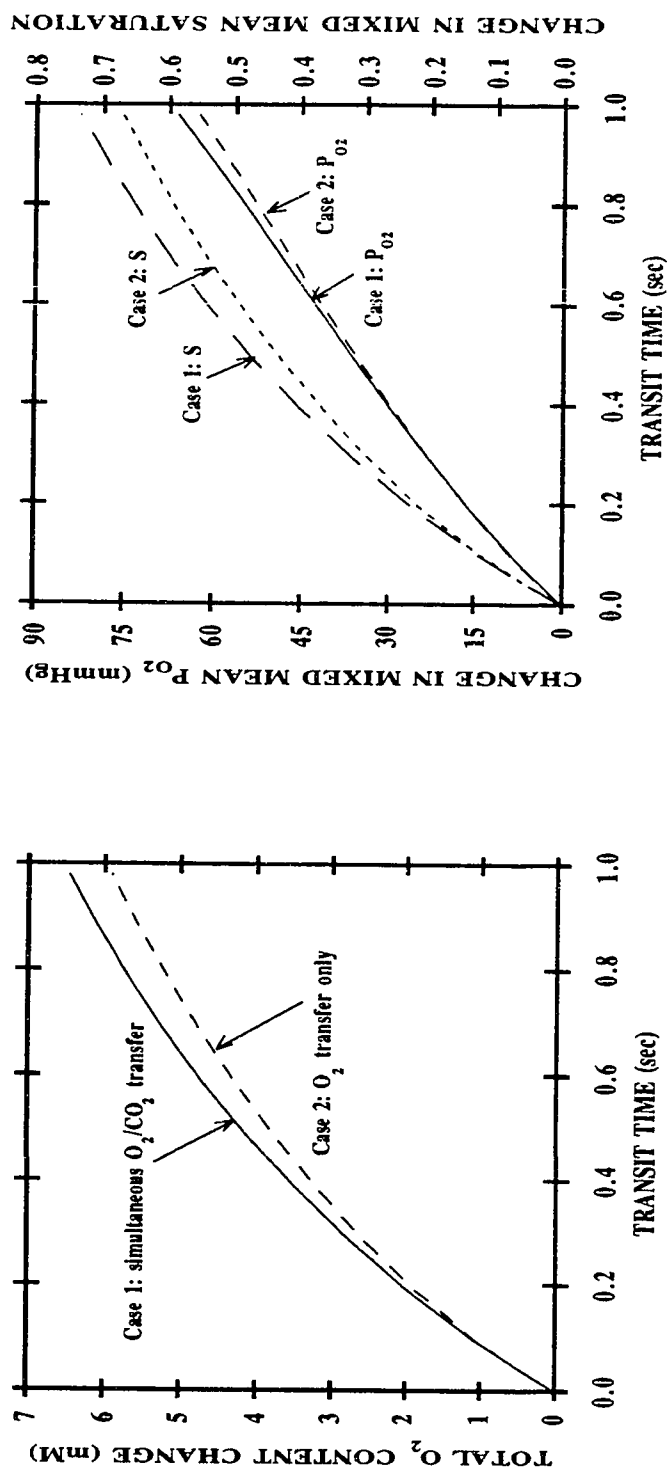


Figure 6.12: Influence of the Bohr effect on rate of O₂ uptake by human whole blood flowing in a Type 2 artificial membrane tube (see Table 6.11). The left panel gives the total O₂ content change as a function of transit time ($[O_2]_{total,in}=1.09$ mM). Curves: theoretical simulation of the situations; (—) O₂ transfer in the presence of CO₂ exchange, (---) O₂ transfer in the absence of CO₂ exchange. The right panel gives both changes in mixed mean P_{O_2} and O₂ saturation as functions of transit time ($P_{O_{2,in}}=14.0$ mmHg, $S_{in}=0.12$). Curves: theoretical simulation of the situations; (—, left-hand scale) and (---, right-hand scale) O₂ transfer in the presence of CO₂ exchange; (---, left-hand scale) and (---, right-hand scale) O₂ transfer in the absence of CO₂ exchange.

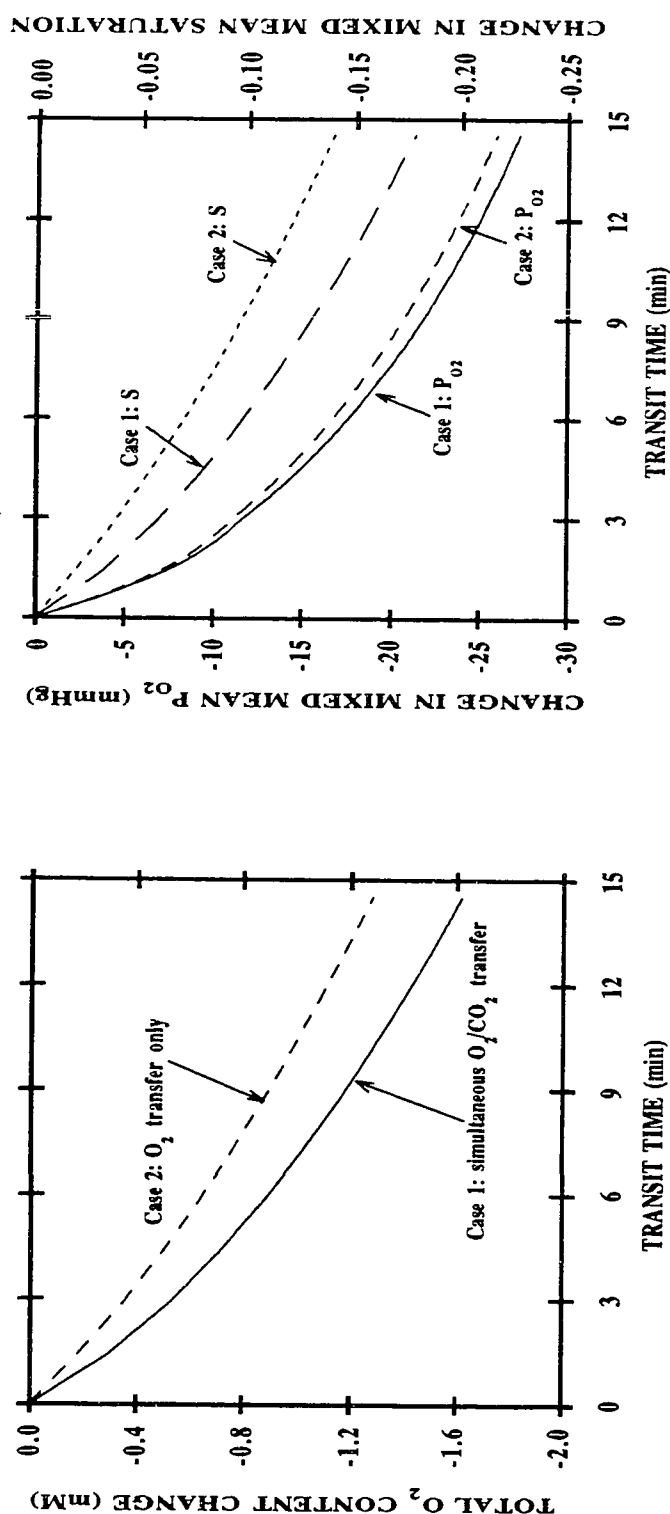


Figure 6.13: Influence of the Bohr effect on rate of O₂ release from human whole blood flowing in a Type 1 artificial membrane tube (see Table 6.11). The left panel gives the total O₂ content change as a function of transit time ($[O_2]_{total,in}=8.43$ mM). Curves: theoretical simulation of the situations; (—) O₂ transfer in the presence of CO₂ exchange, (---) O₂ transfer in the absence of CO₂ exchange. The right panel gives both changes in mixed mean P_{O_2} and O₂ saturation as functions of transit time ($P_{O_{2,i}}=68.1$ mmHg, $S_{i,n}=0.94$). Curves: theoretical simulation of the situations; (—, left-hand scale) and (—, right-hand scale) O₂ transfer in the presence of CO₂ exchange; (---, left-hand scale) and (---, right-hand scale) O₂ transfer in the absence of CO₂ exchange.

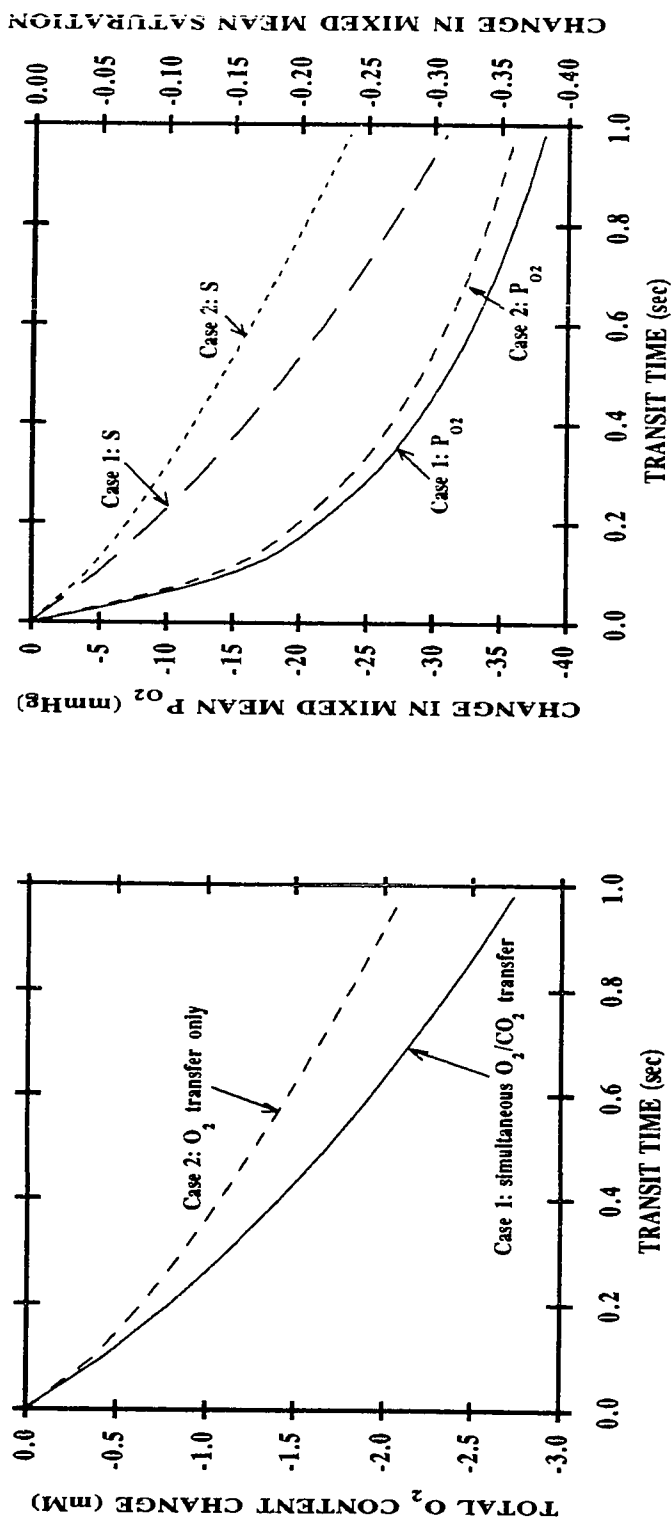


Figure 6.14: Influence of the Bohr effect on rate of O_2 release from human whole blood flowing in a Type 2 artificial membrane tube (see Table 6.11). The left panel gives the total O_2 content change as a function of transit time ($[O_2]_{total, in} = 8.43$ mM). Curves: theoretical simulation of the situations; (—) O_2 transfer in the presence of CO_2 exchange, (---) O_2 transfer in the absence of CO_2 exchange. The right panel gives both changes in mixed mean P_{O_2} and O_2 saturation as functions of transit time ($P_{O_2, in} = 68.1$ mmHg, $S_{in} = 0.94$). Curves: theoretical simulation of the situations; (—, left-hand scale) and (—, right-hand scale) O_2 transfer in the presence of CO_2 exchange; (---, left-hand scale) and (---, right-hand scale) O_2 transfer in the absence of CO_2 exchange.

The magnitude of the Haldane effect on the oxygenation case is given in Figures 6.15 and 6.16 for the Type 1 and 2 membrane tubes, respectively; on the deoxygenation case, Figures 6.17 and 6.18. The left-hand plots of Figures 6.15 - 6.18 present the results of total CO_2 content change versus transit time; and the right-hand plots give the change in mixed mean P_{CO_2} and intracellular hemoglobin carbamate concentration. In the absence of simultaneous O_2 transfer, the total CO_2 content changes calculated are less than the changes that occur under the condition of collateral O_2/CO_2 exchange. The calculated total CO_2 content changes at $z=L$ are tabulated in Table 6.13. As shown in the table, according to this model $\approx 10\%$ of total CO_2 transferred is linked to simultaneous O_2 transfer for the oxygenation case; and $\approx 5\%$ for the deoxygenation case. However, it should be mentioned that the fraction of total CO_2 exchange that is accounted for by the Haldane effect should be larger than what is estimated here. The reason is that only half of the Haldane effect, the effect of O_2 carriage on carbamino compounds, is accounted for in this model. The additional bicarbonate contribution in the presence of simultaneous O_2 exchange which is due to the altered buffering capacity of hemoglobin is not included in this model. The increased acidity of oxyhemoglobin leads to an increase in the intracellular H^+ and allows more intracellular HCO_3^- change. Plasma HCO_3^- would be affected by this effect because of the $\text{HCO}_3^-/\text{Cl}^-$ exchange. This altered buffer capacity of hemoglobin is not completely quantified; as a result, a mathematical description of this relationship is not included in this model.

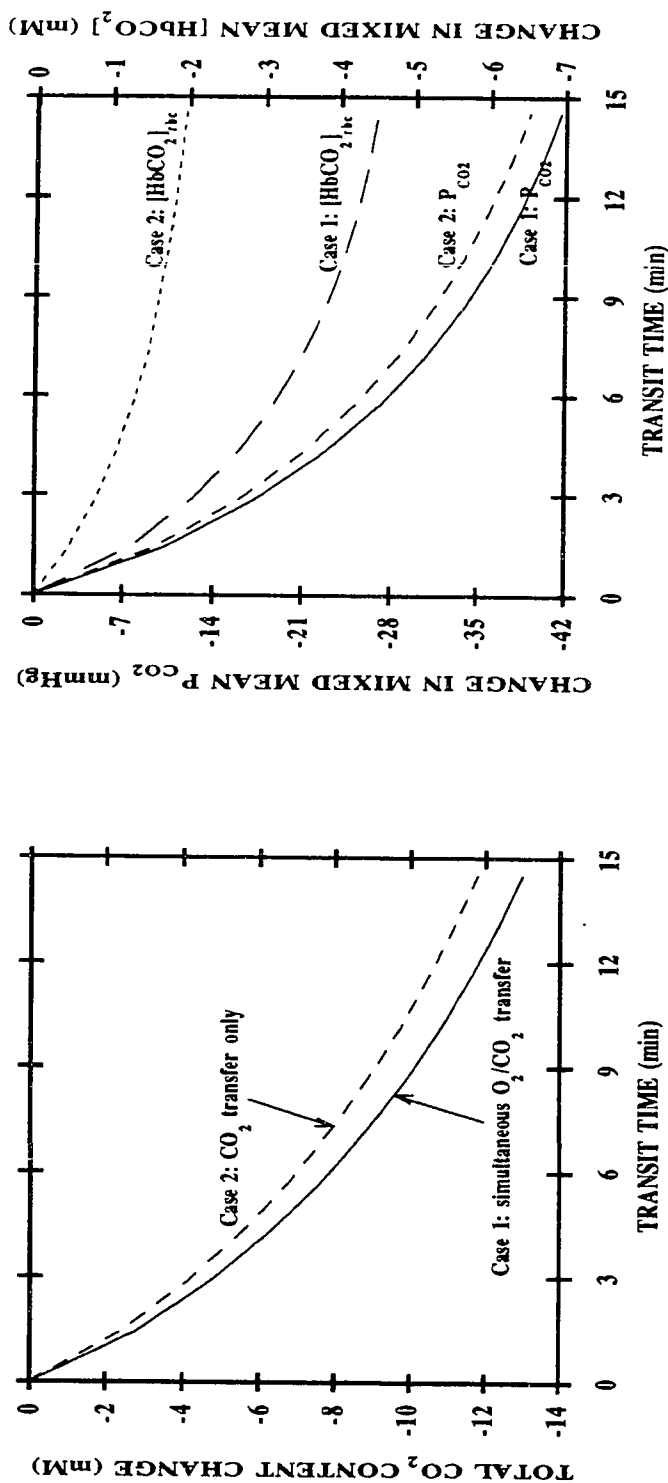


Figure 6.15: Influence of the Haldane effect on rate of CO₂ elimination from human whole blood flowing in a Type I artificial membrane tube (see Table 6.11). The left panel gives the total CO₂ content change as a function of transit time ($[CO_2]_{total,in}=22.4$ mM). Curves: theoretical simulation of the situations; (—) CO₂ transfer in the presence of O₂ exchange, (---) CO₂ transfer in the absence of O₂ exchange. The right panel gives both changes in mixed mean P_{CO2} and $[HbCO_2]_{rbc}$ as functions of transit time ($P_{CO2,in}=52.5$ mmHg, $[HbCO_2]_{rbc,in}=5.08$ mM). Curves: theoretical simulation of the situations; (—, left-hand scale) and (—, right-hand scale) CO₂ transfer in the presence of O₂ exchange; (---, left-hand scale) and (---, right-hand scale) CO₂ transfer in the absence of O₂ exchange.

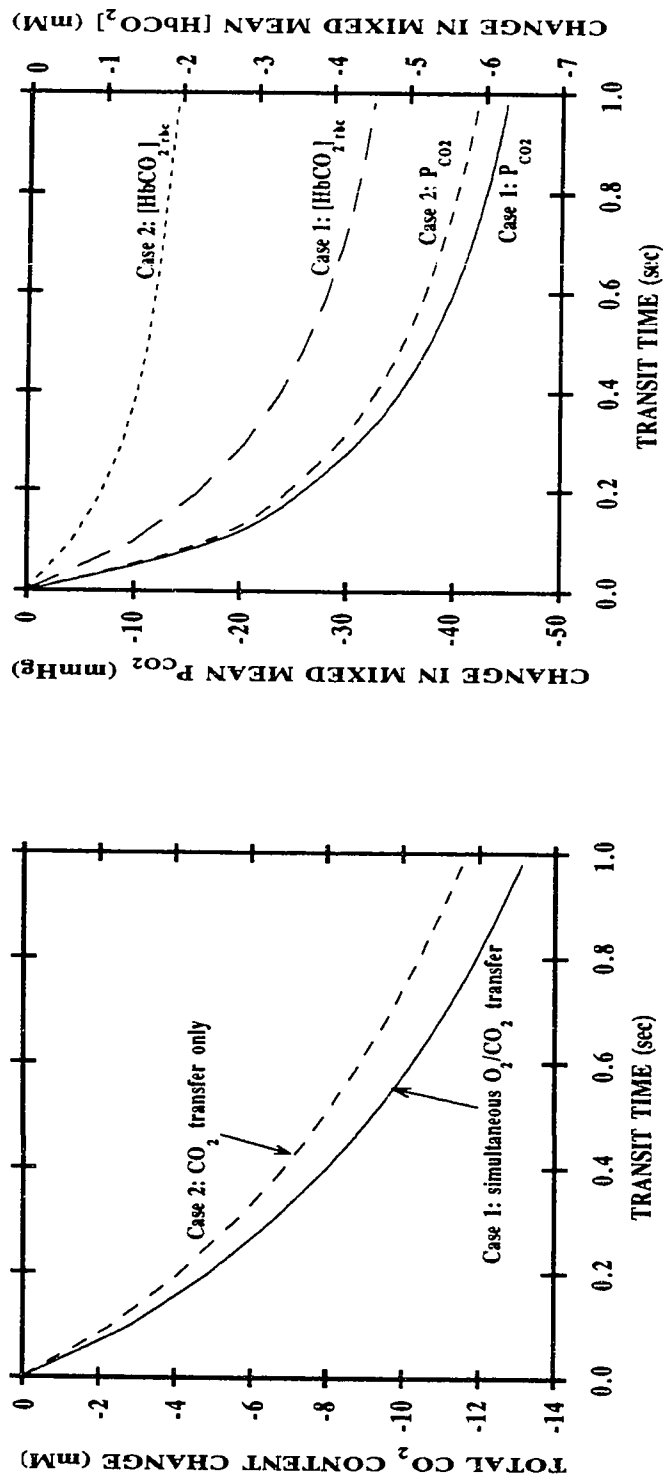


Figure 6.16: Influence of the Haldane effect on rate of CO₂ elimination from human whole blood flowing in a Type 2 artificial membrane tube (see Table 6.11). The left panel gives the total CO₂ content change as a function of transit time ($[CO_2]_{total,in} \approx 22.4$ mM). Curves: theoretical simulation of the situations; (—) CO₂ transfer in the presence of O₂ exchange, (---) CO₂ transfer in the absence of O₂ exchange. The right panel gives both changes in mixed mean P_{CO_2} and $[HbCO_2]_{bc}$ as functions of transit time ($P_{CO_2,in} = 52.5$ mmHg, $[HbCO_2]_{bc,in} = 5.08$ mM). Curves: theoretical simulation of the situations; (—, left-hand scale) and (—, right-hand scale) CO₂ transfer in the presence of O₂ exchange; (---, left-hand scale) and (---, right-hand scale) CO₂ transfer in the absence of O₂ exchange.

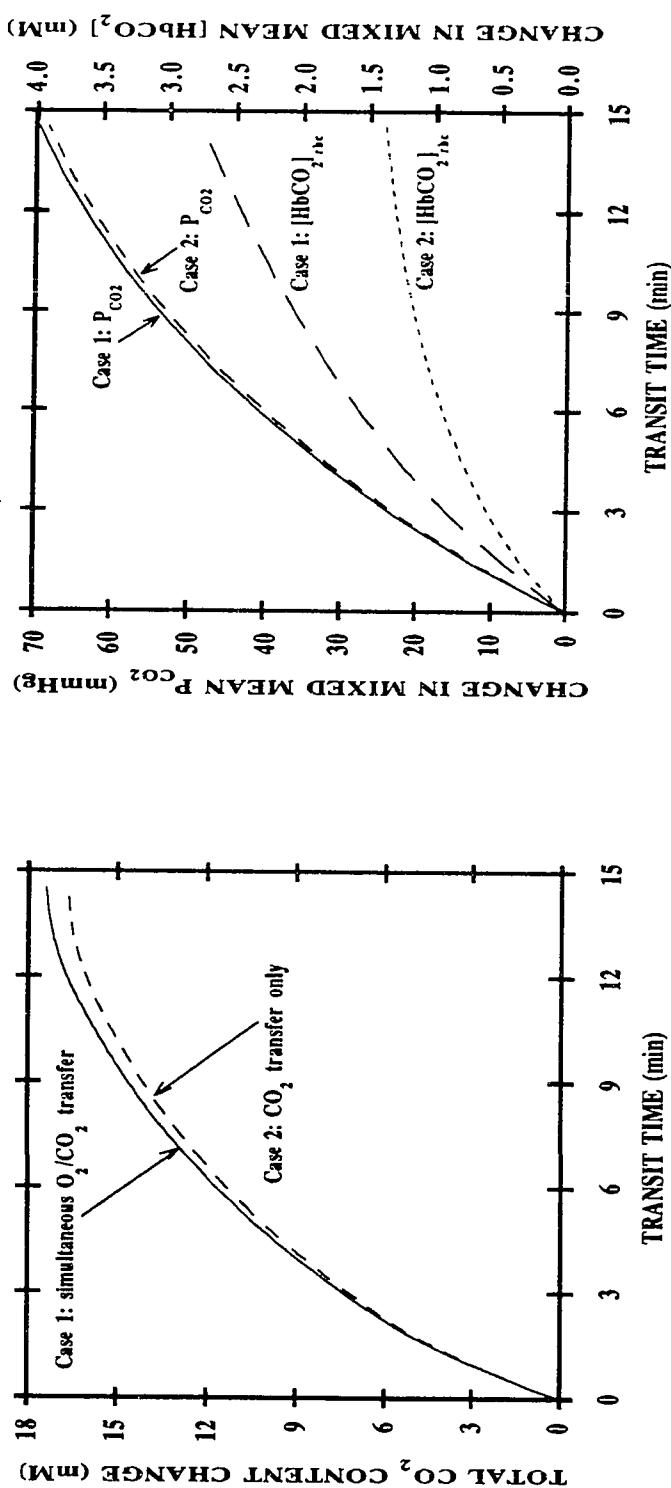


Figure 6.17: Influence of the Haldane effect on rate of CO₂ uptake by human whole blood flowing in a Type 1 artificial membrane tube (see Table 6.11). The left panel gives the total CO₂ content change as a function of transit time ($[CO_2]_{total,in}=24.4$ mM). Curves: theoretical simulation of the situations; (—) CO₂ transfer in the presence of O₂ exchange, (---) CO₂ transfer in the absence of O₂ exchange. The right panel gives both changes in mixed mean P_{CO_2} and $[HbCO_2]_{rbc}$ as functions of transit time ($P_{CO_2,in}=28.8$ mmHg, $[HbCO_2]_{rbc,in}=1.31$ mM). Curves: theoretical simulation of the situations; (—, left-hand scale) and (—, right-hand scale) CO₂ transfer in the presence of O₂ exchange; (---, left-hand scale) and (---, right-hand scale) CO₂ transfer in the absence of O₂ exchange.

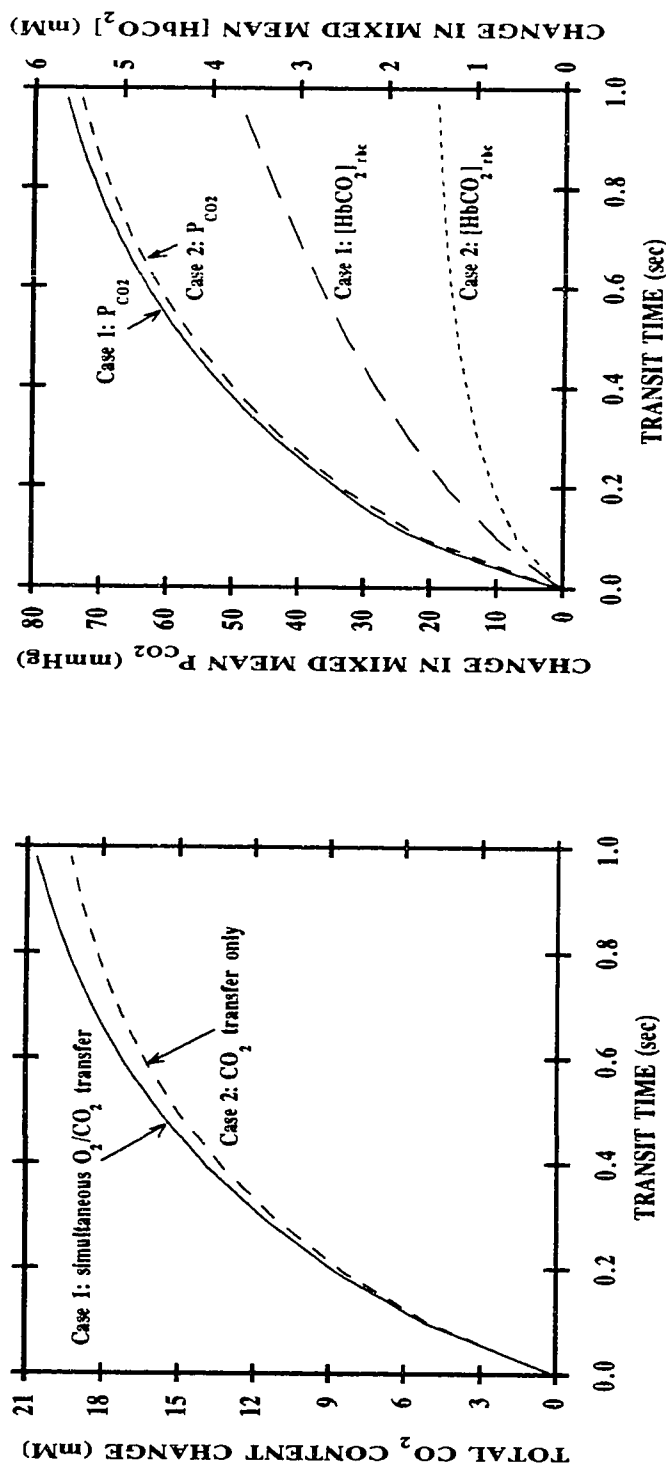


Figure 6.18: Influence of the Haldane effect on rate of CO₂ uptake by human whole blood flowing in a Type 2 artificial membrane tube (see Table 6.11). The left panel gives the total CO₂ content change as a function of transit time ($[CO_2]_{total,in} = 24.4$ mM). Curves: theoretical simulation of the situations; (—) CO₂ transfer in the presence of O₂ exchange, (---) CO₂ transfer in the absence of O₂ exchange. The right panel gives both changes in mixed mean P_{CO_2} and $[HbCO_2]_{bc}$ as functions of transit time ($P_{CO_2,in} = 28.8$ mmHg, $[HbCO_2]_{bc,in} = 1.31$ mM). Curves: theoretical simulation of the situations; (—, left-hand scale) and (—, right-hand scale) CO₂ transfer in the presence of O₂ exchange; (---, left-hand scale) and (---, right-hand scale) CO₂ transfer in the absence of O₂ exchange.

Table 6.13: Influence of the Haldane effect on CO₂ transfer for both oxygenation and deoxygenation cases in artificial membrane tubes.

Cases	$\Delta[CO_2]_{total} = [CO_2]_{total}(z=L) - [CO_2]_{total}(z=0)$	
	CO ₂ transport alone	O ₂ /CO ₂ transport
Oxygenation (I.D.=1.47 mm) [†]	- 11.8 mM	- 13.0 mM (10% ↑) [‡]
Oxygenation (I.D.=27 μm) [*]	- 11.6 mM	- 13.1 mM (11% ↑)
Deoxygenation (I.D.=1.47 mm) [†]	16.6 mM	17.4 mM (5% ↑)
Deoxygenation (I.D.=27 μm) [*]	19.2 mM	20.6 mM (7% ↑)

[†] Type 1 membrane tube: $Q=12.5$ ml/hr.

^{*} Type 2 membrane tube: $Q=9$ μl/hr.

[‡] Values in parentheses denote the % increase in the amount of total CO₂ transfer which is calculated as: $\% \uparrow = \frac{\Delta[CO_2]_{total}(O_2/CO_2 \text{ transfer}) - \Delta[CO_2]_{total}(CO_2 \text{ transfer alone})}{\Delta[CO_2]_{total}(O_2/CO_2 \text{ transfer})}$.

6.2.2.b Effects of Extracellular Carbonic Anhydrase Activity and Buffering Capacity

CO₂ transport in the microvessels as functions of the transit time and extracellular carbonic anhydrase activity for oxygenation situation is shown in Figures 6.19 and 6.20 for Type 1 and Type 2 membrane tubes, respectively; for deoxygenation situation, Figures 6.21 and 6.22. On the left hand side of these figures, the computed change in the total CO₂ content is shown for three different values of the rates of the extracellular CO₂ hydration/dehydration reactions using \hat{A}_{pl} of 1, 100 and 6500; and on the right hand side, the computed changes in plasma HCO₃⁻ concentration and pH . $\hat{A}_{pl}=1$ and $\beta_{pl}=5.5$ mM H⁺/pH represent the case where no carbonic anhydrase activity nor any additional buffers are added to the plasma. As it is illustrated in these figures, CO₂ transfer increases with the enhancement of plasma carbonic anhydrase activity. The calculated total CO₂ content changes at the outlet of the membrane tubes are

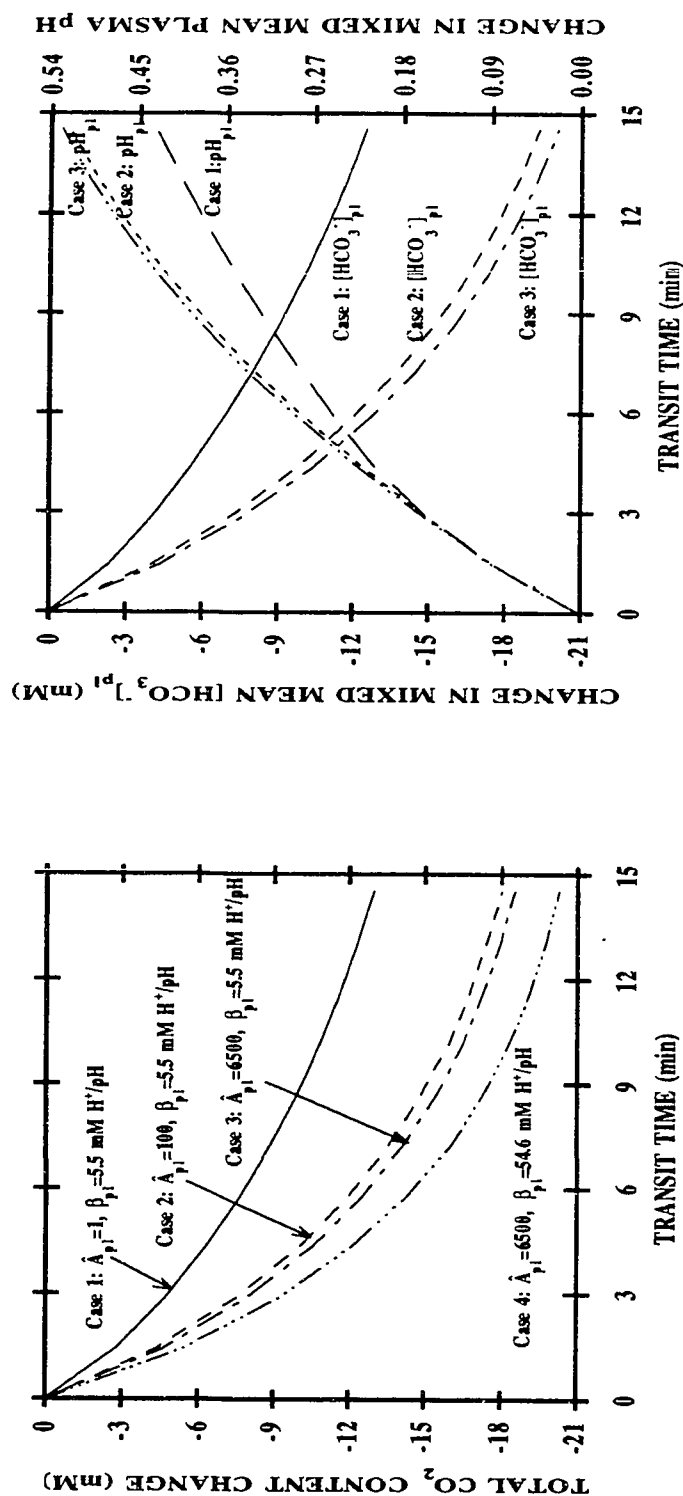


Figure 6.19: Effect of extracellular catalysis of CO₂ hydration/dehydration reactions on rate of CO₂ elimination from human whole blood flowing in a Type 1 artificial membrane tube (see Table 6.11). The left panel gives the total CO₂ content change as a function of transit time ($[CO_2]_{total,in}=22.4$ mM). Curves: theoretical simulation of the situations; (—) $\dot{A}_{pI}=1$, (---) $\dot{A}_{pI}=100$, (— · —) $\dot{A}_{pI}=6500$ and $\beta_{pI}=5.5$ mM H⁺/pH; (····) $\dot{A}_{pI}=6500$ and $\beta_{pI}=54.6$ mM H⁺/pH. The right panel gives both changes in mixed mean $[HCO_3^-]_{pI}$ and pH_{pI} as functions of transit time ($[HCO_3^-]_{pI,in}=25.6$ mM, $pH_{pI,in}=7.28$). Curves: theoretical simulation of the situations; (—, left-hand scale) $\dot{A}_{pI}=1$ and $\beta_{pI}=5.5$ mM H⁺/pH; (---, left-hand scale) $\dot{A}_{pI}=100$ and $\beta_{pI}=5.5$ mM H⁺/pH; (— · —, right-hand scale) $\dot{A}_{pI}=1$ and $\beta_{pI}=5.5$ mM H⁺/pH; (····, right-hand scale) $\dot{A}_{pI}=6500$ and $\beta_{pI}=54.6$ mM H⁺/pH.

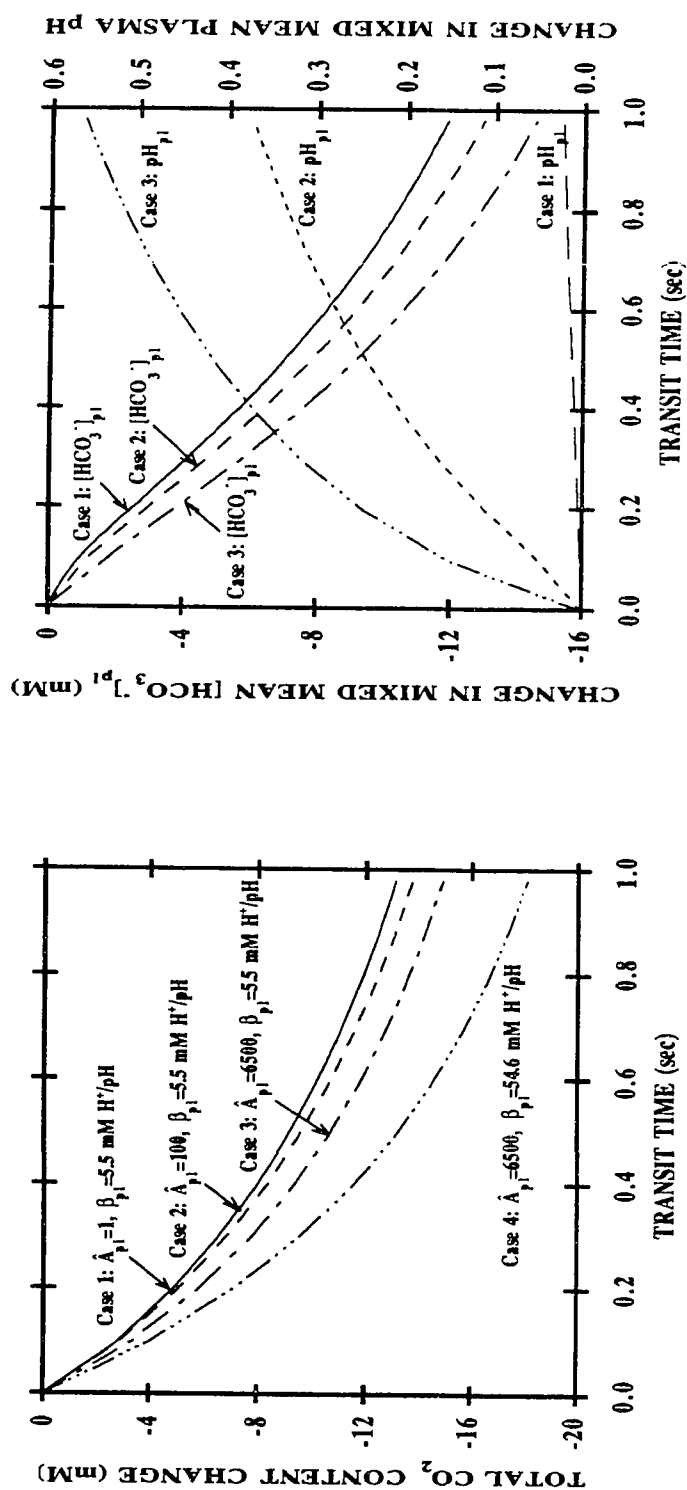


Figure 6.20: Effect of extracellular catalysis of CO₂ hydration/dehydration reactions on rate of CO₂ elimination from human whole blood flowing in a Type 2 artificial membrane tube (see Table 6.11). The left panel gives the total CO₂ content change as a function of transit time ($[CO_2]_{total,in}=22.4 \text{ mM}$). Curves: theoretical simulation of the situations; (—) $\dot{A}_{pI}=1$, (---) $\dot{A}_{pI}=100$, (— · —) $\dot{A}_{pI}=6500$ and $\beta_{pI}=5.5 \text{ mM H}^+/\text{pH}$; (·····) $\dot{A}_{pI}=6500$ and $\beta_{pI}=54.6 \text{ mM H}^+/\text{pH}$. The right panel gives both changes in mixed mean $[HCO_3^-]_{pI}$ and pH_{pI} as functions of transit time ($[HCO_3^-]_{pI,in}=25.6 \text{ mM}$, $pH_{pI,in}=7.28$). Curves: theoretical simulation of the situations; (—, left-hand scale) and (— · —, right-hand scale) $\dot{A}_{pI}=1$ and $\beta_{pI}=5.5 \text{ mM H}^+/\text{pH}$; (---, left-hand scale) and (--- · ---, right-hand scale) $\dot{A}_{pI}=100$ and $\beta_{pI}=5.5 \text{ mM H}^+/\text{pH}$; (·····, left-hand scale) and (·····, right-hand scale) $\dot{A}_{pI}=6500$ and $\beta_{pI}=5.5 \text{ mM H}^+/\text{pH}$.

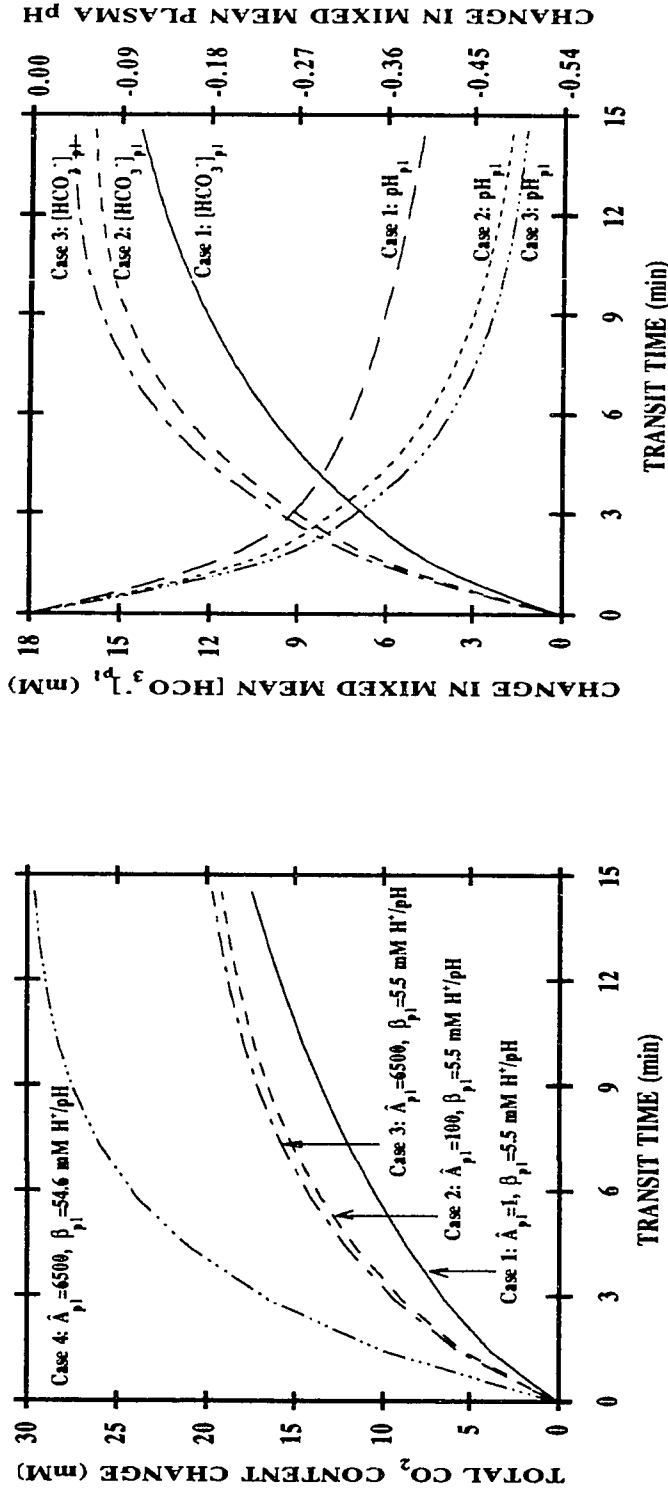


Figure 6.21: Effect of extracellular catalysis of CO₂ hydration/dehydration reactions on rate of CO₂ removal by human whole blood flowing in a Type 1 artificial membrane tube (see Table 6.11). The left panel gives the total CO₂ content change as a function of transit time ($[CO_2]_{total,in}=24.4$ mM). Curves: theoretical simulation of the situations; (—) $\dot{A}_{pI}=1$, (---) $\dot{A}_{pI}=100$, (— · —) $\dot{A}_{pI}=6500$ and $\beta_{pI}=5.5$ mM H⁺/pH; (--- · ---) $\dot{A}_{pI}=6500$ and $\beta_{pI}=54.6$ mM H⁺/pH. The right panel gives both changes in mixed mean $[HCO_3^-]_{pI}$ and pH_{pI} as functions of transit time ($[HCO_3^-]_{pI,in}=31.2$ mM, $pH_{pI,in}=7.66$). Curves: theoretical simulation of the situations; (—, left-hand scale) $\dot{A}_{pI}=1$ and $\beta_{pI}=5.5$ mM H⁺/pH; (---, left-hand scale) $\dot{A}_{pI}=100$ and $\beta_{pI}=5.5$ mM H⁺/pH; (--- · ---, right-hand scale) $\dot{A}_{pI}=6500$ and $\beta_{pI}=5.5$ mM H⁺/pH; (— · —, right-hand scale) $\dot{A}_{pI}=6500$ and $\beta_{pI}=54.6$ mM H⁺/pH.

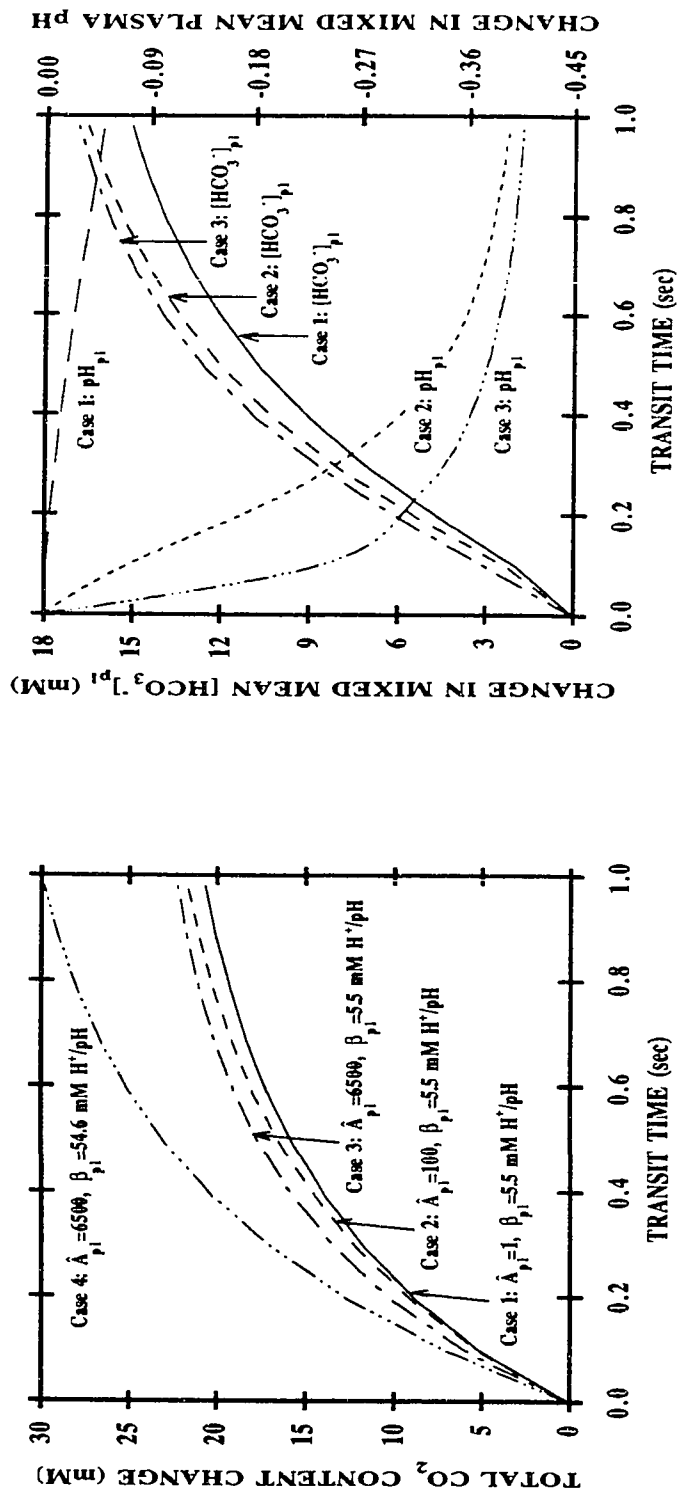


Figure 6.22: Effect of extracellular catalysis of CO₂ hydration/dehydration reactions on rate of CO₂ removal by human whole blood flowing in a Type 2 artificial membrane tube (see Table 6.11). The left panel gives the total CO₂ content change as a function of transit time ($[\text{CO}_2]_{\text{total},in}=24.4 \text{ mM}$). Curves: theoretical simulation of the situations; (—) $\hat{A}_{pI}=1$, (---) $\hat{A}_{pI}=100$, (---) $\hat{A}_{pI}=6500$ and $\beta_{pI}=5.5 \text{ mM H}^+/\text{pH}$; (---) $\hat{A}_{pI}=6500$ and $\beta_{pI}=54.6 \text{ mM H}^+/\text{pH}$. The right panel gives both changes in mixed mean $[\text{HCO}_3^-]_{pI}$ and pH_{pI} as functions of transit time ($[\text{HCO}_3^-]_{pI,in}=31.2 \text{ mM}$, $\text{pH}_{pI,in}=7.66$). Curves: theoretical simulation of the situations; (—, left-hand scale) $\hat{A}_{pI}=1$ and $\beta_{pI}=5.5 \text{ mM H}^+/\text{pH}$; (---, left-hand scale) $\hat{A}_{pI}=100$ and $\beta_{pI}=5.5 \text{ mM H}^+/\text{pH}$; (---, right-hand scale) $\hat{A}_{pI}=6500$ and $\beta_{pI}=5.5 \text{ mM H}^+/\text{pH}$; (---, right-hand scale) $\hat{A}_{pI}=6500$ and $\beta_{pI}=54.6 \text{ mM H}^+/\text{pH}$.

tabulated in Table 6.14. With catalysis similar to that present inside the RBC ($\hat{A}_{pl}=6500$), the increment in CO_2 transfer represent a 12-43% increase for the oxygenation case and 8-13% increases for the deoxygenation case. It is worth noting that the maximum increment in CO_2 transfer for the conditions of $\hat{A}_{pl}=6500$ and $\beta_{pl}=5.5$ mM H^+/pH (normal plasma buffering capacity) is less than the case where $\hat{A}_{pl}=6500$ and $\beta_{pl}=54.6$ mM H^+/pH (buffering capacity equivalent to that inside the RBC). This result is due to the compartmentalization of blood buffers. Normal plasma buffer is only $\approx 10\%$ of that of RBC interior, and with rapid CO_2 dehydration (hydration) of plasma HCO_3^- there is a concomitant reduction (increase) of H^+ , which reduces the speed of the dehydration (hydration) reaction. Therefore, both plasma enzyme and buffering of pH changes are necessary to maintain rapid transfer.

It is interesting to observe that the model predicts a $|\Delta \text{pH}_{pl}|$ of ≈ 0.05 pH units at $z=L$ for 27- μm -diameter vessels which is much smaller in comparison to a $|\Delta \text{pH}_{pl}|$ of ≈ 0.4 pH units for 1.47-mm-diameter vessels. For illustration, consider the case of blood oxygenation accompanied by CO_2 removal. During the gas exchange CO_2 diffuses into the environmental gas space, and P_{CO_2} of blood decreases. Intracellular HCO_3^- falls rapidly as it is converted to CO_2 in the presence of carbonic anhydrase. Plasma HCO_3^- decreases much slowly because the chemical conversion is uncatalyzed, and most of the decrease in HCO_3^- of the plasma is by way of the anion exchange. Within the RBCs, CO_2 , HCO_3^- and H^+ remain essentially in equilibrium; however, the uncatalyzed reaction occurs so slowly that the plasma H^+ concentration changes only slightly while CO_2 and HCO_3^- decreases. The absence of carbonic anhydrase in plasma does not restrict CO_2 exchange; however, it does restrict the rate of plasma pH changes. For the large vessels with diameters of 1.47 mm, the residence time of the RBCs in the membrane tube (\approx several minutes) is long compared to the time scale of the uncatalyzed extracellular CO_2 hydration/dehydration reactions (half time of ≈ 10

Table 6.14

Effect of extracellular catalysis of CO₂ hydration/dehydration reactions (\hat{A}_{pl}) and extracellular buffering capacity (β_{pl}) on CO₂ transfer for both oxygenation (accompanied by CO₂ elimination) and deoxygenation (accompanied by CO₂ uptake) cases in artificial membrane tubes.

Cases	$\Delta[CO_2]_{total} = [CO_2]_{total}(z=L) - [CO_2]_{total}(z=0)$ (mM)			
	$\beta_{pl}=5.5 \text{ mM H}^+/\text{pH}$			$\beta_{pl}=54.6 \text{ mM H}^+/\text{pH}$
	$\hat{A}_{pl}=1$	$\hat{A}_{pl}=100$	$\hat{A}_{pl}=6500$	$\hat{A}_{pl}=6500$
Oxygenation (I.D.=1.47 mm) [†]	- 13.0	- 18.1 (39% ↑) [¶]	- 18.6 (43% ↑)	- 20.3 (56% ↑)
Oxygenation (I.D.=27 μm) [*]	- 13.1	- 13.8 (5% ↑)	- 14.9 (12% ↑)	- 18.1 (38% ↑)
Deoxygenation (I.D.=1.47 mm) [†]	17.4	19.1 (9% ↑)	19.6 (13% ↑)	-29.6 (70% ↑)
Deoxygenation (I.D.=27 μm) [*]	20.6	21.6 (5% ↑)	22.2 (8% ↑)	-29.8 (45% ↑)

[†] Type 1 membrane tube: Q=12.5 ml/hr.

^{*} Type 2 membrane tube: Q=9 μl/hr.

[¶] Values in parentheses denote the % increase in the amount of total CO₂ transfer which is calculated as:

$$\% \uparrow = \frac{\Delta[CO_2]_{total}(\hat{A}_{pl}, \beta_{pl}) - \Delta[CO_2]_{total}(\hat{A}_{pl}=1, \beta_{pl}=5.5 \text{ mM H}^+/\text{pH})}{\Delta[CO_2]_{total}(\hat{A}_{pl}=1, \beta_{pl}=5.5 \text{ mM H}^+/\text{pH})} \cdot 100$$

Table 6.15

Effect of extracellular catalysis of CO₂ hydration/dehydration reactions (\hat{A}_{pl}) and extracellular buffering capacity (β_{pl}) on plasma pH changes for both oxygenation (accompanied by CO₂ elimination) and deoxygenation (accompanied by CO₂ uptake) cases in artificial membrane tubes.

Cases	$\Delta pH_{pl} = pH_{pl}(z=L) - pH_{pl}(z=0)$			
	$\beta_{pl}=5.5 \text{ mM H}^+/\text{pH}$			$\beta_{pl}=54.6 \text{ mM H}^+/\text{pH}$
	$\hat{A}_{pl}=1$	$\hat{A}_{pl}=100$	$\hat{A}_{pl}=6500$	$\hat{A}_{pl}=6500$
Oxygenation (I.D.=1.47 mm) [†]	0.433	0.520 (20% ↑) [¶]	0.528 (22% ↑)	0.260 (51% ↓) [#]
Oxygenation (I.D.=27 μm) [*]	0.023	0.374 (15-fold ↑) [¶]	0.562 (23-fold ↑)	0.250 (56% ↓)
Deoxygenation (I.D.=1.47 mm) [†]	-0.386	-0.467 (21% ↑)	-0.481 (25% ↑)	-0.327 (32% ↓)
Deoxygenation (I.D.=27 μm) [*]	-0.050	-0.394 (7-fold ↑)	-0.407 (7-fold ↑)	-0.300 (26% ↓)

[†] Type 1 membrane tube: $Q=12.5 \text{ ml/hr}$.

^{*} Type 2 membrane tube: $Q=9 \text{ μl/hr}$.

[¶] Values in parentheses denote the increase in the change of plasma pH which is calculated as:

$$(\% \uparrow) \text{ or } (\text{fold } \uparrow) = \frac{\Delta pH_{pl}(\hat{A}_{pl}, \beta_{pl}=5.5 \text{ mM H}^+/\text{pH}) - \Delta pH_{pl}(\hat{A}_{pl}=1, \beta_{pl}=5.5 \text{ mM H}^+/\text{pH})}{\Delta pH_{pl}(\hat{A}_{pl}=1, \beta_{pl}=5.5 \text{ mM H}^+/\text{pH})}$$

[#] Values in parentheses denote % the decrease in the change of plasma pH which is calculated as:

$$\% \downarrow = \frac{\Delta pH_{pl}(\hat{A}_{pl}=6500, \beta_{pl}=5.5 \text{ mM H}^+/\text{pH}) - \Delta pH_{pl}(\hat{A}_{pl}=6500, \beta_{pl}=54.6 \text{ mM H}^+/\text{pH})}{\Delta pH_{pl}(\hat{A}_{pl}=6500, \beta_{pl}=5.5 \text{ mM H}^+/\text{pH})}$$

sec, Klocke (1987)); consequently, plasma pH continues to change as blood travels down the vessels. For the smaller tubes with diameters of 27 μm , the residence time of the RBCs is of the order of one sec; as a result, plasma pH remains essentially unchanged. However, in the cases where additional carbonic anhydrase is added to the plasma of a 27- μm -diameter vessel, the magnitude of ΔpH_{pl} undergoes a 10 - 20 fold increase (Table 6.15).

6.2.2.c *Effects of Red Blood Cell $\text{HCO}_3^-/\text{Cl}^-$ Exchange Kinetics*

Another major determinant of CO_2 transport in blood involves the kinetics of $\text{HCO}_3^-/\text{Cl}^-$ exchange across the RBC membrane. Since under normal physiological conditions, $\approx 80\%$ of CO_2 transfer is derived from the hydration of intra- and extracellular HCO_3^- , the rate of anion exchange is important. The impact of the anion exchange on CO_2 transfer is studied here by varying T_{tot} ; results are shown for T_{tot} ranging from 0.02×10^6 to 1×10^7 . $T_{tot} = 1 \times 10^6$ represents normal RBC membrane; $T_{tot} = 0.02 \times 10^6$ and 0.5×10^6 represent abnormal or drug-inhibited RBC membrane; $T_{tot} = 1 \times 10^7$ represents a 10-fold increase in anion transporters per RBC. The influence of the anion exchange on CO_2 transport is shown in Figures 6.23 and 6.24 for the oxygenation case in the 27- μm -diameter tube; in Figures 6.25 and 6.26 for the deoxygenation case. On the left hand side of Figures 6.23 and 6.25 the computed total CO_2 content and change is given as a function of the transit time and T_{tot} ; and on the right hand side, the changes in both the intra- and extracellular HCO_3^- . Figures 6.24 and 6.26 present effect of anion exchange on pH regulation and Cl^- concentration change; the left-hand plots show changes in both intra- and extracellular pH versus transit time; the right-hand plots, changes in both intra- and extracellular Cl^- . These results illustrate that inhibition of RBC anion exchange affects CO_2 transport and pH changes (also see Tables 6.16 and 6.17). Because some commonly used drugs and anesthetics are known to inhibit the RBC anion exchange, the results may have

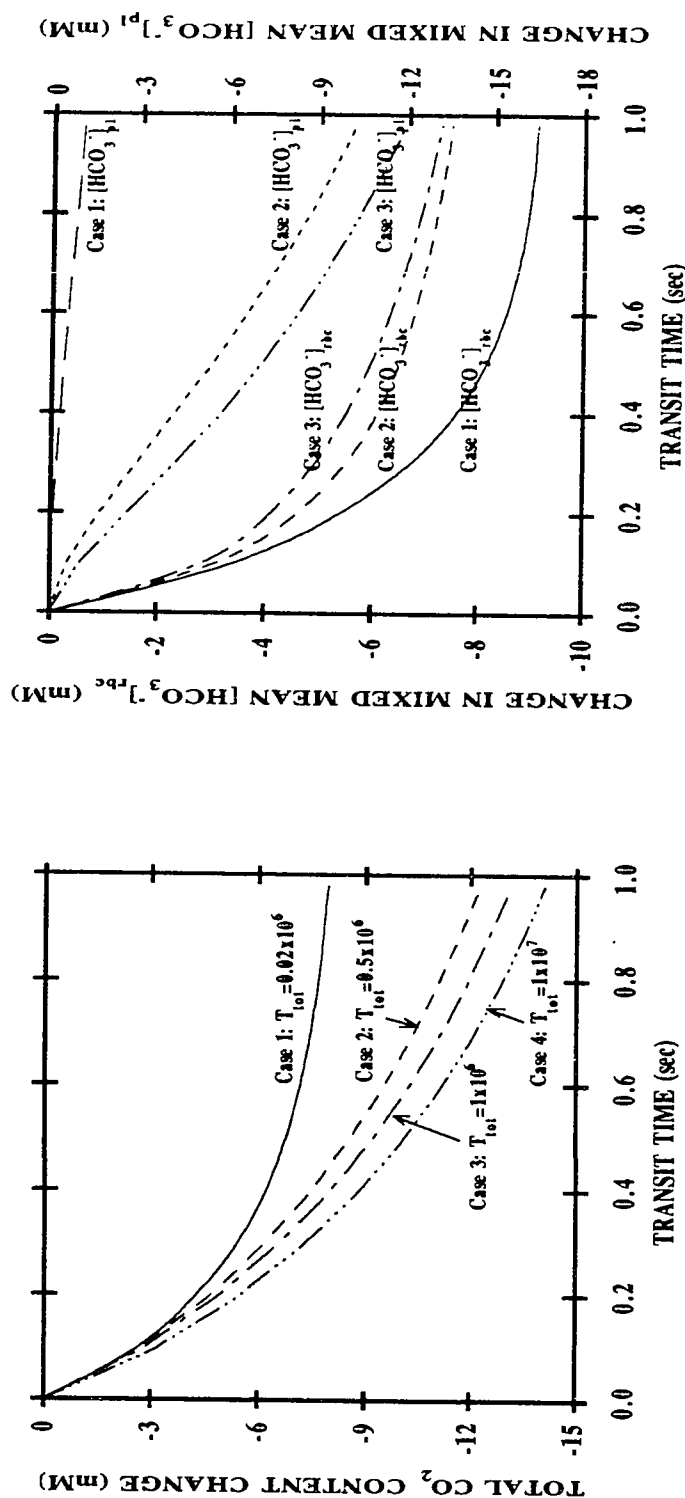


Figure 6.23: Effect of RBC $\text{HCO}_3^-/\text{Cl}^-$ exchange on rate of CO_2 elimination from human whole blood flowing in a Type 2 artificial membrane tube (see Table 6.11). The left panel gives the total CO_2 content change as a function of transit time ($[\text{CO}_2]_{\text{total}, \text{in}} = 22.4 \text{ mM}$). Curves: theoretical simulation of the situations; (—) $T_{\text{tot}} = 0.02 \times 10^6$, (---) $T_{\text{tot}} = 0.5 \times 10^6$, (— · —) $T_{\text{tot}} = 1 \times 10^6$ and (— · · —) $T_{\text{tot}} = 1 \times 10^7$. The right panel gives both changes in mixed mean intra- and extracellular HCO_3^- concentrations as functions of transit time ($[\text{HCO}_3^-]_{\text{rbc}, \text{in}} = 9.42 \text{ mM}$, $[\text{HCO}_3^-]_{\text{pl}, \text{in}} = 25.6 \text{ mM}$). Curves: theoretical simulation of the situations; (—, left-hand scale) and (— · —, right-hand scale) $T_{\text{tot}} = 0.02 \times 10^6$, (---, left-hand scale) and (--- · ·, right-hand scale) $T_{\text{tot}} = 0.5 \times 10^6$, (— · —, left-hand scale) and (— · · —, right-hand scale) $T_{\text{tot}} = 1 \times 10^6$.

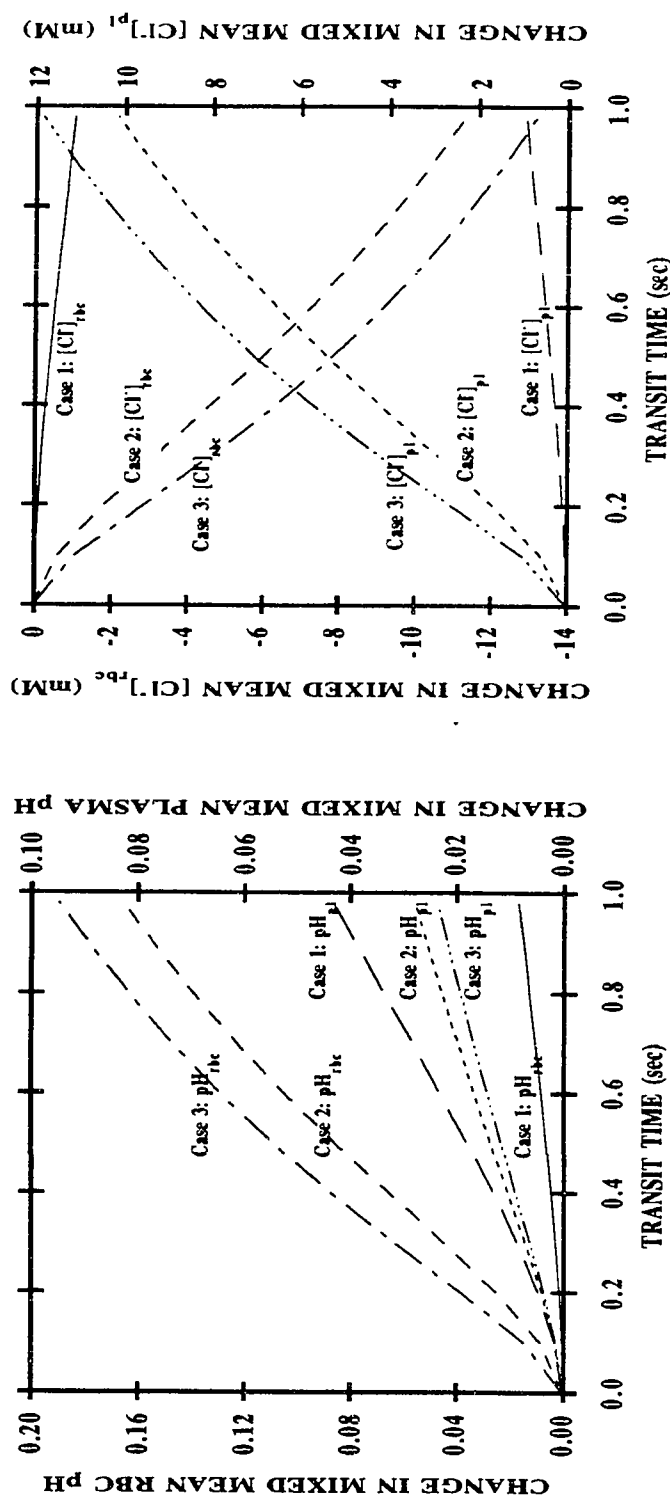


Figure 6.24: Effect of RBC anion exchange on rate of CO_2 elimination from human whole blood flowing in a Type 2 artificial membrane tube (see Table 6.11). The left panel gives both the changes in mixed mean intra- and extracellular pH as functions of transit time ($\text{pH}_{rbc,in} = 7.06$, $\text{pH}_{pl,in} = 7.28$). Curves: theoretical simulation of the situations; (—, left-hand scale) and (---, right-hand scale) $T_{tot} = 0.02 \times 10^6$; (- - - -, left-hand scale) and (- · - · - ·, right-hand scale) $T_{tot} = 0.5 \times 10^6$; (— · — · —, left-hand scale) and (— · — · —, right-hand scale) $T_{tot} = 1 \times 10^6$. The right panel gives both changes in mixed mean intra- and extracellular Cl^- concentrations as functions of transit time ($[\text{Cl}^-]_{rbc,in} = 36.7$ mM, $[\text{Cl}^-]_{pl,in} = 98.2$ mM). Curves: theoretical simulation of the situations; (—, left-hand scale) and (---, right-hand scale) $T_{tot} = 0.02 \times 10^6$; (- - - -, left-hand scale) and (- · - · - ·, right-hand scale) $T_{tot} = 0.5 \times 10^6$; (— · — · —, left-hand scale) and (— · — · —, right-hand scale) $T_{tot} = 1 \times 10^6$.

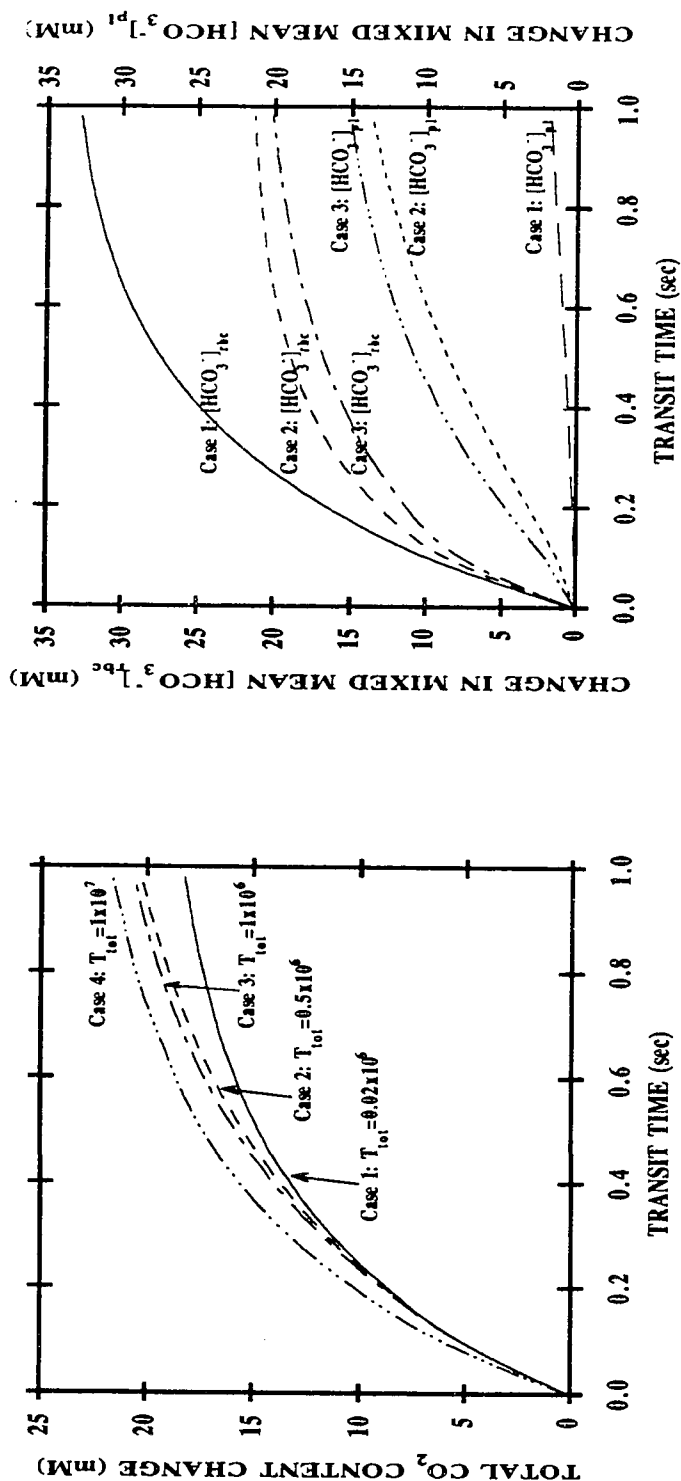


Figure 6.25: Effect of RBC HCO_3^-/Cl^- exchange on rate of CO_2 uptake by human whole blood flowing in a Type 2 artificial membrane tube (see Table 6.11). The left panel gives the total CO_2 content change as a function of transit time ($[CO_2]_{total,in}=24.4$ mM). Curves: theoretical simulation of the situations; (—) $T_{tot}=0.02 \times 10^6$, (---) $T_{tot}=0.5 \times 10^6$, (---) $T_{tot}=1 \times 10^6$ and (---) $T_{tot}=1 \times 10^7$. The right panel gives both changes in mixed mean intra- and extracellular HCO_3^- concentrations as functions of transit time ($[HCO_3^-]_{rbc,in}=12.0$ mM, $[HCO_3^-]_{pl,in}=31.2$ mM). Curves: theoretical simulation of the situations; (—, left-hand scale) and (---, right-hand scale) $T_{tot}=0.02 \times 10^6$; (---, left-hand scale) and (---, right-hand scale) $T_{tot}=0.5 \times 10^6$; (---, left-hand scale) and (---, right-hand scale) $T_{tot}=1 \times 10^6$.

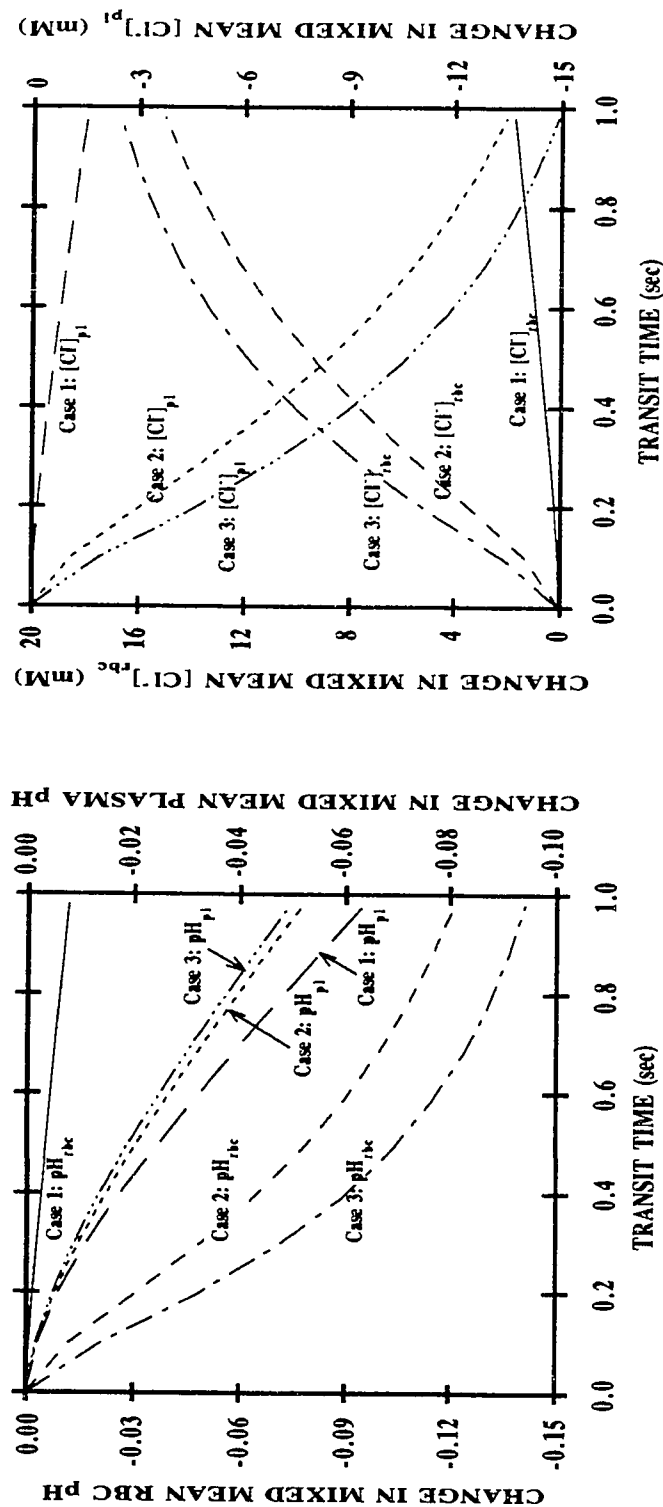


Figure 6.26: Effect of RBC anion exchange on rate of CO_2 uptake by human whole blood flowing in a Type 2 artificial membrane tube (see Table 6.11). The left panel gives both the changes in mixed mean intra- and extracellular pH as functions of transit time ($pH_{rbc,in}=7.44$, $pH_{pl,in}=7.66$). Curves: theoretical simulation of the situations; (—, left-hand scale) and (---, right-hand scale) $T_{tot}=0.02 \times 10^6$; (- - - -, right-hand scale) $T_{tot}=0.5 \times 10^6$; (- · - · - ·, right-hand scale) $T_{tot}=1 \times 10^6$. The right panel gives both changes in mixed mean intra- and extracellular Cl^- concentrations as functions of transit time ($[Cl^-]_{rbc,in}=40.2$ mM, $[Cl^-]_{pl,in}=107.8$ mM). Curves: theoretical simulation of the situations; (—, left-hand scale) and (---, right-hand scale) $T_{tot}=0.02 \times 10^6$; (- - - -, left-hand scale) and (- · - · - ·, right-hand scale) $T_{tot}=0.5 \times 10^6$; (- · - · - ·, right-hand scale) $T_{tot}=1 \times 10^6$.

Table 6.16

Effect of anion exchange on CO₂ transfer for both oxygenation (accompanied by CO₂ elimination) and deoxygenation (accompanied by CO₂ uptake) cases in artificial membrane tubes.

Cases	$\Delta[CO_2]_{total} = [CO_2]_{total}(z=L) - [CO_2]_{total}(z=0)$ (mM)		
	$T_{tot}=0.02 \times 10^6$	$T_{tot}=0.5 \times 10^6$	$T_{tot}=1 \times 10^6$
Oxygenation (I.D.=27 μ m) [†]	- 8.0 (39% ↓)*	- 12.1 (8% ↓)	- 13.1
Deoxygenation (I.D.=27 μ m) [†]	18.1 (12% ↓)	20.1 (2% ↓)	21.6 (5% ↑)

[†] Type 2 membrane tube: Q=9 μ l/hr.

* Values in parentheses denote the % decrease in the amount of total CO₂ transfer which is calculated as:

$$\% \downarrow = \frac{\Delta[CO_2]_{total}(T_{tot}=1 \times 10^6) - \Delta[CO_2]_{total}(T_{tot})}{\Delta[CO_2]_{total}(T_{tot}=1 \times 10^6)} .$$

† Values in parentheses denote the % increase in the amount of total CO₂ transfer which is calculated as:

$$\% \uparrow = \frac{\Delta[CO_2]_{total}(T_{tot}) - \Delta[CO_2]_{total}(T_{tot}=1 \times 10^6)}{\Delta[CO_2]_{total}(T_{tot}=1 \times 10^6)} .$$

Table 6.17

Effect of anion exchange on both intra- and extracellular pH changes for both oxygenation (accompanied by CO_2 elimination) and deoxygenation (accompanied by CO_2 uptake) cases in artificial membrane tubes.

Cases	$\Delta pH_{rbc} = pH_{rbc}(z=L) - pH_{rbc}(z=0)$		
	$T_{tot}=0.02 \times 10^6$	$T_{tot}=0.5 \times 10^6$	$T_{tot}=1 \times 10^6$
Oxygenation (I.D.=27 μm) [†]	0.016 (91% ↓)*	0.165 (13% ↓)	0.189
Deoxygenation (I.D.=27 μm) [†]	-0.012 (92% ↓)	-0.121 (14% ↓)	-0.144
Cases	$\Delta pH_{pl} = pH_{pl}(z=L) - pH_{pl}(z=0)$		
	$T_{tot}=0.02 \times 10^6$	$T_{tot}=0.5 \times 10^6$	$T_{tot}=1 \times 10^6$
Oxygenation (I.D.=27 μm) [†]	0.043 (84% ↑) [‡]	0.028 (18% ↑)	0.023
Deoxygenation (I.D.=27 μm) [†]	-0.064 (28% ↑)	-0.052 (5% ↑)	-0.050

[†] Type 2 membrane tube: $Q=9 \mu\text{l/hr}$.

* Values in parentheses denote the % decrease in the change of RBC pH which is calculated as:

$$\% \downarrow = \frac{\Delta pH_{rbc}(T_{tot}=1 \times 10^6) - \Delta pH_{rbc}(T_{tot})}{\Delta pH_{rbc}(T_{tot}=1 \times 10^6)} \cdot 100$$

[‡] Values in parentheses denote the % increase in the change of plasma pH which is calculated as:

$$\% \uparrow = \frac{\Delta pH_{pl}(T_{tot}) - \Delta pH_{pl}(T_{tot}=1 \times 10^6)}{\Delta pH_{pl}(T_{tot}=1 \times 10^6)} \cdot 100$$

important clinical implications on blood CO_2 transport and pH regulation in small microvessels. Due to the fact that a smaller $\text{HCO}_3^-/\text{Cl}^-$ flux is involved for a 1.47-mm-diameter tube (about 2-3 order of magnitudes smaller than that observed for a 27- μm -diameter tube), changes in the quantity T_{tot} only introduced small changes in CO_2 transport. Those changes, which amount to less than 5% of the total transport, are of minor importance; consequently, those results are not shown.

For illustration, let's consider blood oxygenation accompanied by CO_2 removal in the case where 98% of the $\text{HCO}_3^-/\text{Cl}^-$ exchange is inhibited (case 1 in Figure 6.23). The decrease in the efficiency of anion transport results in a $\approx 39\%$ fall in CO_2 elimination (Table 6.16). In this situation, the accessibility of intracellular carbonic anhydrase activity to the extracellular HCO_3^- is further limited. As a result, CO_2 normally eliminated from blood that had been in the form of plasma HCO_3^- when the blood entered the microvessel is not available to be excreted. The left-hand plot of Figure 6.23 depicts a lowest $\Delta[\text{HCO}_3^-]_{pl}$ and highest $\Delta[\text{HCO}_3^-]_{rbc}$ for case 1 where 98% of the anion transport capability is impaired. Although there is an increase in intracellular HCO_3^- removal from blood, the magnitude of this additional $\Delta[\text{HCO}_3^-]_{rbc}$ is not sufficient to compensate for the decrease in the elimination of plasma HCO_3^- . The reason is that under the "normal" conditions of this computation $\approx 52\%$ of the CO_2 elimination comes from the extracellular HCO_3^- pool, and $\approx 23\%$ comes from the intracellular HCO_3^- . In the case of the impeded anion exchange ($T_{tot}=0.02\times 10^6$), only $\approx 13\%$ of the CO_2 removal is derived from plasma HCO_3^- , and $\approx 48\%$ is derived from red cell HCO_3^- .

In the case where the efficiency of the anion transporter is artificially increased by imposing a 10-fold increase in the total number of anion transporters per RBC, the total amount of CO_2 removal is increased by up to 9% (see Figure 6.23 and Table 6.16). This is due to the fact that during normal operation of the band 3 protein the

plasma HCO_3^- pool is not depleted as much as it theoretically could be due to limitation of the quantity of bicarbonate ions that flow into the RBC to be hydrated. As the capacity of band 3 protein increases this limitation is decreased and blood increasingly behaves as though it had a common HCO_3^- pool (or common carbonic anhydrase pool). In this situation, 56% of the $\Delta[\text{CO}_2]_{\text{total}}$ is attributed to $\Delta[\text{HCO}_3^-]_{\text{pl}}$; and 21%, $\Delta[\text{HCO}_3^-]_{\text{rbc}}$. It is also worth noting that for the blood deoxygenation accompanied by CO_2 uptake cases, $\Delta[\text{CO}_2]_{\text{total}}$ is affected to a lesser extent by the impairment of the $\text{HCO}_3^-/\text{Cl}^-$ exchange. The explanation for this observation is that during the reverse process of CO_2 uptake, intracellular carbonic anhydrase activity is accessible to the incoming bicarbonate source (in the form of CO_2) so that intracellular CO_2 hydration/dehydration reactions continue to occur and HCO_3^- are mostly stored inside the RBCs. Although the extracellular HCO_3^- carriage capacity is not fully utilized in this case, this magnitude of increase in $\Delta[\text{HCO}_3^-]_{\text{rbc}}$ is almost sufficient to compensate for the decrease in the $\Delta[\text{HCO}_3^-]_{\text{pl}}$. For the “normal” deoxygenation case considered here, 42% of the $\Delta[\text{CO}_2]_{\text{total}}$ is attributed to $\Delta[\text{HCO}_3^-]_{\text{pl}}$ and 41% is attributed to $\Delta[\text{HCO}_3^-]_{\text{rbc}}$. For abnormal or drug-inhibited case ($T_{\text{tot}}=0.02 \times 10^6$), only 5% of the $\Delta[\text{CO}_2]_{\text{total}}$ is derived from $\Delta[\text{HCO}_3^-]_{\text{pl}}$ and 75% from $\Delta[\text{HCO}_3^-]_{\text{rbc}}$.

6.2.2.d *Effects of Hematocrit on Gas Transfer*

The model is also used to examine rates of O_2 and CO_2 transfer in microvessels at different levels of discharge hematocrit; the range of hematocrit studied is 20-60%. For the oxygenation situation, O_2 uptake as functions of transit time are given in Figures 6.27 and 6.29 for the Types 1 and 2 artificial membrane tubes, respectively; and CO_2 elimination, Figures 6.28 and 6.30. For the deoxygenation situation, O_2 release results for the Types 1 and 2 artificial membrane tubes are given in Figures 6.31 and 6.33; and CO_2 uptake, Figures 6.32 and 6.34. The right-hand plots of Figures 6.27, 6.29, 6.31 and 6.33 show the computed changes in $[\text{O}_2]_{\text{total}}$; the left-hand plots of

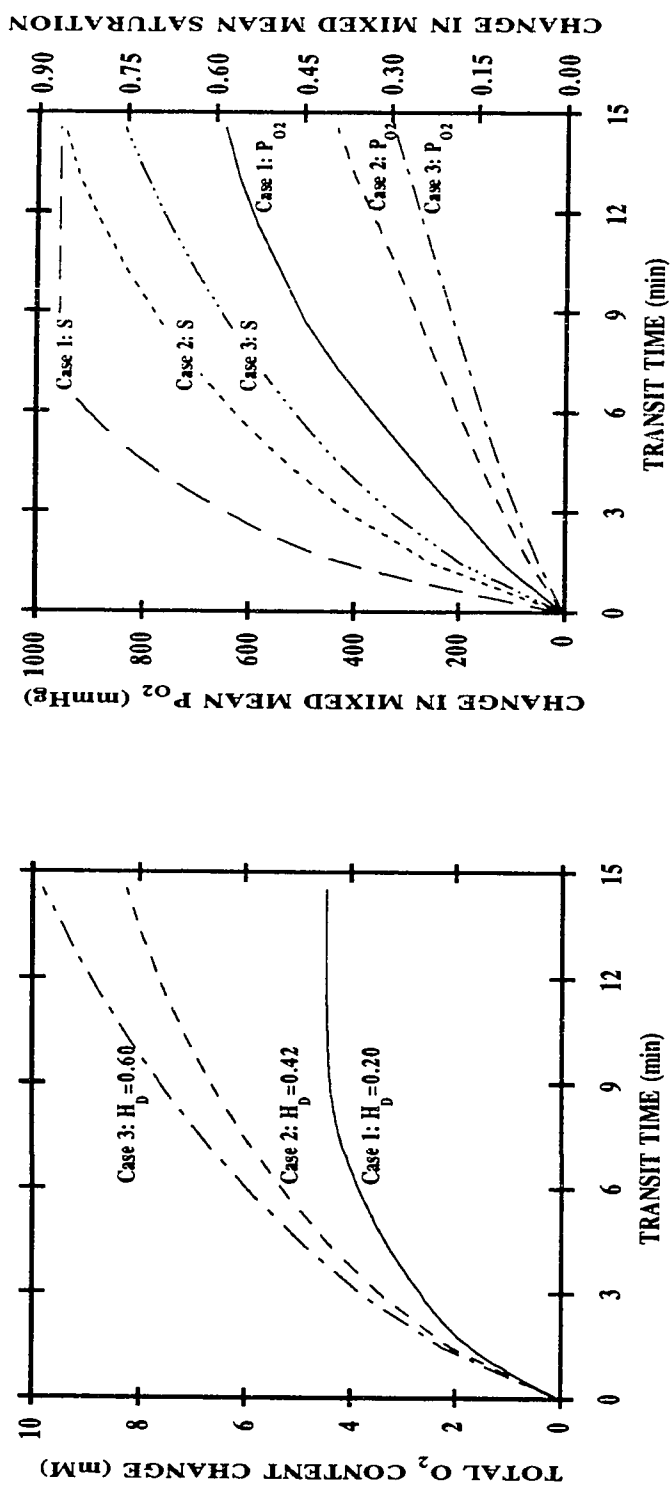


Figure 6.27: Effect of discharge hematocrit on rate of O₂ uptake by human whole blood flowing in a Type 1 artificial membrane tube (see Table 6.11). The left panel gives the total O₂ content change as a function of transit time. Curves: theoretical simulation of the situations; (—) $H_D=0.20$ and $[O_2]_{total,in}=0.53$ mM, (— · — ·) $H_D=0.42$ and $[O_2]_{total,in}=1.09$ mM, (---) $H_D=0.60$ and $[O_2]_{total,in}=14.0$ mmHg, $S_{in}=0.12$). The right panel gives both changes in mixed mean P_{O_2} and O₂ saturation as functions of transit time ($P_{O_2,in}=14.0$ mmHg, $S_{in}=0.12$). Curves: theoretical simulation of the situations; (— · — ·, left-hand scale) and (---, right-hand scale) $H_D=0.20$; (— · — ·, left-hand scale) and (---, right-hand scale) $H_D=0.42$; (— · — ·, left-hand scale) and (---, right-hand scale) $H_D=0.60$.

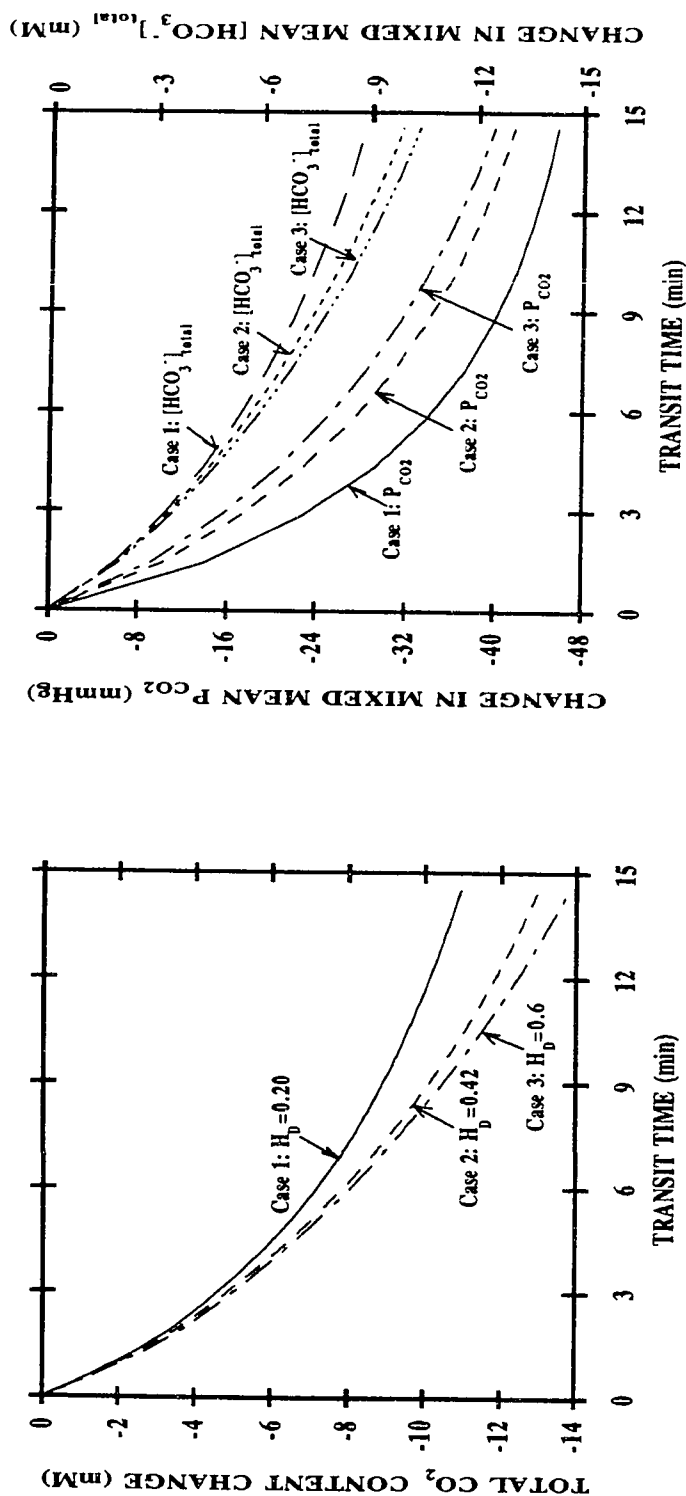


Figure 6.28: Effect of discharge hematocrit on rate of CO_2 elimination from human whole blood flowing in a Type 1 artificial membrane tube (see Table 6.11). The left panel gives the total CO_2 content change as a function of transit time. Curves: theoretical simulation of the situations; (—) $H_D=0.20$ and $[\text{CO}_2]_{\text{total},\text{in}}=24.9$ mM, (---) $H_D=0.42$ and $[\text{CO}_2]_{\text{total},\text{in}}=22.4$ mM, (— · —) $H_D=0.60$ and $[\text{CO}_2]_{\text{total},\text{in}}=20.4$ mM. The right panel gives both changes in mixed mean P_{CO_2} and $[\text{HCO}_3^-]_{\text{total}}$ as functions of transit time ($P_{\text{CO}_2,\text{in}}=52.5$ mmHg). Curves: theoretical simulation of the situations; (—, —, left-hand scale) and (— · —, right-hand scale) $H_D=0.20$ and $[\text{HCO}_3^-]_{\text{total},\text{in}}=22.3$ mM; (---, left-hand scale) and (--- · ---, right-hand scale) $H_D=0.42$ and $[\text{HCO}_3^-]_{\text{total},\text{in}}=18.8$ mM; (— · —, left-hand scale) and (— · — · —, right-hand scale) $H_D=0.60$ and $[\text{HCO}_3^-]_{\text{total},\text{in}}=16.0$ mM.

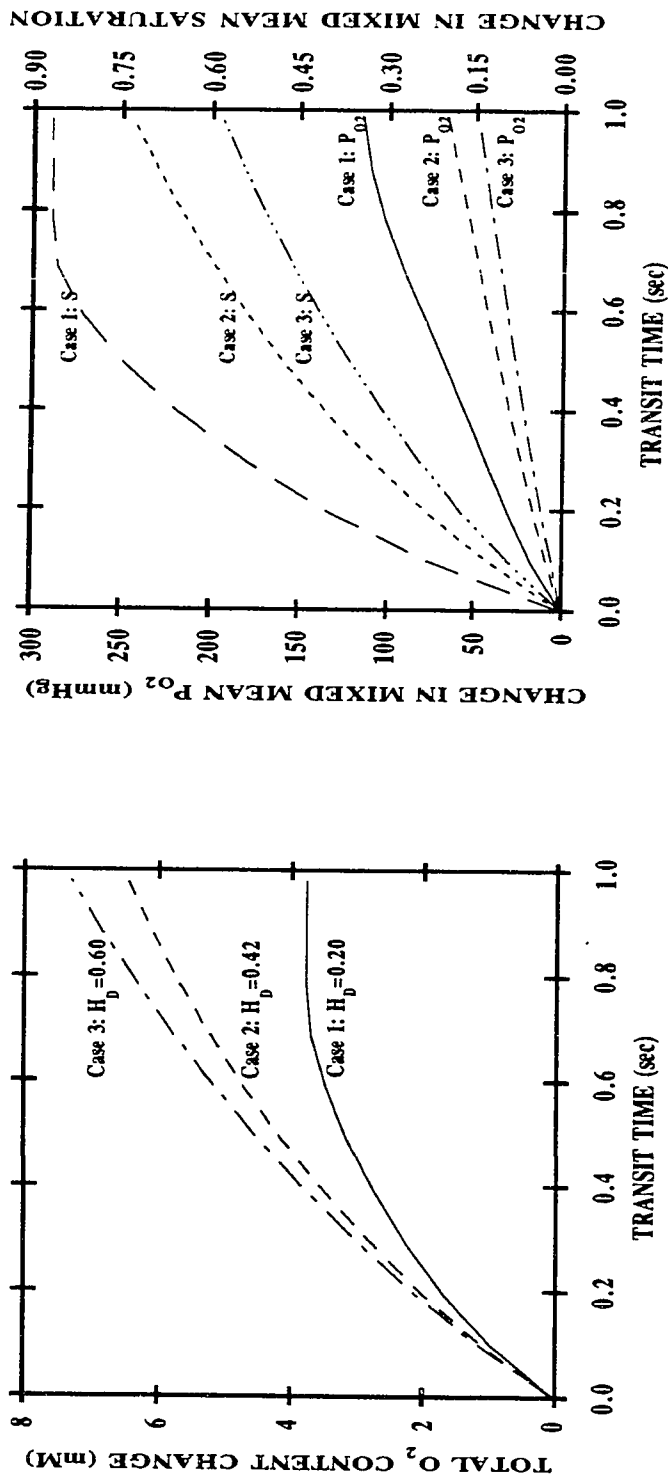


Figure 6.29: Effect of discharge hematocrit on rate of O_2 uptake by human whole blood flowing in a Type 2 artificial membrane tube (see Table 6.11). The left panel gives the total O_2 content change as a function of transit time. Curves: theoretical simulation of the situations; (—) $H_D=0.20$ and $[O_2]_{total,in}=0.53$ mM, (---) $H_D=0.42$ and $[O_2]_{total,in}=1.09$ mM, (— · —) $H_D=0.60$ and $[O_2]_{total,in}=1.55$ mM. The right panel gives both changes in mixed mean P_{O_2} and O_2 saturation as functions of transit time ($P_{O_2,in}=14.0$ mmHg, $S_{in}=0.12$). Curves: theoretical simulation of the situations; (—, left-hand scale) and (---, right-hand scale) $H_D=0.20$; (— · —, left-hand scale) and (---, right-hand scale) $H_D=0.42$; (— · —, left-hand scale) and (---, right-hand scale) $H_D=0.60$.

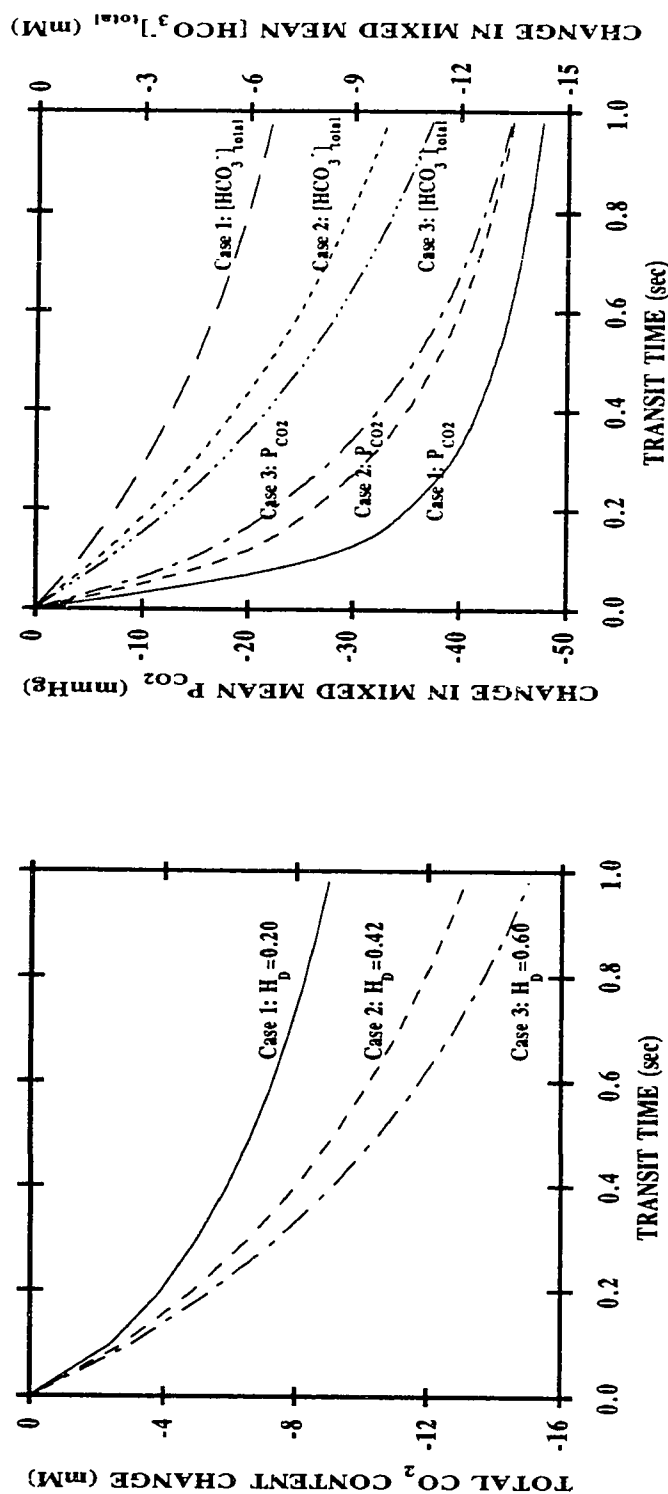


Figure 6.30: Effect of discharge hematocrit on rate of CO₂ elimination from human whole blood flowing in a Type 2 artificial membrane tube (see Table 6.11). The left panel gives the total CO₂ content change as a function of transit time. Curves: theoretical simulation of the situations; (—) $H_D=0.20$ and $[CO_2]_{total,in}=24.9$ mM, (---) $H_D=0.42$ and $[CO_2]_{total,in}=22.4$ mM, (· · ·) $H_D=0.60$ and $[CO_2]_{total,in}=20.4$ mM. The right panel gives both changes in mixed mean P_{CO_2} and $[HCO_3^-]_{total}$ as functions of transit time ($P_{CO_2,in}=52.5$ mmHg). Curves: theoretical simulation of the situations; (—, left-hand scale) and (---, right-hand scale) $H_D=0.20$ and $[HCO_3^-]_{total,in}=22.3$ mM; (· · ·, left-hand scale) and (---, right-hand scale) $H_D=0.42$ and $[HCO_3^-]_{total,in}=18.8$ mM; (—, left-hand scale) and (---, right-hand scale) $H_D=0.60$ and $[HCO_3^-]_{total,in}=16.0$ mM.

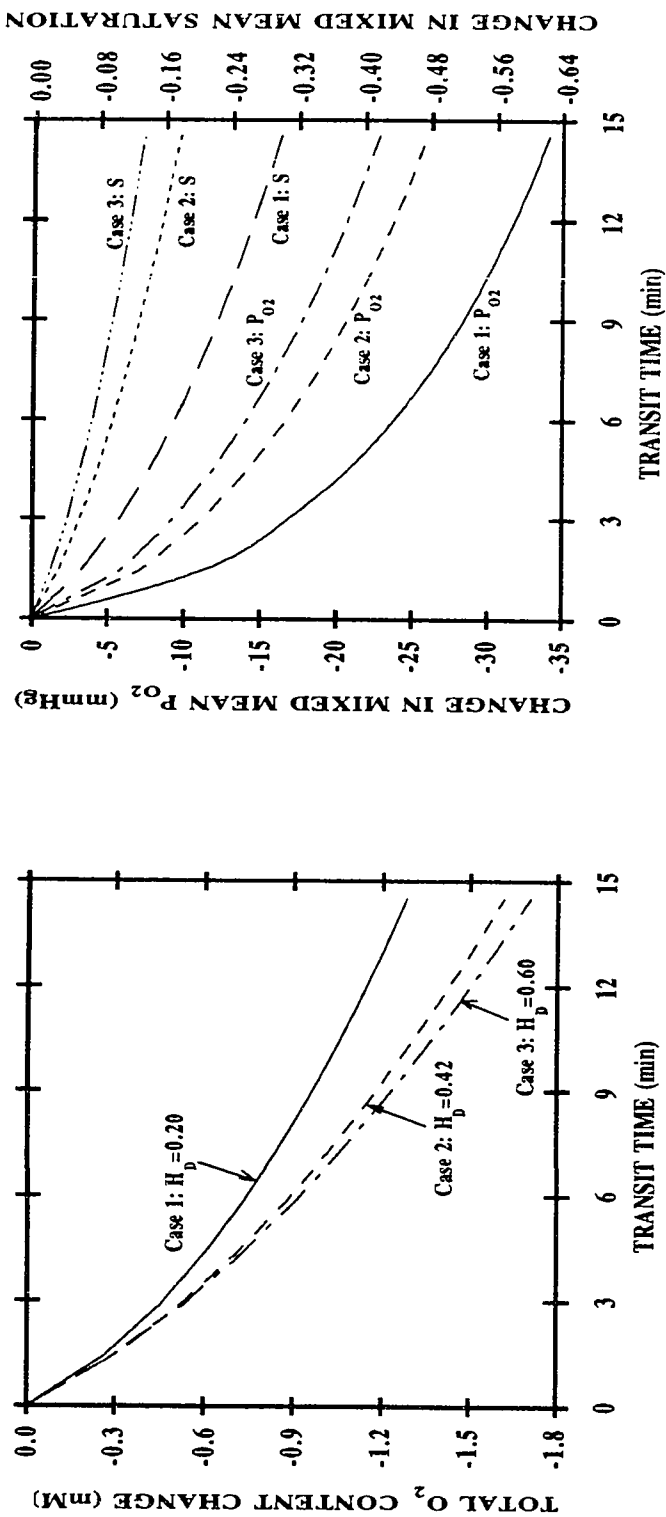


Figure 6.31: Effect of discharge hematocrit on rate of O₂ release from human whole blood flowing in a Type 1 artificial membrane tube (see Table 6.11). The left panel gives the total O₂ content change as a function of transit time. Curves: theoretical simulation of the situations; (—) $H_D=0.20$ and $[O_2]_{total,in}=12.1$ mM, (---) $H_D=0.42$ and $[O_2]_{total,in}=8.43$ mM, (— · —) $H_D=0.60$ and $[O_2]_{total,in}=68.1$ mmHg, $S_{in}=0.94$). The right panel gives both changes in mixed mean P_{O_2} and O₂ saturation as functions of transit time ($P_{O_2,in}=68.1$ mmHg, $S_{in}=0.94$). Curves: theoretical simulation of the situations; (—, left-hand scale) and (---, right-hand scale) $H_D=0.20$; (— · —, left-hand scale) and (— · —, right-hand scale) $H_D=0.42$; (— · —, left-hand scale) and (— · —, right-hand scale) $H_D=0.60$.

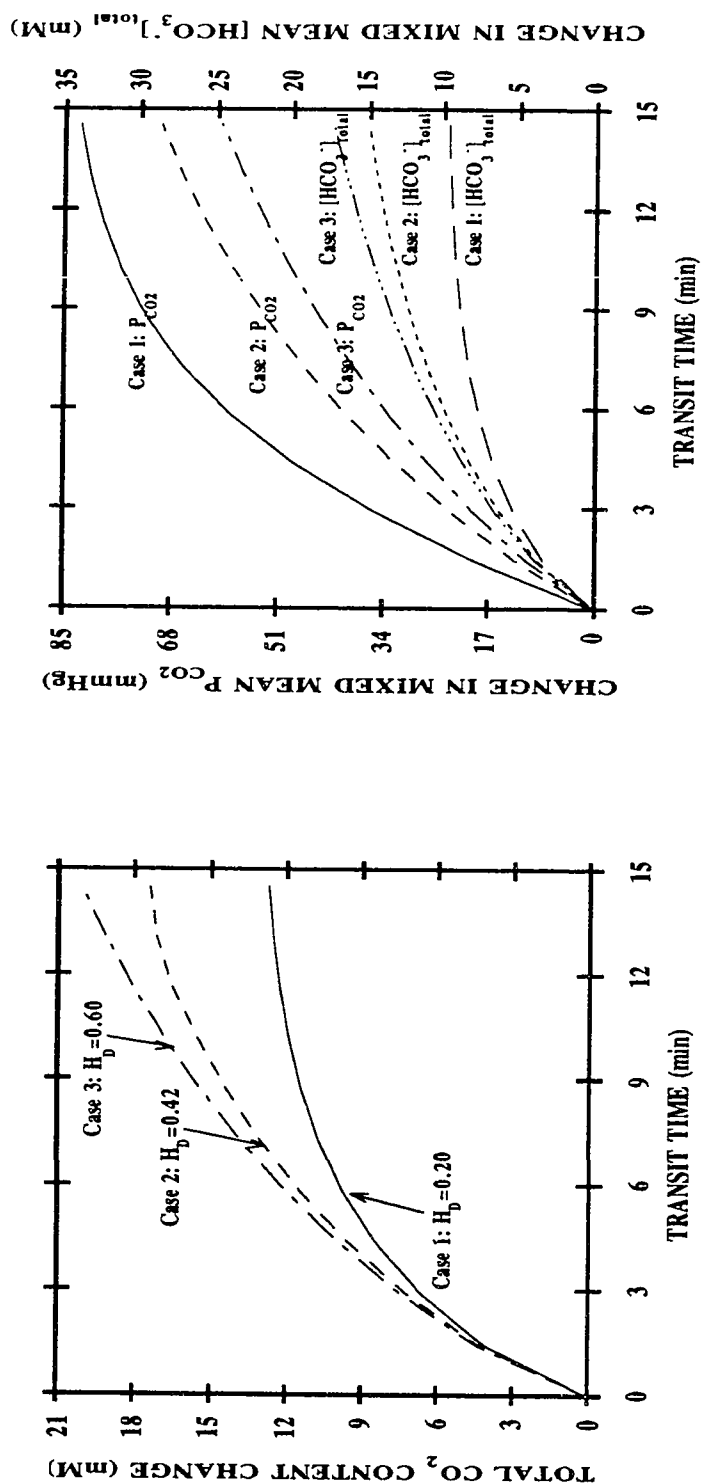


Figure 6.32: Effect of discharge hematocrit on rate of CO₂ uptake by human whole blood flowing in a Type 1 artificial membrane tube (see Table 6.11). The left panel gives the total CO₂ content change as a function of transit time. Curves: theoretical simulation of the situations; (—) $H_D=0.20$ and $[CO_2]_{total,in}=28.4$ mM, (---) $H_D=0.42$ and $[CO_2]_{total,in}=24.4$ mM, (— · —) $H_D=0.60$ and $[CO_2]_{total,in}=21.3$ mM. The right panel gives both changes in mixed mean P_{CO_2} and $[HCO_3^-]_{total}$ as functions of transit time ($P_{CO_2,in}=28.8$ mmHg). Curves: theoretical simulation of the situations; (—, left-hand scale) and (— · —, right-hand scale) $H_D=0.20$ and $[HCO_3^-]_{total,in}=27.4$ mM; (---, left-hand scale) and (--- · ---, right-hand scale) $H_D=0.42$ and $[HCO_3^-]_{total,in}=23.1$ mM; (— · — · —, left-hand scale) and (— · — · — · —, right-hand scale) $H_D=0.60$ and $[HCO_3^-]_{total,in}=19.7$ mM.

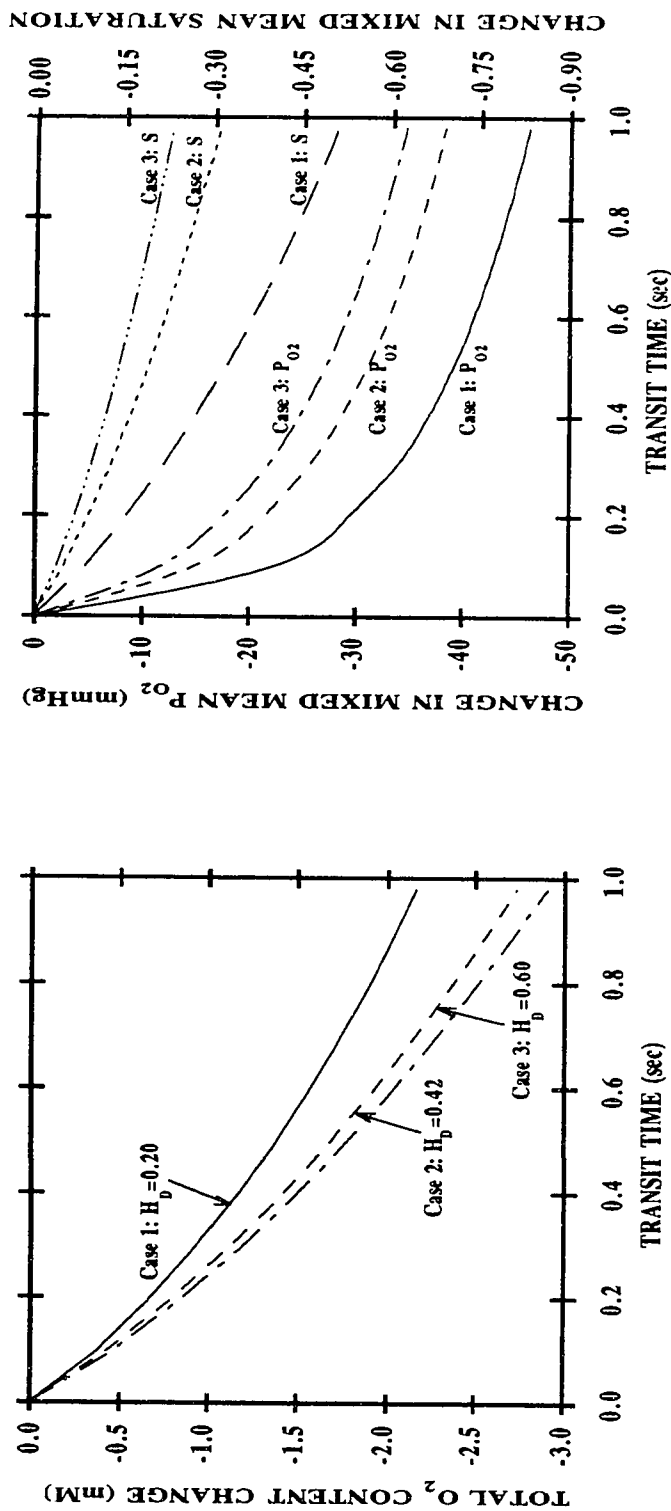


Figure 6.33: Effect of discharge hematocrit on rate of O_2 release from human whole blood flowing in a Type 2 artificial membrane tube (see Table 6.11). The left panel gives the total O_2 content change as a function of transit time. Curves: theoretical simulation of the situations; (—) $H_D=0.20$ and $[O_2]_{total,in}=4.09$ mM, (---) $H_D=0.42$ and $[O_2]_{total,in}=8.43$ mM, (— · —) $H_D=0.60$ and $[O_2]_{total,in}=12.1$ mM. The right panel gives both changes in mixed mean P_{O_2} and O_2 saturation as functions of transit time ($P_{O_2,in}=68.1$ mmHg, $S_{in}=0.94$). Curves: theoretical simulation of the situations; (—, left-hand scale) and (— · —, right-hand scale) $H_D=0.20$; (---, left-hand scale) and (--- · ---, right-hand scale) $H_D=0.42$; (— · —, left-hand scale) and (— · — · —, right-hand scale) $H_D=0.60$.

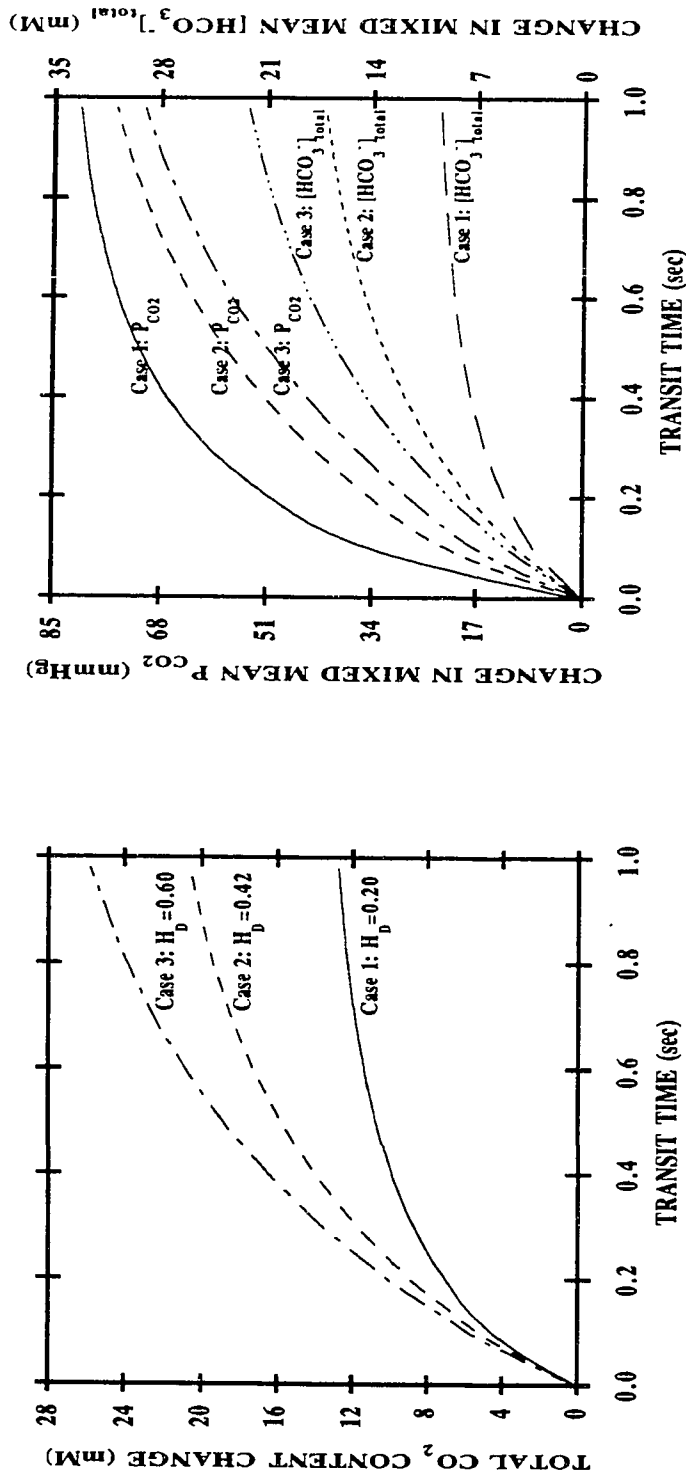


Figure 6.34: Effect of discharge hematocrit on rate of CO_2 uptake by human whole blood flowing in a Type 2 artificial membrane tube (see Table 6.11). The left panel gives the total CO_2 content change as a function of transit time. Curves: theoretical simulation of the situations; (-----) $H_D=0.20$ and $[CO_2]_{total,in}=28.4$ mM, (- - - -) $H_D=0.42$ and $[CO_2]_{total,in}=24.4$ mM, (- - -) $H_D=0.60$ and $[CO_2]_{total,in}=21.3$ mM. The right panel gives both changes in mixed mean P_{CO_2} and $[HCO_3^-]_{total}$ as functions of transit time ($P_{CO_2,in}=28.8$ mmHg). Curves: theoretical simulation of the situations; (——, left-hand scale) and (— — —, right-hand scale) $H_D=0.20$ and $[HCO_3^-]_{total,in}=27.4$ mM; (- - - -, left-hand scale) and (- · · · · ·, right-hand scale) $H_D=0.42$ and $[HCO_3^-]_{total,in}=23.1$ mM; (— · · · —, left-hand scale) and (— · · · —, right-hand scale) $H_D=0.60$ and $[HCO_3^-]_{total,in}=19.7$ mM.

those figures display the computed change in P_{O_2} and S . The right-hand plots of Figures 6.28, 6.30, 6.32 and 6.34 present the computed changes in $[CO_2]_{total}$; the left-hand plots of those figures give the computed change in P_{CO_2} and $[HCO_3^-]_{total}$. These results demonstrate that under the conditions of the computations both $\Delta[O_2]_{total}$ and $\Delta[CO_2]_{total}$ are affected by the discharge hematocrit of blood perfusing the microvessel.

The suspension with lower discharge hematocrit shows a larger change in O_2 saturation; this does not mean better O_2 transport properties. The diluted blood is easier to uptake or release to a given saturation level, because its total transport capacity is smaller. However, after any length z , the suspension with higher hematocrit carries or releases the greater amount of oxygen. The suspension with lower discharge hematocrit also gives a larger change in P_{CO_2} ; this is due to the fact that $\alpha_{CO_2,pl}$ is greater than $\alpha_{CO_2,rbc}$. These results indicate that a reduction in H_D from 42% to 20% leads to a ≈ 21 -46% reduction in $\Delta[O_2]_{total}$ compared with ≈ 16 -38% reduction in $\Delta[CO_2]_{total}$ (Table 6.18). An increase in H_D from 42% to 60% results in ≈ 6 -19% increase in $\Delta[O_2]_{total}$ accompanied by ≈ 7 -25% increase in $\Delta[CO_2]_{total}$ (Table 6.18). The decrement in $\Delta[O_2]_{total}$ with reductions in H_D is caused by a decrease in the O_2 carrying capacity of blood. Concomitant reductions in $\Delta[CO_2]_{total}$ with reductions of H_D are caused mainly due to the decrease in the size of the high buffer capacity intraerythrocyte pool and diminished flux of HCO_3^-/Cl^- across to the RBC membrane.

Table 6.18

Effect of discharge hematocrit (H_D) on O_2 and CO_2 transfer for both oxygenation (accompanied by CO_2 elimination) and deoxygenation (accompanied by CO_2 uptake) cases in artificial membrane tubes.

Cases	$\Delta[O_2]_{total} = [O_2]_{total}(z=L) - [O_2]_{total}(z=0)$ (mM)	
	$H_D=0.20$	$H_D=0.42$
Oxygenation (I.D.=1.47 mm) [†]	4.45 (46% ↓) [‡]	8.23
Oxygenation (I.D.=27 μm) [*]	3.77 (42% ↓)	6.45
Deoxygenation (I.D.=1.47 mm) [†]	- 1.28 (21% ↓)	- 1.62
Deoxygenation (I.D.=27 μm) [*]	- 2.17 (27% ↓)	- 2.73
Cases	$\Delta[CO_2]_{total} = [CO_2]_{total}(z=L) - [CO_2]_{total}(z=0)$ (mM)	
	$H_D=0.20$	$H_D=0.42$
Oxygenation (I.D.=1.47 mm) [†]	- 10.9 (16% ↓) [‡]	- 13.0
Oxygenation (I.D.=27 μm) [*]	- 9.0 (31% ↓)	- 13.1
Deoxygenation (I.D.=1.47 mm) [†]	12.7 (32% ↓)	17.4
Deoxygenation (I.D.=27 μm) [*]	12.7 (38% ↓)	20.6
		$H_D=0.60$
		- 13.9 (7% ↑) [#]
		- 15.0 (14% ↑)
		20.1 (16% ↑)
		25.7 (25% ↑)

[†] Type 1 membrane tube: $Q=12.5$ ml/hr.

^{*} Type 2 membrane tube: $Q=9$ μl/hr.

[‡] Values in parentheses denote the % decrease in the amount of total O_2 or CO_2 transfer which is calculated as:

$$\% \downarrow = \frac{\Delta[C]_{total}(H_D=0.42) - \Delta[C]_{total}(H_D=0.20)}{\Delta[C]_{total}(H_D=0.42)}$$

[#] Values in parentheses denote the % increase in the amount of total O_2 or CO_2 transfer which is calculated as:

$$\% \uparrow = \frac{\Delta[C]_{total}(H_D=0.60) - \Delta[C]_{total}(H_D=0.42)}{\Delta[C]_{total}(H_D=0.42)}$$

6.3 Summary

The blood-gas chemistry has been of interest to numerous investigators (see Chapters 2 and 3). Many investigators made enormous contributions to our understanding of this intricate physicochemical system. In this study, the findings of these other investigators including the simultaneous interactions of hemoglobin with O_2 , CO_2 , H^+ and DPG, CO_2 hydration/dehydration reactions and the buffering action of various buffer systems are incorporated into a mathematical model of gas transport and pH regulation by blood flowing in microvessels. There are a number of refinements in the present analysis compared to previous attempts at a quantitative examination of the chemical and transport processes by blood flowing in microvessels. The transport model developed here takes the particulate, or two-phase, nature of blood into account, while previous analysis assumed blood to be a continuum. This discrete model not only considers the fact that most of the O_2 carried by blood is bound to hemoglobin which is encapsulated inside the RBCs, but also takes into account the compartmentalization of carbonic anhydrase activity and buffers. This analysis also includes the cooperative interactions of various components in the blood, while most of prior studies neglect the Bohr and Haldane effects. Ionic movements (HCO_3^- and Cl^-) across the RBC membrane are described in this work via a simplified ping-pong model, while previous models either did not include this exchange process or otherwise used a phenomenological passive diffusion approach. This model allows us to quantitate the effects of the many simultaneous processes involved in the gas exchange and gain insights not possible using previous approaches.

This discrete model of blood gas transport and pH regulation in microvessels is entirely predictive in the sense that there is no fitting to the O_2/CO_2 transport data. All the parameters are either physical properties or determined by ways independent of the

blood gas exchange experiments. Theoretical calculations simulating Voorhees' experiments show excellent agreement between the measured and predicted changes in $[O_2]_{total}$ and $[CO_2]_{total}$ (Voorhees, 1976) over a range of flowrates, hematocrits and inlet compositions (including P_{O_2} , P_{CO_2} and pH). The computed results of O_2 transport generated by the continuum model also are in good agreement with the O_2 uptake data obtained for blood oxygenation accompanied by simultaneous CO_2 elimination experiments. However, the continuum model underpredicts the amount of O_2 release for the reverse process of blood deoxygenation accompanied with CO_2 uptake. This is due to the fact that the Bohr effect which plays a more important role during deoxygenation is neglected in the continuum model. In addition, the continuum approach yields inaccurate predictions of CO_2 transport. The overprediction of CO_2 transport by the continuum model is attributed to the local chemical equilibrium assumption. Although this assumption is applicable for describing O_2 transport in large vessels, it is determined here not to be appropriate for describing CO_2 transport due to the neglect of the compartmentalization of the carbonic anhydrase activity in blood.

On the basis of the results illustrated in Section 6.2.2.a, it is concluded that the Bohr effect is not of primary importance for blood oxygenation in the presence of simultaneous CO_2 elimination in microvessels (on the order of 10%). However, the Bohr effect is considerably more important for the deoxygenation process accompanied by simultaneous CO_2 uptake by blood (on the order of 20%). The computations also indicate that the Haldane effect (on the order of 10%) is only of secondary importance in CO_2 transfer in microvessels. However, it can potentially become more important upon incorporation of the altered buffering capacity of hemoglobin into the model.

As illustrated in Section 6.2.2.b, an enhancement in CO_2 transfer is observed when carbonic anhydrase activity is available to plasma. However, even in the

presence of large amounts of carbonic anhydrase activity available to plasma, CO_2 elimination and uptake by blood do not undergo a maximum increment. This is due to the fact that the magnitude of extracellular CO_2 hydration/dehydration reactions under these circumstances is limited by the buffer capacity of plasma which is only about 1/10 of that of the hemoglobin-rich RBC interior. Although the fractional changes in total CO_2 exchange are only moderately affected by the extent of catalysis of plasma CO_2 hydration/dehydration reactions in the 27- μm -diameter vessels (on the order of 10%), addition of carbonic anhydrase ($\hat{A}_{pl}=6500$) increases the magnitude of ΔpH_{pl} by over 10 fold.

The relationship between CO_2 transfer and $\text{HCO}_3^-/\text{Cl}^-$ exchange discussed in Section 6.2.2.c demonstrates that a decrease (increase) in total CO_2 transport is linked to a reduced (enhanced) capacity of the anion transporter. The fall in the magnitude of $\Delta[\text{CO}_2]_{total}$ is 39% when the capacity of the anion exchange is reduced by 98% for 27- μm -diameter vessels. It is expected that a reduction of the capacity by as little as 50% may be important in small capillaries where higher fluxes of CO_2 and O_2 are involved. $\Delta[\text{CO}_2]_{total}$ is substantially affected by the inhibition of band 3 protein, and the magnitudes of ΔpH_{rbc} and ΔpH_{pl} are altered to a much greater extent. Even in the cases where $\Delta[\text{CO}_2]_{total}$ is only moderately affected, the magnitudes of ΔpH_{rbc} and ΔpH_{pl} are still altered significantly. Because a number of commonly used drugs are known to inhibit anion exchanges across the human RBC membrane, these observations may have important clinical implications with respect to abnormal gas exchange and disturbed acid/base regulation due to impaired $\text{HCO}_3^-/\text{Cl}^-$ exchange.

The results presented in Section 6.2.2.d show that under the conditions of our computations both O_2 and CO_2 exchange are influenced by the discharge hematocrit of blood perfusing the vessels. The dependence of $\Delta[\text{O}_2]_{total}$ of O_2 transport on cell mass is well established, and these computations show the concomitant $\Delta[\text{CO}_2]_{total}$. Any

decrement in H_D (as with anemia) can, besides reducing $\Delta[O_2]_{total}$, also significantly diminish $\Delta[CO_2]_{total}$. The reduction in $\Delta[CO_2]_{total}$ is due to the decrease in the size of the high buffer capacity intracellular pool and decrease in the total number of anion transporters available for HCO_3^-/Cl^- exchange.

Computations of gas exchange and pH regulation are limited by the model chosen and the data used to characterize the model parameters. Previous attempts to describe this transport system have involved using continuum approximations and lumped-parameter approaches. As a result, effective properties and phenomenological constants are introduced to characterize the events involved in intracapillary exchange. One of the obvious shortcoming with this approach is that the “appropriate” values for the lumped, effective parameters are difficult to estimate, and the “appropriate” values change when the operating conditions change. In addition, this approach is inappropriate due to the fact that it does not include interactions of the different processes involved. Because these models do not incorporate the individual events which are important, it is difficult to quantitate the impact of alteration of an individual step or the interdependence among the many simultaneous processes.

Treating blood as a continuum with all the transferring species in local chemical equilibrium proves to be reasonably satisfactory for predicting O_2 transfer during blood oxygenation accompanied by simultaneous CO_2 elimination. However, this approach significantly underpredicts the amount of O_2 transport during blood deoxygenation accompanied by CO_2 uptake. This poor performance is attributed to the fact that the Bohr effect (alteration of P_{50} by collateral CO_2 transport) which has an important effect on the rate of deoxygenation is not taken into account in the continuum model. Furthermore, the continuum approach is determined here to be a poor representation for the CO_2 transfer network. This was clearly demonstrated when the predictions of the discrete and continuum models were compared with Voorhees'

experimental data. The error of the continuum model can be attributed to neglecting the fact that blood is a two-compartment system and that each compartment has very different reaction and buffering characteristics. It is observed that certain chemical reaction rates have substantial effects on the pH changes (e.g., extracellular CO_2 hydration/dehydration reactions and HCO_3^-/Cl^- exchange kinetics) but modify the overall gas exchange to a lesser extent. The continuum model is inadequate for prediction of $\Delta[CO_2]_{total}$, and even less adequate for prediction of intra- and extracellular ΔpH values which are important with respect to the acid/base status of blood.

Generally speaking, we find that appropriate conclusions depend on the choice of a proper model and that it is important to take into account the two-phase, compartmentalized nature of blood when describing simultaneous gas exchange and pH regulation by blood flowing in microvessels. The discrete model developed here still needs to be critically validated over a range of diameters. Simultaneous development of theoretical models and experimental measurements is, certainly, an excellent way to further our understanding of the complexities of this transport system.

CHAPTER 7

FUTURE DIRECTIONS

Theoretical Refinement and Experimental Validation of the Mathematical Model

Refinements can be introduced to improve the mathematical model developed in Chapter 6. Firstly, updated and more sophisticated blood-gas equilibria for describing the coupled interactions between hemoglobin, O_2 , CO_2 , H^+ and DPG should be implemented to the model if available. Secondly, a major undetermined feature of the kinetic equation for HCO_3^-/Cl^- across the RBC membrane which is the ratio of in-to-out and out-to-in translocation rate constants should be investigated further. Knauf and Mann (1984) proposed that the intrinsic association constants for anions are the same at both membrane surface and suggested that the translocation rates vary with the direction. They arrived at this conclusion in the view of the fact that the asymmetry of anion-bound sites was equal to that for empty sites. For a ping-pong model, the consideration of the asymmetry of band 3 protein will influence the determinations of the macroscopically dissociation constants of the ions.

Critical testing of the discrete model for predicting O_2/CO_2 transport and pH regulation over a range of diameters (20 - 100 μm) needs to be carried out. The *in vitro* microvessel microspectrophotometer system developed in this research program (developed by Boland *et al.* (1987) and currently being modified by McKay and Hellums) allows on-line determination of O_2 flux to and from hemoglobin solutions and RBC suspensions under physiological relevant conditions. Consequently, pH indicator (fluorescent probe or microelectrode) and P_{CO_2} indicator techniques need to be incorporated to the system to allow experimental validation of the model. In addition to a

wide range of diameters, these measurements need to be extended to a range of flow rates, hematocrit and biochemical status of blood samples.

Application of the Experimental and Theoretical Methodologies to Study Gas Transport and Acid/Base Balance by Biochemically Altered Cells, Pathological Cells and RBC Substitutes; and Effect of Drugs on Blood Respiratory Functions

The experimental measurements and theory can be extended to analyze gas transport to and from biochemically altered RBCs, pathological RBCs and RBC substitutes; and to study the effect of drugs. By observing the changes in gas transport and acid/base balance and analyzing data obtained with the help of the model, the key parameters which are affected, which in turn modify the gas transport, can be identified and quantified.

Biochemically Altered RBCs

Several factors involving RBC morphology and physiology influence the rates of its gas transport and *pH* regulation properties. Cell size and shape define the surface area available for O_2/CO_2 and HCO_3^-/Cl^- exchange across the RBC membrane. Intracellular hemoglobin concentration determines the O_2 carriage capacity and intracellular buffering capacity. Changes in intracellular DPG concentration and/or *pH* shift the hemoglobin- O_2 - CO_2 equilibrium relationship. Alterations in the content of intracellular carbonic anhydrase affect the degree of CO_2 retention in blood. The effect of cell size and shape can be studied by measuring the rates of gas exchange of osmotically altered human RBCs or RBCs from other species. The effects of altering intracellular contents of several determining factors can be studied by using reconstituted RBCs tailored made to meet the specified compositions.

Pathological RBCs

The model can be applied to examine gas transport by blood in certain pathological cases. For instance, RBCs from patients with sickle cell anemia may be

studied. Findings that polymerization of *hemoglobin S* is an O_2 -linked function, and that CO_2 has an O_2 -affinity independent effect on *deoxyhemoglobin S* polymerization suggest that varying P_{CO_2} might have different effects on respiratory functions and other RBC properties of blood in sickle cell anemia compared with normal blood. Part of the low affinity associated with sickle cell anemia can be explained by elevated levels of DPG, as seen with many anemic states. In addition, it was reported that the CO_2 -induced Bohr effect of sickle cell blood is considerably larger than normal (Ueda and Bookchin, 1984) which also contributes to the substantially lowering of the O_2 affinity. As another example, blood from patients with the conditions of either respiratory acidosis or alkalosis may be studied. Normal physiological processes occur only within a narrow range of pH ; however, in a number of diseases the acid/base balance may be shifted severely away from the normal acid/base environment. Respiratory acidosis (alkalosis) is an abnormal condition caused by the presence of excessive amounts of acid (alkali) or by reduction of alkali (acid) to a subnormal level; and the acid concerned in the disturbance is H_2CO_3 .

RBC Substitutes

Another application of these experimental and mathematical methodologies is to evaluate the efficiency of various RBC substitutes in delivering O_2 and removing CO_2 . Three classes of synthetic blood substitutes that are presently being tested in various laboratories include perfluorochemical emulsion, crosslinked or polymerized hemoglobin molecules free in solution and artificial RBCs prepared by encapsulating hemoglobin inside lipid bilayer vesicles. These blood substitutes have been studied primarily from an empirical point of view in terms of life support, circulation half-life, shelf life and safety with regard to pyrogens in whole animal transfusion studies. Therefore, the contributions which our experimental and theoretical methods can make is to provide systematic and quantitative analyses on the gas transport properties of these blood

substitutes. For example, transport property of liposome-encapsulated hemoglobin can be measured and analyzed as a function of vesicle size, lipid composition and intracellular compositions (Olson, personal communication).

Effect of Drugs

The key parameters which are modified by drugs, which in turn affect the gas transport and acid/base change of blood can be studied by simulation of the experiments which use the drugs. For example, one can study modification of the O_2 affinity of hemoglobin and normalization of the Bohr effect by some antisickling agents proposed for possible therapeutic roles in sickle cell anemia, such as potassium cyanate. One can also investigate the physiological alterations on CO_2 transport and deviations from the normal state of acid/base balance due to the presence of pharmacological agents, such as furosemide which inhibit RBC anion exchange and carbonic anhydrase activity, or acetazolamide, a more potent inhibitor of carbonic anhydrase activity.

Application of the Experimental and Theoretical Methodologies to Improve the Design of Extracorporeal Blood Oxygenator

Membrane oxygenators used in cardiopulmonary bypass surgery and in membrane lungs involve oxygen transport from relatively large conduits (about 100 μm and larger), and in most of these devices the mass transfer resistance attributable to the blood phase is a significant fraction of the total resistance. Hence, these experimental and mathematical approaches have utility in designing oxygenators and aiding in the interpretation of membrane lung function. In addition, more experimental work is needed to better quantify the O_2 transfer augmentation in blood and the validity of the model presented in Chapter 4 for shear-induced augmentation of O_2 . Furthermore, with additional experimental results a more correct model of augmentation would be appropriate. Finally, a study can be conducted to evaluate the feasibility of oxygenator designs which take advantage of the effects of shear-induced augmentation of O_2 .

REFERENCES

- Adair, G. S. (1925). The hemoglobin system VI. The oxygen dissociation curve of hemoglobin. *J. Biol. Chem.*, **63**, 529-545.
- Ahuja, A. S. (1980). Augmentation of heat and mass transfer in laminar flow of suspensions: A correlation of data. *J. Appl. Phys.*, **51**, 791-795.
- Altman, P. L., and Dittmer, D. S. (1971). "Respiration and Circulation". Bethesda, MD: Federation of American Societies for Experimental Biology.
- Artigue, R. S. (1980). "Mathematical Simulation of the Transport of Oxygen and Important Metabolites in the Human Brain." Ph.D. thesis, Tulane University.
- Artigue, R. S., and Bruley, D. F. (1983). The transport of oxygen, glucose, carbon dioxide and lactic acid in the human brain: Mathematical models. *In* "Oxygen Transport to Tissue IV: Advances in Experimental Medicine and Biology" (D. F. Bruley and H. E. Bischer, Eds.). New York: Plenum Press.
- Arturson, G., Garby, L., Robert, M., and Zaar, B. (1974). The oxygen dissociation curve of normal human blood with special reference to the influence of physiological effector ligands. *Scand. J. Clin. Lab. Invest.*, **26**, 47-52.
- Astarita, G., Savage, D. W., and Bisio, A. (1983). "Gas Treating with Chemical Solvents." New York: John Wiley and Sons.
- Balcerzak, M. J., and Raynor, S. (1961). Steady state temperature distribution and heat flow in prismatic bars with isothermal boundary conditions. *Ann. Biomed. Eng.*, **11**, 401-416.
- Bauer, C., Gros, G., and Bartels, H. (1980). "Biophysics and Physiology of Carbon Dioxide." Heidelberg: Springer-Verlag.

- Baumann, R., Bartels, H., and Bauer, C. (1987). Blood oxygen transport. *In* "Handbook of Physiology" (L. E. Farhi and S. M. Tenney, Eds.), pp. 147-172. Bethesda, MD: American Physiological Society.
- Baxley, P. T., and Hellums, J. D. (1983). A simple model for simulation of oxygen transport in the microcirculation. *Ann. Biomed. Eng.*, **11**, 401-416.
- Benn, J. A. (1974). "Carbon Dioxide Transfer from Weak Acids and Blood: The Effects of Carbonic Anhydrase and Oxygen Uptake on Carbon Dioxide Transfer in an Oxygenator." Ph.D. thesis, Massachusetts Institute of Technology.
- Benn, J. A., Smith, K. A., Drinker, P. A., and Mikic, B. B. (1975). The effects of carbonic anhydrase and oxygen uptake on carbon dioxide transfer in an oxygenator. *Proc. 28th Annu. Conf. Eng. Med. Biol.*, **17**, 241.
- Bidani, A., Crandall, E. D., and Forster, R. E. (1978). Analysis of postcapillary pH changes in blood in vivo after gas exchange. *J. Appl. Physiol.*, **44**, 770-781.
- Bidani, A., and Crandall, E. D. (1985). Kinetic parameters and activity of pulmonary vascular carbonic anhydrase. *Ann. N. Y. Acad. Sci.*, **68**, 565-575.
- Bidani, A., and Crandall, E. D. (1988). Velocity of CO₂ exchanges in the lungs. *Ann. Rev. Physiol.*, **50**, 639-652.
- Bird, R. B., Stewart, W. E., and Lightfoot, E. N. (1960). "Transport Phenomena." New York: John Wiley and Sons.
- Blacerzak, M. J., and Raynor, S. (1961). Steady-state temperature distribution and heat flow in prismatic bars with isothermal boundary conditions. *Int. J. Heat Mass Transfer*, **3**, 113-125.
- Boland, E. J., Nair, P. K., Lemon, D. D., Olson, J. S., and Hellums, J. D. (1987). An in vitro capillary system for studies on microcirculatory O₂ transport. *J. Appl. Physiol.*, **62**, 791-797.

- Bradley, C. G. (1969). "The Transport of Oxygen and Carbon Dioxide in Blood Flowing in a Permeable Tube." Ph.D. thesis, Louisiana State University.
- Bradley, C. G., and Pike, R. W. (1971). The transport of oxygen and carbon dioxide in blood flowing in a permeable tube. *J. Assoc. Adv. Med. Instrum.*, **5**, 230-242.
- Brahm, J. (1977). Temperature-dependent changes of chloride transport kinetics in human red cells. *J. Gen. Physiol.*, **70**, 283-306.
- Brahm, J. (1986). The physiology of anion transport in red cells. *Progress in Hematology*, **XIV**, 1-21.
- Buckles, R. G. (1966). "An Analysis of Gas Exchange in a Membrane Oxygenator." Ph.D. thesis, Massachusetts Institute of Technology.
- Buckles, R. G., Merrill, E. W., and Gilliland, E. R. (1968). An analysis of oxygen absorption in a tubular membrane oxygenator. *Am. Inst. Chem. Eng. J.*, **14**, 703-708.
- Buerk, D. G. (1985). An evaluation of Easton's parameter for the oxyhemoglobin equilibrium curve. In "Advances in Experimental Medicine and Biology" (D. Bruley, H. I. Bircher, and D. Reneau, Eds.), pp. 333-344. New York: Plenum Press.
- Buerk, D. G., and Bridges, E. W. (1986). A simplified algorithm for computing the variation in oxyhemoglobin saturation with pH, P_{CO_2} , T and DPG. *Chem. Eng. Commun.*, **47**, 113-124.
- Bugliarello, G., and Sevilla, J. (1970). Velocity distribution and other characteristics of steady and pulsatile blood flow in fine glass tubes. *Biorheology*, **7**, 85-107.
- Bunn, H. F., and Briehl, R. W. (1970). The interaction of 2,3-diphosphoglycerate with various human hemoglobins. *J. Clin. Invest.*, **49**, 1088-1095.
- Bunn, H. F., Ransil, B. J., and Chao, A. (1971). The interactions between erythrocyte organic phosphates, magnesium ion and hemoglobin. *J. Biol. Chem.*, **246**, 5273-5279.
- Butler, J. N. (1964). "Solubility and pH Calculations." Palo Alto, CA: Addison-Wesley.

- Byrne, G. D., Hindmarsh, A. C., Jackson, K. J., and Brown, H. G. (1977). A comparison of two ODE codes: GEAR and EPISODE. *Comp. Chem. Eng.*, **1**, 133-147.
- Cabantchik, Z. I., Knauf, P. A., and Rothstein, A. (1978). The anion transport system of the red blood cell: The role of membrane protein evaluated by the use of probes. *Biochim. Biophys. Acta*, **515**, 239-302.
- Caro, C. G., Pedley, T. J., Schroter, R. C., and Seed, W. A. (1978). "The Mechanics of the Circulation." New York: Oxford University Press.
- Chanutin, A., and Curnish, R. R. (1967). Effects of organic and inorganic phosphates on the oxygen equilibrium of human erythrocytes. *Arch. Biochem. Biophys.*, **121**, 96-102.
- Chen, S. S. (1972). "Transport Processes in a Membrane Oxygenator and a Tapered Tube with Suction and Injection." Ph.D. thesis, Kansas State University.
- Chow, E. I., Crandall, E. D., and Forster, R. E. (1976). Kinetics of bicarbonate-chloride exchange across the human red blood cell membrane. *J. Gen. Physiol.*, **68**, 633-652.
- Christoforides, C., and Hedley, W. J. (1969). Effect of temperature and hemoglobin concentration on solubility of oxygen in blood. *J. Appl. Physiol.*, **27**, 592-596.
- Clark, A., Federspiel, W. J., Clark, P. A. A., and Cokelet, G. R. (1985). Oxygen delivery from red cells. *Biophys. J.*, **47**, 171-181.
- Coin, J. T., and Olson, J. S. (1979). The rate of oxygen uptake by human red blood cells. *J. Biol. Chem.*, **25**, 1178-1190.
- Cokelet, G. R. (1987). The rheology and tube flow of blood. In "Handbook of Bioengineering" (R. Skalak and S. Chien, Eds.), pp. 14.1-14.17. New York: McGraw-Hill.
- Colton, C. K., and Drake, R. F. (1971). Effect of boundary conditions on oxygen transport to blood flowing in a tube. *Chem. Engr. Prog. Symp. Ser.*, **67**, 88-95.

- Crandall, E. D., Klocke, R. A., and Forster, R. E. (1971). Hydroxyl ion movements across the human erythrocyte membrane. *J. Gen. Physiol.*, **57**, 664-683.
- Crandall, E. D., and O'Brasky, J. E. (1978). Direct evidence for participation of rat lung carbonic anhydrase in CO₂ reaction. *J. Clin. Invest.*, **62**, 618-622.
- Crandall, E. D., and Bidani, A. (1981). Effects of red blood cell HCO₃⁻/Cl⁻ exchange kinetics on lung CO₂ transfer: Theory. *J. Appl. Physiol.: Respirat. Envir. Exercise Physiol.*, **50**, 265-271.
- Crandall, E. D., Mathew, S. J., Fleischer, R. S., Winter, H. I., and Bidani, A. (1981). Effects of inhibition of RBC HCO₃⁻/Cl⁻ exchange on CO₂ excretion and downstream pH disequilibrium in isolated rat lungs. *J. Clin. Invest.*, **68**, 853-862.
- Crandall, E. D., Winter, H. I., Schaeffer, J. D., and Bidani, A. (1982). Effects of salicylate on HCO₃⁻/Cl⁻ exchange across the human erythrocyte membrane. *J. Membr. Biol.*, **65**, 139-145.
- Dalmark, M. (1976). Effects of halides and bicarbonate on chloride transport in human red blood cells. *J. Gen. Physiol.*, **67**, 223-234.
- Davenport, H. (1969). "The ABC of Acid-Base Chemistry." Chicago, IL: University of Chicago Press.
- Defares, J. G., and Visser, B. F. (1962). On the form of the physiological CO₂ dissociation curve, the physiological O₂ dissociation curve and the diffusion curves of O₂ and CO₂ along the capillary path. *Ann. N. Y. Acad. Sci.*, **96**, 939-955.
- Diller, T. E. (1977). "Oxygen Diffusion through Flowing Blood." Sc.D. thesis, Massachusetts Institute of Technology.
- Diller, T. E., Mikic, B. B., and Drinker, P. A. (1980). Shear-induced augmentation of oxygen transfer in blood. *J. Biomech. Eng.*, **102**, 67-72.
- Diller, T. E., and Mikic, B. B. (1983). Oxygen diffusion in blood: A translational model of shear-induced augmentation. *J. Biomed. Eng.*, **105**, 346-352.

- Diller, T. E., Pattantyus, I. A., and Britts, W. C. (1984). Augmentation and facilitation of oxygen transfer in flowing hemoglobin solutions. *Adv. Exp. Med. Biol.*, **180**, 545.
- Dodgson, S. J., and Forster II, R. E. (1983). Carbonic anhydrase activity of intact erythrocytes from seven mammals. *J. Appl. Physiol.: Respirat. Environ. Exercise Physiol.*, **55**, 1292-1298.
- Dorson, W. J., Larsen, K. G., Elgas, R. J., and Voorhees, M. E. (1971). Oxygen transfer to blood: Data and theory. *Trans. Amer. Soc. Artif. Int. Organs*, **XVII**, 309-316.
- Dorson, W. J., and Voorhees, M. (1974). Limiting models for the transfer of CO₂ and O₂ in membrane oxygenators. *Trans. Amer. Soc. Artif. Int. Organs*, **XX**, 219-226.
- Easton, D. M. (1979). Oxyhemoglobin dissociation curve as expo-exponential paradigm of asymmetric sigmoid function. *J. Theor. Biol.*, **76**, 335-349.
- Eckstein, E. C., Bailey, D. G., and Shapiro, A. H. (1977). Self-diffusion of particles in shear flow of a suspension. *J. Fluid Mech.*, **79**, 191-208.
- Effros, R. M., Chang, R. S. Y., and Siverman, P. (1978). Acceleration of plasma bicarbonate conversion to carbon dioxide by pulmonary carbonic anhydrase. *Science*, **199**, 427-429.
- Ellsworth, M. L., Popel, A. S., and Pittman, R. N. (1988). Assessment and impact of heterogeneities of convective oxygen transport parameters in capillaries of striated muscle: Experimental and theoretical. *Microvas. Res.*, **35**, 341-362.
- Fair, J. C., and Weissman, M. H. (1971). Oxygen transfer to blood flowing in round tubes including Bohr and Haldane effects. *Chem. Eng. Sci.*, **26**, 963-967.
- Falke, J. J., and Chan, S. I. (1985). Evidence that anion transport by band 3 proceeds via a ping-pong mechanism involving a single transport site. *J. Biol. Chem.*, **260**, 9537-9544.

- Falke, J. J., Kaness, K. J., and Chan, S. I. (1985). The kinetic equation for the chloride transport cycle of band 3. *J. Biol. Chem.*, **260**, 9545-9551.
- Federspiel, W. J., and Popel, A. S. (1986). A theoretical analysis of the effect of the particulate nature of blood on oxygen release in capillaries. *Microvas. Res.*, **32**, 164-189.
- Fell, D. A. (1979). Computer simulation of the mixing technique and nonlinear optimization used in the analysis of oxyhemoglobin dissociation. *Math. Biosci.*, **46**, 59-69.
- Ferguson, J. K. W. (1936). Carbamino compounds of carbon dioxide with human hemoglobin and their role in the transport of CO₂. *J. Physiol. (London)*, **88**, 40-55.
- Forster, R. E. (1957). Exchange of gases between alveolar air and pulmonary diffusing capacity. *Physiol. Rev.*, **37**, 391-403.
- Forster, R. E. (1969). Rate of reactions of CO₂ with human hemoglobin. In "CO₂: Chemical, Biological and Physiological Aspects", pp. 55-64. Washington, DC: National Aeronautics and Space Administration.
- Forster, R. E., and Crandall, E. D. (1975). Time course of exchanges between red cells and extracellular fluid during CO₂ uptake. *J. Appl. Physiol.*, **38**, 710-718.
- Forster, R. E. (1982). Diffusion of chemical reaction as limiting factors in CO₂ equilibration in lungs. *Federation Proc.*, **41**, 2125-2127.
- Frohlich, O., and Gunn, R. B. (1986). Erythrocyte anion transport: The kinetics of a single-site obligatory exchange system. *Biochim. Biophys. Acta*, **864**, 169-194.
- Funder, J., and Weith, J. O. (1976). Chloride transport in human erythrocytes and ghosts: A quantitative comparison. *J. Physiol.*, **262**, 679-698.
- Gahtgens, P., Albrecht, K. H., and Kreutz, F. (1978). Fahraeus effect and cell screening during tube flow of human blood. I. Effect of variation of flow rate. *Biorheology*, **15**, 147-154.

- Gaetgens, P., Duhrssen, C., and Albrecht, K. H. (1980). Motion, deformation, and interaction of blood cells and plasma during flow through narrow capillaries. *Blood Cells*, **6**, 799-812.
- Garby, G., and de Verdier, C. H. (1971). Affinity of human hemoglobin A to 2,3-diphosphoglycerate. Effect of hemoglobin concentration and pH. *Scand. J. Clin. Lab. Invest.*, **27**, 345-350.
- Garg, L. C., and Maren, T. H. (1972). The rates of hydration of carbon dioxide and dehydration of carbonic acid at 37 °C. *Biochim. Biophys. Acta*, **261**, 70-76.
- Gibbson, B. H., and Edsall, J. T. (1963). Rate of hydration of carbon dioxide and dehydration of carbonic acid at 25 °C. *J. Biol. Chem.*, **238**, 3502-3507.
- Goldsmith, H. L. (1968). The microrheology of red blood cell suspensions. *J. Gen. Physiol.*, **52**, 5s-28s.
- Goldsmith, H. L., and Marlow, J. C. (1979). Flow behavior of erythrocytes: II Particle motions in concentrated suspensions of ghost cells. *J. Colloid Interface Sci.*, **71**, 383-407.
- Goldsmith, H. L., and Turitto, V. T. (1986). Rheological aspects of thrombosis and haemostasis: Basic principles and applications. *Thrombosis and Haemostasis*, **55**, 415-435.
- Goldstick, T. K., and Fatt, I. (1970). Diffusion of oxygen in solutions of blood proteins. *Chem. Engr. Prog. Symp. Ser.*, **66**, 101-113.
- Gros, G., and Moll, W. (1971). The diffusion of carbon dioxide in erythrocyte and hemoglobin solutions. *Pfluegers Arch.*, **324**, 249-266.
- Gros, G., and Moll, W. (1974). Facilitated diffusion of CO₂ across albumin solutions. *J. Gen. Physiol.*, **64**, 356-371.

- Gros, G., Forster, R. E., and Lin, L. (1976). The carbamate reaction of glycylglycine, plasma and tissue extracts evaluated by a pH stopped-flow apparatus. *J. Bio. Chem.*, **251**, 4398-4407.
- Gunn, R. B., Dalmark, M., Tosteson, D. C., and Weith, J. O. (1973). Characteristics of chloride transport in human red cells. *J. Gen. Physiol.*, **51**, 185-206.
- Gunn, R. B., and Frohlich, O. (1976). Asymmetry in the mechanism for anion exchange in human red blood cell membranes: Evidences for reciprocating sites that react with one transported anion at a time. *J. Gen. Physiol.*, **74**, 351-374.
- Hashitani, T., and Kigoshi, K. (1965). Measurement of the self diffusion coefficient of carbon dioxide, hydrogen carbonate ions, and carbonate ions in an aqueous solution. *Bull. Chem. Soc. Jap.*, **38**, 1395-1396.
- Hellums, J. D. (1977). The resistance to oxygen transport relative to that in the surrounding tissue. *Microvas. Res.*, **13**, 131-136.
- Hill, A. V. (1910). The possible effects of the aggregation of hemoglobin of the molecules of hemoglobin on its dissociation curves. *J. Physio. (London)*, **41**, iv.
- Hill, E. P., Power, G. G., and Longo, L. D. (1973a). A mathematical model of carbon dioxide transfer in the placenta and its interaction with oxygen. *Am. J. Physiol.*, **224**, 283-229.
- Hill, E. P., Power, G. G., and Longo, L. D. (1973b). Mathematical simulation of pulmonary O₂ and CO₂ exchange. *Am. J. Physiol.*, **224**, 904-917.
- Hill, C. G. (1977). "An Introduction to Chemical Engineering Kinetics and Reactor Design." New York: John Wiley and Sons.
- Hill, E. P., Gros, G., and Gilbert, R. D. (1977). Rate of pH changes in blood plasma in vitro and in vivo. *J. Appl. Physiol.*, **42**, 928-934.
- Hlastala, M. P. (1973). Significance of the Bohr and Haldane effects in the pulmonary capillary. *Respir. Physiol.*, **17**, 81-92.

- Hlastala, M. A., and Woodson, R. D. (1975). Saturation dependency of the Bohr effect: Interactions among H^+ , CO_2 , and DPG. *J. Appl. Physiol.*, **38**, 1126-1131.
- Hlastala, M. P., and Woodson, R. D. (1983). Bohr effect data for blood gas calculations. *J. Appl. Physiol.*, **55**, 1002-1007.
- Hlastala, M. P. (1984). Interactions between O_2 and CO_2 in blood. *In* "Oxygen Transport in Red Blood Cells" (C. Nigolau, Ed.), pp. 95-103. New York: Pergamon Press.
- Honig, C. R., Gayeski, T. E. J., Federspiel, W., Clark, A., and Clark, P. (1984). Muscle oxygen gradients from hemoglobin to cytochrome: New concepts, new complexities. *Adv. Exp. Med. Biol.*, **169**, 23-28.
- Horvath, A. L. (1985). "Handbook of Aqueous Electrolyte Solutions: Physical Properties, Estimation and Correlation Methods." New York: John Wiley and Sons.
- Illsley, N. P., and Verkman, A. S. (1987). Membrane chloride transport measured using a chloride-sensitive probe. *Biochemistry*, **26**, 1215-1219.
- Itada, N., and Forster, R. E. (1977). Carbonic anhydrase activity in intact red blood cells measured with ^{18}O exchange. *J. Biol. Chem.*, **252**, 3881-3890.
- Ivanon, K. P., Derry, A. N., Vovenko, E. P., Samoilov, M. O., and Semionov, D. G. (1982). Direct measurements of oxygen tension at the surface of arterioles, capillaries and venules of the cerebral cortex. *Pflugers Arch.*, **393**, 118-120.
- Jennings, M. L. (1982). Stoichiometry of a half-turnover of band 3, the chloride transport of human erythrocytes. *J. Gen. Physiol.*, **79**, 169-185.
- Jennings, M. L. (1985). Kinetics and mechanism of anion transport in red blood cells. *Ann. Rev. Physiol.*, **47**, 519-533.
- Jennings, M. L. (1989). Structure and function of the red blood cell anion transport protein. *Ann. Rev. Biophys. Biophys. Chem.*, **18**, 397-430.

- Kagawa, T., and Mochizuki, M. (1982). Numerical solution of partial differential equation describing oxygenation rate of the red blood cell. *Jpn. J. Physiol.*, **32**, 197-218.
- Keller, K. H., Canales, E. R., and Yum, S. (1971). Tracer and mutual diffusion coefficients of proteins. *J. Phys. Chem.*, **75**, 379-387.
- Keller, K. H. (1971). Effect of fluid shear on mass transport in flowing blood. *Federation Proc.*, **30**, 1591-1599.
- Kelman, G. R. (1966). Digital computer subroutine for the conversion of oxygen tension into saturation. *J. Appl. Physiol.*, **21**, 1375-1386.
- Kernohan, J. C. (1965). The pH-activity curve of bovine carbonic anhydrase and its relationship to the inhibition of the enzyme by anions. *Biochim. Biophys. Acta*, **96**, 304-317.
- Kilmartin, J. V., and Rossi-Bernardi, L. (1973). Interaction of hemoglobin with hydrogen ions, carbon dioxide, and organic phosphates. *Physiol. Rev.*, **53**, 836-890.
- Klocke, R. A. (1973). Mechanism and kinetics of the Haldane effect in human erythrocytes. *J. Appl. Physiol.*, **35**, 673-681.
- Klocke, R. A. (1976). Rate of bicarbonate-chloride exchange in human red cells at 37 °C. *J. Appl. Physiol.*, **40**, 707-714.
- Klocke, R. A. (1980). Equilibrium of CO₂ reactions in pulmonary capillary. *J. Appl. Physiol.*, **48**, 972-976.
- Klocke, R. A. (1987). Carbon dioxide transport. In "Handbook of Physiology" (L. E. Farhi and S. M. Ternney, Eds.), pp. 173-198. Bethesda, MD: American Physiological Society.
- Knauf, P. A., and Mann, N. A. (1984). Use of niflumic acid to determine the nature of the asymmetry of the human erythrocyte anion exchange system. *J. Gen. Physiol.*, **83**, 703-725.

- Kotyk, A., Janacek, K., and Koryta, J. (1988). "Biophysical Chemistry of Membrane Functions". New York: John Wiley and Sons.
- Kreuzer, F. (1970). Facilitated diffusion of oxygen and its possible significance: A review. *Respir. Physiol.*, **9**, 1-30.
- Lambert, A., and Lowe, A. G. (1978). Chloride/bicarbonate exchange in human erythrocytes. *J. Physiol.*, **275**, 51-63.
- Lambert, A., and Lowe, A. G. (1980). Chloride-bicarbonate exchange in human red cells measured using a stopped flow apparatus. *J. Physiol.*, **306**, 431-443.
- Leal, L. G. (1973). On the effective conductivity of a dilute suspension of spherical drops in the limit of low particle Peclet number. *Chem. Eng. Commun.*, **1**, 21-31.
- Lee, T. Q., Schmid-Schonbein, G. W., and Zweifach, B. W. (1983). The application of an improved dual-slit photometric analyzer for volumetric flow rate measurements in microvessels. *Microvas. Res.*, **26**, 351-361.
- Lehninger, A. L. (1975). "Biochemistry." New York: Worth Publishers.
- Lemon, D. D., Nair, P. K., Boland, E. J., Olson, J. S., and Hellums, J. D. (1987). Physiological factors affecting oxygen transport by hemoglobin in an in vitro capillary system. *J. Appl. Physiol.*, **62**, 798-806.
- Lemon, D. D. (1989). "Oxygen and Carbon Dioxide Exchange by Human Hemoglobin and Erythrocytes." Ph.D. thesis, Rice University.
- Lih, M. M. (1969). A mathematical model for the axial migration of suspended particles in tube flow. *Bull. Math. Biophys.*, **31**, 143-150.
- London, R. D., Lipkowitz, M. S., and Abramson, R. G. (1987). $\text{Cl}^-/\text{HCO}_3^-$ antiporter in red cell ghosts: A kinetic assessment with fluorescent probes. *Am. J. Physiol. (Renal Fluid Electrolyte Physiol. 21)*, **252**, F844-F855.
- Lowe, A. G., and Lambert, A. (1983). Chloride-bicarbonate exchange and related transport processes. *Biochim. Biophys. Acta*, **694**, 353-374.

- Madsen, M. K., and Sincovec, R. F. (1975). Software for non-linear partial differential equations. *ACM Trans. Math. Software*, **1**, 232-260.
- Margaria, R. (1963). A mathematical treatment of the blood dissociation curve for oxygen. *Clin. Chem.*, **9**, 745-762.
- Martin, D. W. (1981). Structure and function of a protein - hemoglobin. In "Harper's Review of Biochemistry" (D. W. Martin, P. A. Mayes, and V. W. Rodwell, Eds.), pp. 40-50. Los Altos, CA: Lange Medical Publications.
- McCracken, T. A., Bruley, D. F., Reneau, D. D., Bicher, H. I., and Kinsely, M. H. (1972). System analysis of transport processes in human brain; O₂, CO₂, glucose. In "Proceedings of 1st Pacific Chemical Engineering Congress." New York: American Institute of Chemical Engineers.
- Meldon, J. H., and Garby, L. (1975). The blood oxygen transport system. *Acta Med. Scand. Suppl.*, **578**, 19-29.
- Meldon, J. H. (1984). Computerized analysis of blood-gas equilibria: CO₂ titration of oxygenated whole blood. *Chem. Eng. Commun.*, **27**, 157-172.
- Meldon, J. H., Silverman, S. M., and Myers, L. A. (1986). Computerized analysis of blood-gas equilibria: Prediction and interpretation of experimental results. *Chem. Eng. Commun.*, **47**, 125-133.
- Merchuk, J. C., Tzur, Z., and Lightfoot, E. N. (1983). Diffusional resistances to oxygen transfer in whole blood. *Chem. Eng. Sci.*, **38**, 1315-1321.
- Middleman, S. (1972). "Transport Phenomena in the Cardiovascular System." New York: John Wiley and Sons.
- Milhorn, H. T., and Pulley, P. E. (1968). A theoretical study of pulmonary capillary gas exchange and venous admixture. *Biophys. J.*, **8**, 337-357.
- Mochizuki, M. (1966). Study on the oxygenation velocity of human red cell. *Jpn. J. Physiol.*, **16**, 658-666.

- Mochizuki, M. (1984). "Programs for solving O₂ and CO₂ diffusions into and out of the erythrocytes." Yamagata, Japan: Yamagata Medical Society.
- Moll, W. (1969). The influence of hemoglobin diffusion on oxygen uptake and release by red cells. *Respir. Physiol.*, **6**, 1-15.
- More, J. J., Garbow, B. S., and Hillstrom, K. E. (1980). "User Guide for MINPACK-1 (No. ANL-80-74)". Argonne National Laboratory.
- Nair, P. (1988). "Simulation of Oxygen Transport in Capillaries." Ph.D. thesis, Rice University.
- Nair, P. K., Hellums, J. D., and Olson, J. S. (1989). Prediction of oxygen transport rates in blood flowing in large capillaries. *Microvasc. Res.*, **38**, 269-285.
- Nair, P. K., Huang, N. S., Hellums, J. D., and Olson, J. S. (1990). A simple model for prediction of oxygen transport rates by flowing blood in large capillaries. *Microvasc. Res.*, **39**, 203-211.
- Nelder, J. A., and Meads, R. (1965). A simplex method for function minimization. *Comp. J.*, **7**, 308-321.
- Nir, A., and Acrivos, A. (1976). Effective thermal conductivity of sheared suspensions. *J. Fluid Mech.*, **78**, 33-48.
- Nunn, J. F. (1987). "Applied Respiratory Physiology." New York: Butterworths.
- O'Riordan, J. F., Goldstick, T. K., Ditzel, J., and Ernest, J. T. (1983). Characterization of oxygen-hemoglobin equilibrium curves using nonlinear regression of the Hill equation: parameter values for normal adults. *Adv. Exp. Med. Biol.*, **159**, 435-444.
- O'Riordan, J. F., Goldstick, T. K., Vida, L. N., Honig, G. R., and Ernest, J. T. (1985). Modeling whole blood oxygen equilibrium: Comparison of nine different models fitted to normal human data. In "Advances in Experimental Medicine and

- Biology" (F. Kreuzer, S. M. Cain, Z. Turek, and T. K. Goldstick, Eds.), pp. 505-522. New York: Plenum Press.
- Obaid, A. L., and Crandall, E. D. (1979). $\text{HCO}_3^-/\text{Cl}^-$ exchange across the human erythrocyte membrane: Effects of pH and temperature. *J. Membr. Biol.*, **50**, 23-41.
- Otto, N. C., and Quinn, J. A. (1971). The facilitated transport of carbon dioxide through bicarbonate solutions. *Chem. Eng. Sci.*, **26**, 949-961.
- Passow, H. (1986). Molecular aspects of band 3 protein-mediated anion transport across the red blood cell membrane. *Rev. Physiol. Biochem. Pharmacol.*, **103**, 62-203.
- Perutz, M. F. (1978). Hemoglobin structure and respiratory transport. *Sci. Am.*, **239**, 92-125.
- Pittman, R. N., and Ellsworth, M. L. (1986). Estimation of red cell flow in microvessels: Consequences of the Baker-Wayland spatial averaging model. *Microvas. Res.*, **32**, 371-388.
- Pittman, R. N. (1987). Oxygen delivery and transport in the microcirculation. In "Microvascular Perfusion and Transport in Health and Disease" (McDonagh, Ed.). Basel: Karger.
- Popel, A. S., and Gross, J. F. (1979). Analysis of oxygen diffusion from arteriolar networks. *Am. J. Physiol.*, **237**, H681-H689.
- Popel, A. S. (1989). Theory of oxygen transport to tissue. *CRC Crit. Rev. Biomed. Engr.*, **17**, 257-321.
- Reich, J. G., and Zinke, I. (1984). Analysis of kinetic binding measurements. IV. Redundancy of model parameters. *Studia Biophysica*, **43**, 91-107.
- Reneau, D. D., Bruley, D. F., and Knisely, M. H. (1967). A mathematical simulation of oxygen release, diffusion, and consumption in the capillaries and tissue of human brain. In "Chemical Engineering in Medicine and Biology" (D. Hershey, Ed.), pp. 135-241. New York: Plenum Press.

- Reneau, D. D., Bruley, D. F., and Knisely, M. H. (1969). A digital simulation of transient oxygen transport in capillaries - tissue systems (cerebral grey matter). *Am. Inst. Chem. Eng. J.*, **15**, 916-925.
- Rossi-Bernardi, L., and Roughton, F. J. W. (1967). The specific influence of carbon dioxide and carbamate compounds on the buffer power and Bohr effects in human hemoglobin solutions. *J. Physiol. (London)*, **189**, 1-29.
- Roth, A. C., and Wade, K. (1986). The effects of transmural transport in the microcirculation: A two gas species model. *Microvasc. Res.*, **32**, 64-83.
- Roughton, F. J. W. (1935). Recent work on carbon dioxide transport by the blood. *Physiol. Rev.*, **15**, 241-296.
- Roughton, F. J. W., and Forster, R. E. (1957). Relative importance of diffusion and chemical reaction rates in determining the rate of exchange of gases in the human lung. *J. Appl. Physiol.*, **11**, 290-302.
- Roughton, F. J. W. (1959). Diffusion and simultaneous chemical reaction velocity in hemoglobin solutions and red cell suspensions. *Prog. Biophys. Chem.*, **9**, 55-67.
- Ryan, U. S., and Ryan, J. W. (1984). Cell biology of pulmonary endothelium. *Circulation (suppl. III)*, **70**, 46-62.
- Salathe, E. P., Fayad, R., and Schaffer, S. W. (1981). Mathematical analysis of carbon dioxide transport by blood. *Math. Biosci.*, **57**, 109-153.
- Salhany, J. M., and Rauenbuehler, P. B. (1983). Kinetics and mechanism of erythrocyte anion exchange. *J. Biol. Chem.*, **258**, 245-249.
- Samaja, M., and Winslow, R. M. (1979). The separate effects of H^+ and 2,3-DPG on the oxygen equilibrium curve of human blood. *Brit. J. Haematology*, **41**, 373-381.
- Samaja, M., Mosca, A., Luzzana, M., Rossi-Bernardi, L., and Winslow, R. M. (1981). Equations and nomogram for the relationship of human blood P_{50} to 2,3-diphosphoglycerate, CO_2 , and H^+ . *Clin. Chem.*, **27**, 1856-1861.

- Schmid-Schonbein, H., and Wells, R. E. (1971). Rheological properties of human erythrocytes and their influence upon the anomalous viscosity of blood. *Ergebnisse der Physiologie*, **63**, 146-219.
- Schmukler, R., and Chien, S. (1985). Rapid deoxygenation of red cells and hemoglobin solution using hollow capillary fibers. *Biorheology*, **22**, 21-29.
- Schnell, K. F., Gerhardt, S., and Schoppe-Fredenburg, A. (1977). Kinetic characteristics of sulfate self-exchange in human red blood cells and red blood cell ghosts. *J. Membr. Biol.*, **30**, 319-350.
- Sendroy, J., Dillion, R. T., and Van Slyke, D. D. (1934). Studies of gas and electrolyte equilibria in blood. XIX. The solubility and physiological state of uncombined oxygen in blood. *J. Biol. Chem.*, **105**, 597-632.
- Sharan, M., Aminataei, A., and Singh, M. P. (1987). A numerical study of the nonsteady transport of gases in the pulmonary capillaries. *J. Math. Biol.*, **25**, 433-452.
- Siggaard-Anderson, O. (1971). Oxygen-linked hydrogen ion binding of human hemoglobin. Effects of carbon dioxide and 2,3-diphosphoglycerate. I. Studies on erythrocytes. *Scand. J. Clin. Lab. Invest.*, **27**, 351-360.
- Singh, M. P., Khetarpal, K., and Sharan, M. (1980). A theoretical model for studying the rate of oxygenation of blood in pulmonary capillaries. *J. Math. Biol.*, **9**, 305-330.
- Sinha, R. (1936). *Kolloid Z.*, **76**, 16.
- Sirs, J. A. (1970). The interaction of carbon dioxide with rate of exchange of oxygen by red blood cells. In "Blood Oxygenation" (D. Hershey, Ed.), pp. 116-139. New York: Plenum Press.
- Sosa, O., and Merchuk, J. C. (1972). Transfer of O₂ and CO₂ in a membrane artificial lung. Part I - Theoretical; Part II - Experimental. In "Proceedings of 1st Pacific Chemical Engineering Congress", pp. 151-161. New York: American Institute of Chemical Engineers.

- Spaan, J. A. E., Kreuzer, F., and Van Wely, F. K. (1980). Diffusion coefficients of oxygen and hemoglobin as obtained simultaneously from photometric determination of oxygenation of layers of hemoglobin solutions. *Pflugers Arch.*, **384**, 241-251.
- Spaeth, E. E., and Friedlander, S. K. (1967). The diffusion of oxygen, carbon dioxide, and inert gas flowing in blood. *Biophys. J.*, **7**, 827-851.
- Spaeth, E. E. (1973). Blood oxygenation in extracorporeal devices: Theoretical considerations. *CRC Crit. Rev. Bioeng*, **1**, 383-417.
- Tyuma, I., and Ueda, Y. (1975). Nonlinear relationship between oxygen saturation and proton release, and equivalence of the Bohr and Haldane coefficients in human hemoglobin. *Biochem. Biophys. Res. Commun.*, **65**, 1278-1283.
- Ueda, Y., and Bookchin, R. M. (1984). Effects of carbon dioxide and pH variations in vitro on blood respiratory functions, red blood cell volume, transmembrane pH gradients, and sickling in sickle cell anemia. *J. Lab. Clin. Med.*, **104**, 146-159.
- Van Slyke, D. D. (1922). On the measurement of buffer values and on the relationship of buffer value to the dissociation content of the buffer and the concentration and reaction of the buffer solution. *J. Biol. Chem.*, **52**, 525-570.
- Van Slyke, D. D., Wu, H., and McLean, F. C. (1923). Studies of gas and electrolyte equilibria in the blood. Factors controlling the electrolyte and water distribution in the blood. *J. Biol. Chem.*, **56**, 765-849.
- Vandegriff, K. D., and Olson, J. S. (1984a). A quantitative description in three dimensions of oxygen uptake by human red blood cells. *Biophys. J.*, **45**, 825-835.
- Vandegriff, K. D., and Olson, J. S. (1984b). The kinetics of O₂ release by human red blood cells in the presence of external sodium dithionite. *J. Biol. Chem.*, **259**, 12609-12618.

- Vandegriff, K. D., and Olson, J. S. (1984c). Morphological and physical factors affecting oxygen uptake and release by red blood cells. *J. Biol. Chem.*, **259**, 12619-12627.
- Villarroel, F. (1970). "Gas Transport to Blood Flowing in Semipermeable Tubes under Steady and Pulsatile Flow Conditions." Ph.D. thesis, University of Maryland.
- Villarroel, F., Lanham, C. E., Bischoff, K. B., Regan, T. M., and Calkins, J. M. (1971). Gas transport to blood flowing in semipermeable tubes under steady and pulsatile flow conditions. *Chem. Eng. Progr. Symp. Ser.*, **67**, 96-104.
- Villarroel, F., and Lanham, C. E. (1973). A design calculation method for capillary-tube oxygenators. *Med. Biol. Eng.*, **11**, 732-742.
- Voorhees, M. E. (1976). "Mutal Transfer of Carbon Dioxide and Oxygen to and from Blood Flowing in Macrochannel Devices." Ph.D. thesis, Arizona State University.
- Wagner, P. D., and West, J. B. (1972). Effects of diffusion impairment on O₂ and CO₂ time courses in pulmonary capillaries. *J. Appl. Physiol.*, **33**, 62-71.
- Wang, N. L., and Keller, K. H. (1985). Augmented transport of extracellular solutes in concentrated erythrocyte suspensions in couette flow. *J. Colloid Interface Sci.*, **71**, 210-225.
- Weerappuli, D. P. V., and Popel, A. S. (1989). A model of oxygen exchange between an arteriole or venule and the surrounding tissue. *J. Biomech. Eng.*, **111**, 24-31.
- Weissman, M. H., and Mackros, L. F. (1967). Oxygen transfer to blood flowing in round tubes. *Journal of Engineering Mechanics Division; A.S.C.E.*, **93**, 225-244.
- Weissman, M. H., and Mockros, L. F. (1969). Oxygen and carbon dioxide transfer in membrane oxygenators. *Med. Biol. Engng.*, **7**, 169-184.
- Weith, J. O. (1979). Bicarbonate exchange through the human red cell membrane determined with [¹⁴C]bicarbonate. *J. Physiol.*, **294**, 521-539.

- Weith, J. O., Brahm, J., and Funder, J. (1980). Transport and interactions of anions and proteins in the red blood cell membrane. *Ann. N.Y. Acad. Sci.*, **341**, 394-418.
- Weith, J. O., and Brahm, J. (1980). Kinetics of bicarbonate exchange in human red cells - physiological implications. In "Membrane Transport in Erythrocytes" (U. V. Lassen, H. H. Ussing, and J. O. Weith, Eds.), pp. 467-487. Copenhagen: Munksgaard.
- Weith, J. O., Andersen, O. S., Brahm, J., Bjerrum, P. J., and Borders, C. L. (1982). Chloride-bicarbonate exchange in the red cells: Physiology of transport and chemical modification of binding sites. *Phil. Trans. R. Soc. Lond.*, **299**, 383-399.
- Weith, J. O., and Bjerrum, P. J. (1982). Titration of transport and modifier sites in the red cell anion transport system. *J. Gen. Physiol.*, **79**, 253-282.
- Weith, J. O., and Brahm, J. (1985). "Cellular Anion Transport." New York: Raven Press.
- Winslow, R. M., Swenberg, M., Berger, R. L., Shrager, R. I., Luzzana, M., Samaja, M., and Rossi-Bernardi, L. (1977). Oxygen equilibrium curve of normal human blood and its evaluation by Adair equation. *J. Biol. Chem.*, **252**, 2331-2337.
- Winslow, R. M., Samaja, M., Winslow, N. J., Rossi-Bernardi, L., and Shrager, R. I. (1983). Simulation of continuous blood O₂ equilibrium curve over physiological pH, DPG, and PCO₂ range. *J. Appl. Physiol.: Respirat. Environ. Exercise Physiol.*, **54**, 524-529.
- Wyman, J. (1964). Linked functions and reciprocal effects in hemoglobin: A second look. *Adv. Protein Chem.*, **19**, 223-286.
- Zemaitis, J. F., Clark, D. M., Rafal, M., and Scrivner, N. C. (1986). "Handbook of Aqueous Electrolyte Thermodynamics: Theory and Application". New York: American Institute of Chemical Engineers.

Zwart, A., Kwant, G., Oeseburg, B., and Zijlstra, W. G. (1984). Human whole-blood oxygen affinity: Effect of temperature. *J. Appl. Physiol.: Respirat. Environ. Exercise Physiol.*, **57**, 429-434.

Zydney, A. L., and Colton, C. K. (1988). Augmented solute transport in the shear flow of a concentrated suspension. *Hydrodynamics*, **10**, 77-96.

APPENDIX A

Validation of Space Average Oxygen Saturation Calculation Involved in Simulation of Boland *et al.*'s System

In Boland *et al.*'s dual wavelength microspectrophotometric system, the extent of oxygenation of the RBC suspension was monitored by measuring absorbance changes at two different wavelengths. Because of the small path length ($30 \leq \mu\text{m}$) of the absorbing solution, measurements were made at the Soret region wavelengths of 414 and 430 nm; these wavelengths represent the absorption maxima of oxy- and deoxyhemoglobin, respectively. The dual wavelength measurements were carried out on fully saturated (100%) and unsaturated (0%) specimens flowing under the same conditions as the test specimen (exp). All light intensity measurements were made after the steady-state condition was reached. The change in absorbance at each wavelength, $\Delta A_{exp-100\%}^{430}$ or $\Delta A_{exp-100\%}^{414}$, was calculated from the negative logarithm of the ratio of the transmittance voltage of the sample under the O_2 transport condition to that for the fully oxygenated sample. The $\Delta A_{exp-100\%}$ values at each wavelength were then subtracted to reduce light scattering artifacts and to enhance the resultant signals, since the absorbance changes are in opposite directions. The change in absorbance in passing from the fully deoxygenated state to the fully oxygenated state at both wavelengths are $\Delta A_{0\%-100\%}^{430}$ and $\Delta A_{0\%-100\%}^{414}$. The difference between $\Delta A_{0\%-100\%}$ at 430 and 414 nm represents the maximum possible signal; this quantity was used to normalize the difference between $\Delta A_{exp-100\%}^{430}$ and $\Delta A_{exp-100\%}^{414}$ and to compute the fractional degree of saturation of hemoglobin in the following equation:

$$\langle S \rangle_{measured} = 1 - \frac{\Delta A_{exp-100\%}^{430} - \Delta A_{exp-100\%}^{414}}{\Delta A_{0\%-100\%}^{430} - \Delta A_{0\%-100\%}^{414}} \quad (\text{A.1})$$

which is equivalent to Equation (A.2a) or (A.2b).

$$\langle S \rangle_{measured} = 1 - \frac{\ln\left(\frac{V_{100\%}^{430}}{V_{exp}^{430}}\right) - \ln\left(\frac{V_{100\%}^{414}}{V_{exp}^{414}}\right)}{\ln\left(\frac{V_{100\%}^{430}}{V_{0\%}^{430}}\right) - \ln\left(\frac{V_{100\%}^{414}}{V_{0\%}^{414}}\right)} \quad (A.2a)$$

$$\langle S \rangle_{measured} = 1 - \frac{\ln\left(\frac{q_{100\%}^{430}}{q_{exp}^{430}}\right) - \ln\left(\frac{q_{100\%}^{414}}{q_{exp}^{414}}\right)}{\ln\left(\frac{q_{100\%}^{430}}{q_{0\%}^{430}}\right) - \ln\left(\frac{q_{100\%}^{414}}{q_{0\%}^{414}}\right)} \quad (A.2b)$$

where V 's and q 's are the transmittance voltage and light intensity at different wavelengths and conditions, respectively.

In comparison of theoretical results with experimental results, the radially varying O_2 saturations from the mathematical model must be averaged over the cross section in a suitable fashion. In analyzing Boland *et al.*'s data, space averaged O_2 saturations from the theory are calculated so that the comparison can be made directly with the microspectrophotometric determinations of O_2 saturations. The space average saturation is calculated as

$$\langle S \rangle_{sa} = \frac{1}{\pi r_c^2 H_T} \int_0^{r_c} 2 \pi r h(r) S(r) dr \quad (A.3)$$

The primary objective of the following calculation is to rigorously validate the above averaging method. It is proposed to use the O_2 saturation profile, $S(r)$, generated from the model and the basic equation for describing energy transport in absorbing media to

calculate the experimentally measured absorbance. As a result, it is then possible to directly compare the average O₂ saturation calculated by Equations (A.2b) and (A.3).

In order to describe energy transport in nontransparent media, Bird *et al.* (1960) wrote differential equations for the local rate of energy as viewed both from the material and the radiation standpoint. For the electromagnetic radiation phase, they wrote the following equation for describing the local rate of radiant-energy density U :

$$\frac{\partial U}{\partial t} = -(\nabla \cdot q) + (E - \psi) \quad (\text{A.4})$$

where

q is the radiant energy flux.

E is the energy lost by the material phase resulting from the emission of photons by molecules of the material phase.

ψ is the local gain of energy by the material phase resulting from photon absorption by the molecules of the material phase.

Equation (A.4) can also be written for the radiant energy within a frequency range λ to $\lambda+d\lambda$:

$$\frac{\partial U^\lambda}{\partial t} = -(\nabla \cdot q^\lambda) + (E^\lambda - \psi^\lambda) \quad (\text{A.5})$$

The conditions which are applicable to Boland *et al.*'s spectrophotometric system are described below. It is a steady-state system in which a monochromatic radiant beam of frequency λ , focused parallel to the y -axis, passes through an absorbing fluid (see Figure A.1). In addition, the absorbing media can be assumed to be at temperatures sufficiently low enough that emission by the media is unimportant. Furthermore, the local rate of volumetric energy absorption, ψ^λ , is given by $m^\lambda q^\lambda$, in which m^λ is the

extinction coefficient of the pigment in the medium at frequency λ . Then Equation (A.5) becomes

$$\frac{dq^\lambda}{dy} = -\psi^\lambda \quad (\text{A.6})$$

Rearranging Equation (A.6) and integration with respect to y gives

$$\ln \left(\frac{q^\lambda}{q_{ref}^\lambda} \right) = \int_{y = -\sqrt{r_c^2 - x^2}}^{y = \sqrt{r_c^2 - x^2}} m^\lambda dy \quad (\text{A.7})$$

where

q^λ is the light intensity at wavelength λ after passing through the medium.

q_{ref}^λ is the incident light at wavelength λ .

x and y are the coordinate system (see Figure A.1).

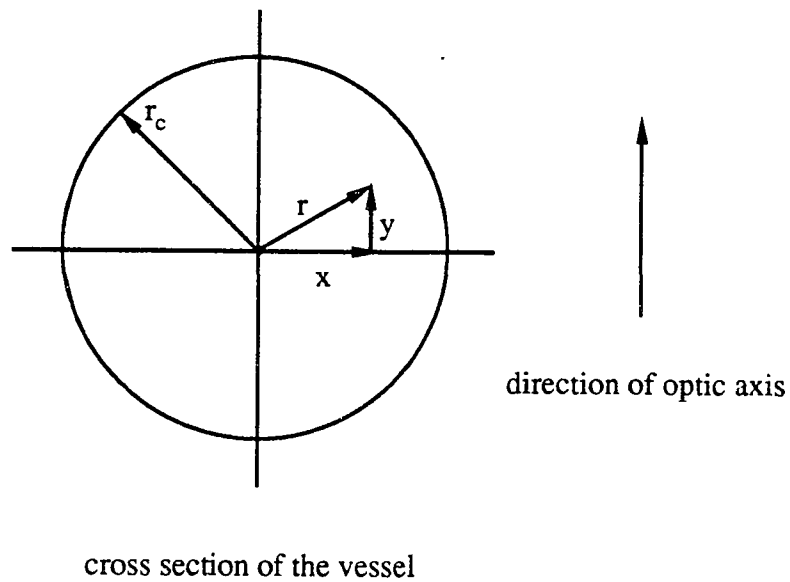


Figure A.1: Explanation of coordinates.

If the system contains two non-interacting pigments, oxygenated and deoxygenated hemoglobin, the concentrations of oxygenated hemoglobin ($[HbO_2]$) and deoxyhemoglobin ($[Hb]$) can be related to their respective extinction coefficients at wavelength λ ($\epsilon_{HbO_2}^\lambda$ and ϵ_{Hb}^λ),

$$m^\lambda = \epsilon_{HbO_2}^\lambda [HbO_2] + \epsilon_{Hb}^\lambda [Hb] \quad (A.8)$$

Equation (A.8) can be rewritten in terms of O_2 saturation and hemoglobin concentration.

$$m^\lambda(r) = \left\{ \epsilon_{HbO_2}^\lambda S(r) + \epsilon_{Hb}^\lambda [1 - S(r)] \right\} C_{Hb,rbc} h(r) \quad (A.9)$$

where $C_{Hb,rbc}$ is the intracellular hemoglobin concentration, and $h(r)$ is the hematocrit profile. Because the experimental determinations were obtained over a rectangular field of view of approximately $28 \times 40 \mu m$ to yield fractional saturation of hemoglobin, one needs to integrate Equation (A.7) with respect to x over the domain of $x = -r_c$ to $x = r_c$.

$$\left\langle \ln \left(\frac{q^\lambda}{q_{ref}^\lambda} \right) \right\rangle = \frac{C_{Hb,rbc}}{2 r_c} \int_{x=-r_c}^{x=r_c} \int_{y=-\sqrt{r_c^2-x^2}}^{y=\sqrt{r_c^2-x^2}} \left\{ \epsilon_{HbO_2}^\lambda S(r) + \epsilon_{Hb}^\lambda [1 - S(r)] \right\} h(r) dy dx \quad (A.10)$$

The above integral can be more easily evaluated by changing to polar coordinate.

$$\left\langle \ln \left(\frac{q^\lambda}{q_{ref}^\lambda} \right) \right\rangle = \frac{C_{Hb,rbc}}{r_c} \int_{\theta=-\pi/2}^{\theta=\pi/2} \int_{r=0}^{r=r_c} \left\{ \epsilon_{HbO_2}^\lambda S(r) + \epsilon_{Hb}^\lambda [1 - S(r)] \right\} h(r) r dr d\theta \quad (A.11)$$

Therefore, the quantities listed in Equation (A.12) can then be calculated using either Equation (A.10) or (A.11); $\langle S \rangle_{measured}$ can then be computed using Equation (A.2b).

$$\left\langle \frac{q_{exp}^{\lambda}}{q_{ref}^{\lambda}} \right\rangle, \left\langle \frac{q_{100\%}^{\lambda}}{q_{ref}^{\lambda}} \right\rangle, \text{ and } \left\langle \frac{q_{0\%}^{\lambda}}{q_{ref}^{\lambda}} \right\rangle \quad \text{for } \lambda = 430 \text{ and } 415 \text{ nm.} \quad (\text{A.12})$$

Given $h(r)$ and $S(r)$ for situations of either O₂ uptake or release experiments (runs R1, R2, U1 and U2 presented in Figures 4.1 - 4.4), the comparison of the O₂ saturation computed via Equation (A.2b) is plotted against the O₂ saturation computed via Equation (A.3). The fact that all the points fall on the 45° line indicates Equation (A.3) is an appropriate method for calculating space-average O₂ saturation.

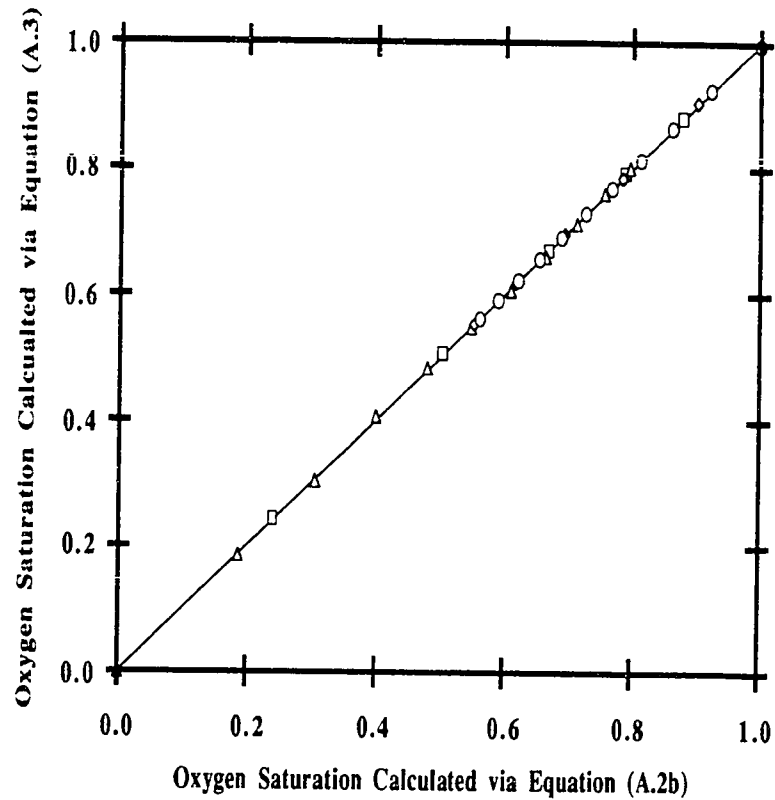


Figure A.2: Comparison of O_2 saturation values computed by two independent methods. The ordinate is O_2 saturation calculated via Equation (A.3), and the abscissa is O_2 saturation calculated via Equation (A.2b). Results are given for Boland *et al.*'s experimental data which are presented in Figures 4.1 - 4.4.

APPENDIX B

Estimation of the Extracellular Mass Transfer Coefficient of CO₂ in A Stopped-flow Rapid-mixing Apparatus

Evidence which supports the fact that unstirred solvent layers account for almost entirely for the small mass transfer coefficient for O₂ at the cell surface in a stopped-flow apparatus had been discussed by Coin and Olson (1979). As pointed out by Vandegriff and Olson (1984a) that the magnitude of the external diffusion effect can be estimated from a simple boundary analysis:

$$k_{O_2} \approx \frac{\alpha_{p,O_2} D_{O_2,pl}}{\Delta x} \quad (B.1)$$

where

k_{O_2} and $D_{O_2,pl}$ are the extracellular mass transfer coefficient and extracellular diffusivity of O₂, respectively.

α_{p,O_2} is the partition coefficient of O₂ between the phases, and $\alpha_{p,O_2} \approx 1$.

Δx represents the thickness of the unstirred layers.

Furthermore, Vandegriff and Olson (1984a) examined O₂ uptake by RBCs in a stopped-flow rapid-mixing experiments by developing a detailed three-dimensional model and using previously developed hydrodynamic theories to describe the unstirred solvent layer. An initial 1 μm unstirred layer was postulated to occur during mixing and expanded with time by a $(t)^{0.5}$ function when flow stops. This formula in combination with the their cylindrical disk model was reported to fit a wide range of experimental conditions. Their result indicated that there is much less turbulent mixing after flow stops and that the diffusion sublayer is between 8-20 μm during most of the reaction

they studied. If the properties in Equation (B.1) were replaced by that of CO_2 , $D_{\text{CO}_2,pl} \approx 1.85 \times 10^{-5} \text{ cm}^2/\text{sec}$ and Δx taken to be $\approx 14 \text{ }\mu\text{m}$, k_{CO_2} is then calculated to be $\approx 0.013 \text{ cm/sec}$.

In this study, to simplify the mathematical analysis and neglect the detailed description of the incomplete stirring layer adjacent to the cell surface, the flux of CO_2 across the boundary layer which includes the RBC membrane and the unstirred layer is written as the followings:

$$\text{Flux}_{\text{CO}_2} = \eta_{\text{CO}_2} \left(\frac{[\text{CO}_2]_{\text{rbc}}}{\alpha_{\text{CO}_2,\text{rbc}}} - \frac{[\text{CO}_2]_{\text{pl}}}{\alpha_{\text{CO}_2,\text{pl}}} \right) \quad (\text{B.2})$$

where

η_{CO_2} is the lumped mass transfer coefficient for CO_2 , and it is related to k_{CO_2} through the following relationship: $\eta_{\text{CO}_2} = k_{\text{CO}_2} \alpha'_{\text{CO}_2,\text{pl}}$. $\alpha'_{\text{CO}_2,\text{pl}}$ is the CO_2 solubility coefficient in the extracellular phase, and in this equation it has the unit of $(\text{mmHg})^{-1}$.

$\alpha_{\text{CO}_2,\text{rbc}}$ and $\alpha_{\text{CO}_2,\text{pl}}$ are the intracellular and extracellular solubility coefficients for CO_2 , respectively. $\alpha_{\text{CO}_2,\text{pl}}$ is related to $\alpha'_{\text{CO}_2,\text{pl}}$ through the molar volume of CO_2 .

From Equation (B.1), a simple boundary analysis, η_{CO_2} is estimated to be $\approx 8 \times 10^{-6} \text{ cm/sec/mmHg}$. Additionally, the magnitude of this external diffusion effect is also calculated from the following two methods. The first approach incorporates Kagawa and Mochizuki's calculation for η_{O_2} which was obtained from modeling the oxygenation rate of RBCs in a stopped-flow reactor (Kagawa and Mochizuki, 1982). The second method involves the usage of the low Reynolds number asymptotic solution for diffusion from a disc to the surrounding fluid.

Kagawa and Mochizuki's calculation

This differential equations which consists of two components, e.g., the diffusion and chemical reaction components, as given in a two-dimensional cylindrical-disk model by Equation (B.3) was used by Kagawa and Mochizuki (1982) to estimate η_{O_2} .

$$\left(1 + \frac{d[HbO_2]_{rbc}}{d[O_2]_{rbc}}\right) \frac{\partial [O_2]_{rbc}}{\partial t} = D_{O_2,rbc} \left[\frac{1}{r} \frac{\partial}{\partial r} \left(r \frac{\partial [O_2]_{rbc}}{\partial r} \right) + \frac{\partial^2 [O_2]_{rbc}}{\partial x^2} \right] \quad (B.3)$$

where

$[O_2]_{rbc}$ and $[HbO_2]_{rbc}$ are the dissolved O_2 and oxyhemoglobin concentrations in the RBC, respectively.

$d[HbO_2]_{rbc}/d[O_2]_{rbc}$ is the slope of the ODC.

$D_{O_2,rbc}$ is the diffusivity for O_2 in the RBC.

They used the O_2 transfer data obtained by Mochizuki's (1966) which was obtained from stopped-flow rapid-reaction apparatus to estimate η_{O_2} . Because of the symmetry of radial and vertical diffusion, the P_{O_2} gradient at $r=0$ and $z=0$ becomes zero; and the diffusion rate across the boundary layer was expressed by the transfer coefficient, η_{O_2} . Let the distances of the origin be $r=c$, and $z=\pm d$, respectively. The boundary conditions were given by

$$D_{O_2,rbc} \frac{\partial [O_2]_{rbc}}{\partial r} \Big|_{r=R_{rbc}} = \eta_{O_2} (P_{O_2} \Big|_{r=R_{rbc}} - P_{O_2,pl}) \quad (B.4a)$$

$$D_{O_2,rbc} \frac{\partial [O_2]_{rbc}}{\partial z} \Big|_{z=\pm t_{rbc}} = \eta_{O_2} (P_{O_2} \Big|_{z=\pm t_{rbc}} - P_{O_2,pl}) \quad (B.4b)$$

where

R_{rbc} is the RBC radius (3.5 μm).

t_{rbc} is the RBC thickness (1.6 μm).

$P_{O_2,pl}$ is the P_{O_2} in the surrounding medium; $P_{O_2,pl}$ can be taken as approximately constant because volume ratio of suspending buffer to RBCs was $\gg 1$ Mochizuki's experiment.

Kagawa and Mochizuki (1982) computed the oxygenation process by varying the η_{O_2} value, while initial and boundary conditions were given according to Mochizuki's data (1966). According to them, the O_2 saturation-time curve calculated by use of $\eta_{O_2}=2.5 \times 10^{-6}$ cm/sec/mmHg coincided the best with the experimental data.

The above approach is obviously an oversimplification of the real situation in stopped-flow rapid-mixing experiments. Even after convective mixing had ceased to occur, the O_2 concentration gradient in the external aqueous layer is not a linear function of the distance from the cell surface (Vandegriff and Olson, 1984a). In addition, the thickness of the unstirred layer varied with the time. In the initial turbulent flow within the mixing chamber, the cells were well mixed and only a thin layer of solution surrounding the cell surface remained unstirred. As flow continued into the observation chamber and the turbulence began to dissipate, the cells became entrained in microscopic eddies that grew even larger after laminar flow stopped. The unstirred layer is empirically determined to be projecting in the following manner (Vandegriff and Olson, 1984c):

$$d(t) = d(0) + K t^{0.5} \quad (\text{B.5})$$

where

$d(t)$ is the thickness of the unstirred layer at time t .

$d(0)$ is the thickness of the unstirred layer during turbulent flow in the mixer.

K is a proportionality constant and has to be determined empirically; and $K \approx R_{rbc}^{1/3} D_{O_2}^{1/3} \nu^{7/12}$ where ν is the kinematic viscosity.

However, for a first order approximation, the detailed description of incomplete stirring of the aqueous layer adjacent to cell surface is neglected. The mass transfer resistance to O_2 that exists at this unstirred layer is assumed to be lumped into the empirical, effective mass transfer coefficient, η_{O_2} . Due to the lack of stopped-flow data on CO_2 transport, the value of η_{CO_2} is taken to be the same as that of η_{O_2} .

Low Reynolds number asymptotic solution for diffusion from a disc to the surrounding fluid

η_{CO_2} can also be approximated from Nusselt number correlations for mass transfer from disc to the surrounding fluid (Merchuk *et al.*, 1983)

$$\frac{k_{CO_2} t_{rbc}}{D_{CO_2,pl}} = \frac{8}{\pi} \quad (B.6)$$

where

k_{CO_2} is the extracellular mass transfer coefficient of CO_2 , and it is related to η_{CO_2} through the following relationship: $\eta_{CO_2} = k_{CO_2} \alpha_{CO_2,pl}$.

t_{rbc} is the thickness of the RBC.

The $8/\pi$ term is the asymptotic value of the Nusselt number for pure diffusion from the disc to a stationary medium around it. From Equation (B.6), η_{CO_2} is calculated to be about 6×10^{-6} cm/sec/mmHg.

APPENDIX C

Dedimensionalization of Type I Discrete Model Which Consists of Equations (6.1.1) - (6.1.10)

In this section, Type I discrete model, Equations (6.1.1) - (6.1.10), for describing simultaneous O_2/CO_2 transport and acid/base regulation by blood flowing in microvessels is dedimensionalized. It is convenient to introduce the following dimensionless variables [given in Equation (6.33)]:

$$\begin{aligned}
 t &= \frac{z}{L}, \quad x = \frac{r}{r_r}, \quad x' = \frac{r_c - r}{r_c - r_r}, \\
 u &= \frac{[O_2]_{rbc}}{[O_2]_o}, \quad v = \frac{[CO_2]_{rbc}}{[CO_2]_o}, \quad w = \frac{[H^+]_{rbc}}{[H^+]_o}, \quad s = \frac{[Cl^-]_{rbc}}{[Cl^-]_o}, \\
 w' &= \frac{[H^+]_{pl}}{[H^+]_o}, \quad r' = \frac{[HCO_3^-]_{pl}}{[HCO_3^-]_o}, \quad s' = \frac{[Cl^-]_{pl}}{[Cl^-]_o}, \\
 v'' &= \frac{[CO_2]_{pl}'}{[CO_2]_o}, \quad w'' = \frac{[H^+]_{pl}'}{[H^+]_o}, \quad r'' = \frac{[HCO_3^-]_{pl}'}{[HCO_3^-]_o}
 \end{aligned}$$

When the equations of continuity are written in terms of these dimensionless variables, we obtain Equations (C.1) - (C.10).

$$\left(\left(\frac{\alpha_{O2,rbc}}{\alpha_{O2,pl}} \right) h(x) D(1-slp)(1-Bb^2x^2) \left[1 + \left(\frac{C_{cheme,rbc}}{[O_2]_o} \right) \frac{\partial S}{\partial u} \right] + (1-h(x)) D(1-Bb^2x^2) \left(\left(\frac{[O_2]_o}{L} \right) \frac{\partial u}{\partial t} = \left(\frac{D_{O2,pl}[O_2]_o}{r^2} \right) \frac{1}{x} \frac{\partial}{\partial x} \left(x \frac{\partial u}{\partial x} \right) \right) \right) \quad (C.1)$$

$$\left\{ h(x) D(1-slp)(1-Bb^2x^2) \left[1 + \left(\frac{C_{cheme,rbc}}{4[CO_2]_o} \right) \frac{\partial \phi}{\partial v} + \left(\frac{K' f_{water}}{[H^+]_o} \right) \frac{1}{w} \right] + \left(\frac{\alpha_{CO2,pl}}{\alpha_{CO2,rbc}} \right) (1-h(x)) D(1-Bb^2x^2) \left(\left(\frac{[CO_2]_o}{L} \right) \frac{\partial v}{\partial t} = \left(\frac{D_{CO2,pl}[CO_2]_o}{r^2} \right) \left(\frac{\alpha_{CO2,pl}}{\alpha_{CO2,rbc}} \right) \frac{1}{x} \frac{\partial}{\partial x} \left(x \frac{\partial v}{\partial x} \right) + h(x) \left(\frac{s}{v} \right)_{rbc} Flux_{HCO3} - (1-h(x)) R_{HCO3,pl} \right) \right\} \quad (C.2)$$

$$D(1-slp)(1-Bb^2x^2) \left[\left(\frac{\beta_{rbc}}{2.303 [H^+]_o} \right) \frac{1}{w} + \left(\frac{K' f_{water}}{[H^+]_o} \right) \left(\frac{[CO_2]_o}{[H^+]_o} \right) \frac{v}{w^2} - 2 \left(\frac{[H^+]_o}{L} \right) \frac{\partial w}{\partial t} = - \left(\frac{s}{v} \right)_{rbc} Flux_{HCO3} \right] \quad (C.3)$$

$$D(1-slp)(1-Bb^2x^2) \left(\frac{[Cl^-]_o}{L} \right) \frac{\partial s}{\partial t} = - \left(\frac{s}{v} \right)_{rbc} Flux_{HCO3} \quad (C.4)$$

$$(1-h(x)) D(1-Bb^2x^2) \left(\frac{[H^+]_o}{L} \right) \frac{\partial w'}{\partial t} = \left(\frac{D_{H,pl} [H^+]_o}{r^2} \right) \frac{1}{x} \frac{\partial}{\partial x} \left(x \frac{\partial w'}{\partial x} \right) + \left(\frac{2.303 [H^+]_o}{\beta_{pl}} \right) (1-h(x)) w' R_{HCO3,pl} \quad (C.5)$$

$$(1-h(x)) D(1-Bb^2x^2) \left(\frac{[HCO_3^-]_o}{L} \right) \frac{\partial r'}{\partial t} = \left(\frac{D_{HCO3,pl} [HCO_3^-]_o}{r^2} \right) \frac{1}{x} \frac{\partial}{\partial x} \left(x \frac{\partial r'}{\partial x} \right) - h(x) \left(\frac{s}{v} \right)_{rbc} Flux_{HCO3} + (1-h(x)) R_{HCO3,pl} \quad (C.6)$$

$$(1-h(x)) D(1-Bb^2x^2) \left(\frac{[Cl^-]_o}{L} \right) \frac{\partial s'}{\partial t} = \left(\frac{D_{Cl,pl} [Cl^-]_o}{r^2} \right) \frac{1}{x} \frac{\partial}{\partial x} \left(x \frac{\partial s'}{\partial x} \right) + h(x) \left(\frac{s}{v} \right)_{rbc} Flux_{HCO3} \quad (C.7)$$

$$A(1-b)[2-(1-b)x']x'\left(\frac{[CO_2]_o}{L}\right)\frac{\partial v''}{\partial t} = \left[\frac{D_{CO_2,pl}[CO_2]_o}{(r_c-r_r)^2}\right]\frac{\partial^2 v''}{\partial x'^2} - \left\{\frac{D_{CO_2,pl}[CO_2]_o}{[r_c-(r_c-r_r)x']}\frac{\partial v''}{\partial x'} - R_{HCO_3,pl}'\right\} \quad (C.8)$$

$$A(1-b)[2-(1-b)x']x'\left(\frac{[H^+]_o}{L}\right)\frac{\partial w''}{\partial t} = \left[\frac{D_{H,pl}[H^+]_o}{(r_c-r_r)^2}\right]\frac{\partial^2 w''}{\partial x'^2} - \left\{\frac{D_{H,pl}[H^+]_o}{[r_c-(r_c-r_r)x']}\frac{\partial w''}{\partial x'} + \left(\frac{2.303[H^+]_o}{\beta_{pl}}\right)w''R_{HCO_3,pl}'\right\} \quad (C.9)$$

$$A(1-b)[2-(1-b)x']x'\left(\frac{[HCO_3^-]_o}{L}\right)\frac{\partial r''}{\partial t} = \left[\frac{D_{HCO_3,pl}[HCO_3^-]_o}{(r_c-r_r)^2}\right]\frac{\partial^2 r''}{\partial x'^2} - \left\{\frac{D_{HCO_3,pl}[HCO_3^-]_o}{[r_c-(r_c-r_r)x']}\frac{\partial r''}{\partial x'} + R_{HCO_3,pl}'\right\} \quad (C.10)$$

where

$$h(x) = h_m(1-x^m).$$

If modified Hill model is used, then $\frac{\partial S}{\partial u} = n\left(\frac{[O_2]_o}{C_{50}}\right)^n u^{n-1} / \left[1 + \left(\frac{[O_2]_o}{C_{50}}\right)^n u^n\right]^2$.

If modified Easton model is used, then

$$\frac{\partial S}{\partial u} = \left(\frac{\kappa[O_2]_o}{\alpha_{O_2,rbc}}\right)(S_{max} - S_{min}) \exp\left[\kappa P_{O_2}^* - \left(\frac{\kappa[O_2]_o}{\alpha_{O_2,rbc}}\right)u\right] \exp\left\{-\exp\left[\kappa P_{O_2}^* - \left(\frac{\kappa[O_2]_o}{\alpha_{O_2,rbc}}\right)u\right]\right\}.$$

$$\frac{\partial \phi}{\partial v} = \frac{2\lambda_\alpha[CO_2]_o + 4\lambda_\alpha^2[CO_2]_o^2 v}{(1 + \lambda_\alpha[CO_2]_o v)^2} + \frac{2\lambda_\beta[CO_2]_o(1 + K_{DPG}[DPG]) + 4\lambda_\beta^2[CO_2]_o^2 v}{(1 + \lambda_\beta[CO_2]_o v + K_{DPG}[DPG])^2}.$$

$$\begin{aligned}
Flux_{HCO_3} &= \frac{T_{tot} k_{trans} K_A [HCO_3^-]_o (s' r' - s' r)}{(s + s') + \left(\frac{[HCO_3^-]_o}{[Cl^-]_o} \right) (r + r') + 2 \left(K_A [Cl^-]_o s s' + \left(\frac{K_A [HCO_3^-]_o^2}{[Cl^-]_o} \right) r' r + (K_A [HCO_3^-]_o) (s' r' + s' r) \right)} \\
R_{HCO_3,pl} &= \hat{A}_{pl} \left[k_u \left(\frac{\alpha_{CO_2,pl}}{\alpha_{CO_2,rbc}} \right) [CO_2]_o v - \left(\frac{k_v}{K_1} \right) [H^+]_o [HCO_3^-]_o w' r' \right] \\
R'_{HCO_3,pl} &= \hat{A}_{pl} \left[k_u [CO_2]_o v'' - \left(\frac{k_v}{K_1} \right) [H^+]_o [HCO_3^-]_o w'' r'' \right]
\end{aligned}$$

Rewriting the above equations in terms of the dimensionless groups (a 's, d 's, u_{ext} and v_{ext} which are listed in Section 6.1.4) yields Equations (6.34) - (6.43).

For the discrete model, mixed mean concentrations of species i inside the RBC ($[C_i]_{mm,rbc}$), in the plasma ($[C_i]_{mm,pl}$) and in the whole blood ($[C_i]_{mm,wb}$) are calculated by Equations (6.73a), (6.73b) and (6.73c), respectively. By introducing the normalization quantities listed in Equation (C.11), Equations (6.73a) - (6.73c) can be rewritten in terms of the dimensionless variables.

$$C_i = \frac{[C_i]_{rbc}}{[C_i]_o}, \quad C'_i = \frac{[C_i]_{pl}}{[C_i]_o}, \quad C''_i = \frac{[C_i]_{pl}}{[C_i]_o}, \quad x = \frac{r}{r_r}, \quad x' = \frac{r_c - r}{r_c - r_r} \quad \text{and} \quad b = \frac{r_r}{r_c} \quad (C.11)$$

Normalized mixed mean concentration of species i inside the RBC

$$\frac{\langle C_i \rangle_{mm,rbc}}{[C_i]_o} = \frac{2 b^2 h_m D (1-s/p)}{H_T \langle V \rangle_{rbc}} \int_0^1 x (1 - x^m) (1 - B b^2 x^2) C_i(x) dx \quad (C.12)$$

Normalized mixed mean concentration of species i in the plasma

$$\begin{aligned} \frac{\langle C_i \rangle_{mm,pl}}{[C_i]_o} = & \frac{2 b^2 D}{(1 - H_T) \langle V \rangle_{pl}} \int_0^1 x [1 - h_m(1 - x^m)] (1 - B b^2 x^2) C_i'(x) dx \\ & + \frac{2 (1-b)^2 A}{(1 - H_T) \langle V \rangle_{pl}} \int_0^1 x' [1 - (1 - b)x'] [2 - (1 - b)x'] C_i''(x') dx' \end{aligned} \quad (C.13)$$

Normalized mixed mean concentration of species i inside the vessel

$$\begin{aligned} \frac{\langle C_i \rangle_{mm,wb}}{[C_i]_o} = & \frac{2 b^2 h_m D (1-s/p)}{\langle V \rangle} \int_0^1 x (1 - x^m) (1 - B b^2 x^2) C_i(x) dx + \frac{2 b^2 D}{\langle V \rangle} \int_0^1 x [1 - h_m(1 - x^m)] (1 - B b^2 x^2) C_i'(x) dx \\ & + \frac{2 (1-b)^2 A}{\langle V \rangle} \int_0^1 x' [1 - (1 - b)x'] [2 - (1 - b)x'] C_i''(x') dx' \end{aligned} \quad (C.14)$$